Title
Low-Dimensional Materials at the Nanoscale: Transition Metal Chalcogenides, Carbon Nanomaterials and Organic Semiconductors

Author
Onishi, Seita

Publication Date
2017

Peer reviewed|Thesis/dissertation

Low-Dimensional Materials at the Nanoscale: Transition Metal Chalcogenides, Carbon Nanomaterials and Organic Semiconductors

By

Seita Onishi

A dissertation submitted in partial satisfaction of the

requirements for the degree of

Doctor of Philosophy

in

Physics

in the

Graduate Division

of the

University of California, Berkeley

Committee in charge:
Professor Alex Zettl, Chair
Professor Michael Crommie
Professor Vivek Subramanian

Summer 2017

Low-Dimensional Materials at the Nanoscale:
Transition Metal Chalcogenides, Carbon Nanomaterials and Organic Semiconductors

by

Seita Onishi

Abstract

Low-Dimensional Materials at the Nanoscale:
Transition Metal Chalcogenides, Carbon Nanomaterials and Organic Semiconductors

by

Seita Onishi

Doctor of Philosophy in Physics

University of California, Berkeley

Professor Alex Zettl, Chair

The overall theme of this dissertation is the electronic transport and electromechanical study of low dimensional materials at the nanoscale. The dissertation is divided into three parts based on the class of materials: I. collective ground states in ultrathin materials, II. carbon nanomaterials based nanomechanical resonators and III. organic semiconductors.

In part I, the superconductivity and charge density waves in transition metal chalcogenides are introduced. Crystal synthesis of transition metal chalcogenides by chemical vapor transport is presented. The materials have quasi-low dimensional crystal structure: either quasi-two dimensional (e.g. $NbSe_2$, TaS_2, WTe_2, FeSe) or quasi-one dimensional (e.g. $NbSe_3$, TaS_3, $(NbSe_4)_3I$). Monolayer $NbSe_2$, grown by molecular beam epitaxy, shows a superconducting transition at T_c=2K and is studied down to 50mK with magnetic fields. The sliding charge density waves in $NbSe_3$ nanoribbons are studied with narrowband noise, which directly probes the order parameter. A proposal to scale down the contactless conductivity measurement technique for nanoscale samples with lithographically fabricated planar coils is presented.

In part II, microstructures of suspended carbon nanotubes and graphene are studied as nanomechanical resonators. Carbon nanotubes are clamped on one end and the other end is free to enable field emission. The field emission provides a means of electrical readout. Fabrication of carbon nanotube field emitting mechanical resonators on an integrated platform are explored. The platform is designed to allow the study of the nanomechanical motion across multiple characterization techniques. Graphene nanomechanical resonators are studied as a first step in the development of a microactuator-based platform to control strain fields in graphene. In particular, non-uniaxial strains for large pseudo-magnetic field effects are intended.

In part III, organic nanowire formation with DPP-TPA molecules for use in photovoltaics is explored. The nanowire's charge carrier mobility is characterized in a field effect transistor. In addition, the use of rubrene single crystals for the study of photophysics at the interface with novel acceptor molecules is explored.

To Mika and Morihisa Onishi,
my parents

Table of contents

List of figures

List of tables

Acknowledgements

The best part of research in the Zettl group is that I could work on a wide range of topics and freely interact with many fellow researchers. I have learned much from discussions with everyone in the group and thank them for all the pleasant interactions.

Brian Kessler, Keith Ray, Kris Erickson, Kwanpyo Kim, Allen Sussman and Benji Alemán for being supportive senior students when I started in the group. Matthias Loster, Anna Zaniewski and Maria Schriver for teaching me about solar cells. Will Regan and Will Gannett for teaching me everything I know about the SEM. Jiyoung Chang, Oscar Vazquez-Mena, Hamid-Reza Barzegar, Jairo Velasco Jr., Jongmin Yuk, Hiroya Ishida and Hu Long for wise advice on research and life. Qin Zhou for teaching me much about microfabrication and always approaching things with a unique perspective. Qin successfully predicted one of the least-expected but important question in my qual. Aiming Yan and Nasim Alem for teaching me about TEM. Jianhao Chen, Claudia Ojeda-Aristizabal and Wu Shi for teaching me about transport experiments. Anna Goldstein for sharing the appreciation for angular momentum and parabolic motion with me. Ashley Gibb for introducing me to many opportunities that the world offers. Aidin Fathalizadeh for showing me how to approach the theoretical limit of an efficient lunch. Onur Ergen for the fun times at Kirchberg. Gabe Dunn for making a snowboarder out of me in one winter. Brian Shevitski for always being honest and direct. Thang Pham for always being so open in our conversations. I working on experiments together with Thang was particularly enjoyable and stimulating. Matt Gilbert for being a good labmate and a fellow Villager. Sally Turner for being the first sign that the future of Zettl group is bright. Donez Horton-Bailey and Scott Meyer for proving it will be even brighter. Donez has patiently responded to my efforts to maintain our office's legacy as a garrulous office.

I am particularly thankful to Çağlar Girit for giving me great support when I was looking for an opportunity to work in the Zettl group.

I would like to thank Prof. Fréchet for allowing me to work as a jointly-funded student in his lab. Working in such a strongly interdisciplinary setting during an early part of my education was stimulating and taught me much. I thank David Okawa, the previous Zettl/Fréchet student, for facilitating my transition. I also thank many Fréchet group members, who have worked with me and taught me about organic chemistry. Claudia Piliego, Claire Woo, Alan Yiu and Jeremy Niskala taught me about organic semiconductor devices. Justin Mynar and Jill Millstone taught me about molecular self-assembly. Tom Holcombe, Dave Kavulak and Pierre Beaujuge taught me about organic solar cells. Mark Chen, Olivia Lee and Jessica Douglas taught me how to (try to) read chemical structures in organic chemistry.

My most interesting collaborators have been the undergraduate students: Joey Barreto, Corey Shih, Owen Chiatai Chen, Sissi Xiyue Wang, Jacob Bryon, Patrick Stetz, Kevin Nuckolls and Albert Hsiung. While training and working with them, I learned much and the process was essential for my growth as a physicist. They have worked hard and enabled projects to progress much further than I could have by myself. Being a former Berkeley undergraduate myself, working with them has made me proud to have been a Berkeley undergraduate.

The completion of a doctoral dissertation is an important step for my identity as a physicist and I would like to use this opportunity to acknowledge some outstanding teachers, who were particularly important for my journey to this point. From early in life: Sally Draper-Tough (6th

grade science teacher), Daniel Mendes and Sarfaraz Svar (high school physics teachers). When I was an undergraduate student, Ofer Naaman closely mentored me and taught me the importance to “have fun” in physics. I still think back on the advice they gave me and their lessons are still a large part of what drives me in physics.

Last but not least, I thank Prof. Alex Zettl for all the guidance he has provided me. The last eight years have been a period of important scientific, professional and personal growth for me. Alex has played a large role in all three aspects. I will always value the lessons I learned from him and hope to have a similar impact on others one day.

Introduction

The understanding of how a large ensemble of atoms results in the physical properties of materials is one of the fundamental themes of condensed matter physics. The task is well articulated in what is often called Dirac's challenge [1]:

> "The underlying physical laws necessary for the mathematical theory of a large part of physics and the whole of chemistry are thus completely known, and the difficulty is only that the exact application of these laws leads to equations much too complicated to be soluble. It therefore becomes desirable that approximate practical methods of applying quantum mechanics should be developed, which can lead to an explanation of the main features of complex atomic systems without too much computation."

Most macroscopic ("cm"-scale) objects, which are made of $>10^{23}$ number of atoms, behave according to classical physics. The wavefunctions of atoms decohere over small length scales and at first glance, it appears the quantum mechanical effects are irrelevant, when the ensemble is viewed as a whole. However, collective ground states (e.g. superconductivity, charge density waves) is evidence that the laws of quantum mechanics is not trapped to the atomic length scale. The electrons in a material collectively behave as a quantum mechanical object, which results in the manifestation of very noticeable quantum mechanical effects at the "cm"-scale. In particular, when collective grounds states enable the transport of quasi-particles (e.g. zero resistance), the quantum mechanical transportation of energy and information is interesting for applications in technology. Intrigued by collective transport phenomena, this work focuses mainly on electronic transport in crystalline solids.

Even, when restricted to crystalline solids, there is still a great variety in the possible crystal structure and combinations of elements. Their dimensionality is an attractive classification scheme for its simplicity. The behavior of collective ground states are heavily dependent on the dimensionality of the system. For example, the Aslamazov-Larkin equation (see section 1.1.1) successfully describes the effects of order parameter fluctuations in many superconductors [2]. The equation does not require any knowledge of the material's crystal structure, except its dimension. If the anisotropy of the chemical bonds confine the electrons, such that it is effectively a sheet (wire), it is considered a 2D (1D) system. Often, the theoretical model is simpler in low dimensions. The exact solution for the Ising model of ferromagnetism was found for 1D in 1925 [3] and for 2D in 1944 [4]. Low dimensional systems are not simply cross-sections of the 3D case and, for some cases, results in fundamentally different behavior. Electrons in 1D systems are expected to behave as a Luttinger liquid [5] rather than a Fermi gas in conventional metals. Theoretically, a metallic state of fermions should not exist in 2D but experimental observations of metallic states suggest the emergence of fundamentally different conduction mechanisms [6]. Hence, low dimensional systems have the potential to yield new electronic phases that do not occur in 3D materials. In particular, the driving mechanism of CDW (i.e. Peierls instability) is the strongest in 1D. It is also intriguing that the high T_c superconductivity occurs in cuprates, which have quasi-2D crystal structure.

Theoretically, 1D systems are modeled as a chain of atoms (see Fig. 1-9). The experimental realization of a well-ordered chain of atoms, which are electronically decoupled from a substrate,

is highly challenging. Similarly, 2D systems are often modeled as sheets of atoms. Historically, three materials classes have emerged as promising systems for experimental studies: transition metal chalcogenides, carbon nanomaterials and solids organic molecules. In this section, the material classes are introduced in order of historical occurrence with the context of realizing a low dimensional system. This work studies each of the three materials classes through synthesis, device fabrication and electronic transport/electromechanical measurements to understand their strengths and weaknesses for the study of 2D and 1D systems. The low dimensional effects in some of the materials were studied predominantly before the availability of nanoscale characterization. Hence, the focus of this work will be on studying the materials from a nanoscale perspective.

The diversity of carbon bonds (i.e. sp^3, sp^2 and sp^1) [7] anticipates the creation of materials with much more complex structures than commonly found in binary and ternary compounds of other elements. The vast knowledge in organic chemistry enables molecular structures to be altered in steps to tune the electronic interactions. In 1964, Little [8] theoretically proposed that a polymer with the right interaction between the side-chain and the backbone, could realize superconductivity with T_c well above room-temperature. Organic charge transfer salts (e.g. TTF-TCNQ) [9] were one of the first materials to experimentally realize the CDW state, which was a theoretical conjecture [10]. Two types of molecules, a donor and an acceptor, assemble into a crystal by charge transfer. The delicate sharing of charge between the acceptor and donor molecules results in the formation of a 1D conduction channel. Numerous members of this materials class enabled the experimental study of a rich spectrum of CDW and superconducting behavior.

Blue bronzes (i.e. $K_{0.3}MoO_3$ and $Rb_{0.3}MoO_3$) followed the organic charge transfer salts as their inorganic analogs. Charge transfer with the MoO_3 clusters create an atomic chain of alkali metal ions [10]. The drawback of the charge transfer salts is that charge transfer is crucial for both electronic confinement and structural support. Hence, any attempt to isolate the 1D conduction channel from the material would completely destroy it. In contrast, the atomic chains in transition metal trichalcogenides (e.g. $NbSe_3$, TaS_3) are weakly bound to the rest of the chains. Within each chain, the charge balance is satisfied and the inter-chain attraction is through weak van der Waals forces. These materials are quasi-1D, since they are technically an ensemble of chains and inter-chain interactions complicate the study of the single chain properties. Experimental techniques to isolate, identify and contact atomic chains need to be developed. A similar technical development was demanded for conducting polymers [11]. When measuring the conductivity of a collection of atomic chains, the measurement is complicated by the contributions of inter-chain hopping and the role of interaction with the chains running in parallel [12,13].

An indirect way of extracting the role of inter-chain interactions is by reducing the sample size and studying the size dependence. At the nanoscale, the sample size becomes comparable to or below the critical length scales of some electronic states (e.g. correlation length for CDW). This approach is explored for $NbSe_3$ in section 6.1. In addition, electron beam lithography can create contacts with nanoscale separation (typically ~100nm). Techniques to reach below this length scale is highly specialized and under development [14]. There could be 1D materials, which are too short to contact without nanofabrication but long enough to bridge across the nanofabricated contacts. Hence, advances in nanofabrication prompts for the search of 1D systems to be revisited at the nanoscale.

The discovery of carbon nanotubes enabled the study of materials at the true 1D limit. A single walled carbon nanotube can have diameters as small as 0.4nm [15]. The entire tube is a single molecule in that the carbon atoms are covalently bonded and electrons are delocalized across the whole tube. The large aspect ratio yields tubes long enough to bridge across lithographically fabricated contacts. The electronic transport in single walled carbon nanotubes show signatures of a Luttinger liquid, a uniquely 1D phenomenon [16]. Depending on the chirality of the tubes, single walled carbon nanotubes are semiconducting or metallic [15], which enables the study of materials with a variety of band structures at the true 1D limit. In addition, the semiconducting tubes are susceptible to the modulation of carrier concentration by electrostatic gating.

The early studies of 2D systems were in thin films [17,18] and charges confined to heterostructure interfaces [19,20]. Similar to quasi-1D materials, these systems were bound to the substrate and could not be isolated. Transition metal dichalcogenides are layered materials, in which the inter-layer forces are weak. Many of the materials [21] (e.g. $NbSe_2$, TaS_2) support collective ground states with low dimensional effects (e.g. CDW and superconductivity with anisotropic properties). Most of the studies were in the quasi-2D regime, in which a stack of many layers were used. In principle, a single layer could have been extracted from the material without destroying it but a monolayer was not isolated [22].

In 2004, graphene was isolated from the layered material, graphite [23]. Graphene is the truly 2D limit of graphite since it is a one atom thick sheet of covalently bonded carbon atoms. Graphene exhibits quantum Hall effects similar to the heterostructure based systems [24]. The massless Dirac fermions emerging from graphene's special band structure actually allow quantum Hall effect to be observed at room temperature, making the phenomenon more accessible. To clarify, the massless Dirac fermions are not a consequence of low dimensionality and could arise in a 3D system, as well [25]. In this sense, graphene is special for its band structure and not a representative 2D metal. Mechanical exfoliation (Scotch tape method [26]) and the study of layered materials at the ultrathin limit is found in older literature (e.g. ultrathin $NbSe_2$ study in 1972 [22]) but a single atomic layer was not successfully isolated until graphene. The isolation of graphene is attributed to the combination of: 1) the Scotch tape method, 2) an ingenious way to identify thin films by optical interference [27] and 3) advances in micro/nanofabrication.

Carbon nanomaterials (i.e. carbon nanotubes, graphene) are at the forefront in the effort to realize truly low dimensional materials. Their low dimensional behaviors are already confirmed by electronic transport. The natural next step in complication would be the study of other physical properties (e.g. optical [28,29] and thermal [30]). In particular, the combination of electrical conductivity and high Young's modulus makes them interesting for electromechanical studies. Nanomechanical resonators of carbon nanomaterials have been demonstrated as sensitive probes for its mechanical properties [31–33]. For quasi-1D materials, the study of the Young's modulus in TaS_3 and $NbSe_3$ [34] demonstrated that the CDW significantly impacts the mechanical properties. At the nanoscale, the CDW transition was detected in nanomechanical resonators of $NbSe_2$ [35]. While carbon nanomaterials do not undergo CDW transitions, the electromechanical measurements could be an effective probe for their electronic states. The readout of a single electron spin with carbon nanotube nanomechanical resonators have been theoretically proposed [36]. The extreme mechanical strength of graphene allows it to be manipulated with large strains [37,38]. Through strain, the lattice parameter can be continuously tuned and, depending on the strain directions, even the lattice symmetry can be manipulated. While graphene is a 2D honeycomb lattice of carbon atoms, its manipulation with strain could

yield a whole spectrum of materials, which span different lattice constants and symmetries. To explore these prospects, this work studies the electromechanical properties of carbon nanotubes and graphene in Part II.

Recently, monolayers of other layered materials have been isolated with mechanical exfoliation and 2D materials "beyond graphene" [39–41] has become a popular topic. The popularity is partly driven by the need for materials with band gaps to further scale down the semiconductor based electronic devices. For these purposes, semiconductors (e.g. MoS_2 [42] and black phosphorous [43]) are interesting. From a low dimensionality perspective, metallic transition metal dichalcogenides (e.g. $NbSe_2$, TaS_2) are even more interesting. Neither graphite nor graphene do not possess collective ground states. Superconductivity was "induced" in them by proximity effects [44,45]. In contrast, the transition metal chalcogenides are rich with CDW and superconductivity phases in the bulk. The effect of approaching the monolayer limit in a layer-by-layer manner would provide great insight into the effect of dimensionality on the collective ground states. Many studies on the CDW at the monolayer limit have recently emerged [46–49]. For the study of CDW, the quasi-1D transition metal chalcogenides are distinct, as many of them support sliding CDW. A desirable extension of the CDW study at the monolayer limit is to study the CDW at the single chain limit of quasi-1D materials. If a sliding CDW persists to the single chain limit, both static and dynamic CDW properties could be studied. With the recently reported isolation of single chain TiS_3 [50], similar interests in the field appear to be emerging. The study of collective ground states towards the atomic 2D and 1D limit of transition metal chalcogenides are discussed in Part I.

Parallel to the developments in inorganic low dimensional materials, interest in organic semiconductors have recently emerged. The interest is driven by applications in flexible electronics and photovoltaics. Unlike the charge transfer salts, the molecules are not designed to be metals but semiconductors. The inter-molecular hopping of charge carriers are enhanced by increasing the π orbital overlap between molecules. To implement this strategy, there have been extensive studies to control the self-assembly of molecules to optimize the charge transport mechanism [51]. By tuning the steric interaction of the molecules with the selection of functional groups, the self-assembly can yield 1D nanostructures [52]. As the band gaps [53] and dielectric constants [54] of organic solids can be modified by slightly changing the functional groups, there is a potential to create a wide spectrum of 1D nanostructure of various electronic properties. A spectrum of materials would provide insight into the structure-property relationships, as the organic charge transfer salts have. It is of interest whether the enhancement of charge transport through π orbital overlap is enough to support delocalized transport across molecules. Attempts to create such a system is discussed in Part III.

Part I

Collective ground states in ultrathin chalcogenides

1 Collective ground states in solids

Electrical currents in a solid are carried by charge carriers that behave similarly to free charged particles in vacuum but are actually quasiparticles. Quasiparticles exist within a crystalline lattice and their free particle-like behavior is an emergent phenomenon [55] from the crystal structure. Unlike a free particle in a vacuum, there are bandgaps in a material, in which certain range of energy and momenta are forbidden for quasiparticles [56]. Although solids are composed of electrons, protons and neutrons, some materials yield exotic quasiparticles (e.g. fractional charge [19,20], massless Dirac fermions [57] and Weyl fermions [58,59]). It is interesting that emergent behavior allows the study of exotic particles at energy scales far below that of high energy particle physics experiments.

A collective ground state forms, when bosonic quasiparticles (e.g. Cooper pairs [60]) emerge and condense to the ground state. Collective transport phenomena occur when the collective ground state is driven by an electric field and results in charge conduction. Compared to electrical conduction by electrons and holes, collective transport yields fundamentally different behavior, such as zero resistance and an interesting coupling of dc and ac response.

The physical characteristics of the two examples of collective ground states: superconductivity and charge density waves (CDW) are introduced in this chapter. While collective transport in superconductors are well known, sliding CDW [10] is introduced as another example of collective transport. This chapter provides background for the subsequent chapters in Part I.

1.1 Superconductivity

Superconductivity is characterized by zero electrical resistance and perfect diamagnetism (Meissner effect). Below the critical temperature (T_c), the electrons in a metal form pairs ("Cooper pairs"), which condense to a superfluid. In the first class of superconductors that were discovered, the mechanism for Cooper pair formation was the attraction between a pair of charge carriers mediated by phonons. This class of phonon-mediated superconductivity is well understood by BCS theory [61] and is called "conventional superconductivity".

There are superconductors, which cannot be explained by phonon-mediated pairing called "unconventional superconductors" [62]. Among unconventional superconductors, there are various classes of exotic superconductivity (e.g. cuprate, iron-based, heavy fermion and organic) and a single pairing mechanism does not necessarily apply to all of them. Fig. 1-1 shows a representative sample of superconductors. The superconductors are presented as a timeline as there have been extensive efforts to raise the T_c up to room temperature. The figure shows both conventional superconductors (circles) and unconventional superconductors (diamonds, stars and squares). The fullerene superconductors[1] (triangles pointing down) and strongly covalent material based superconductors[2] (triangles pointing up) cannot be definitively determined as conventional or unconventional at this point. The figure is not an exhaustive list[3] of superconductors but illustrates some of the significant developments in the history of superconductivity research. In particular, many more conventional superconductors than those shown in Fig. 1-1 were discovered in the early years of superconductivity.

[1] It is debated whether fullerene superconductors are unconventional, as the evolution of T_c with lattice parameter is consistent with phonon-mediated pairing but the normal state has a phase diagram similar to cuprates [280].
[2] The applicability of phonon-mediated pairing is ambiguous [281] and there are suggestive data for unconventional superconductivity [282].
[3] References to literature on many superconductors are compiled on the Superconducting Materials Database [283] and can be accessed free of charge.

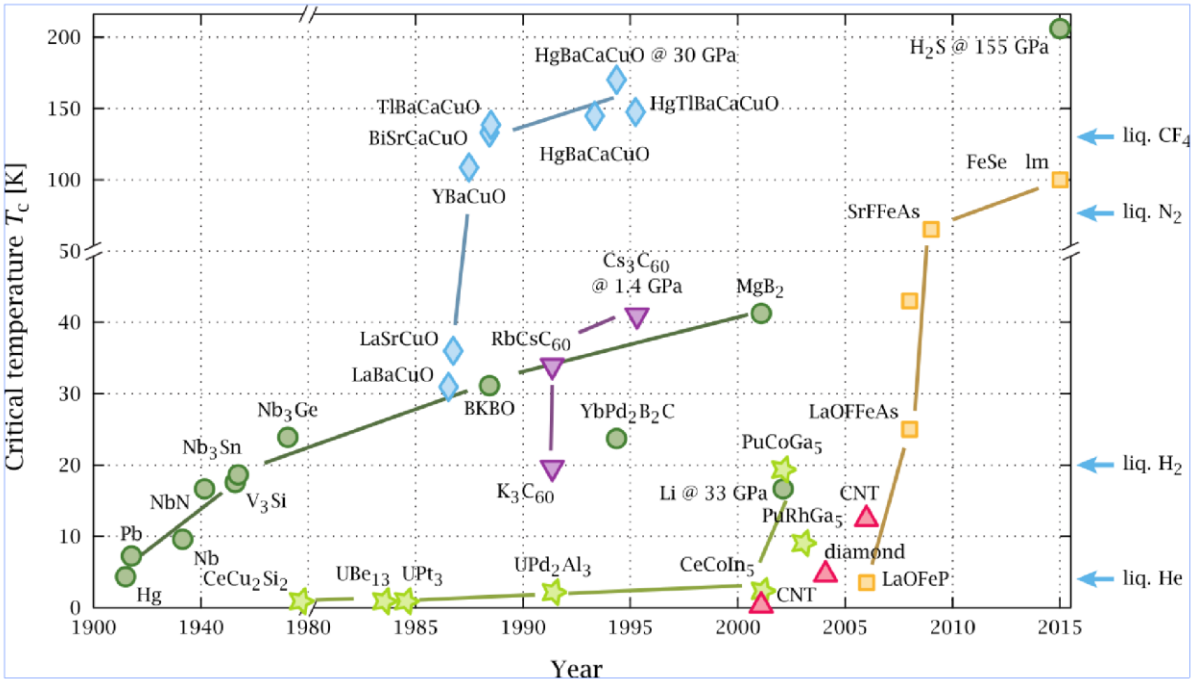

Fig. 1-1 Timeline of superconductivity.
Fig. 2.4, Jensen Ray Master's thesis [286]. The left, vertical axis corresponds to the critical temperature (T_c). The bottom, horizontal axis corresponds to the year of discovery. The right vertical axis is marked with the boiling point of cryogens. Conventional superconductors (circles), cuprates (diamonds), heavy fermion superconductors (diamonds), fullerene superconductors (triangles pointing down), strongly covalent materials based superconductors (triangles pointing up) and iron-based superconductors (squares) are shown.

1.1.1 Superconducting transition

When a material undergoes a phase transition to a superconductors, its resistance drops to zero at $T<T_c$. Experiments on currents circulating in a superconductor indicate that the decay time is >100,000 years [63], implying that superconductors possess practically perfect conductivity.

Fig. 1-2 schematically shows R(T) of a material when it undergoes a superconducting transition. Typically, the resistivity in metals settle to a temperature independent constant value ("residual resistivity") at low T due to impurity scattering. For a superconductor, the resistance drops lower than the normal state resistance (R_n) and T_{onset} is the highest temperature at which this occurs, marking the onset of superconductivity. The transition width is the range of temperature from T_{onset} to T_{zero}, where the resistance reaches zero. The R(T) curve has an inflexion point at the middle of the transition, which defines T_c. Below T_c, the resistance gradually flattens to zero resistance. The finite resistance that persists for $T_{zero}<T<T_c$ is caused by phase slip events [2]. The resistance drop at $T_c<T<T_{onset}$ is driven by fluctuations of the superconducting order parameter [2]. In this temperature range, the whole sample is not yet superconducting but the dynamics of fluctuating superconducting domains result in excess conductivity. The temperature dependence of the fluctuation enhanced conductivity (ΔS_{SC}) depends on the dimensionality of the system, according to the Aslamazov-Larkin formula [64]

$$\Delta S_{SC} = \bar{t}^{-(4-D)/2} \qquad \text{Eq. 1-1}$$

where $\bar{t} = (T - T_c)/T_c$, the reduced temperature and D is the dimensionality of the system (i.e. D=1,2,3). The fluctuation enhanced conductivity is found from R(T) by

$$\Delta S_{SC} = \frac{1}{R} - \frac{1}{R_n} \qquad \text{Eq. 1-2}$$

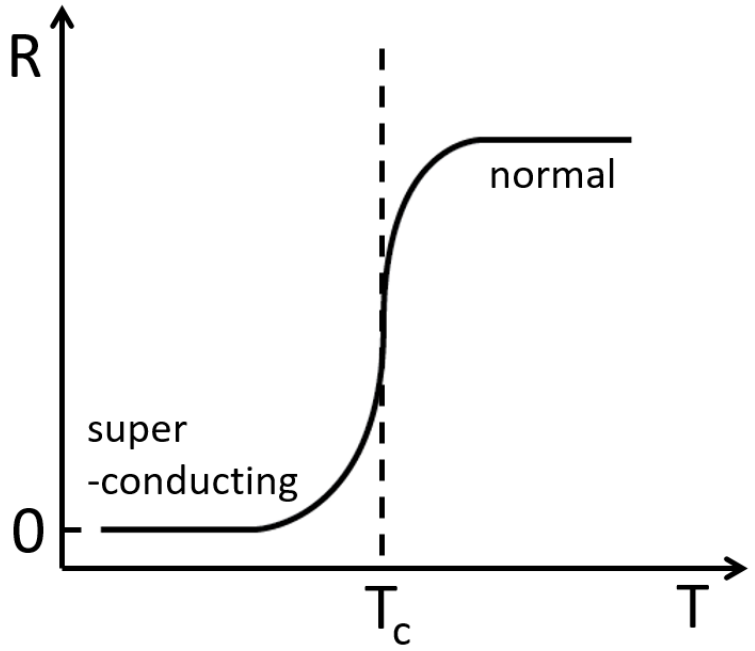

Fig. 1-2 Resistive superconducting transition.
R(T) of a system transitioning from the finite resistance (normal) state to the zero resistance (superconducting) state as it is cooled below T_c. T_c is defined as the inflection point in the middle of the transition.

1.1.2 Magnetic properties of a superconductor

When cooled to the superconducting state, the magnetic susceptibility of the superconductor drops to $-1/4\pi$ [63]. The Meissner effect should be distinguished from shielding, as it is often confused. According to Lenz's law [65], all conductors responds to a change in magnetic flux with current flow, which sets up a magnetic field to counteract the change in flux. In the case of a normal metal, the current decays after the magnetic field reaches steady state. For a superconductor, the current continues to circulate without dissipation and *shield* the flux, even in the steady state. In contrast, the Meissner effect is caused by perfect diamagnetism *without* a time dependent magnetic field. Shielding and Meissner effect is distinguished by controlling when the magnetic field is turned on. Suppose a metal is cooled from the normal state ($T>T_c$) to the superconducting state ($T<T_c$). If the magnetic field is turned on *after* entering the superconducting state, the field is cancelled by shielding. If the magnetic field is turned on *before* entering the superconducting state, the superconductor does not see the change in flux because the field is already in the steady state before the transition. Instead, the flux is spontaneously expelled from the material during the superconducting transition. This effect

cannot be explained by shielding and is called Meissner effect. The Meissner effect fundamentally distinguishes superconductivity from other zero resistance phenomena (e.g. ballistic transport).

Superconductors fail to completely expel magnetic flux if the external magnetic field (B_{ext}) is greater than a material dependent value called the critical field (B_c). The penetration of flux occurs in two different ways, depending on whether the superconductor is type I or type II. In type I superconductors, the superconducting state is completely destroyed when $B_{ext}>B_c$ and the material becomes a normal metal, despite $T<T_c$. In type II superconductors, the superconductivity is suppressed by a magnetic field in two stages. Above the lower critical field (B_{c1}), the material still exhibits zero resistance but flux lines penetrate the superconductor as vortices. As B_{ext} is further increased, the density of vortices increase. At the upper critical field (B_{c2}), the vortices connect and the superconducting state is completely destroyed.

Fig. 1-3 summarized the difference between type I and II. In both type I (Fig. 1-3a) and II (Fig. 1-3b) the magnetization (M) decreases to a more negative value in response to increasing B_{ext} for $B_{ext}<B_c$ and $B_{ext}<B_{c1}$, respectively. M(B) is consistent with the diamagnetic response of a superconductor. For $B_{ext}>B_c$ in type I, M=0 immediately, indicating the complete penetration of flux. For $B_{ext}>B_c$ in type II, M approaches 0 slowly until it hits zero at $B_{ext}=B_{c2}$. There is actually a third critical field B_{c3} related to surface properties [66] but type II superconductors are primarily characterized by B_{c1} and B_{c2}. For the development of electromagnets or power transmission lines, B_{c2} is an important figure of merit, as it determines the highest achievable fields or currents [67].

There is a theoretical limit on the B_c, called the "Pauli paramagnetic" or "Chandrasekhar-Clogston" limit [68,69]

$$B_P = 1.84T_c \qquad \text{Eq. 1-3}$$

In Cooper pairs with singlet pairing, the particles in the pair have opposite spins. When a magnetic field is applied, one particle can align its spin to the field but its partner would have to anti-align its spin. For $B_{ext}>B_P$, B_{ext} overcomes the Zeeman splitting energy and flips the sign of the anti-aligned spin. Altering the spin symmetry breaks the Cooper pair and the superconductivity is no longer sustained.

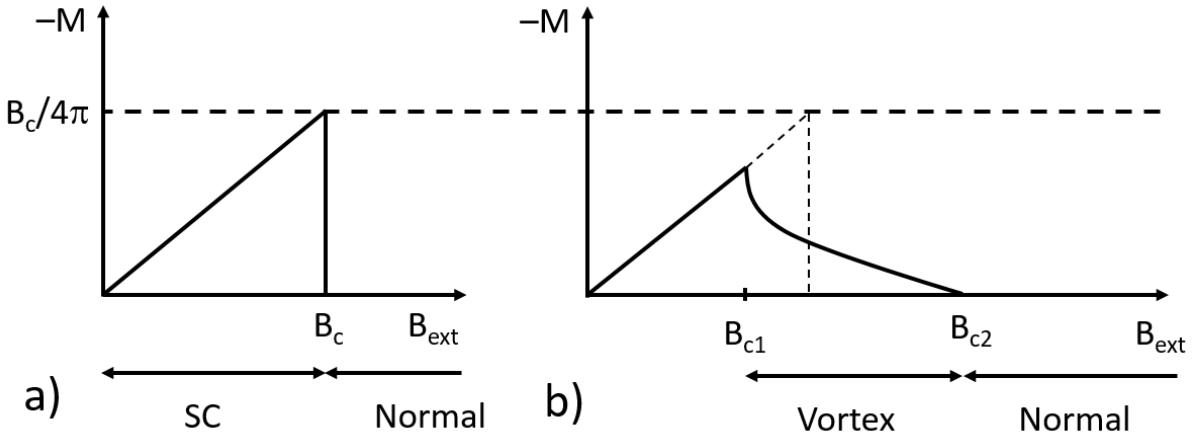

Fig. 1-3 Critical fields of superconductors.
Figure based on Fig. 4, Ch. 10, Kittel [287]. Magnetization (M) dependence on external magnetic field (B_{ext}) of a) type I superconductor and b) type II superconductor.

1.1.3 Conventional superconductors

More than 27 elements in the periodic table are known to be superconductors and the list grows when elements, which become superconductors under high pressure [70] are included. As presented in the 1963 review by Matthias *et al*. [71], there are many compounds and alloys, which are conventional superconductors. In the review, many compounds, superconductors and non-superconductors, are sorted by their crystal structure and compared to form the basis of an empirical search rule for superconductors ("Matthias' rule" [72]).

Currently, the record for the highest T_c is held by H_2S under pressure[4] with T_c=203K [73]. Prior to the discovery, cuprates held the record for ~20 years (see Fig. 1-1). In the past, it was believed that there was a theoretical upper bound to the T_c in conventional superconductors based on the McMillan equation. As shown in Fig. 1-4, the McMillan equation (dotted line) saturates as the electron-phonon coupling (λ) increases. However, according to Moussa and Cohen [74], the McMillan formula is valid for $\lambda \leq 1$. The line, dashed line and dashed/dotted line are the results of using the correct Eliashberg T_c formula for large λ with each corresponding to different assumptions for the phonon spectrum. The three lines both indicate that the upper bound for T_c continues to increase with the increase of λ. Hence, BCS superconductors with high T_c are theoretically possible.

[4] H_3S, which emerges from H_2S at high pressure, has been found to be responsible for the high T_c from X-ray diffraction experiments [284].

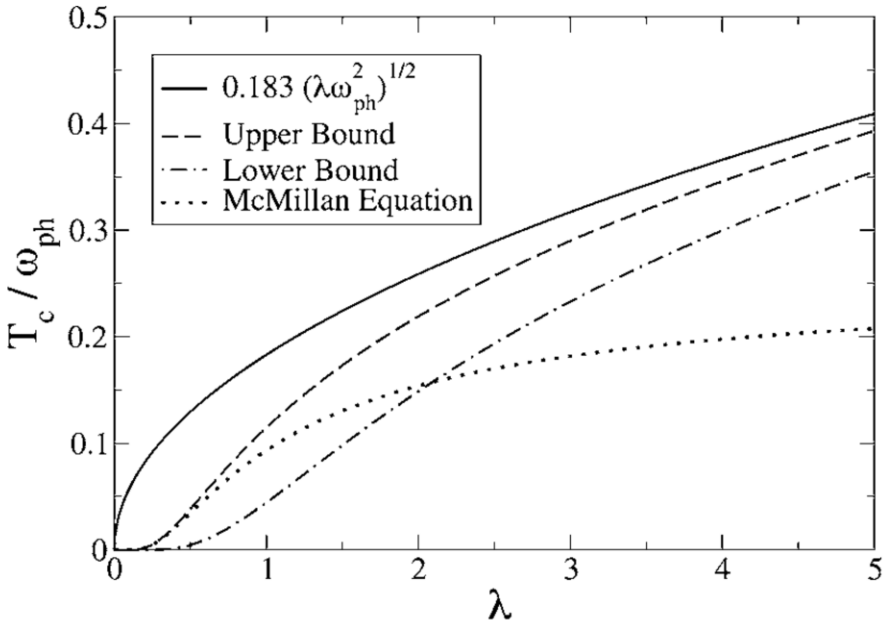

Fig. 1-4 Theoretical bound of T_c at high λ.
Fig. 1, Moussa and Cohen [74]. The vertical axis is the critical temperature (T_c) divided by the phonon frequency (ω_{ph}). The horizontal axis is the electron-phonon coupling (λ). The dotted line is the McMillan formula. The line is the upper bound for the T_c from the Eliashberg equation corresponding to infinite phonon hardening. The dashed (dashed/dotted) line is the upper (lower) bound corresponding to more extensive theoretical considerations.

1.1.4 Unconventional superconductors

As shown in Fig. 1-1, the landscape of superconductors is rich with unconventional superconductors. The cuprates (diamond markers) have had a particularly strong impact on the field of superconductivity. The record T_c was rapidly increased to 93K by YBCO in 1987 [75]. At that time, the record T_c for conventional superconductors had remained at 23K in Nb_3Ge for 14 years. Since then, many cuprates with high T_c have been discovered and unconventional pairing mechanisms became a popular route towards high temperature superconductivity. However, the mechanism of Cooper pair formation in cuprates is still under debate [62]. As shown in Fig. 1-5, the physical picture of cuprates is complicated further by the rich phase diagram that contains exotic phases.

More recently, iron-based superconductors were discovered. The discovery was unexpected as magnetism was believed to be detrimental to superconductivity [76]. Matthias' rule advised to avoid magnetism [72] and many compounds containing iron exhibit magnetic phases. Currently, the highest T_c in iron-based superconductors has not exceeded the record T_c in cuprates. However, the comparison of iron-based superconductors with cuprates could refine the theoretical understanding of unconventional superconductivity. One interesting difference is that in the iron-based superconductor phase diagram, as shown in Fig. 1-6, the superconducting phase is directly next to the antiferromagnetic phase.

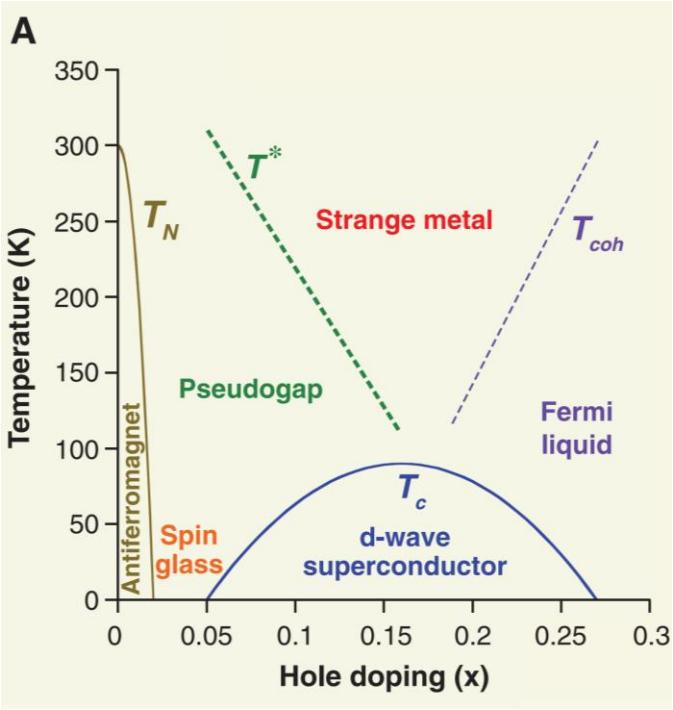

Fig. 1-5 Schematic phase diagram of cuprates.
Fig. 3A, Norman [62].

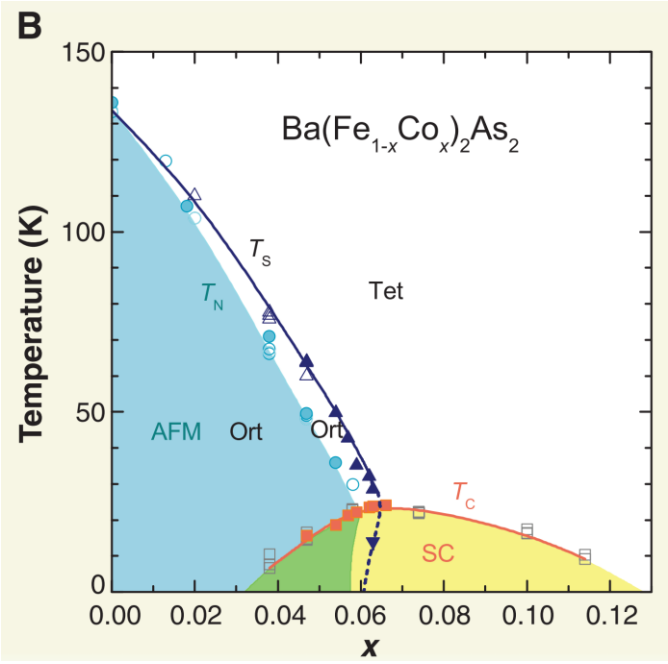

Fig. 1-6 Phase diagram of the iron-based superconductor $Ba(Fe_{1-x}Co_x)_2As_2$.
Fig. 4B, Norman [62].

1.1.5 Two-dimensional superconductivity

Fig. 1-7 shows the change in R(T) of a bismuth film as the film thickness is changed [17]. For the thinnest film, the sheet resistance is highest and R(T) shows thermally activated behavior of an insulator. For thinner films, the sheet resistance is lower. Below $R=h/4e^2=6.45k\Omega$, R(T) switches to superconducting behavior, marked by sharp drops to zero. Interestingly, there is no metallic state between the insulating and superconducting states. A metallic state would result in R(T), which extrapolates to R(T=0)=0 or saturate to a finite value as $T\rightarrow 0$ but such states cannot be found in Fig. 1-7. The "superconductor-insulator transition" (SIT) [17] has been seen in many two-dimensional systems.

Magnetic fields also drive the SIT by quenching the superconducting state in 2D superconductors [18]. Fig. 1-9 shows the R(T) switches from a superconducting to thermally activated behavior, as the magnetic field is increased. Interpretation is complicated by the existence of parallel channels of "fermionic excitations" [18] but SIT behavior in this system was supported through analysis of how R scales with B and T.

It was expected that the electrons in 2D systems either localize to yield insulators or condense to a superconducting state and a metallic state should not exist. However, there have been experimental observations of intervening metallic states in SIT, which has been challenging theoretical understanding [6]. Recently, with the possibility of isolating ultrathin layers of superconductors from layered materials, the study of two-dimensional superconductivity has experienced a re-emergence of interest [77].

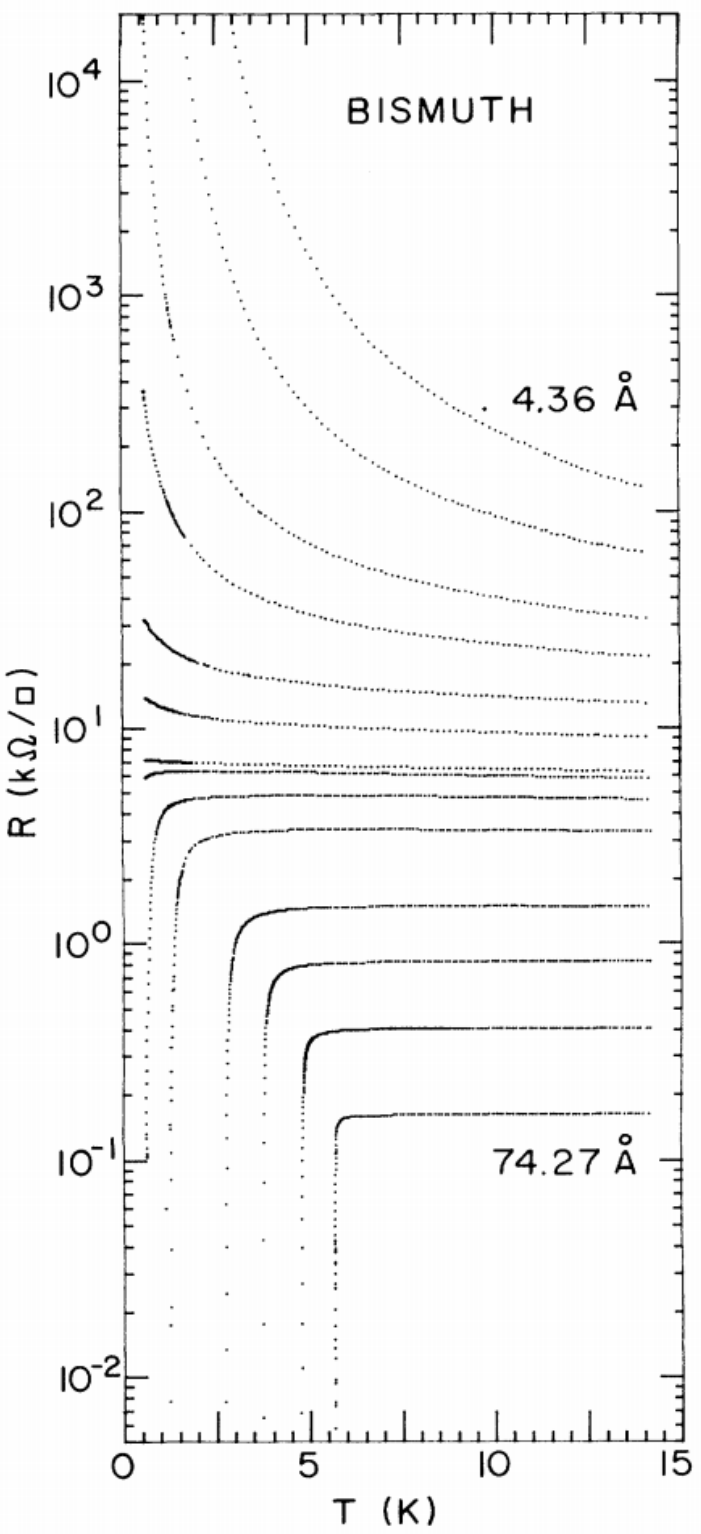

Fig. 1-7 Disorder driven SIT.
Fig. 1, Haviland, Liu and Goldman [17]. SIT tuned by sheet resistance. From the top to bottom curve, bismuth film thickness varies from 4.36Å to 74.27Å.

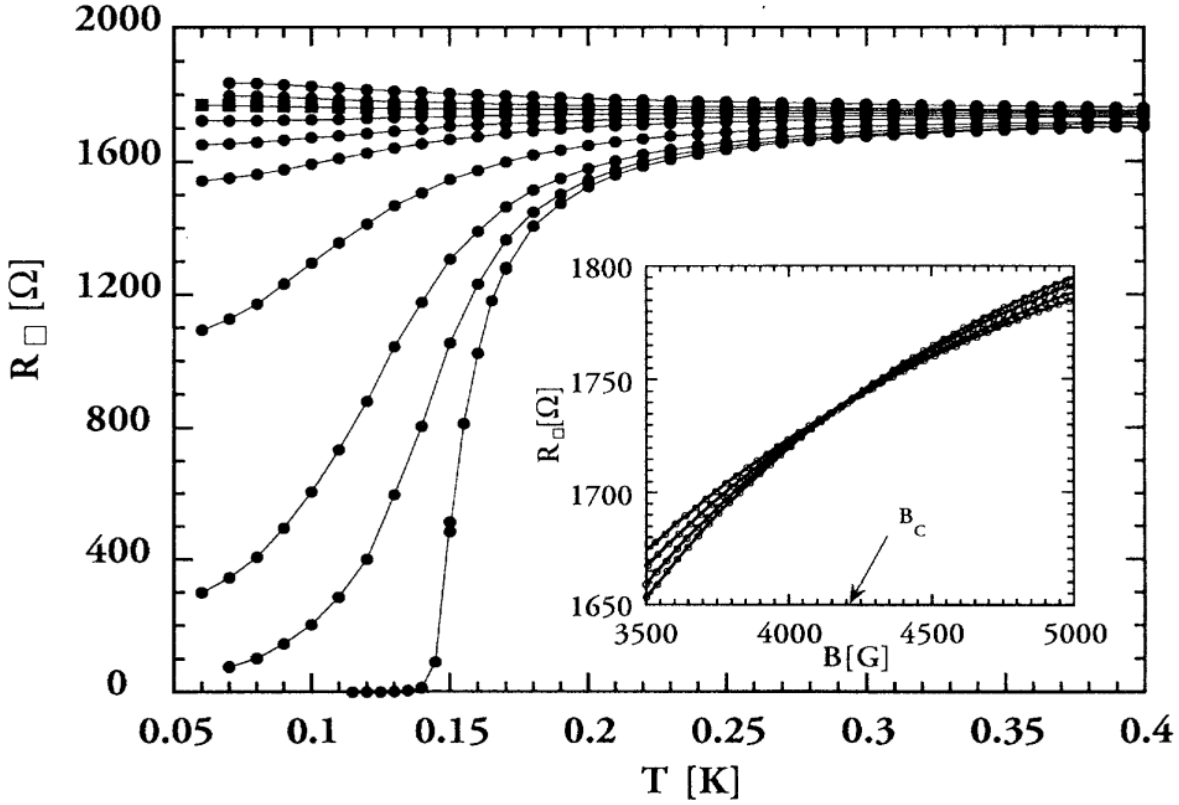

Fig. 1-8 Magnetic field driven SIT.
Fig. 1, Yazdani and Kapitulnik [18]. SIT tuned by magnetic field in MoGe film. In the main panel, from the top to bottom curve, magnetic field varies from 0.6T, 0.55T, 0.45T, 0.44T, 0.40T, 0.30T, 0.20T, 0.10T, 0.05T and 0T.

1.2 Charge density wave (CDW)

When a material is cooled below the transition temperature (T_P) to the CDW state, the charge density spontaneously distorts to produce a periodic lattice with a new periodicity, which appears as a peak in a diffraction pattern. The emergence of a CDW superlattice in real space has been confirmed by scanning tunneling microscopy [78]. In a material with atomic lattice spacing *a*, the CDW wavelength λ could be either commensurate (λ/*a* is a simple rational fraction) or incommensurate (λ/*a* is *not* a simple rational fraction) [10]. For example, the CDW in 1T-TaS_2 is incommensurate at high temperature and commensurate at low temperature [79].

The CDW transition is driven by instabilities in the electron-phonon coupling, which occur for low dimensional systems. CDW occur in quasi-1D (e.g. $NbSe_3$ [80]) and quasi-2D (e.g. $NbSe_2$ [81]) materials where anisotropies in bonding configuration causes a quasi-low D electronic structure. Compared to superconductors, many CDW materials are more robust against thermal fluctuations. For example, the NbS_3 has a CDW transition at around 620-650K [82].

The emergence of a new periodicity by the CDW opens a bandgap at the Fermi level. The CDW transition is a metal-insulator transition, where the system is a metal for $T>T_P$ and insulator for $T<T_P$. However, a real material might not be a pure insulator, even at $T<T_P$, due to ungapped portions of the Fermi surface. The CDW is normally pinned relative to the atomic lattice of the material. However, in some materials, the CDW can be made to slide with an electric field above a certain threshold field (E_T). The sliding CDW results in excess conductivity, which adds to the ohmic response of the material, and the makes the I(V) curve nonlinear. The sliding CDW is found mostly in quasi-1D materials and rarely occurs in quasi-2D materials (see Table 2-1).

1.2.1 Low dimensional effects

Suppose there is a one dimensional chain of atoms, which are spaced evenly at a distance of *a* from each other. Fig. 1-9a shows a 1D metal, where the charge distribution is uniform along the chain. At low-D, this configuration is actually unstable against a spatially periodic perturbation with wave vector $q=2k_F$. Fig. 1-9b shows the electrons spontaneously bunch up with their nearest neighbors and form a chain of spacing 2*a*. This distortion of the lattice is called "Peierls distortion". The charge distribution is no longer uniform and fluctuate periodically along the chain as a "charge density wave" (CDW). The new 2*a* periodicity of the distorted lattice results in a bandgap formation at the Fermi surface and the system becomes an insulator.

The instability against $q=2k_F$ perturbations can be justified by the dimensional dependence of the Lindhard response function F(q) [78]. To illustrate the dimensional dependence, the derivation by Mihaila [83] is partially reproduced below. The potential $\Phi^{ext}(\boldsymbol{r},\omega)$ due to an external field on a collection of charges induces a field, which gives rise to a potential $\Phi^{ind}(\boldsymbol{r},\omega)$. The total potential of the system is

$$\Phi^{tot}(\boldsymbol{r},\omega) = \Phi^{ext}(\boldsymbol{r},\omega) + \Phi^{ind}(\boldsymbol{r},\omega) \qquad \text{Eq. 1-4}$$

The total, external and induced charge distribution also follow a similar relationship.

$$\rho^{tot}(\boldsymbol{r},\omega) = \rho^{ext}(\boldsymbol{r},\omega) + \rho^{ind}(\boldsymbol{r},\omega) \qquad \text{Eq. 1-5}$$

The potential and the charge distribution are related by the Poisson equation.

$$-\nabla^2\Phi^{tot,ext\ or\ ind}(\boldsymbol{r},\omega) = 4\pi\rho^{tot,ext\ or\ ind}(\boldsymbol{r},\omega) \quad \text{Eq. 1-6}$$

From a linear response approximation

$$\rho^{ind}(\boldsymbol{r},\omega) = e^2\int d^{\mathrm{D}}r'\chi(\boldsymbol{r},\boldsymbol{r}',\omega)\Phi^{tot}(\boldsymbol{r}',\omega) \quad \text{Eq. 1-7}$$

For a fermion gas at the static response limit, the response function $\chi(\boldsymbol{r},\boldsymbol{r}',\omega)$ in momentum space is called the Lindhard response function $F(\mathrm{q}) = -\chi(\mathrm{q},\omega=0)$,

$$F(\mathrm{q}) = 2\int_{\mathrm{k}\le\mathrm{k_F}}\frac{d^{\mathrm{D}}\mathrm{k}}{(2\pi)^{\mathrm{D}}}\frac{f_{\mathbf{k+q}}-f_{\mathbf{k}}}{\epsilon_{\mathbf{k+q}}-\epsilon_{\mathbf{k}}} \quad \text{Eq. 1-8}$$

where f is the Fermi-Dirac function and ϵ is the energy. For dimensions D=1, 2 and 3,

$$F_{\mathrm{D}=1}(\mathrm{q}) = \frac{2\mathrm{k_F}}{\pi\epsilon_{\mathrm{F}}}\frac{1}{2\mathrm{q}}\log\left|\frac{1+\frac{1}{2}\mathrm{q}}{1-\frac{1}{2}\mathrm{q}}\right| \quad \text{Eq. 1-9}$$

$$F_{\mathrm{D}=2}(\mathrm{q}) = \begin{cases}\dfrac{\mathrm{k_F^2}}{2\pi\epsilon_{\mathrm{F}}} & \text{for } \mathrm{q}<2\\ \dfrac{\mathrm{k_F^2}}{2\pi\epsilon_{\mathrm{F}}}\left(1-\sqrt{1-\left(\dfrac{2}{\mathrm{q}}\right)^2}\right) & \text{for } \mathrm{q}>2\end{cases} \quad \text{Eq. 1-10}$$

$$F_{\mathrm{D}=3}(\mathrm{q}) = \frac{\mathrm{k_F^3}}{3\pi^2\epsilon_{\mathrm{F}}}\frac{3}{4}\left[1+\frac{1-\left(\frac{1}{2}\mathrm{q}\right)^2}{\mathrm{q}}\log\left|\frac{1+\frac{1}{2}\mathrm{q}}{1-\frac{1}{2}\mathrm{q}}\right|\right] \quad \text{Eq. 1-11}$$

Fig. 1-10 shows F(q) for D=1, 2 and 3. Each curve is normalized by F(0) for comparison. At q = $2\mathrm{k_F}$, the function becomes more mathematically well-behaved as D increases: there is a divergence for D=1, a discontinuity for D=2 and a continuous function at D=3. Hence, a 1D system is most unstable to perturbations of periodicity q=$2\mathrm{k_F}$.

Materials with quasi-2D structure have been experimentally discovered but cannot be completely explained by the Peierls distortion, since Eq. 1-10 does not diverge. The general form of the Lindhard response function (Eq. 1-8), suggests a divergence at $\epsilon_{\mathrm{k+q}} = \epsilon_{\mathrm{k}}$. This occurs when parts of the Fermi surface run parallel to each other and is called Fermi surface nesting. For 2D systems, it is generally believed that nesting drives the system to a CDW transition. However, many of the experimental reports are inconsistent with this model and the mechanism is still under debate [84]. For example, $NbSe_2$ has been studied as a prototypical 2D CDW material but the size and location of the energy gap and nesting vectors still do not agree well with theory. Alternative CDW mechanisms such as saddle point [85] and electron-phonon coupling [86] have been proposed.

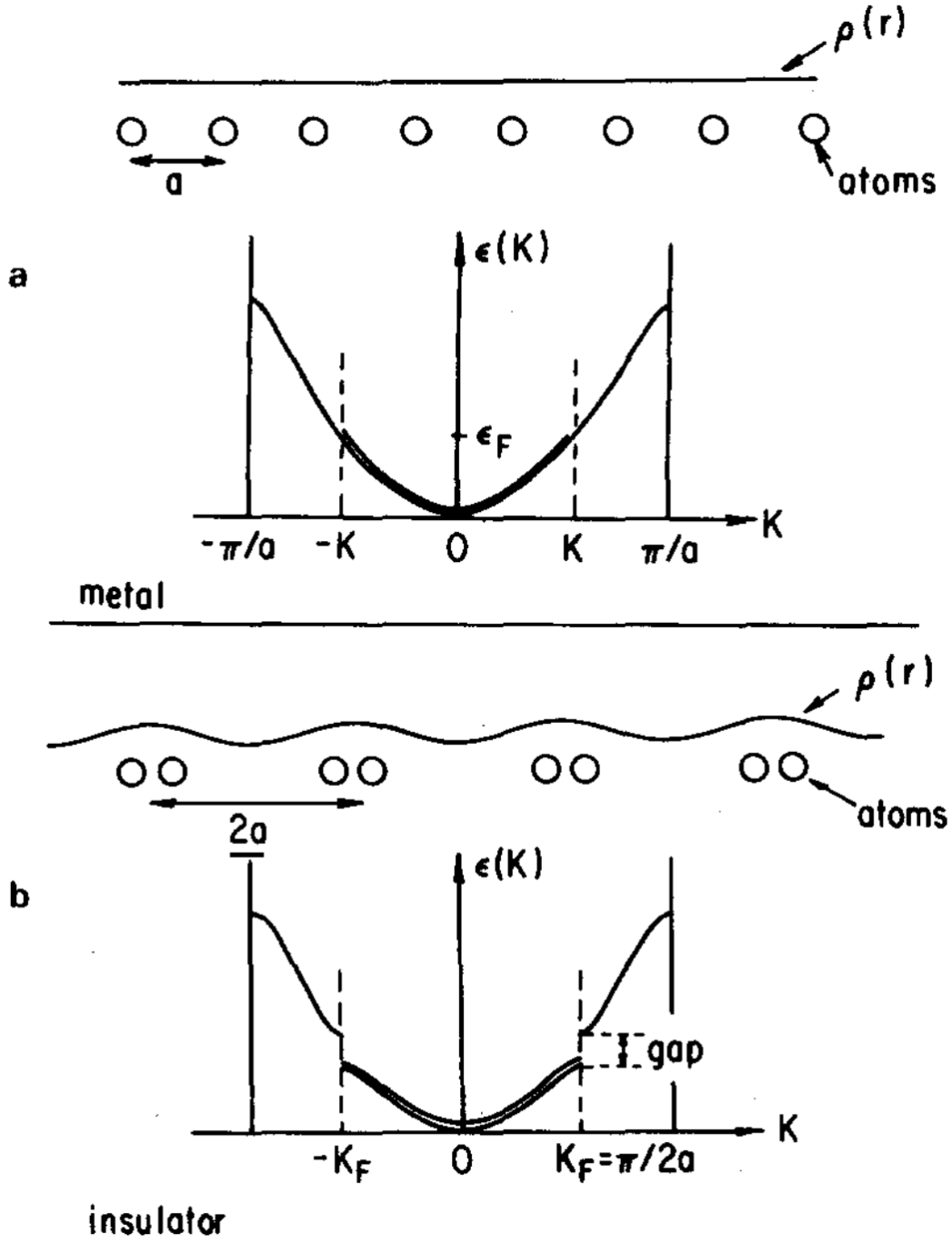

Fig. 1-9 Peierls distortion of 1D electron gas.
Fig. 2.1, Grüner and Zettl [10]. Position of the atoms, charge distribution and band structure for a) before Peierls distortion and b) after Peierls distortion.

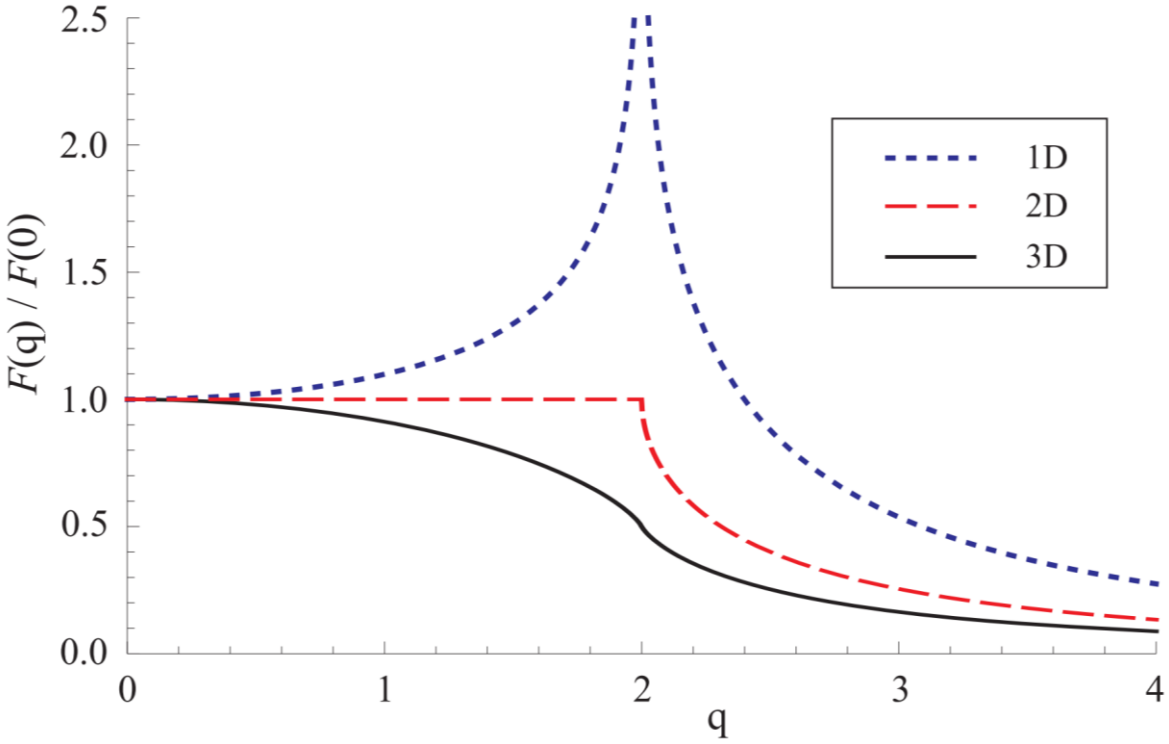

Fig. 1-10 Dimensional dependence on the Lindhard dielectric function.
Fig. 1, Mihaila [83]. Lindhard response function $F(q)$ is plotted for dimensions D=1 (Eq. 1-9 with blue, short dashed line), D=2 (Eq. 1-10 with red, long dashed line) and D=3 (Eq. 1-11 with black, solid line). $F(q)$ is normalize by $F(0)$ and q (horizontal axis) is in units of k_F.

1.2.2 Sliding CDW

In the CDW state, the charge density ρ is modulated in space as [10]

$$\rho(x) = \rho_0 \cos(2k_F x + \phi) + \text{const} \qquad \text{Eq. 1-12}$$

As the energy does not depend on the phase of the wave (ϕ), the CDW could slide without dissipation. Fröhlich proposed conduction by sliding CDW as a possible mechanism for the zero resistance in superconductivity [87] but the model did not account for the Meissner effect [88,89]. Experimentally, sliding CDW has been observed but only when driven by electric fields greater than a threshold field (E_T) because the CDW is pinned by defects for $E<E_T$ [10]. It is believed that the unavoidable presence of defects has so far prevented the realization of the perfect conductivity for sliding CDW.

Sliding CDW has been experimentally observed in only a special subset of materials with CDW transitions [10,78] (see Table 2-1). In the rest of the CDW materials, the CDW is believed to be either impossible to depin or E_T lies beyond the experimentally testable range. At this point, it is unknown whether all CDW states are capable of sliding, when driven with a high enough electric field, or there are inherently "static" CDW. The majority of the materials with sliding CDW have a quasi-1D crystal structure (e.g. $NbSe_3$, TaS_3). Generally, it is believed that the pinning is stronger in 2D systems and hinders sliding. However, sliding CDW have been discovered recently in quasi-2D materials [90].

1.2.2.1 Experimental signatures of sliding CDW

An experimental signature of a sliding CDW is the appearance of non-linearity in the I(V) curve, which exceeds the linear ohmic behavior at high voltage bias. The dc conductivity follows the empirical formula

$$\sigma_{\text{total}} = \sigma_A + \sigma_B \left(1 - \frac{E_T}{E}\right) \exp\left(-\frac{E_0}{E - E_T}\right) \qquad \text{Eq. 1-13}$$

where σ_A is the ohmic component and σ_B and E_0 are free parameters. In Fig. 1-11, the current (triangles, right axis) is plotted against the electric field, obtained by dividing the bias voltage by the contact separation. The I(E) curve is practically the same as an I(V) curve. The curve is linear below $E<E_T$=5.2mV/cm but grows super-linearly with E for $E>E_T$ due to the added contribution from the sliding CDW. The differential resistance (dV/dI) is shown in the same graph (circles, left axis). This quantity is commonly measured directly by a lock-in amplifier. The derivative is more sensitive to non-linear effects and enables measurement with a lower current through the sample. Heating effects need to be minimized as it also results in a super-linear increase in conductivity with field. Consistent with the I(V) curve, dV/dI is flat for $E<E_T$ and decreases by more than 50% as E is increased above E_T.

Sliding CDW leads to conduction, despite the system being in an insulating CDW state at $T<T_P$. Another possible interpretation is that the CDW state is destroyed for $E>E_T$ and the conduction is recovered from closing the CDW energy gap. In Fig. 1-12, ρ(T) for T = 60~30K exhibits an anomaly, where the resistivity (ρ) increases with cooling. The anomaly is caused by the CDW opening an energy gap at the Fermi level and decreasing the number of carriers available. The anomaly is more suppressed for j = 11.6A/mm^2 (open circles) than for j = 0.116A/mm^2 (filled circles) because the high current excitation biases the sample with $E>E_T$. The suppression of the CDW signature in ρ(T) at $E>E_T$ might be interpreted as the suppression of the CDW order parameter itself. However, the X-ray diffraction peak from the lower CDW superlattice, is the same for low and high current bias in Fig. 1-12. The normalized temperature evolution of the lower CDW is similar to that of the upper CDW, which means the CDW order parameter is unaffected by the strength of the electric field [91]. The X-ray diffraction result is strong evidence for a sliding CDW.

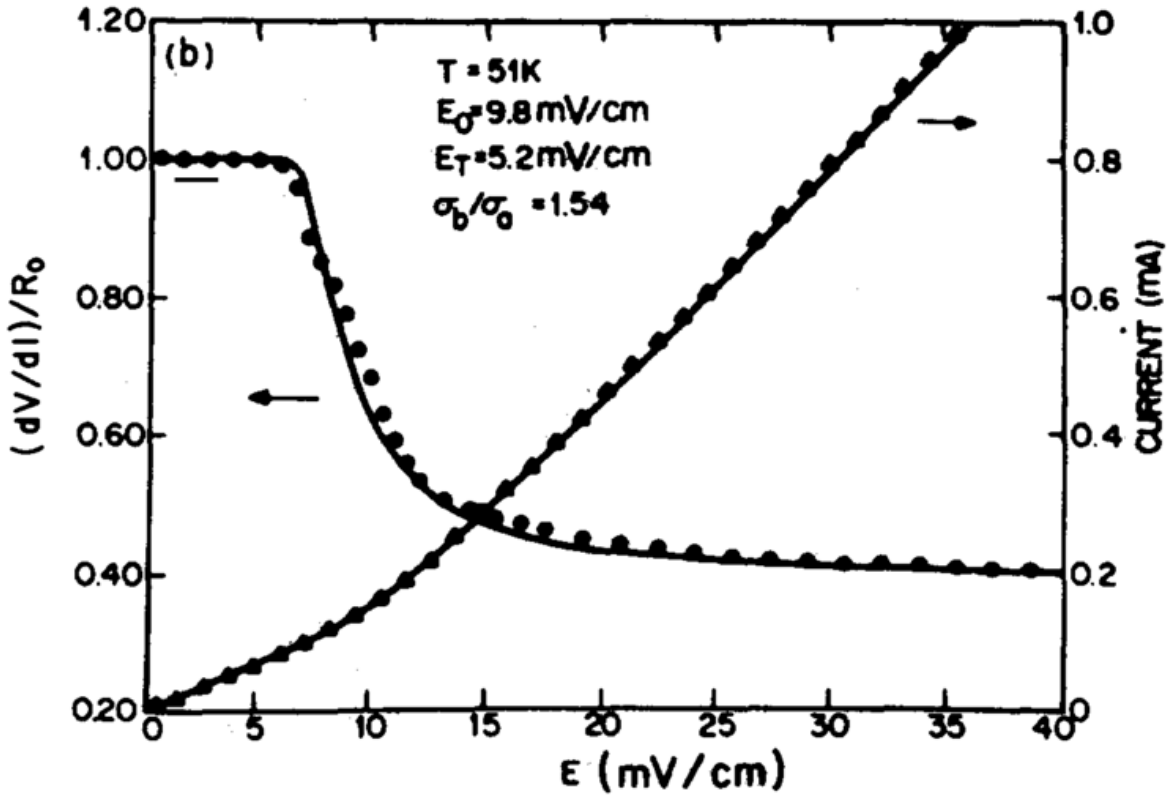

Fig. 1-11 Non-linear I(V) curve of sliding CDW in $NbSe_3$.
Fig.5.2b, Grüner and Zettl [10]. Current (right axis) and normalized differential resistance (left axis) response to the electric field (bottom axis) from a dc bias voltage. T=51K, below the lower CDW transition temperature in $NbSe_3$ (T_{P2}=59K). Non-linearity appears at $E>E_T$ for the current and $E>E_0$ for the differential resistance.

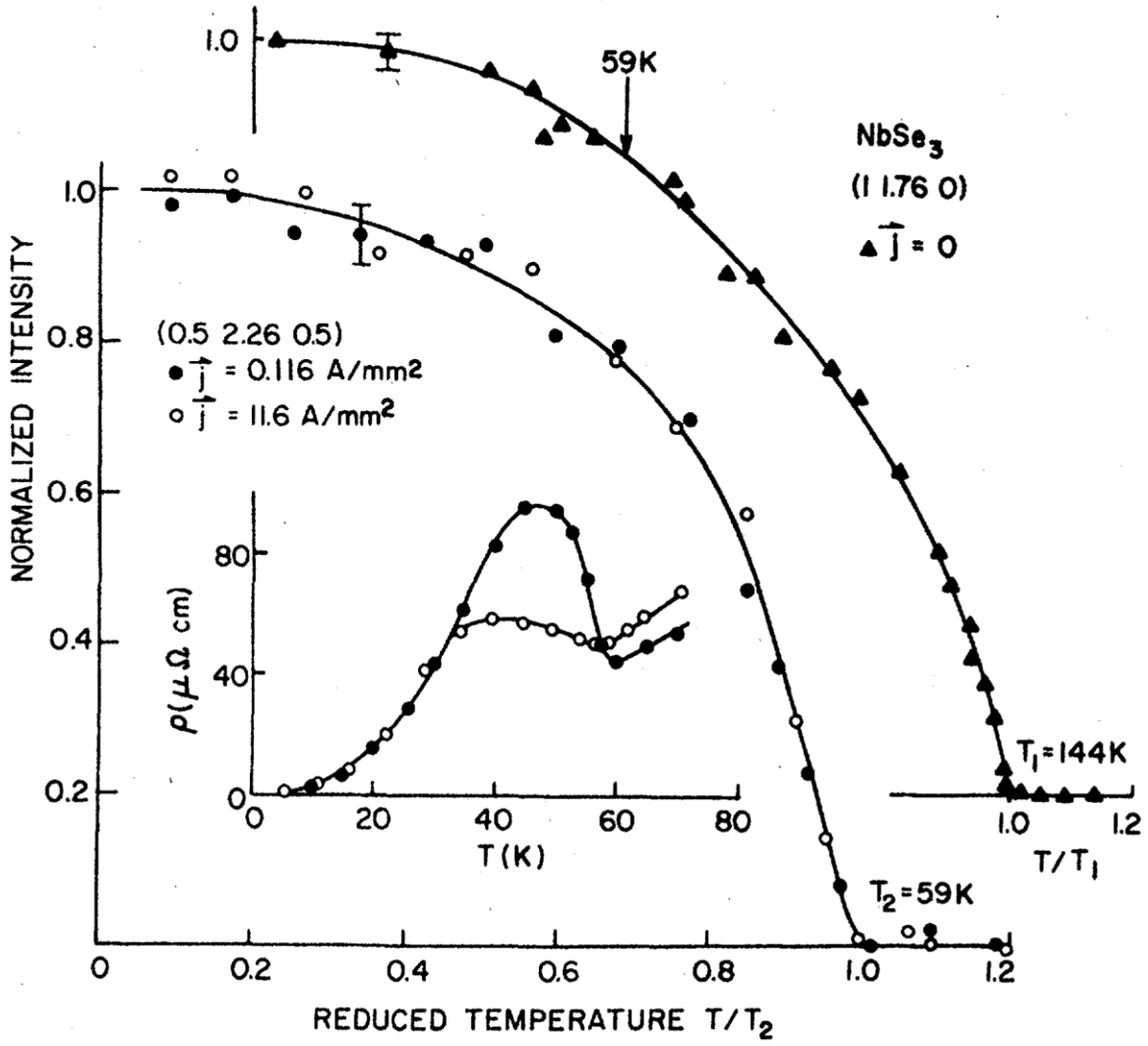

Fig. 1-12 Temperature dependence of X-ray peak intensity for CDW in $NbSe_3$.
Fig. 2, Fleming *et al*. [91]. Peak intensities from X-ray diffraction corresponding to the upper CDW transition (triangles) and lower CDW transition (circles). The points corresponding to the pinned CDW (solid circles) and sliding CDW (open circles) follow the same temperature dependence. Inset: temperature dependence of resistivity.

1.2.2.2 Threshold field

For $E<E_T$, the CDW is pinned by impurities and the type of pinning is divided into strong and weak pinning. The phase correlation length L_0 is defined as [10]

$$\langle\phi(x)\phi(0)\rangle \sim \exp\left(-\frac{x}{L_0}\right) \quad \text{Eq. 1-14}$$

where $\phi(x)$ is the phase of the CDW at position x. For strong pinning, L_0 is the average distance between the impurities. For weak pinning, L_0 is much larger than the average distance between the impurities, as the CDW adjusts its phase to minimize energy over multiple impurities. The threshold field increases with the impurity concentration (n_i). For weak pinning,

$$E_T \sim n_i^2 \quad \text{Eq. 1-15}$$

For strong pinning,

$$E_T \sim n_i \quad \text{Eq. 1-16}$$

Fig. 1-13 shows the temperature dependence of E_T in $NbSe_3$. E_T is determined either from dV/dI measurements similar to Fig. 1-11 or the onset of narrowband noise (see section 1.2.2.3). For the upper CDW, $E_0(T)$ from Eq. 1-13 is shown, as well. Comparison with R(T) (dashed line), shows that the $E_T(T)$ curve on the right corresponds to the upper CDW transition and the curve on the left to the lower CDW. When cooled below T_P, both the upper and lower $E_T(T)$ first dip down to a minimum value and gradually increase again when cooled further. $E_T(T)$ for other materials (e.g. TaS_3, NbS_3, $(TaSe_4)_2I$, $NbSe_4)_{3.33}I$ and $K_{0.3}MoO_3$) shows the same general trend [10]. E_T diverges as $T \rightarrow T_P$ from $T<T_P$ due to $\Delta(T)$. The dependence of E_T on Δ is determined by the tradeoff between the CDW strain ($\sim\Delta^2$) and the impurity interaction strength ($\sim\Delta$). The difference in scaling leads to the divergence of E_T as Δ collapses while approaching T_P.

The theoretical explanation for the increase of E_T as $T \rightarrow 0$ is still under debate. Two models and their comparison to experimental data have been discussed by McCarten *et al.* [92]. In the model by Maki and Virosztek [93,94], the thermal fluctuation of the CDW order parameter at finite temperature weakens the coupling of the CDW to the pinning potential. Hence, the CDW is pinned the strongest at T=0 and the pinning is weakened as the thermal fluctuation effects become stronger at higher temperature. In the model by Lee and Rice [95], $E_T(T)$ is attributed to the temperature dependence of the carriers in the CDW state (n_c). At finite temperature, $n_c \rightarrow n_c^{eff}$ by the interaction of the CDW condensate and normal carriers. E_T is affected by the variation in charge density, as the force on the CDW condensate varies as $F_{CDW} = en_c^{eff}E$ and the model predicts $E_T(T) \sim \frac{1}{n_c^{eff}(T)}$. When compared with experiment [92], n_c^{eff} (obtained from narrowband noise measurements) reached a maximum at the middle of the CDW transition and decreased as $T \rightarrow 0$ but $\frac{1}{n_c^{eff}(T)}$ did not exactly match the $E_T(T)$ data.

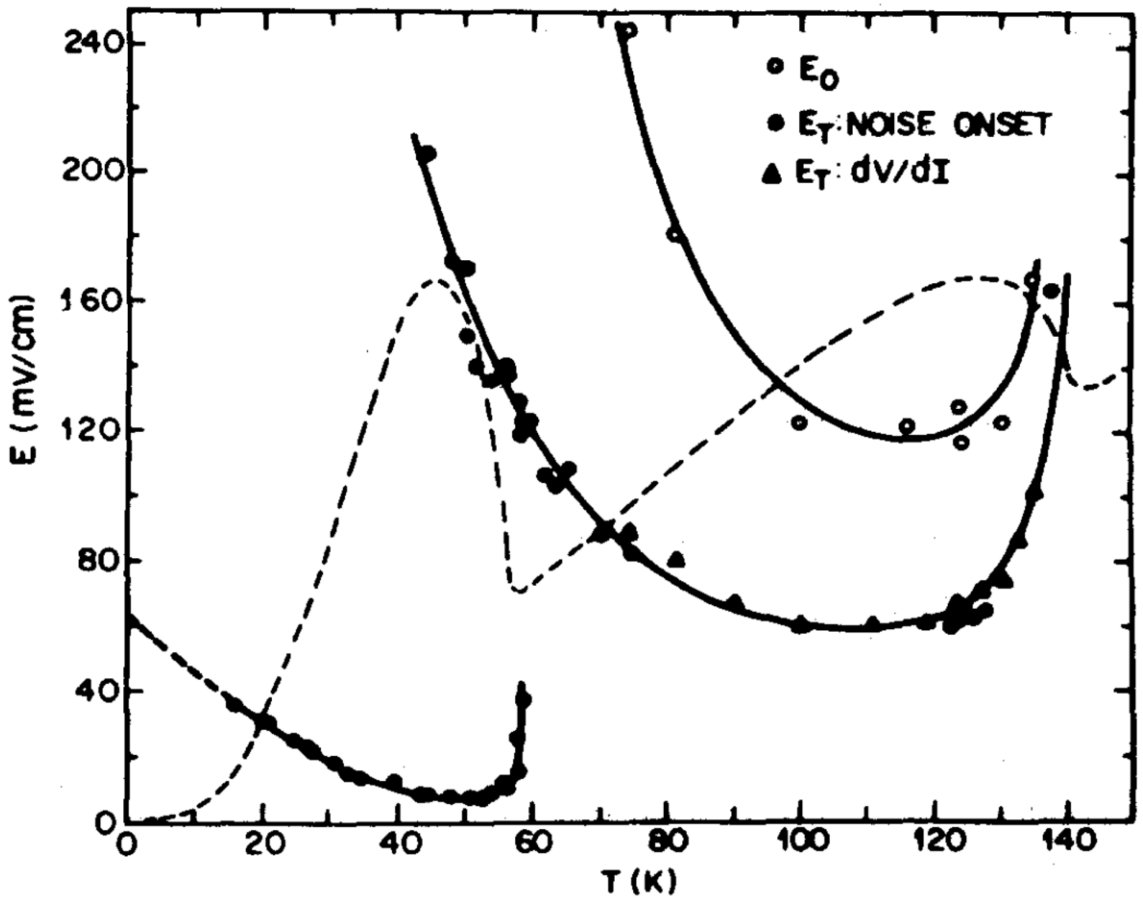

Fig. 1-13 E_T(T) of bulk $NbSe_3$.
Fig. 5.3, Grüner and Zettl [10]. E_T from the upper and lower CDW are determined by dV/dI measurement (triangles) and onset of narrowband noise (circles). E_0(T) for the upper CDW shows a similar temperature dependence as E_T. The dotted line is R(T), showing the resistive anomalies from the upper and lower CDW.

1.2.2.3 ac response

The CDW conduction is also strongly frequency dependent, which has been observed experimentally in multiple materials [10]. The system behaves similar to a semiconductor with an energy gap $\hbar\omega_0$, where ω_0 is associated with pinning potential. For $\omega > \omega_0$, the conductivity increases with frequency, consistent with [10]

$$\text{Re } \sigma_{ac}(\omega) = \frac{n_c e^2 \tau}{m^*} \frac{\omega^2/\tau^2}{(\omega_0^2 - \omega^2)^2 + \omega^2/\tau^2}$$
$$\text{Im } \sigma_{ac}(\omega) = \frac{n_c e^2 \tau}{m^*} \frac{(\omega_0^2 - \omega^2)\omega/\tau^2}{(\omega_0^2 - \omega^2)^2 + \omega^2/\tau^2} \quad \text{Eq. 1-17}$$

where n_c is the density of carriers condensed in the CDW state, τ is the CDW damping time constant and m^* is the effective mass of the CDW. For $\omega < \omega_T$, there is no frequency dependence but the dielectric constant is strongly enhanced by the CDW (e.g. 2×10^8 in $NbSe_3$ at T = 42K) [10]. The dielectric constant in the static limit is

$$\varepsilon_1(\omega \to 0) = 1 + \frac{4\pi n_c e^2}{m^* \omega_0^2} \quad \text{Eq. 1-18}$$

ω_0 increases with impurity concentration (n_i), as denser impurity means a traveling CDW encounters them with higher frequency. Hence, $\varepsilon_1(\omega \to 0)$ decreases as n_i increases. In contrast, E_T increases as n_i increases. The product of the two are actually independent of n_i [10]

$$\varepsilon_1 E_T = 0.58 n_c e \lambda \quad \text{Eq. 1-19}$$

Another characteristic ac response of the CDW is narrowband noise. Sliding CDW emit an ac signal, which is narrowly centered at a specific frequency, called "narrowband noise" [10]. Interestingly, a material under *dc bias* results in the emission of an *ac signal*. Although the exact origin of the narrowband noise has not been revealed, it is believed to be generated by the interaction of the sliding CDW and the pinning potential. Fig. 1-14 shows the noise spectrum of $NbSe_3$. At zero bias (Fig. 1-14e), the noise spectrum does not show any peak. However, when driven with $E>E_T$ (Fig. 1-14a-d), the system shows narrowband peaks in the noise spectrum. The fundamental frequency and its harmonics can be clearly seen and the narrowband noise shifts to higher frequency as the excitation is increased.

As shown in Fig. 1-15, there is a linear relationship between the narrowband noise frequency and the current carried by the sliding CDW. Denoted as I_{CDW} or J_{CDW} for current density, this quantity is measured by subtracting the ohmic contribution of the normal carriers from the current under $E>E_T$. The relation can be rationalized from [10]

$$I_{CDW} = e n_c A v_d \quad \text{Eq. 1-20}$$

where A is the cross-sectional area of the materials and v_d is the drift velocity of the CDW. Given the narrowband noise frequency (f_{NBN}) and the wavelength of the pinning potential ($\bar{\lambda}$), we can substitute $v_d = f_{NBN}\bar{\lambda}$

$$I_{CDW} = e n_c A f_{NBN} \bar{\lambda} \quad \text{Eq. 1-21}$$

The ratio I_{CDW}/f_{NBN} is proportional to n_c, the number of carriers condensed in the CDW state. As $n_c \sim \Delta$, the CDW order parameter [96], narrowband noise measurements provides a direct probe of the order parameter. Fig. 1-16 shows the amplitude of the X-ray diffraction peak

corresponding to the lower CDW in $NbSe_3$ (asterisks). The X-ray amplitude, and hence Δ, grows as the material is cooled below the transition temperature and the BCS gap equation fits the data well near the transition temperature. When plotted together, I_{CDW}/f_{NBN} (open circles), shows a similar temperature dependence.

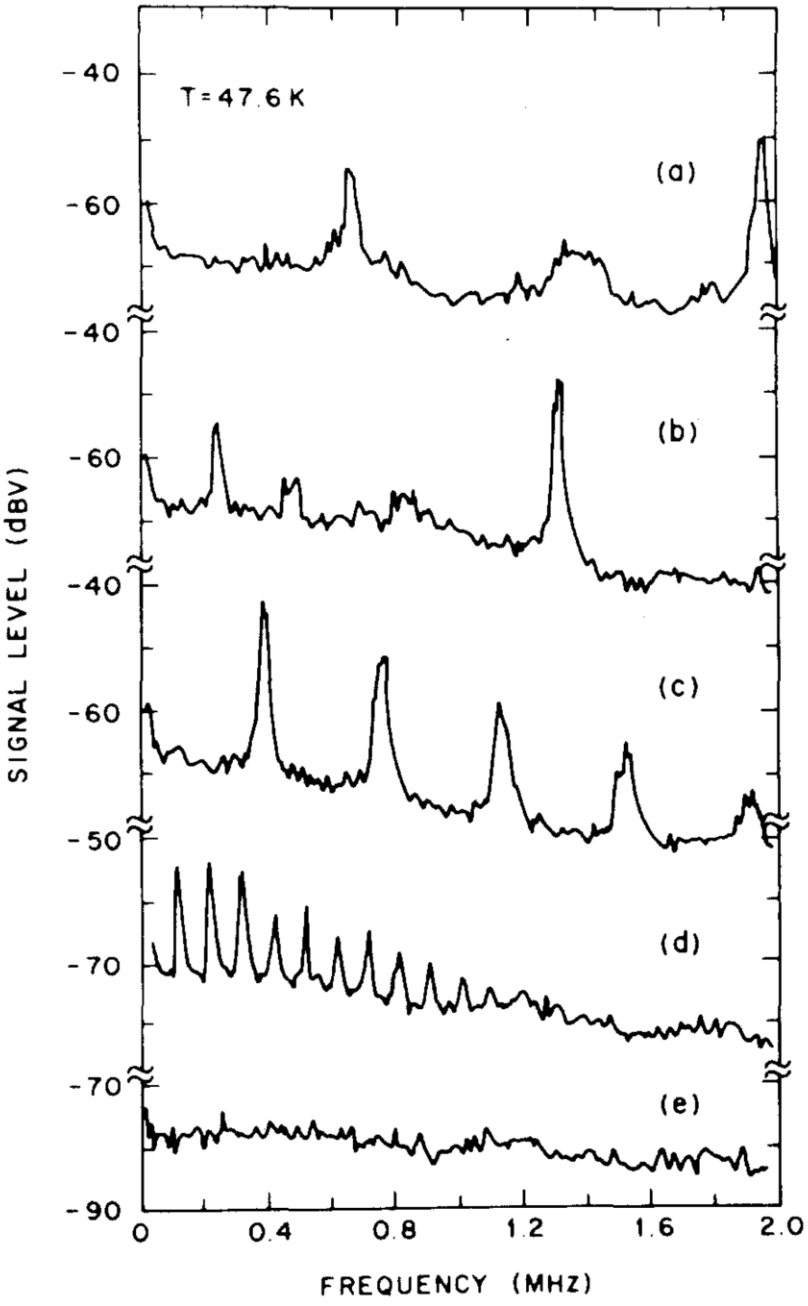

Fig. 1-14 Narrowband noise of bulk $NbSe_3$.
Fig. 5.10, Grüner and Zettl [10]. Noise spectrum of $NbSe_3$ with currents and voltages (a) I=270μA, V=5.81mV; (b) I=219μA, V=5.05mV; (c) I=154μA, V=4.07mV; (d) I=123μA, V=3.40mV; (e) I=V=0.

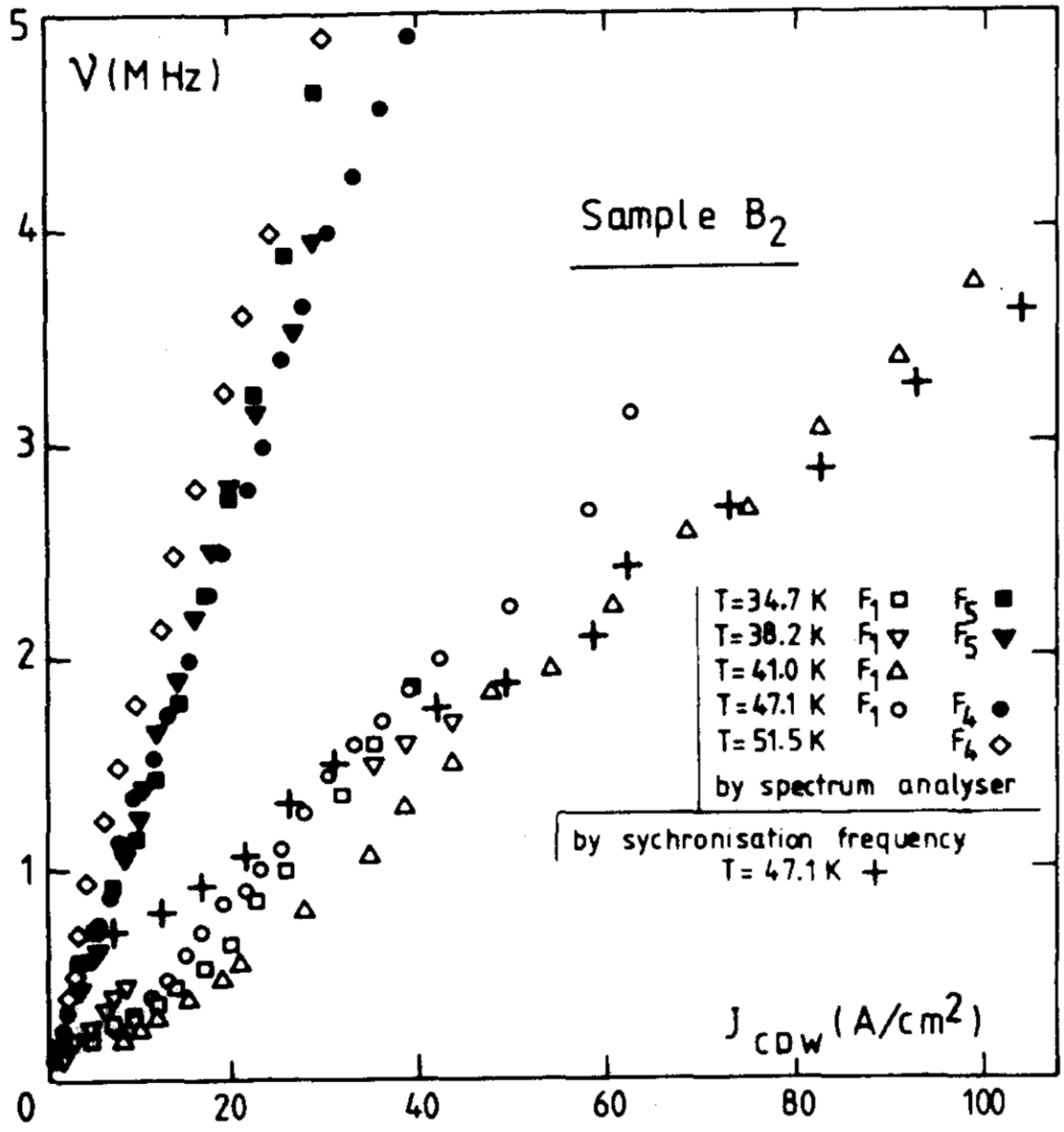

Fig. 1-15 Narrowband noise frequency vs J_{CDW} of bulk $NbSe_3$.
Fig. 5.13, Grüner and Zettl [10]. J_{CDW} is the current density corresponding to the excess current due to sliding CDW. F_1 is the fundamental frequency of the narrowband noise.

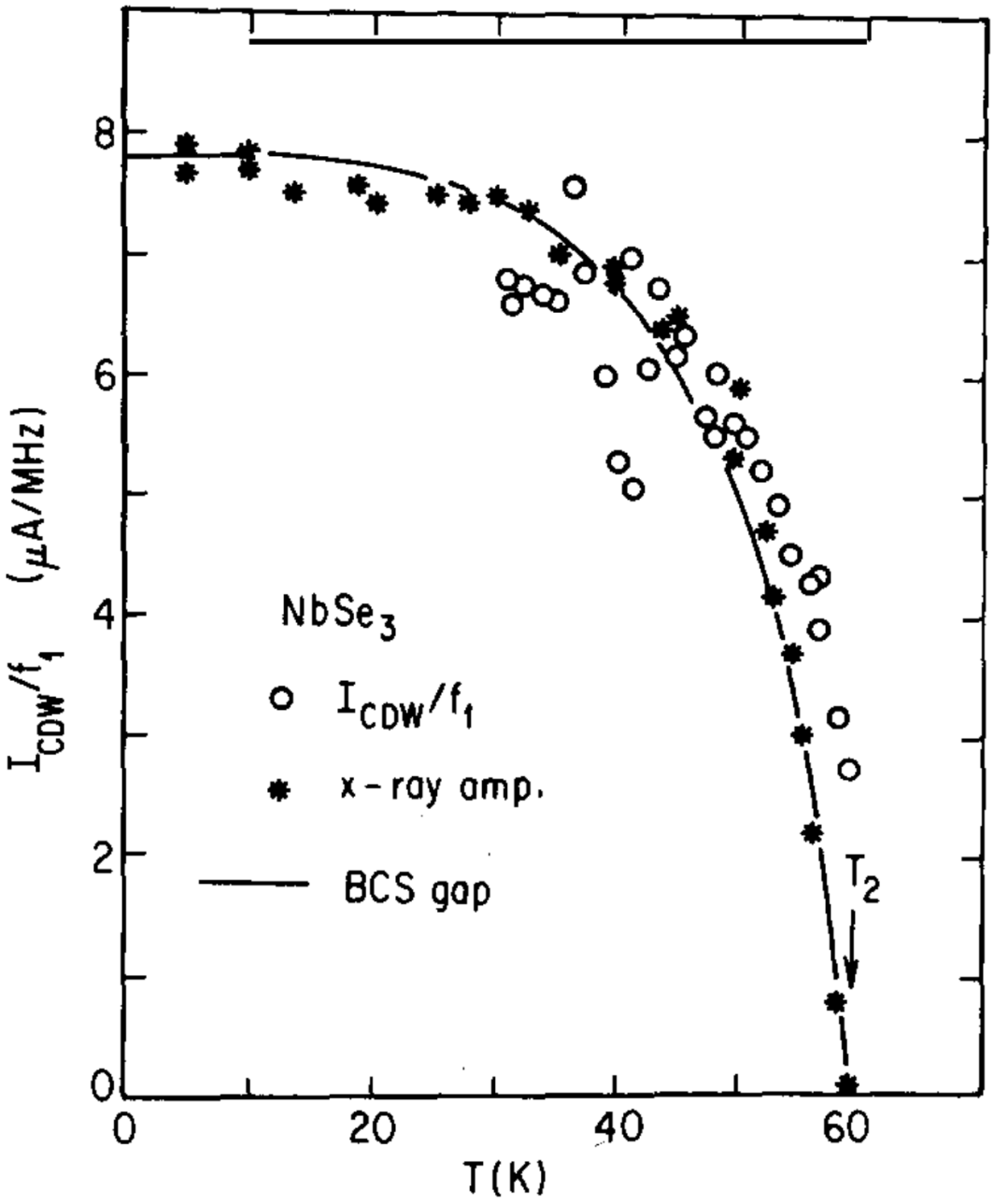

Fig. 1-16 CDW order parameter evolution with temperature.
Fig. 5.16, Grüner and Zettl [10]. I_{CDW} is the excess current from sliding CDW and f_1 is the fundamental narrowband noise frequency. X-ray amplitude is amplitude of X-ray diffraction peak corresponding to the CDW state. The BCS gap equation describes the temperature dependent evolution of the CDW order parameter.

2 Transition metal chalcogenides

Compounds formed by transition metals (e.g. molybdenum, tantalum, tungsten and niobium) and chalcogens (e.g. sulfur, selenium and tellurium) are called transition metal chalcogenides (TMC). Denoting *M* for transition metal and *X* for chalcogen, compounds belonging to *MX*, MX_2, MX_3 and MX_4 are discussed in this chapter. TMC form quasi-low D materials with highly anisotropic electronic structure [97]. The TMC introduced here possess interesting electronic states (e.g. superconductivity, CDW, Weyl fermions), which are summarized in Table 2-1.

In quasi-2D crystals, the atoms form layers, which stack along an axis perpendicular to the layers. The chemical bonds are strong covalent bonds in the plane of the layers but weak van der Waals bonds perpendicular to the layers. As the bonding between the layers are weak, quasi-2D crystals are easily cleaved parallel to the layers, analogous to peeling off sheets from a stack. Most quasi-2D TMC are MX_2 (e.g. $NbSe_2$, TaS_2, WTe_2), but a *MX* (i.e. FeSe) is introduced as well.

In a quasi-1D crystals, the atoms form chains, which run parallel to each other. The chemical bonds are strong covalent bonds along the length of the chains but are weak van der Waals bonds between neighboring chains. Similar to quasi-2D materials, the weak inter-chain bonding allows the crystal to cleave easily along the chain to yield bundles of fewer chains [50]. Quasi-1D materials with MX_3 (e.g. $NbSe_3$, TaS_3) and MX_4 (e.g. $(NbSe_4)_2I$, $(NbSe_4)_3I$, $(NbSe_4)_{3.33}I$) formula are introduced in this chapter.

It could be argued that the quasi-low D materials are not truly low-D systems because some electronic interaction between the layers/chains take place. Recently, many studies have focused on studying them in the ultrathin limit, towards truly low-D effects, and some background on the topic will be introduced in this chapter.

	Material	Characteristic transition/electronic state	Transition temperature (K)
Quasi-2D	2H-$NbSe_2$	CDW	T_P=33
		Superconductivity	T_c=7.2
	1T-TaS_2	Incommensurate CDW	T_P~352 (warming)
		Nearly commensurate CDW	T_P~348 (cooling) T_P~240 (warming)
		Commensurate CDW	T_P~140 (cooling)
	1T'-WTe_2	Extreme magnetoresistance	Note1
		Insulating state	T*=38 at B=2T ('turn on' temperature)
	FeSe	Superconductivity	T_c=8
Quasi-1D	$NbSe_3$	Sliding CDW	T_{P1}=144
		Sliding CDW	T_{P2}=59
	TaS_3 (orthorhombic)	Sliding CDW	T_P=215
	TaS_3 (monoclinic)	Sliding CDW	T_{P1}=240
		Sliding CDW	T_{P2}=160
	$(TaSe_4)_2I$	Sliding CDW	T_P=265
	$(NbSe_4)_2I$	Sliding CDW	T_P=210
	$(NbSe_4)_3I$	Ferrodistortive, structural	$T_{structural}$=274
	$(NbSe_4)_{3.33}I$	Sliding CDW	T_P=285

Table 2-1 Summary of quasi-low materials.
Note 1: It is unclear whether WTe_2 transitions to extreme magnetoresistance from a "normal" state at a certain temperature.

2.1 Quasi-2D Materials (stacked sheets)

As illustrated[5] in Fig. 2-1a, quasi-2D TMC have a layered crystal structure. In graphite and hexagonal boron nitride (h-BN), each layer is one atom thick [23,98]. For TMC, each layer is three atoms thick: a plane of transition metals is sandwiched by chalcogen atoms from top and bottom, as shown by the side view of one layer in Fig. 2-1b. The transition metals do not directly bond to each other but are held in place by bonding with the chalcogen atoms in between. In most quasi-2D TMC (e.g. NbS_2, $NbSe_2$, TaS_2, $TaSe_2$, MoS_2, WS_2 [99]), the atoms from MX_2 layers with the crystal structure shown in Fig. 2-1b,c. When one layer is isolated and viewed from the top, the atoms form a hexagonal lattice which resembles h-BN. However, it should be noted that the bonding configuration is very different because the small, green spheres represent the top and bottom chalcogens. Two of the materials discussed in this chapter are exceptions to the rule above: WTe_2 forms MX_2 layers but do not form the hexagonal lattice and FeSe form MX layers.

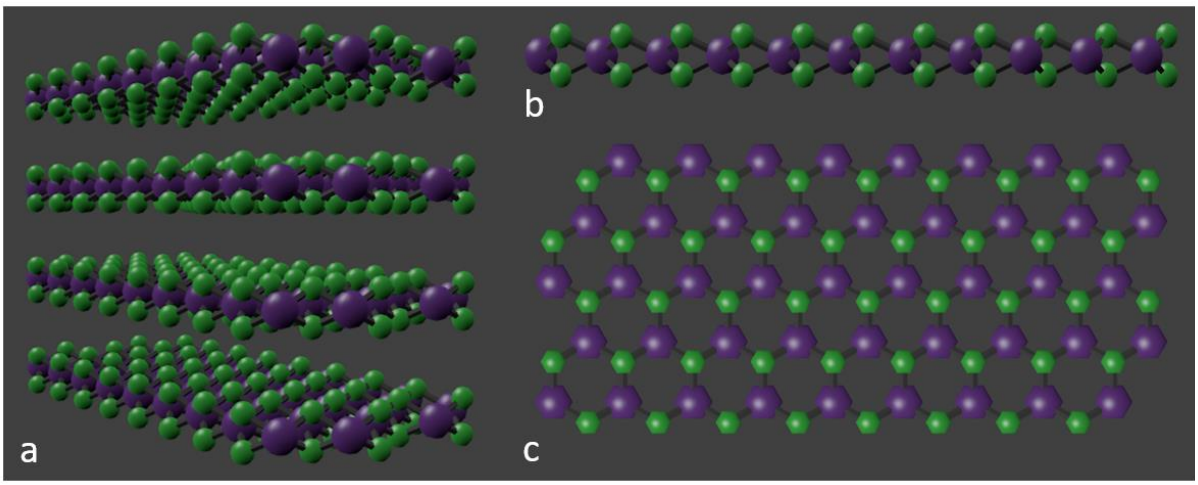

Fig. 2-1 Crystal structure of MX_2.
Small, green spheres are chalcogen atoms (e.g. sulfur, selenium) and large, purple spheres are transition metal atoms (e.g. tantalum, sulfur). a) Stack of four tri-atomic layer sheets. b) Orthographic side view of one sheet of tri-atomic layer. c) Orthographic top view of one sheet of tri-atomic layer.

[5] Figure created by free and open source 3D graphics software Blender (https://www.blender.org/).

2.1.1 Polytypes

Polymorphism is commonly known as the existence of different crystal structure for an element or a compound. Polytypes are a subset of polymorphs, in which the crystals vary along only one dimension [100]. Specifically, this is realized in layered materials with sheets that stack differently. The variation is illustrated in Fig. 2-2 and depends on alignment of the metal atoms between stacked sheets and bonding configuration with the chalcogens (octahedral or trigonal). Polytypes are commonly referred with Ramsdell notation [100], consisting of the number of layers in the unit cell and the lattice type (e.g. 2H(a), 1T). In Fig. 2-2, the symmetry group (e.g. D_{6h}^4, D_{3d}^3) for each polytype is shown as well. As exemplified by TaS_2, electronic properties differs significantly between polytypes.

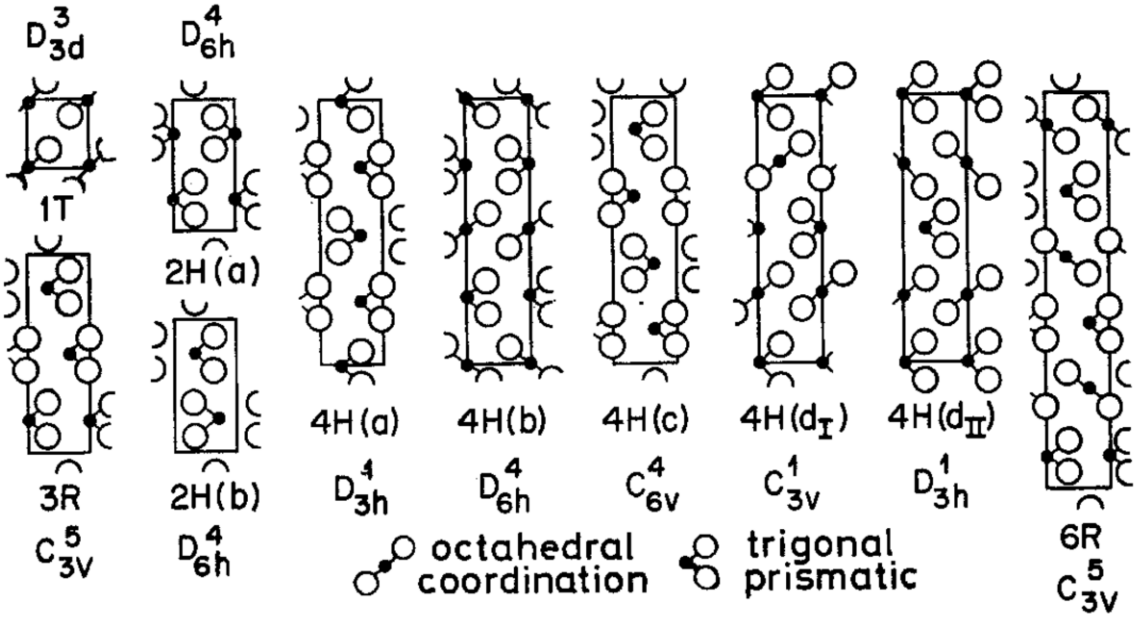

Fig. 2-2 Polytypes of MX_2.
Fig. 1, Wilson *et al*. [106]. Side view of unit cell. Open circle represents chalcogen atom. Solid circle represents transition metal atom. Each polytype is labeled by Ramsdell notation [100] and space group.

2.1.2 $NbSe_2$

Niobium diselenide ($NbSe_2$) consists of MX_2 layers shown in Fig. 2-1b,c with niobium for the transition metal (large, purple spheres) and selenium for the chalcogen (small, green spheres). The 2Ha stacking has been the most widely studied and easily obtained polytype of $NbSe_2$ (see Fig. 2-2). In the discussion below "$NbSe_2$" refers to 2Ha-$NbSe_2$. $NbSe_2$ at the ultrathin limit is discussed in chapter 5.

$NbSe_2$ is a metal with CDW transition at T_P=33K. Fig. 2-3 show the signatures of the CDW transition in R(T) and heat capacity measurement. The resistivity increases slightly when the sample is cooled below T_P=33K but metallic behavior persists with further cooling. Since the CDW is a metal-insulator transition, the resistivity should continue to increase with cooling below T_P. In $NbSe_2$, only a small portion of the Fermi surface is gapped by the CDW and the rest

remains metallic. The CDW resistive anomaly is detectable in only high quality samples with residual resistivity ratio >30 [101]. The mechanism of the CDW transition in $NbSe_2$ has been extensively studied but is still debated [49].

$NbSe_2$ is superconducting below T_c=7.2K, as indicated by the sharp drop in resistivity. Other MX_2 (i.e. MoS_2 and TaS_2) need to be intercalated with dopants to become a superconductor but $NbSe_2$ does not require doping [102]. Due to its layered structure, B_{c2} is highly anisotropic and $B_{c2}^{\parallel} > B_{c2}^{\perp}$ [103]. The coherence length is typically calculated from B_{c2} with the Ginzburg-Landau equation. For $NbSe_2$, the theory is inconsistent with the experimentally observed temperature dependence of $B_{c2}^{\parallel}/B_{c2}^{\perp}$ [104]. The Doniach-Lawrence model is commonly applied to layered superconductors but Toyota *et al*. [105] have argued that the interlayer coupling is too strong to be Josephson coupling.

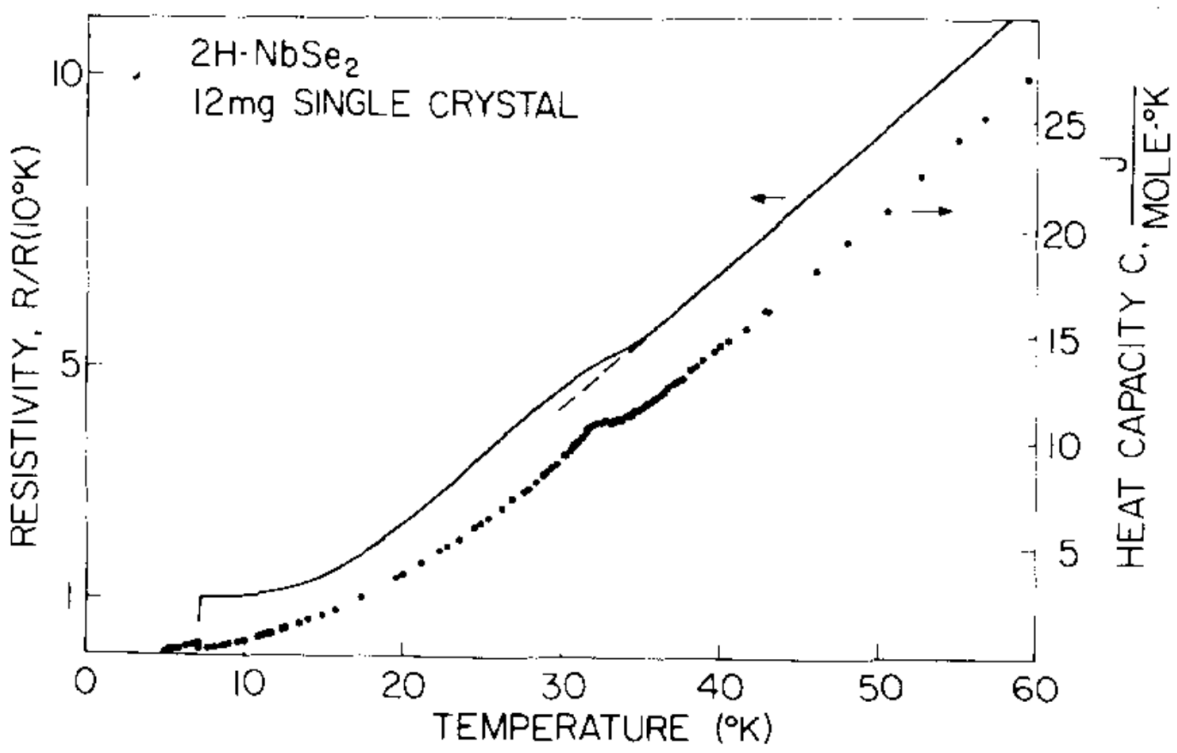

Fig. 2-3 R(T) and C(T) of 2H(a)-$NbSe_2$.
Fig. 2, Harper *et al*. [81].

2.1.3 TaS_2

Tantalum disulfide (TaS_2) consists of layers with MX_2 structure shown in Fig. 2-1b,c. Various polytypes of TaS_2 (e.g. 1T, 4Hb, 6R) have been studied [106], but we focus on 1T-TaS_2. 1T-TaS_2 exhibit characteristic hysteretic CDW transition [107]. Fig. 2-4 shows R(T) of 1T-TaS_2. On cooling from 400K, the resistivity rapidly increases at T=350K and T=240K. On warming from low temperature, the resistivity drops at T=140K and T=350K. For standard CDW anomalies, the CDW transition should occur at the same temperature on cooling and warming. In contrast, 1T-TaS_2 has a 5K wide hysteresis loop centered at 350K and a 100K wide loop at 190K.

Scanning tunneling microscopy studies show that the hysteresis is caused by transitions between the incommensurate, "nearly commensurate" and commensurate phase.

In ultrathin 1T-TaS_2, T_P have been reported to vary with thickness and charge carrier density [47,108]. In addition, ultrathin 1T-TaS_2 becomes superconducting when tuned to high carrier density with liquid gating [108] (see section 6.2).

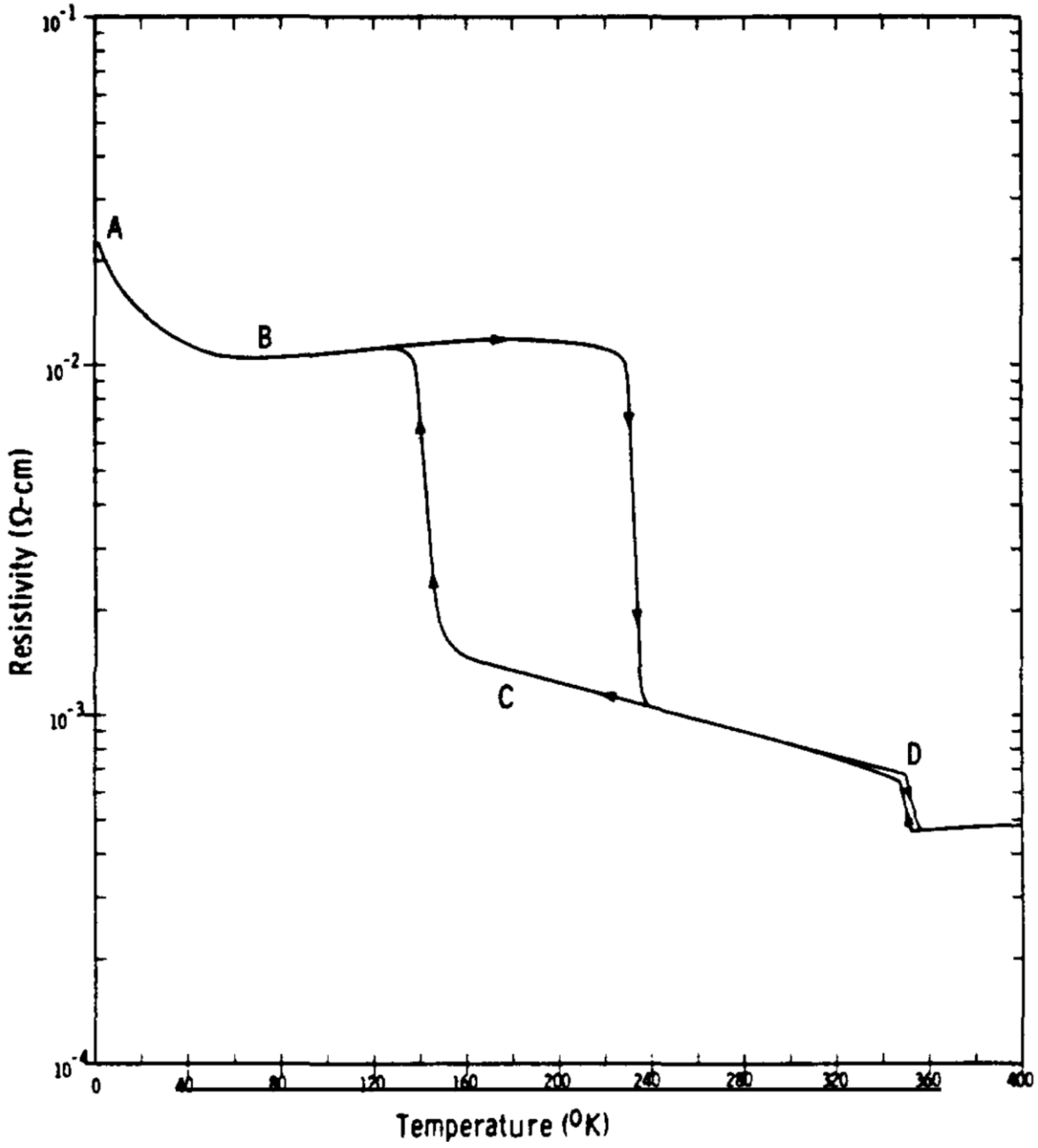

Fig. 2-4 R(T) of 1T-TaS_2.
Fig. 3, Thompson *et al*. [107]. Arrows on the curve indicate direction of temperature change.

2.1.4 WTe_2

WTe_2 forms MX_2 layers but occurs as the distorted 1T (1T') polytype [109]. When a standard MX_2 layer is viewed from the top (see Fig. 2-1c), the metal atoms form a hexagonal lattice. Fig. 2-5 shows the tungsten atoms in 1T'-WTe_2 bunch up with their neighbors and form a chain of tungsten atoms, which run along the MX_2 layer.

WTe_2 has been known as a semimetal since 1966 [110]. Recently, high quality crystals exhibited interesting magnetoresistance effects. In typical metals, the resistance increases with the application of a magnetic field but saturates above a specific field [111]. In WTe_2, the resistance continues to increase, even when the field is as high as 60T [112]. Fig. 2-6 shows R(T) of WTe_2, which is metallic with no magnetic field. When a magnetic field is applied perpendicular to the layers, R(T) switches to thermally activated behavior below the 'turn on' temperature (T*). As shown in the top inset, T* increases linearly with magnetic field. This behavior is seen in other materials, such as Cd_3As_2, $PtSn_4$ and LaSb, and classifies WTe_2 as an extreme magnetoresistance material [113].

After the discovery of Weyl semimetals in TaAs [59,113], Soluyanov *et al*. [114] predicted WTe_2 to be a type II Weyl semimetal, in which Weyl nodes occur at the intersection of electron and hole pockets. Subsequently, Fermi arcs were experimentally observed in WTe_2 [115]. Due to the topologically protected close interaction of top and bottom surfaces of a Weyl semimetal, the interlayer interaction in WTe_2 is of special interest. Comparison of the carrier effective mass at $B^{\parallel}$ and $B^{\perp}$ showed that they only differed by a factor of 2 at T>100K, despite being a layered material [116].

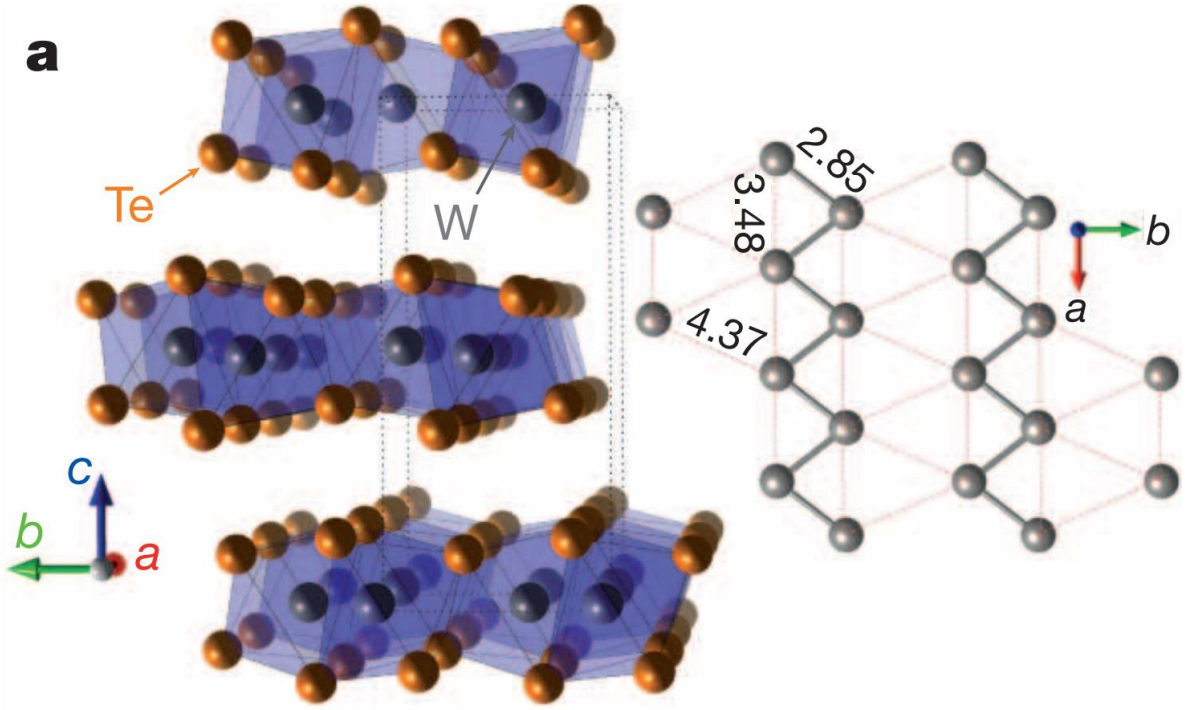

Fig. 2-5 Crystal structure of WTe_2.
Fig. 1a, Ali *et al*. [112]. Left: side view. Right: top view of only the tungsten atoms.

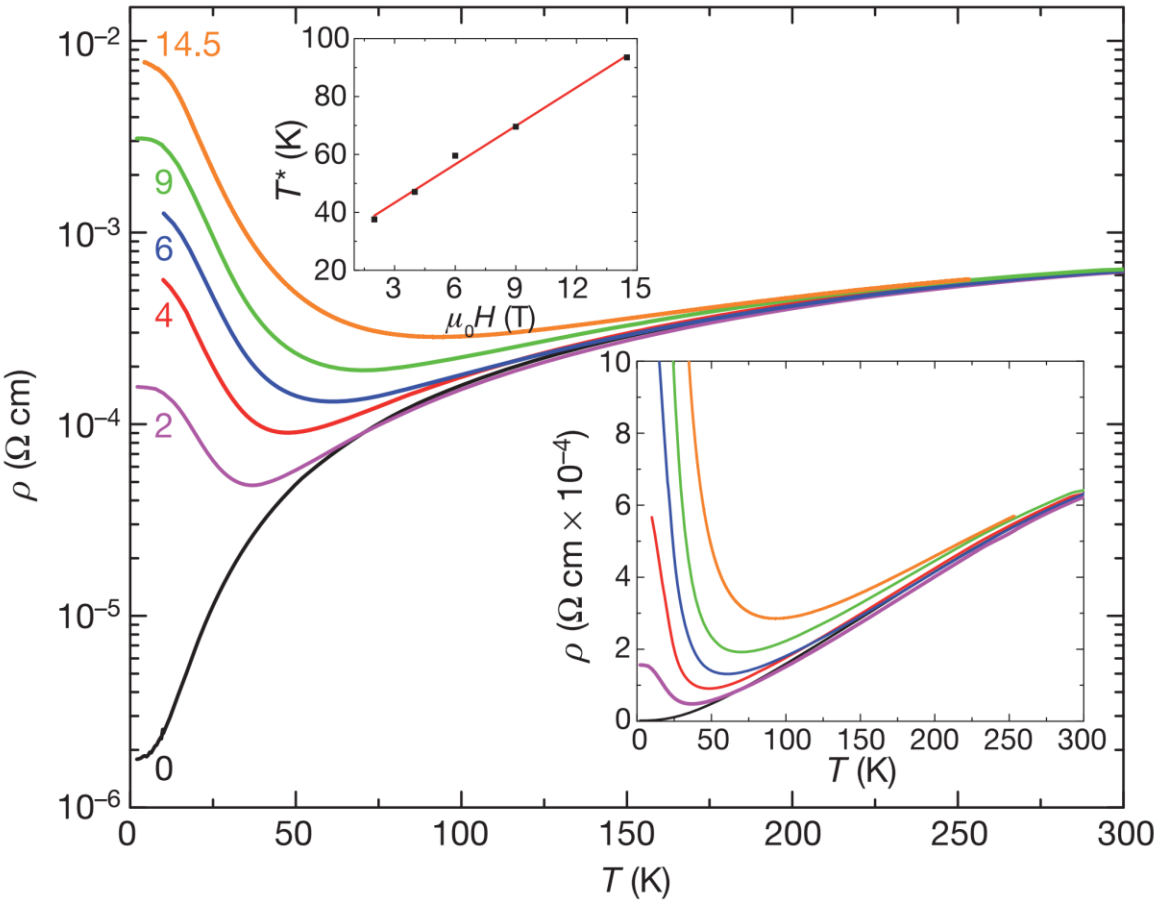

Fig. 2-6 R(T,B) of WTe_2. Ali *et al.* [112]**.**
R(T) curve labeled by the magnetic field strength (from top to bottom): 14.5T, 9T, 6T, 4T, 2T and 0T. Magnetic field is perpendicular to the WTe_2 layers. Top inset: 'turn on' temperature (T*) vs magnetic field.

2.1.5 FeSe

Unlike other transition metal chalcogenides, FeSe forms *MX* layers, as shown in Fig. 2-7a. In MX_2 layers, one chalcogen atom bonds to three neighboring metal atoms, whereas in *MX* layers, one chalcogen atom bonds to four neighboring metal atoms. Viewing from the top, one FeSe layer appears as a square lattice with alternating iron and selenium atoms, as shown in Fig. 2-7b. FeSe is commonly referred as β iron selenide to distinguish it from other compounds of the Fe-Se phase diagram but the Greek symbol varies among literature. It is more reliable to refer to FeSe by its crystal structure (tetragonal FeSe or "PbO-type").

Fig. 2-8 shows examples of an iron-based superconductor (see section 1.1.4). All the compounds share a layered crystal structure, consisting of iron containing sheets. Similar to cuprates, the iron-based superconductor family differ only by the molecules between the sheets called "blocking layers". T_c is sensitive to the blocking layers because they tune the lattice spacing and charge density in the iron containing layer. In iron arsenide compounds, the blocking

layers need to exist to balance the charge. In contrast, FeSe does not need a blocking layer and has the simplest structure among the iron-based superconductors.

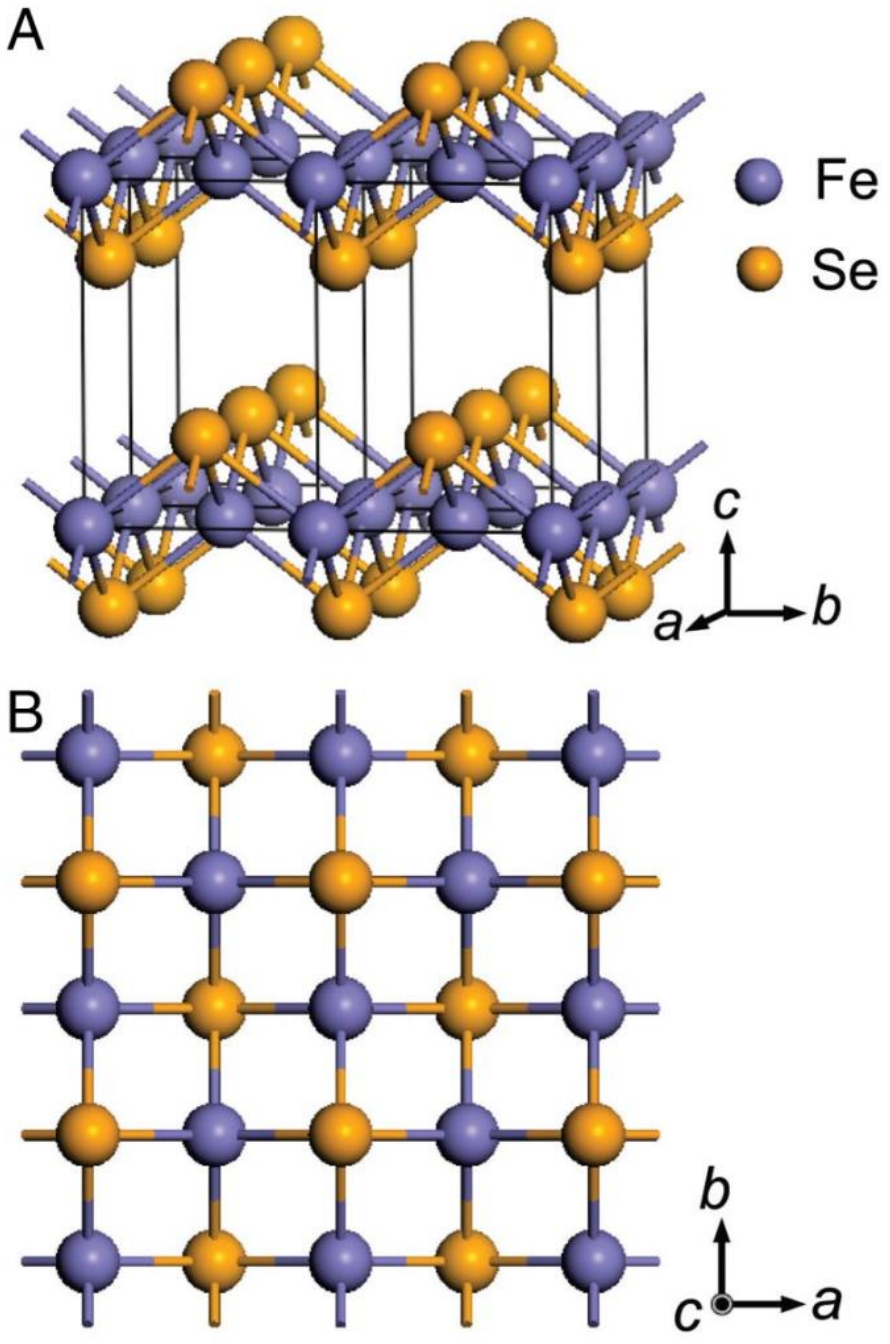

Fig. 2-7 Crystal structure of FeSe.
Fig. 1, Hsu *et al.* [117]. a) Side view. The unite cell is outlined by black lines. b) Top view.

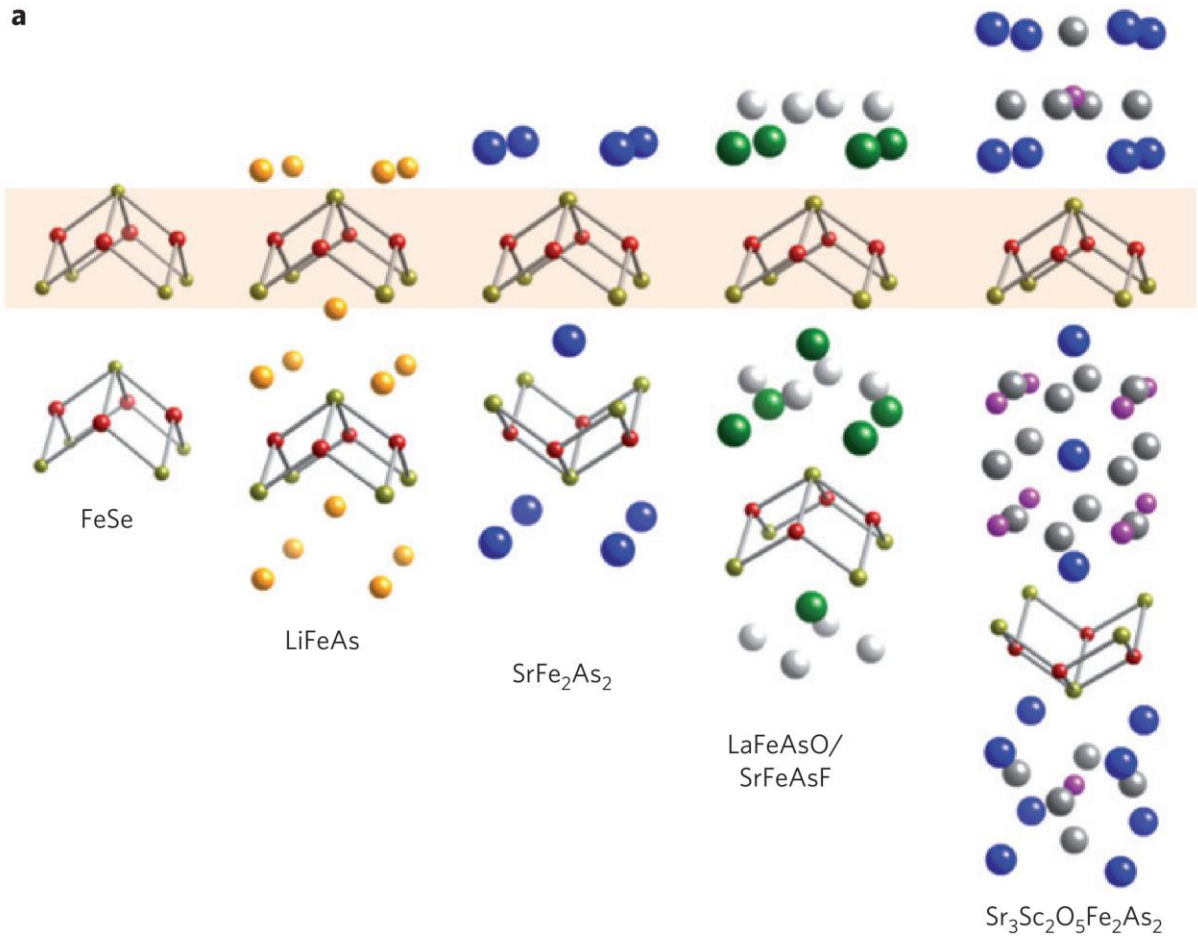

Fig. 2-8 Crystal structure of iron-based superconductors.

Fig. B1a Paglione and Greene [76].

FeSe is a superconductor with T_c=8K [117]. Fig. 2-9 shows M(T). Below T~8K, the susceptibility (χ) drops to χ<0 during the zero field cooling (ZFC) measurement due to shielding currents in the superconducting state. The field cooling (FC) curve also sharply drop at the same temperature, indicating the Meissner effect (see section 3.3.2). The magnetic anomaly at T~105K is attributed to a structural phase transition. For T<105K, FC shows χ increases with cooling. The inset shows the change in M during a magnetic field sweep. The hysteresis and the collapsed diamond shape is evidence for superconductivity. The diagonal tilt of the pattern is interpreted as the coexistence of a paramagnetic phase, which could be the cause of anomalous M(T) during FC.

Similar to many layered materials, the T_c of FeSe can be raised to 32K by intercalation of alkali metals [118]. Surprisingly, an anomalously large superconducting gap was observed in 2012 for monolayer FeSe grown on strontium titanate by molecular beam epitaxy [119]. Subsequently, a resistive superconducting transition at 100K was reported [120]. The role of the substrate/FeSe interface is still unclear. Shiogai *et al.* reported T_c=40K in ultrathin FeSe obtained by controlled electrochemical etching with an ionic liquid. The T_c was enhanced for both $SrTiO_3$ and MgO substrates but the FeSe carrier density could have been significantly affected by the ionic liquid in the device. The mechanism for T_c enhancement in the FeSe/$SrTiO_3$ system is still unknown [121] and there is suggestive experimental evidence that it is a conventional superconductor [122,123].

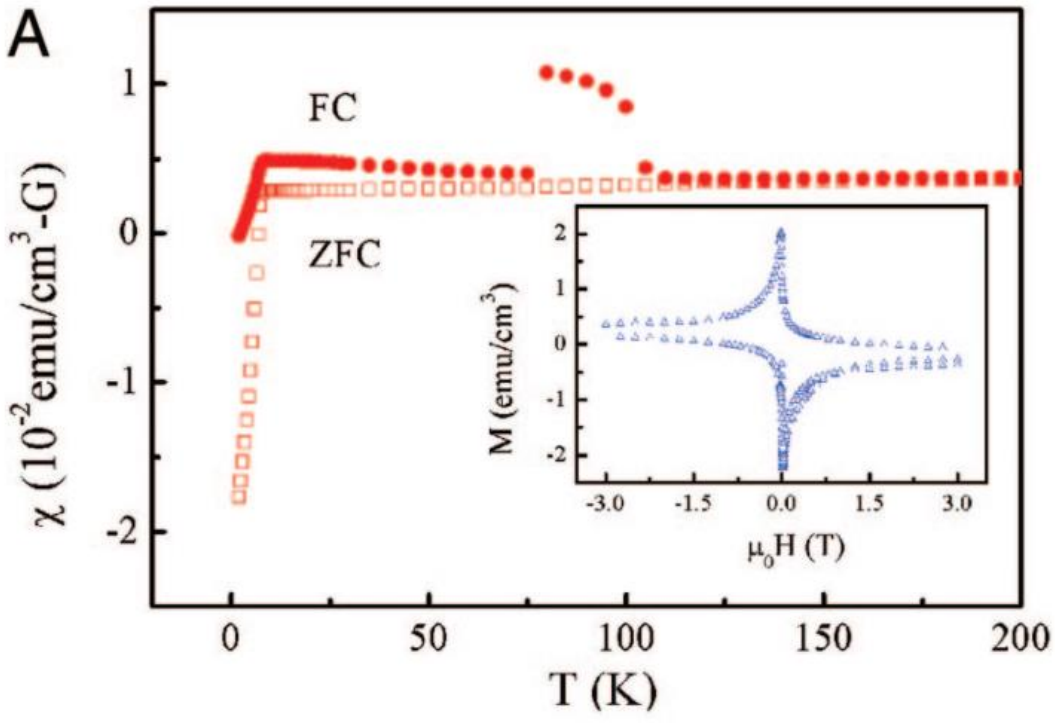

Fig. 2-9 χ(T) of FeSe.
Fig. 4A, Hsu *et al*. [117]. "ZFC" is short for zero field cooldown and "FC" is short for field cooldown with B=3mT. Inset: M(B) at T=2K.

2.2 Quasi-1D Materials (bundled chains)

There has been interest in quasi-1D materials due to theoretical predictions of exotic phenomena in 1D many-body systems (e.g. Peierls instability, Luttinger liquid [5]). Materials include conducting polymers [12], carbon nanotubes [29] and $NbSe_3$ [124]. In some materials, such as conducting polymers, the 1D object is difficult to extract from the bulk. In blue bronze ($K_{0.3}MoO_3$) [10], the 1D conduction channel is supported by charge transfer to the surrounding chemical species and extraction from the bulk would destroy the material.

In contrast, TMC form MX_3 chains, which are bound to other chains through weak van der Waals forces. As illustrated in Fig. 2-10 with $NbSe_3$ as an example, a Nb (metal) atom bonds to three Se (chalcogen) atoms and another Nb atom bonds to the Se on the other side. The chain grows longer in this manner and results in a covalently bonded chain of Nb atoms with triangular planes of Se in between. $(NbSe_4)_nI$ does not have the same structure as MX_3 but is introduced below as an analog to MX_3-like chains with inter-chain bonds mediated by charge transfer.

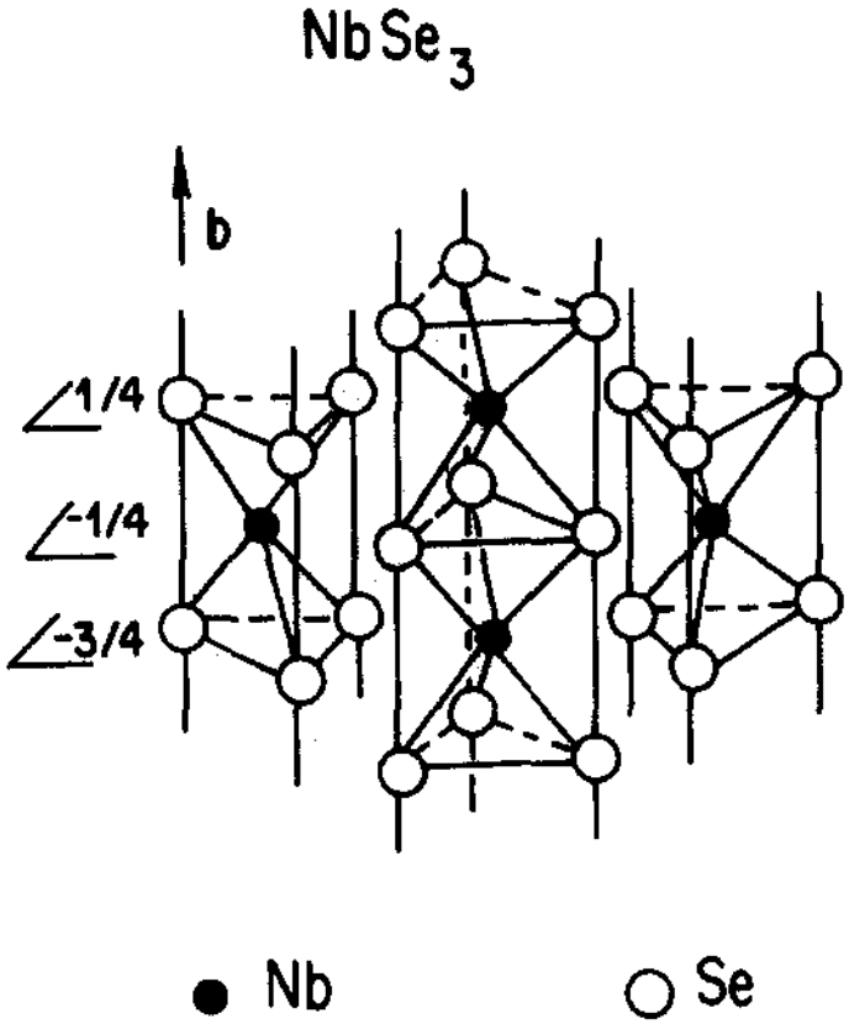

Fig. 2-10 Crystal structure of $NbSe_3$.
Fig. 3.1, Grüner and Zettl [10].

2.2.1 $NbSe_3$

$NbSe_3$ forms atomic chains shown in Fig. 2-10. As shown in Fig. 2-11, R(T) is overall metallic with sudden increases in resistance at T_{P1}=144K and T_{P2}=59K, corresponding to the upper and lower CDW transitions, respectively. For both transitions, the increase in resistance is consistent with the CDW gap opening but the system recovers metallic behavior as it is cooled further. The Fermi surface of $NbSe_3$ is not completely gapped and the remaining metallic part of the Fermi surface dominates over the gapped part.

Both the upper and lower CDW in $NbSe_3$ slide when biased with $E>E_T$ (see section 1.2.2). $NbSe_3$ has been a prototypical material for sliding CDW studies and deeper understanding of the phenomena (e.g. narrowband noise [125] and plasticity [126,127]).

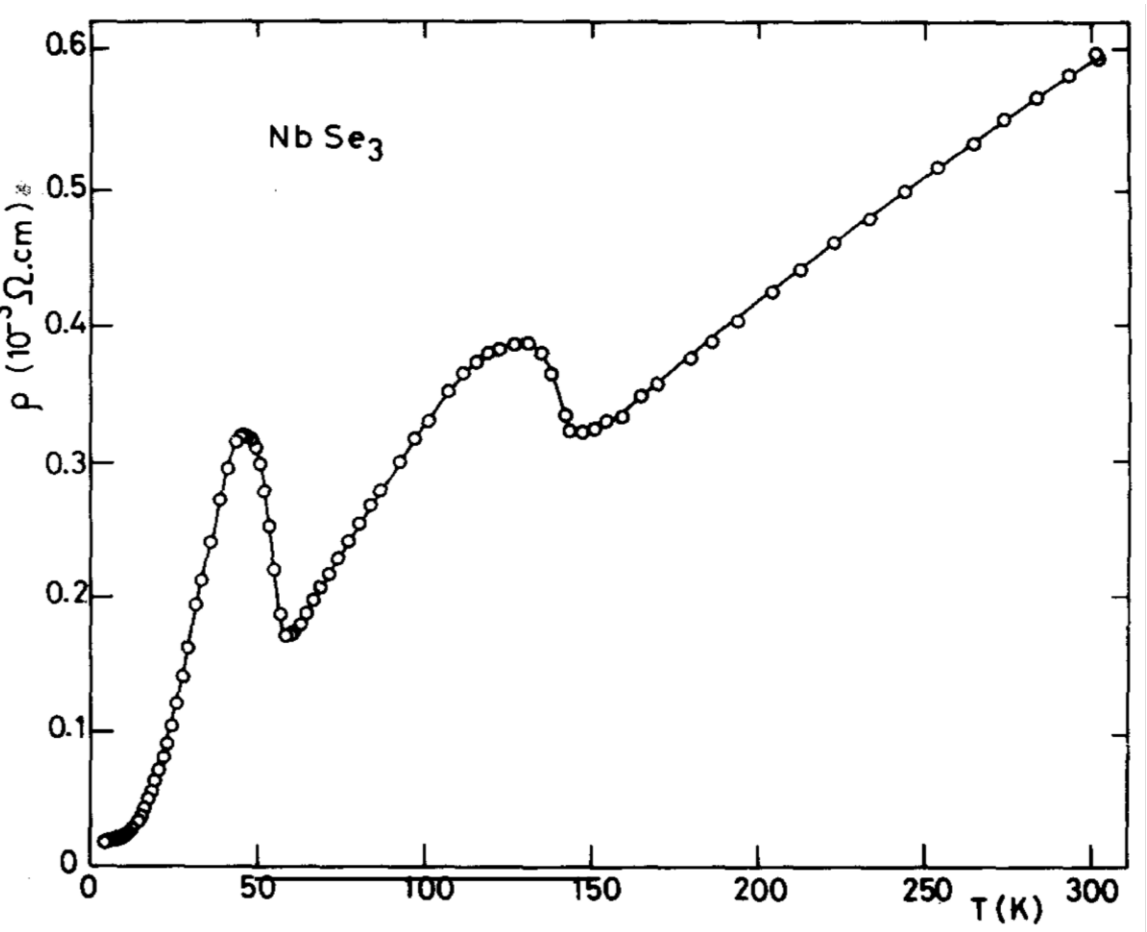

Fig. 2-11 R(T) of $NbSe_3$.
Fig. 2, Chaussy *et al*. [80].

2.2.2 TaS_3

TaS_3 has a similar crystal structure to $NbSe_3$ (see Fig. 2-10), where Ta replace the Nb atoms and S replace the Se atoms. Fig. 2-12 shows the normalized conductivity of TaS_3 against 1/T. As increasing 1/T corresponds to lowering T, the graph indicates a sharp decrease in conductivity below T_P. The CDW transition appears as a peak at T_P=215K in the numerical derivative shown in the inset. Similar to $NbSe_3$, sliding CDW behavior was observed [128]. In contrast to $NbSe_3$, the conductivity of TaS_3 continues to decrease for $T>T_P$=215K, which indicates that the Fermi surface is completely gapped. Transport study of the CDW conduction in TaS_3 is simplified by the absence of a metallic portion. TaS_3 with T_P=215K is distinguished as orthorhombic TaS_3, with the subsequent discovery of monoclinic TaS_3, which exhibits two CDW transitions at T_{P1}=240K and T_{P2}=160K.

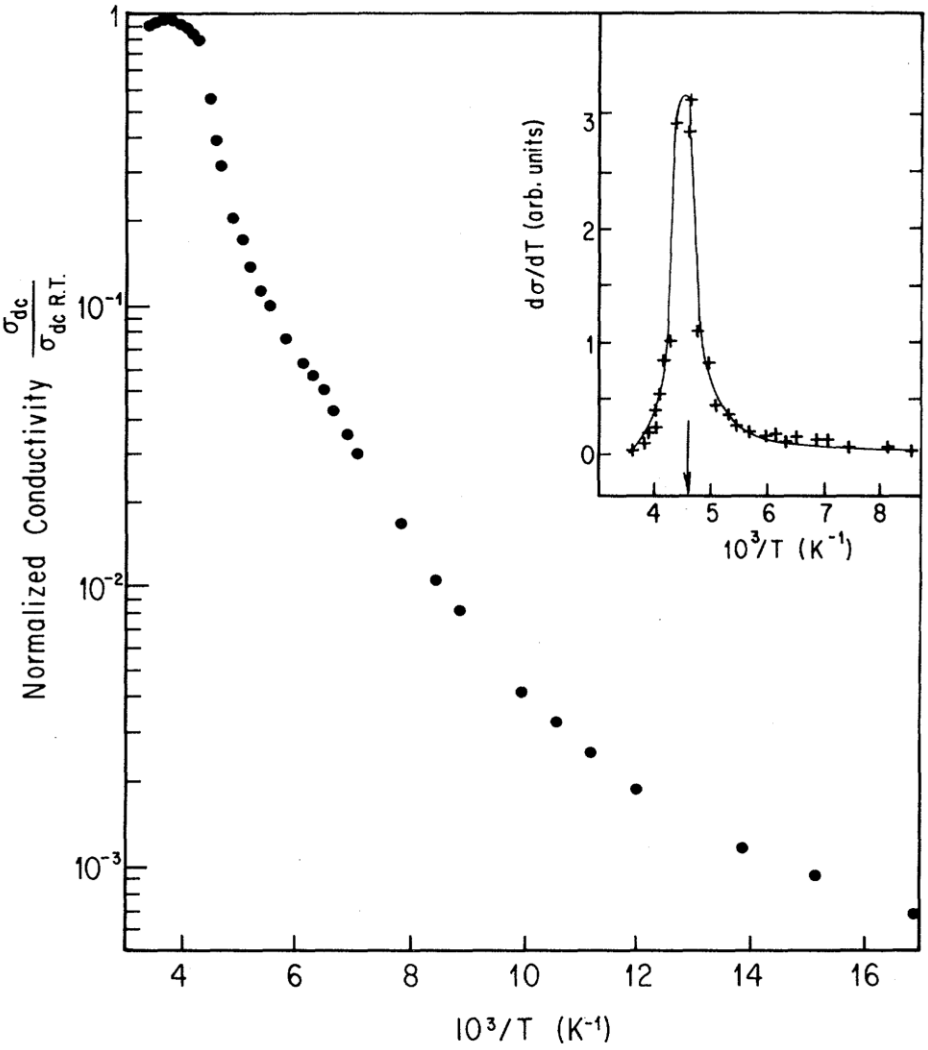

Fig. 2-12 σ(1/T) of TaS_3.

Fig. 1, Thompson *et al*. [128]. Inset: numerical derivative of σ(T) indicates a metal-insulator transition at T_P=215K.

2.2.3 $(NbSe_4)_nI$

$(NbSe_4)_nI$ belongs to the class of $(MX_4)_nY$, where Y is either iodine or bromine (not yttrium). As shown by the structure on the right of Fig. 2-13, $(MX_4)_nY$ forms MX_4 chains, which are charge balanced by the Y chemical species between the chains. n is the coordination number between the MX_4 chains and periodically occurring Y species. As the inter-chain interactions are mediated by charge transfer, the MX_4 chains are more closely electronically coupled to each other than MX_3 chains.

$(NbSe_4)_2I$, $(NbSe_4)_{3.33}I$ and $(TaSe_4)_2I$) are known to have a sliding CDW at T_P=210K, 285K and 265K, respectively [78]. $(NbSe_4)_3I$ exhibits an anomalous kink in R(T) at T=274K, but the behavior is thermally activated for both above and below the kink. Unlike its n=2 variant, $(NbSe_4)_3I$ is a semiconductor, which undergoes a ferrodistortive structural transition at T=274K [78].

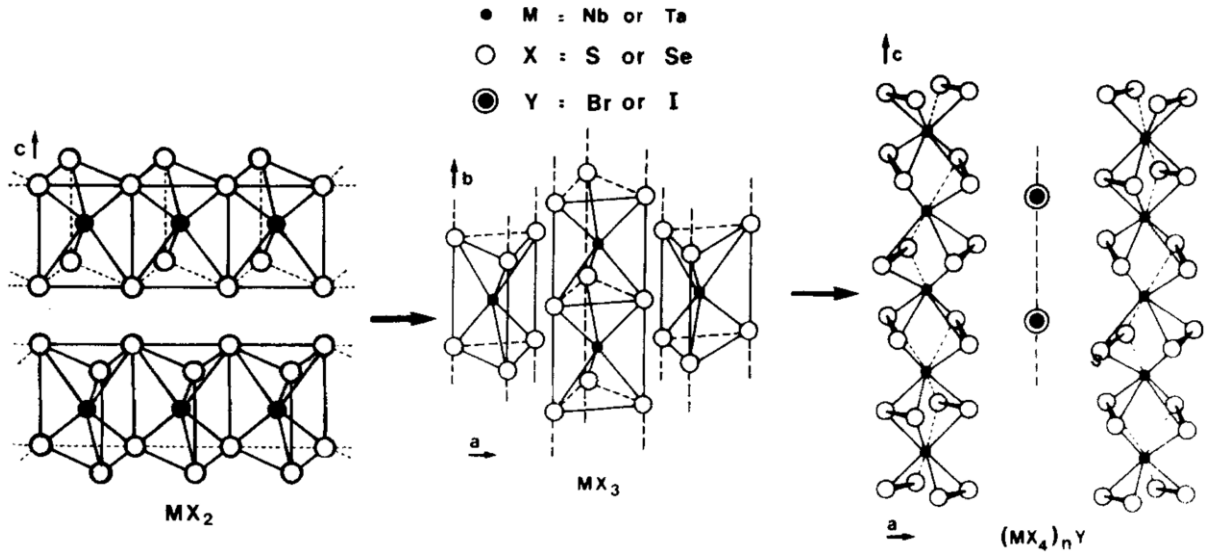

Fig. 2-13 Comparison of MX_2, MX_3 and $(MX_4)_nY$ crystal structure.
Fig. 1, Gressier *et al*. [288].

2.3 Ultrathin limit

Since the isolation of graphene from graphite by mechanical exfoliation in 2004 [23], the study of layered materials at the ultrathin limit (~10nm) has been a popular field. In particular, materials at the monolayer limit have exhibited extraordinary electronic properties. The manipulation of ultrathin layered materials has evolved to the creation of creation of van der Waals (vdW) heterostructures. Background on mechanical exfoliation, the monolayer limit and vdW heterostructures are provided in this section, as they are relevant to the motivation behind the experiments discussed in Chapters 4-7.

2.3.1 Mechanical exfoliation

Often called the "Scotch tape" method, mechanical exfoliation has been applied to many layered materials [129]. With mechanical exfoliation, materials have been studied at the ultrathin limit, where their collective ground states become strongly dependent on thickness [46,47,96,130]. The thickness dependence of collective ground states provides insight into the role of interlayer coupling for the collective ground states [22].

As illustrated in Fig. 2-14, an adhesive tape is first pressed on to the layered material. When the tape is peeled off, some layers of the material remain stuck on the tape. Often, the portion of the tape with the layered material is pressed onto other clean parts of the tape and peeled off multiple times to "thin down" the material. Finally, the tape is pressed onto a substrate and removed. With this method, thin flakes of the layered material are transferred to a substrate and some monolayers can be found among the flakes. For further details on mechanical exfoliation are presented in the doctoral dissertation by Çağlar Girit (section 2.1 [131]).

The identification of graphene was equally important as mechanical exfoliation for isolating graphene. Intuition might suggest that any material would be difficult to see with an optical microscope if it is only a single atom thick. However, optical interference effects enable graphene to be seen by an optical microscope when it is on top of a silicon wafer coated with a 300nm thick layer of SiO_2 [27]. This effect is applicable to other materials (e.g. transition metal dichalcogenides [132]), given that the SiO_2 thickness is adjusted to match the optical properties of the material. Since graphene, many layered materials have thinned down to the monolayer limit [42,43,133].

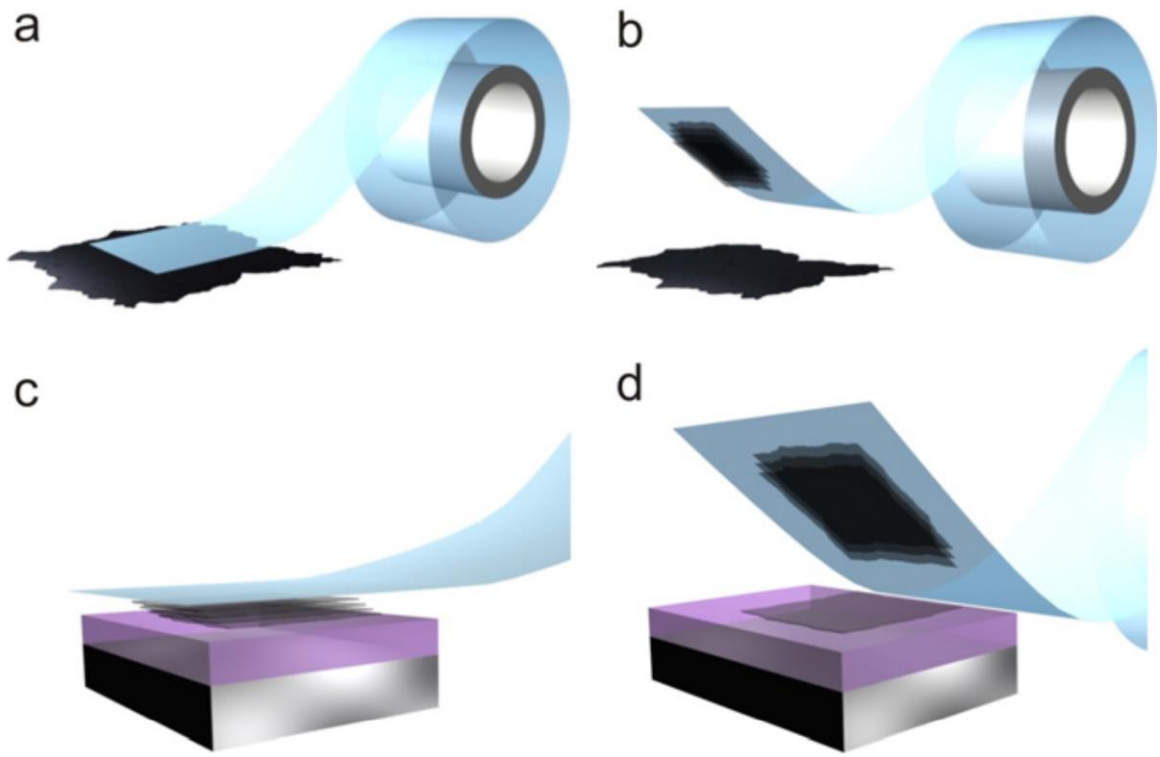

Fig. 2-14 Mechanical exfoliation schematic.
Fig. 1, Novoselov and Neto [289].

2.3.2 Monolayer limit

A layered material's behavior usually changes significantly when it is isolated as a monolayer. Even at the ultrathin length scale, the monolayer is distinct because a unique crystal symmetry is realized only in the absence of other layers. The bandgap in MoS_2 is direct for the monolayer but is indirect for bilayer and thicker [134]. The unique electronic structures in some monolayers have given rise to remarkable physical properties. In graphene, the charge carriers behave as massless Dirac fermions [57]. Photoluminescence is exceptionally strong in monolayer MoS_2 from spin-orbit coupling effects, which are unique to the monolayer [134].

2.3.3 van der Waals heterostructure

In ultrathin materials, the surface and interface effects play larger roles as the surface/bulk ratio is reduced. It is anticipated that novel phenomena can be probed at the interface of different ultrathin materials. For example, the moiré pattern formed by lattice mismatch in a graphene/h-BN stack led to the realization of the Hofstadter butterfly, a theoretically predicted quantum fractal phenomenon [135,136]. The proposed assembly of "van der Waals heterostructures" formed by stacking layered materials as illustrated in Fig. 2-15 has attracted attention [41]. As shown in Table 2-2, there is a rich landscape of layered materials in which combinations of materials can be selected to form interfaces mediated by vdW forces.

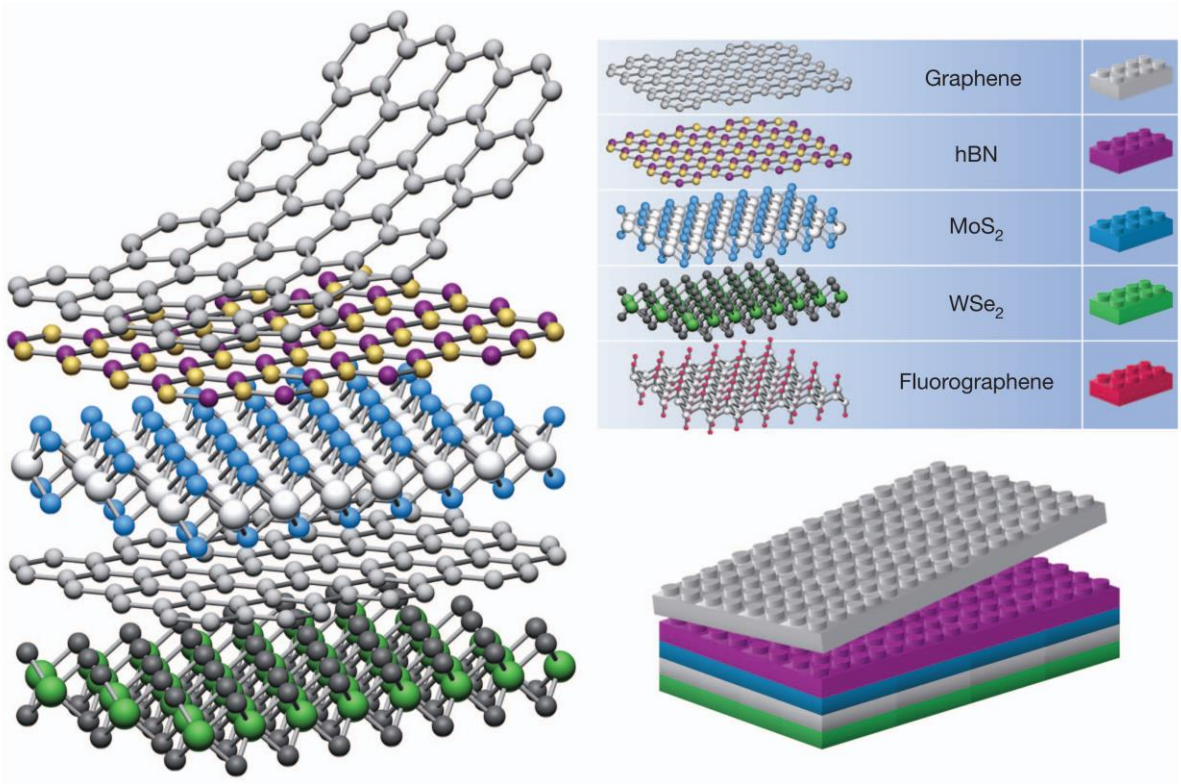

Fig. 2-15 van der Waals heterostructure schematic.
Fig. 1, Geim and Grigorieva [41].

Graphene family	Graphene	hBN 'white graphene'	BCN	Fluorographene	Graphene oxide
2D chalcogenIdes	MoS_2, WS_2, $MoSe_2$, WSe_2	Semiconducting dichalcogenides: $MoTe_2$, WTe_2, ZrS_2, $ZrSe_2$ and so on		Metallic dichalcogenides: $NbSe_2$, NbS_2, TaS_2, TiS_2, $NiSe_2$ and so on	
				Layered semiconductors: GaSe, GaTe, InSe, Bi_2Se_3 and so on	
2D oxides	Micas, BSCCO	MoO_3, WO_3	Perovskite-type: $LaNb_2O_7$, $(Ca,Sr)_2Nb_3O_{10}$, $Bi_4Ti_3O_{12}$, $Ca_2Ta_2TiO_{10}$ and so on	Hydroxides: $Ni(OH)_2$, $Eu(OH)_2$ and so on	
	Layered Cu oxides	TiO_2, MnO_2, V_2O_5, TaO_3, RuO_2 and so on		Others	

Table 2-2 Library of quasi-two dimensional materials.
Fig. 2, Geim and Grigorieva [41].

Sophisticated techniques for creating van der Waals heterostructures have been developed and adopted by many research groups [43,137,138]. Many of the early use of heterostructures were for protection from impurities [137] and air degradation [43], using h-BN as a substrate and capping layer. Wang *et al*. demonstrates that encapsulation in h-BN minimizes impurity effects in graphene [137]. The superior quality is due to the h-BN providing an atomically smooth substrate and the manipulation of graphene without using polymers. In addition, Cao *et al*. shows that when air sensitive materials (e.g. black phosphorous and monolayer $NbSe_2$) are encapsulated with h-BN, they are protected from degradation in air [43].

Currently, vdW heterostructures of layered materials with h-BN are the most prevalent. However, h-BN is an insulator and it is often used to facilitate access to the pristine physical properties of another material. There is increasing interest in vdW heterostructures, in which both components are electronically active [139,140]. If two collective ground states, which normally reside in different materials are made to interact at the interface, novel electronic state could arise. The materials introduced in this chapter are rich in many-body effects (e.g. superconductivity, CDW and Weyl fermions) and are synthesized, as discussed in Chapter 4, to study their interaction in van der Waals heterostructures.

3 Low temperature measurement apparatus

Many of the sample characterization and measurement in the subsequent chapters involve measurement at low temperatures: from room temperature down to liquid helium temperature (4.2K) or sometimes 50mK. Low temperatures are required since the characteristic electronic ground states of the materials studied (e.g. transition metal chalcogenides) often occur below room temperature. Specialized instruments (cryostats) and techniques are required to reach low temperatures and this chapter details the instruments employed. In principle, cryostats can be adapted to host a wide range of characterization techniques. Most of the cryostats presented in this chapter are for electrical transport and magnetoresistance measurements. As an exception, the MPMS measures magnetization.

3.1 Electrical transport measurements

Samples are primarily characterized by electrical transport measurements. Often the transition to electronic ground states of interest show signatures in the temperature dependence of the sample resistance R(T). For example, superconductivity results in a drop to zero resistance as the sample is cooled below the critical temperature and CDW exhibits a "resistive anomaly", in which the resistance rapidly increases with cooling below the CDW transition. For sliding CDW, electrical transport is one of the clearest ways to demonstrate its occurrence. Various other physical probes (e.g. magnetization, thermal conductivity and heat capacity) have been established as general low temperature measurement techniques in experimental condensed matter but electrical transport is the simplest measurement to set up.

3.1.1 Sample preparation

Wires are attached to the electrical contacts of the samples, which allows a continuous electrical pathway from the sample to the measurement instruments located outside the cryostat. Samples are typically wired up as shown in Fig. 3-1. The work should be performed under a stereo microscope with tweezers. TDI-5A-SA-I tweezers and No.11 scalpels are recommended for manipulation of the gold wires. With this technique, electrical contacts can be made to samples of size >200μm.

The sample is electrically contacted by attaching Ø25μm gold wires with silver paste. It is crucial to use wires of small diameter to prevent them from popping off while changing the sample temperature. If cooling to liquid helium temperature, thermal contraction/expansion significantly moves the relative position of the wires. In such a case, a thin, flexible wire allows the strain to be relieved by bending whereas a thick, rigid wires would not. In addition, the gold wires should be annealed by flowing current through it until it grows red hot. The annealed wires are pliable and easily guided to the desired placement, whereas unannealed wires are too springy to stay in their guided configurations. The silver paste is Dupont 4929 with thinners either Dupont 4987 or 2-n-butoxyethyl acetate to tune the consistency. The consistency should be thick enough to prevent silver paste from flowing to other undesired locations on the sample and thin enough to allow time to paint with it before drying. A wooden stick with a piece of Ø25μm (unannealed) gold wire attached at the end makes a good "paint brush".

An alternative to painting gold wires to the sample is to wire bond. This often requires contact pads to be pre-made on the sample by evaporating metal and often used for lithographically fabricated devices of nanoscale materials (Part II9.1). The contact pads need to be clean and flat for successful bonding. 50-100nm thick gold pads of width and length 200μm are best for comfortably making contact with wire bonding. The drawback of wire bonding is that it could damage the material since it sends substantial energy as ultrasonic waves during the bonding process. Although it lacks the versatility of silver paste, wire bonding can rapidly contact many samples for which the bonding parameters are optimized.

From the sample, the wires are connected to the quartz that the sample is attached to. The junction between the wires and the quartz serves as "anchor points" which act as stress relief when the relative position of the components change by thermal expansion/contraction. The wires between the sample and anchor points should bow as shown in Fig. 3-1 to minimize stress on the junctions. The anchor points are important for their mechanical purpose and have no electrical purpose. In practice, it is simpler to first glue down the sample with superglue to the

quartz and then glue down wires, cut to the appropriate length, at the anchor points. Finally, guide the wires to the desired placement on the sample and paint the junctions between the wires and the sample. From the anchor points, gold wires should be connected to contacts on the cryostat, which ultimately interface to measurement instruments.

The sample is attached to a copper block in the cryostat with GE varnish (VGE 7031) to ensure good thermal contact to the copper. GE varnish allows mounted samples to be removed by applying a little force and the remaining GE varnish can be cleaned off with isopropanol. Since copper has good thermal conductivity, the temperature is assumed to be the same anywhere on the copper and the sample temperature is measured by a temperature sensor located on the copper block, close to the sample. The sample temperature is controlled by controlling the temperature of the copper block with heaters.

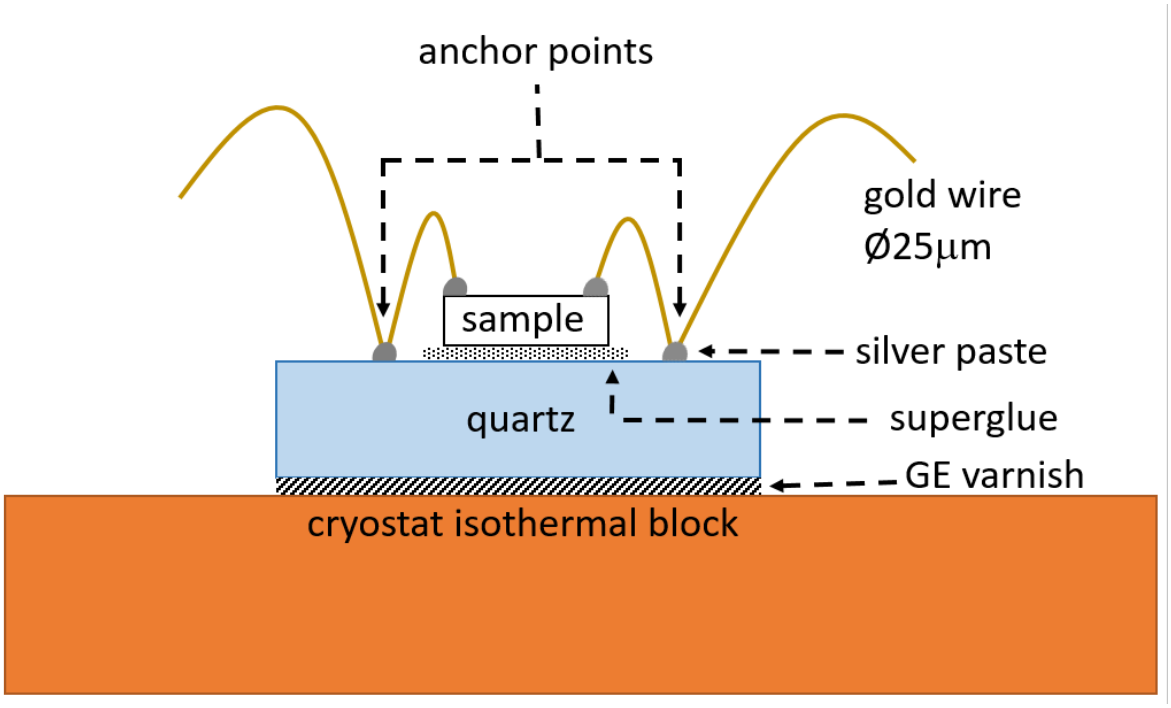

Fig. 3-1 Sample mounted for low temperature transport.
The sample is mounted to be in good thermal contact with a copper block in the cryostat and electrically contacted with silver paste and gold wire.

3.1.2 Nb test sample

To test the thermometry of the homemade systems, a sample of known R(T) is measured. Since niobium is a superconductor below 9.2K [141], the sharp drop in resistance provides a well-defined feature to check the accuracy of temperature measurement. The niobium sample is a RF sputtered thin film on Si/SiO_2, provided by Aritoki Suzuki, a post-doctoral researcher in the Adrian Lee group. Niobium thin film deposition with the electron beam evaporator did not show superconductivity. Niobium thin film deposition is notoriously sensitive to deposition conditions and the superconductivity was likely quenched by heavy disorder. The thin film form is desirable

since the small cross-section makes the sample resistance high enough to yield a measurable voltage drop for the nanovoltmeter. Although with a thickness of >200nm, the thin film T_c should be comparable to the bulk, there are reports where the film deposition conditions could raise the T_c to 9.7K [142]. In hindsight, a wire of narrow diameter would have avoided complications from film deposition conditions.

Four contacts are placed on the corners of the niobium film by wirebonding. A thin layer of niobium oxide forms on the surface, which is a conductor at room temperature but an insulator at low temperature. Hence, it is necessary to break through the oxide with wirebonding and silver paint cannot be used.

3.1.3 Resistance measurement

To measure the dc resistance of the sample, the sample is measured in a four-point probe configuration. Excitation is supplied by the current source (Keithley 2400 or 2602) and the voltage is measured by the nanovoltmeter (Keithley 181). The current leaving the current source is measured and recorded for each measurement. If the sample resistance becomes too high, the current source is unable to provide the programmed value of the current. The drop in source current appears as a drop in voltage and could be misinterpreted as a drop in resistance if we do not track the actual value of the sourced current.

When the sample is at low temperature, there is a significant temperature difference between the sample and the measurement electronics, which is always at room temperature. The thermal gradient causes a thermoelectric voltage ξ across the wires that connect the sample and the measurement electronics. The voltage for the current bias (I_{exc}) in one direction (V_+) and in the reversed direction (V_-) is measured for each temperature to cancel voltage offset ξ according with the formula:

$$R = \frac{V_+ + \xi - (V_- + \xi)}{2|I_{exc}|} \qquad \text{Eq. 3-1}$$

To ensure that the sample settles from any transient response, the voltage is measures 1s after the switch in current direction.

3.2 Homemade system

Before the commercial systems became prevalent, homemade cryostats were the standard for experiments at low temperature. Homemade systems are simpler in design and can be easily customized for a desired purpose. The equipment introduced below were made and used by past Zettl group members but needed to be refurbished as they were not in use for some time. The gas flow cryostat and the bath cryostat are introduced in this section. The gas flow cryostat is well-suited for fast cooldowns of multiple samples, as the sample can be exchanged without taking out the cryostat from the helium bath. The gas flow cryostat cannot hold a sample at low temperature for a long time, as it consumes the most helium at low temperature. In contrast, the bath cryostat is well-suited for maintaining the sample at low temperature for a long period of time and temperature sweeps of low sweep rates. However, the probe needs to be taken out of the helium bath when loading a new sample and significant amount of helium is lost when reinserting the probe. In addition, the doping vessel is introduced in this section. It is a module, which fits in the bath cryostat probe for *in situ* measurement of samples after chemical modification in a sealed environment.

3.2.1 Gas flow cryostat

The gas flow cryostat cools the sample with a flow of cold helium gas. As shown in Fig. 3-2, the cryostat is a tube with a double concentric tubes running from the gas inlet end (magnified in bottom panel) to the sample space (magnified in top panel). The gas inlet end of the cryostat goes inside a bath of liquid helium (e.g. a storage dewar). Considering the length of the cryostat, a standard 60L storage dewar is the most suitable. A resistor (R~500Ω) is attached to the bottom of the cryostat and immersed inside the liquid helium. Wires, running up from the resistor to outside the dewar, is connected to a variac. The resistor works as a gas flow control heater, where the power to the heater controls the rate of cold helium gas release. The power is controlled by the variac setting (100% power corresponds to the 120V ac, from the electrical outlet). The resistor should be a metal film type and ceramic resistors should not be used as they will become insulating in liquid helium.

When the flow control heater is powered, helium evaporates and pressurizes the dewar. As shown in the bottom magnification panel, the helium gas goes: 1) into the cryostat through a hole at above liquid level, 2) down to the opening of the inner tube at the bottom and 3) back up through the inner tube. The helium gas is cooled when it goes down the outer tube to the inner tube since the outer tube is in thermal contact with a bath of liquid helium. The cold helium gas is carried to the sample space at room temperature through the inner tube, while the superinsulation and vacuum jacket between the inner and outer tube provides thermal insulation.

As shown in the top panel, the cold helium gas shoots out to the sample space at the top of the cryostat. The probe is mounted in a way, such that the rubber stopper plugs up the hole at the top of the cryostat (facing the right side of the image) and the sample is placed in the stream of cold helium gas. As indicated by the blue arrows, the cold gas goes: 1) through the sample space, 2) back through the space between the inner and outer cylinder and 3) out through the exit ports on the left side of the image. The exit ports should be open during a cooldown and regulation of flow through the ports can provide a coarse control over the temperature. When the cryostat is not in use, the exit ports should be closed and the hole on the right should be plugged up to avoid ice blocks.

Fig. 3-3 shows the probe for the gas flow cryostat. The probe is essentially a rubber stopper, which fits into the opening of the gas flow cryostat, and a support rod which holds the sample. The support rod is made of thermally insulating material, such as wood or stainless steel. Twisted pairs of wires run along the support rod to provide electrical connection from the sample end of the probe to BNC connectors on the other end. #40 AWG copper wire with enamel insulation are used, as wires of large diameter leak in too much heat from room temperature. At the sample end, the wires connect to contact pads on the copper plate. The contact pads are circles of silver epoxy (H20E) on top of Stycast (2850FT), which insulates the silver epoxy from the copper. The sample is mounted on a copper plate by GE varnish and electrical contacts are made to the contact pads. A silicon diode is placed on the bottom side of the copper plate, close to the sample to monitor the sample temperature.

The sample is protected from the direct stream of cold gas with a copper can, which attaches to a rubber stopper. The copper can and the stopper does not form a complete seal and some gas can leak in and fill the inside of the gas with helium. Ø0.008in manganin wire is non-inductively wound around the copper can to work as the temperature control heater. The temperature of the sample is finely controlled by controlling the power to this heater. When incorporated in a PID loop based temperature controller (Lakeshore 340), the probe can hold a constant temperature or ramp temperature up and down with controlled ramp rates. When using the PID loop, the temperature feedback should be based on the "control diode", which is placed on the can to provide close feedback to the change in heater power. The sample diode does not respond quickly enough to the change in heater power and causes the system to oscillate in temperature. The control diode is placed on the inside of the can because direct exposure to the stream of cold gas results in large temperature gradients.

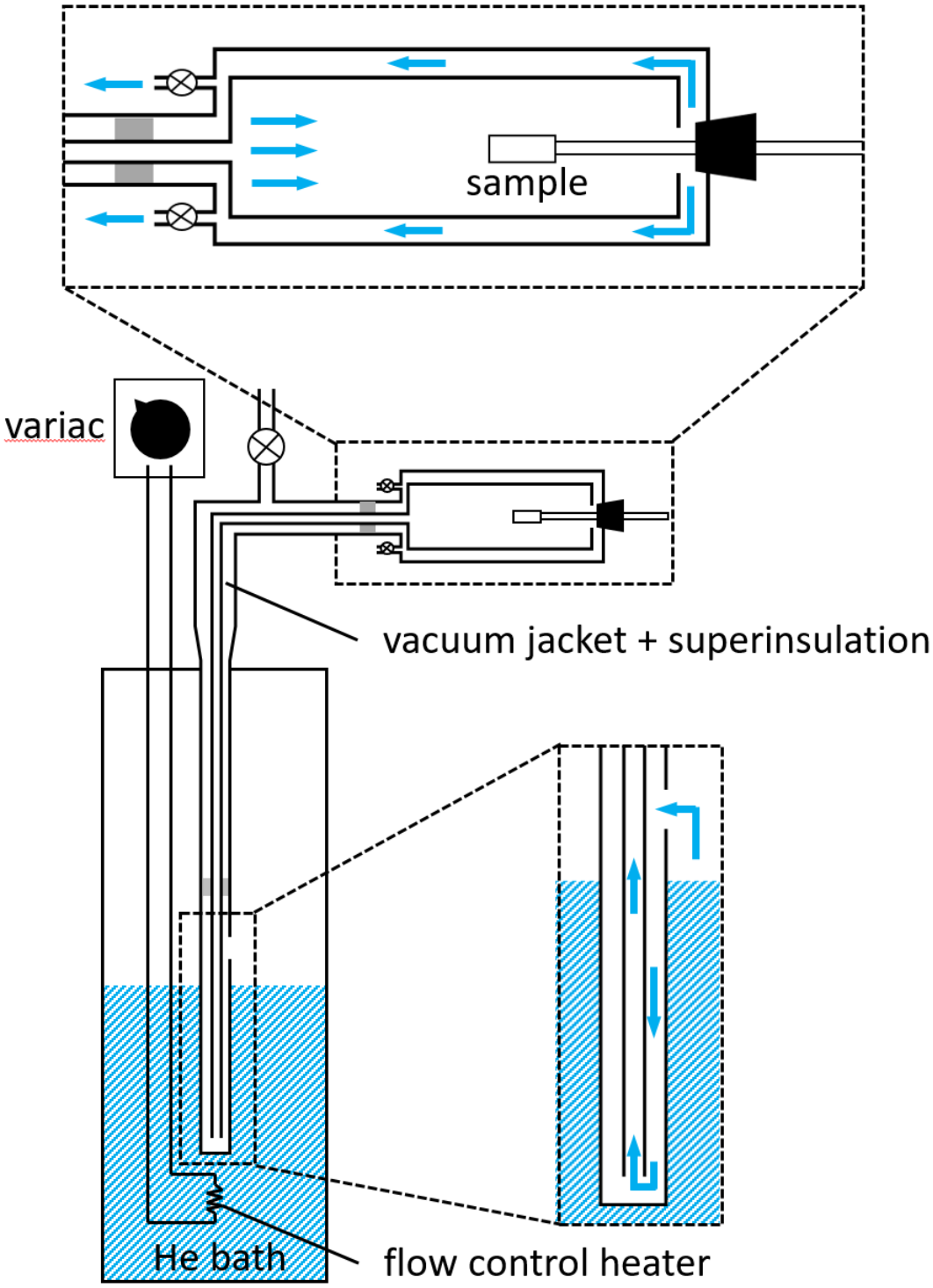

Fig. 3-2 Gas flow cryostat.
The gas intake portion and sample space are magnified and blue arrows are added to indicate helium gas flow.

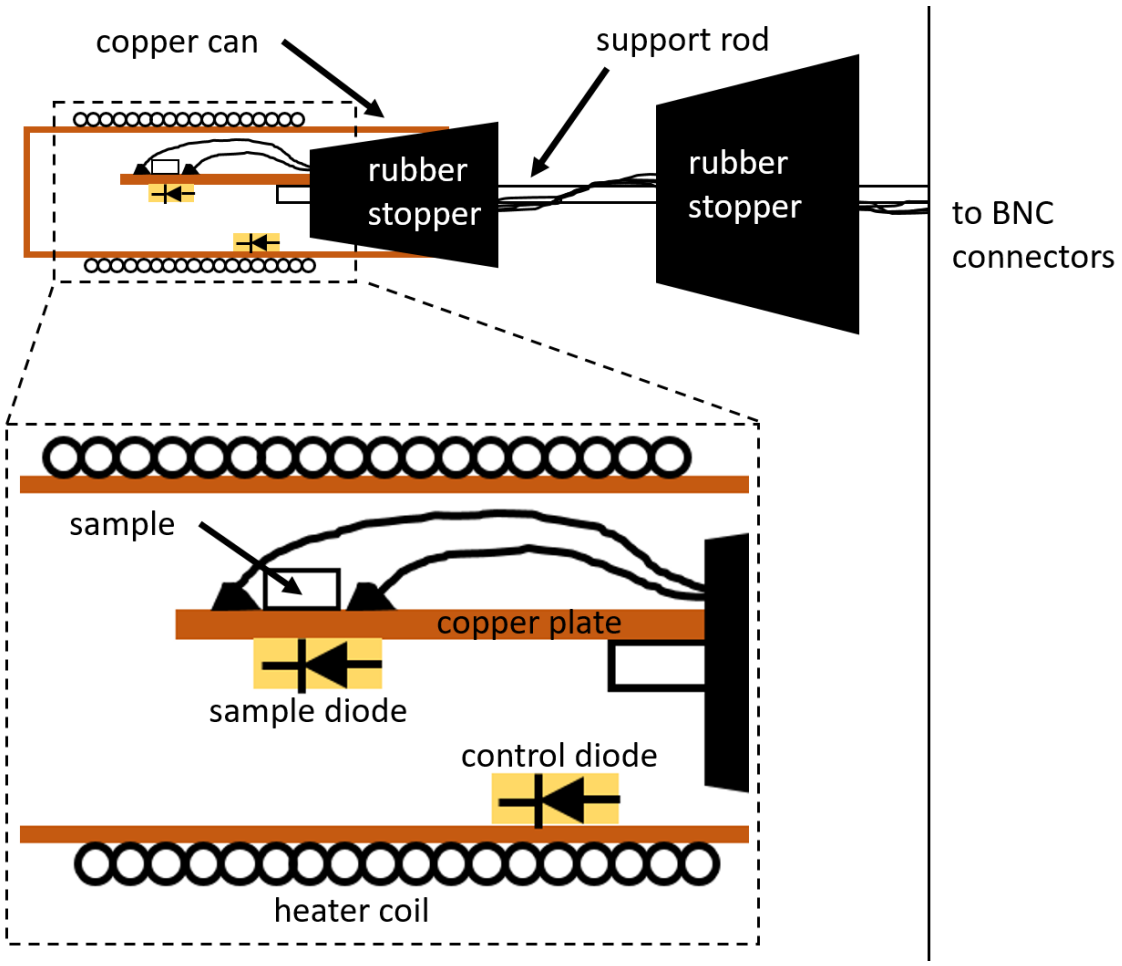

Fig. 3-3 Probe for gas flow cryostat.
The large rubber stopper (right) fits into the opening of the gas flow cryostat sample space. Sample is mounted on a copper plate and twisted pairs run along the support rod to provide electrical connection from the sample to BNC connectors. The sample diode reads the sample temperature and the control diode is part of a feedback loop based temperature control system.

The cryostat enables rapid cooldown, as the sample is immersed in cold gas and makes good thermal contact with the coolant. Fig. 3-4 shows a typical cooldown time of the gas flow cryostat. At time=5min, the power to the flow control heater (P_{heat}) is increased from 0% to 20% with the variac. Cold gas begins to flow into the sample chamber and the sample temperature decreases rapidly to T~25K in 5min. The cooling rate slows down after reaching T~25K but the temperature drops further to T~15K when P_{heat} is increased to 50%. At time=15min, the temperature is increased by slowly ramping down P_{heat}. At high flow (P_{heat} =80%) and longer cooling time (~30min), the cryostat can reach T=4.7K. The gas flow rate can be increased by pressurizing the helium dewar with helium gas, as typically done while transferring liquid helium to another dewar. However, this results in an *increase* in sample temperature, as the heating effect of introducing warm helium gas is greater than the benefits of increased flow rate.

Even without a feedback loop, well-controlled temperature ramps can be performed by controlling the power to the flow control heater. Fig. 3-5 shows the resistance of a niobium thin

film (see section 3.1.2) for T=290-8K. The resistance is measured by four wirebonded contacts with 100μA dc current bias. R(T) is overall metallic and the resistance drops to zero at 9.3K, consistent with the superconducting transition in niobium. For low temperature, the temperature ramp rate is limited to <0.5K/min. The inset shows a magnification of the superconducting transition. The hysteresis between the cooldown and warmup R(T) curve of ~0.04K is small and indicates the sample and the temperature sensor is in good thermal contact to the cryostat.

The temperature stability with a PID loop was characterized in collaboration with Jacob Bryon. Fig. 3-6 shows the temperature reading from the sample diode while the temperature controller is set to hold the temperature fixed at ~30K. The temperature controller uses the input from the control diode to adjust the heater power. The temperature fluctuation is less than ±0.1K from the mean value. After 4min, the mean value drifts by ~0.1K.

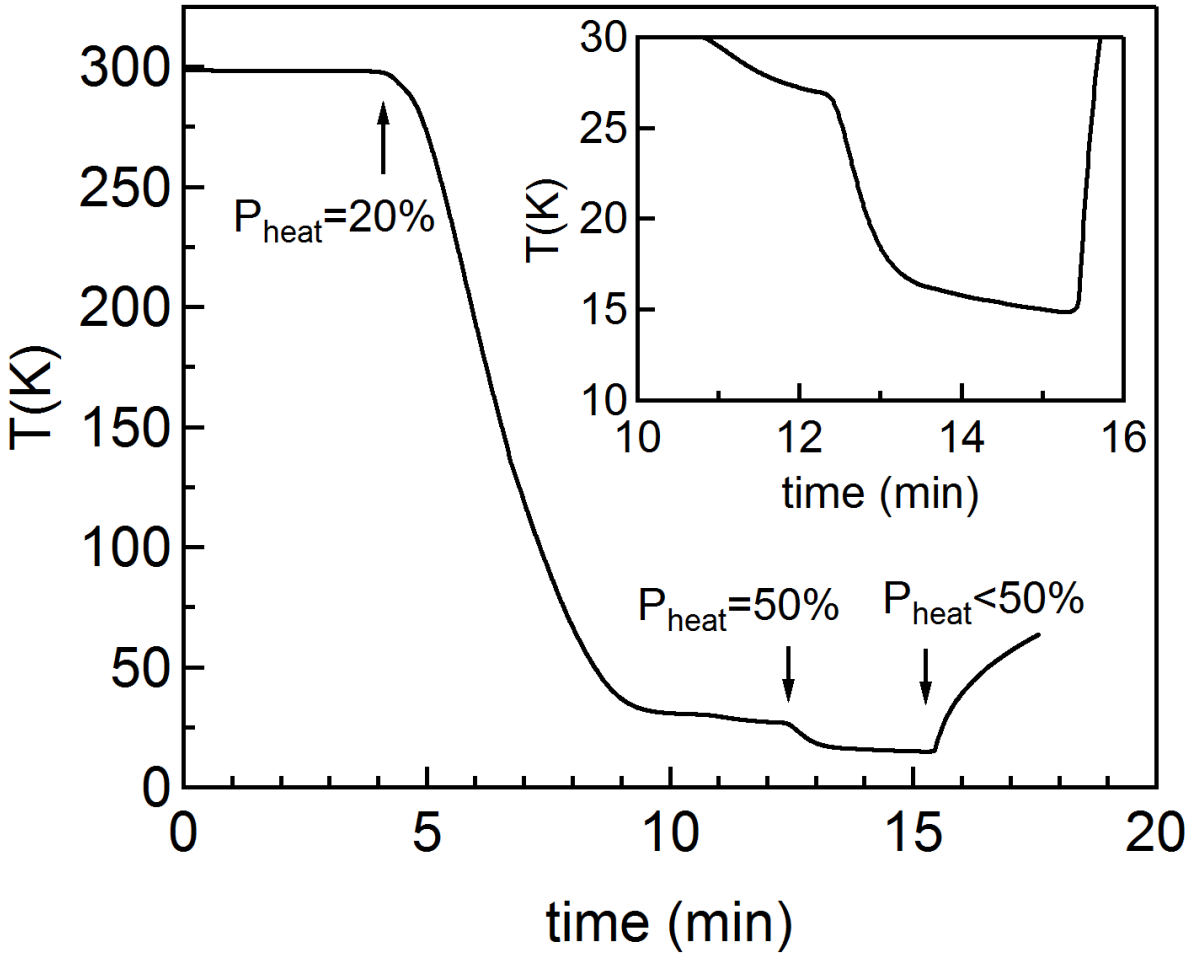

Fig. 3-4 Cooldown time of gas flow cryostat.
The power to the helium flow control heater (P_{heat}) is adjusted with a variac. The arrows mark the points at which P_{heat} was changed. Inset: magnification of low temperature data at time=10-16min.

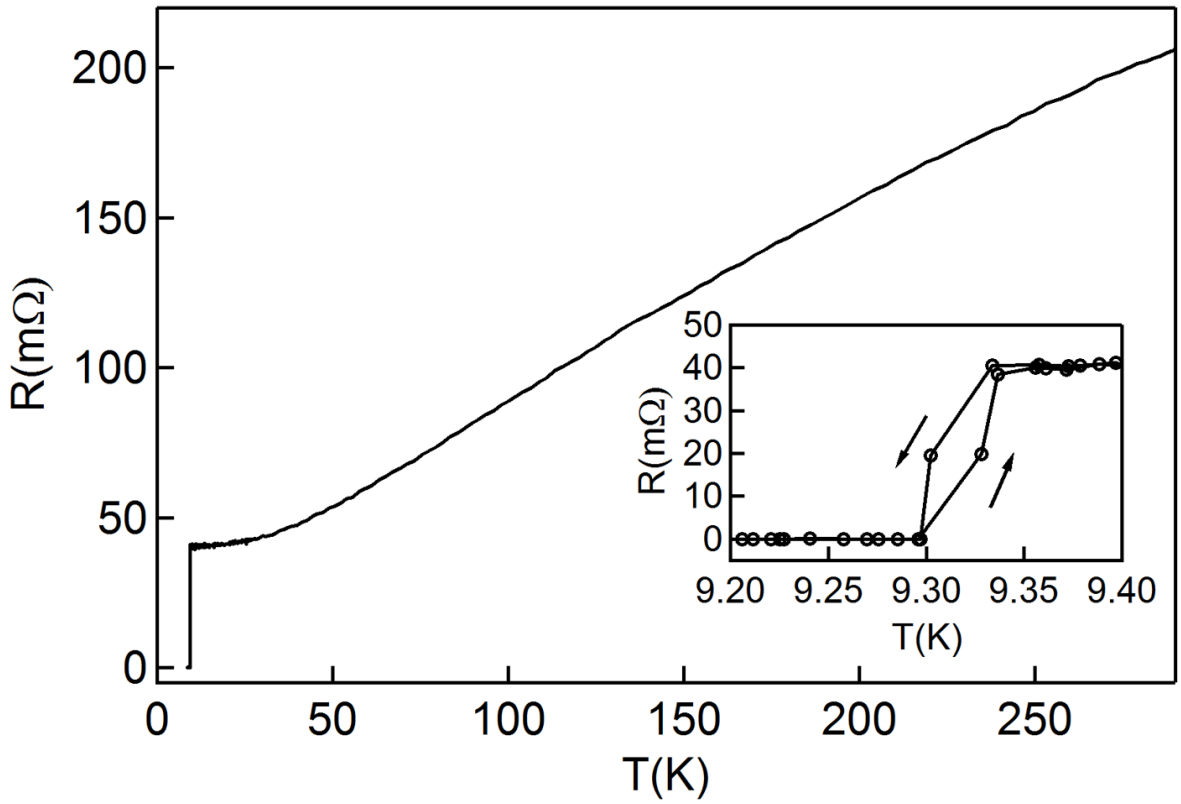

Fig. 3-5 R(T) of Nb measured with gas flow cryostat.
Resistance of RF sputtered Nb film for T=290-8K. Inset: superconducting transition at 9.3K. Arrows indicate direction of temperature change.

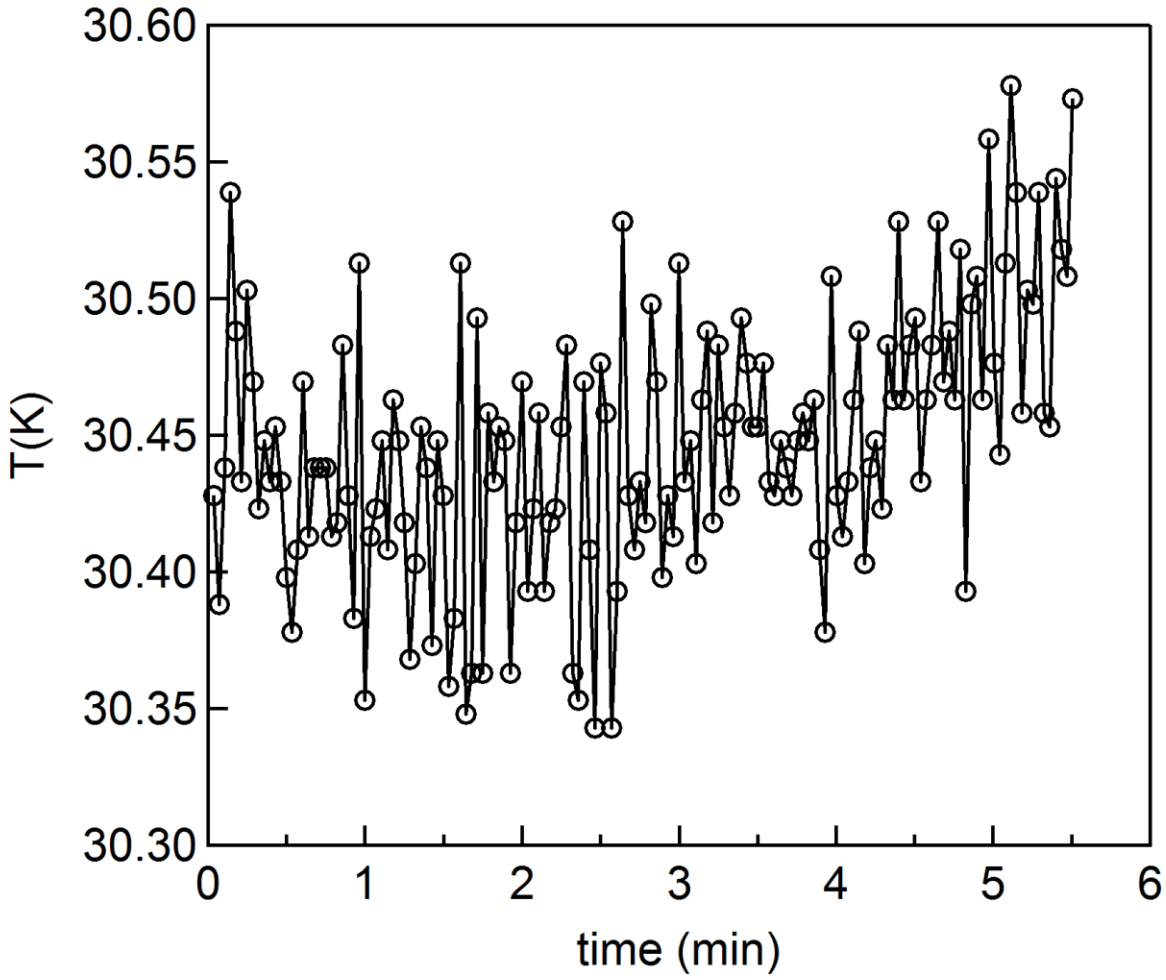

Fig. 3-6 Temperature stability of gas flow cryostat.
Temperature held constant by controlling heater output with PID loop.

3.2.2 Bath cryostat

The bath cryostat cools the sample by placing it in a probe, which is immersed into a bath of liquid helium. The sample is placed inside the probe, thermalized to a block, which is thermally connected to the helium bath outside of the probe. The sample can be maintained at low temperature as long as the liquid helium is replenished. Heat from the environment at room temperature leaks into the dewar and slowly boils off the helium but the loss can be minimized to make the helium last for many days between filling.

The probe for the bath cryostat was previously designed and fabricated by Kasra Khazeni, a former graduate student in the Zettl group (PhD 1997), but after many years of use, the probe needed to be refurbished. Kevin Nuckolls, an undergraduate researcher in the Zettl group, restored the function of the probe and detailed the work in his Undergraduate Honors Thesis [143]. The work in this section is a collaboration with Kevin and all figures are either adapted or reproduced from Nuckolls [143]. Kevin created the designs for components that needed to be fabricated after discussing with me. The components of the cryostat were fabricated by the Physics Department Machine Shop and assembled by Kevin. Kevin and I tested the cryostat and characterized its performance.

Fig. 3-7 shows the overview of the cryostat components. The probe is a stainless steel tube with electrical and vacuum connections at the top and sample space at the bottom. The magnified view of the sample space is shown (outlined by dashed lines). The "probe end attachment" connects to the bottom of the probe and houses thermometry components and "sample shelves". The sample shelves can be removed from the probe end attachment to mount samples under a microscope. When sealed with the inner can, the sample space is isolated from the environment and can be evacuated with a pump connected to the port at V1. The electrical wires from the sample shelves run up the length of the probe to the breakout box, which connects the wires to BNC connectors to interface with measurement instruments. When the bottom of the probe is at cryogenic temperature, the blackbody radiation from the top of the probe is a significant heat source since room temperature is hotter by hundreds of Kelvins. The radiation baffles are placed in the probe to block the radiation.

The probe fits into a stainless steel can called the "outer can". The outer can comes into direct contact with liquid helium and provides adequate thermal contact between the probe and the bath. The thermal contact should be large enough to cool the sample to the bath temperature (T=4.2K) but limited so that the sample temperature can be varied with a heater. When the outer can is evacuated with a pump connected to V2, the heat exchange by convection is disabled and the probe is significantly decoupled from the bath. Limited thermal contact is still provided by conduction through springy beryllium copper contacts ("thermal links"), which are attached to the probe and touch the walls of the can. To reach the base temperature of the cryostat, the thermal coupling to the bath is maximized by leaking in some helium gas through the V2. The helium gas significantly improves the thermal contact by convection.

The can is designed to fit inside a dewar equipped with a superconducting magnet, which can provide magnetic fields up to 17T. The bottom part of the can is copper to minimize the screening of the magnetic field. When the dewar is connected to a vacuum pump at V3, lower temperatures than 4.2K can be reached by evaporative cooling (e.g. 1.5K). As this process involves evacuating a large volume, specialized pumps and vacuum lines are required.

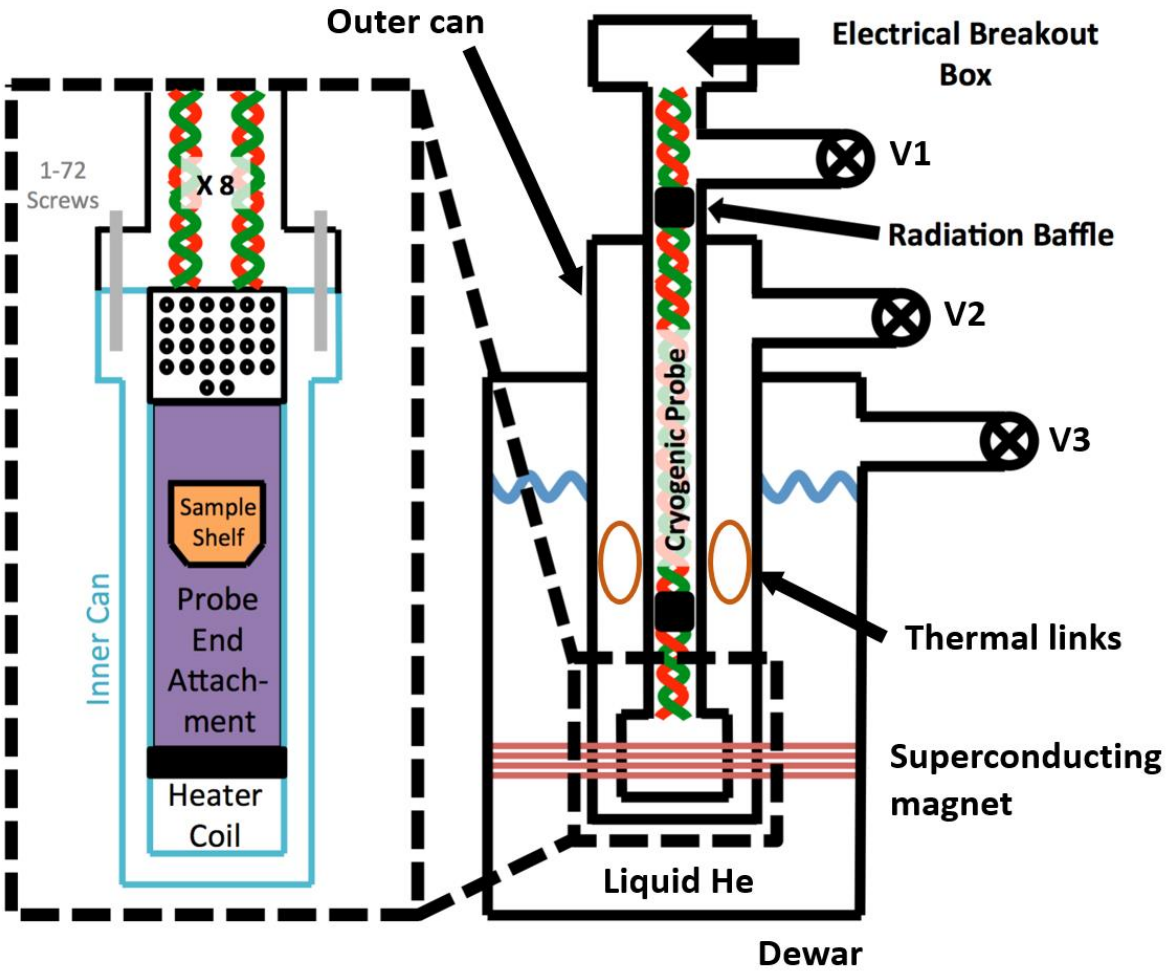

Fig. 3-7 Overview of bath cryostat.

Adapted from Fig. 4.1, Nuckolls [143] with modifications. V1, V2 and V3 are valves to ports where a vacuum pump is connected. The probe is a long stainless steel tube with multiple twisted pairs of wires (red and green wavy lines) running along it. At the top, the wires connect to a breakout box. At the bottom, the wires connect to the sample. The details of the probe bottom are magnified in the panel on the left (outlined by the dashed line). The inner can enables the sample space to be placed under vacuum with a pump at V1. The probe fits in a can called the "outer can" and is immersed in a bath of liquid helium while enclosed in the outer can. The dewar, which holds the probe is equipped with a superconducting magnet.

Fig. 3-8 shows the wiring of the cryostat. Inside the cryostat, wires are soldered to a 26 pin connector at the top and travel down the probe as twisted pairs[6]. The number of wires[7] along the probe is limited to 8 twisted pairs (i.e. 16 wires). As the wires carry heat from room temperature to the sample, running too many wires compromises the cooling power of the cryostat. The twisted pairs are bundled inside a Teflon tube to facilitate pushing the bundle along the probe. The pair for the heater is in a bundle by itself, as it is more prone to damage from the high currents required for heater operation.

At the bottom of the probe, the twisted pairs are soldered to pin connectors, which plug into a matrix of pin connectors. Pin connectors, which uses an alloy with very small magnetic response, are selected for use at high magnetic fields [8]. Components on the probe end attachment (i.e. samples, temperature sensors and heater) are connected to the wires from the top of the probe with twisted pairs, which plug into the back side of the matrix. At the probe end attachment, the 8 twisted pairs are distributed among the components as needed. Wiring configurations is easily changed by plugging and unplugging pin connectors. For example: 5 pairs (10 wires) can be allocated to a single sample, while reserving a pair for the heater and 2 pairs for sample temperature sensor.

Outside of the probe, a breakout box connects to the 26 pin connector at the top. Each twisted pair from the probe is connected to one of the BNC connectors from an array of 14, housed in a metal box. The breakout box interfaces the twisted pairs to BNC cables connected to measurement instruments. Each twisted pair is wired to a switch controlled circuit (Fig. 3-8, outlined by the dashed line) to protect the sample from unwanted electrical biases and pulses. In the diagram, $1P_+$ corresponds to the positive signal wire of the twisted pair and $1P_-$ to the negative signal wire of the *same* pair. The two wires are connected to a double pole double throw (DPDT) switch S1. Practically, the switch snaps to 3 positions: connect, open and short[9]. In the "connect" position, $1P_+$ connects to the inner pin and $1P_-$ to the outer shell of the isolated BNC. In the "open" position both are $1P_+$ and $1P_-$ are floating because they are not connected to anything. In the "short" position, $1P_+$ and $1P_-$ are shorted to each other. When S2 is closed, the wires are shorted to the box as well.

Fig. 3-9 shows the breakout box assembled from the components listed in Table 3-1. Fig. 3-9a shows the front of the box. Each BNC connector corresponds to a twisted pair and are labeled according to the pin naming convention of the 26 pin connector. Fig. 3-9b shows the back of the box with the cover removed. The wires from the 26 pin connector to each BNC are made into twisted pairs and shielded by aluminum foil. When the cover is placed, the aluminum box provides additional shielding from environmental noise.

[6] When soldering to the 26 pin connector, the pins should be appropriately heat sunk with a hemostat to prevent deformation of the plastic that house the pins. If the plastic is deformed, the vacuum seal at the connector is compromised.

[7] #40 AWS copper wire, coated with enamel.

[8] Mill-Max Manufacturing Corp. 310-13-164-41-001000. Alloy: 61.5% Cu, 35.4% Zn and 3.1% Pb

[9] It is called DPDT because conventionally the open position is not counted as a "throw".

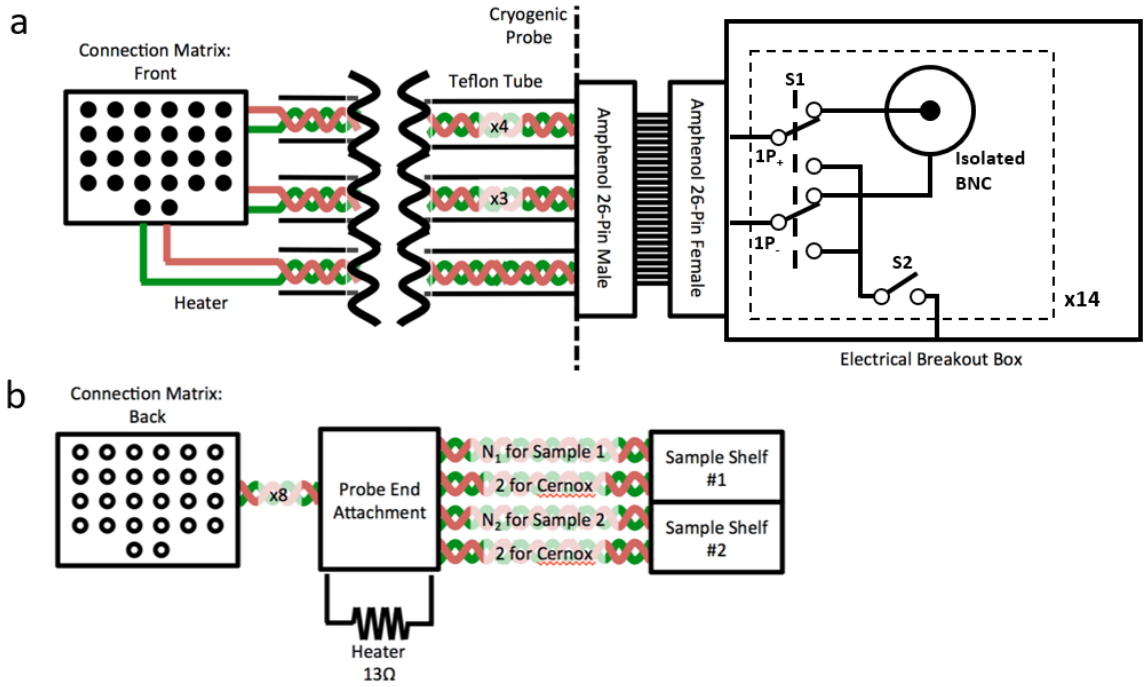

Fig. 3-8 Electrical wiring of bath cryostat.
Adapted from Fig. 4.5, Nuckolls [143] with modifications. Red and green wavy lines represent twisted pairs of wires and are labeled with the number of *pairs* it represents. a) Schematic of electrical wiring from along the whole probe. The right (left) side of the figure corresponds to the top (bottom) of the probe. Electrical breakout box is located outside of the probe and consists of 14 copies of the electrical circuit outlined by the dashed line. The wires run down the probe to the matrix at the bottom. b) Bottom of the probe. All twisted pairs branch out from the back of the matrix. The pairs are distributed among the two sample shelves with the constraint $N_1+2+N_2+2=8-1$ (one pair is dedicated to the heater).

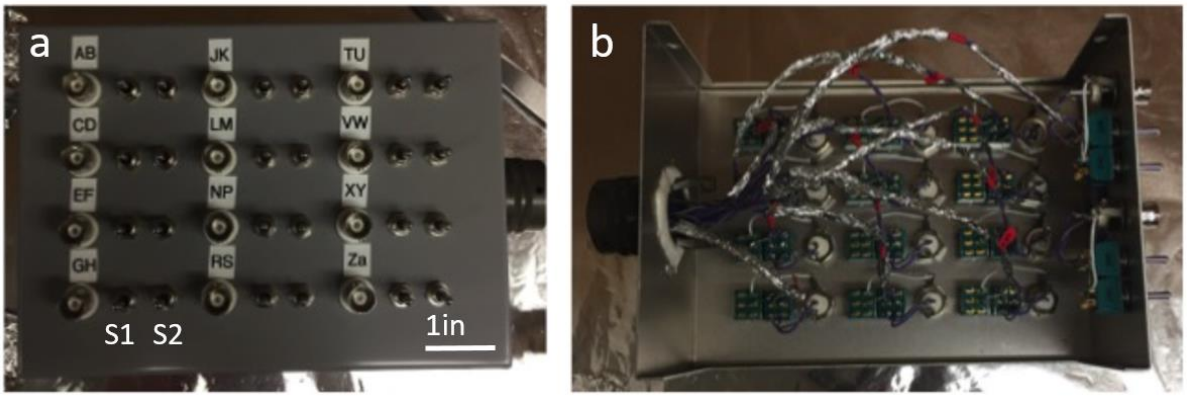

Fig. 3-9 Electrical breakout box.
Adapted from Fig. 4.8, Nuckolls [143] with modifications. Box dimensions =7x5x3in. a) Front of the box with a 3x4 array of a unit composed of a BNC connector and two switches. Two more units (not shown) and a 26 pin connector are attached to the side. Each unit is a circuit shown on the top right of Fig. 3-8a. The switch, located closer (further) to the BNC, corresponds to S1 (S2). b) Back of the box with the cover removed. Each pair of wire, corresponding to a twisted pair in the probe, are twisted and shielded with aluminum foil.

Component	Manufacturer	Part number
Enclosure (box)	Bud industries	CU-3008-A
Isolated BNC	Amphenol RF Division	31-10-RFX
DPDT switch	TE Connectivity	MTA206P
26-pin connector	Amphenol	JMS3116M16-26S

Table 3-1 List of parts for breakout box.
Components used for making the breakout box shown in Fig. 3-9.

Fig. 3-10a shows a CAD design model[10] of the probe end attachment from two perspectives. The cylindrical portions at the top and bottom have grooves to wind heaters for temperature control. The diameter of the cylinders are close to the diameter of the inner can opening, so heaters wires cannot protrude beyond the cylinder diameter. The top cylindrical portion has four holes (4-40 through), surrounding the large hole in the center, to attach the piece to the bottom of the matrix of pin connectors. The wires from the matrix comes through the large hole at the center. The blade-like portion in the middle has two holes (8-32 through) to mount the sample shelves, which are shown in Fig. 3-10b. Each shelf has a tapped hole and mounted by putting an 8-32 screw into the sample tapped hole on the shelf through the probe attachment and tightening. This design enables the sample to be mounted at a tilt of θ=0-90^o with respect to a magnetic field. The two shelves need to be mounted on opposite sides of the blade-like piece to leave clearance for $\theta \neq 0$ mounting. Both the probe end attachment and the samples shelves are made of copper to minimize temperature gradients.

Fig. 3-10c shows the fabricated probe end attachment. The heater is wound only on the bottom groove, as we believed only the bottom heater would be sufficient for temperature control. The heater is a non-inductively wound coil of manganin wire[11] with a total resistance of 13Ω. The whole coil is coated with Stycast (2850FT) for good thermal contact to the probe. The rectangular black pieces are pin connectors attached to the copper by Stycast to thermalize the wires to low temperature. The top of the pin connectors are soldered to wires from the matrix and pin connectors corresponding to various components (i.e. heater, temperature sensor and sample) plug in from below.

In Fig. 3-10c, one sample shelf is mounted on the bottom hole. The image on the right is a magnified view of the sample shelf. The edge of the top shelf surface is covered with a line of Stycast to electrically insulate from the copper. Twisted pairs of wires attach to the circles of silver epoxy (H20E). The silver circles are contact pads to paint on wires from the sample. On the back side of the top shelf surface (not visible in image), a temperature sensor is mounted by GE varnish (VGE 7031). The Cernox (Lakeshore CX1050-BG-HT) temperature sensor is used for its low magnetic field induced errors. The sensor is in bare chip form to avoid possible incorporation of magnetic materials in other packaging options. The designs of the probe end attachment and sample shelf are detailed in Fig. 3-11 and Fig. 3-12.

[10] Made with AutoCAD by Kevin Nuckolls.

[11] Ø0.008in manganin wire with Kapton coating.

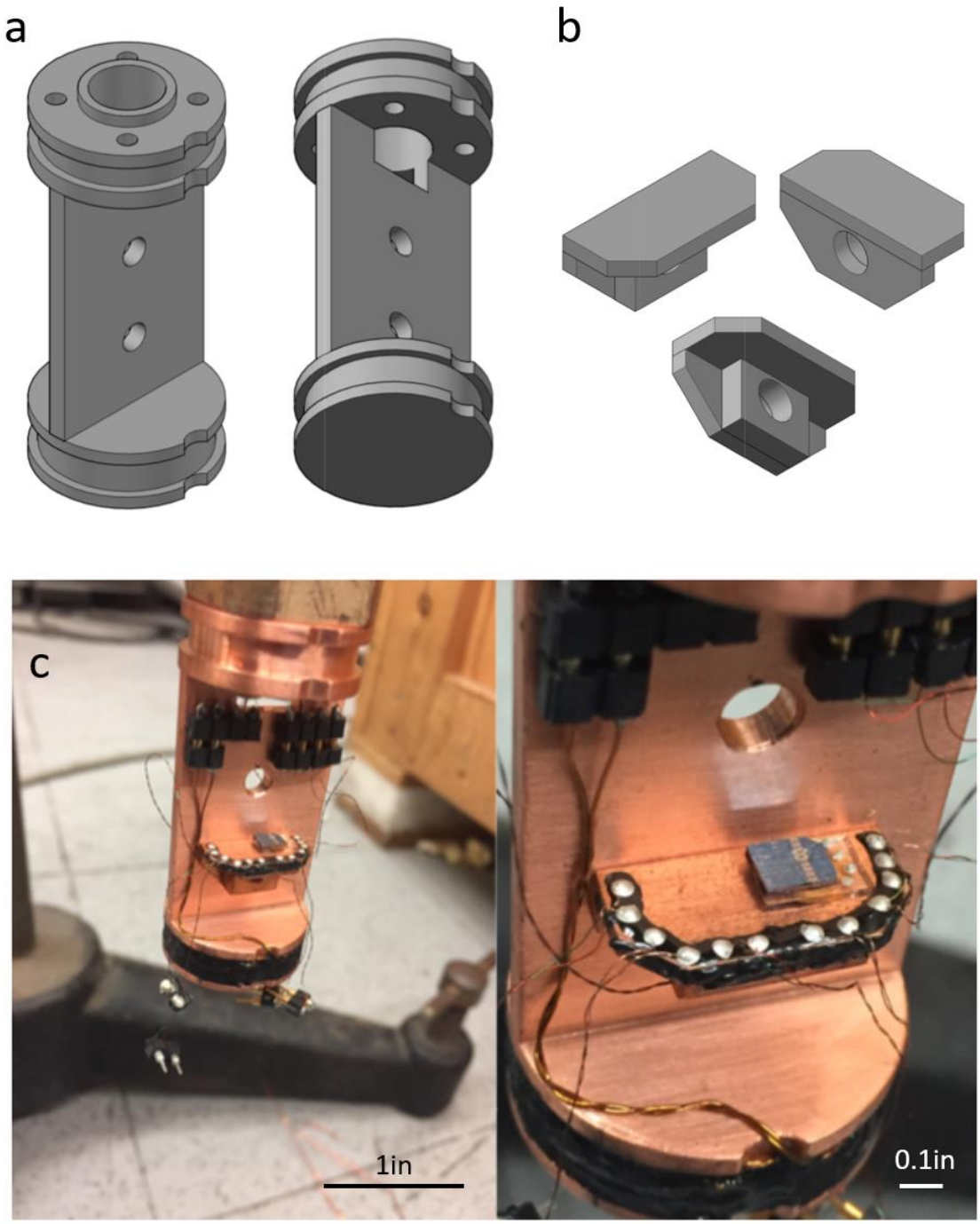

Fig. 3-10 Probe end attachment and sample shelf image.
a) Fig. 4.13, Nuckolls [143]. CAD based model of the probe end attachment from two perspectives b) Fig. 4.15, Nuckolls [143]. CAD based model of the sample shelves from three perspectives c) Fig. 6.11, Nuckolls [143] with scale bars added for clarity. Optical image of the probe end attachment with sample shelf, electrical wiring and sample attached.

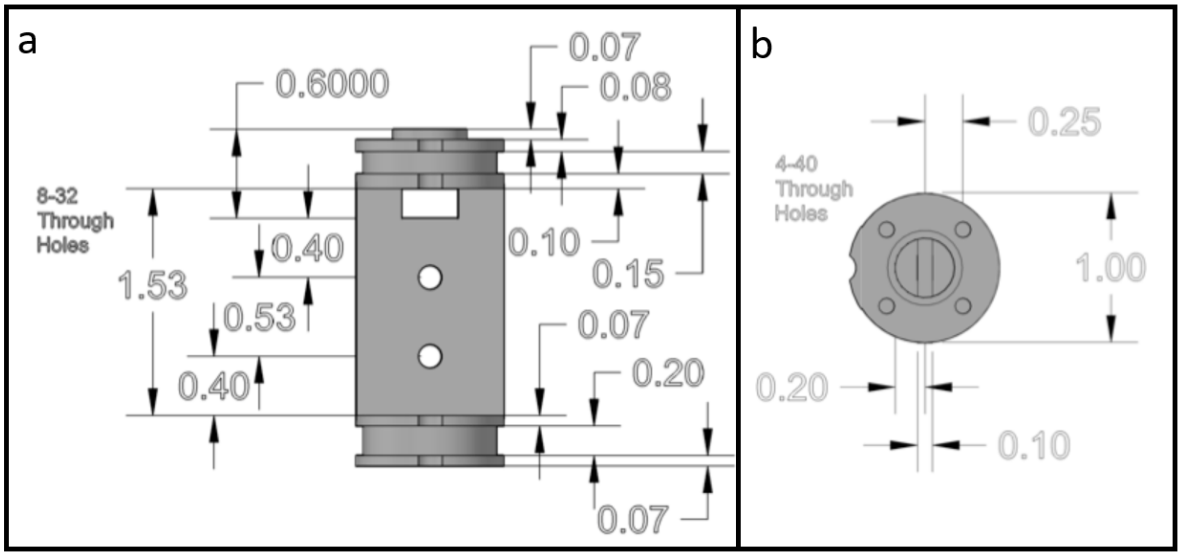

Fig. 3-11 Probe end attachment design.
Adapted from Fig. 4.14, Nuckolls [143]. All dimensions are in inches. a) Side view and b) top view.

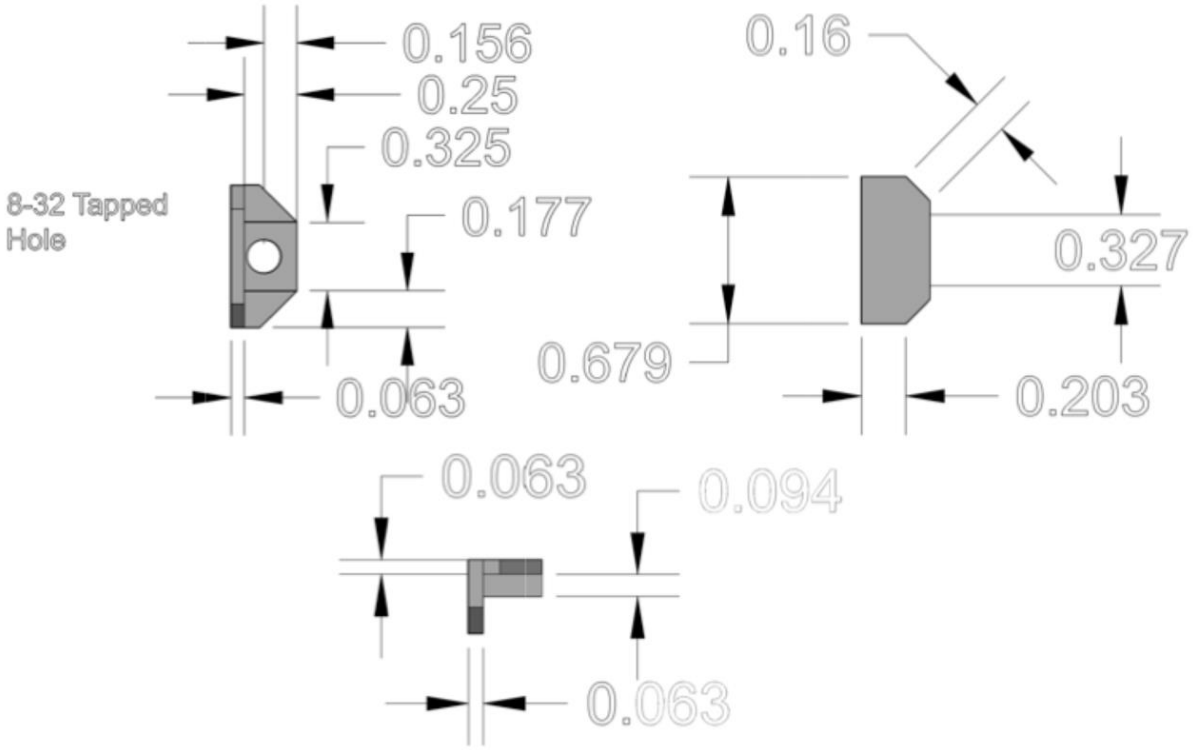

Fig. 3-12 Sample shelf design.
Fig. 4.16, Nuckolls [143]. All dimensions are in inches.

Fig. 3-13 shows the bottom of the probe, where the inner can attaches to. At the bottom half of the image, the matrix of pin connectors are shown. The probe end attachment (not shown in image) is mounted below the matrix. The inner can forms a seal with the cylindrical flange above the matrix. Ø0.5mm indium wire is placed at the junction between the probe and the inner can and squeezed by tightening the eight 1-72 screws to form an indium seal for vacuum.

Fig. 3-14a shows the inner can, which is made of copper. At the top, there are 8 tapped holes for 1-72 screws. Fig. 3-14b shows the dimensions of the inner can. It is important that the inner diameter of the can closely matches the diameter of the cylinder protruding from the flange in Fig. 3-13 to form a vacuum seal. The space, enclosed by the inner can and the interior of the probe up to V1, is isolated and can be evacuated with a pump connected at V1. The lowest pressure reached at room temperature is 9×10^{-6}torr after pumping overnight with a turbo pump (Pfeiffer HiCube 80 Eco). The procedure for forming the indium seal, developed by Kevin, is detailed in Nuckolls [143] and reproduced here.

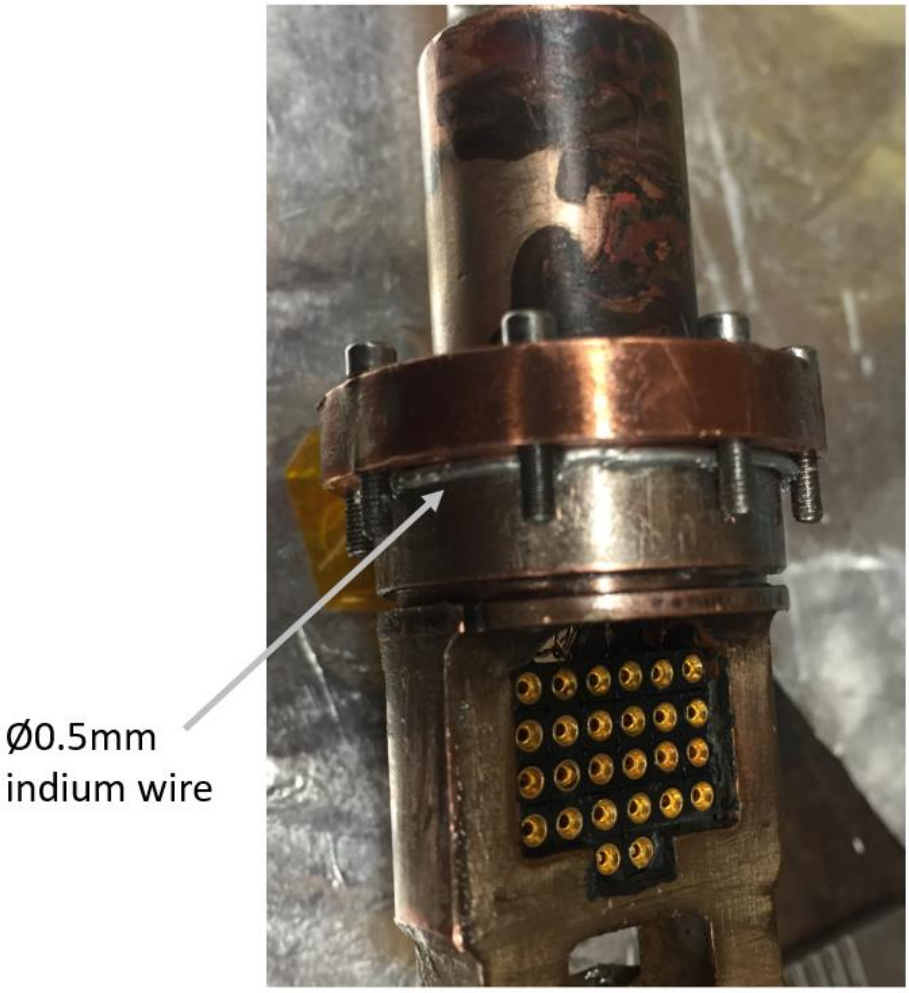

Fig. 3-13 Indium seal before sealing inner can.
Adapted from Fig. 4.12, Nuckolls [143] with modifications. Indium wire is placed at the junction between the bottom of the probe and inner can (not shown) to form a vacuum seal.

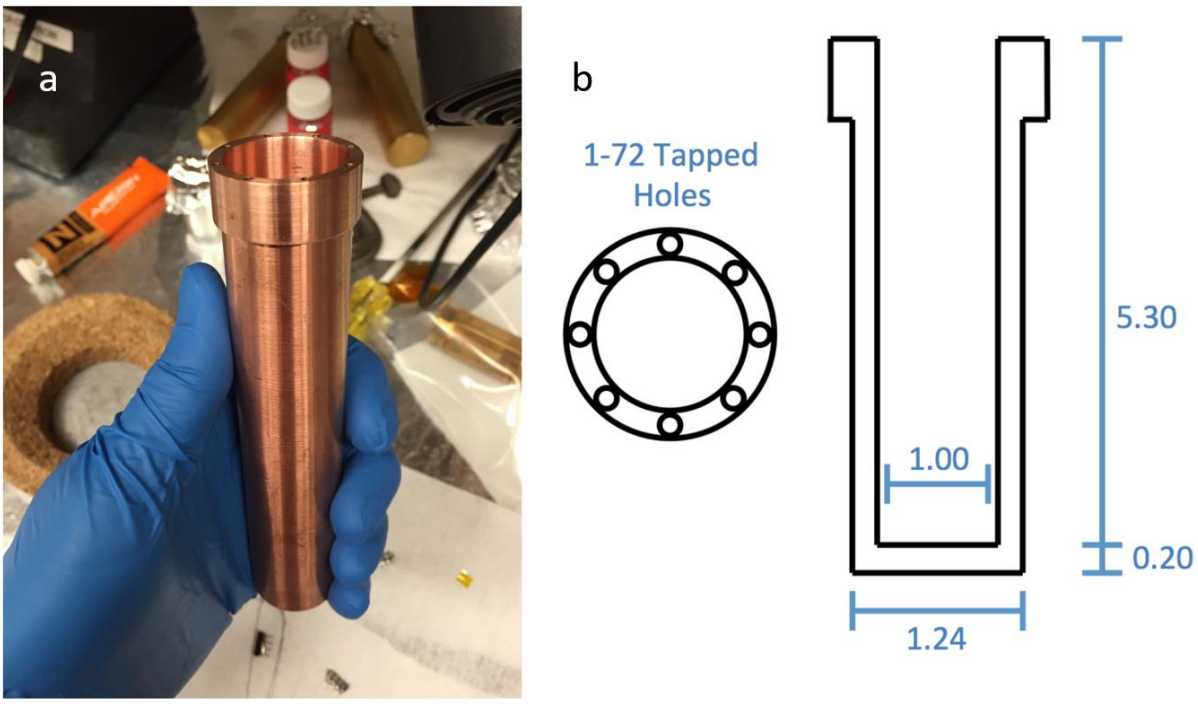

Fig. 3-14 Inner can.
a) Fig. 4.10, Nuckolls [143]. Optical image of inner can. b) Fig. 4.9, Nuckolls [143]. Schematic of inner can. All dimensions are in inches.

Excerpt from page 39-41 of Nuckolls [143]

Indium Seal Forming Procedure

1. Grease the base of the probe end attachment, the inside of the inner can, inside about 2 inches from the top, and the top surface. Also, place a very thin layer of vacuum grease on the probes end, where the indium will be placed. This helps when one wishes to remove it later.
2. Carefully slide the inner can up the probe staff, tucking wires into the can with a set of tweezers as you go. Slide it up until there is about half an inch of space between the top of the inner can and the sealing surface of the probe.
3. Place all eight, 1-72 screws into their respective holes, only about 0.5mm below the probe's bottom surface.
4. Cut roughly 3.5 inches of the 0.5mm indium wire and begin to tuck this wire between the small portions of the screws that stick out and the probes outer surface, as shown in [Fig. 3-13]. The 3.5 inch indium wire will be slightly too long, but allows the ends to be cut at a slant to be pressed into one another. Make sure that this cut lines up between screws.
5. Slide the inner can up the probe staff and align one of the screws with about a half twist into the threaded hole of the inner can. Firmly press on the base of the inner can to make some seal and tighten the screws using the star pattern method until inner can is securely fastened to the end of the probe.
6. Now, open the probe back up to the point where the inner can is half an inch below the sealing interface. On top of the original, now flattened indium ribbon, repeat the above steps to install a second indium wire, again 0.5mm in diameter.

Fig. 3-15 shows the sample temperature ramp up and down for T=8.5-9.2K. The temperature is controlled with a PID loop based controller (Lakeshore 340). The controller adjusts the output of the heater with feedback from the temperature sensor reading. For both temperature ramps up and down, a linear rate of ~0.06K/min is maintained. At the end of the temperature ramp down near the cooldown rate slows down in preparation for holding a constant temperature at 8.5K.

Fig. 3-16 shows R(T) of a test sample of niobium thin film (see section 3.1.2). The resistance is measured by four-point probe technique with 100μA dc current bias. However, there is a thin layer of niobium oxide between the niobium and the contacts. Wirebonding would have broken through the oxide but the sample was contacted with silver paint. The drop in resistance below T=9.04K is in agreement with the T_c=9.2K from literature [141]. The resistive transition does not drop to zero and broadens out to a tail due to contact effects. There is very little hysteresis between R(T) measured on warmup (red squares) and cooldown (green triangles), indicating good thermal contact between the temperature sensor and the sample.

In principle, the base temperature of the cryostat should be 4.2K, the temperature of the helium bath. However, the lowest base temperature reached by this system is 5.1K and requires further development to reach lower temperatures. Two reasons have been proposed: 1) there are too many wires (16 #40 AWG copper wires) that run down the probe or 2) there is an unobstructed optical path from the top of the probe to the sample space and blackbody radiation heats the

sample space. Regarding reason 1), we have not tried any cooldowns with less than 16 wires. To address reason 2, cylinders of copper have been placed inside the probe to serve as radiation baffles. The baffles should absorb the radiated heat from above and conduct it away to the inner walls of the probe. However, placing the baffles raised the base temperature to 5.6K. It is possible that the baffles did not thermalize well with the inner walls of the probe due to poor contact. For future work, a spring based mechanism for improved contact should be explored.

Fig. 3-17 shows the warmup of the cryostat to 220K with the heater. The outer can is evacuated to weaken the thermal coupling between the probe and the helium bath. For future experiments, it is useful to evaluate the maximum temperature achievable with the 13Ω heater. Higher heater resistance would enable higher power outputs but the heater resistance is limited by the amount of wire that fit inside the groove on the probe end attachment (see Fig. 3-10). When operated at 1W, the heater allows the sample to reach 220K in <10hours. Operating the heater at 1.3W caused damage after 2hours of continuous operation. The heater was actually not damaged but the wires in the twisted pair from the 26 pin connector to the matrix was shorted to each other. With ~300mA of current the insulation of the wires melted.

Although room temperature cannot be reached with the heater, 220K is the glass transition temperature of DEME-TFSI [144], a commonly used ionic liquid for strong electrostatic gating (see section 6.2). It is convenient to reversibly reach the glass transition temperature, as the ionic liquid responds to a change in gate voltage only at above its glass transition temperature.

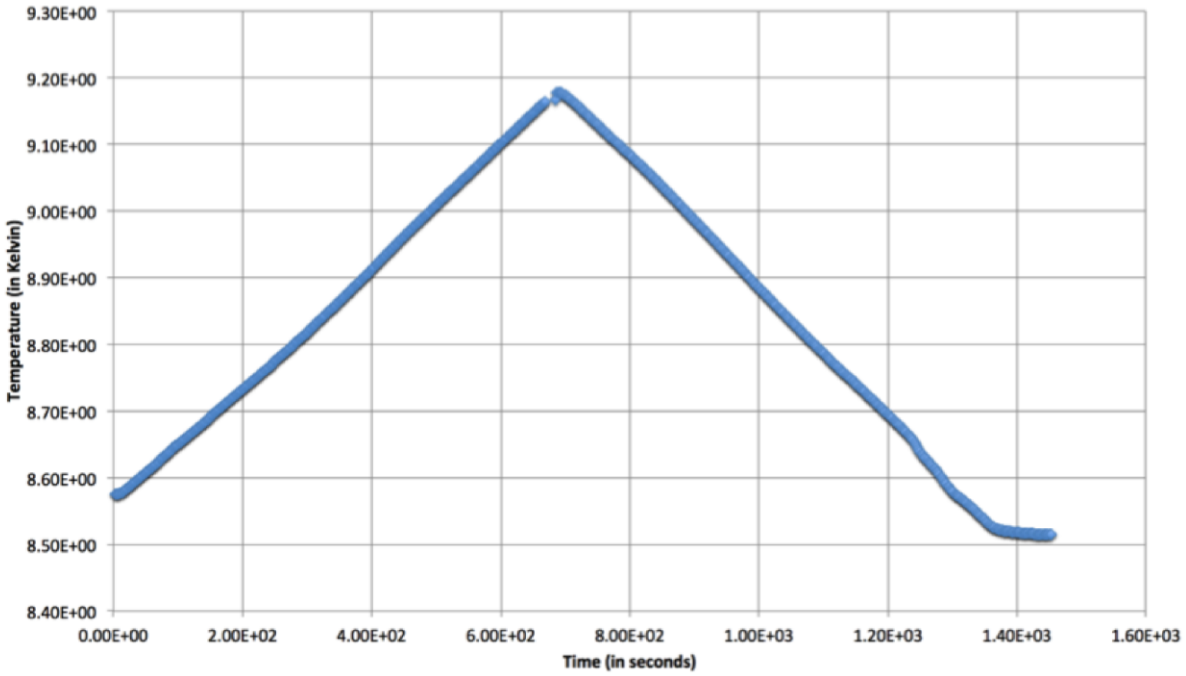

Fig. 3-15 Bath cryostat temperature control.
Fig. 6.1, Nuckolls [143]. Sample temperature is ramped up and down with a linear rate of ~0.06K/min, controlled with a PID loop.

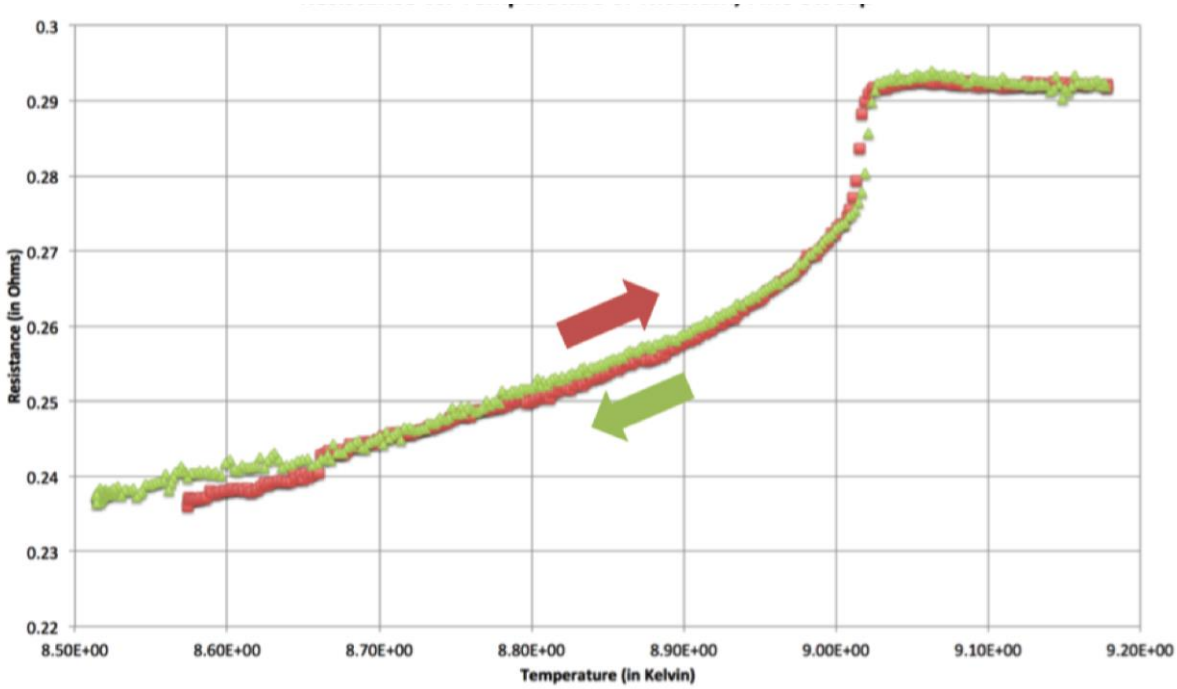

Fig. 3-16 R(T) of Nb measured by bath cryostat.
Fig. 6.13, Nuckolls [143]. Niobium contacted by silver paint and measured by four-probe. Silver paint contacts cause significant contact resistance. Cooldown (green triangles) and warmup (red squares) are shown.

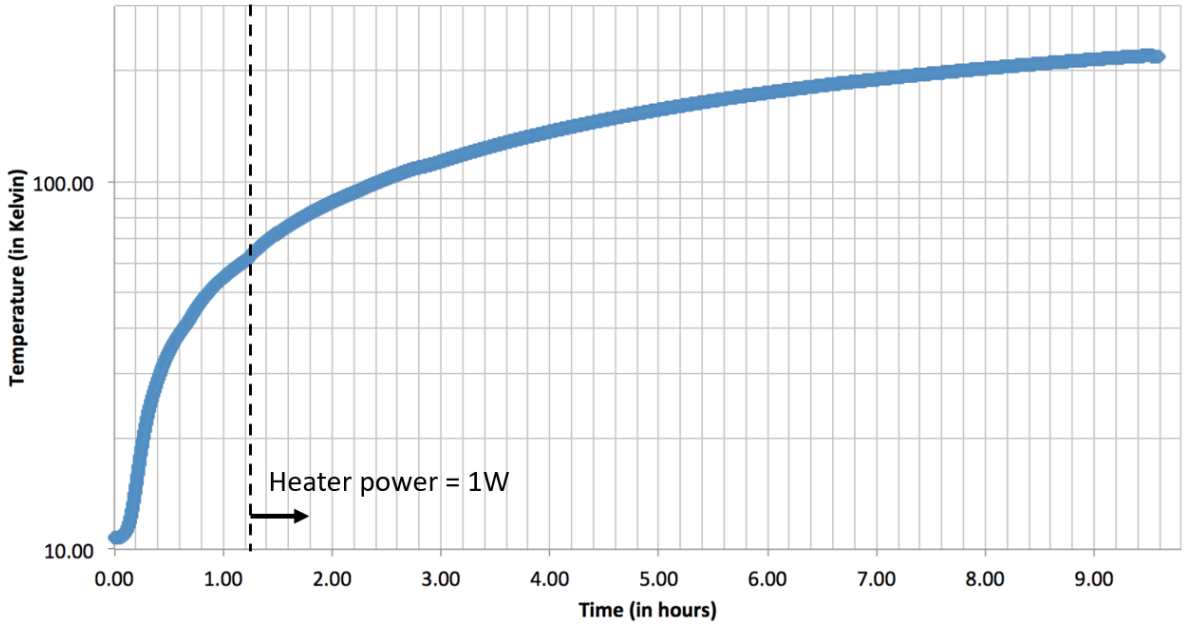

Fig. 3-17 Bath cryostat warmup to 220K with heater.
Adapted from Fig. 6.2, Nuckolls [143] with modifications. Before time=1.2hrs (dashed line), power to the heater is increased manually to 1W. After time=1.2hrs, power to the heater is maintained at 1W.

3.2.3 Doping vessel

For materials, which are sensitive to doping, the sample can be exposed to chemical species in a "doping vessel" and directly mounted (i.e. without taking it out of the vessel) to a cryostat for low temperature measurements. The doping vessels were used by Michael Fuhrer, a former graduate student in the Zettl group (PhD1998), for studying superconductivity in alkali metal doped C_{60} crystals [145]. Careful study of superconductivity in Rb-doped C_{60} crystals was enabled by high quality samples obtained with the doping vessel [145]. Synthesis conditions were optimized because the crystal resistance was monitored during doping and independent control of sample and alkali metal temperatures were possible.

Recently, interest in graphite intercalation and C_{60} crystal doping has re-emerged, since it can now be applied to carbon materials at the ultrathin limit (e.g. bilayer graphene, C_{60}/graphene hybrid structure [146]). The doping vessels are reproduced[12] based on the design shown in Fuhrer [145] with slight modifications. The stainless steel parts are made of 316 stainless steel to be non-magnetic. Fig. 3-18 shows the doping vessel design and Fig. 3-19 shows the photograph of the fabricated doping vessel. The sample is mounted on the stage and wires from the sample travel outside along the feedthrough. Torr Seal is applied to the feedthrough opening to seal it for vacuum. The Swagelok connection on the tube fits into the stage to make a vacuum seal. The tube is a metal tube mated to a Pyrex tube. The glass end of the tube is initially open and connected to a valve via a Quick-Connect fitting[13]. The valve enables air sensitive materials (e.g. Rb) to be loaded into the vessel inside a glovebox and carried to the sealing setup without

[12] Fabricated by Department of Physics Machine Shop
[13] Kurt J. Lesker Company, QF25XVC050

exposure to air (see Fig. 4-2). The glass end is sealed with a torch, while maintaining vacuum inside the vessel, similar to ampoules (see section 4.1.1).

The temperature sensor assembly screws into the backside of the stage to probe the sample temperature through the 0.050in thick stainless steel. The threading is changed to 6-32 (from 6-40 in Fuhrer [145]) as it is a more commonly used size. Temperature sensors are mounted on the copper portion to thermally couple to the sample. The opening on the copper portion is designed to tightly fit around the cylindrical "AA" package from Lakeshore Cryotronics. Multiple sensor assemblies are prepared to quickly switch between sensor types (e.g. thermocouple for high temperature and Cernox for low temperature).

After the doping vessel is sealed, the alkali metal vapor is obtained by heating with a heating tape around the Pyrex. The ability to monitor the sample resistance and temperature provides good control over the doping conditions. After doping the sample, the doping vessel is mounted on a cryostat for low temperature measurement. The Ø0.25in tubing protruding from the Swagelok connection is clamped onto the bottom of a probe, similar to one described in section 3.2.2, and cooled in a bath cryostat.

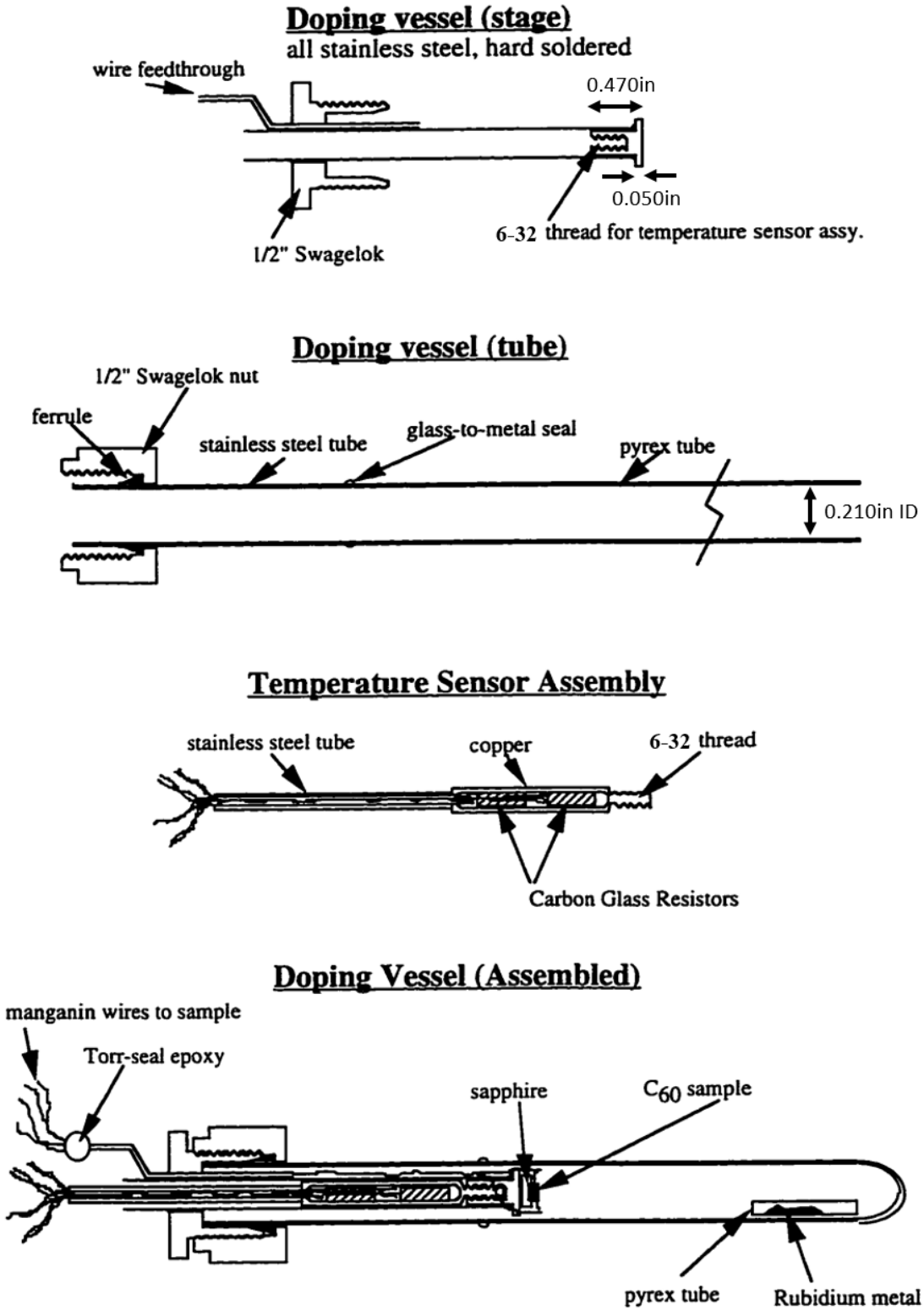

Fig. 3-18 Doping vessel design.
Adapted with modifications from Fig. 9-4, Fuhrer [145].

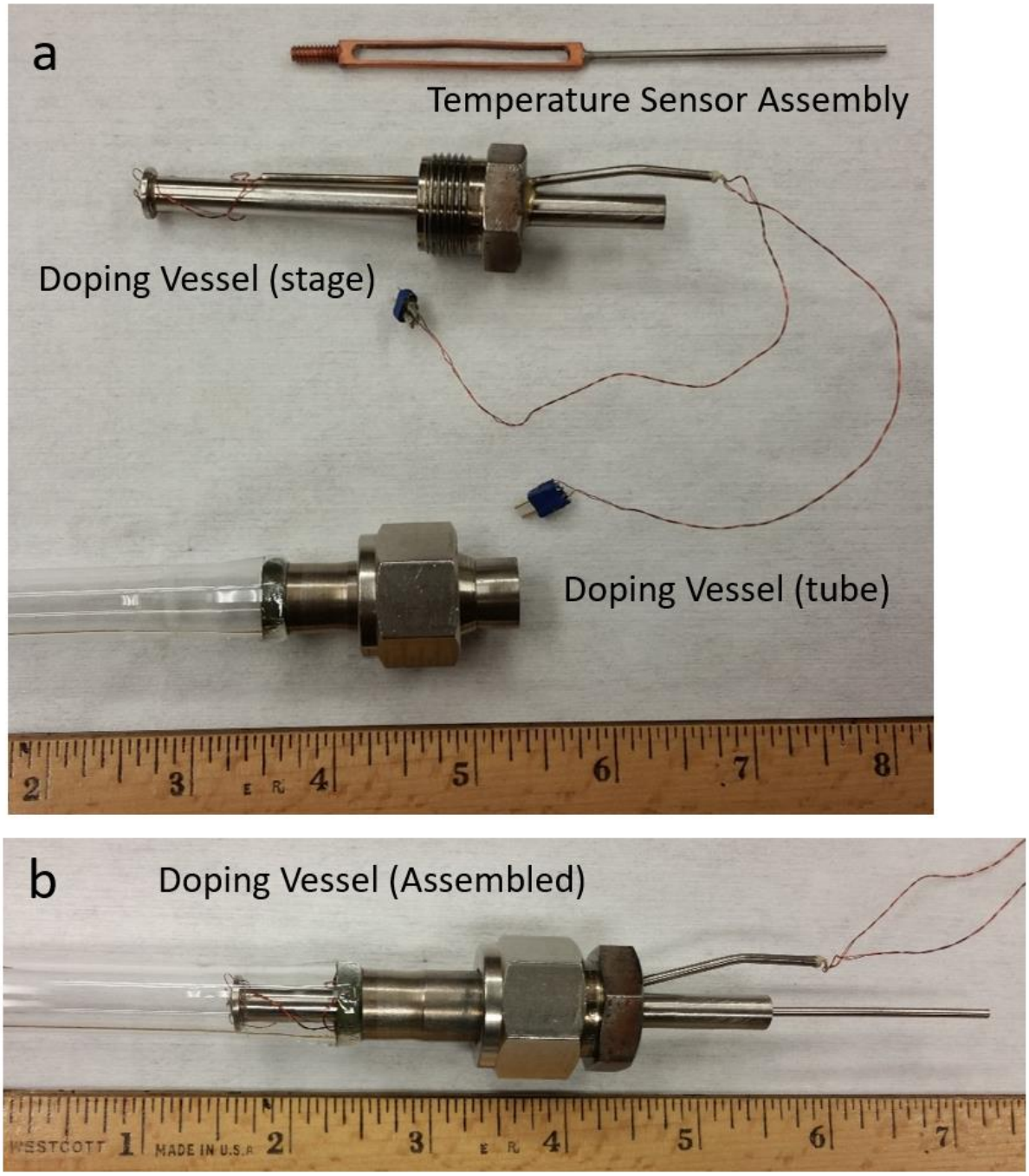

Fig. 3-19 Doping vessel image.
Optical image of the doping vessel. Ruler is in inches.

3.2.4 UHV cryostat

Chapter 5 describes low temperature transport measurements for a sample in ultra-high vacuum (~10^{-10}torr). The cryostat is part of a variable temperature STM with a minimum temperature of 4.2K and works essentially as a bath cryostat. The STM sample space is thermally coupled to a metal block immersed in liquid helium. Since the STM must be isolated from mechanical vibrations, a copper braid provides the thermal coupling and some optimization is required to reach a base temperature of 4.2K. For transport measurements, the sample is mounted on the same sample space for STM measurements and its resistance is measured through an electrical feedthrough in the UHV chamber. The equipment is built and maintained by members of the Crommie group, who have provided me assistance for the measurement.

3.3 Commercial systems

Commercial systems are configured for user-friendly, automated processes of routine measurements. The PPMS Dynacool is an automated cryostat, which allows measurements of R(T) for T=400-1.8K, without much expertise in cryogenics. Due to its closed circuit cryogen design, it does not need to be filled with liquid helium and its cryogenic capabilities can be maintained with very little cost. In addition, the temperature range is extended down to 50mK with the D850 module. The MPMS is another automated cryostat equipped with a SQUID magnetometer and enables magnetization measurement of the sample for T=400-1.5K.

3.3.1 PPMS Dynacool

The physical property measurement system (PPMS, Quantum Design) is an automated cryostat with electrical connections to the sample and a superconducting magnet to apply high magnetic fields. The Dynacool is a version of the system, which does not need to be filled with liquid helium to replenish its cryogen. The helium is condensed by a gas flow based system and circulated in a closed circuit. Among the cryostats discussed in this chapter, the Dynacool requires the least amount of helium and consumes at most one K-type cylinder per month. The system allows control of sample temperature for T=400-1.8K and magnetic fields up to B=±9T, with automated control.

Lower temperatures down to 50mK are reached with dilution refrigeration (DR). The mixture of He^4 and He^3 isotopes enables cooling to temperatures far below the boiling point of helium [147]. The DR module (D850, Quantum Design) fits inside the Dynacool and allows sample temperature control for T=4-0.05K. The D850 cools down from 300K to base temperature in ~6 hours and has a cooling power of 0.25μW at 100mK. D850 controls temperature with DR for T=1.1-0.05K and evaporative cooling of pure He^4 liquid for T=4-1K. The switch between the two modes of operation is automated by the instrument but requires some waiting time.

Fig. 3-20 shows the cryostat temperature as it is switched from evaporative cooling to DR. T=4K initially and the D850 begins the switch to DR for setpoint ≤1K. While the He^4-He^3 mixture is condensed, the temperature cannot be controlled. After 150 minutes, the D850 enters DR mode (signaled by the spike in T) and control for T=1.1-0.05K is possible.

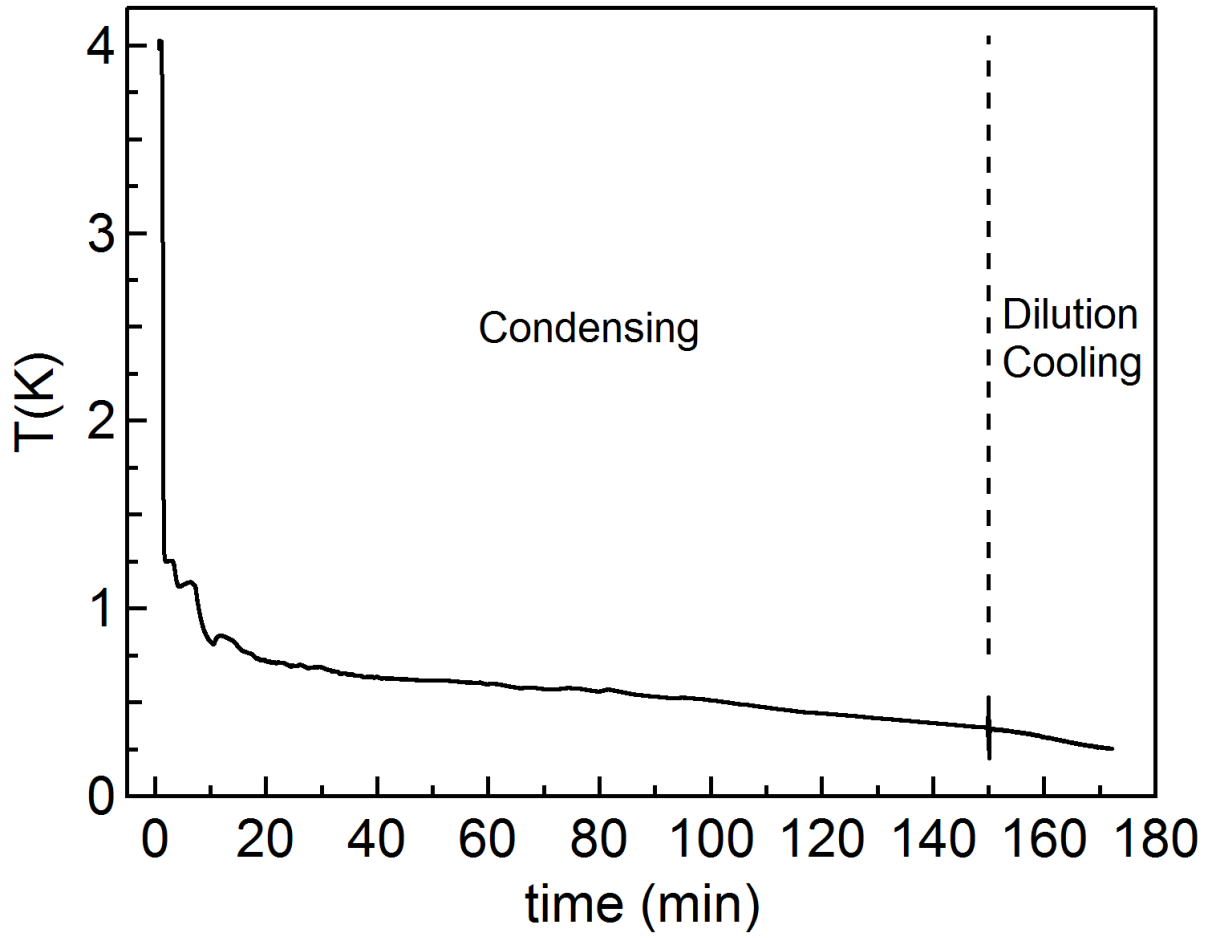

Fig. 3-20 Cooldown from 4K to dilution cooling.
Cryostat is initially at T=4K (time=0) and prepares for dilution cooling when setpoint <1K is entered. To the left of the dashed line, He^3-He^4 mixture is condensing and temperature control is disabled. To the right, the cryostat enables temperature control for T=1.1-0.05K by dilution cooling.

Fig. 3-21 shows the switch from DR to evaporative cooling. T~0.8K initially and the D850 begins the switch to evaporative cooling for setpoints ≥1.1K. In the first step, the pump for the dilution of He^3 out of the mixture is stopped and to condense the He^3 into the He^4-He^3 mixture. This process, which takes ~100min is called "Condensing for Evaporative Cooling". In the second step, called "Distilling Mixture", the He^3 is pumped out of the mixture, so that a liquid of pure He^4 remains and the He^3 is flowed back into a storage tank. After 60min, T settles to the setpoint (e.g. 4K) and control for T=4-1K by evaporative cooling is possible.

The detail below, which could not be found in our copy of the manual, may be useful for future experiments. For setpoints = 2-1.1K, only the "Condensing for Evaporative Cooling" step is executed and control for T=2-1K is possible. If T=4-2K is desired, while in the T=2-1K range, D850 enters the "Distilling Mixture" and T remains constant at 2K until the process is complete. Once the system is in the T=4-2K range, T=4-1K can be reached continuously.

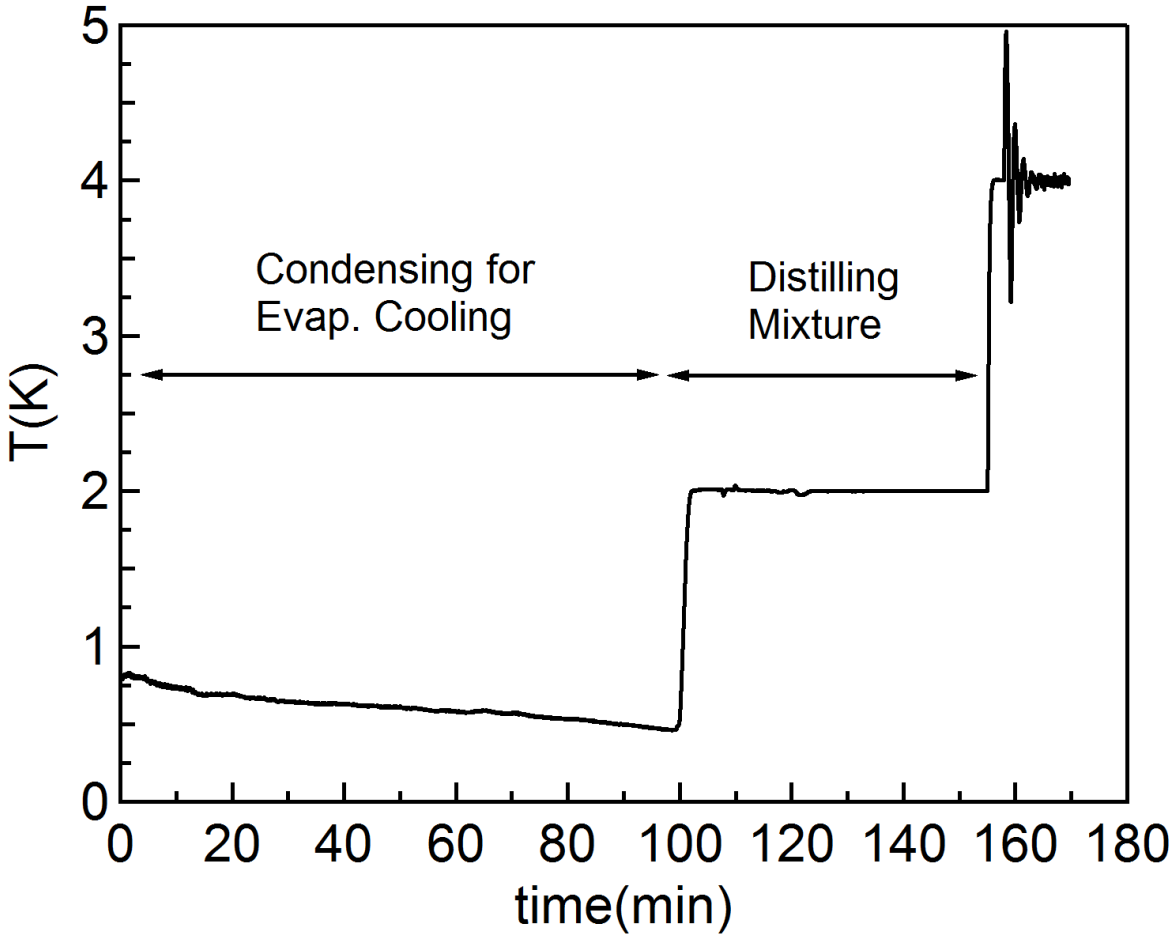

Fig. 3-21 Warmup to 4K from dilution cooling.
Cryostat is initially at T~0.8K (time=0) and prepares for evaporative cooling after setpoint=4K is entered. The condensation and distillation processes are automatically controlled by the instrument and temperature cannot be controlled during these processes.

In principle, the combined capabilities of the Dynacool and D850 enables control over T=400-0.05K. However, the sample location is different for T=400-1.8K and T=4-0.05K by design. If measurements at T=400-4K are desired for a sample characterized in the D850, it needs to be removed from the cryostat and remounted into the Dynacool after the D850 module is removed. For an air sensitive sample (e.g. monolayer $NbSe_2$, see section 5.3.3), the sample behavior would change, every time it is removed from the inert environment of the cryostat. Hence, a method is devised to measure R(T) for T=300-0.05K without removing the sample from the cryostat.

For T=400-4K, the sample temperature cannot be measured with D850 because its sensor is uncalibrated for T>4K. The electrical connection to the sample is available at all times during the D850 operation. To resolve this problem, a diode (DT670, Lakeshore Cryotronics) is mounted on the D850 sample space and the diode readout is used to measure the sample temperature for T>4K. This method allows both R and T data to be collected but the sample temperature cannot be effectively controlled for T>4K. During D850's cooldown (warmup) to (from) T=4K, the system controls the temperature with a feedback loop based on the sensor located at the

Dynacool sample space. Since there is poor thermal connection between the Dynacool and D850 sample spaces, a method to run the Dynacool temperature control system with input from the D850 sample temperature needs to be developed.

Fig. 3-22 shows the D850 sample temperature during warmup to 300K. The sample is initially at T=2.5K and begins an automated warmup procedure to 300K for removal of the D850 when a setpoint=300K is entered. During this warmup, the Dynacool only displays the temperature of the Dynacool sample space. T in Fig. 3-22 is measured by the silicon diode mounted on the D850. As shown in the inset, the temperature changes very rapidly for T>10K, starting with a jump from 2.5K to 6K. Such a fast change makes the reading unreliable since the sample and sensor might not have sufficient time to thermalize to the same temperature. The ramp rate appears to be slow enough for T>10K and could be slowed down further by changing the temperature ramp rate of the Dynacool.

Fig. 3-23 shows the D850 sample temperature during cooldown from 300K. The sample is loaded at room temperature with the D850 module into the Dynacool and the Dynacool lowers the chamber temperature to T<4K to enable the D850 to enter DR mode. The inset shows the temperature change for T<10K is much slower for the cooldown compared to the warmup (see Fig. 3-22 inset). Temperature data for T=10-4K are much more reliable, when measured during cooldown from 300K. The silicon diode needs to be forward biased at 10μA for temperature measurement but the heat load from the bias exceeds the D850 cooling power and base temperature becomes limited to T~3K. If the diode bias is turned off at this point, the sample can be cooled to 50mK.

It should be noted that mounting the silicon diode actually puts a small magnetic field on the sample. Fig. 3-24 shows R(B) for -10mT≤B≤10mT for a sample with positive magnetoresistance. The minimum should all be located at B=0T but the R(B) scans at different temperatures show the minimum occurs at B~1.5mT. The packaging of the diode is contains a ferromagnetic material, which adds an offset to the applied magnetic field. For measurements which require precise control of the magnetic field, it would be better to obtain a diode in the "bare die" form (e.g. DT670-BR, Lakeshore Cryotronics), which would be free of ferromagnetic material.

A material's dependence on the magnetic field direction (B) often provides valuable information. It is common to change the sample orientation, so that the magnetic field is pointed either perpendicular ($B^{\perp}$) or parallel ($B^{\parallel}$) to the sample plane. The sample holder for D850 enables only $B^{\perp}$. To apply $B^{\parallel}$, an L-shaped copper piece has been mounted on the sample holder. Fig. 3-25 shows the modified sample holder. The yellow block, mounted horizontally is the silicon diode for measuring the sample temperature. The L-piece is mounted by two holes where brass screws screw into the tapped holes on the sample holder (only one screw shown in image). The sample orientation is changed by removing the screws and rotating the L-piece by 90^{o} anti-clockwise. The plane with the sample attached becomes horizontal (wall → floor) and the plane with the diode becomes vertical (floor → wall). There are mounting holes on both sides of the L-piece (i.e. floor and wall) that match the configuration of tapped holes in the sample holder. The wires from the sample go to contact pads[14] along the edges of the L-piece. Form the contacts pads, wires connect to the contact pads on the sample holder. The wires are long enough that the sample orientation can be changed without reconfiguring the wiring.

[14] Made with Stycast (2850FT) and silver epoxy (H20E). See section 3.2.1 and 3.2.2.

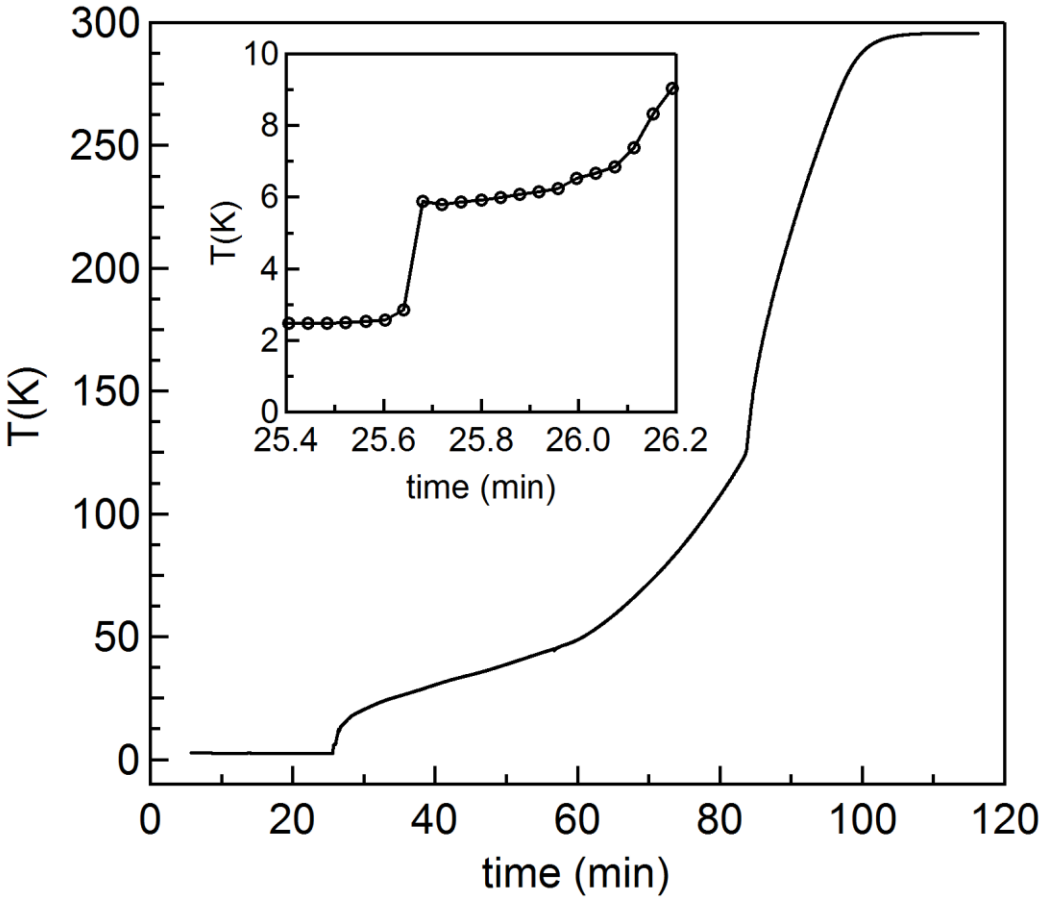

Fig. 3-22 Warmup from dilution cooling to 300K.
Temperature measured with silicon diode mounted on the sample holder.

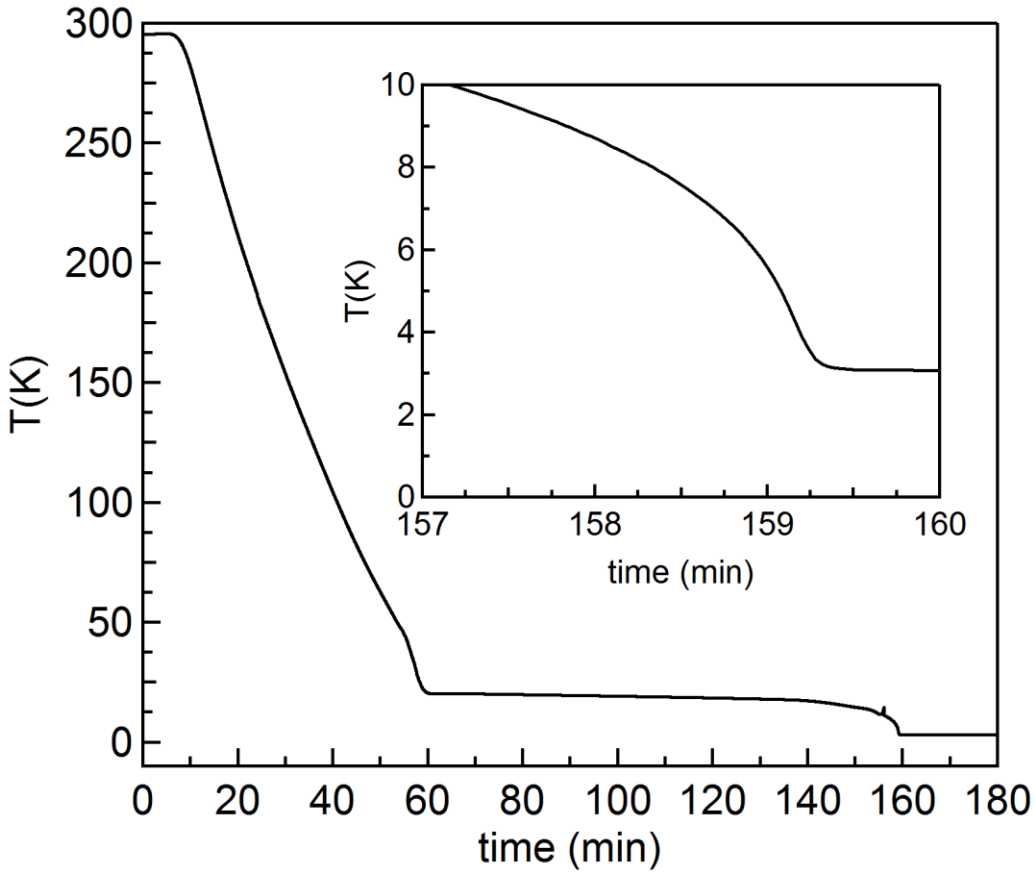

Fig. 3-23 Cooldown from 300K to dilution cooling.
Temperature measured with silicon diode mounted on the sample holder. Curve settles to T~3K after reaching dilution cooling, due to heat load from the 10μA bias to the diode.

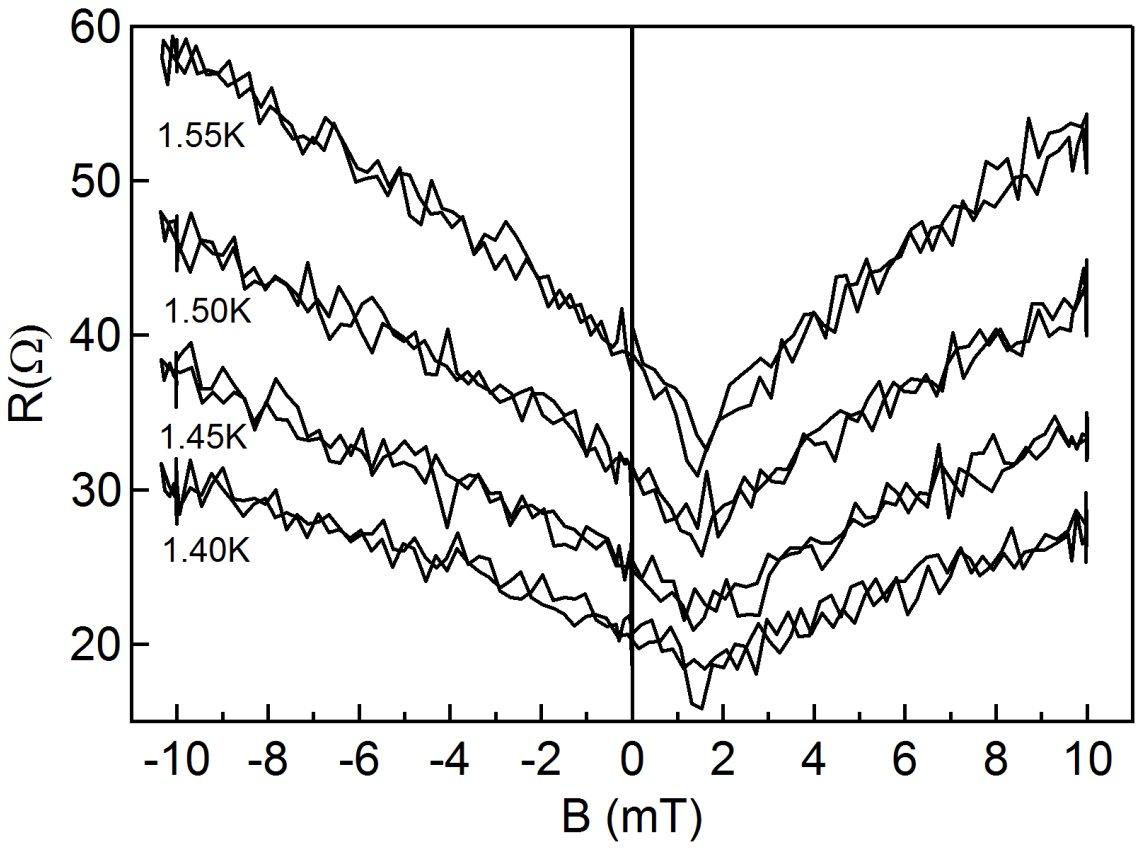

Fig. 3-24 Magnetic field offset from silicon diode.
R(B) at T=1.40, 1.45, 1.50 and 1.55K of a sample with positive magnetoresistance. Magnetic materials in silicon diode package adds ~1.5mT offset.

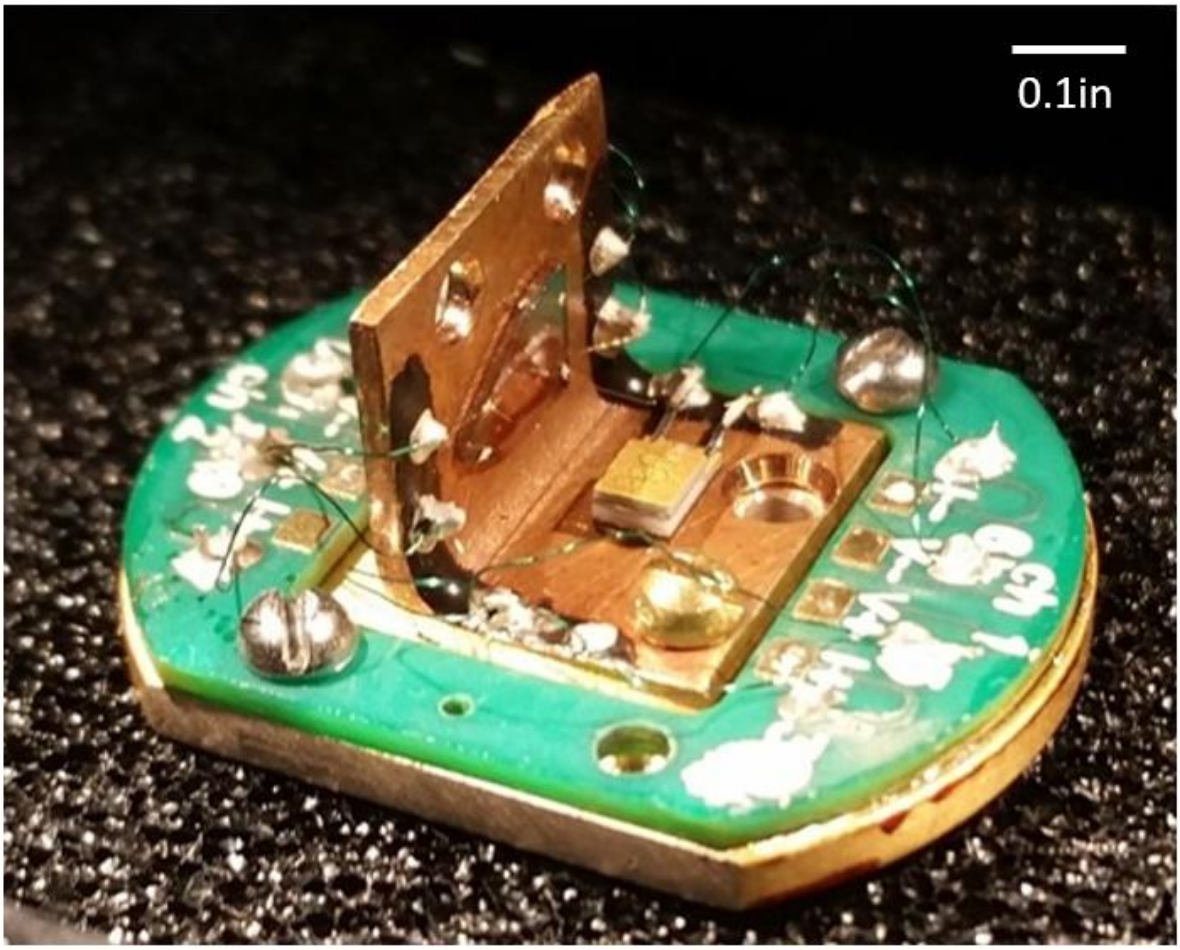

Fig. 3-25 Sample holder for $B^{\parallel}$ and $B^{\perp}$ in dilution refrigerator.
Sample is mounted vertically on the side wall of the L-shaped copper piece. On the horizontal face is a silicon diode for temperature measurement at T<4K.

3.3.2 MPMS

The magnetic property measurement system (MPMS, Quantum Design) is an automated cryostat equipped with a SQUID magnetometer. SQUID magnetometry is a sensitive measurement of sample magnetization (M) and particularly well-suited for measurements of samples under a low magnetic field[15]. Based on experience, samples with M as low as ~10^{-4}emu could be measured. Sample temperature is controlled for T=400-1.8K and magnetic fields up to B=±2T can be applied. The system uses liquid helium as the cryogen, which needs to be refilled every few days. Temperature control at T=4-1.5K is limited to 2 hours, as the system utilizes a smaller volume of helium cooled by evaporative cooling for this temperature range.

The SQUID magnetometer measurement is well-suited for samples which are difficult to make electrical contacts to, such as small samples, and electrical insulators. In samples with multiple

[15] For samples under high magnetic fields, torque magnetometry has remarkable sensitivity.

domains, it is possible that there are small superconducting domains that are isolated from each other. Such domains are difficult to detect from R(T) if they do not form a percolation network that bridges across the contacts but magnetometry does not require contacts.

Signatures of ferromagnetism and superconductivity are detected in zero-field cooldown (ZFC)/field cooldown (FC) measurements. ZFC measurement is performed with the following steps: 1) the sample is cooled under zero magnetic field to below its transition temperature, 2) the magnetic field B_{ext} is turned on at the lowest temperature and 3) M of the sample is measured, while warming up and under B_{ext}. Subsequently, FC measurement is performed by measuring M, while cooling and under B_{ext}. For ferromagnetism, the M(T) curves are different for ZFC and FC below the Curie temperature. For superconductivity, the magnetization becomes negative below the critical temperature due to diamagnetism. As the ZFC diamagnetic signal is due to shielding and FC is due to Meissner effect, the two curves do not necessarily overlap (see section 1.1.2).

Magnetization is measured by moving the sample through the detection loops with a stepper motor [148]. The detection loops is a superconducting wire wound in a second-order gradiometer configuration and inductively coupled to the SQUID. As shown in Fig. 3-26a, the loops are wound in one direction for the top and bottom, and in the opposite direction for the middle two. The SQUID translates magnetic flux to voltage for each sample position. The V vs position graph of Fe_2O_3 in Fig. 3-26b is a typical result for a sample with positive magnetization. The SQUID voltage peaks to a positive voltage at 1.5cm and 4.5cm, and dips down to a negative voltage at 3cm. The shape of the curve corresponds to the sample passing through the bottom loop at 1.5cm, the middle two loops at 3cm and the top loop at 4.5cm. The sign of the SQUID voltage reverses as the winding directions of the loops reverse and the peaks are half the height of the dip because the middle loop is wound twice.

A curve is fit to the V vs position data, assuming the sample is a point dipole of magnetization M. The measured M is the result of this fitting. It should be noted that one scan of the sample position through the detection loops yields *one* value of magnetization. In order to obtain M(T), at least one SQUID voltage vs sample position graph must be collected at each temperature. For every measurement of M, the fit should be checked to ensure that it reasonably follows the data. If the sample location is not correctly centered, the fit could even yield a magnetization in the opposite direction.

Samples are loaded into the MPMS by inserting a steel rod with the sample mounted on the bottom with a plastic straw and a gel cap. The vacuum seal of the MPMS chamber is able to form a seal around the steel rod to maintain the sample space under vacuum, as oxygen results in undesired paramagnetic signals at low temperature. The plastic straw is attached to the steel rod by polyimide tape (Kapton) and the gel cap holds the sample at the middle of the straw by tightly fitting inside the straw. The use of a plastic drinking straw may appear crude but the measurement sensitivity is unaffected as long as the sample is held by a non-magnetic material shaped as a cylinder with uniform mass distribution along its length. The uniformity of the cylinder is important because the pickup coils are configured to be sensitive to the spatial gradient of magnetization.

The sample undergoes three cycles of pumping out the air and purging with helium to flush out the oxygen. At this step, it is possible that a pressure difference develops along the length of the straw and the gel cap is sucked out from the bottom of the straw. To avoid losing the sample in this manner some holes should be made at the top of the straw and the bottom of the straw should be covered, but not sealed with polyimide tape. The top and bottom of the straw should

be sufficiently far from the sample to prevent the non-uniformity from affecting the measurement.

The MPMS can perform measurement at above room temperature up to 400K. For such measurements, a quartz tube should be used instead of a plastic straw. When heated to above room temperature, the straw expands significantly and loosens its grip around the gel cap. Hence, the gel cap could move around during measurement, due to vibrations. In contrast, a quartz tube would not expand as much as the straw.

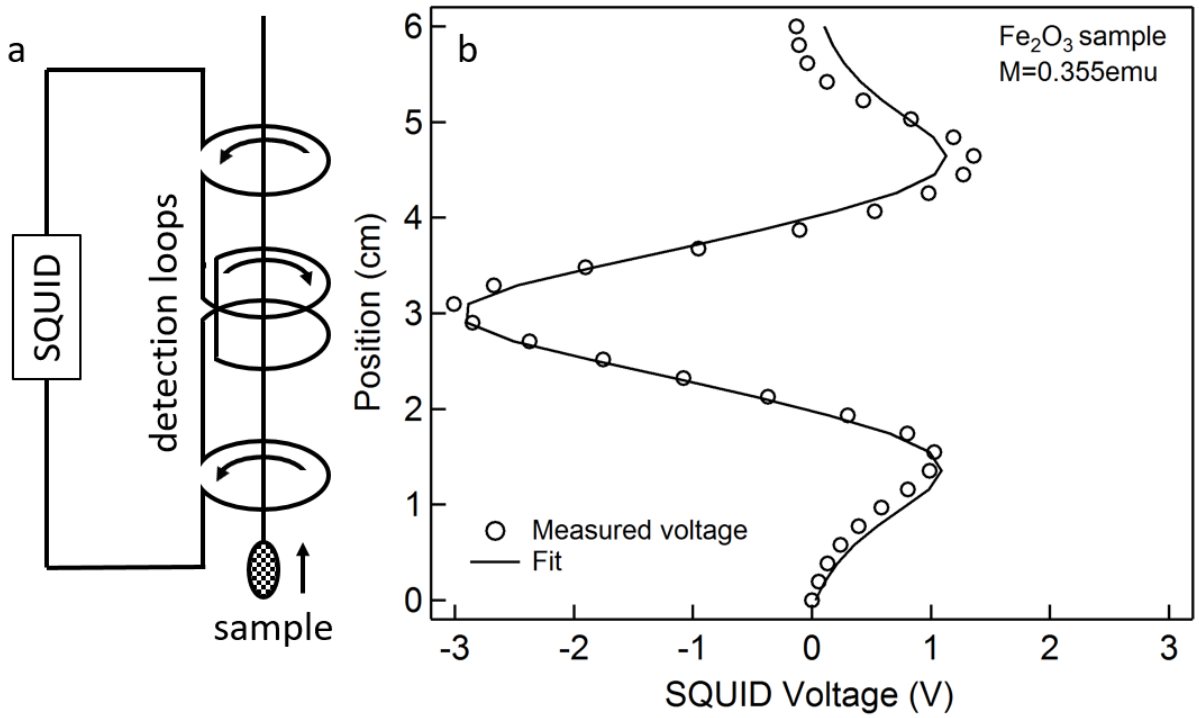

Fig. 3-26 MPMS measurement process.
a) The sample is vertically moved through superconducting detection loops in a second-order gradiometer configuration. The SQUID is inductively coupled to the detection coils and translates the magnetic flux to voltage at each position of the sample. The curved arrows accentuate the difference in winding direction between the middle two loops and the top and bottom loops. b) Moving the sample (e.g. Fe_2O_3) produces the graph shown. From the fit (solid line), the magnetization of the sample is calculated.

4 Crystal growth

High quality crystals are often necessary for observation of novel physical phenomena. As illustrated by Bloch's theorem [149], periodic order of a crystalline lattice is essential for the formation of a band structure. Emergent phenomena (e.g. CDW, superconductivity, massless Dirac fermions [57] and Weyl fermions [58,59]) are the results of a material's characteristic band structure (see Chapter 1). When the crystalline order is compromised, the characteristic physical phenomena are obscured and dominated by disorder effects. For example, when measuring R(T) in a metal, resistivity decreases with cooling from the suppression of electron-phonon scattering. In a disordered metal, the resistivity increases with cooling because "Anderson localization" [150] made the system into an insulator.

Crystal growth of organic semiconductors and transition metal chalcogenides (TMC) are presented in this chapter. Organic crystal growth (specifically rubrene) is motivated by the project discussed in Chapter Part III15. TMC crystals are grown for study at the ultrathin limit (see section 2.3). Specifically, TMC grown are $NbSe_2$, 1T-TaS_2, $NbSe_3$, TaS_3, $(NbSe_4)_3I$, WTe_2, FeSe, Fe_3Se_4, and $FeSe_2$. The synthesis methods are based on synthesis methods found in the literature but sometimes modified to match the needs of ultrathin study. In particular, some synthesis methods have been developed to quickly produce small crystals.

4.1 Growth techniques

Crystal growth often starts with the condensation of the source material molecules from a mobile state (e.g. gas or ions in a solution) into a solid. However thin film deposition processes, such as electron beam evaporation, does not necessarily result in crystallization. The substrate is much colder than the source temperature and when the molecules encounter the substrate, their kinetic energy is immediately quenched. The molecules adhere at the site where they first encounter the substrate and are unable to explore the most energetically stable configuration. In contrast, crystallization occurs when the molecules have enough time/energy to explore its neighborhood for the most energetically favorable site. To realize this condition, the molecules are slowly formed into a well ordered crystal.

To realize such crystal growth conditions, two techniques have been employed: vapor transport and flux growth. The apparatus for crystals growth for both methods are homemade. Vapor transport successfully grows crystals of all materials presented here. Since there is a possibility that flux growth is more suitable for WTe_2 and FeSe growth, flux growth syntheses are explored as well.

4.1.1 Vapor transport

Crystal growth by vapor transport involves the transport of source material in vapor form across a temperature gradient from hot to cold. Two variations are introduced: physical and chemical vapor transport. Physical vapor transport is used when the source material can vaporize or sublime at easily attainable temperatures (i.e. <1000^{o}C). Here, it is used in the growth of organic crystals. Fig. 4-1a schematically shows the physical vapor transport of rubrene. At the hottest part of the gradient, the source material in powder form is heated to give off vapors of the source material. A continuous flow of inert gas (e.g. N_2) carries the source material vapor along the temperature gradient from the hot zone to the cool zone. At some point in the temperature gradient, the vapor is cooled to the condensation temperature of the source material. At this point in the temperature gradient, the material slowly deposits on the walls of the furnace and grows as crystals.

Chemical vapor transport is used when vapors of the source materials cannot be easily obtained. For TMC crystal growth, a transport agent is necessary because most of the transition metals have melting points $\gtrsim$2,500^{o}C [151]. The transport agent vaporizes at a lower temperature and reacts with the source material to form a chemical complex, which diffuses as a gas. As shown in Fig. 4-1b, the complex forms at the hot zone and dissociates at the cool zone, depositing the materials for crystal growth. After dissociation, the free transport agent complexes with new source material at the hot zone and carries it to the cool zone. This cycle continuously feeds material to the growing crystal. Taking $NbSe_2$ as an example, the suggested chemical reaction is [152]

$$NbSe_{2(s)} + 5/2 I_{2(g)} \rightleftharpoons NbI_{5(g)} + 2Se_{(g)} \qquad \text{Eq. 4-1}$$

In this case, the starting material is $NbSe_2$ powder. As the transport agent (iodine) reacts with $NbSe_2$ to form a gaseous complex and selenium is a gas at >685^{o}C [151]. In literature, the exact composition of the intermediate complex are often not determined. Iodine is commonly used as a transport agent for its low boiling point (184^{o}C [151]) and chemical reactivity.

During vapor transport, the material is simultaneously synthesized and purified by the temperature gradient. Most of the impurities in the source material have a different condensation temperature than the source material. Hence, the impurities are deposited at different parts of the temperature gradient and separated from the target crystal. The target crystal grows at a point, where the molecules' kinetic energies are too low to remain in the gas phase but still high enough to explore the energy landscape for the most stable configuration. A well-ordered crystal lattice is the most energetically stable form for a solid and the temperature gradient enables the chemical species to find this state. Slow growth is essential for minimizing structural defects (e.g. dislocations). Typical growth durations are 2 weeks to a month for ~1mm crystals. To realize the conditions above, a long furnace with a shallow temperature gradient is desired.

Physical vapor transport uses an open system, where inert gas from an external source can flow through the open ends of a tube (Fig. 4-1a). In contrast, chemical vapor transport is a closed system, in which both ends of the tube are sealed (ampoule) and transport occurs with the diffusion of the pre-loaded transport agent (Fig. 4-1b). Ampoules are made by first sealing one end of a quartz tube with a hydrogen torch and loading the ingredients for crystal growth. Subsequently, the open end of the quartz tube is connected to the adapter of a vacuum station at the point labeled "quartz piece" in Fig. 4-2 and evacuated. Finally, the quartz piece is heated at a point near the quartz piece/vacuum junction with a hydrogen torch until the tube is sealed. While the quartz piece is evacuated, heating the quartz makes the wall cave inward. The purpose is to make the walls collapse from all sides to seal the tube. However, if the wall caves in too rapidly, the material becomes overstretched and a hole is pulled. Particularly for ampoules of large diameter, it is necessary to deform the prospective sealing point of the quartz piece into a "neck" with a hydrogen torch before attaching it to the vacuum station.

As ampoules are sealed systems, some reactions could result in explosions. If too much transport agent is added, pressure could build up at high temperature due to thermal expansion and cause the ampoule to explode. Ampoules are also used for reacting elements together to form the source material powder. In this case, caution should be exercised when ramping up the temperature. If the metal and the chalcogenide reacts quickly (e.g. niobium and selenium) the chalcogenide vapors at high temperature condense into a solid metal chalcogenide. However, if the reaction is slow (e.g. tantalum and sulfur), the ampoule fills with chalcogenide vapor and pressure builds up as the temperature is raised. When exploring a reaction for the first time, it is advised to seal an ampoule within a larger ampoule, in case the smaller ampoule breaks. The system should be closely monitored during the first temperature ramp up.

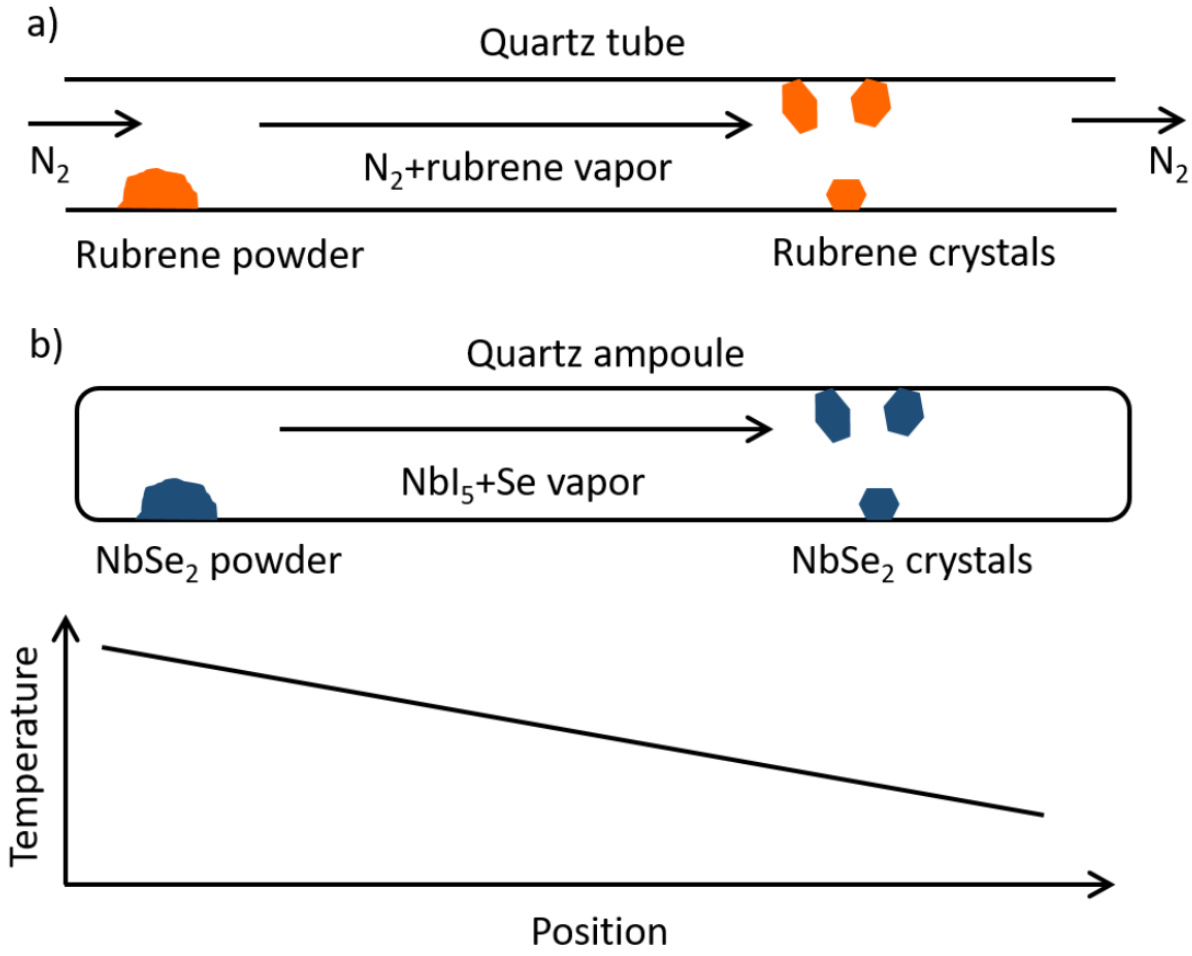

Fig. 4-1 Vapor transport schematic.
a) Physical vapor transport for rubrene crystal growth. b) Chemical vapor transport for $NbSe_2$ crystal growth with iodine as transport agent. The temperature vs position graph at the bottom indicates the systems in a) and b) are placed in a temperature gradient.

The vacuum station, shown in Fig. 4-2, is developed with the help of Jacob Bryon. The quartz piece is evacuated with the turbomolecular pump, while valves V1 and V3 are open and V2 is closed. Before sealing the ampoule, the gate valve V3 is closed to protect the pump. If a hole is pulled during the ampoule sealing process, the rapid loss of vacuum would damage the pump. The setup reaches ~10^{-6}torr, while pumping, but the vacuum degrades without actively pumping. The large volume of the ballast stabilizes the vacuum to ~10^{-2}torr while sealing the ampoule. The vacuum would be improved if a cryo-pump is used instead. However, we found vacuum <10^{-1}torr is sufficient for the growth of high quality crystals (see section 2.1.2). For loading air sensitive materials, such as alkali metals or $AlCl_3$, the setup can be disconnected at flange F1 to load the ingredients inside a glovebox. After coming out of the glovebox, the materials in the quartz piece are protected from air as long as V1 is closed. Some crystal growth processes are accelerated by the presence of argon compared to vacuum. To seal the ampoule with some argon, the system is first flooded with argon by opening V2. Then, the pump is started and V2 is closed.

Before all the argon is pumped out, V3 is closed when the desired pressure of argon is indicated by the gauge.

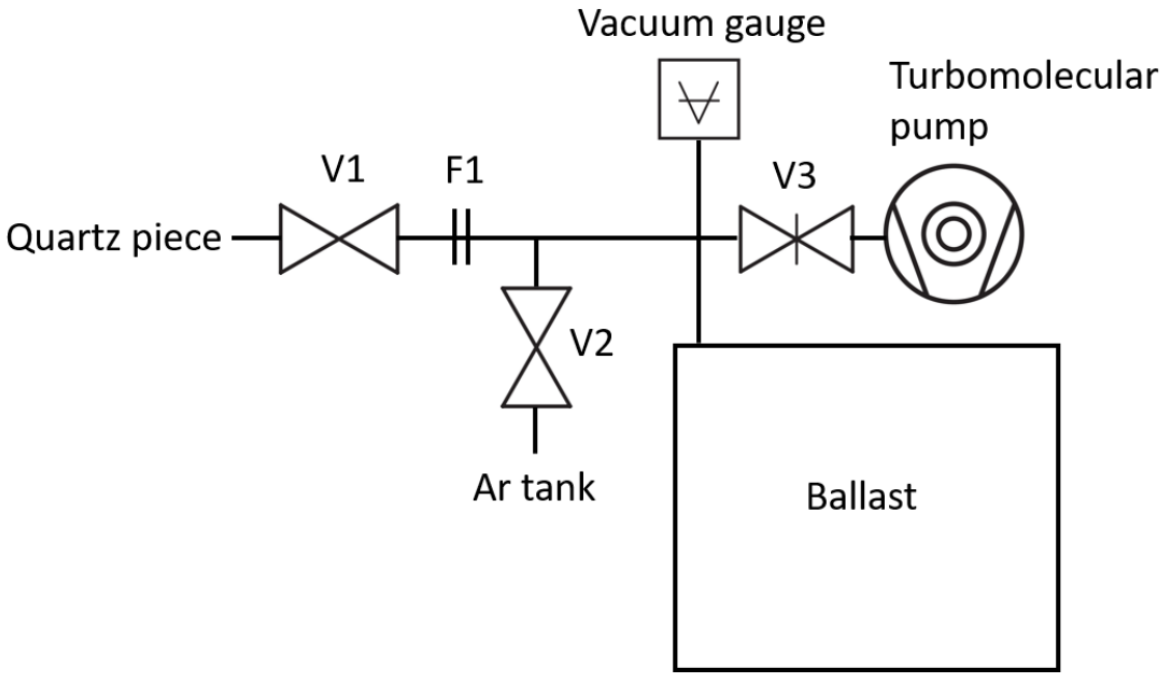

Fig. 4-2 Ampoule sealing station.
Valves are labeled by V1, V2 and V3. F1 indicates a flange.

The temperature gradient is created by a homemade temperature gradient furnace (see Fig. 4-3). The furnace consists of two quartz tubes of different diameters concentrically arranged. For physical vapor transport, adapters for flowing inert gases are connected at both ends and another tube is placed inside the inner tube to load ingredients and extract crystals. For chemical vapor transport, ampoules are placed in the inner tube. The outer tube serves as thermal insulation to trap the heat from the heating coil around the inner tube. Fiberglass insulation is inserted at the ends as thermal insulation and to separate the inner tube from the outer tube wall. Quartz is used for its stability up to high temperature and optical transparency. The furnace is designed, so that we can look through the furnace walls and the crystal growth progress can be monitored without interrupting the growth.

The heating coil is Ø0.5mm nichrome (Chromel C) wire wound with spacing, which gradually grows from left to right. The temperature is highest (lowest) in the region with the smallest (largest) distance between coil windings. The coil is fixed in place by alumina paste, which runs along the length of the inner tube. The coil remains in place due to friction at room temperature but at high temperature, the wire in the coil expands and moves around. As the strain on the coil is trapped from the winding process, the coil would completely loosen from the setup if it is not fixed in place. Three parallel lines of alumina paste, which are equally separated from each other provide this mechanical support. Placing asbestos tape between the coil and the inner tube during the winding process is a known solution but a substitute had to be found due to unavailability of asbestos tape. The alumina paste (Ceramabond 569, AREMCO Products Inc.) is stable at high temperature but coats the outer tube with a thin layer of yellowish material after a few weeks of

running the furnace. According to the manufacturer, the alumina paste does not outgas and the yellow coating is likely due to a chemical reaction between components in the alumina paste and the nichrome wire. An alternative product (Pyro-Paint 634-ZO, AREMCO Products Inc.) has been suggested but has not been used in a furnace yet.

The temperature along the length of the furnace for different power settings of the variac are measured to obtain a calibration of the variac power to temperature profile. The gradient furnace has been operated at ~1000^{o}C but the inner tube becomes cloudy, possibly due to the changes in the quartz crystal structure. In practice, the furnaces are limited to <800^{o}C for routine operation, which proves sufficient for TMC growth. Once the synthesis parameters for successful crystal growth is identified, the outer tube is wrapped with aluminum foil to enhance the heating efficiency. In this manner, multiple furnaces could be powered from a single 120V, 20A circuit. In some instances, commercial furnaces without a deliberate temperature gradient have been used (e.g. Lindberg 59344 box furnace and Barnstead International F21135 tube furnace). The temperature inhomogeneity inside the furnaces have proven sufficient for some vapor transport growths.

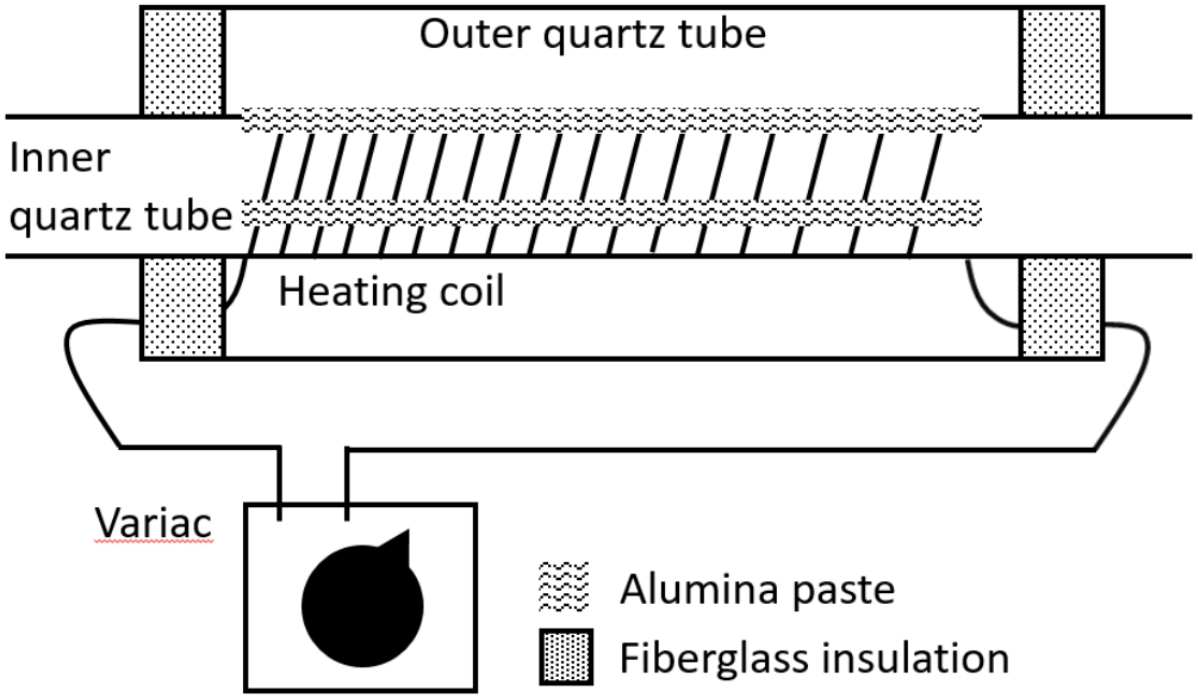

Fig. 4-3 Temperature gradient furnace schematic.
Homemade temperature gradient furnace consists of concentric quartz tubes separated by fiberglass insulation (dots pattern). The heating coil is wound on the inner tube and powered by a variac. The gradual variation in coil winding spacing results in a temperature gradient. The coils are fixed in place by alumina paste (wavy lines pattern).

4.1.2 Flux growth

In flux growth, materials are crystallized in solution. The growth starts at high temperature, when the source material is completely dissolved in a solution ("flux"). As the temperature is lowered, the solubility of the source material in flux is reduced. At some temperature, the flux is saturated and the materials, begin to precipitate out of the flux. When the temperature decrease is slow, the precipitate forms very slowly, enabling them to grow into crystals. The temperature is decreased until the flux solidifies. At this point, the flux grown crystals are embedded in a solid piece of flux. In most cases, the flux is water soluble (e.g. KCl) and the crystals are extracted by dissolving the flux.

The advantage of flux growth compared to vapor transport is that it does not depend on the chemistry of the transport agent. It is well-suited for the crystal growth of compounds, which are more complex than binary compounds, as many ingredients can be simultaneously dissolved in the flux [153]. The drawback of flux growth is that the impurities in the flux or the source material can be trapped in the crystal. Crystals grown by vapor transport are often regarded as "cleaner" than flux growth. However, there are instances in which flux growth yields higher quality crystals than vapor transport [154].

Since the cooling rate translates to crystal growth rate, it is important that the materials are slowly cooled. The furnaces in the lab were limited to cooling rates of $\geq 6^{o}$C/hr, as the control electronics were not designed for slower rates. To enable slower cooling rates, a control unit for flux growth has been designed, constructed and tested by Patrick Stetz (see Fig. 4-4). The control unit is based on a feedback loop, which adjusts power to the furnace heating coils with a relay. The temperature reading from a type K thermocouple is sent back to the control unit. The ampoule for flux growth is placed inside a copper block (~7kg) to smooth out rapid changes in temperature by adding thermal mass. Ampoule temperature is measured by a thermocouple placed closed to the ampoule, inside the copper block, and logged by a commercial readout system. Another thermocouple is placed near the heating elements, outside of the copper block, to serve as the temperature feedback. The feedback thermocouple is necessary because the thermal response of the copper block is too slow to use for feedback control and causes temperature oscillations.

As shown in Fig. 4-4, the Fuji Electric PXR3 is the central piece of the feedback electronics. Large currents for heating the furnace goes through the relay and heats it up. While the relay (Crydom D1225) is designed to operate up to 80^{o}C, it is isolated in a separate enclosure to avoid overheating the other electronic components. The heat sink actually dissipates heat efficiently enough that the relay temperature only increases slightly. The temperature controller maintains temperature at a setpoint and carries out automated temperature ramping. Fig. 4-5 shows the temperature of the ampoule during a cooldown at 0.9^{o}C/hr. The line in the inset represents data points taken every 2 minutes, demonstrating a linear cooling rate is maintained for >100 hours. The main panel is the time=16-22hrs section of the cooldown with a linear fit with slope 0.9^{o}C/hr. In summary, cooling rates much slower than the previous limit, 6^{o}C/hr has been realized by making a new temperature controller.

Currently, the system is controlled by a commercial software, which executes a pre-defined temperature ramp process. For more flexibility, a custom program should be developed (e.g. with LabVIEW) to control the temperature by continuously renewing the setpoint. A temperature ramp would be executed by periodically renewing the setpoint to a value calculated from the

initial temperature, final temperature and ramp rate. For large enough thermal mass, the stepwise change in temperature is smoothed out to a continuous, slow change in temperature.

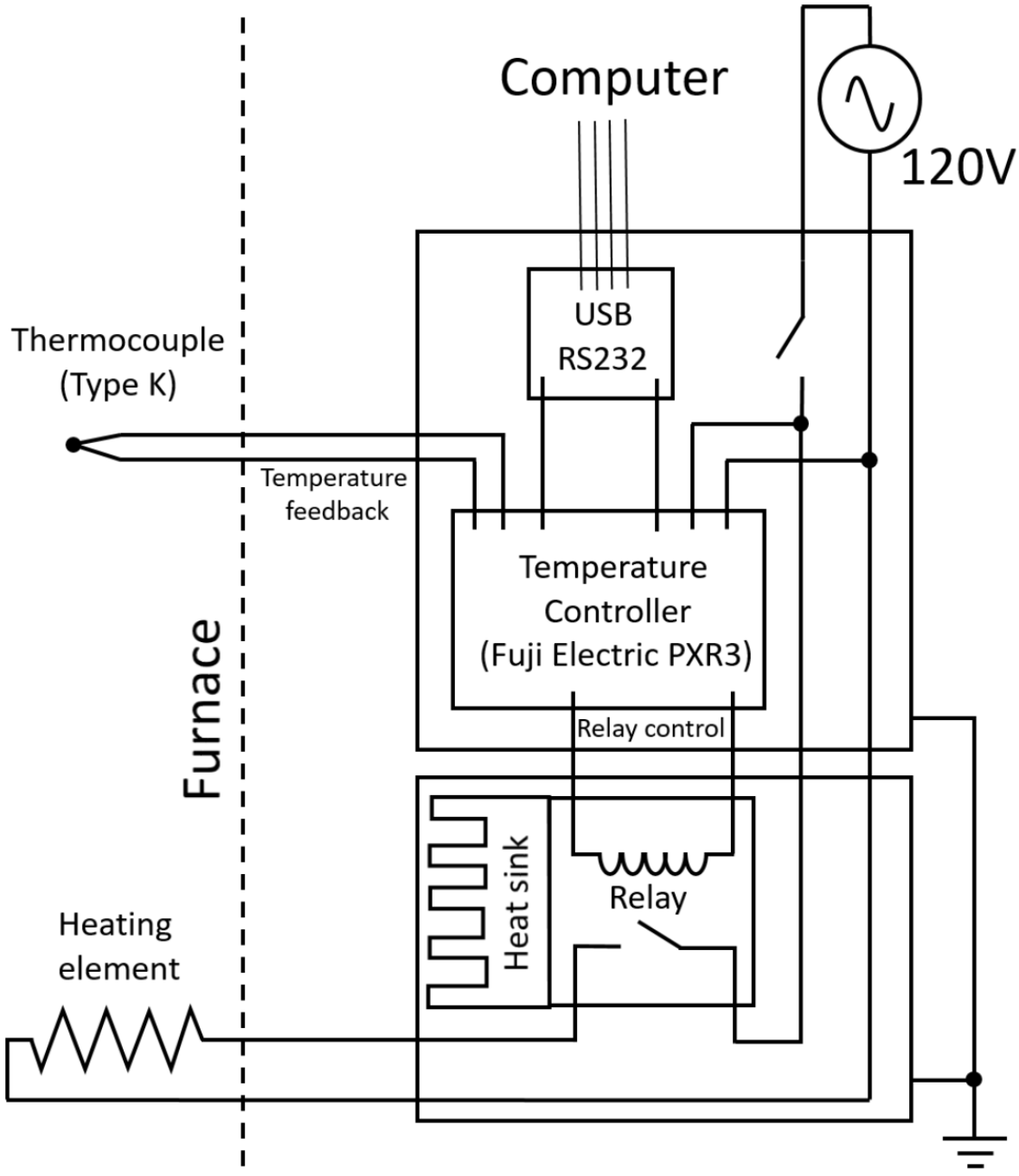

Fig. 4-4 Flux growth control unit schematic.
The temperature controller interfaces with the computer and controls furnace temperature through the relay. The control is based on a feedback loop with the thermocouple reading as feedback.

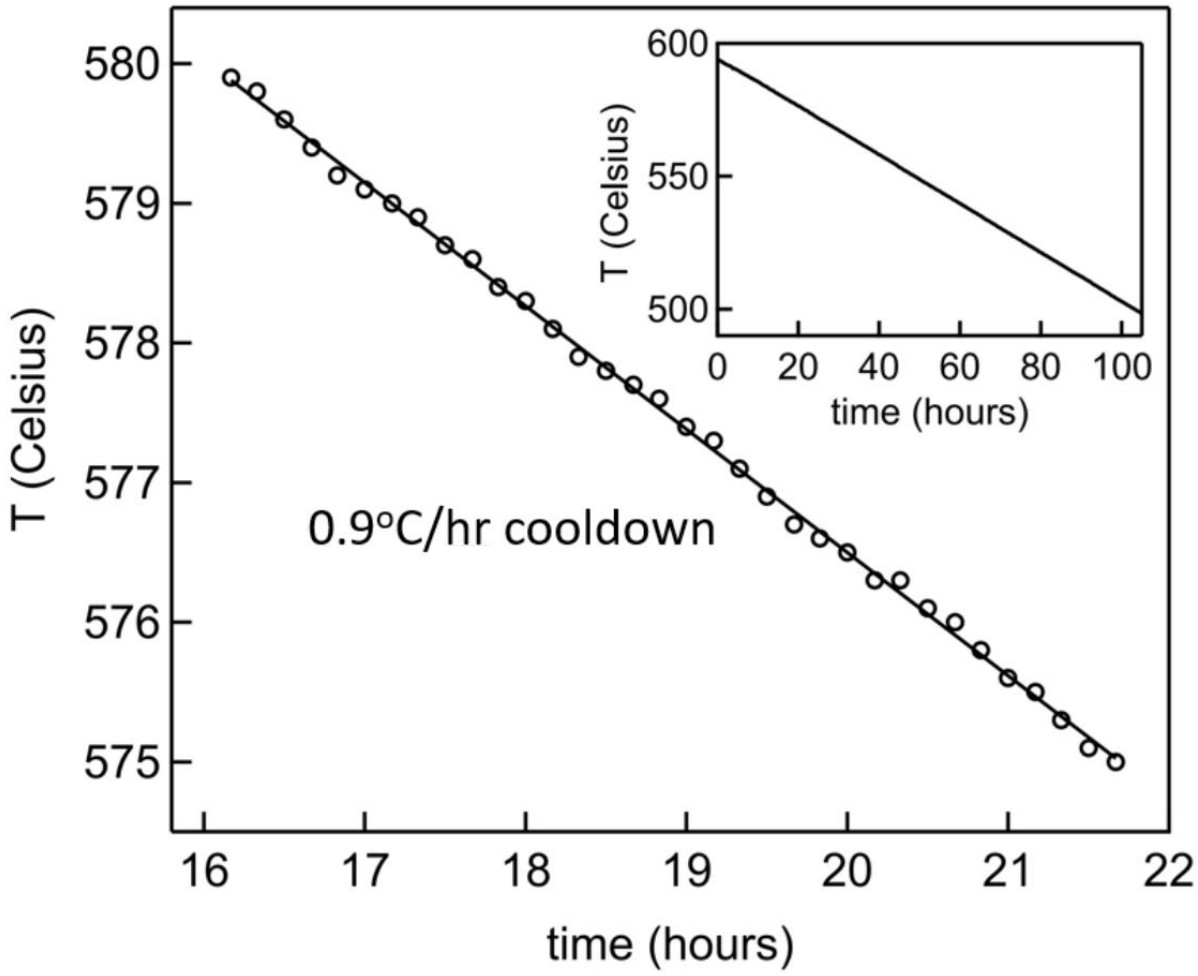

Fig. 4-5 Flux growth control unit test run.
The line in inset is from data points, taken every 2min. The main panel is the 16-22hrs section of the cooldown displayed in inset. The open circles are data points and the line is a linear fit with slope -0.9°C/hr.

4.2 Characterization

Crystals are primarily characterized by R(T) measurements. The characteristic superconducting or charge density wave transition temperatures of the material are compared with previous studies. The crystals are glued to a quartz substrate and 25μm (1mil) diameter annealed gold wires are attached to the crystal with silver paste (see section 3.1.1). Each contacted crystal is loaded into a commercial, automated cryostat (Quantum Design PPMS Dynacool, see section 3.3.1) and R(T) is measured with the current switching method (see section 3.1.3).

The magnetic properties of synthesized crystals are characterized by a SQUID magnetometer (Quantum Design MPMS, see section 3.3.2). The samples are loaded in a gel cap and snugly fit to a plastic straw. Signatures of superconductivity, ferromagnetism/ferrimagnetism and antiferromagnetism are confirmed by ZFC/FC cycles and M(B) hysteresis loops.

For some samples, the crystal structures are deduced from X-ray diffraction (XRD). XRD is performed by Antonio DiPasquale at the X-ray Crystallography Facility in College of Chemistry, UC Berkeley.

4.3 Organic crystal (rubrene)

Rubrene crystals (see "Rubrene" in Fig. 13-1) are grown by physical vapor transport for the photoconductivity experiment described in Chapter Part III15. The synthesis is based on Laudise *et al*. [155]. Rubrene powder is placed at the hottest zone of a temperature gradient with 2.5cm^3/min N_2 gas flows from the hot zone to the cool zone. The temperature gradient is stabilized by a PID feedback loop based temperature controller, which maintains the thermocouple reading at 180^{o}C. The thermocouple does not indicate the actual temperature of rubrene, as it is not in direct contact with it, but the hot zone temperature is assumed to ~300^{o}C, the source temperature used by Podzorov *et al*. [156]. The thermocouple location is unchanged throughout all growths for reproducibility of thermal conditions. The temperature setting for growth was initially found by ramping up the power until small crystallites appeared on the cooler zone.

It is challenging to reach into the long furnace tube with tweezers to extract the crystals. To facilitate crystal extraction, short quartz tubes, with slightly smaller diameters than the gradient furnace, are inserted at the growth zone. The crystals grow on the inner walls of the inserted tubes. After growth, the tubes are taken out of the furnace to extract the crystals. After 4 days of growth, orange crystals of ~2mm x 1mm x 10μm (see Fig. 4-6) are obtained. The inter-molecular forces are weak van der Waals forces, making the crystals extremely fragile. $NbSe_2$ crystals of thickness ~10μm are strong enough to be picked up with tweezers. In contrast, rubrene crystals of similar thickness break, when they are pinched with tweezers. Instead, they are manipulated by a hypodermic needle connected to a vacuum.

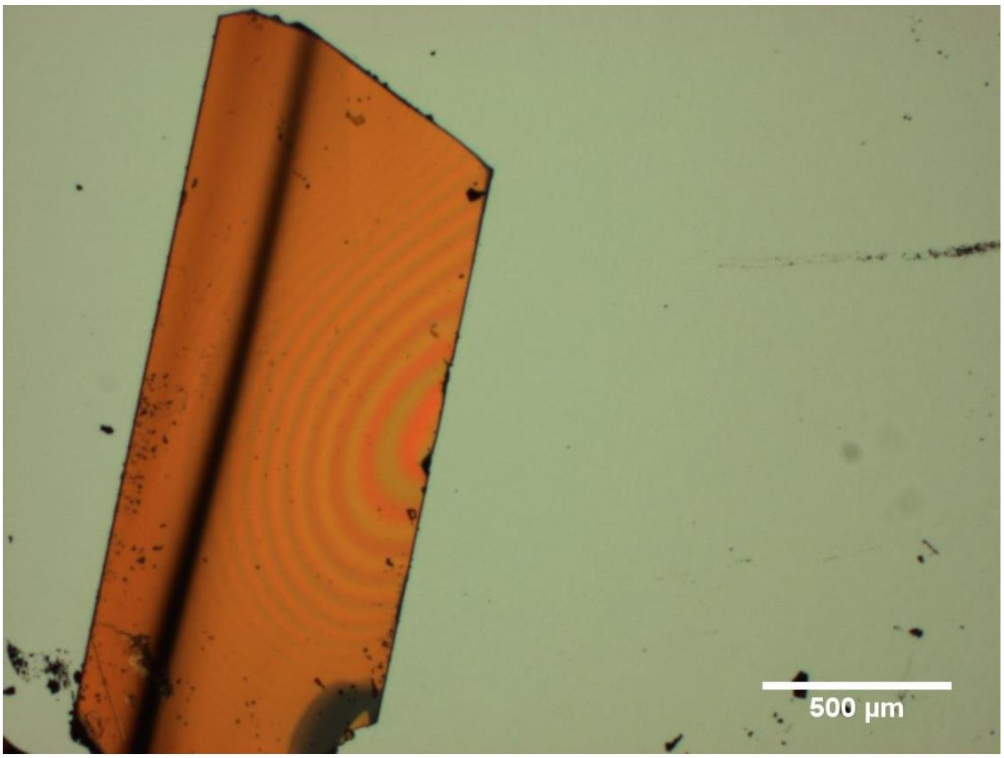

Fig. 4-6 Synthesized rubrene crystal.
Thickness~10μm.

4.4 Transition metal chalcogenide crystals

The crystal structures and electronic properties of the transition metal chalcogenides are introduced in Chapter 2. Many of the compounds in Table 2-1 are synthesized to study collective ground states (e.g. superconductivity and CDW, see Chapter 1) at the ultrathin limit. The synthesis parameters and characterization results are presented in this section. The crystals were synthesized mostly by a team of undergraduate researchers in the Zettl group: Joey Barreto, Corey Shih, Xiyue Wang, Patrick Stetz and Jacob Bryon and characterized with their help. Magnetization measurement are in collaboration with Owen Chen, an undergraduate researcher in the Zettl group. The synthesis parameters for the crystals grown are summarized in Table 4-1 and Table 4-2.

Synthesis	**I**	**II**	**III**	**IV**
Description	Thick $NbSe_2$	High quality $NbSe_2$	Thick 1T-TaS_2	Fast 1T-TaS_2 growth
Materials (purity)	$NbSe_2$ powder (99.8%) 65.4mg Iodine crystals (99.999%) 27.0mg	Nb powder (99.99%) 49.0mg ($0.5x10^{-3}$mol) Se powder (99.999%) 126.1mg ($1.6x10^{-3}$mol) Iodine crystals (99.999%) 51.8mg ($0.4x10^{-3}$mol)	Ta powder (99.9%) 323.5mg ($1.8\ x10^{-3}$mol) Sulfur powder (sublimed) 132.3mg ($4.1\ x10^{-3}$mol) Iodine crystals (99.999%) 134.4mg ($1.1\ x10^{-3}$mol)	TaS_2 powder (99.8%) 421.7mg Sulfur powder (sublimed) 15.7mg Iodine crystals (99.999%) 140.0mg
Ampoule size (Ø x length)	0.64cm x 13.5cm	1.27cm x 17cm	1.27cm x 20cm	1.27cm x 20cm
Vacuum (torr)	10^{-1}	10^{-1}	10^{-1}	10^{-1}
Temperature conditions	Homemade gradient (Fig. 4-7) T_{source}=713ºC T_{growth}=700-670ºC	Box furnace (Lindberg 59344) 700ºC	Tube furnace (Barnstead International F21135) 1. 1050ºC for 1 day. 2. 950ºC for 28 days. 3. Quench in ice water.	
Growth time (days)	56	12	29	7

Table 4-1 Crystal synthesis parameters.
Syntheses I-IV. Table continues on next page.

Synthesis	**V**	**VI**	**VII**	**VIII**
Description	Gradient grown $NbSe_3$	Box furnace grown $NbSe_3$	TaS_3	$(NbSe_4)_3I$
Materials (purity)	Nb powder (99.99%) 48.8mg ($0.5x10^{-3}$mol) Se powder (99.999%) 125.4mg ($1.6 x10^{-3}$mol)	Nb powder (99.99%) 42.0mg ($0.6x10^{-3}$mol) Se powder (99.999%) 130.1mg ($1.6x10^{-3}$mol)	TaS_2 powder (99.8%) 121.7mg ($0.6x10^{-3}$mol) Sulfur powder (sublimed) 53.0mg ($1.7x10^{-3}$mol) Iodine crystals (99.999%) 126.6mg ($1.0x10^{-3}$mol)	$NbSe_2$ powder (99.8%) 301.6mg Iodine crystals (99.999%) 99.8mg
Ampoule size (dia. x length)	1.27cm x 15cm	1.27cm x 11cm	1.27cm x 20cm	1.27cm x 20cm
Vacuum (torr)	10^{-1}	10^{-1}	Argon filled	10^{-1}
Temperature conditions	Homemade gradient (Fig. 4-13) T_{source}=707°C T_{growth}=664-653°C	Box furnace (Lindberg 59344) 700°C	Homemade gradient (Fig. 4-16) T_{source}=666°C T_{growth}=545-534°C	Homemade gradient (Fig. 4-19) T_{source}=689°C T_{growth}=544-539°C
Growth time (days)	19	12	7	55

Table 4-1 continued. Syntheses V-VIII. Table continues on next page.

Synthesis	**IX**		**X**	
Description	WTe_2		FeSe	
Materials (purity)	W wire	170.1mg ($0.9x10^{-3}$mol)	FeSe powder (Table 4-2XII)	268.4mg
	Te shots	223.8mg ($1.8x10^{-3}$mol)	$AlCl_3$ powder (99.99%)	281.1mg
	Iodine crystals (99.999%)	106.1mg ($0.8x10^{-3}$mol)		
Ampoule size (dia. x length)	1.27cm x 20cm		1.27cm x 15cm	
Vacuum (torr)	10^{-1}		Ar+H_2O filled	
Temperature conditions	Homemade gradient (Fig. 4-22) T_{source}=696ºC T_{growth}=696-668ºC		Homemade gradient (Fig. 4-26) T_{source}=363ºC T_{growth}=268-252ºC	
Growth time (days)	33		24	

Table 4-1 continued. Syntheses IX-X.

Synthesis	XI		XII	
Description	TaS_2 powder		FeSe powder	
Materials (purity)	Ta powder (99.9%)	1,423.9mg ($7.9x10^{-3}$mol)	Fe grains (99.999%)	1,119.7mg ($20x10^{-3}$mol)
	Sulfur powder (sublimed)	497.9mg ($15.6x10^{-3}$mol)	Se powder (99.999%)	1,551.2mg ($20 x10^{-3}$mol))
Ampoule size (dia. x length)	1.27cm x 20cm		1.27cm x 17cm	
Reaction condition	1.600°C for 4 days. 2.1,050°C for 1 day. 3.920°C for 5 days.		1.750°C for 1 day. 2.1,075°C for 1 day. 3.Cool to 400°C for 1 day.	

Table 4-2 Powder source material synthesis parameters.

4.4.1 Quasi-2D CDW material

$NbSe_2$ and 1T-TaS_2 are classified as quasi-2D CDW materials, as they form plate-like crystals and exhibit CDW phase transitions. The background on the crystal structure and characteristic transitions are discussed in section 2.1. Synthesis parameters are more sensitive for quasi-2D CDW materials than for the quasi-1D CDW materials and more trials are required before successful crystal synthesis. Large crystals are obtained from month-long growths. An alternate accelerated growth method is also presented. With this method, crystals of ~1mm x 1mm are obtained in ~1 week without a gradient furnace.

4.4.1.1 $NbSe_2$

$NbSe_2$ crystals are grown with the help of Jacob Bryon, Joey Barreto and Corey Shih.

Fig. 4-8a shows large crystals grown from pre-reacted $NbSe_2$ powder and iodine sealed in an ampoule, while in a temperature gradient (see Fig. 4-7) for 56 days. The source material is placed at the hottest zone at 713°C, the crystals grow at the 700-670°C zone. The synthesis parameters are summarized in Table 4-1I. Since the crystals grow close to the hot zone, it is likely that temperature inhomogeneity in a box furnace is sufficient for crystal growth.

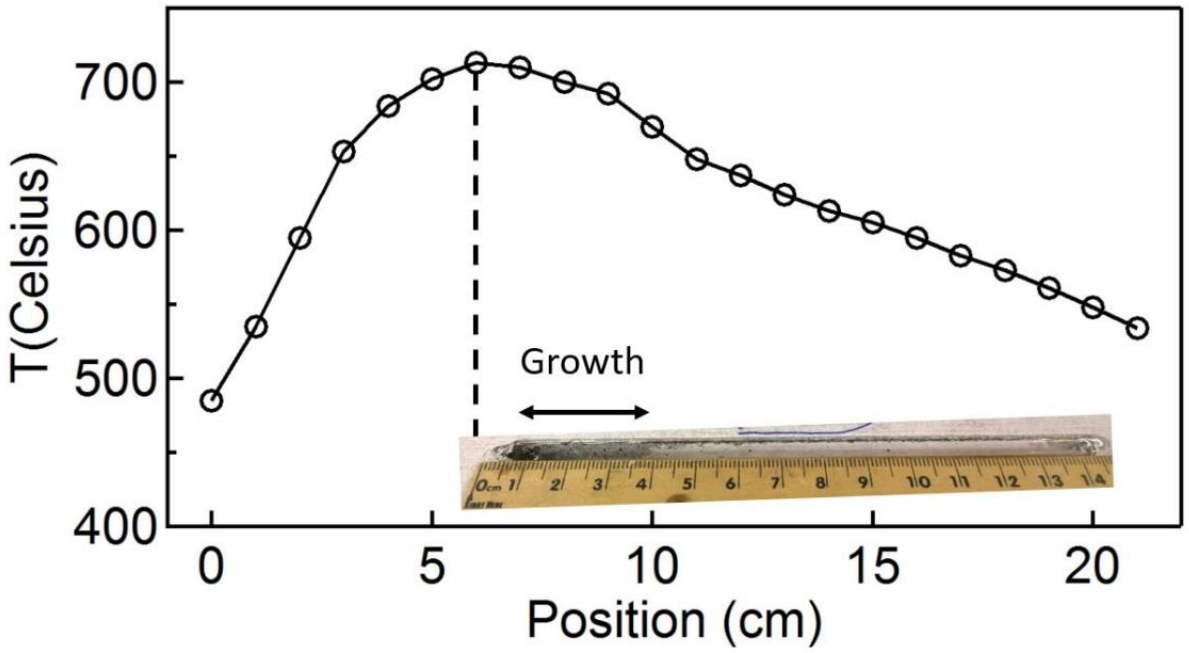

Fig. 4-7 $NbSe_2$ crystal synthesis temperature profile.
Image of the ampoule after synthesis is scaled and placed according to its placement in the gradient furnace. T_{source}=713°C, T_{growth}=700-670°C.

Fig. 4-8b shows crystals of ~1mm are obtained from a 12 day growth in a box furnace at 700°C (Table 4-1II). Instead of using pre-reacted $NbSe_2$, niobium and selenium in their elemental form can be used. Interestingly, with a stoichiometry of Nb:Se=1:3, growth of $NbSe_3$ is expected but only $NbSe_2$ is obtained. A possible reason is that $NbSe_3$ does not grow when iodine is present (see section 4.4.2.1). Comparing the images in Fig. 4-8a,b, the crystal from a 56 day growth and 12 day growth have similar lateral dimensions. However the 56 day growth is 400μm thick, whereas the 12 day growth is <100μm thick.

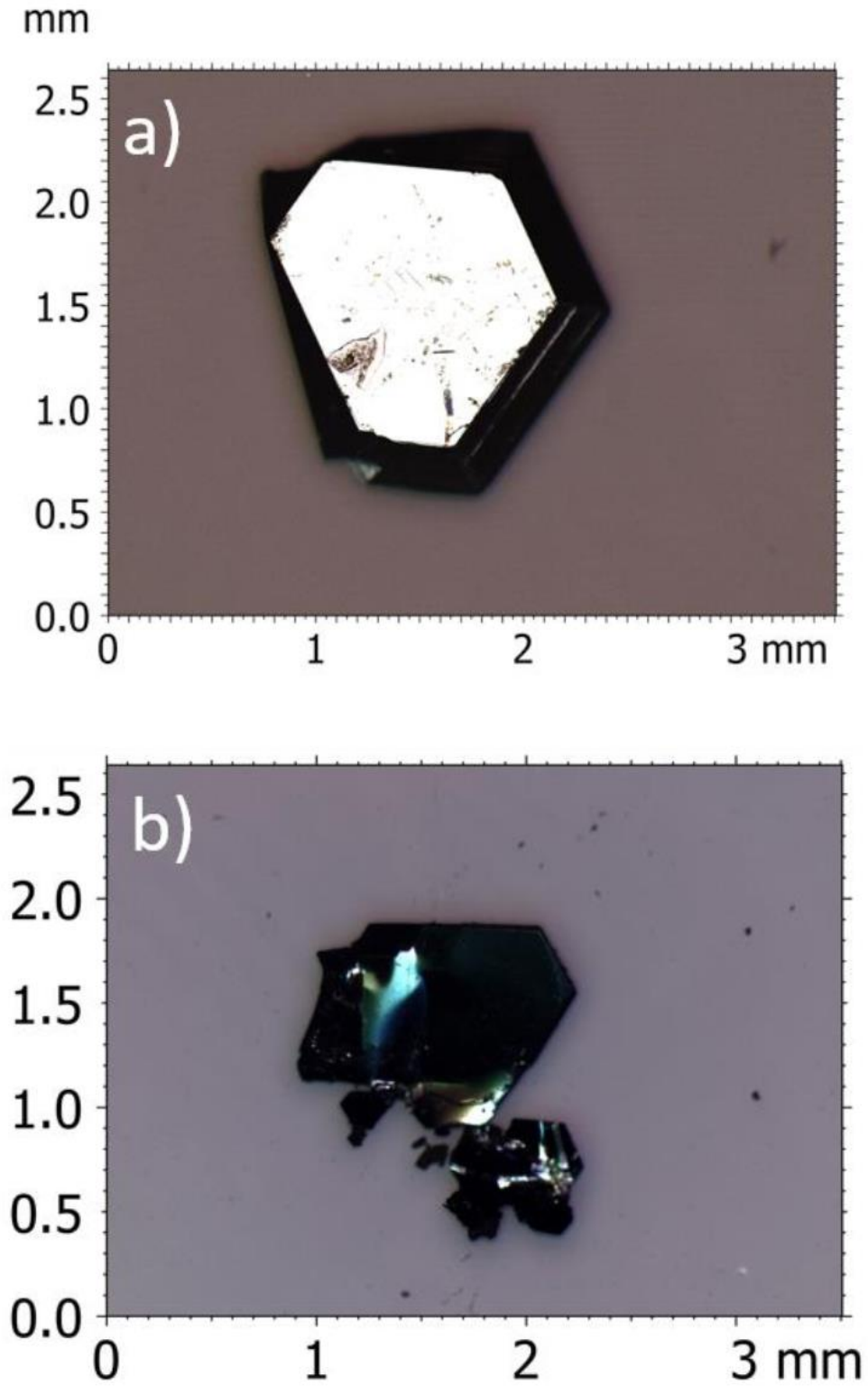

Fig. 4-8 Synthesized $NbSe_2$ crystals optical images.
a) Grown for 56 days in gradient furnace. b) Grown for 12 days in box furnace.

The reported T_c in literature for $NbSe_2$ is 7.2K [81] (see section 2.1.2). However, the R(T) in Fig. 4-9 shows depressed T_c<5.5K. A crystal grown in 10^{-5}torr (solid line) actually has a lower residual resistivity ration (RRR) than a crystal grown in 10^{-1}torr (dotted line). As shown in the inset, the crystal from 10^{-5}torr has a lower T_c as well. The depression in T_c appears not to be caused by contaminants in vacuum. Both crystals are grown from commercially obtained pre-reacted $NbSe_2$ powder with a purity of 99.8%.

Fig. 4-10 shows R(T) of a crystals grown from 99.99% Nb powder and 99.999% Se powder (Table 4-1II). The right on the right shows the onset of superconductivity at 7.2K. Hence, the depression of T_c is due to the impurities in the source material. A small anomaly is seen at ~32K in the main panel. In the left inset, the anomaly is accentuated by comparing with $R_{HT}(T)$ (red, dotted line). $R_{HT}(T)$ is obtained by fitting a polynomial at higher temperature (T=35-40K) and extrapolating for T<35K. The resistive anomaly slightly diverges to a resistance higher than $R_{HT}(T)$ for T~32-25K. This anomaly is a signature of the CDW transition [81] (see Fig. 2-3). In Fig. 2-3, the resistance continues to remain above the $R_{HT}(T)$, whereas R(T) recovers $R_{HT}(T)$ for T<25K in Fig. 4-10.

The CDW resistive anomaly in $NbSe_2$ is known to appear only in high quality crystals (RRR≥30), as discussed by Staley *et al*. [101]. In a previous study [101], the superconducting transition is at T_c=7.2K for crystals with RRR=10 but the CDW anomaly is absent in the R(T). With RRR=66, our $NbSe_2$ crystals are high quality compared to crystals reported in literature (see Table 4-3).

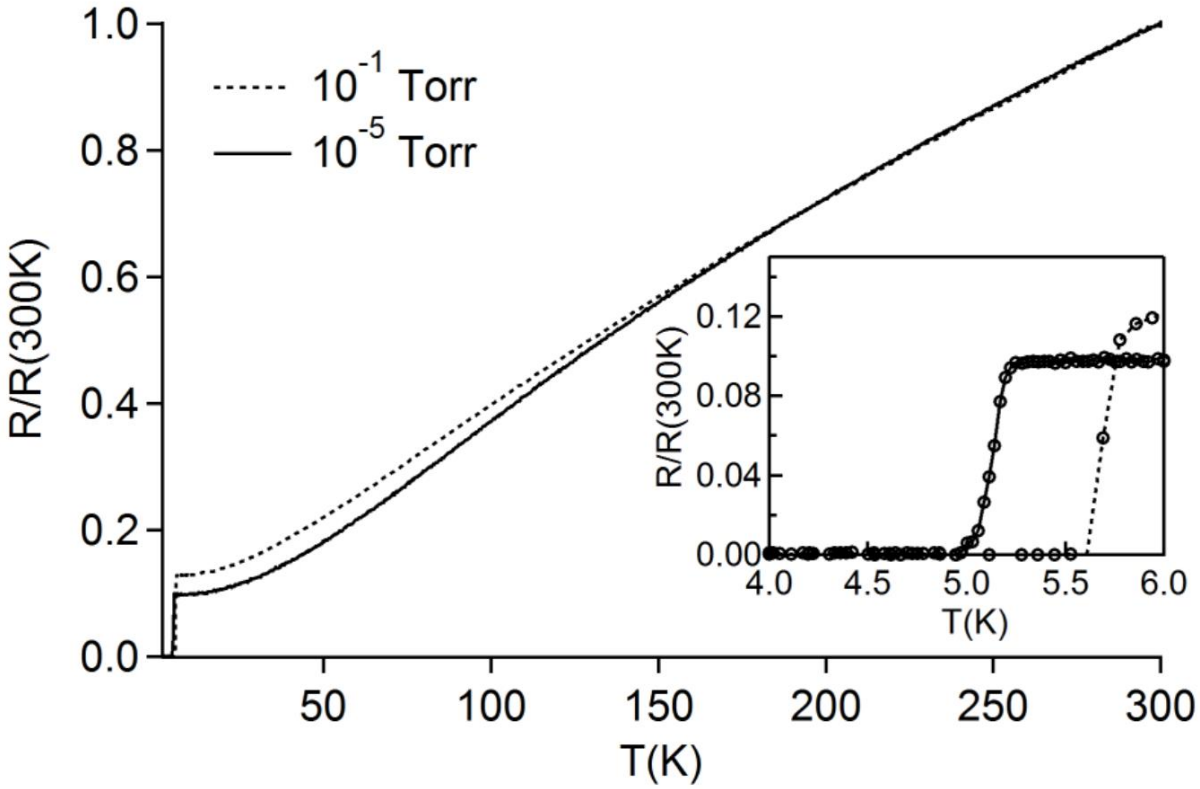

Fig. 4-9 Effect of vacuum condition on $NbSe_2$ synthesis.
Resistance for each sample is normalized to its resistance at 300K. $NbSe_2$ crystals synthesized in 10^{-1}torr (dotted line) and 10^{-5}torr (solid line) are compared. Both samples are synthesized from $NbSe_2$ powder (99.8%). Inset: same data from T=6-4K, with magnified view of the superconducting transition.

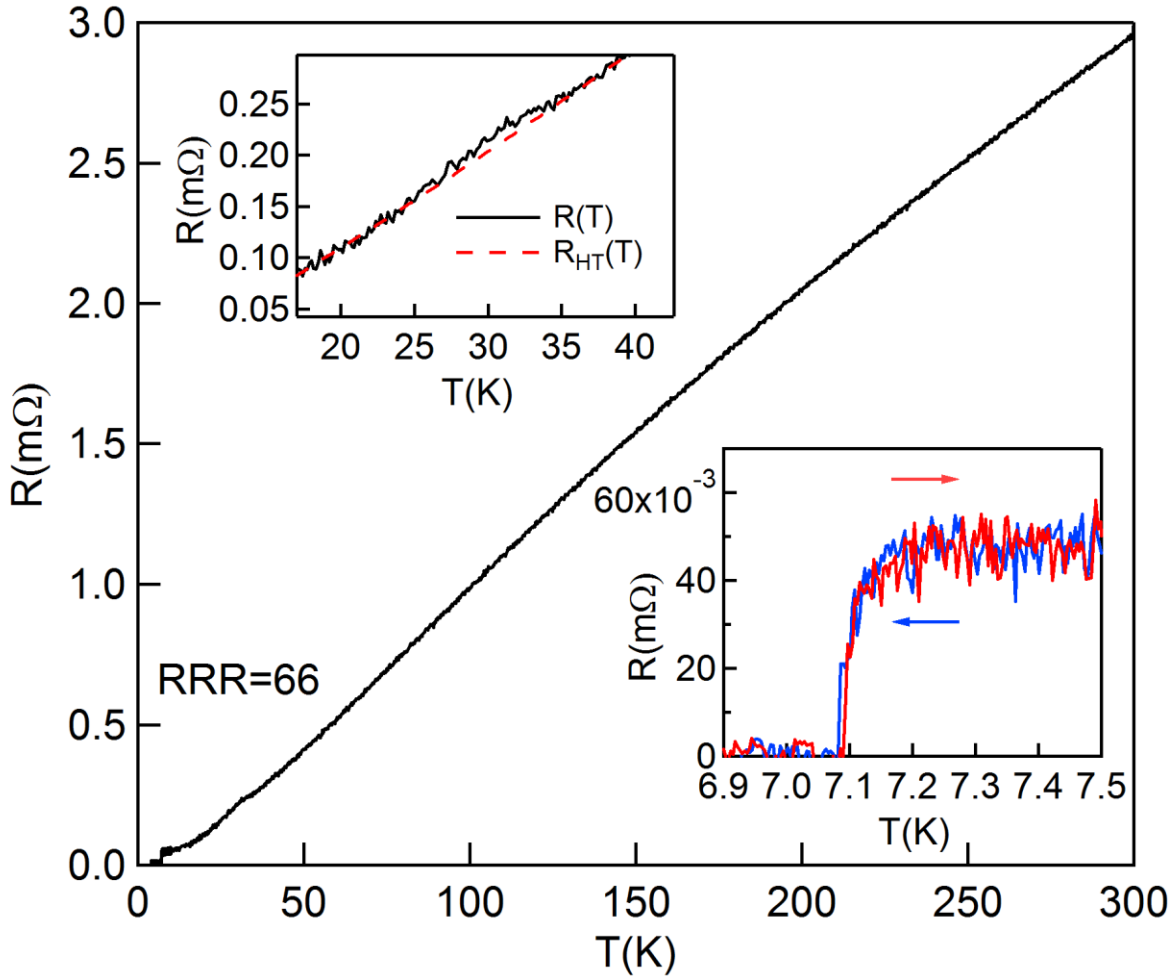

Fig. 4-10 R(T) of synthesized $NbSe_2$.
$NbSe_2$ crystal synthesized with high purity materials (Table 4-1II). Main panel: resistance of $NbSe_2$ crystal from 300K to 2K. Left inset: resistance from 45K to 15K. The red dashed line is $R_{HT}(T)$, a fit to the data for T=35-40K to accentuate the resistance anomaly. Right inset: resistance from 7.5K to 6.9K. The blue line is the resistance on cooldown and red line is the resistance on warmup.

Year	RRR	Reference
2010	13-67	[290]
2009	10	[101]
2003	10-100	[291]
1994	18-61	[292]

Table 4-3 $NbSe_2$ RRR from literature.
Courtesy of Jacob Bryon.

4.4.1.2 1T-TaS_2

1T-TaS_2 crystals are grown with the help of Corey Shih and Joey Barreto. Our synthesis methods are based on Enomoto *et al*. [157] and the information in the notebooks of Brian Burk, a former graduate student in the Zettl Group (PhD 1994).

For trials with the hot zone at <800^{o}C, the growth rate is slow and only very small crystals are obtained after a week of growth. Best results are obtained with the condition summarized in Table 4-1III with a tube furnace at 950^{o}C, using the temperature inhomogeneity of the furnace (see section 4.1.1). The ampoule is held at 1050^{o}C for a day at the start of the growth to react the Ta and S for synthesis from elemental Ta and S. This step is unnecessary when starting with pre-reacted TaS_2 powder but is kept the same for consistency. As the 1T polytype is stable only at high temperatures [158], the ampoule is immediately quenched with ice water after synthesis. As shown in Fig. 4-11a, plate-like crystals as large as 8mm are grown from elemental Ta, S and iodine (as transport agent) after 29 days. Excess sulfur is added to preferentially grow the 1T-polytype [158].

The synthesis time is shortened when pre-reacted TaS_2 is used instead of elemental Ta and S, with the parameters listed in Table 4-1IV. With only 7 days, the crystal shown in Fig. 4-11b is made from TaS_2 powder, elemental sulfur (to provide excess sulfur) and iodine (as transport agent). After initially using commercial TaS_2 powder, recipes for reacting elemental Ta and S are developed to obtain higher purity source material. The recommended material amounts for a synthesis run are shown in Table 4-2XI. The temperature should be varied according to the steps shown in Table 4-2XI. The ampoule will explode if the temperature is increased too rapidly because the reaction between tantalum and sulfur is slow (section 4.1.1). Without sufficient time to be captured by the tantalum, the ampoule is filled with unreacted sulfur gas at high temperature and pressure builds up due to thermal expansion. Hence, the ampoule is held at 600^{o}C to let the elemental sulfur react with the tantalum. The subsequent steps at high temperature are annealing steps to homogenize the tantalum + sulfur compound.

Fig. 4-12 shows R(T) of a 1T-TaS_2 crystal (image of sample shown in Fig. 4-11b). R(T) recorded on cooldown (warmup) is marked with an arrow pointing left (right). There are two hysteresis loops, one centered at 355K and the other at 190K, which are attributed to two CDW transitions (see section 2.1.3). R(T) increases non-linearly on cooldown for T<100K since the material is an insulator at this temperature range [107]. The above features in R(T) are consistent with Thompson *et al*. [107] (see Fig. 2-4). One difference is the kink at 160K in Fig. 4-12, which is causes by some domains with a higher CDW transition temperature than the rest.

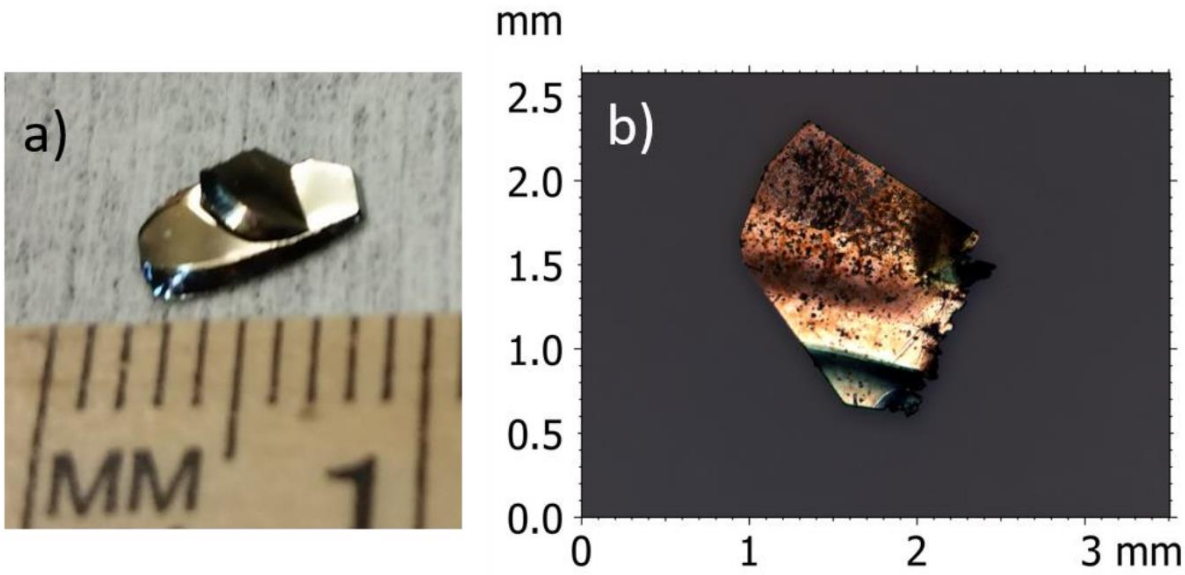

Fig. 4-11 Synthesized 1T-TaS_2 crystals optical image.
a) Grown for 29 days. b) Grown for 7 days.

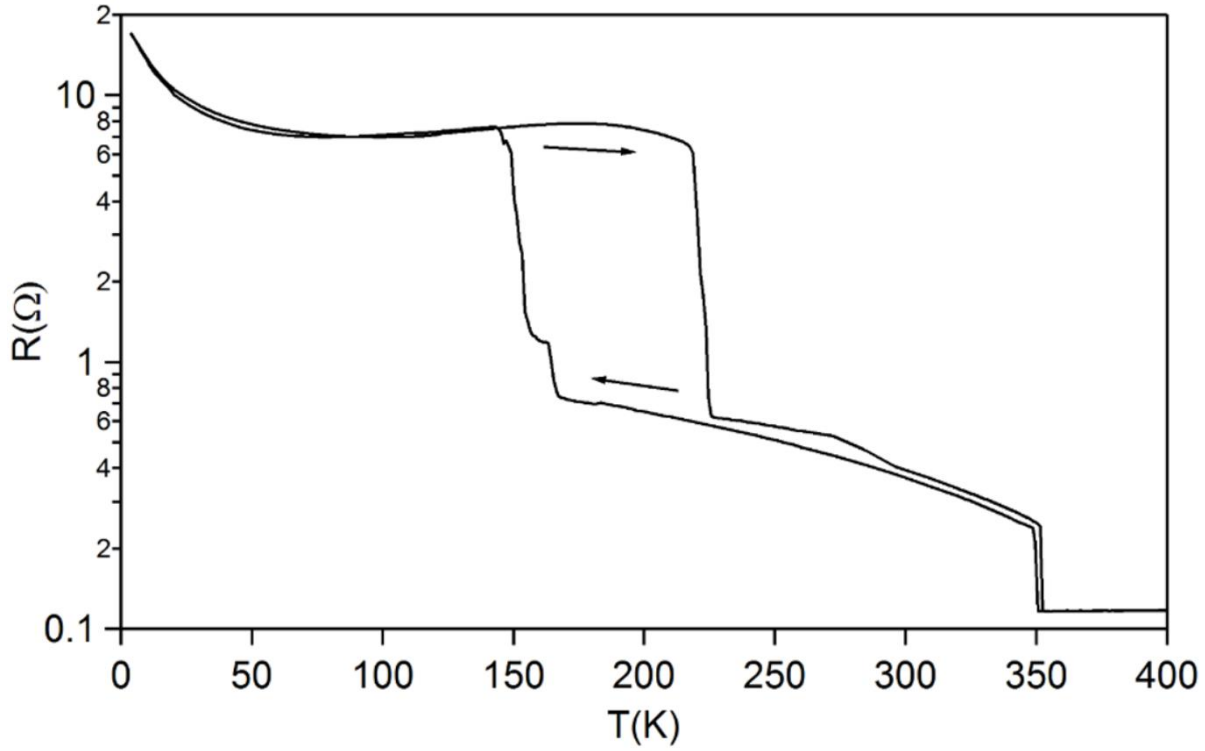

Fig. 4-12 R(T) of synthesized 1T-TaS_2.
From thick TaS_2 crystal (Table 4-1III).

4.4.2 Quasi-1D CDW material

Due to the quasi-1D crystal structure of $NbSe_3$ and TaS_3, they form fibrous whiskers in their crystalline form. In contrast to the faceted plate-like crystals of $NbSe_2$ and TaS_2, the quasi-1D CDW materials look similar to black cotton balls. The background on the crystal structures and electronic properties are discussed in section 2.2.

4.4.2.1 $NbSe_3$

$NbSe_3$ is synthesized with the help of Jacob Bryon. The crystals are grown by loading stoichiometric amounts of Nb and Se in an ampoule and placing the ampoule in a temperature gradient (see Fig. 4-13). The source material is located at the 707ºC zone and the crystal grows at the 664-653ºC zone. The synthesis parameters are summarized in Table 4-1V. As an alternative, $NbSe_3$ is also grown in a box furnace set to 700ºC (Table 4-1VI), using its temperature inhomogeneity (see section 4.1.1). It is important that iodine is *not* used for the synthesis of $NbSe_3$. The presence of iodine preferentially grows $NbSe_2$, even when the source material is loaded with the molar ratio Nb:Se=1:3. For $NbSe_3$ growth, Se appears to act as a transport agent.

Fig. 4-14 shows $NbSe_3$ grown in the gradient furnace for 19 days (Table 4-1V). Consistent with the quasi-1D crystal structure, the crystals look fibrous. The R(T) in Fig. 4-15 shows an overall metallic behavior with CDW resistive anomalies at T_{P1}=144K and T_{P2}=59K. The R(T) features are consistent with the R(T) from Chaussy *et al*. [80] (see Fig. 2-11).

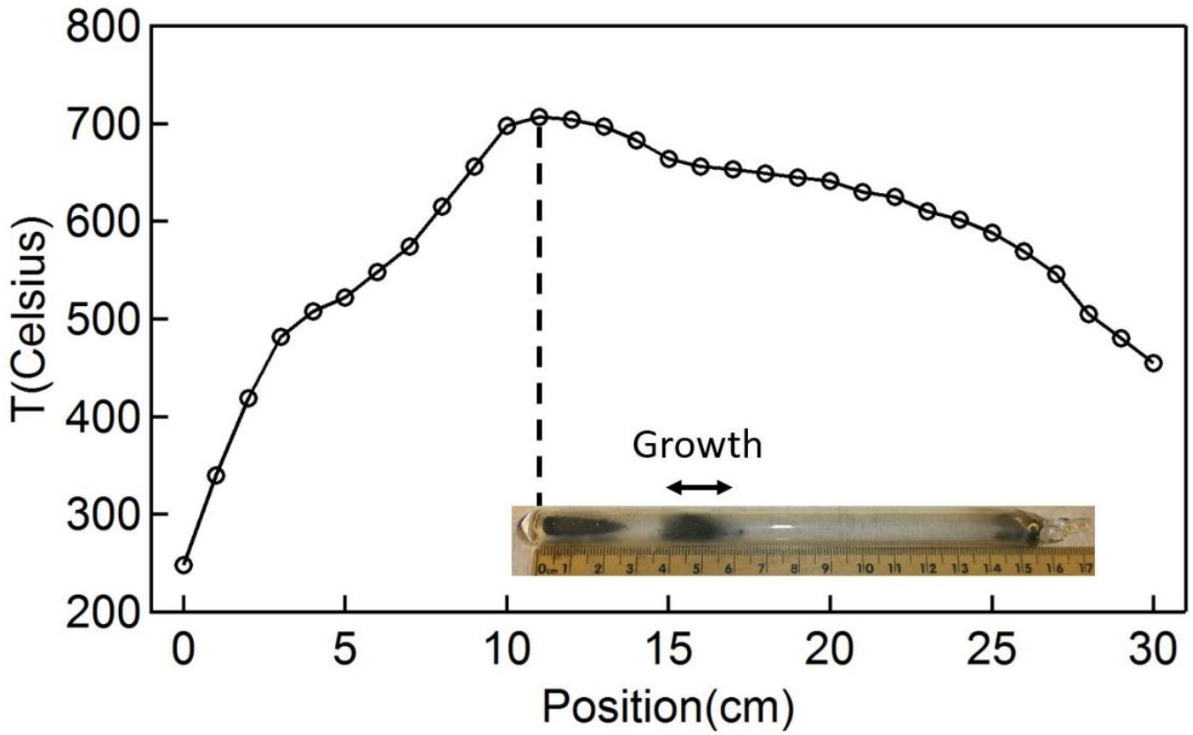

Fig. 4-13 Temperature profile for $NbSe_3$ crystal synthesis.
Optical image of the ampoule after synthesis is scaled and placed according to its placement in the gradient furnace. T_{source}=707ºC, T_{growth}=667-653ºC.

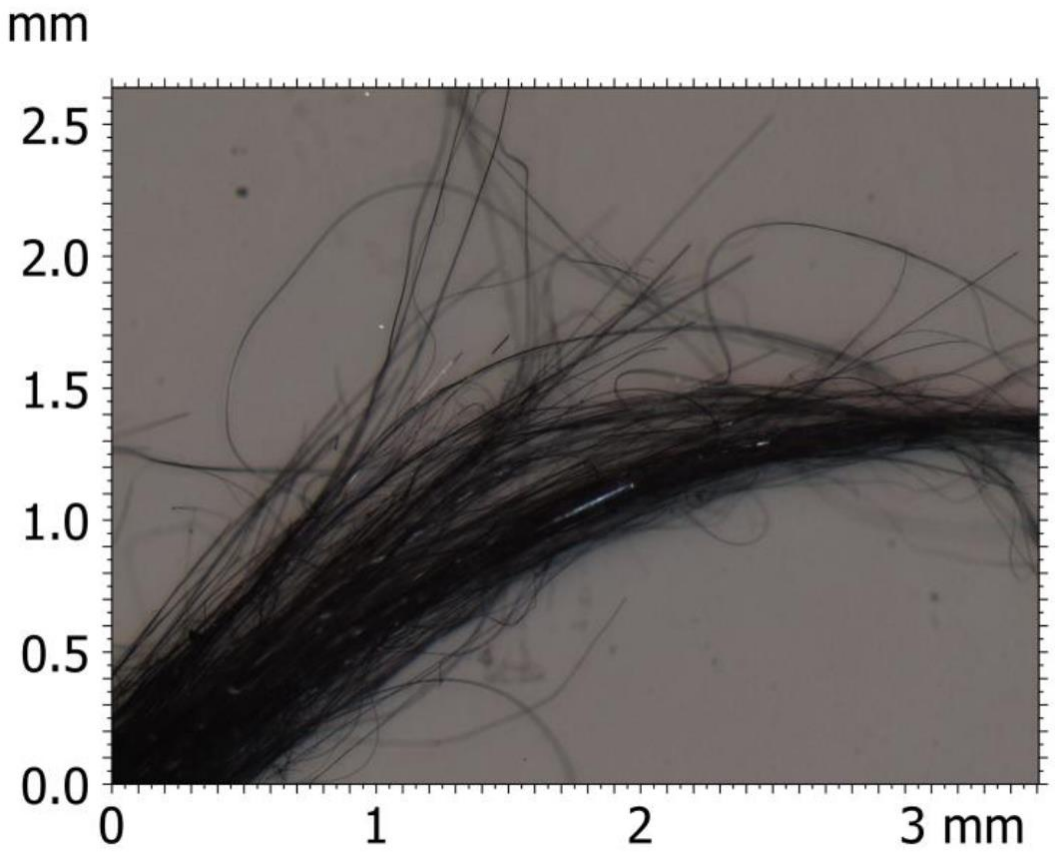

Fig. 4-14 Synthesized $NbSe_3$ optical image.
Grown in gradient furnace (Table 4-1V).

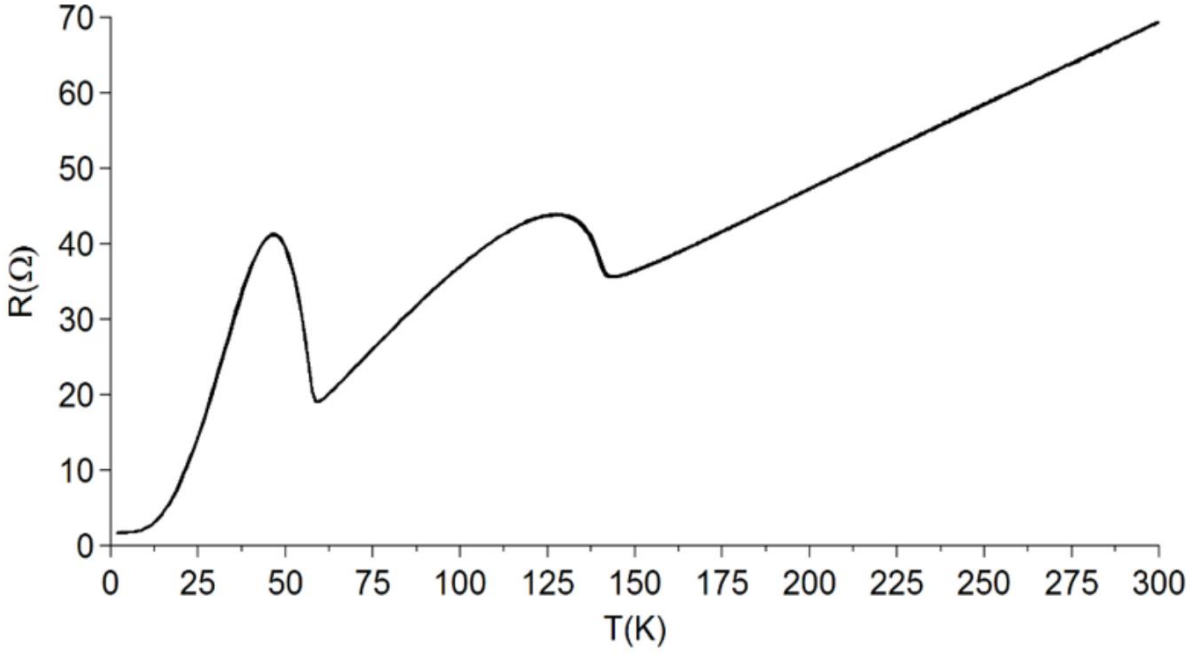

Fig. 4-15 R(T) of synthesized $NbSe_3$.
Grown in box furnace (Table 4-1VI).

4.4.2.2 TaS_3

TaS_3 is synthesized with help from Corey Shih. TaS_2 and elemental sulfur are loaded in an ampoule according to stoichiometry and iodine is added as a transport agent (see Table 4-1VII). The ampoule is filled with some argon to accelerate the growth and placed in a temperature gradient. Fig. 4-16 shows the gradient. The line is an interpolation based on a fit on the 6 data points shown as circles markers. The source material is at 666ºC and the crystal grows at the 545-534ºC zone. Cotton-like crystals (see Fig. 4-17) are grown in 7 days.

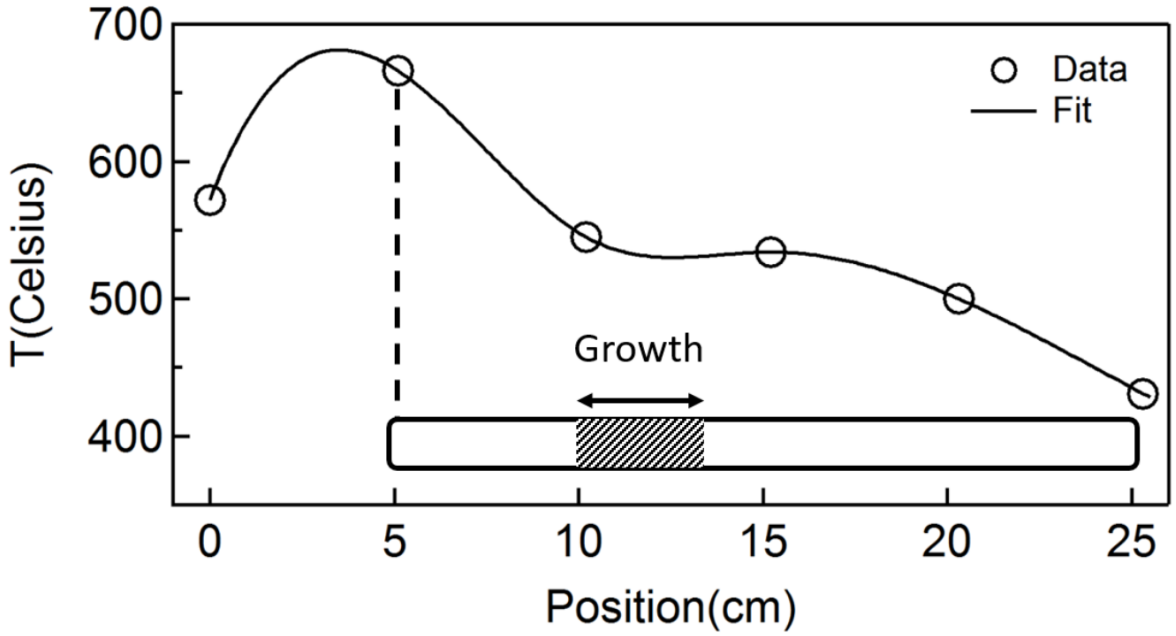

Fig. 4-16 Temperature profile for TaS_3 crystal synthesis.
The black curve shows a cubic spline interpolation between the data points (open circles) as a guide to the eye. The rectangle at the bottom represents the ampoule. Crystals grow in the shaded region. T_{source}=666ºC, T_{growth}=545-534ºC.

Fig. 4-17 Synthesized TaS_3 crystals optical image.

Fig. 4-18a shows R(T) of the synthesized crystals. A third order polynomial (red line) is fit to the data for T=220-200K. Using the numerical derivative of the fit, the quantity $\frac{1}{R}\frac{dR}{dT}$ is calculated and displayed in the inset. The curve in the inset peaks at 214K, indicative of a transition, which is consistent with the T_P=215K CDW transition reported in Thompson *et al.* [128]. Fig. 4-18b shows the Arrhenius plot of the TaS_3 resistance. Due to the CDW gap formation, the resistance follows the thermally activated behavior $R \sim e^{-2\Delta/k_B T}$. The energy gap Δ=788K obtained from the slope in the Arrhenius plot is consistent with Δ=740K from Thompson *et al*. [128].

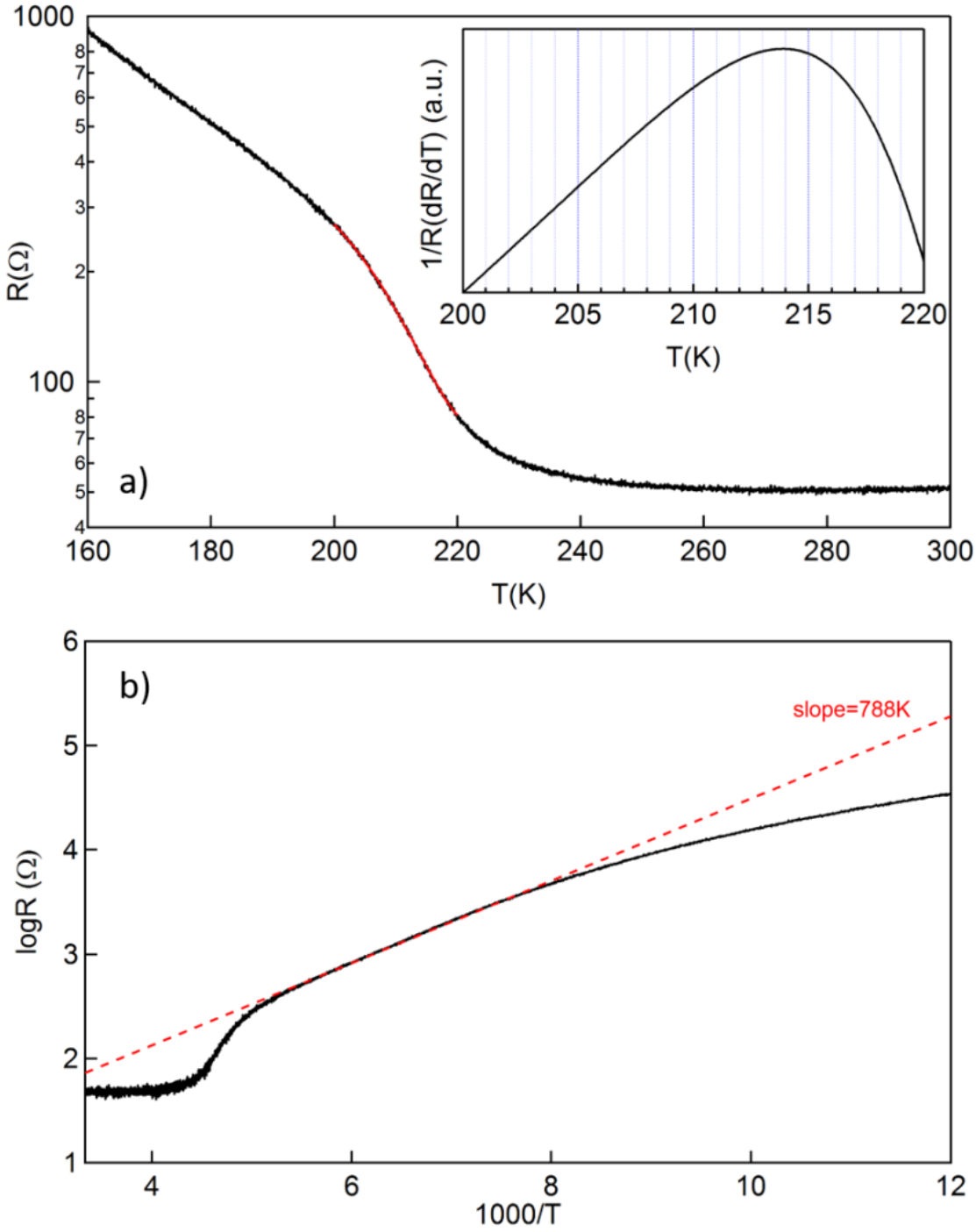

Fig. 4-18 R(T) of synthesized TaS_3.

a) Resistance at T=300-60K. Red line is a fit to the T= 220-200K data. Inset: $\frac{1}{R}\frac{dR}{dT}$ from numerical derivative of the fit. b) Arrhenius plot for T=300-83K. Red, dotted line is a linear fit to T=190–123K range. Δ=788K from slope.

4.4.2.3 $(NbSe_4)_3I$

$(NbSe_4)_3I$ was synthesized, while working on $NbSe_2$ synthesis with Joey Barreto. This material is formed when iodine, which is usually included as a transport agent, becomes part of the crystal, instead of dissociating at the crystal growth zone. $NbSe_2$ powder and iodine are loaded in an ampoule (see Table 4-1VIII) and placed in a temperature gradient shown (see Fig. 4-19). The hot zone is at 689°C and the crystals grow at the 544-539°C zone. $NbSe_2$ requires higher temperatures (see Fig. 4-7) and does not grow during $(NbSe_4)_3I$ synthesis. Hence, the synthesis parameters described in Table 4-1VIII yield only $(NbSe_4)_3I$. Fig. 4-20 shows crystals, which were grown for 55 days. They are shiny, needle-like crystals, which are thicker and straighter compared to $NbSe_3$, possibly due to the increased inter-chain interaction by the iodine.

The crystals are characterized by electrical transport. As silver paste does not make good electrical contact to this material, contacts are formed by evaporating 50nm of gold through a shadow mask and painting wires to the gold contacts with silver paste. Fig. 4-21 shows R(T), which indicates thermally activated hopping behavior from T=300-200K. The kink at 272K is attributed to the ferrodistortive structural transition known to occur at T=274K [78] (see section 2.2.3). I(V) curves measured at 230K does not show any non-linear conduction for E≥15V/cm, which is an order of magnitude higher than E_T=3V/cm reported for $(NbSe_4)_{3.33}I$ [159]. $(NbSe_4)_2I$ or $(NbSe_4)_{3.33}I$ would exhibit sliding CDW behavior at T=230K (see Table 2-1).

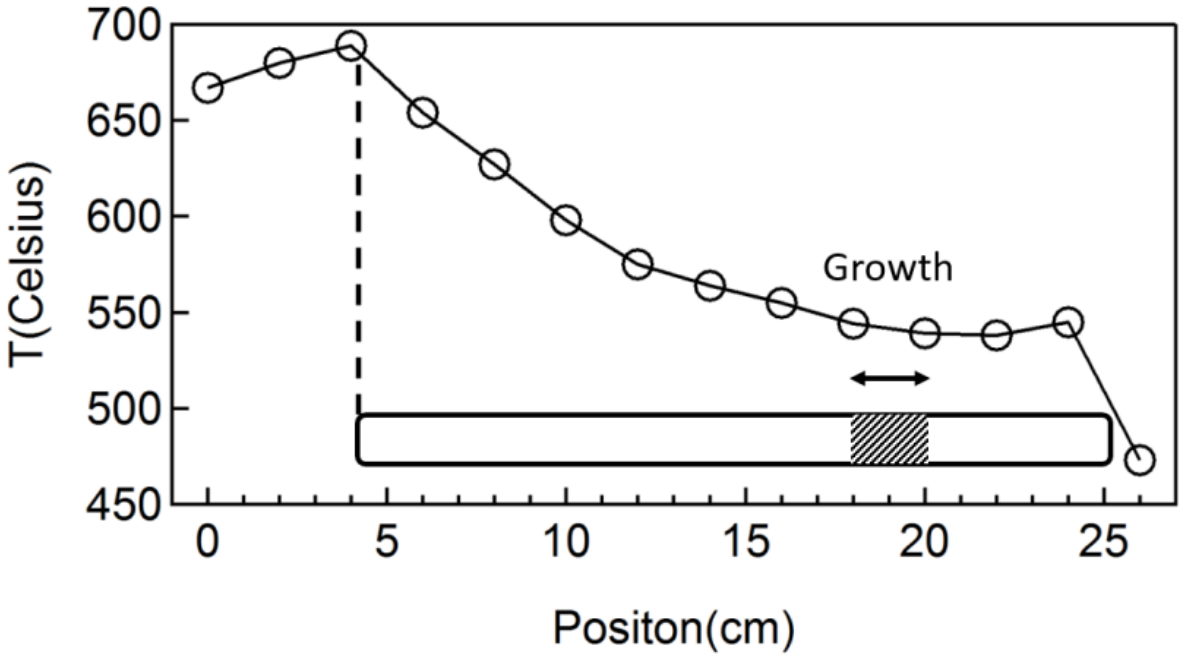

Fig. 4-19 Temperature profile for $(NbSe_4)_3I$ growth.
The rectangle at the bottom represents the ampoule. Crystals grow in the shaded region. T_{source}=689°C, T_{growth}=544-539°C.

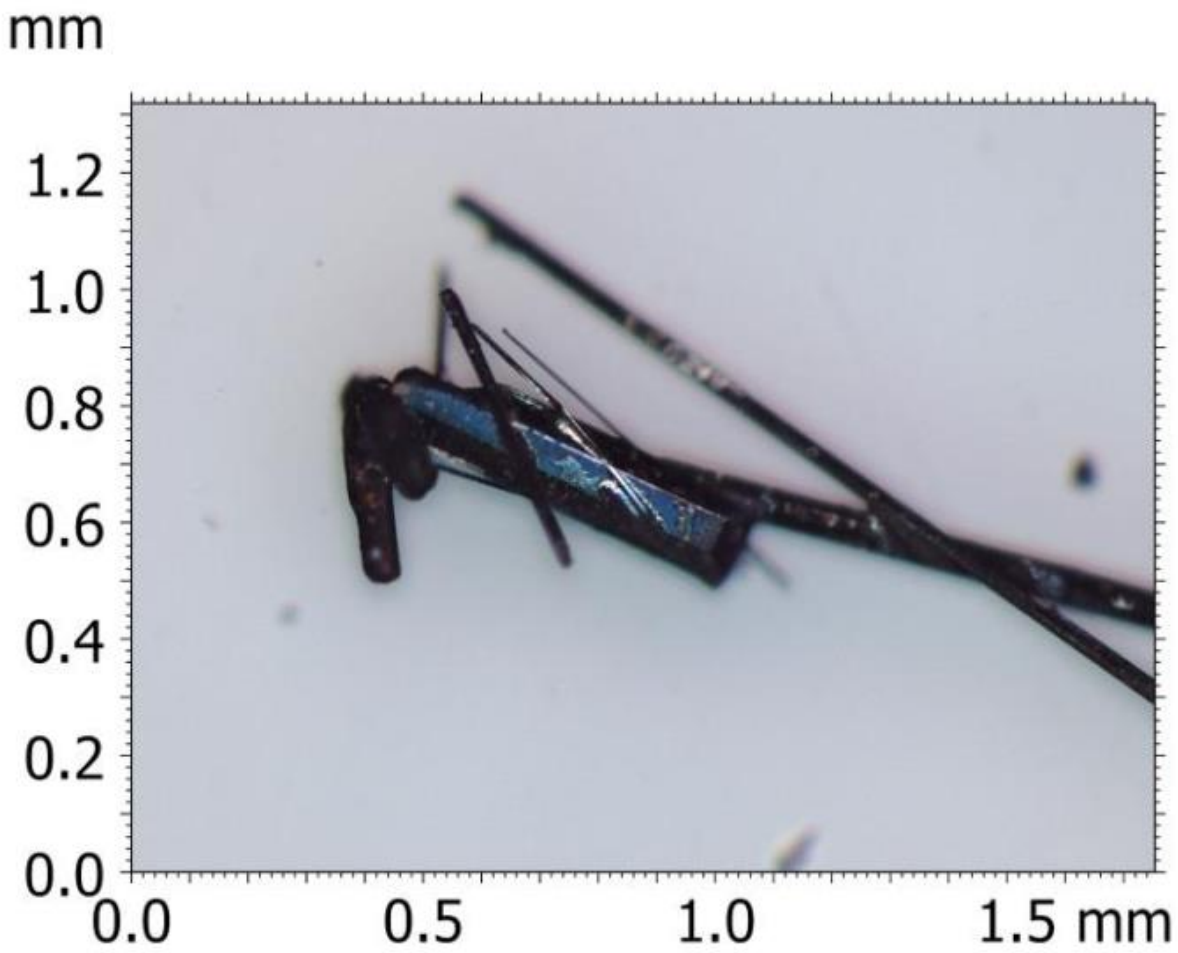

Fig. 4-20 Synthesized $(NbSe_4)_3I$ crystals optical image.

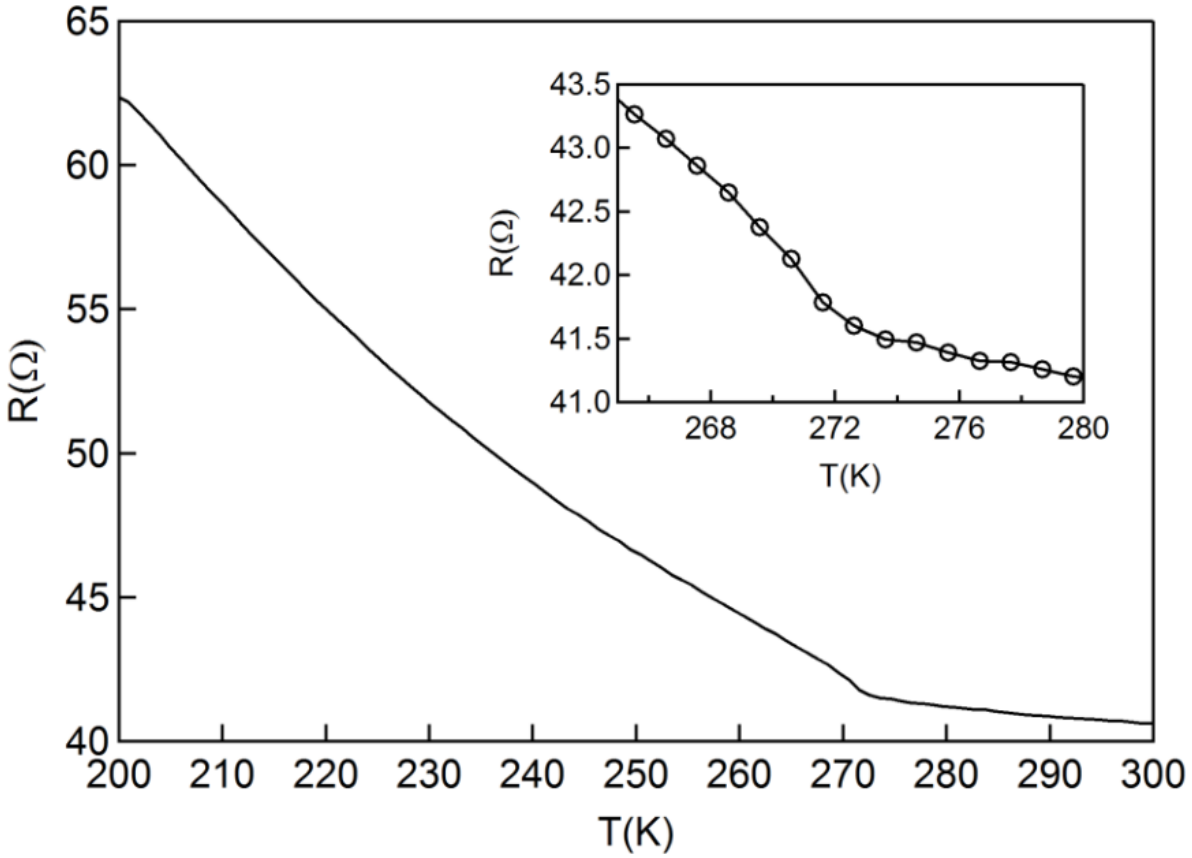

Fig. 4-21 R(T) of synthesized $(NbSe_4)_3I$.
The kink at 272K is from a structural phase transition. Inset: magnified view of the transition.

4.4.3 WTe_2

WTe_2 crystals are grown with help from Patrick Stetz. Tungsten wire and tellurium shots are sealed in an ampoule with iodine as transport agent (see Table 4-1IX). The synthesis reported by Ali *et al.* [112] use bromine for the transport agent but iodine appears to be an acceptable alternative. The ampoule is placed in a temperature gradient (see Fig. 4-22) for 33 days. The source materials are placed close to the hottest zone at 696ºC and crystal growth occurs close to the source materials in the 696-668ºC zone. Needle like crystals are obtained (see Fig. 4-23).

Fig. 4-24a shows R(T) of the synthesized WTe_2 crystals under $B^{\perp}$=0, 2, 4, 6, 9T. R(T) is metallic for $B^{\perp}$=0 down to 2K. For $B^{\perp}\geq$4T, there is a 'turn on' temperature T*, below which the resistance increases with cooling. This behavior is consistent with previous study [112] (see Fig. 2-6). However, the 'turn on' effect is weaker in our samples. In Fig. 4-24a, the residual resistance (i.e. R(T→0)) for $B^{\perp}$=9T increases by a factor ~10 compared to $B^{\perp}$=0, whereas the factor is more than ~100 in Fig. 2-6. This is attributed to the difference in quality of the crystals. The RRR=38 for our crystals, whereas RRR=370 for the crystals in Fig. 2-6 [112].

Fig. 4-24b shows magnetoresistance $\mathrm{MR} = \frac{\mathrm{R(B)-R(0)}}{R(0)} \times 100\%$ at T=1.8K. For |B|>6.5T, wiggles can be seen in the MR curve. A second order polynomial, MR_{fit}, is fit to the data and subtracted. The result, $MR-MR_{fit}$, is plotted against 1/B in the inset for B=6.25-9T. The data for increasing and decreasing B both exhibit periodic oscillations, which are identified as Shubnikov-de Haas oscillations. The Shubnikov-de Haas oscillations are similar to those reported by Ali *et al*. [112].

To obtain higher quality crystals, flux growth should be explored. Although flux growth is usually thought to be more prone to contamination by impurities, reports of flux growth in excess tellurium has yielded very high quality crystals [154]. The vapor transport grown crystals by Ali *et al*. [112] have RRR ~370, whereas the flux grown crystals by Wu *et al*. report RRR>900 [154]. It is possible that vapor grown WTe_2 suffers from Te vacancies, similar to $MoTe_2$ [160]. Growth in a Te rich environment is more suitable for filling the vacancies. We have developed a setup for flux growth and began trials to replicate the process but have not obtained crystals from flux growth yet (see section 4.1.2).

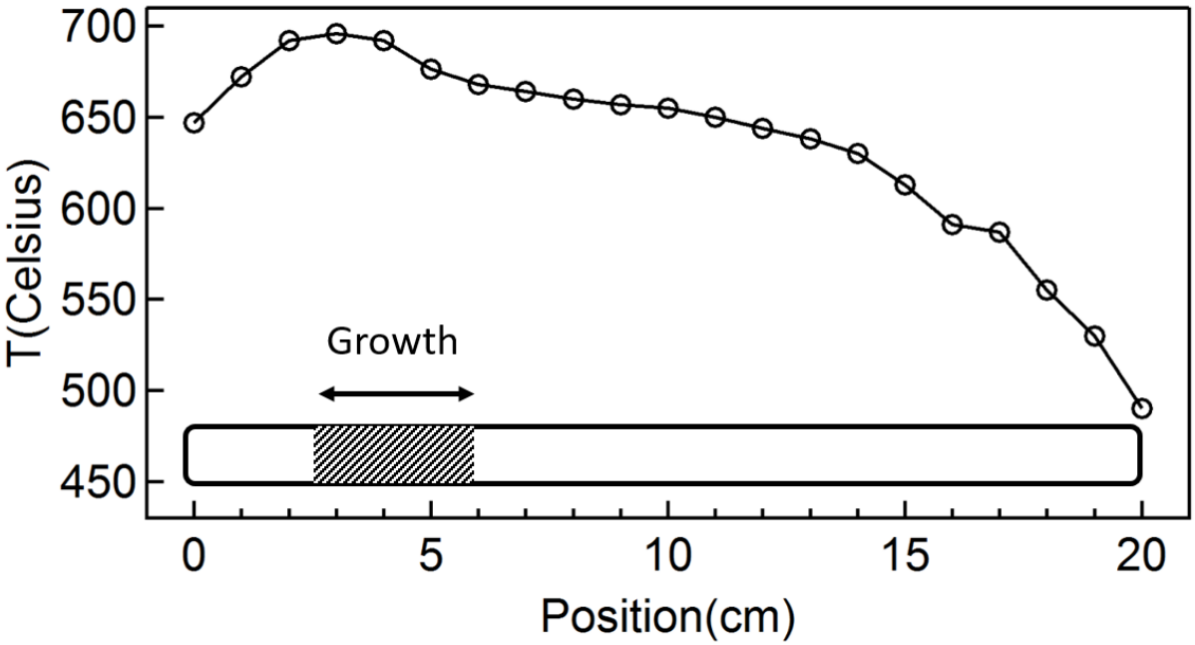

Fig. 4-22 Temperature profile for WTe_2 crystal synthesis.
The rectangle at the bottom represents the ampoule. Crystals grow in the shaded region. T_{source}=696ºC, T_{growth}=696-668ºC.

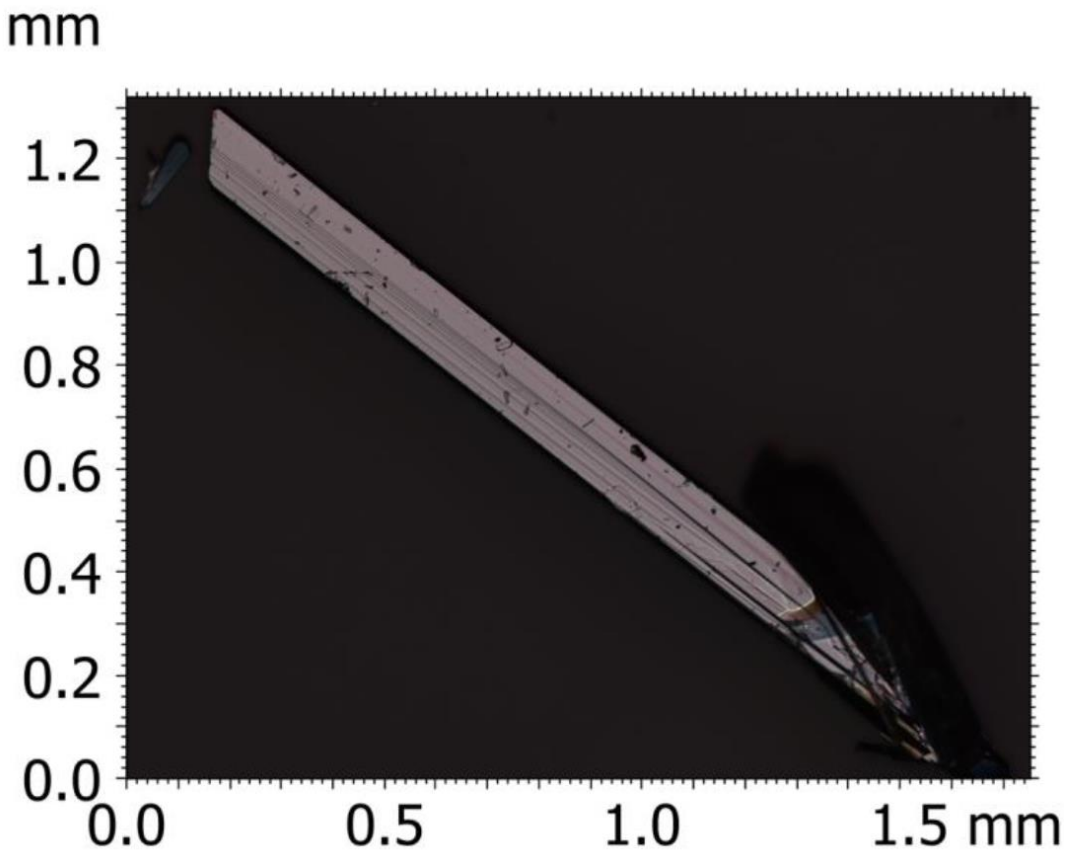

Fig. 4-23 Synthesized WTe_2 crystal optical image.

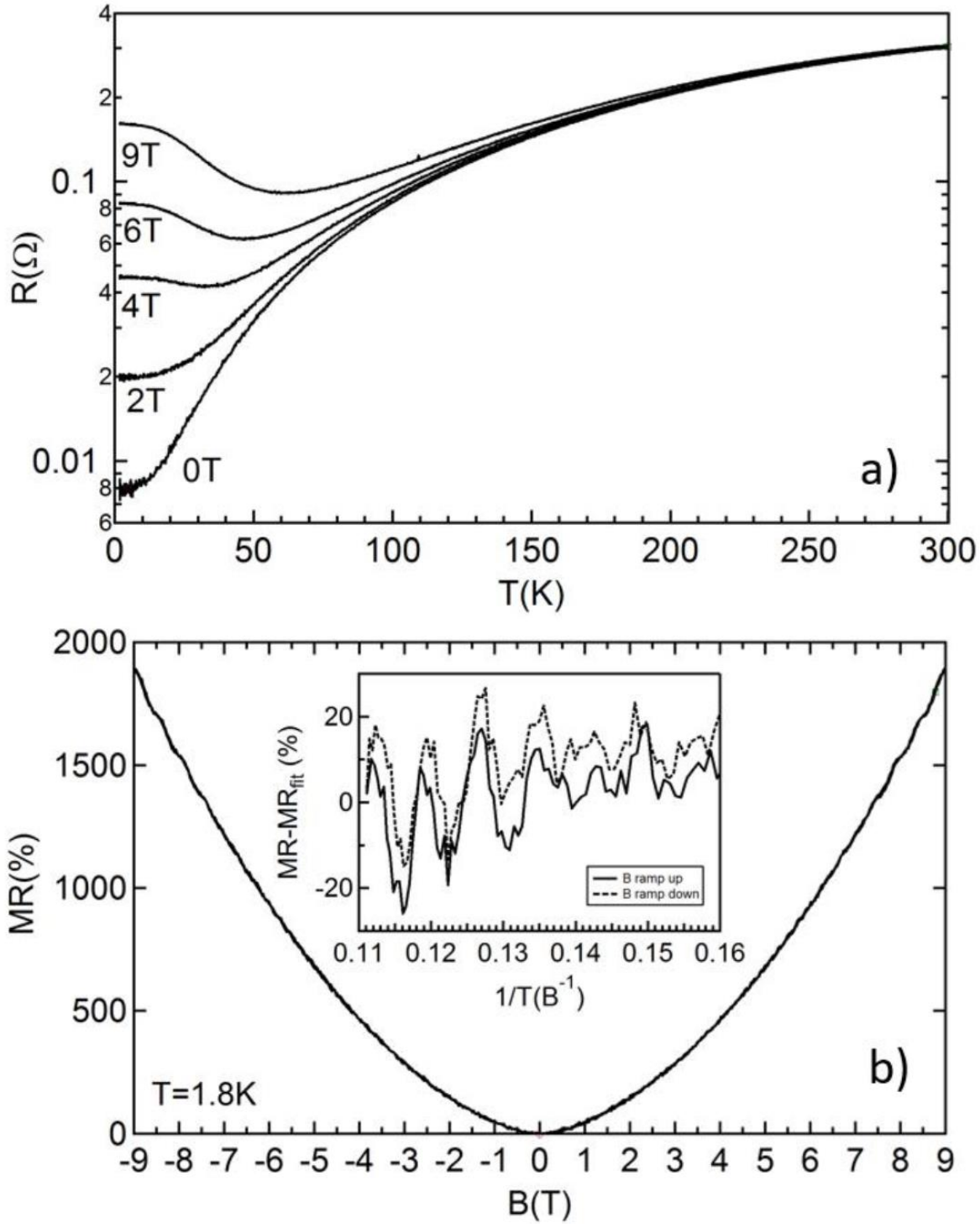

Fig. 4-24 Electrical transport of synthesized WTe_2.
a) R(T) of synthesized WTe_2 crystal under a magnetic field oriented perpendicular to the plate-like crystal face. b) Magnetoresistance (MR) for -9T≤B≤9T at T=1.8K.

4.4.4 FeSe

FeSe is synthesized with help from Xiyue Wang, Joey Barreto, and Patrick Stetz. Owen Chen assisted with the magnetic property characterization. As shown in Fig. 4-25, the Fe-Se phase diagram is complex with many phases. The target phase is the tetragonal FeSe (labeled as β). While developing the synthesis parameters for FeSe, we accidentally synthesized other Fe-Se compounds. The synthesis methods for $FeSe_2$ and Fe_3Se_4 are also presented.

Tetragonal FeSe synthesis is based on Koz *et al.* [161]. Pre-reacted FeSe powder and $AlCl_3$ are loaded in an ampoule (see Table 4-1X). According to Koz *et al*., $AlCl_3$ releases HCl when heated by reacting with water, which is released from the ampoule walls.

$$Al_2Cl_{6(g)} + 3H_2O_{(g)} \rightarrow Al_2O_{3(s)} + 6HCl_{(g)} \qquad \text{Eq. 4-2}$$

HCl is the transport agent, which complexes to FeSe

$$2HCl_{(g)} + FeSe_{(s)} \rightleftharpoons FeCl_{2(g)} + H_2Se_{(g)} \qquad \text{Eq. 4-3}$$

$AlCl_3$ is protected from air during ampoule loading and sealing process (see section 4.1.1) to avoid it reacting with the moisture in the air.

At the same time, crystal growth is facilitated by high water content in the ampoule for increased HCl production during synthesis. Argon gas is bubbled through water and leaked into the ampoule before sealing. The ampoule is placed in a temperature gradient shown in Fig. 4-26, with the source material at 363°C. The crystals grow in the 268-252°C zone. Fig. 4-27 shows rectangular crystals up to 250μm x 150μm large, which are obtained after 24 days. The rectangular shape is consistent with the habit of the tetragonal crystal structure.

For the synthesis described above, tetragonal FeSe grows only when the source material is pre-reacted FeSe powder. Starting with elemental Fe and Se results in $FeSe_2$ crystals (see section 4.4.4.1). FeSe powder is synthesized by sealing elemental Fe and Se into an ampoule and heating the ampoule according to the program listed in Table 4-2XII. To avoid the ampoule exploding during synthesis, the amount of ingredients should not exceed those listed in Table 4-2XII for an ampoule with diameter 1.27cm and length 17cm. The 2 step temperature is also a precaution against an explosion (see section 4.1.1).

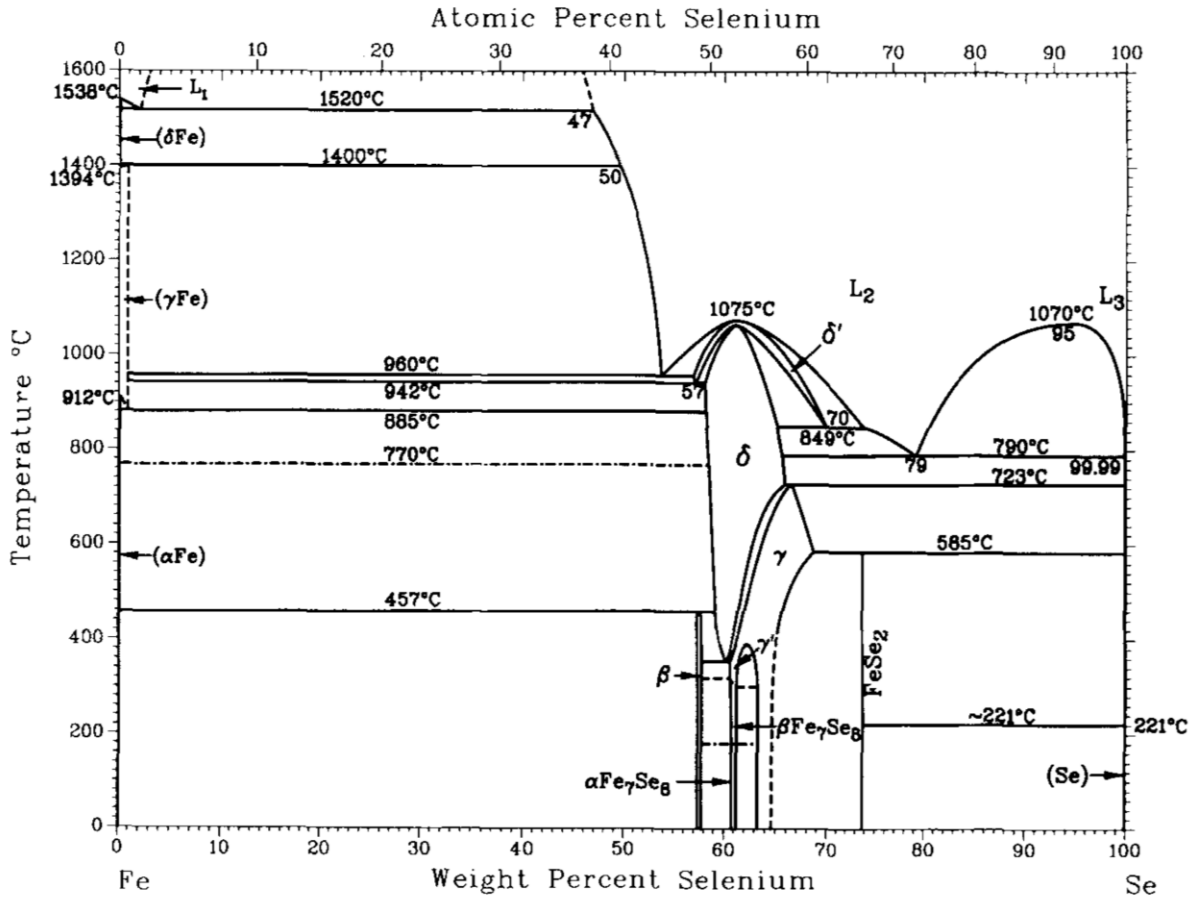

Fig. 4-25 Fe-Se phase diagram.
Fig. 1, Okamoto [293]. Tetragonal FeSe phase labeled as β.

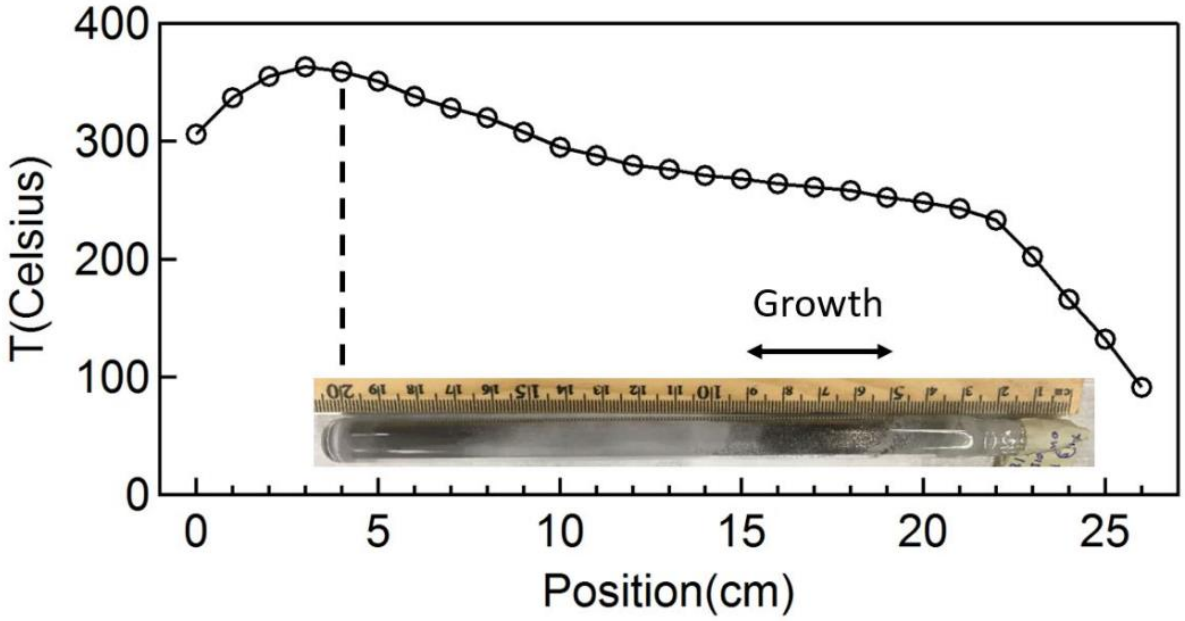

Fig. 4-26 Temperature profile for FeSe crystal synthesis.
Image of the ampoule after synthesis is scaled and placed according to its placement in the gradient furnace. Crystals grow at the dark region 15-19cm. T_{source}=363ºC, T_{growth}=268-252ºC

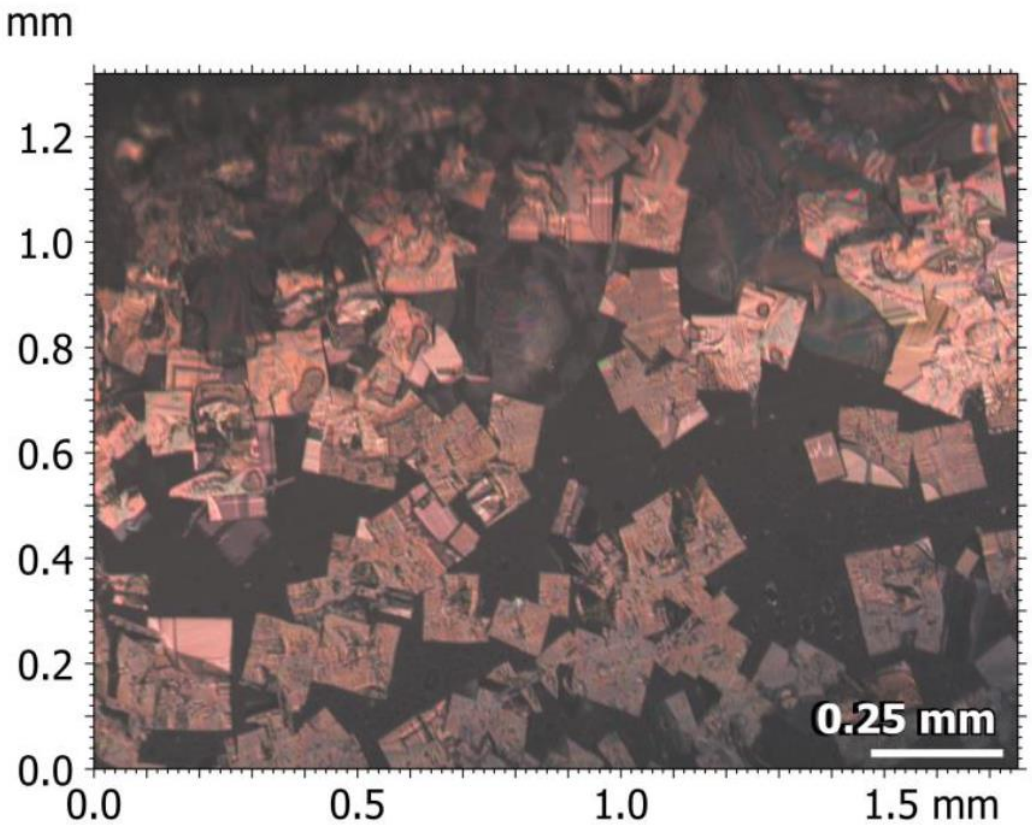

Fig. 4-27 Synthesized FeSe crystals optical image.

Fig. 4-28 shows the magnetic susceptibility (χ) measurement for T=10-5K. For ZFC, χ drops to negative below 8.5K and approaches $-1/4\pi$, demonstrating almost complete shielding. The diamagnetic signal below 8.5K is consistent with the onset of superconductivity in tetragonal FeSe [117]. Magnetization at 5K for magnetic fields $-1T \leq B \leq 1T$ is shown in the inset. M(B) is hysteretic and the collapsed diamond shape is characteristic of superconductivity. At high magnetic field, the curves asymptote to a diagonal line, indicating the coexistence of a paramagnetic behavior. Paramagnetic behavior is discussed in Hsu *et al*. as well [117]. χ for FC does not drop at 8.5K and even slightly increases. For lower temperatures, χ is slightly negative but negligible compared to the ZFC. This suggests the superconducting volume fraction is low, as Meissner effect should have reduced the FC curve as low as the ZFC curve. The report by Hsu *et al*. [117], observe similar behavior with a more pronounced increase of χ during FC (see Fig. 2-9). The anomaly at 100K is not observed in our samples.

As vapor transport growth of FeSe is very slow, we believe flux growth [162] is more suitable for obtaining large crystals. We have developed a setup for flux growth (see section 4.1.2) but our synthesis trials for FeSe flux growth is still in its early stages.

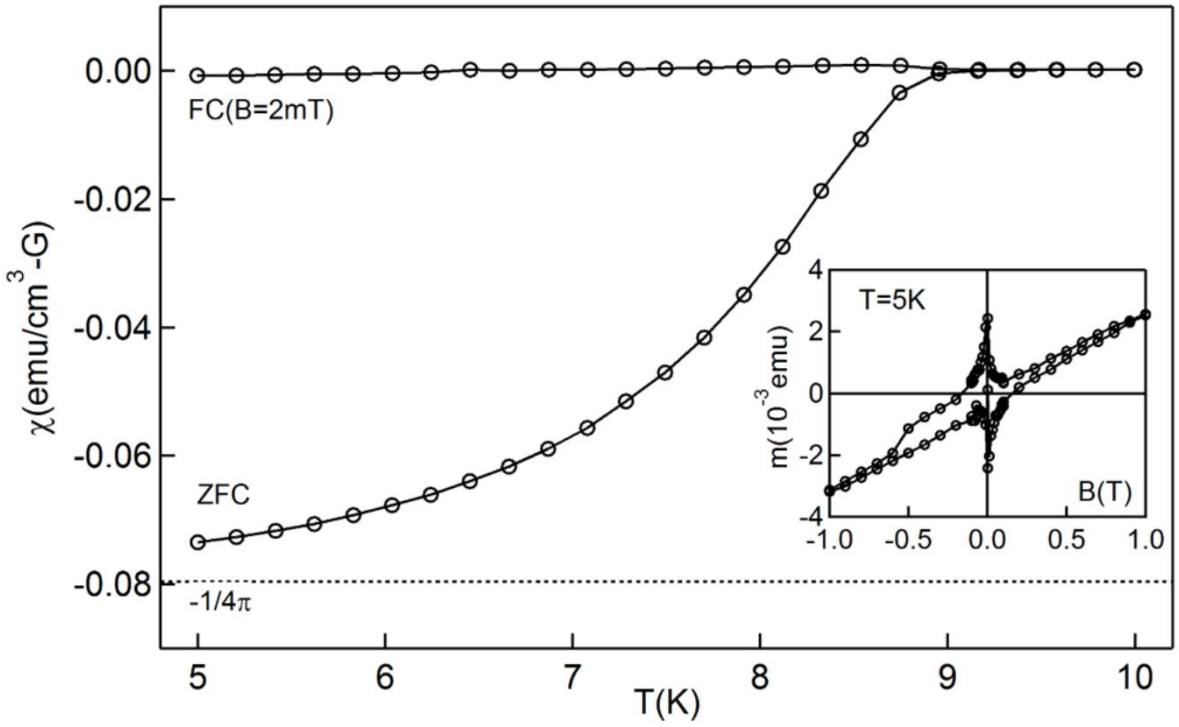

Fig. 4-28 Magnetic property of synthesized FeSe crystal.
Magnetic susceptibility of synthesized FeSe for T=10-5K. Sample is measured after zero-field cooling (ZFC) and during field cooling (FC) with a magnetic field B=2mT. The dotted line is drawn at $\chi=-1/4\pi$, the value for complete shielding. Inset: sample magnetization at T=5K as the field is scanned between -1T and 1T.

4.4.4.1 $FeSe_2$

When elemental Fe and Se with Fe:Se=1:1 are used as the source material instead of pre-reacted FeSe, needle-like $FeSe_2$ crystals grow instead of tetragonal FeSe (see Fig. 4-29). All other synthesis parameters are the same: $AlCl_3$ is added for vapor transport and the same temperature gradient (see Fig. 4-26) is used. The crystals are confirmed to be $FeSe_2$ with single crystal XRD. The crystals structure is "marcasite structure" (orthorhombic, Pnnm) with lattice parameters a=4.7Å, b=5.8Å, c=3.6Å [163]. $FeSe_2$ (marcasite structure) is a semiconductor with bandgap 0.5-1.0eV [164,165]. Wu Shi proposed using ionic liquid gating (see section 6.2) to explore if superconductivity could be induced in $FeSe_2$, as it has been in other semiconductors [144]. If superconductivity is induced, it is interesting whether it will be iron-based or BCS (see section 1.1).

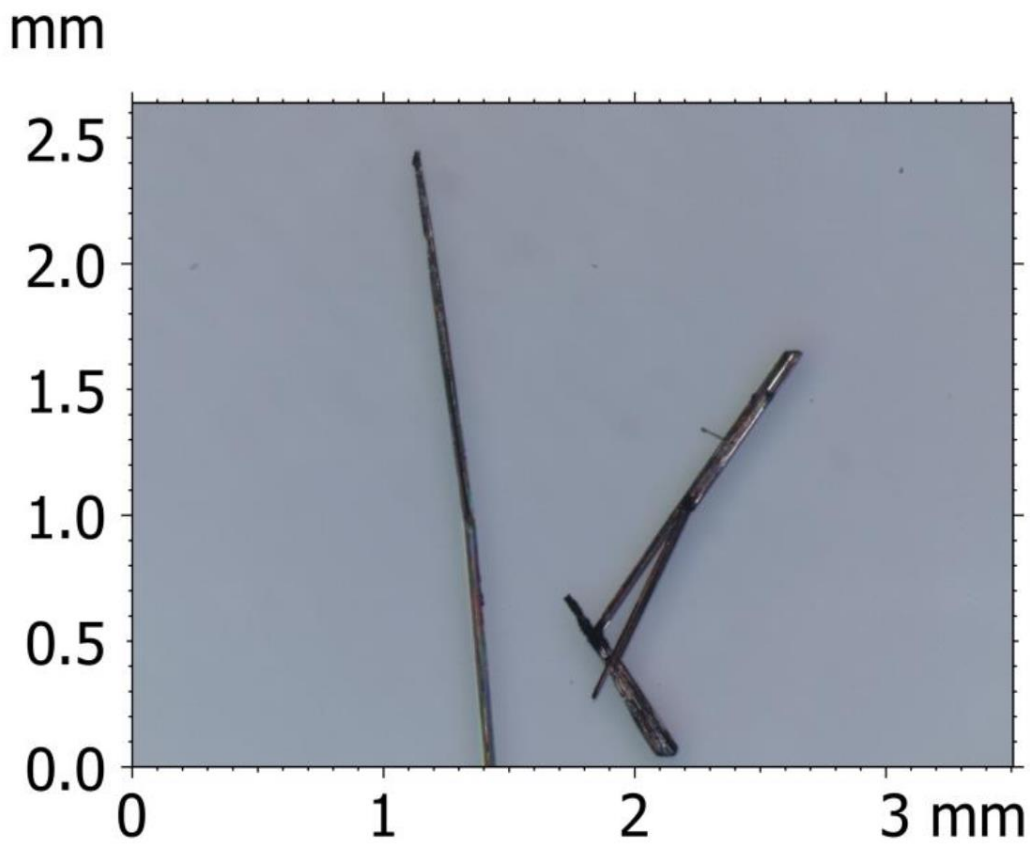

Fig. 4-29 Synthesized $FeSe_2$ crystals optical image.

4.4.4.2 Fe_3Se_4

Fe_3Se_4 is obtained in our attempt to grow tetragonal FeSe with iodine (transport agent) and pre-reacted FeSe powder. Adopting similar conditions as other TMC crystal growth, the hot zone is set at 667^{o}C. The synthesis did not yield rectangular FeSe crystals but yielded hexagonal, plate-like crystals. According to single crystal XRD, the synthesized crystal has a "NiAs structure" (monoclinic, C2/m), with lattice parameters a=12.7Å, b=3.5Å, c=5.2Å [163]. This Fe_3Se_4 is labeled as γ in the Fe-Se phase diagram (see Fig. 4-25). FeSe is not produced because it is only stable below 457^{o}C and high growth temperature is not suitable for its growth. Karkin *et al*. [166] reports difficulties with iodine vapor transport, as well. $AlCl_3$ based vapor transport or flux growth is more promising for growing large crystals.

Magnetic properties of crystals from another trial with a slightly cooler hot zone of 620^{o}C is characterized. Fig. 4-30a shows the ZFC and FC curves do not overlap below 192K. The history dependence is an indication of ferromagnetism/ferrimagnetism. Fig. 4-30b shows M(B) at T=4.2K and the characteristic hysteresis of ferromagnetism is seen. However, M(B) at T=290K shows a small hysteresis. It is possible that there is a domain with a higher Curie temperature than 290K but a weaker magnetic signal. The kink at 123K is interesting, as it is possibly the signature for transition to the anti-ferromagnetic state [167]. From the magnetic behavior, we believe the crystal is a mixture of Fe_3Se_4 domains and Fe_7Se_8 domains. According to the magnetic phase diagram in Fig. 4-31, a ferrimagnetic to anti-ferromagnetic transition with Néel temperature at 123K is possible. Since the paramagnetic to ferrimagnetic transition for Fe_7Se_8 occurs at T>400K, it is possible the crystal is still ferrimagnetic at 290K. The transition at 192K is attributed to Fe_3Se_4. This section included for possible future interests in magnetic materials (i.e. anti-ferromagnetism and ferrimagnetism). However, the current synthesis parameters need to be further refined if a pure Fe_7Se_8 crystal is required.

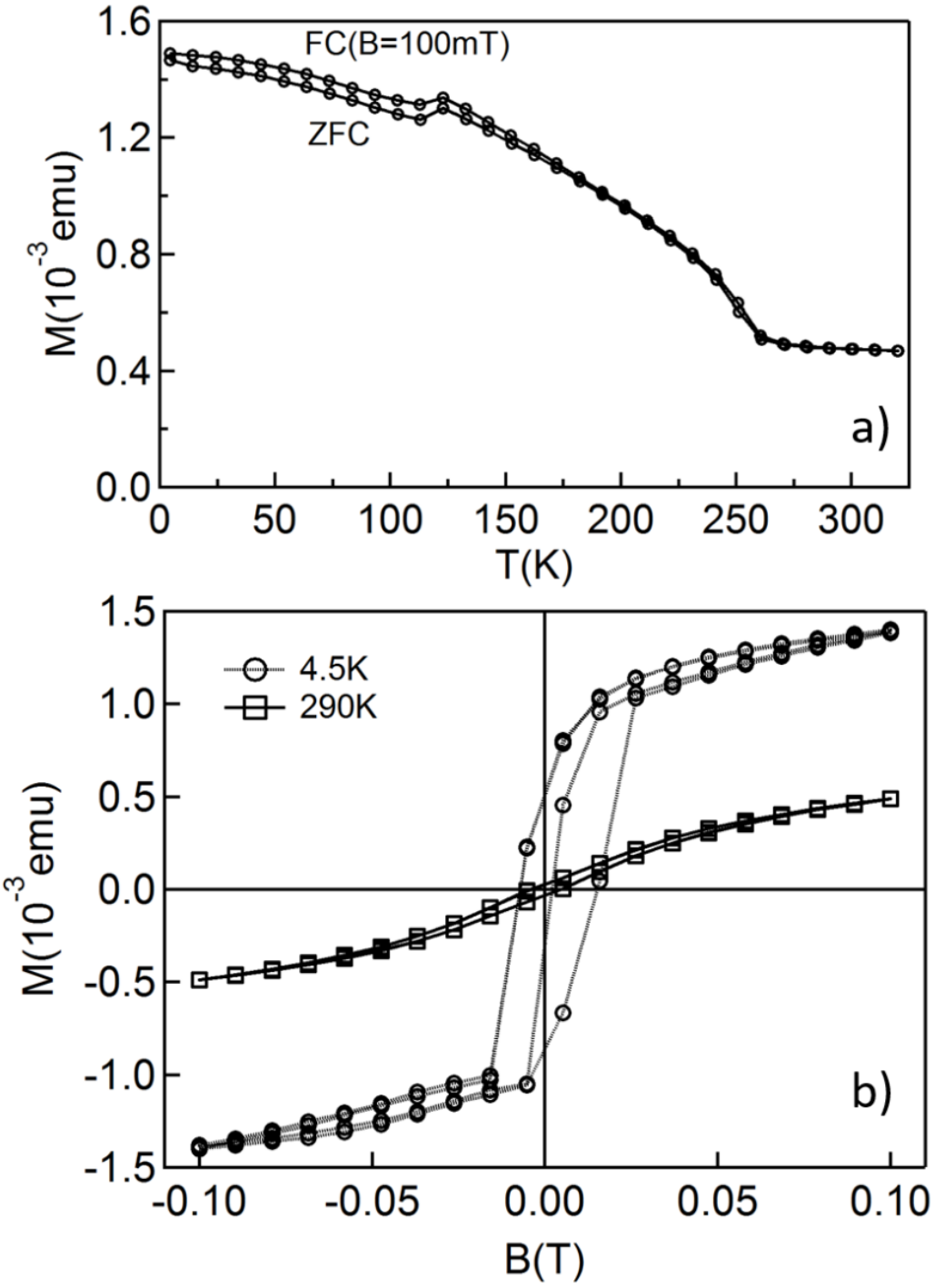

Fig. 4-30 Magnetic properties of synthesized Fe_3Se_4/Fe_7Se_8.
a) Magnetization for T=320-4.5K after zero-field cooling (ZFC) and during field cooling (FC) with magnetic field B=100mT. b) Magnetization as magnetic field is scanned between 0.1T and -0.1T at 4.5K (circles) and 290K (squares).

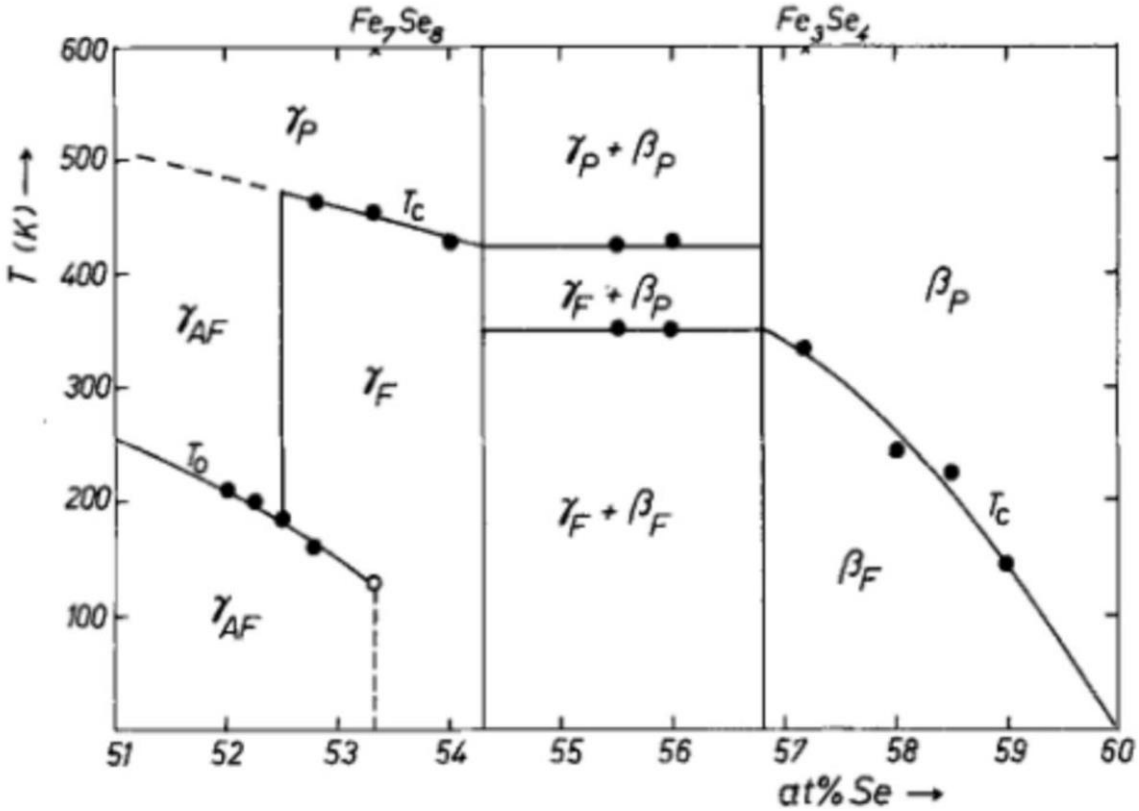

Fig. 4-31 Magnetic phase diagram for FeSe with NiAs structure.
Fig. 1, Terzieff & Komarek [294].

5 Monolayer $NbSe_2$ (MBE grown)

$NbSe_2$ was studied as one of the prototypical layered material with anisotropic superconducting properties [168]. Since then, many other superconductors with layered structure have emerged (e.g. cuprates, MgB_2 and iron based superconductors, see section 1.1). The discovery of the "Scotch tape" method has renewed interest in collective ground states at the ultrathin limit (see section 2.3). The thickness dependence of the CDW phase has recently been a topic of extensive study in 1T-TaS_2 [47]. The isolation of an atomic layer of a superconductor is of great relevance to the study of two-dimensional superconductivity, previously pursued primarily with molecular beam epitaxy (see section 1.1.5). As both superconducting and CDW phases exist in $NbSe_2$, it is an interesting material for the study of collective ground states in the ultrathin limit.

Recent studies on monolayer $NbSe_2$ obtained samples by mechanical exfoliation [130,169]. We have explored a complementary sample structure using monolayer $NbSe_2$ grown by MBE. Samples were grown by Yi Zhang, a post-doctoral researcher in the Shen group, and Hyejin Ryu, a post-doctoral researcher at the Advanced Light Source. Our samples offer unique advantages for surface sensitive and *in situ* vacuum studies. Transport in MBE grown monolayer $NbSe_2$ was studied in a UHV cryostat with the help of Miguel Ugeda, a post-doctoral researcher in the Crommie group, Aaron Bradley, a graduate student in the Crommie group, and Yi Chen, a graduate student in the Crommie group. Subsequently, I extended the transport study to lower temperatures using a dilution refrigerator to study superconductivity. Miguel, Aaron and Yi Chen characterized the samples with STM. In particular, they studied the CDW at the monolayer limit with STM and a short discussion on their results are included in the end.

5.1 Ultrathin $NbSe_2$

Superconductivity in ultrathin $NbSe_2$ was reported in 1972 [22]. Frindt proposed that the layer number dependence of superconductivity would elucidate the role of interlayer coupling. Fig. 5-1 shows the decrease in T_c as the number of layers are reduced. The thickness of the sample was estimated by dividing the sheet resistance by the bulk resistivity. The estimated thickness (filled circles), are shown together with nearest integer multiple of the monolayer thickness (open circles). The T_c was measured down to the bilayers and an extrapolation predicts T_c=3.8K in monolayer $NbSe_2$.

In 2015, superconductivity in monolayer $NbSe_2$ with T_c=2K was reported [169] (see Fig. 5-2). The thickness was characterized by height measurements with atomic force microscopy. Subsequently, a higher T_c=3.1K was reported by Xi *et al*. [48]. The discrepancy in T_c is possibly due to the presence of graphene. In the first study [169], ultrathin $NbSe_2$ was covered by graphene to protect it from the environment. For 3 and 4 layer thick $NbSe_2$, covering with graphene or h-BN made no difference. However, it is possible that graphene has some effect for monolayer $NbSe_2$.

The recent study of monolayer $NbSe_2$ by Xi *et al*. [130] report, for magnetic fields pointing parallel to the layer, $B_{c2}^{\parallel} > B_P$ exceeds B_P (see section 1.1.2). A similar effect is reported for ionic liquid gated MoS_2 as well [170]. According to Xi *et al*. [130], the carrier spins are protected by a combination of spin-orbit coupling effect and the unique crystal symmetry of the monolayer. It is interesting to note that, $B_{c2}^{\parallel} > B_P$ has been reported in *bulk* $NbSe_2$ for magnetic fields directed parallel to the layers [171,172]. Magnetoresistance experiments indicate $B_{c2}^{\parallel} \sim 6.5 B_P$ for monolayer [130] and $B_{c2}^{\parallel} \sim 1.5 B_P$ for bulk [171]. However, the measurement and definition of $B_{c2}^{\parallel}$ differ between the two studies and further study is needed for a fair comparison.

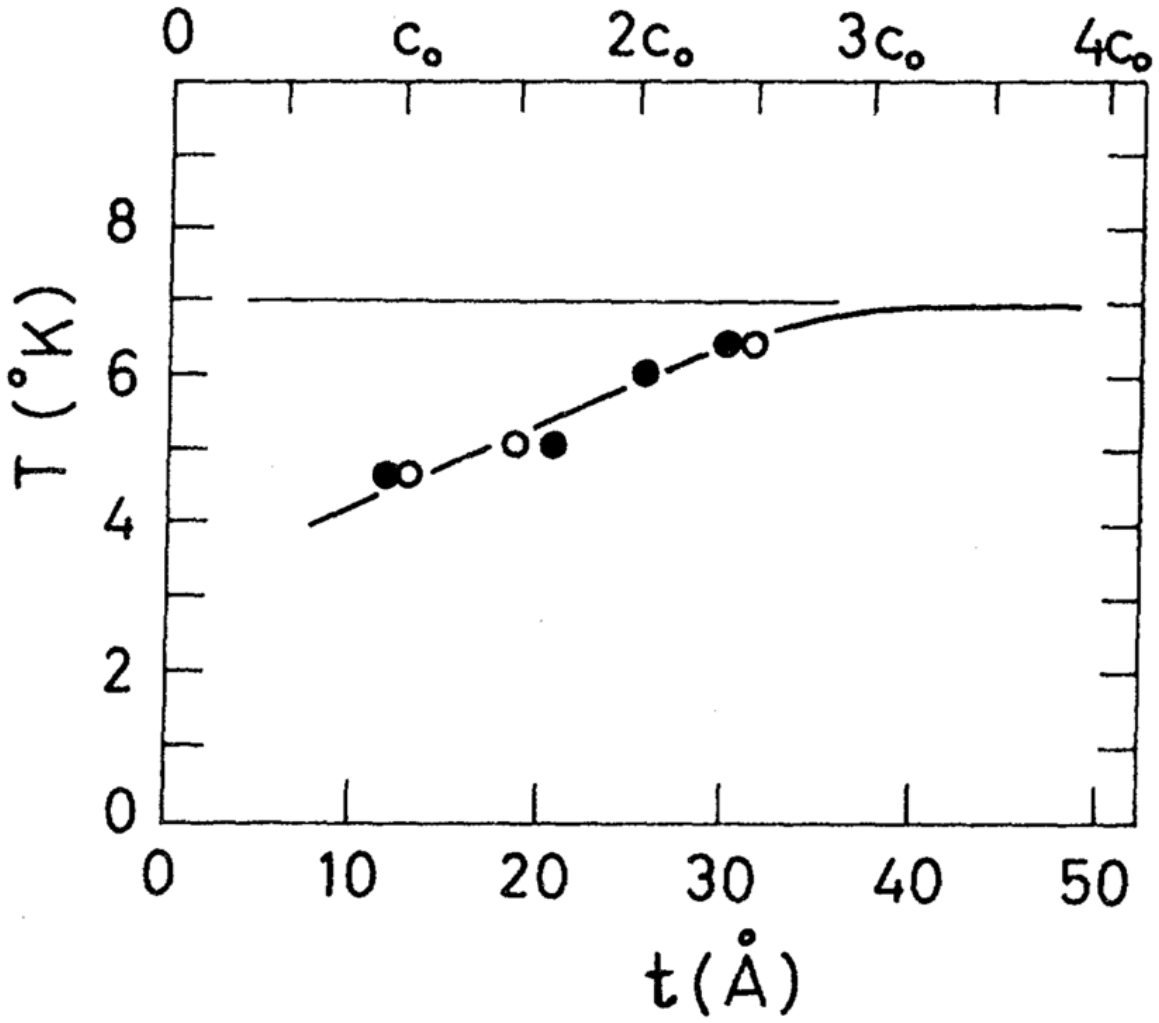

Fig. 5-1 T_c vs $NbSe_2$ thickness (1972).
Fig. 2, Frindt [22]. The vertical axis is T_c from the resistive superconducting transition. The horizontal axis is the sample thickness (t). The top label c_0=12.6Å is the unit cell dimension corresponding to two $NbSe_2$ layers. Filled circles are placed at thicknesses deduced from resistivity. Open circles are placed at the nearest multiple of single layer thickness ($c_0/2$) with the same T as its nearest filled circle. The line extrapolates to T_c=3.8K in the single layer.

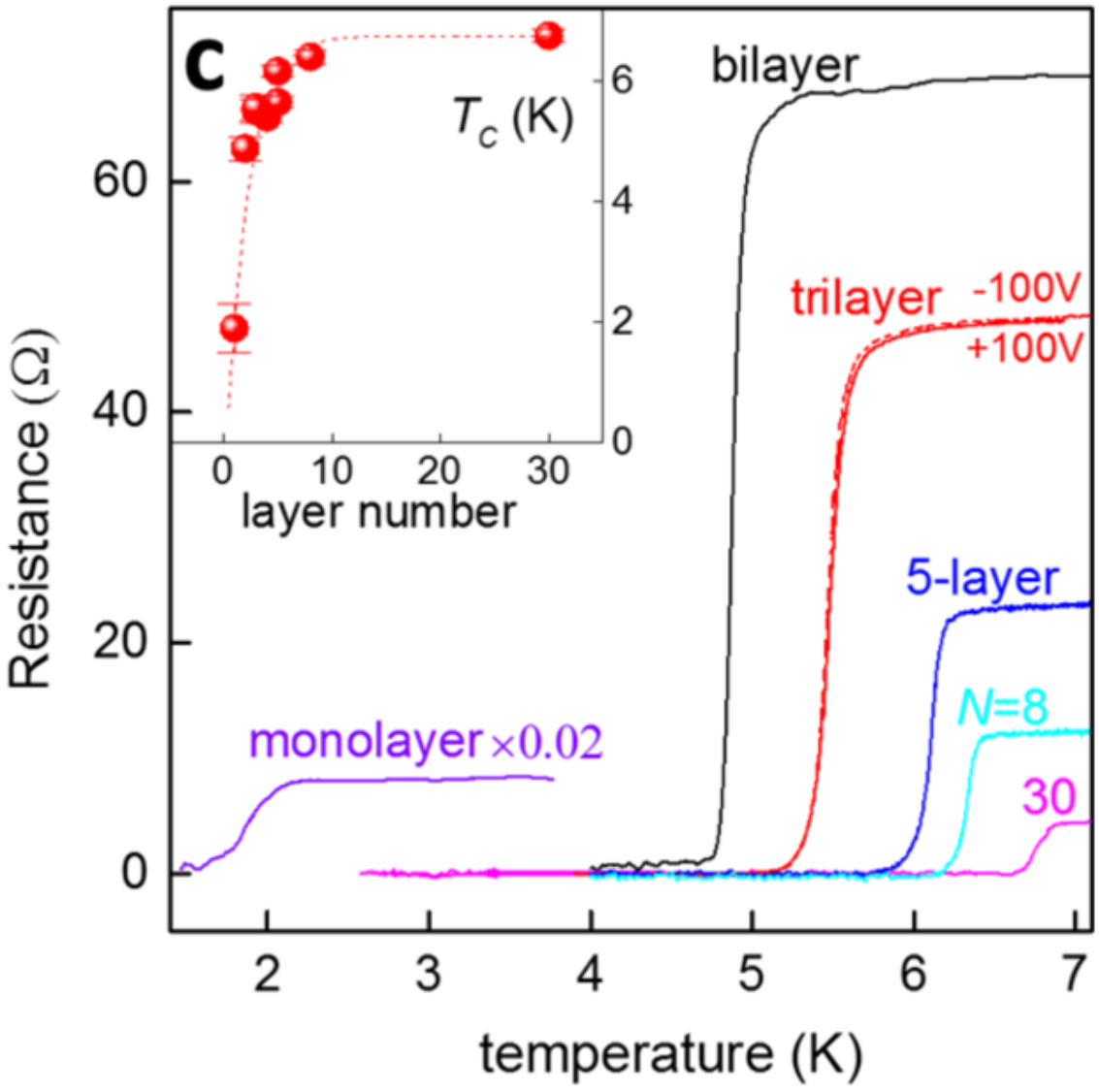

Fig. 5-2 T_c vs $NbSe_2$ thickness (2015).
Fig. 4c, Cao *et al*. [169]. The resistive superconducting transition from 30 layer $NbSe_2$ down to monolayer. The monolayer transition is centered at T_c~2K. The layer thicknesses are measured by atomic force microscopy.

5.2 MBE grown monolayer $NbSe_2$

Although many layered materials are susceptible to mechanical exfoliation down to the ultrathin limit (Table 2-2), Geim and Grigorieva warn that materials does not necessarily possess the chemical stability of its bulk form at the ultrathin limit [41]. Electrical devices of ultrathin $NbSe_2$ fabricated in air exhibit insulating behavior [77,101]. However, when $NbSe_2$ is exfoliated and encapsulated by h-BN or graphene [169], it remains metallic and superconducting down to the monolayer limit. $NbSe_2$ at the few unit cell thickness range decomposes if exposed to air, possibly due to photo-oxidation effects, which produce Nb_2O_5 and selenium precipitates [173,174]. Many of the recent studies [130,169,175] on ultrathin $NbSe_2$ protects the sample from air exposure by encapsulating it in h-BN.

We study a complimentary device structure to the mechanically exfoliated and h-BN capped devices. Monolayer $NbSe_2$ are grown on bilayer graphene (BLG) with MBE by Yi Zhang and Hyejin Ryu [28]. As illustrated in Fig. 5-3, the device consists of a silicon carbide (SiC) substrate, BLG, monolayer $NbSe_2$ (1ML $NbSe_2$) and selenium capping layer (Se cap). The BLG is epitaxially grown on the SiC and serves as a flat substrate that minimizes structural defects in $NbSe_2$. The ~10nm thick selenium capping layer is deposited at the end of the growth in order to protect the $NbSe_2$ after removing it from the UHV growth chamber. The advantage of the selenium capping layer is that it can be easily removed to re-expose the $NbSe_2$ surface, making it amenable to *in situ* studies with surface sensitive probes, such as scanning tunneling microscopy and photoemission.

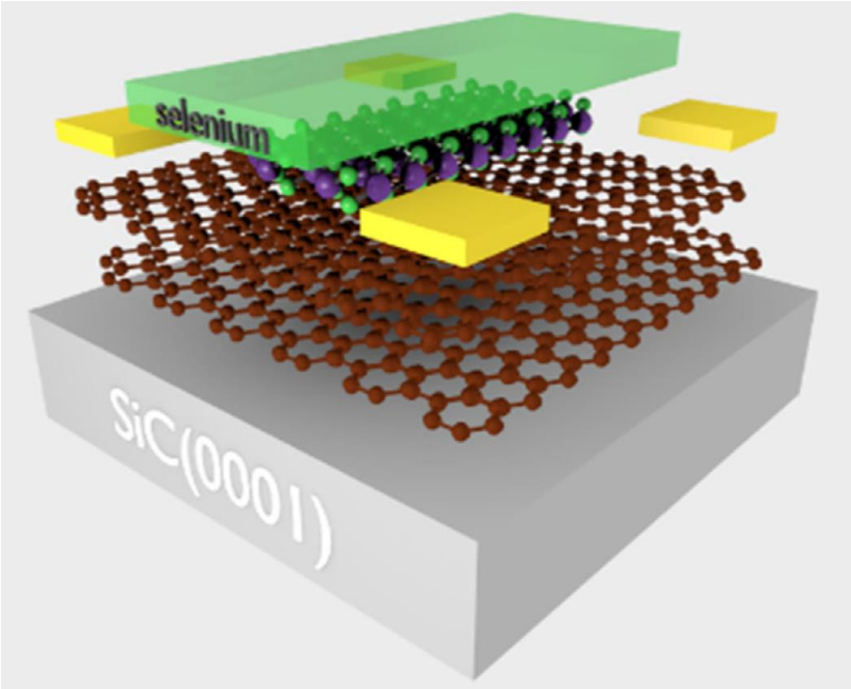

Fig. 5-3 MBE 1ML $NbSe_2$.
Adapted from Fig. 1, Onishi *et al*. [295]. The layers shown are (from bottom to top): silicon carbide substrate/epitaxially grown bilayer graphene/MBE grown monolayer $NbSe_2$/selenium capping layer (~10nm). Metal contacts (yellow plates) are on the four corner of the sample.

Fig. 5-4 shows an STM scan of a representative sample area obtained by Miguel, Aaron and Yi Chen in the Crommie group. Monolayer $NbSe_2$ forms a continuous network on top of BLG. Parts of the substrate are masked during MBE growth, to obtain exposed areas of graphene. As shown in Fig. 5-5, contacts are placed in a four-point probe configuration to the exposed graphene to study the transport behavior. 5nm/100nm of Ti/Au is evaporated through a shadow mask and the contacts are connected to cryostat wiring either by wire bonding or with silver paste.

Fig. 5-6 shows R(T) for T=50-5K of the MBE 1ML $NbSe_2$ (Fig. 5-3), before removal of the Se capping layer (solid line). The behavior is metallic for T=50-30K but R(T) switches to a thermally activated behavior for T=30-5K, possibly due to localization effects (see section 5.4). It is possible that the heat treatment during Se cap removal would alter the chemical composition of the $NbSe_2$ film to $NbSe_{x>2}$. To address this concern, R(T) of the sample before and after selenium capping layer removal are compared. After measuring R(T) with the Se cap, the same sample is heated in a UHV chamber at 330^{o}C to remove the Se cap and R(T) is measured *in situ*. To emphasize, the sample before and after removal of the Se cap are measured in the *same* UHV chamber (see section 3.2.4) with the *same* contact geometry and the sample without the Se cap is never exposed to air. As shown in Fig. 5-6 inset, the sample after Se cap removal (dotted line) has a lower resistance than the sample before Se cap removal (solid line). We attribute the difference to annealing effects during the selenium evaporation. R(T) of the sample without Se cap shows that the system is overall metallic for T=30-200K with a switch to thermally activated behavior for T=30-5K, similar to the sample with Se cap.

In order to compare the sample with Se cap and without Se cap, the resistance of each sample is normalized by the resistance at 50K (R(T)/R(50K)). Both curves are similar in their switch from metallic to thermally activated behavior at T~30K. Closer inspection reveals that the resistance minimum shifts slightly from T~30K for the sample with selenium to T~33K for the sample without Se cap. However, the difference is subtle, as the dip is broad and the minima are not well defined. With a change in chemical composition, much more dramatic change in R(T) is expected. Hence, we conclude that the transport behavior is not affected by the presence of selenium and does not change significantly during the removal of the Se cap. In hindsight, R(T) data for T>50K from the sample with Se cap would have been useful, as the electron-phonon coupling can be extracted from the slope (dR/dT) at high temperature, where R(T) is linear [176]. After the measurement in Fig. 5-6, the sample is imaged with STM in situ and looked similar to the typical samples in STM studies (see Fig. 5-4).

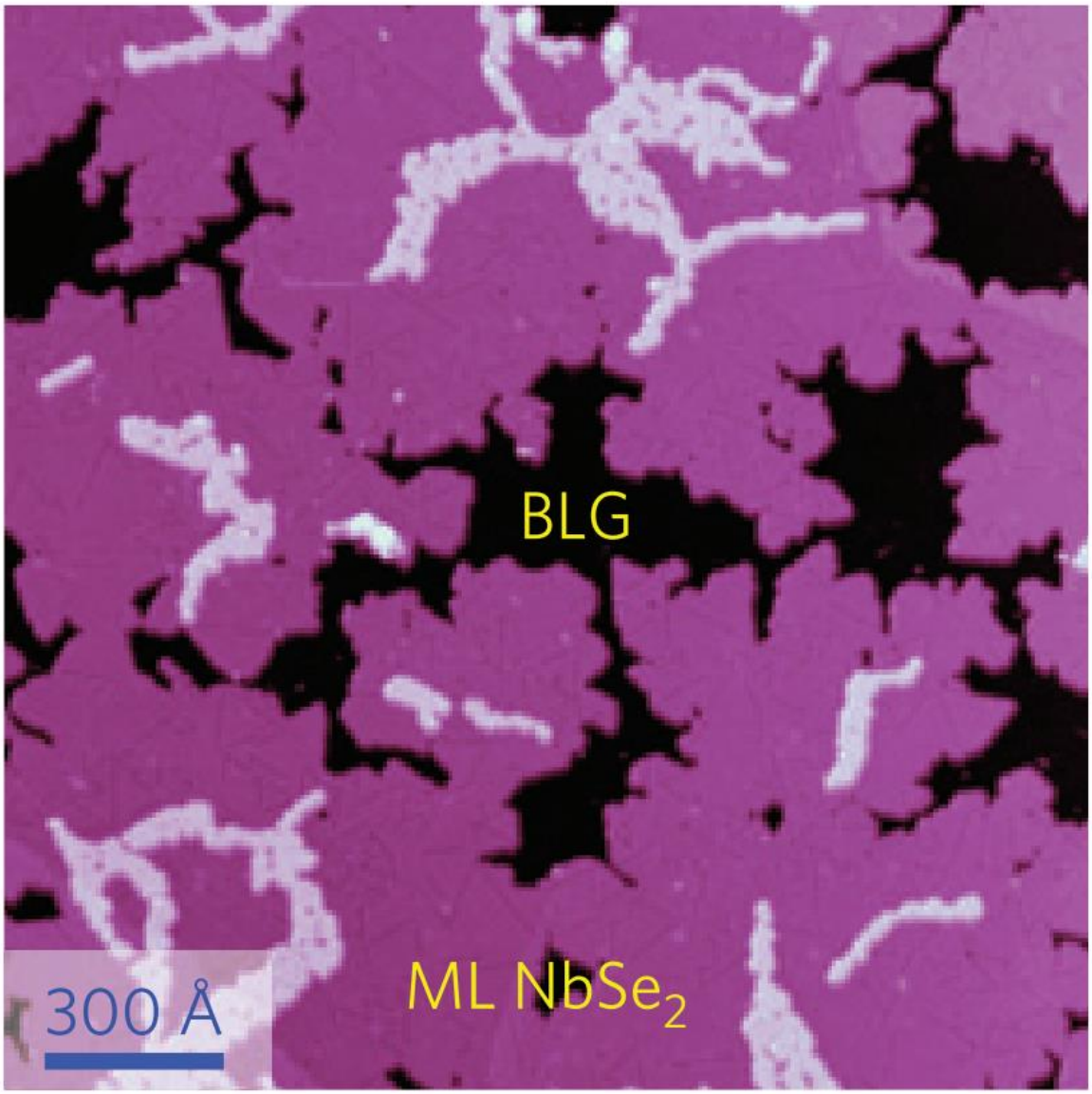

Fig. 5-4 STM image of MBE 1ML $NbSe_2$.
Fig. 1b, Ugeda *et al*. [49]. The monolayer $NbSe_2$ domains (purple region) cover most of the bilayer graphene (black region).

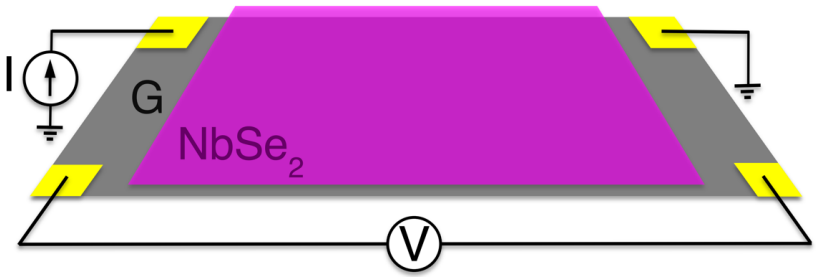

Fig. 5-5 Contact geometry on MBE 1ML $NbSe_2$.
Fig. S3, Ugeda *et al*. [49]. The contacts are evaporated on the exposed parts of graphene.

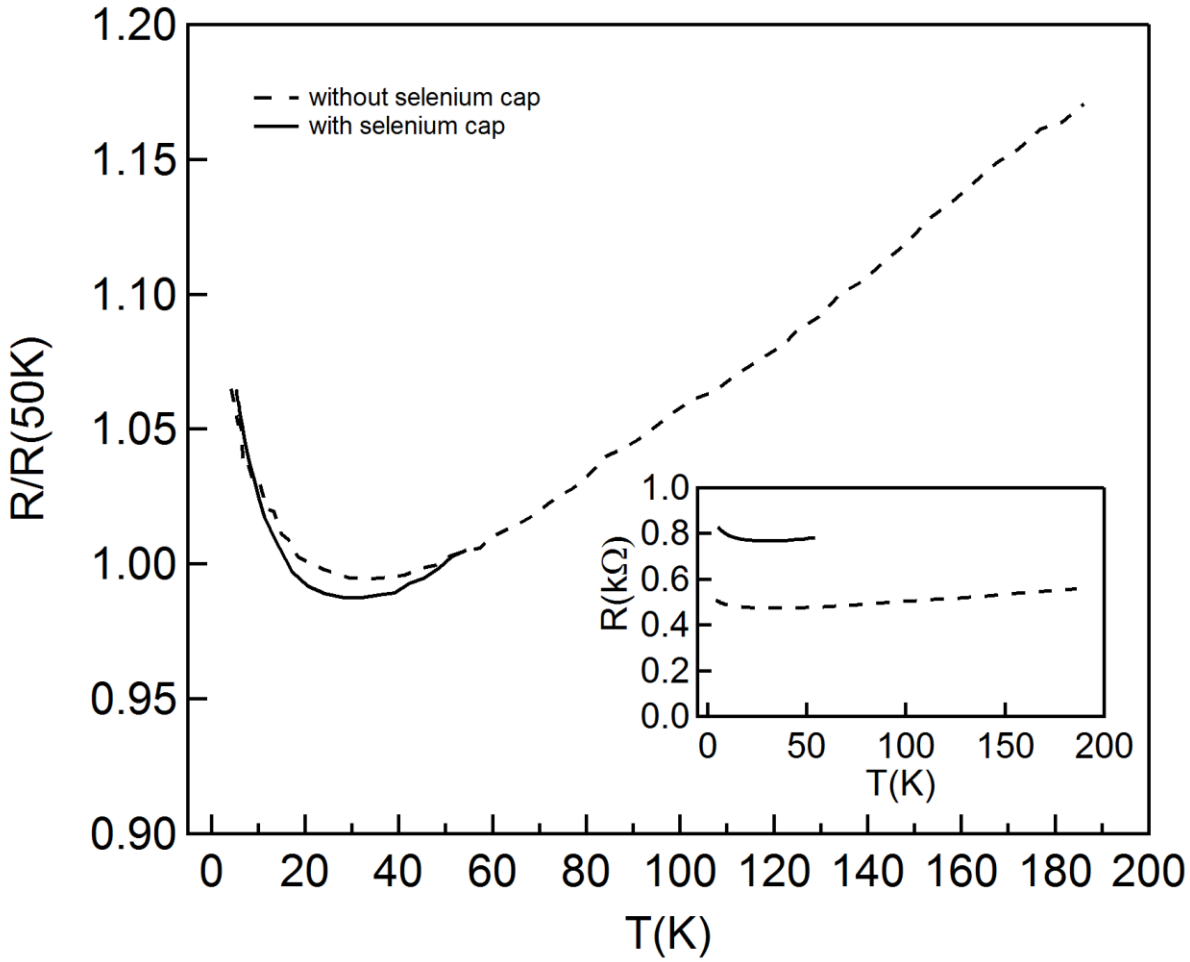

Fig. 5-6 Comparison of MBE 1ML $NbSe_2$ with and without Se cap.
R(T) first measured with Se cap (solid line). Subsequently, Se cap is evaporated off the same sample in UHV and R(T) is measured *in situ* (dashed line). Both R(T) are normalized to their resistance at 50K for comparison. Inset: resistances of the sample without normalization.

5.3 Superconductivity

Fig. 5-7 shows R(T) of MBE 1ML $NbSe_2$ for T=4-0.05K. The selenium capping layer is kept on the sample during measurement. At high temperature, the sample is in the normal state and resistance increases with cooling, possibly due to localization (see section 5.4). Below T_{onset}=2.6K, the resistance begins to drop and diverges from the extrapolated normal state behavior (upper dashed line), consistent with the onset of superconductivity. The midpoint temperature (T_{mid}=1.9K) is where the resistance falls to half of the normal state resistance. We define the normal state resistance as $R_n=R(T_{onset}=2.6K)$. Upon further cooling, the resistance falls to a constant value of R=15Ω (lower dashed line). The value of this constant resistance varies between samples and is very close to zero for some. For a superconductor, the resistance should remain at zero for $T< T_{zero}$. We believe the temperature independent residual resistance for some samples originates from the graphene portion, which is in series with the $NbSe_2$. The superconducting part of the sample falls to zero resistance for $T<T_{zero}$=1.3K. Our observed transition temperature is in agreement with T_c=2K reported by Cao *et al.* [169] but lower than the T_c=3.1K reported by Xi *et al.* [48].

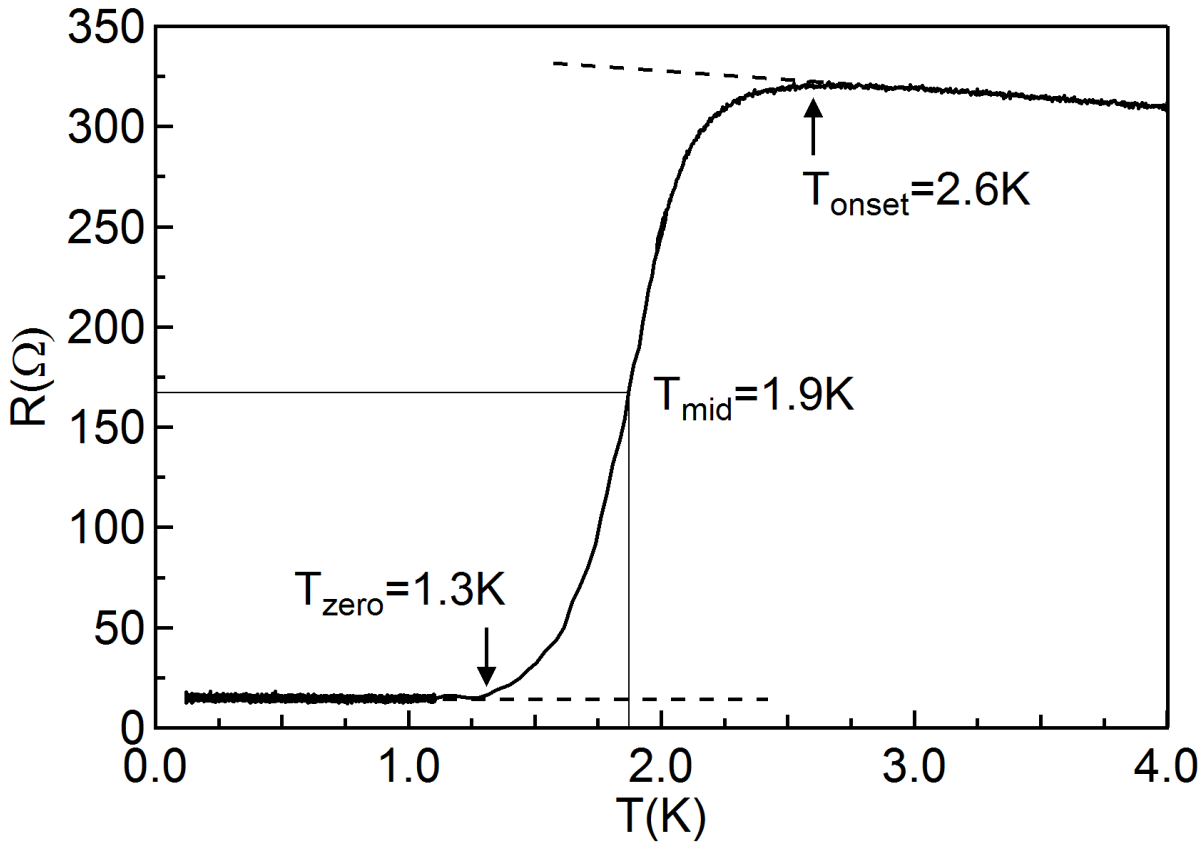

Fig. 5-7 Resistive superconducting transition in MBE 1ML $NbSe_2$.
Sample R(T) measured by four-point probe (see Fig. 5-5). The dashed line at the upper part of the graph is extrapolated R(T) from the normal state (T>2.6K). The dashed line at the lower part of the graph is a horizontal line at R=15Ω. T_{mid} for $R(T_{mid})=0.5R(T_{onset})$ is determined from the thin, horizontal and vertical construction lines.

5.3.1 Perpendicular magnetic field dependence

Fig. 5-8 shows R(T) of MBE monolayer $NbSe_2$ under a magnetic field directed perpendicular to the film ($B^{\perp}$). As $B^{\perp}$ increases, the transition gradually shifts to lower temperatures and broadens. At 3T, the superconductivity is completely quenched and R(T) switches to a thermally activated behavior. At 6T, the resistance increases more rapidly with cooling. The switch to insulating behavior is suggestive of a SIT (see section 1.1.5) in 2D superconductors. For our samples, we cannot confirm the large divergence in R at low T, which were seen in disorder induced SIT of Bi (see Fig. 1-7). However, R(T)of our samples resemble the magnetically tuned SIT in MoGe films (see Fig. 1-8).

Recently, in bilayer $NbSe_2$, the emergence of a quantum metal state between the superconducting and insulating state was observed [175]. The state is characterized by the resistance settling to a temperature independent, magnetic-field dependent value at low temperature. As our system has a complicated structure of bilayer graphene and $NbSe_2$, further study is needed to investigate how the system behaves when superconductivity is quenched.

Fig. 5-9 shows $B^{\perp}$-dependence of the resistance at T=0.15-3K. At low magnetic field ($|B|<2T$) and $T<T_c$, the resistance increases rapidly with $B^{\perp}$, due to the destruction of the superconducting order parameter. For a superconductor, the resistance should saturate to a constant value after superconductivity is completely quenched at high magnetic field. Our samples exhibit a slight positive magnetoresistance at high fields ($|B|>2T$) but the dependence is much weaker compared to the superconducting state. For the sample at 3K, well above T_c, only the small positive magnetoresistance is seen for both low and high fields. At a high magnetic field, the R decreases as T increases, consistent with the insulating behavior in Fig. 5-8 at high field.

Further details on R(B) in the superconducting state are shown on Fig. 5-10. There is little difference between the R(B) measured during field ramp up and down (labeled by arrows). Hence, the 100nA excitation is below the threshold of vortex motion. For the curve measurement at 0.15K, the data from ramp up and down are combined as the dataset is incomplete by themselves. At 0.15K, the change in magnetic field causes the sample to heat up and data points, which were measured without a well-controlled sample temperature is discarded. Even for 0.15K, R(B) from the ramp up and down look identical, when reliable data for both ramp directions are available. To minimize heating during magnetic field ramps, ramp rates are limited to 0.01T/s for T>0.15K and 0.001T/s for T=0.15K.

Fig. 5-15 shows $B_{c2}^{\perp}(T)$ extracted from R(B). The $B_{c2}^{\perp}$ is defined as $R(B_{c2}^{\perp})=0.5R_n$. $B_{c2}^{\perp}$ increases as the temperature is lowered and extrapolates to $B_{c2}^{\perp}(T=0)\sim1.3T$. The decrease in slope below 0.5K is consistent with the trend seen in bulk $NbSe_2$ [172]. Near T_c, the linear extrapolation from the data near T_c (dashed line) intercepts $B_{c2}=0$ at $T\sim1.75K<T_c=1.9K$. However, $B_{c2}(T)$ has been known to exhibit positive curvature near T_c in bulk layered superconductors [102]. It is possible that a similar effect occurs for monolayer $NbSe_2$.

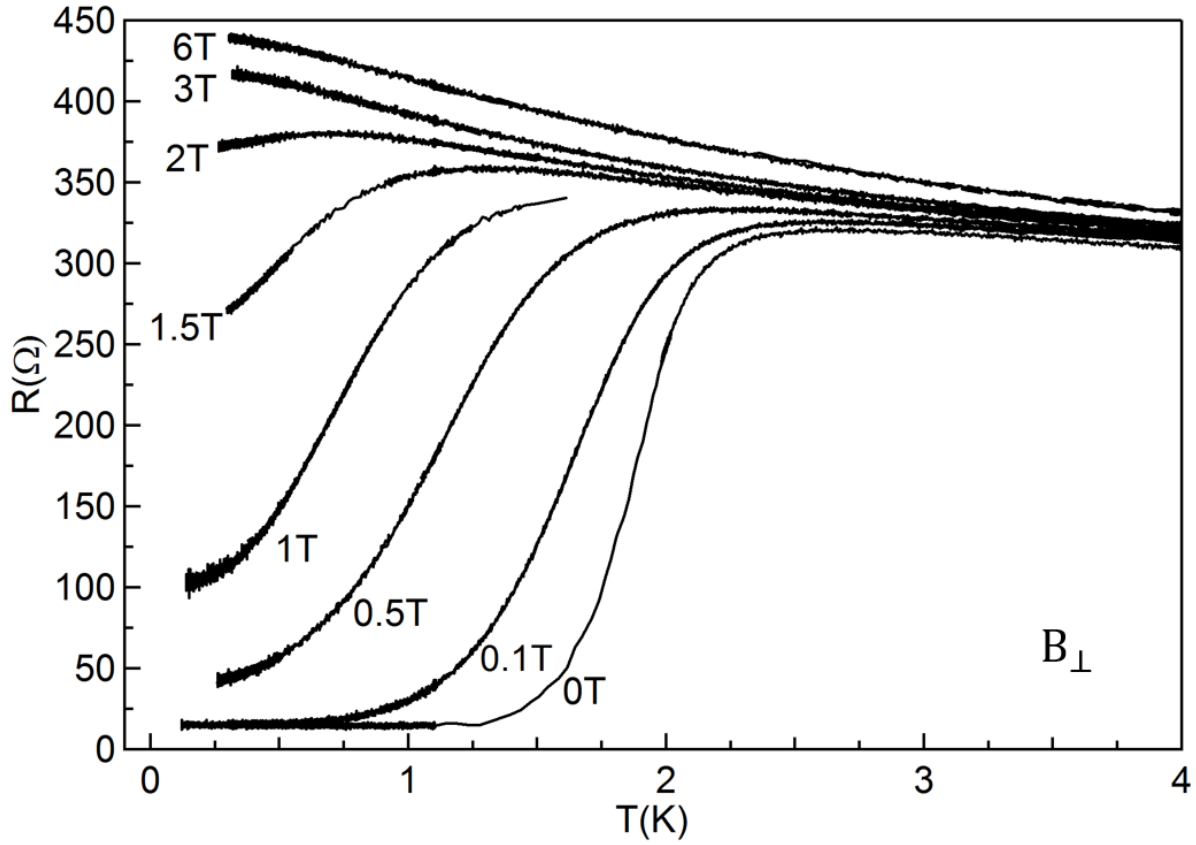

Fig. 5-8 R(T) of MBE 1ML $NbSe_2$ under $B^{\perp}$.
Each R(T) curve is labeled by $B^{\perp}$ strength. The sample geometry is SiC/BLG/1ML $NbSe_2$/Se, with Se cap still on the sample during measurement.

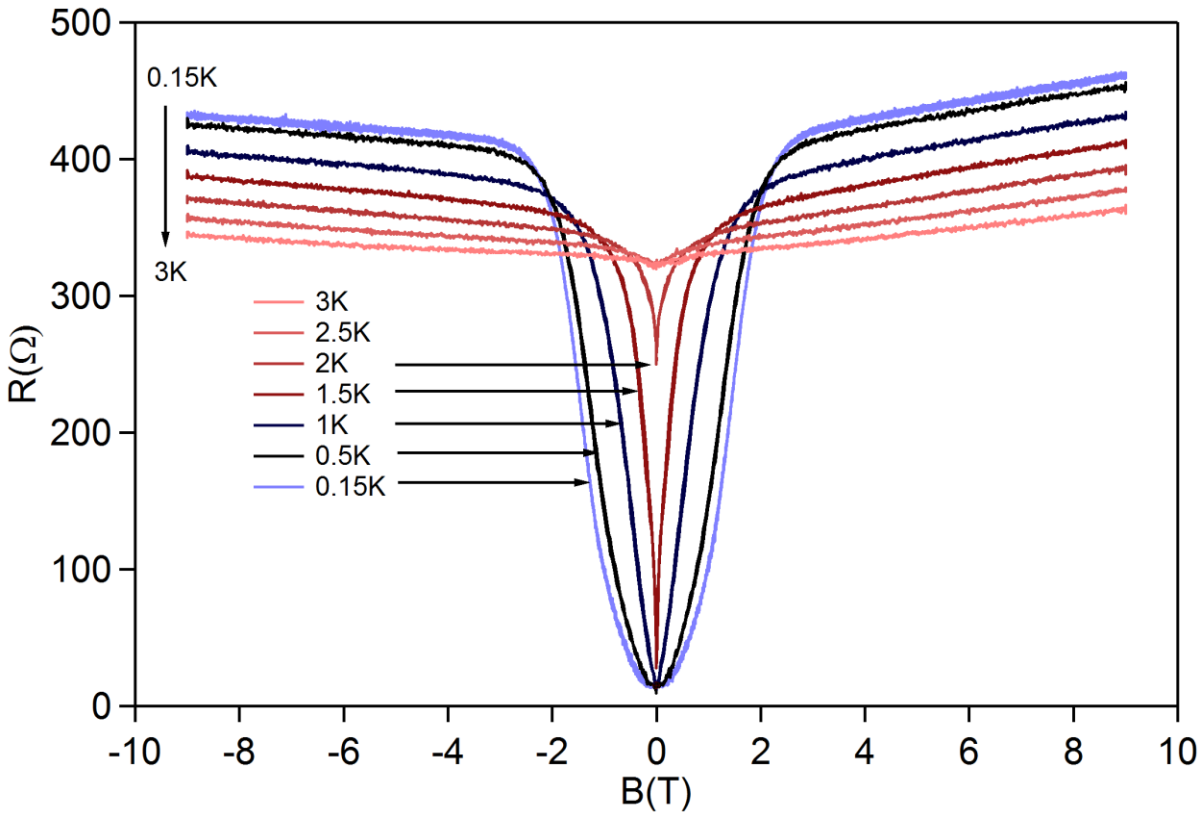

Fig. 5-9 R(B), -9T≤B$^{\perp}$≤9T of MBE 1ML $NbSe_2$.
Resistance is measured as the magnetic field is varied at constant temperature. R(B) for T=0.15K, 0.5K, 1K, 1.5K, 2K, 2.5K and 3K are shown. At low magnetic field, the resistance increases with temperature, whereas at high magnetic field, the resistance decreases with temperature.

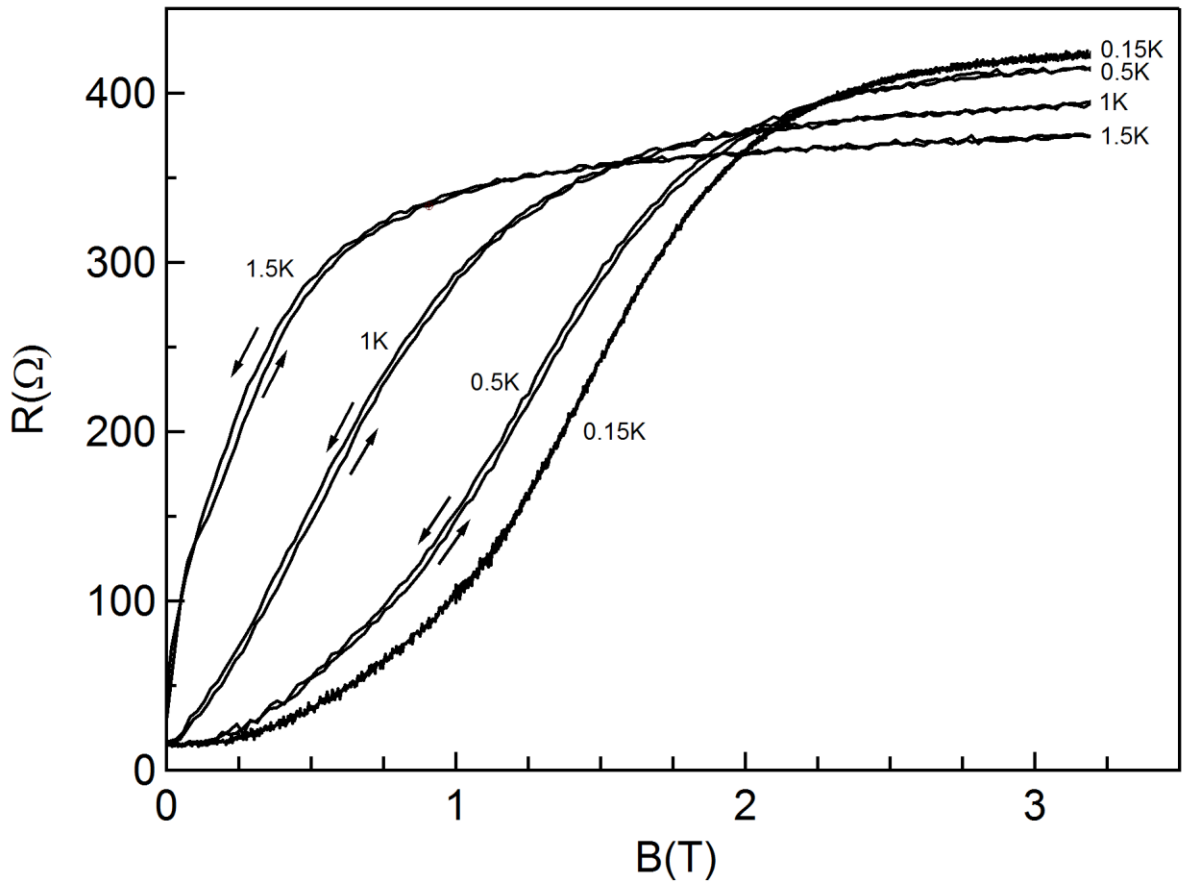

Fig. 5-10 R(B), $B^{\perp}$=0-3.5T of MBE 1ML $NbSe_2$.
Magnification of R(B) shown in Fig. 5-9 for low magnetic field. Each curve is labeled by the sample temperature during measurement. The arrows show the direction of magnetic field sweep.

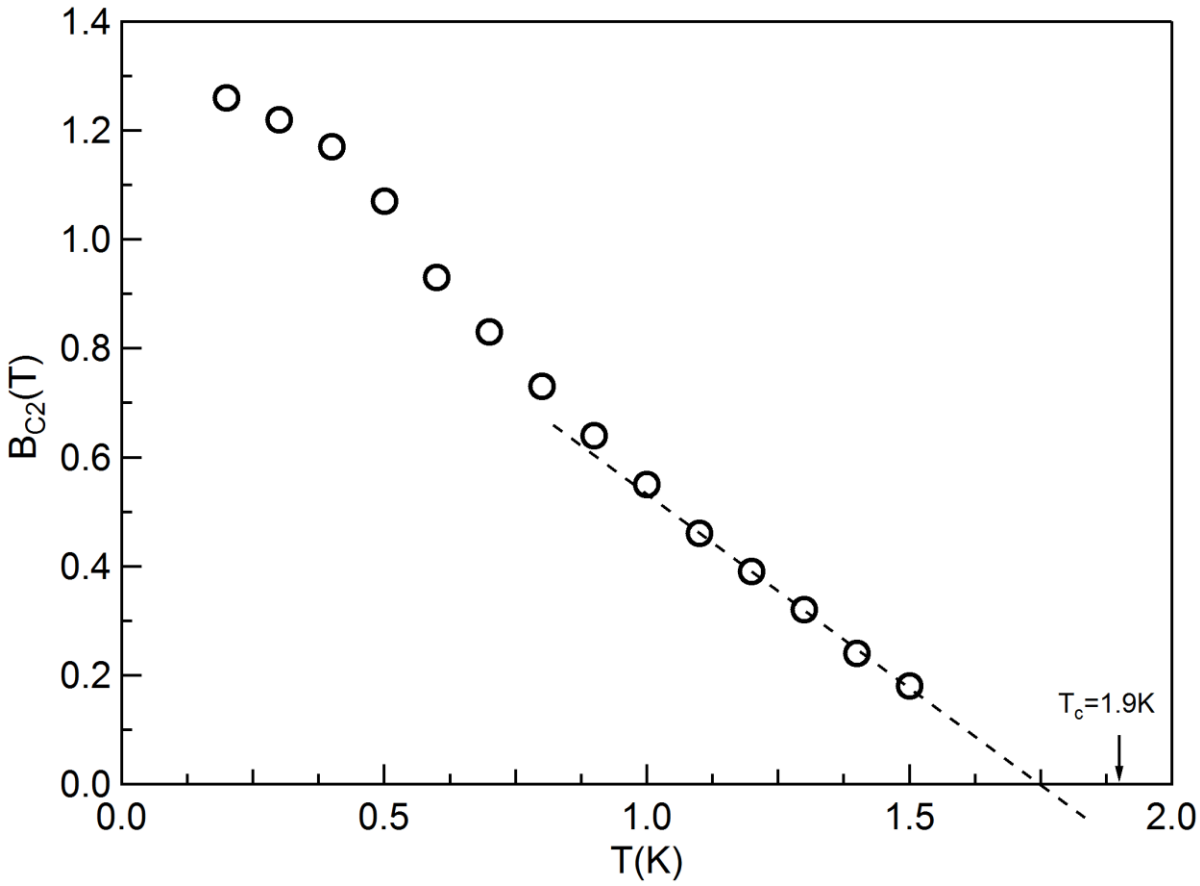

Fig. 5-11 $B_{c2}^{\perp}$(T) of MBE 1ML $NbSe_2$.
Each data point corresponds to $R(B_{c2})=0.5R_n$, where R_n is the normal state resistance with no magnetic field, and is extracted from R(B) similar to Fig. 5-10. T_c=1.9K from the superconducting transition at B=0T in Fig. 5-7, is marked by an arrow. The dashed line is a linear extrapolation to B_{c2}=0.

5.3.2 Parallel magnetic field dependence

For a superconductor of atomic thickness, $B_{c2}^{\parallel} > B_{c2}^{\perp}$ with a very large $B_{c2}^{\parallel}/B_{c2}^{\perp}$ is expected. $B_{c2}^{\parallel}$>31.5T was reported in exfoliated monolayer $NbSe_2$ [130] and the remarkably high $B_{c2}^{\parallel}$ is attributed to protection provided by the unique symmetry of the monolayer $NbSe_2$ (see section 5.1).

Fig. 5-12 shows R(T) with magnetic fields parallel to the sample. T_c shifts to lower temperature for higher magnetic field. For $B^{\perp}$>3T, superconductivity is completely quenched and R(T) switches to thermally activated behavior (see Fig. 5-8). In contrast, superconductivity survives even at $B^{\parallel}$=9T.

Fig. 5-13 shows R($B^{\parallel}$) of the sample. The positive magnetoresistance is interpreted as the suppression of superconductivity. As the field increases, the R(B) curves for T=0.7-1.2K emerge from a horizontal line of constant resistance at R=15Ω. The finite resistance is due to the portion of the sample, where graphene is in series with the $NbSe_2$. The lower (higher) the temperature for R(B) measurement, higher (lower) the field at which the curve emerges out of the R=15Ω threshold. For T<0.7K, the resistance remains at R=15Ω for B=0-9T because 9T is not strong enough to suppress the superconductivity to R>15Ω.

For R($B^{\parallel}$), B=9T is not high enough to reach R_n. For a large enough B, R should rapidly increase with B and saturate to a constant value, similar to R($B^{\perp}$) (see Fig. 5-10). Since R($B_{c2}^{\parallel}$)=0.5R_n cannot be defined, $B_{c2}^{\parallel}$ cannot be studied without higher magnetic fields. It would be interesting to compare $B_{c2}^{\parallel}$(T) in our MBE monolayers and in exfoliated monolayers.

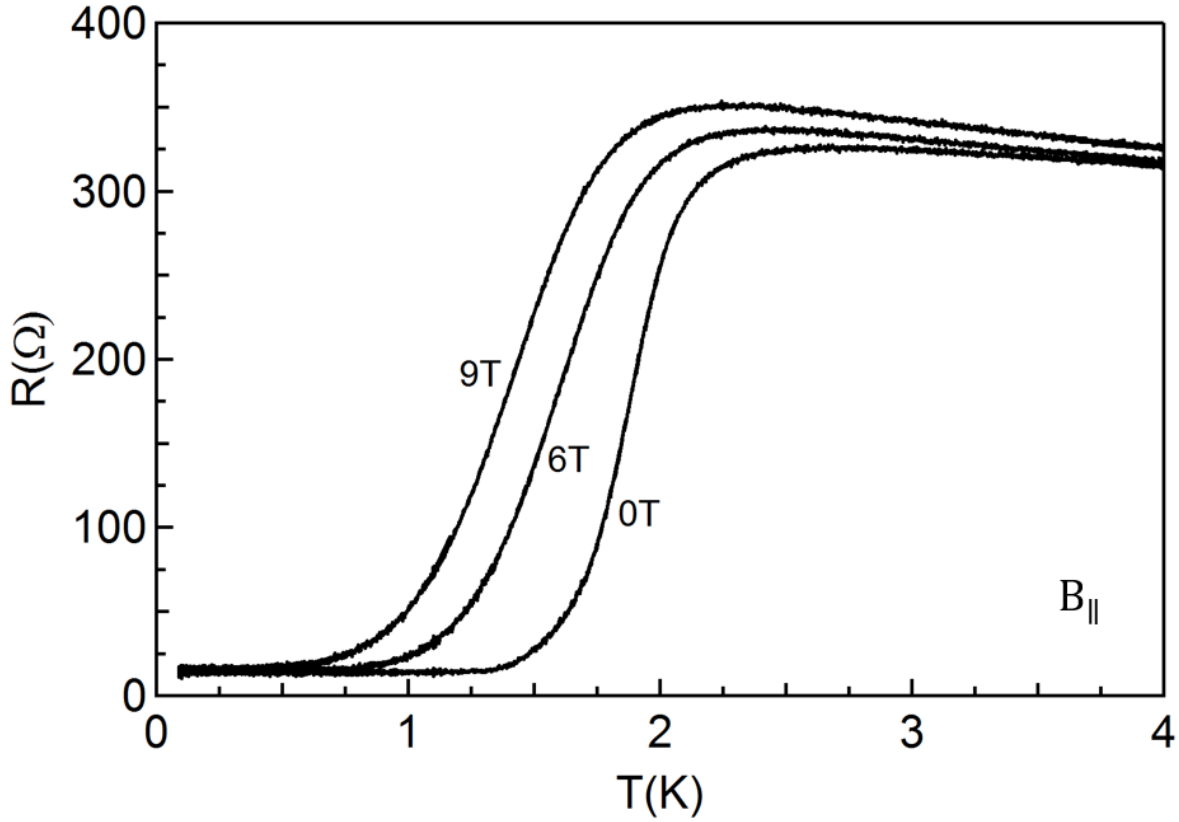

Fig. 5-12 R(T) with $B^{\parallel}$ of MBE 1ML $NbSe_2$.
Each R(T) measured at constant magnetic field in the parallel to the sample.

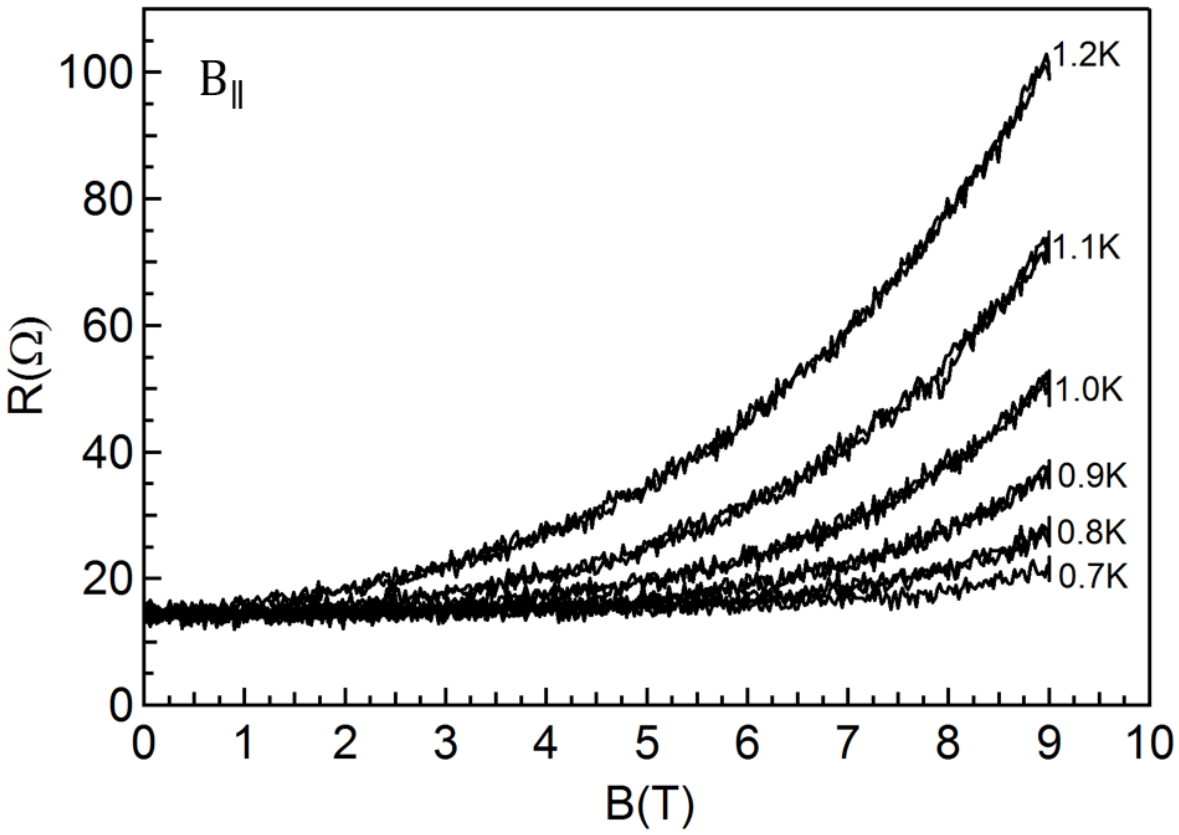

Fig. 5-13 R($B^{\parallel}$) of MBE 1ML $NbSe_2$.
Each R(B) curve is measured at constant temperatures from 0.7K to 1.2K in 100mK steps. R(B) for T<0.7K shows no change in resistance for B=0-9T.

5.3.3 Monolayer $NbSe_2$ exposed to air

A sample is exposed to air for 15min after Se cap removal in UHV. Fig. 5-14 shows the comparison between R(T) of the air exposed sample and a sample with Se cap (see Fig. 5-7). T_c for the air exposed sample (blue, dotted line) is depressed to 0.65K. To compare the change in transition width, the resistance in each sample is normalized by its R_n and the temperature is normalized by its $T_c=T_{mid}$. As expected, the transition is broader for the air exposed sample due to disorder effects. Most of the broadening occurs for $T>T_c$, where the transition is driven by fluctuation enhanced conductivity, and the behavior is surprisingly unchanged for $T<T_c$, where resistance is dominated by phase-slips (see section 1.1.1).

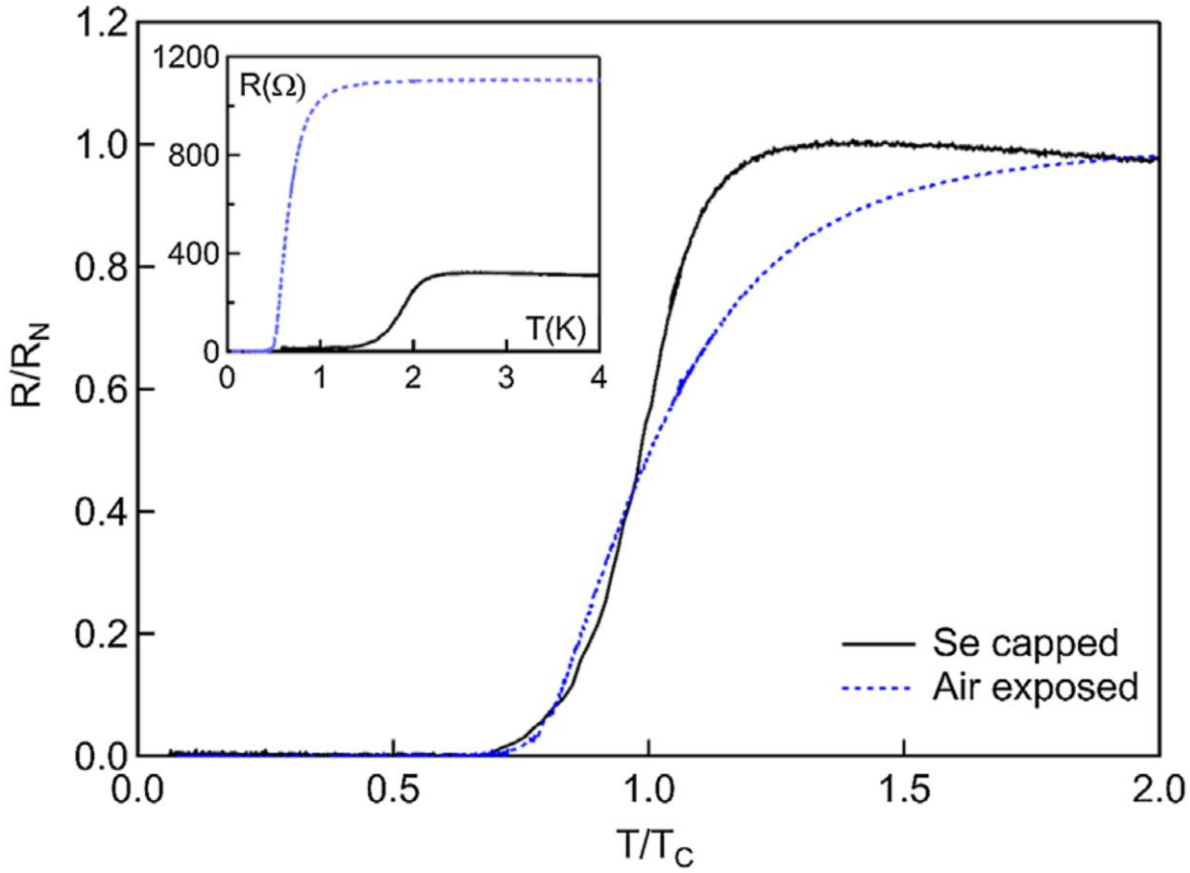

Fig. 5-14 Superconductivity in air exposed MBE 1ML $NbSe_2$.
Fig. 3, Onishi *et al*. [295]. Resistance of samples (shown in inset) is normalized by the normal state resistance by $R_n=R(T_{onset})$. The temperature is normalized by T_c. Two samples: one with selenium cap (black, solid line) and one exposed to air without selenium cap (blue, dotted line), are compared.

Fig. 5-15 compares $B_{c2}(T)$ of the air exposed sample and a sample protected with Se cap. As expected, the sample exposed to air (blue, squares) has an overall lower $B_{c2}(T)$ with $B_{c2}(T=0)$~0.2T. The reduced B_{c2} of the air exposed sample could be the result of reduced T_c. The B_{c2} for the air exposed sample and sample with Se cap are each normalized by $B_P=1.84T_c$ (Eq. 1-3, see section 1.1.2). The two samples are compared in the inset with the T normalized by T_c. Even after normalizing, B_{c2}/B_P of the air exposed sample reaches only half the value of the selenium capped sample.

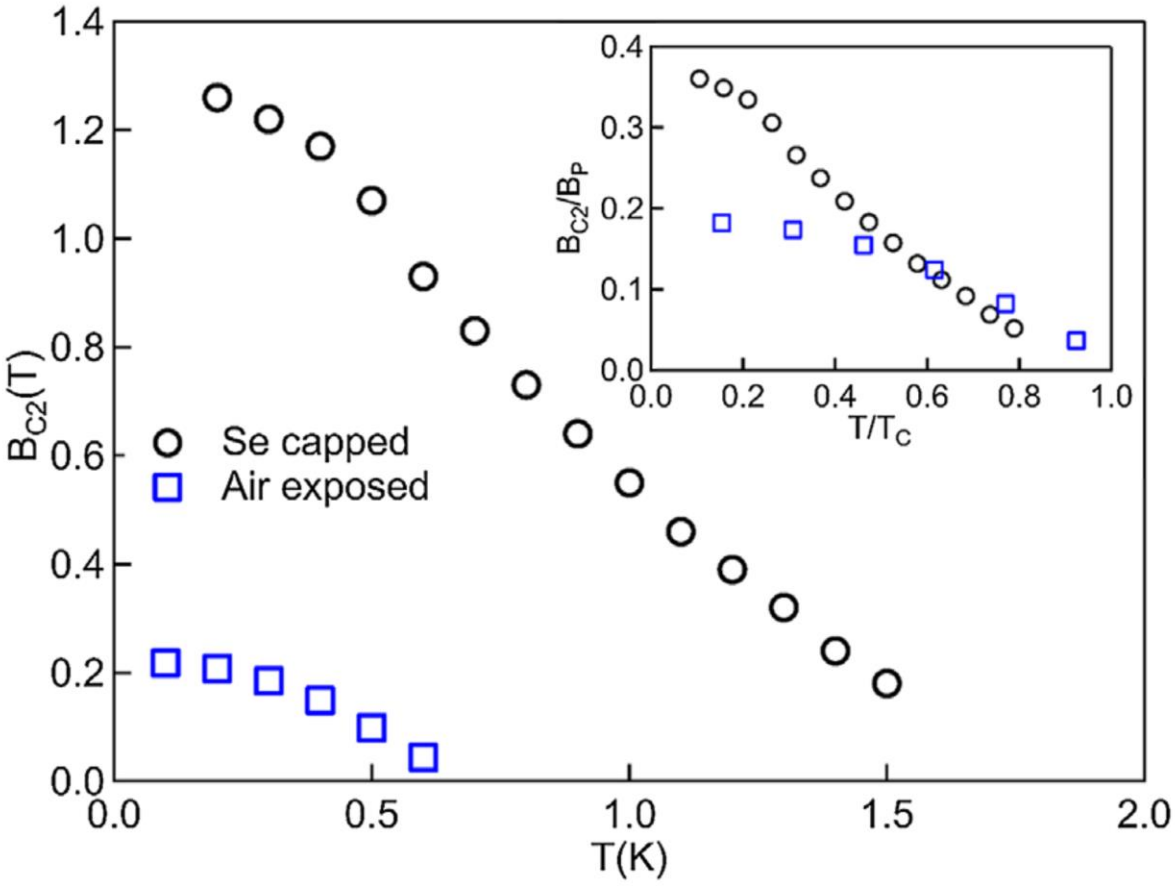

Fig. 5-15 $B_{c2}(T)$ of air exposed MBE 1ML $NbSe_2$.
Fig. 4, Onishi *et al*. [295]. Upper critical field (B_{c2}) defined as $R(B_{c2})=0.5R_n$. Two samples: one with selenium cap (black circles) and one exposed to air without selenium cap (blue squares), are compared. Inset: B_{c2} is normalized by the Pauli paramagnetic limit $B_P=1.84T_c$ and temperature is normalized by T_c.

Fig. 5-16 shows $R(B^{\perp})$ of the air exposed sample. A series of curves from 100mK to 1K in 100mK intervals are shown, with the line color progressing from dark to light blue as they correspond to higher temperature. The red dashed line corresponds to R(B) at 4K, which represents normal state behavior at $T >> T_c$. As with the Se capped sample (see Fig. 5-9), the R(B) curves for T≤1K show positive magnetoresistance due to the suppression of superconductivity. The R(B) curves measured during increasing and decreasing magnetic field are identical. At B>0.8T, all the curves adopt behavior of weak positive magnetoresistance as the superconductivity is completely suppressed and the resistance saturates to the normal state value. The inset shows R(T) at different values of B. Superconductivity is completely quenched for B>0.8T. The slope of the weak positive magnetoresistance is similar to the normal state magnetoresistance at 4K. At B>0.8T, R(B) at 4K has a lower resistance than R(B) at T≤1K because the system switches to thermally activated behavior when superconductivity is quenched at high magnetic fields.

In the superconductivity literature, the most common criterion for extracting B_{c2} from R(B) is $R(B_{c2})=0.5R_n$, where R_n is the normal state resistance. However, other criteria (e.g. $R(B_{c2})=0.9R_n$ and $R(B_{c2})=0.1R_n$) are found in the literature [177–182]. The comparison of $B_{c2}(T)$ based on different criteria has aided in interpreting the interplay between the superconducting domains and global behavior of the sample in past studies [182]. We have extracted $B_{c2}(T)$ with various criteria but do not propose a complete interpretation as further study is needed for this system. The horizontal line labeled with "90%" and "50%" in Fig. 5-16 correspond to the values from R(B) used to extract the B_{c2} with the $R(B_{c2})=0.9R_n$ and $R(B_{c2})=0.5R_n$ criterion, respectively.

In Fig. 5-17, $B_{c2}(T)$ from $R(B_{c2})=0.9R_n$ (green, open triangles) and $R(B_{c2})=0.5R_n$ (blue, open squares) are shown. In addition, $B_{c2}(T)$ from the "onset" criterion (black, open circles) is shown. The "onset" criterion determines B_{c2} as the field, at which finite resistance emerges from the zero resistance state. R(B) near this point is linearly extrapolated, as shown by the construction in the inset and the intersection with R=0 and the linear extraction is taken as B_{c2}. This criterion is of particular relevance to $NbSe_2$, as the characterization of B_{c2} in bulk $NbSe_2$ was based on this criterion [103]. $B_{c2}(T)$ behavior is similar across all three criterion. For $R(B_{c2})=0.5R_n$, linear extrapolation to $B_{c2}=0$ (blue, dotted line) intersects at T=678mK, close to T_{mid}=650mK.

Monolayer $NbSe_2$ from exfoliation were confirmed to undergo 2D superconducting transitions by applying the Aslamazov-Larkin formula (Eq. 1-1) [130]. It is interesting whether the air exposed monolayer $NbSe_2$ still shows a 2D superconducting transition. Fig. 5-18a shows the superconducting transition at B=0 (solid line) and R(T) of the sample under $B^{\perp}$=3T (dashed line). The superconductivity is completely quenched at 3T and R(T) shows a slight thermally activated behavior. R(T) at B=3T is taken as R_n and the excess conductivity (ΔS) is extracted from the data using Eq. 1-2. Fig. 5-18b shows ΔS vs $\bar{t} = (T - T_c)/T_c$. From the slope in the log-log plot, the dimension of the system is found from the Aslamazov-Larkin formula (Eq. 1-1). For $\bar{t}$=0.2-1, the closest fit is for D=1.9 but for $\bar{t}$=1-5, the fit indicates D=2.6. Lines with slopes corresponding to D=2 (blue, double dotted/single dashed line) and D=3 (triple dotted/single dashed line) are shown for comparison. In contrast to the study of K_3C_{60} thin films [183], we find that the slope for of our sample in Fig. 5-18b is sensitive to the value of T_c. We believe T_c=678mK is the most physically relevant because $B_{c2}^{\perp}(T_c)=0$ (see Fig. 5-17) and close to T_{mid}=650mK.

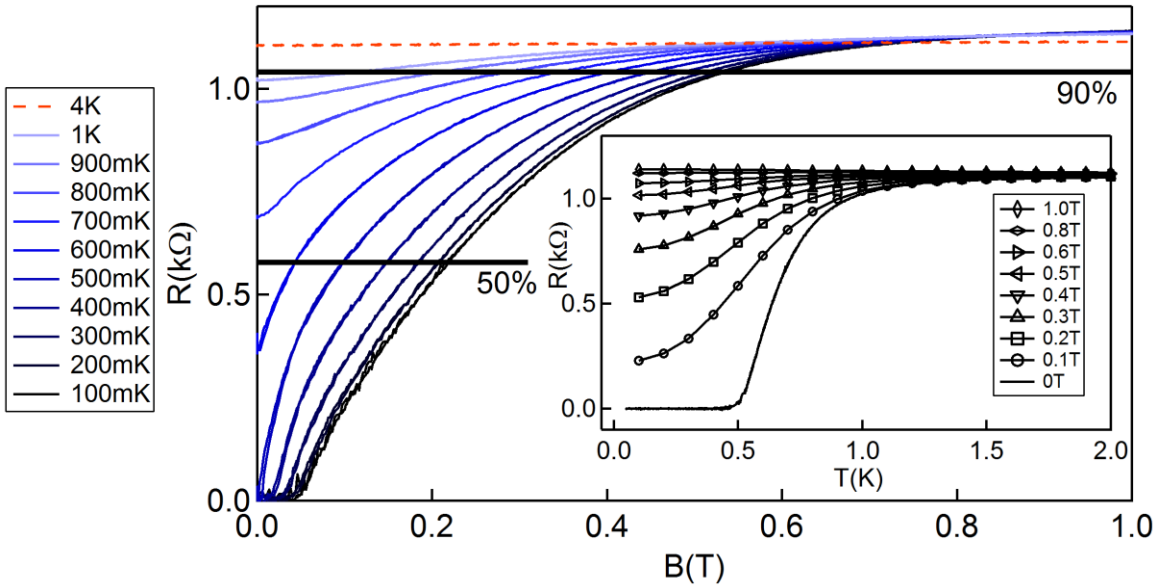

Fig. 5-16 R($B^{\perp}$) of air exposed MBE 1ML $NbSe_2$.
Each R(B) curve is measured at constant temperatures from 100mK to 1K in 100mK steps. As the line color is varied from black to lighter shades of blue, the temperature increases. The red, dashed line corresponds to R(B) at 4K. The upper horizontal line is drawn at $0.9R_n$ and the lower horizontal line is drawn at $0.5R_n$. Inset: R(T) at constant magnetic fields from 0 to 1T in 0.1T steps.

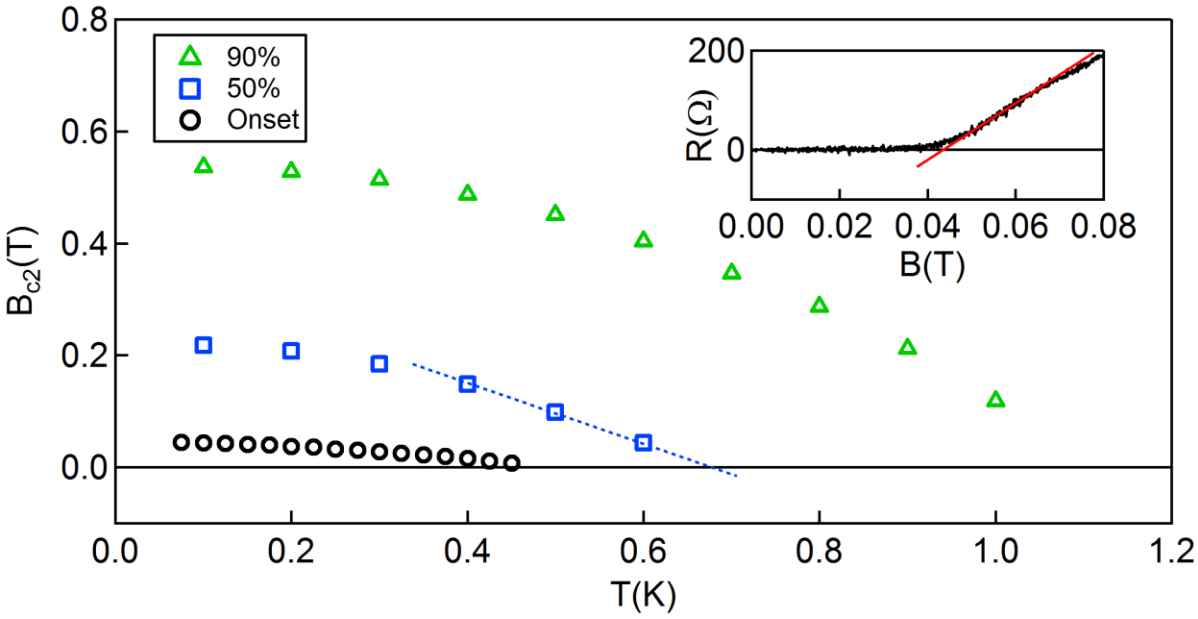

Fig. 5-17 B_{c2}(T) of air exposed MBE 1ML $NbSe_2$.
Triangles, squares and circles represent B_{c2} defined as $0.9R_n$, $0.5R_n$ and R_{onset}, respectively. Blue, dotted line is the linear extrapolation to B_{c2}=0, which intersects at T=678mK. Inset: R(B) for B=0-0.08T at 100mK. Red line is linear extrapolation to R=0. Each B_{c2} for R_{onset} is found by this construction.

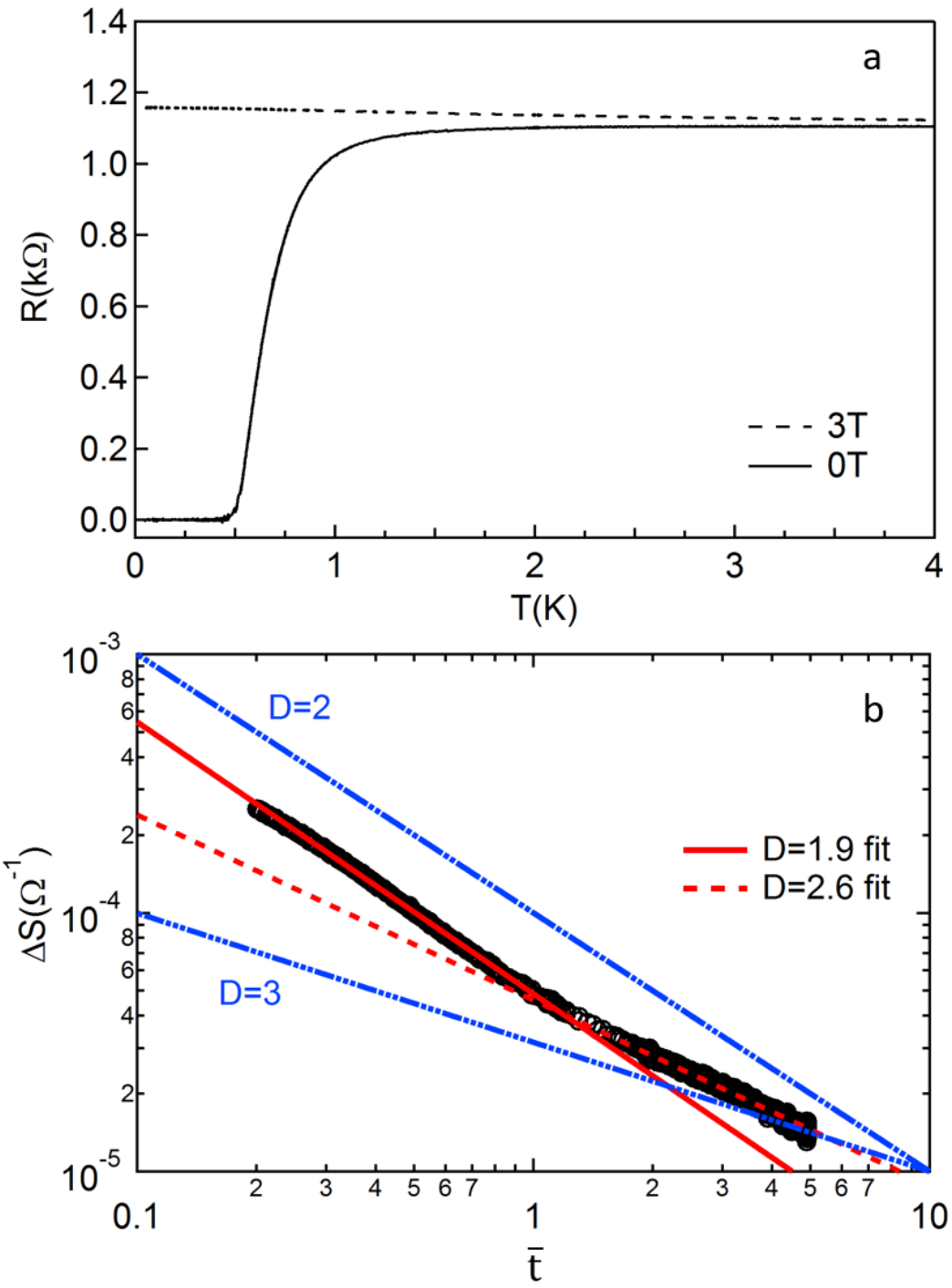

Fig. 5-18 Dimensionality of MBE 1ML $NbSe_2$ superconducting transition.
a) R(T) used to evaluate the excess conductivity (ΔS). Dotted line shows R(T) when superconductivity is quenched with $B^{\perp}$=3T. b) log-log plot of ΔS vs $\bar{t} = (T - T_c)/T_c$, with T_c=678mK. Data points are displayed as open circles. Eq. 1-1 is fit to the data with D=1.9 (red, solid line) and 2.6 (red, dashed line). Lines corresponding to D=2 (blue, double dotted/single dashed line) and D=3 (triple dotted/single dashed line) are shown.

5.4 Localization effects

R(T) of the 1ML MBE $NbSe_2$ switches from metallic behavior to thermally activated behavior (see Fig. 5-6). The resulting dip in R(T) reaches a minimum at T~30K. Fig. 5-19 shows R(T) of a sample, which is exposed to air for 15min (red, dashed line), 30min (green, dashed/single dot line) and 45min (blue, dashed/double dot line). As the air exposure time increases, the dip in R(T) at T~30K becomes progressively more pronounced. Although it is interesting that the dip occurs near the bulk $NbSe_2$ CDW transition temperature, the growth of the feature with increasing disorder suggests that it is caused by localization effects.

The formula for weak localization in 2D is [184]

$$\Delta S_{WL} = \frac{W}{L}\frac{e^2}{2\pi^2\hbar}\alpha p \ln\left(\frac{T}{T_0}\right) \qquad \text{Eq. 5-1}$$

where α, p and T_0 are fit parameters and W, L are width and length of the sample, respectively. ΔS_{WL} is the excess conductance

$$\Delta S_{WL} = \frac{1}{R} - \frac{1}{R_0} \qquad \text{Eq. 5-2}$$

$R_0(T)$ is metallic component of the sample resistance without weak localization effects. Since weak localization causes an increase in resistance, the excess conductivity is actually negative ($\Delta S_{WL} \leq 0$). For each curve in the R(T) shown in Fig. 5-19, R_0 is obtained by fitting

$$R_0 = a + bT^p \qquad \text{Eq. 5-3}$$

to the temperature range with metallic behavior. The fitting ranges are 58K to 74K for the sample at UHV and 50K to 80K for the sample after air exposure. p is close to 1 for all the R(T) curves (see Table 5-1).

Fig. 5-20 shows the Eq. 5-1 fit (red line) to the data in Fig. 5-19. The sample in UHV matches the fit to 4K but the sample after air exposure follows the fit for T=10-40K and turns away to higher conductivity for T<10K. The fit parameters are shown in Table 5-1. T_0 progressively increases for longer exposure to air but the sample at UHV (i.e. the limit of no air exposure) has higher T_0 than the sample with 15min exposure. Despite the $\ln(T/T_0)$ behavior, the value of αp for each fit is unusually large [184] and indicates that conventional weak localization does not explain the dip in R(T). Further study with controlled introduction of disorder is needed to determine the relationship between disorder and the switch to thermally activated behavior.

Sample	T_0(K)	p	α	αp
Ultrahigh vacuum	39.9	0.96	18.1	17.3
15min air exposure	39.3	0.92	9.4	8.7
30min air exposure	43.4	1.01	3.5	3.5
45min air exposure	44.9	1.07	2.5	2.6

Table 5-1 Weak localization fit parameters.
Fit parameters for Eq. 5-3 displayed as red lines in Fig. 5-20.

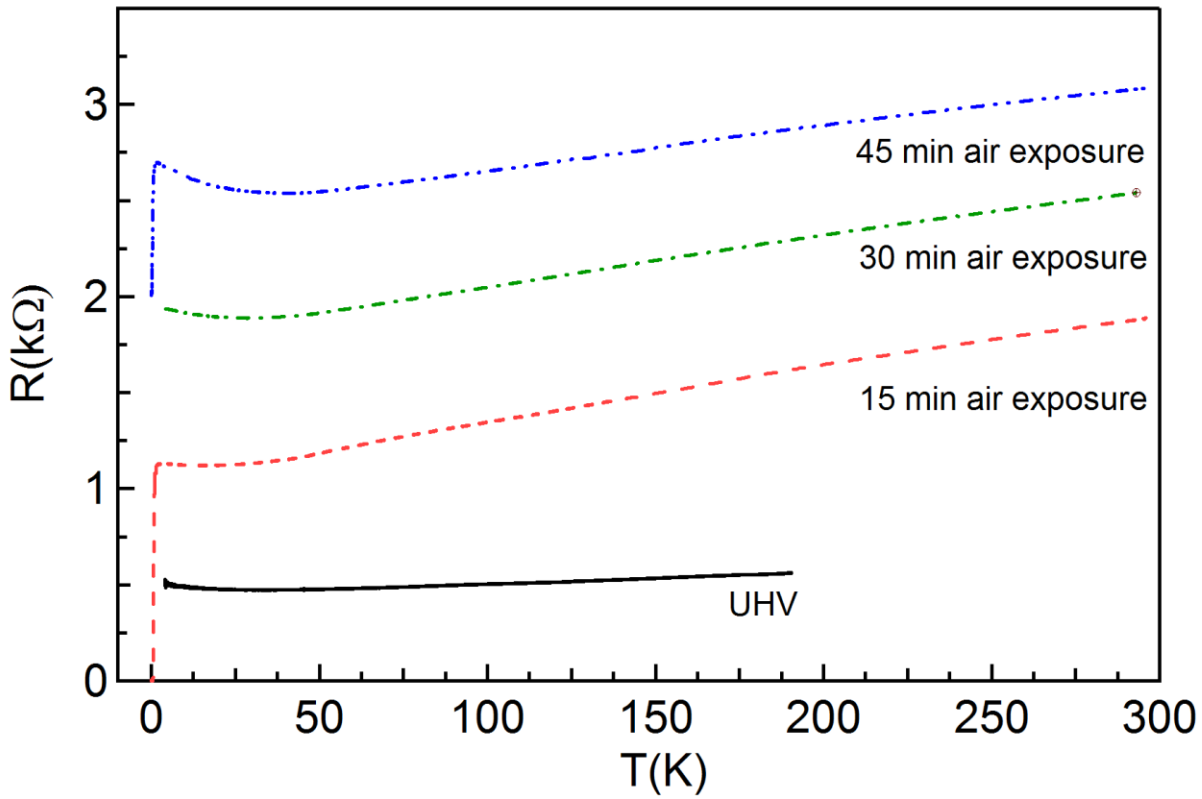

Fig. 5-19 Effect of air exposure on MBE 1ML $NbSe_2$.
R(T) of sample in ultrahigh vacuum (black, solid line), after 15min air exposure (red, dashed line), after 30min air exposure (green, dashed/single dot line) and after 45min air exposure (blue, dashed/double dot line).

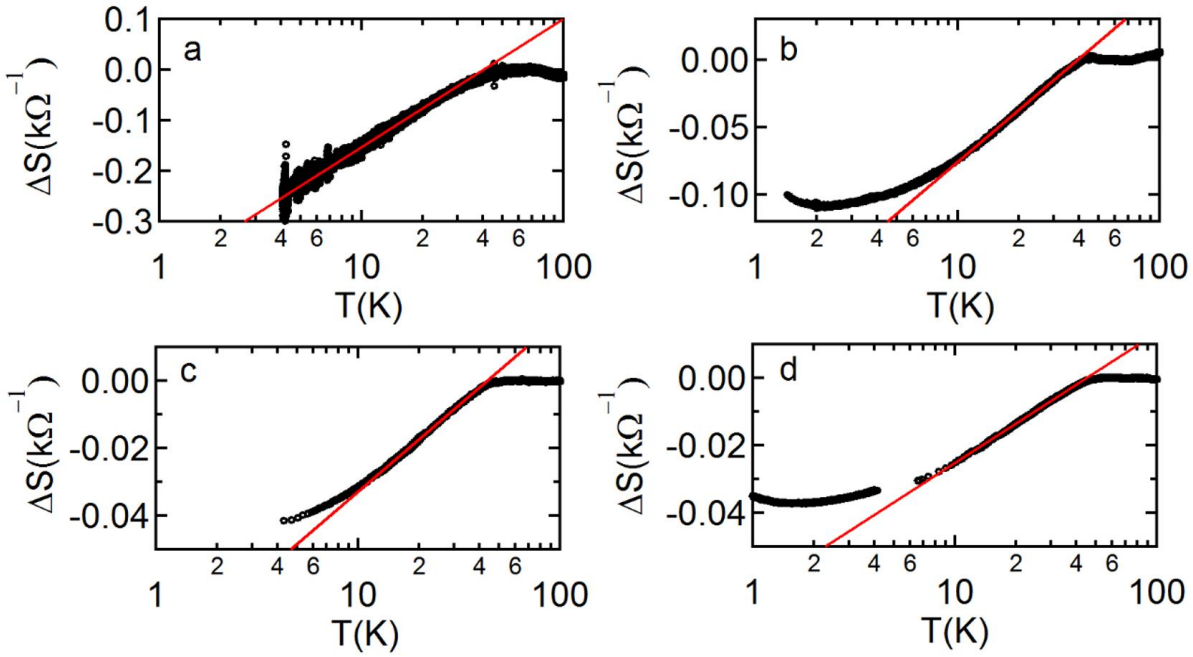

Fig. 5-20 Weak localization fit to R(T).

Excess conductivity (ΔS) calculated from data shown in Fig. 5-19 for a) UHV, b) 15min air exposure, c) 30min air exposure and d) 45min air exposure. Red line is the fit to $\ln(T/T_0)$ dependence.

5.5 CDW

The signature of CDW transition appears in R(T) of bulk $NbSe_2$ only as a weak resistive anomaly and high quality crystals are required to see the effect (see section 4.4.1.1). Non-linear conduction from sliding CDW would be a clear signature of the CDW state (see section 1.2.2). However, sliding behavior has not been observed in bulk $NbSe_2$. We attempted to slide the CDW in our MBE 1ML $NbSe_2$ by applying electric fields up to 4V/cm at 4.2K but did not see nonlinear conduction.

STM provides a direct probe of the CDW as it measures the local charge density. Fig. 5-21 shows STM scans of MBE 1ML $NbSe_2$ at different temperatures obtained by Miguel, Aaron and Yi Chen in the Crommie group. At 4K (Fig. 5-21e), a 3x3 reconstruction pattern, marked by the blue rhombus, can be clearly seen in addition to the $NbSe_2$ atomic lattice. The inset shows that the 3x3 reconstruction appears as a peak in the fast Fourier transform (FFT) of the image. This superlattice is consistent with the CDW superlattice seen in bulk $NbSe_2$ [49]. Hence, the CDW state exists at 4K in monolayer $NbSe_2$. The scan at 25K in Fig. 5-21d shows the CDW signature is still present. However, at 45K, the CDW signature is faded and only the $NbSe_2$ atomic lattice is visible, as shown in Fig. 5-21c. The CDW transition temperature for monolayer $NbSe_2$ is in the range $25K \leq T < 45K$, close to the bulk $T_P = 33K$.

There is a discrepancy between the STM result [49] and results based on optical properties [48]. The optical study used terahertz Raman spectroscopy and reported that the CDW transition is strongly enhanced to 145K in monolayer $NbSe_2$. The STM results are supported by *ab initio* calculations from Mauri *et al.* [185].

Theoretically, a phase transition at finite temperature for a two dimensional system is only possible for a Kosterlitz-Thouless transition due to the Mermin-Wagner theorem [186–189]. As STM is a local measurement, which probes the system at the atomic scale, it would be interesting to expand the study with complimentary techniques, which probe longer length scales (e.g. microwave transmission and optics).

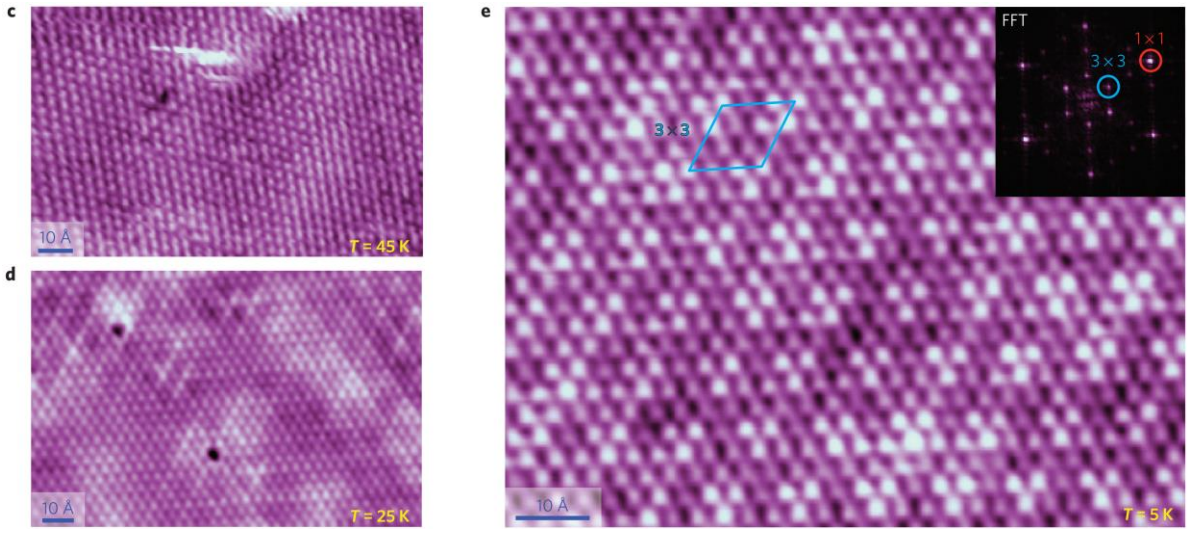

Fig. 5-21 Temperature dependent STM image of MBE 1ML $NbSe_2$.
Fig. 1c, d and e, Ugeda *et al*. [49]. STM image of $NbSe_2$ at c) T=45K, d) T=25K and e) T=5K. 3x3 reconstruction illustrated by blue lines and confirmed by FFT in the inset in e) are clearly visible at T=25, 5K but absent in T=45K.

6 Ultrathin $NbSe_3$

Recent studies on ultrathin transition metal chalcogenides have focused on mechanical exfoliation of quasi-2D MX_2 materials (e.g. $NbSe_2$, TaS_2, see section 2.1) [46,134,190,191]. However, it is possible to mechanically exfoliate $NbSe_3$ (an MX_3 material, see section 2.2) to obtain nanoribbons as thin as 18nm [96]. For the study of CDW in the ultrathin limit, MX_3 materials are of significant interest because many of them enable the CDW to slide (see Table 2-1). In addition to the static CDW properties (e.g. transition temperature and magnitude of resistive anomaly), the CDW dynamics (e.g. threshold field and narrowband noise) provide further insight into the nature of the CDW state.

This chapter discusses the effects of nanoribbon thickness on sliding CDW in $NbSe_3$. Narrowband noise measurements, which reliably probes the CDW order parameter for bulk crystals, has been applied to $NbSe_3$ nanoribbons. Preliminary results from fabrication of nanoribbon devices for studying the system under ionic liquid gating are shown. Another promising route towards obtaining $NbSe_3$ in the single atomic chain limit is the synthesis of $NbSe_3$ in a spatially confined environment, (e.g. inside of a nanotube). Interesting preliminary results of $NbSe_x$ confined in a boron nitride nanotube are presented.

6.1 Mechanically exfoliated $NbSe_3$

Previous studies have obtained nanowires and nanoribbons of $NbSe_3$ by direct synthesis [192] or ultrasonic exfoliation [124]. We have obtained $NbSe_3$ nanoribbons by mechanical exfoliation and studied the thickness dependence of CDW parameters (i.e. transition temperature, resistive anomaly magnitude, threshold noise and narrowband noise). The nanoribbons have a length to width ratio of 10:1, where the width is at least ten times the thickness for each one. The thickness ranges from 55nm to 18nm. As the material is thinned down, the resistive anomaly is suppressed and threshold field (E_T) increases, as reported in previous studies [92,124]. The thickness dependence of narrowband noise has not been previously studied and the results of probing the CDW order parameter with narrowband noise in ultrathin $NbSe_3$ are discussed.

Mehdi Jamei, a fellow graduate student in the Zettl group (PhD 2015), carried out the experiments and obtained the results shown in section 6.1.2. Subsequently, I analyzed his results to interpret the effect of thickness dependence in the CDW of $NbSe_3$ nanoribbons. His experimental methods are reproduced from his doctoral dissertation [193] to provide background information for section 6.1.2.

6.1.1 Experimental methods

$NbSe_3$ nanoribbons obtained by mechanical exfoliation were contacted by electron beam lithography (see section 9.1). In/Cr/Au trilayer contacts were evaporated on surfaces treated with nitrogen plasma to obtain the best contact. The threshold fields were detected by measuring the differential resistance with a lock-in amplifier and the pulse method. The narrowband noise was studied by measuring the output of the dc biased sample with a spectrum analyzer. A custom circuit was built to overcome the high impedance of the sample.

6.1.1.1 Device fabrication

Mechanical exfoliation of $NbSe_3$, electron beam lithography and contact deposition are detailed in pages 19-20 of Mehdi Jamei's doctoral dissertation [193] and reproduced below.

1.2.1.2 The exfoliation technique

My experience with exfoliating graphene helped me refine the exfoliation process in order to apply it to $NbSe_3$ crystals. Single crystalline $NbSe_3$ usually comes in thin, ribbon-shaped whiskers, and are several centimeters in length. Since the bonds between quasi-one-dimensional chains in $NbSe_3$ are very weak, this material can be exfoliated very easily. I started with a few long ribbons of $NbSe_3$ and placed them on a piece of scotch tape. After folding the tape onto itself several times, it was covered with thin $NbSe_3$ ribbons, which formed a grey film on the tape. I transferred a small amount of this film by exfoliating with a new tape. I repeated this process until the $NbSe_3$ film on the tape became semi-transparent. Next, I applied the final tape, containing thin $NbSe_3$ ribbons onto the target substrate. After applying pressure with my thumb, and leaving it for 15 minutes, I slowly removed the tape, and examined the exfoliated crystals under the optical and electron microscope. Figure 1.15 shows a thin $NbSe_3$ crystal, exfoliated on a $Si\text{-}SiO_2$ substrate with pre-patterned gold alignement marks.

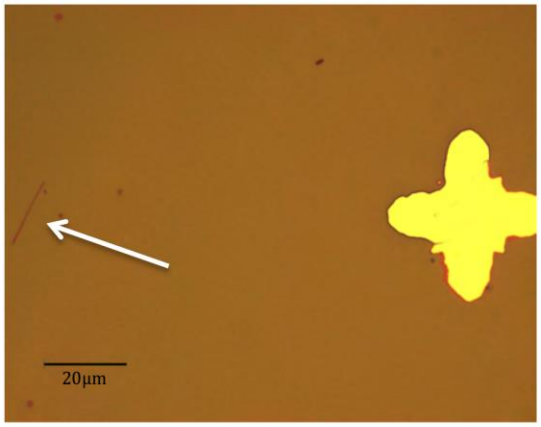

Figure 1.15: The SEM micrograph of $NbSe_3$ crystals on a $Si\text{-}SiO_2$ substate with pre-patterened gold alignment marks

1.2.1.3 E-beam lithography and nitrogen plasma treatment

For this experiment, I used silicon wafers with a 285Å silicon dioxide layer on top, as the substrate. Before transferring the crystals to the substrate, I patterned a network of gold alignment marks, using conventional photolithography and lift-off techniques. I designed a photolithography mask, containing a network of 2×2 μm crosses separated by 200 μm. The UV exposure step was completed in Marvell Nanolab Facilities, using the ksaligner photolithography machine. The metal evaporation and lift-off steps were carried out in the Zettl lab.

After transferring the exfoliated crystals to the substrate, I located the thinnest crystals by using a combination of optical microscopy, Scanning Electron Microscopy (SEM), and Atomic Force Microscopy (AFM) techniques. Next, using SEM, I mapped the selected crystals to find their relative position with the alignment marks network. After that, I fabricated the electrical contacts, using e-beam lithography and lift-off procedures.

First, I experimented with the standard e-beam resist, a bilayer of MMA-PMMA. After exposing the resist with an electron beam, and subsequently developing it in a MIBK-IPA solution, I deposited a thin film of indium-chromium-gold tri-layer using e-beam evaporation technique. Indium has been proven to form a great electrical contact with a large variety of crystals including the blue bronze [57]. The final contact patterns were formed with a lift-off step in acetone.

I selected the indium-chromium-gold tri-layer, because it created the most uniform metal film on $NbSe_3$ crystals. If deposited on $NbSe_3$ crystals alone, indium does not form a uniform film, but forms isolated balls. I also tried depositing indium at liquid nitrogen temperature, using a thermal evaporation machine equipped with a sample cooling system. This also did not improve the quality of the indium film.

However, even with the tri-layer metal film, the contact resistances of the final devices were too high. In order to solve the high contact resistance problem, right before placing the samples in the e-beam evaporation chamber, I performed a plasma treatment step. However, since PMMA has a very weak physical structure when placed in a reactive plasma environment, it gets etched and re-deposited, and hence, does not hold its pattern. Therefore, I changed the e-beam resist to ZEP, which has better resistance in etching environments than PMMA. Section 2.2.4 provides an overview of different e-beam resists and advantages of each. Table 1.2 compares the properties of PMMA and ZEP e-beam resists [58].

The e-beam lithography step with the ZEP resist is as follows: A spin coating technique was used to coat a bi-layer of MMA EL6 and ZEP-520A, at 4000 rpm and 3000 rpm respectively, on substrates with previously mapped $NbSe_3$ crystals. Next, samples were baked at 180°C in air on a hot plate. For large patterns (i.e. contact pads), the e-beam lithography step was carried out in a NPGS system in the Zettl lab. For small features, I used the Crestec machine in the Nanolab, as described in section 2.2.4. The nitrogen plasma treatment step was performed in a 50 sccm flow of nitrogen, at 50 W power and for 30 seconds. In this condition, the plasma treatment step had a minor effect on the ZEP e-beam resist film. For this step, I used a Reactive Ion Etching (RIE) machine in the Zettl lab.

Sensitivity to e-beam	ZEP is ~5x more sensitive
Resolution	Almost equivalent
Edge roughness	ZEP has a greater line edge roughness (LER)
Durability	Etch selectivity of Si/ZEP is ~3x higher

Table 1.2: Comparison between ZEP and PMMA e-beam resists [58].

Page 22 of Jamei [193]

After the RIE step, I immediately transferred the samples to an e-beam evaporation chamber where I deposited metal contact layers. The final thicknesses of indium, chromium, and gold films were 15nm, 5nm and 30nm, respectively. The deposition rate was maintained at 1 Å/s, for all metal films. For metal deposition, I used the e-beam evaporation machine in Zettl lab. Figure 1.16 shows a schematic of the entire fabrication process.

A similar schematic to Figure 1.16 in Mehdi's doctoral dissertation [193] is shown in Fig. 9-1. Although Mehdi suggests to use ZEP over PMMA as the resist for its chemical resistance to nitrogen plasma, PMMA was also found to be an acceptable resist for the same device fabrication process (see section 6.2).

The procedure described above begins with identifying $NbSe_3$ exfoliated nanoribbons, as shown in Fig. 6-1. The nanoribbons appear as orange ribbons with a well-defined rectangular shape on Si/SiO_2 wafer (identified by circles). The wispy shapes are tape residue, which results from the tape adhesive remaining on the SiO_2 surface after exfoliation. Fig. 6-2 shows $NbSe_3$ nanoribbons, which are contacted with metal. The size and room temperature resistance for the devices are listed in Table 6-1. The thickness is measured by atomic force microscopy and the lateral dimensions are measured with a scanning electron microscope. The resistance is measured by two-probe and the contact resistances are calculated to be <20% by comparing the two-probe resistance and with the bulk $NbSe_3$ resistivity.

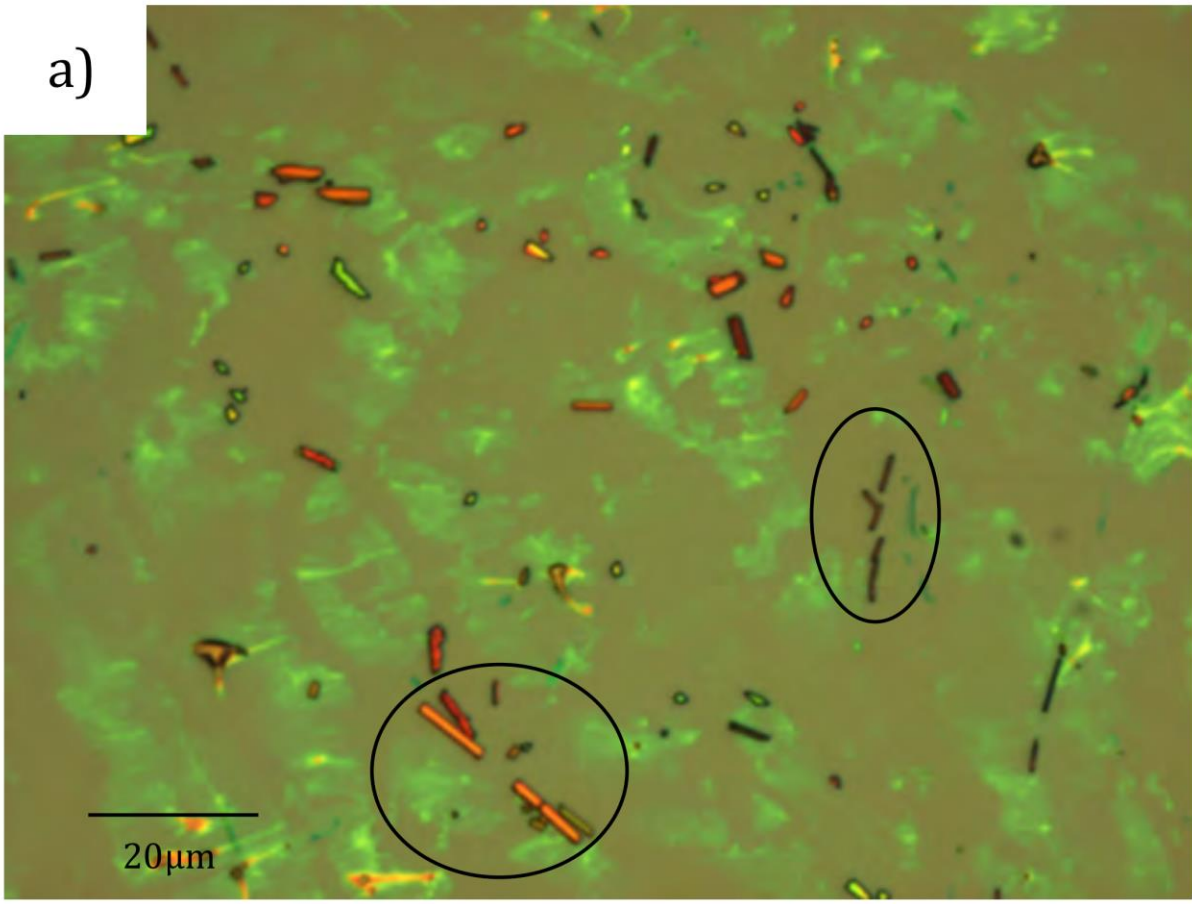

Fig. 6-1 Optical image of $NbSe_3$ nanoribbons obtained by mechanical exfoliation.
Fig. 1.25a, Jamei [193]. The substrate is a silicon wafer with a thin film of silicon dioxide on top. The orange rectangular ribbons are $NbSe_3$ nanoribbons and the green wispy shapes are tape residue. The $NbSe_3$ nanoribbons, selected for device fabrication, are circled.

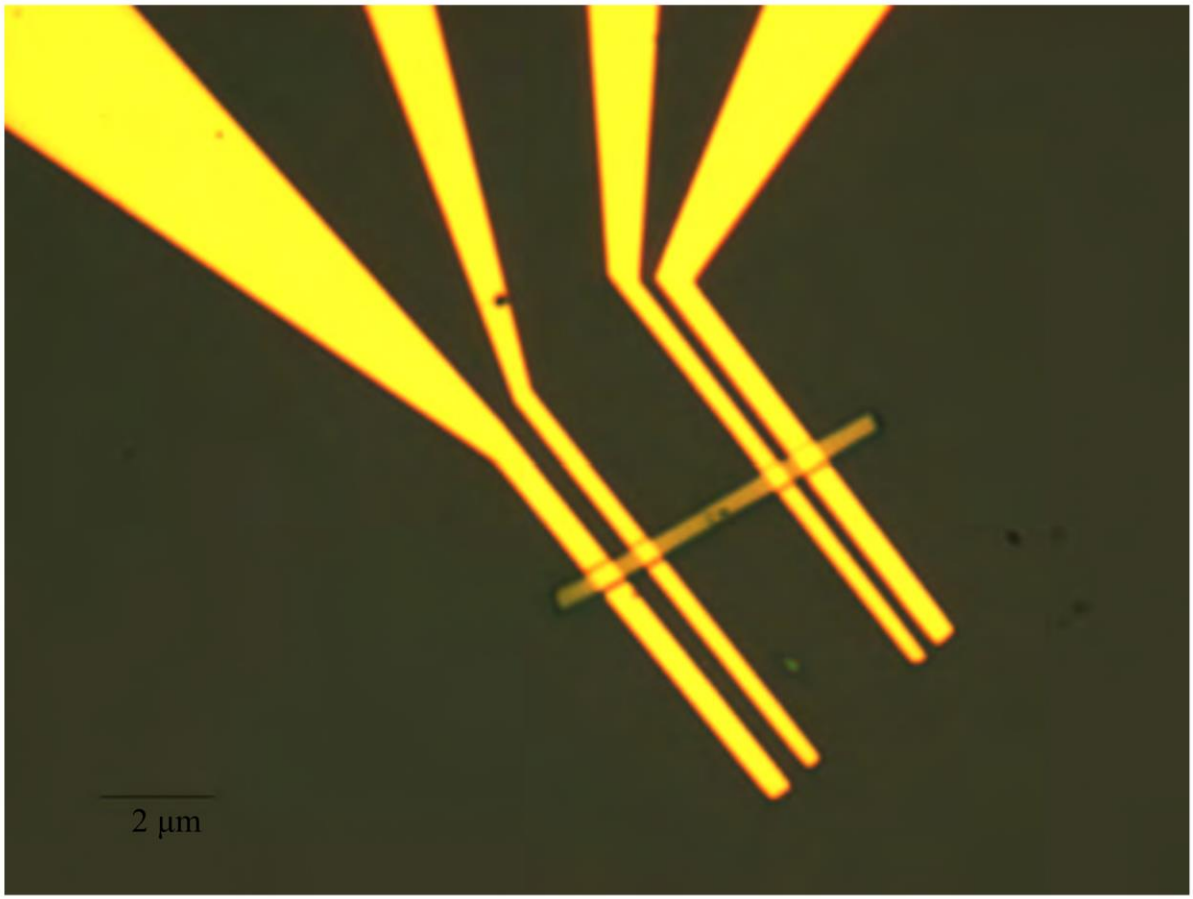

Fig. 6-2 Optical image of lithographically contacted $NbSe_3$ nanoribbons.
Fig. 1.29, Jamei [193]. Four strips of In/Cr/Au trilayer contacts (yellow strips) are placed on top of an $NbSe_3$ nanoribbon (orange ribbon).

Sample #	Thickness (nm)	Width (nm)	Length (μm)	Resistance at RT (kΩ)	Contact Resistance (%)
1	55	550	7.4	0.76	19.5
2	34	450	4.6	0.92	18.3
3	31	280	3.2	1.08	14.6
4	18	150	1.1	1.20	15.1

Table 6-1 Size and resistance of fabricated $NbSe_3$ nanoribbon devices.
Table 1, Onishi *et al.* [96]. The contact resistance is calculated by comparison to the bulk $NbSe_3$ resistivity $2.5 \times 10^{-4}\Omega$ cm [10].

6.1.1.2 Measurement techniques

R(T) was measured with the current switching technique (see section 3.1.3) in a gas flow cryostat (see section 3.2.1). As the contact resistance was low, the measurements are two-probe. The threshold field was measured in two ways to minimize heating effects [193]: lock-in amplifier (P=0.01nW and f=500Hz) and the pulse method using low duty cycle pulses (1μs pulse width with 1Hz repetition rate). The narrowband noise was measured with a spectrum analyzer and a custom amplifier. The threshold field measurement and narrowband noise measurement methods are detailed in pages 25-28 of Mehdi Jamei's doctoral dissertation [193] and reproduced below.

Page 25 of ref. [193]

Threshold field detection

Figure 1.20 (a) shows the measurement setup that was used to detect the threshold field. This measurement technique is based on the fact that, above the threshold field, a crystal with a charge density wave becomes a non-linear conductor where the charge densities carry the excess current. Figure 1.21 shows a typical $NbSe_3$ I-V curve at 36K. The deviation from the linear conductivity starts at the threshold field.

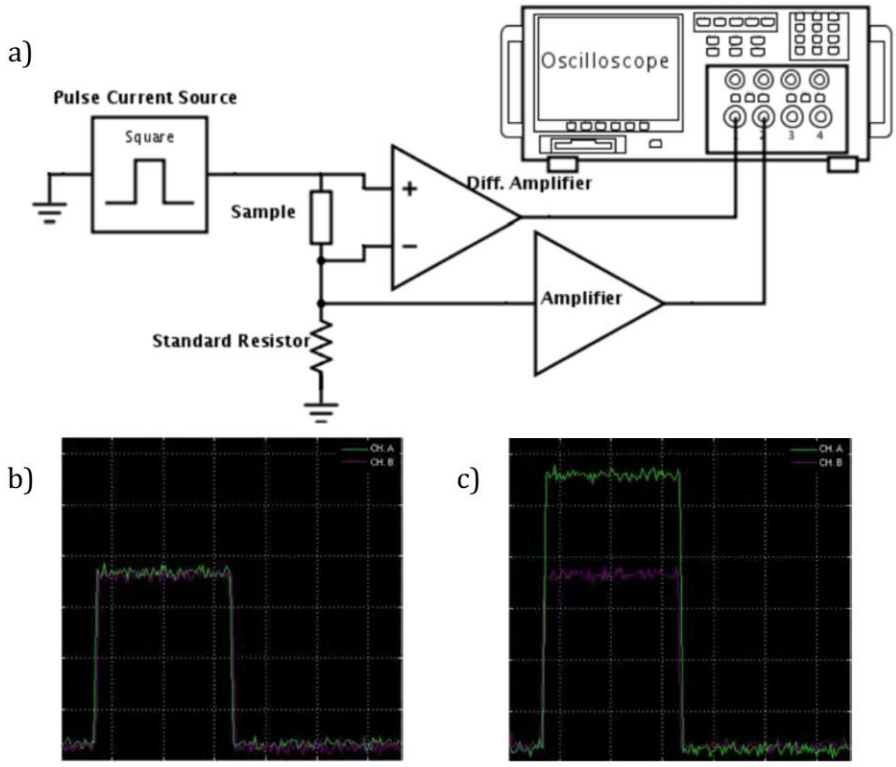

Figure 1.20: (a) The setup used to measure the threshold field. (b) The output signals from the two amplifiers follow each other closely, while the sample is in the linear regime. (c) As soon as the sample becomes non-linear (above the threshold field), the two pulses separate on the oscilloscope display.

In the measurement setup shown in Figure 1.20 (a), amplifier gains can be fine-tuned such that, in a low-field regime, the output signal from the sample and the standard resistor (which is chosen to be close to the low-field resistance of the sample) on the oscilloscope precisely follow each other. While the sample is in the linear regime, increasing the current source power will increase, both V_{sample} and $V_{resistor}$, at the same rate, and therefore their respective pulse shapes on the oscilloscope will follow each other. However, above the threshold field, the increasing current source power will cause a faster increase in $V_{resistor}$ versus V_{sample}. This is because, above the threshold field, sliding CDW carriers will decrease the total resistance of the crystal and hence the lower voltage. Therefore, the threshold field can be measured by measuring the bias current at

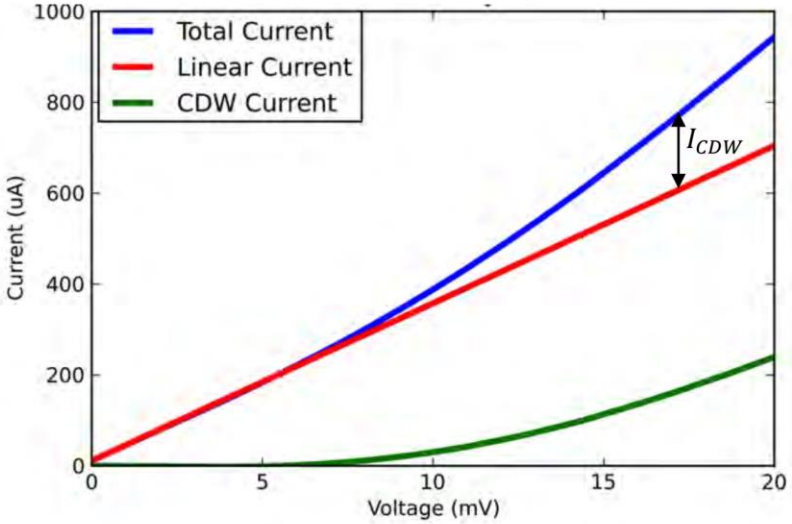

Figure 1.21: Current versus voltage characteristic of a bulk $NbSe_3$ crystal at 36°K. The crystal becomes non-linear above the threshold field, where the CDW carriers slide and carry the excess current.

which the two signals on the oscilloscope display start to separate. In order to minimize the heating effect, a microsecond current pulse, with a low duty-cycle, was employed as the bias source.

Noise measurement circuit

Charge density wave states have been shown to have interesting Narrow Band Noise (NBN) characteristics. A spectrum analyzer was used to detect the NBN signal from the sample. However, since the input impedance of most spectrum analyzers are 50 Ω, the direct measurement of the low-power NBN signal was not possible, and a low-noise amplifier was required.

In order to fix the above problem, I built a low noise, large bandwidth amplifier circuit, similar to the circuit used in a previous study on bulk crystals with charge density waves [59]. The overall structure of the circuit was kept intact. However, the input impedance and the gain of the circuit were increased to support the higher impedance and the weaker signal of the thin film crystals.

A schematic of the low-noise measurement circuit is shown in Figure 1.22. The overall size and the relative position of different components were important to achieve the desired bandwidth. At the heart of the circuit a UA733 low-noise video differential amplifier was used. Figure 1.23 (a) shows the gain vs. frequency for a UA733 IC. After amplification, the next module is a follower circuit, which utilizes a NTE108 NPN RF transistor and provides sufficient power for the spectrum analyzer. The output impedance of the circuit was designed to be close to 50Ω to match the input impedance of the spectrum analyzer. The circuit was tested to amplify signals up to 50MHz.

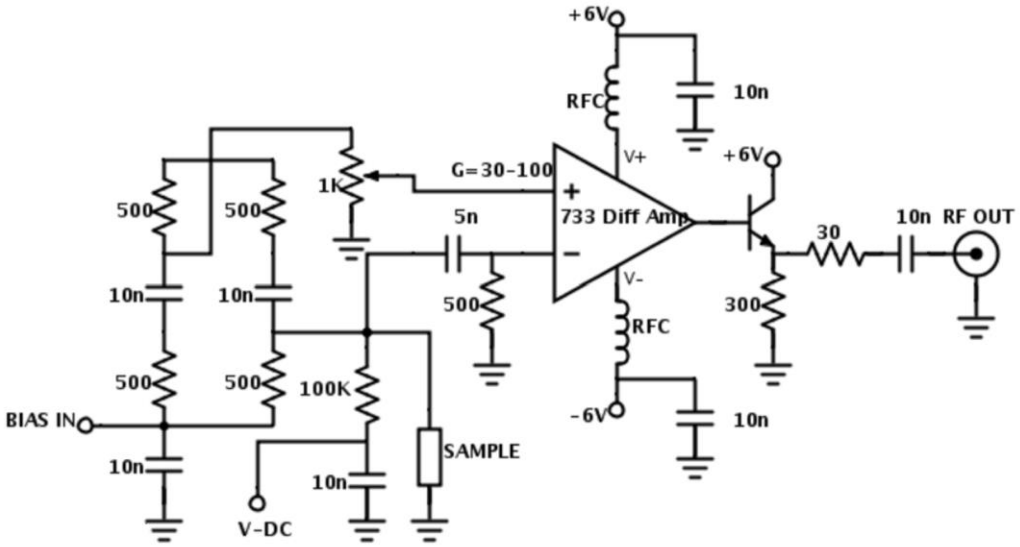

Figure 1.22: Noise measurement circuit. First, UA733 amplifies the signal. Next, a follower circuit provides the required power for the spectrum analyzer. The circuit was built similar to [59] with some modifications.

In order to measure the NBN signal, the sample was biased with a dc electric current

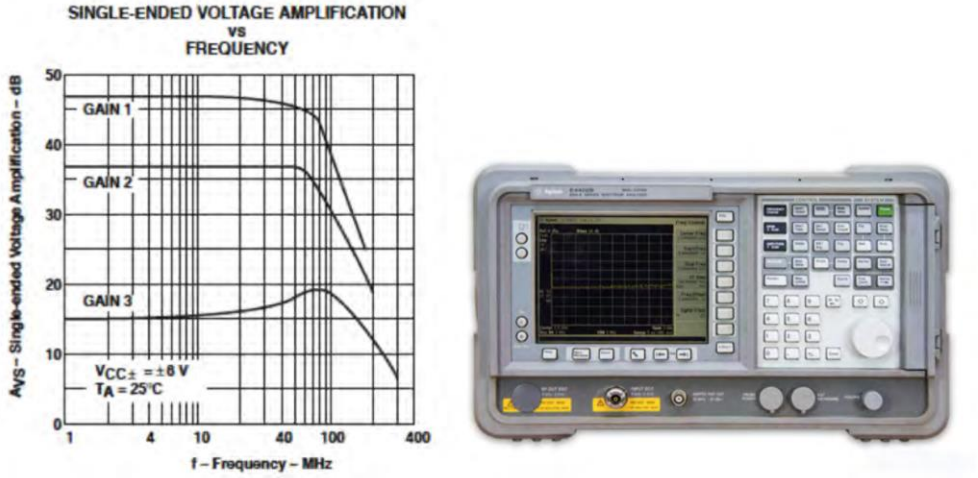

Figure 1.23: (a) UA733 gain versus frequency characteristics [61] and (b) an Agilent E4402B spectrum analyzer [62]

Page 28 of ref. [193]

using a Keithley 2602A system. A SMA coaxial cable transferred the noise signal to the noise measurement circuit. An Agilent E4402B spectrum analyzer (Figure 1.23 (b)) detected the amplified NBN signal. A Labview program was written to read and store the bias data from the Keithley, signal data from the spectrum analyzer, and temperature from the sample diode. The NBN detection setup is shown in Figure 1.24.

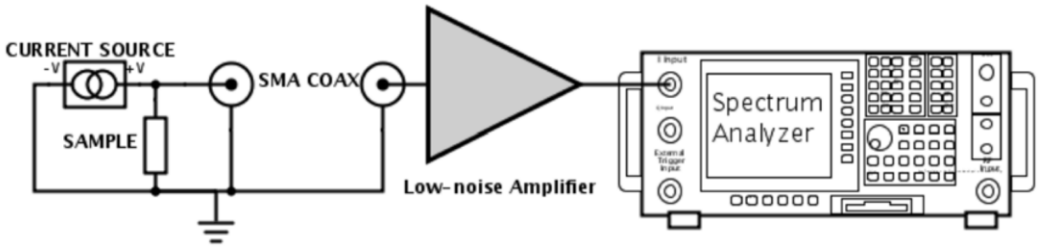

Figure 1.24: Narrow-band noise measurement setup. The noise signal from the dc-biased sample was transferred to the noise measurement circuit. After amplification, the signal was detected in a spectrum analyzer.

6.1.2 Thickness dependence

From previous studies [92,124], it is known that the CDW resistive anomaly is suppressed and the E_T increases as the $NbSe_3$ sample size is made smaller, below the micron length scale. The mechanically exfoliated $NbSe_3$ nanoribbons show the same finite size effects, which become more pronounced for thinner nanoribbons. It is unclear whether these effects are caused by enhancement of surface pinning or the collapse of the CDW order parameter. Since narrowband noise is a well-established technique to directly probe the CDW order parameter for bulk $NbSe_3$, it is applied to $NbSe_3$ nanoribbons to answer this question.

6.1.2.1 CDW resistive anomaly

The R(T) of bulk $NbSe_3$ has an overall metallic behavior but exhibits two anomalies below T_{P1}=144K and T_{P2}=59K, which correspond to the upper and lower CDW, respectively (see section 2.2.1). Previous studies [92,124] on finite size effects in $NbSe_3$ demonstrate that the resistive anomalies becomes more suppressed as the sample size is made smaller. Fig. 6-3 shows R(T) of $NbSe_3$ nanowires obtained by ultrasonic cleaving [124]. Each curve corresponds to nanowires of different width and the width decreases, going from the bottom curve to the top. As the sample width decreases, the CDW anomalies are suppressed progressively. The sample size is classified by the number of $NbSe_3$ chains running along the sample, calculated from the room temperature resistance. Below 2000 chains, the threshold indicated by the dotted line, R(T) switches to a different behavior, in which resistance increases with cooling in a power law relationship. The power law behavior is attributed to the one-dimensional form of the system. The inset shows the slight decrease in T_{P1} and T_{P2} with sample size.

The R(T) of $NbSe_3$ nanoribbons obtained by mechanical exfoliation show both similarities and differences to ultrasonically cleaved nanowires. Fig. 6-4a shows the change in resistance of

$NbSe_3$ nanoribbon samples for T=220-10K. The nanoribbons have thickness t=55, 34, 31 and 18nm and the data from bulk $NbSe_3$ are shown for comparison. For each sample, the resistance is normalized by its resistance at 220K. Consistent with common $NbSe_3$ R(T), the bulk sample shows a resistive anomaly at T_{P1}=144K and T_{P2}=59K. In the nanoribbons, the anomalies are suppressed, showing a smaller increase in resistance before returning to metallic behavior. For the upper CDW, the anomaly is progressively suppressed as the sample becomes thinner. As shown in Fig. 6-4b, t=55nm has the most pronounced anomaly among the nanoribbons and t=18nm has the least pronounced anomaly. t=34, 31nm with the intermediate anomaly height have similar values. In contrast, the anomaly for lower CDW is severely suppressed in the nanoribbons. As shown in Fig. 6-4c, even the thickest nanoribbon (t=55nm) is already as suppressed as the t=18nm sample. No clear progression in anomaly height with variation in thickness can be seen, as the suppression effect seems to set in at a greater thickness but a slight resistive anomaly is still visible for all the samples.

In the nanoribbons, the power law behavior of the nanowires are not observed. Assuming a square cross-section, the dimensions for the 2000 chains nanowire (the threshold chain number for power law behavior in [124]) is width=thickness=$\sqrt{2000}$=45 chains. To compare, the measured dimensions of our nanoribbon samples are translated to chain numbers, using the $NbSe_3$ monoclinic unit cell dimensions a=1.0nm, c=1.56nm and θ =109.5^o, which contains six chains. The same unit cell parameters were used in the nanowire study [124]. The height of one chain is estimated as $\frac{1}{2} \times 1.0\text{nm} \times \sin(70.5^o) = 0.47\text{nm}$. From Table 6-2, we see that in the t=18nm nanoribbon, the system is confined to 38 chains in the thickness direction. However, as the width is much greater than the thickness, the total number of chains 10,800>>2000. Since the power law is attributed to one-dimensional confinement effects, the absence of power law behavior in the nanoribbons is possibly due to the lack of confinement in the width direction. Hence, the nanoribbons from mechanical exfoliation impose a more two-dimensional confinement effect compared to the nanowires from ultrasonic cleaving.

For the nanowires, the upper and lower CDW anomalies seem to be equally sensitive to the sample size reduction. The increased sensitivity to sample size reduction of the lower CDW anomaly is possibly characteristic to the two-dimensional confinement effects of the nanoribbons.

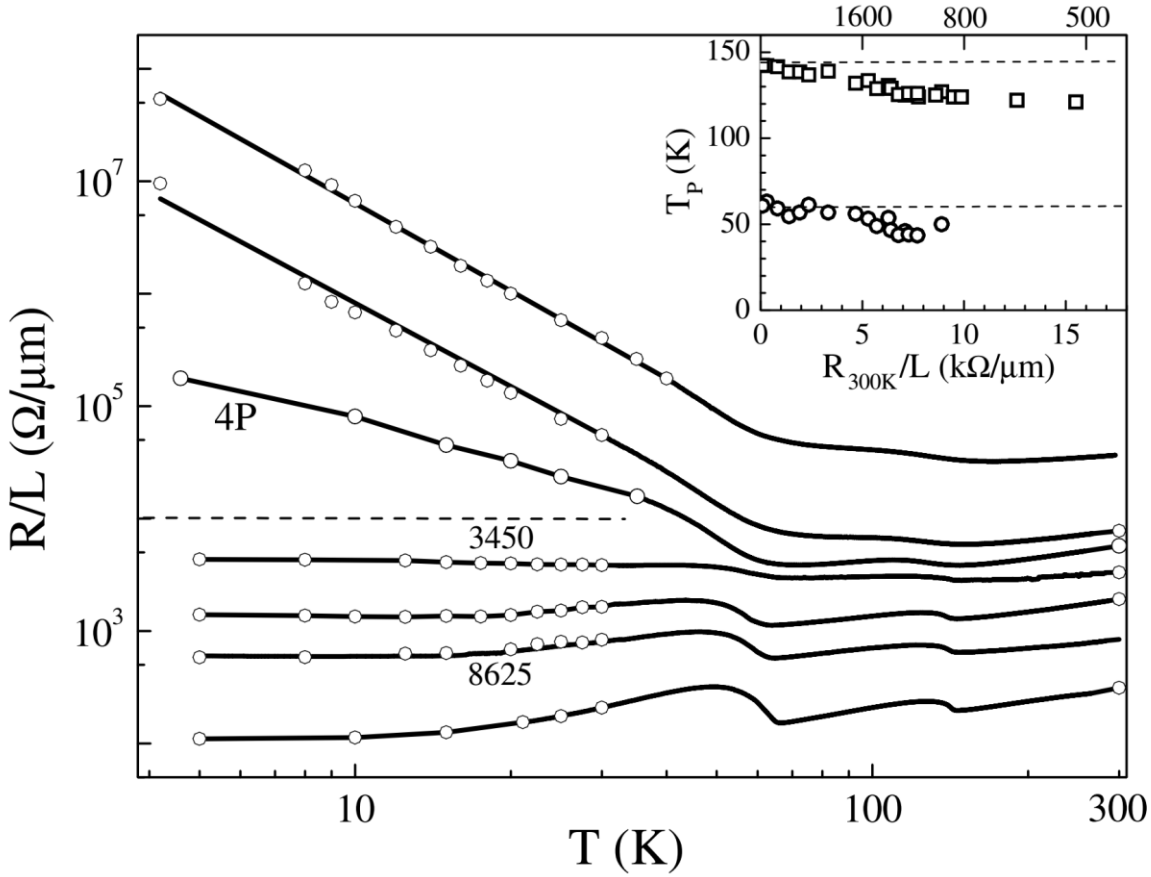

Fig. 6-3 R(T) of ultrasonically cleaved $NbSe_3$ nanowires.
Fig. 2, Slot *et al.* [124]. Temperature dependence of resistance per sample length (R/L) for $NbSe_3$. Each curve corresponds to a sample with different chain numbers deduced from room temperature resistance. From bottom to top the chain numbers are: 25640, 9490, 4170, 2430, 1400, 1030 and 220. Two of the curves are labeled by chain numbers found from Shapiro-step measurements. Each open circle corresponds to the point where an I(V) curve was measured. Inset shows the sample size dependence of the CDW transition temperature (T_P) for the upper CDW (squares) and lower CDW (circles).

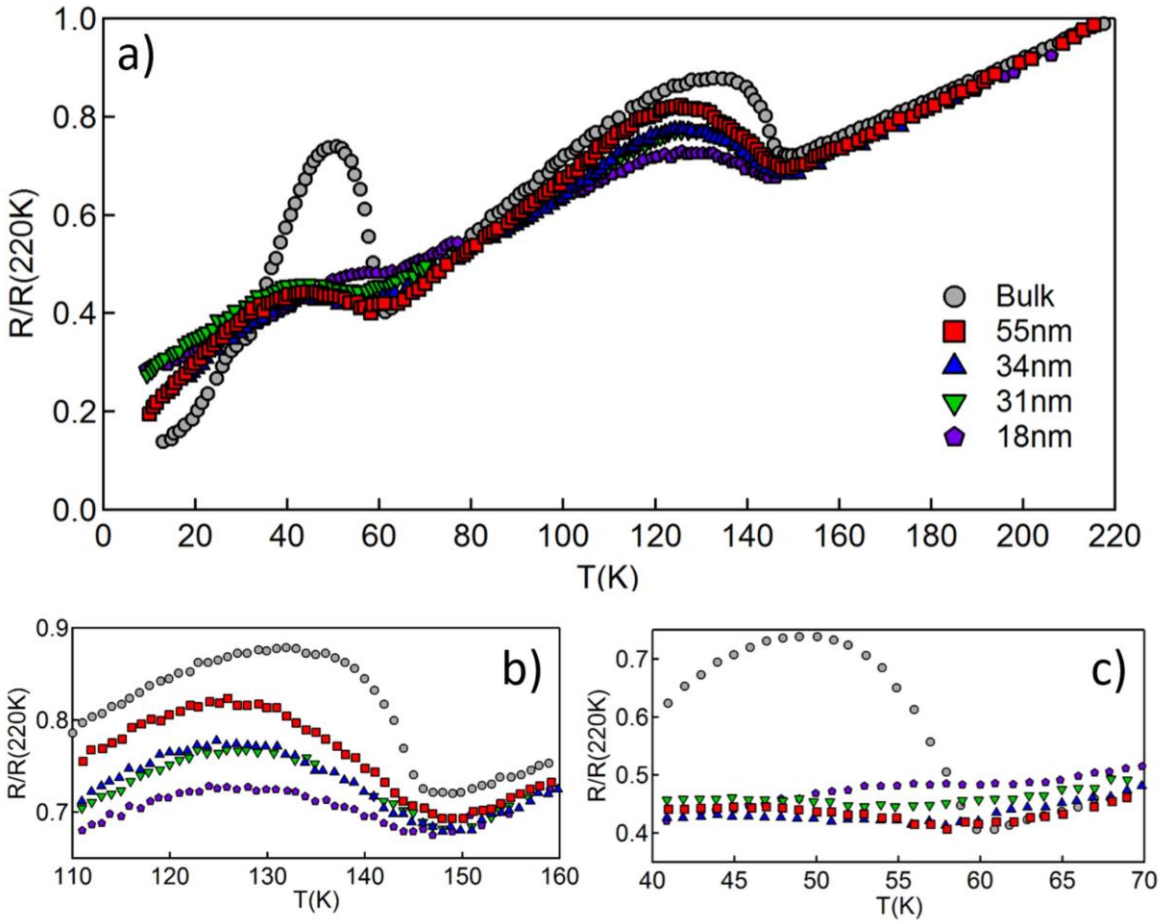

Fig. 6-4 R(T) of mechanically exfoliated $NbSe_3$ nanoribbons.
Figure 1, Onishi *et al.* [96]. Each marker corresponds to data from samples of various thickness with bulk (gray circle) and nanoribbons of thickness 55nm, 34nm, 31nm and 18nm. The resistance for each sample is normalized by its resistance at 220K. a) Overall (220-10K) temperature dependence with resistive anomalies at the upper and lower CDW transitions. The resistive anomalies are magnified for the b) upper and c) lower transition.

Thickness (nm)	Thickness (# of chains)	Width (nm)	Cross-sectional area (nm^2)	Total # of chains
55	117	550	30,250	121,000
34	72	450	15,300	61,200
31	66	280	8,680	34,720
18	38	150	2,700	10,800

Table 6-2 Number of chains in $NbSe_3$ nanoribbons.
For each sample, thickness is in nm, as measured, and in # of chains, assuming each chain is 0.47nm high. The cross-sectional area is found by A = thickness x width. The total # of chains is calculated assuming the unit cell, consisting of 6 chains, has a cross-sectional area of $1.5nm^2$ [124].

The CDW transition temperature is conventionally determined from R(T) as the temperature at which $\frac{1}{R}\frac{dR}{dT}$ is minimum. To find the derivative numerically, a third order polynomial is fit to the resistive anomalies for each sample (bulk, t=55, 34, 31 and 18nm). Fig. 6-5a shows the fit to the upper CDW and Fig. 6-6a for the lower CDW. The data range for the fit is restricted to the temperature range, at which the resistance increases with cooling. The metallic behavior, occurring at temperatures above and below the CDW transition are excluded. The temperature range for each fit is shown in Table 6-3. As the transition width differs between sample thicknesses, a different temperature range is chosen for each sample to produce the best fit. In particular, the transitions are much broader in the nanoribbon samples than the bulk $NbSe_3$. A fit over $\Delta T=8K$ is sufficient to encompass the whole transition in bulk $NbSe_3$ but a temperature range as large as $\Delta T=22K$ is required for the upper CDW of the t=31nm sample. Variation of the fitting range by 1K does not result in any significant change in the calculated T_P.

The derivative is found by taking the derivative of the polynomial fit and evaluating it at each temperature. Fig. 6-5b shows the calculated $\frac{1}{R}\frac{dR}{dT}$ for the upper CDW and Fig. 6-6b for the lower CDW. Both figures show smooth curves, which dip to a minimum. Higher order polynomials might enhance the fit to the data but are not suitable since they follow the noise of the data too closely and results in sharp wiggles. The wiggles of the fit contribute significantly to the derivative term and produces a derivative with many sharp peaks. A cubic spline fit was attempted but was not successful for this reason. Although the dips are not as sharp and well defined as that of the bulk sample, the nanoribbons also show notable dips. In Fig. 6-4c, the resistive anomaly is greatly suppressed and obscured but the minimum in Fig. 6-6b indicates that the CDW transition still occurs.

T_{P1} and T_{P2}, determined from the minima in Fig. 6-5b and Fig. 6-6b are listed in Table 6-3. Their thickness dependences are shown in Fig. 6-7. T_{P1} appears to decrease with thickness, consistent with previous study [124] but T_{P2} does not show any clear trend. The error from the polynomial fit process is translated to error in finding T_P and displayed as error bars for each data point in Fig. 6-7. The error bars indicate that the variation in T_P is still within error and further study is required to determine the relationship with nanoribbon thickness.

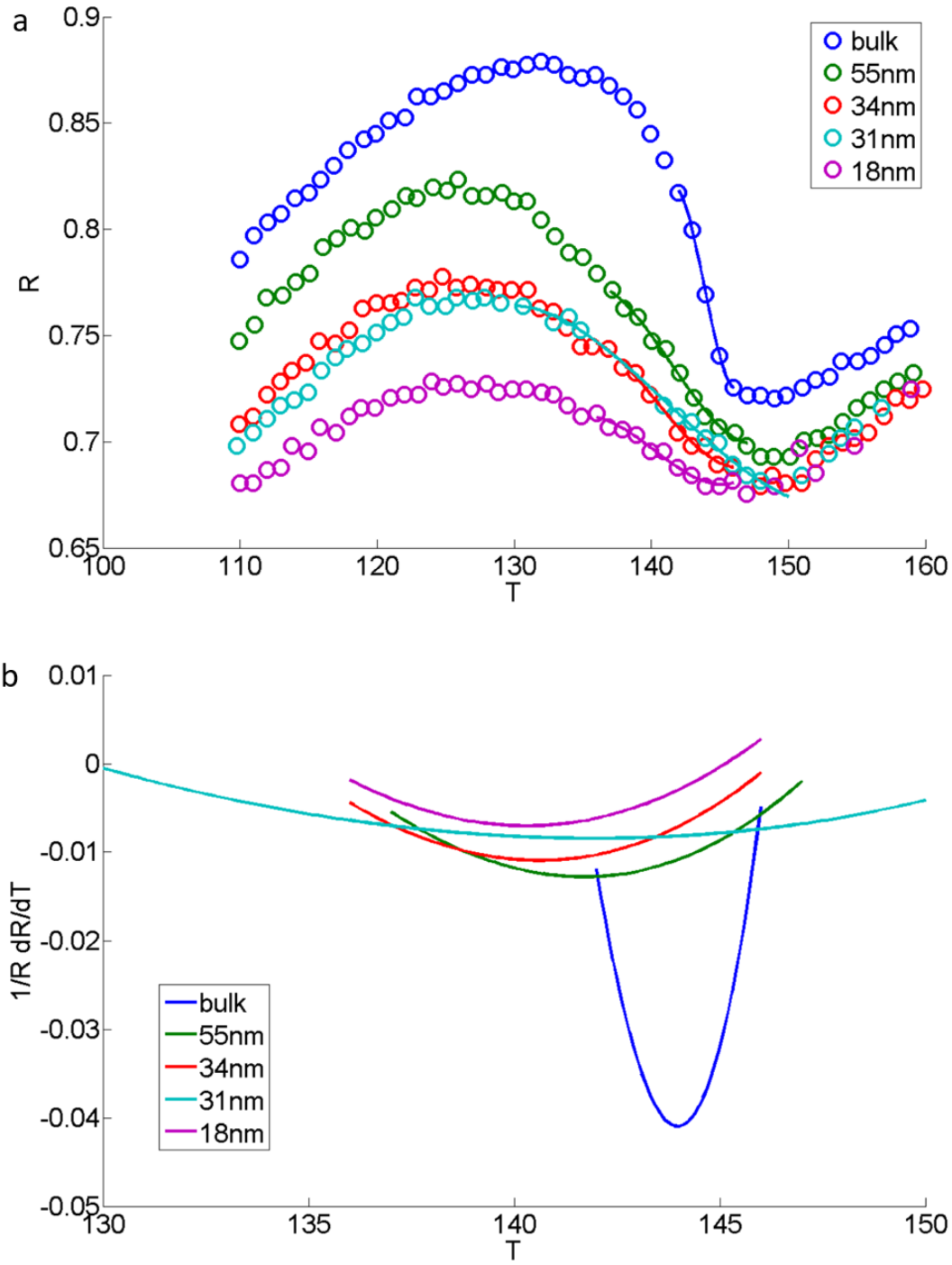

Fig. 6-5 Numerical derivative of upper CDW resistive anomaly.
a) Upper CDW R(T)/R(220) from Fig. 6-4b with 3rd degree polynomial fits. The temperature range for fitting are shown in Table 6-3. b) $\frac{1}{R}\frac{dR}{dT}$ of the fitted polynomials. The temperature corresponding to the minimum of each curve is interpreted as T_{P1}.

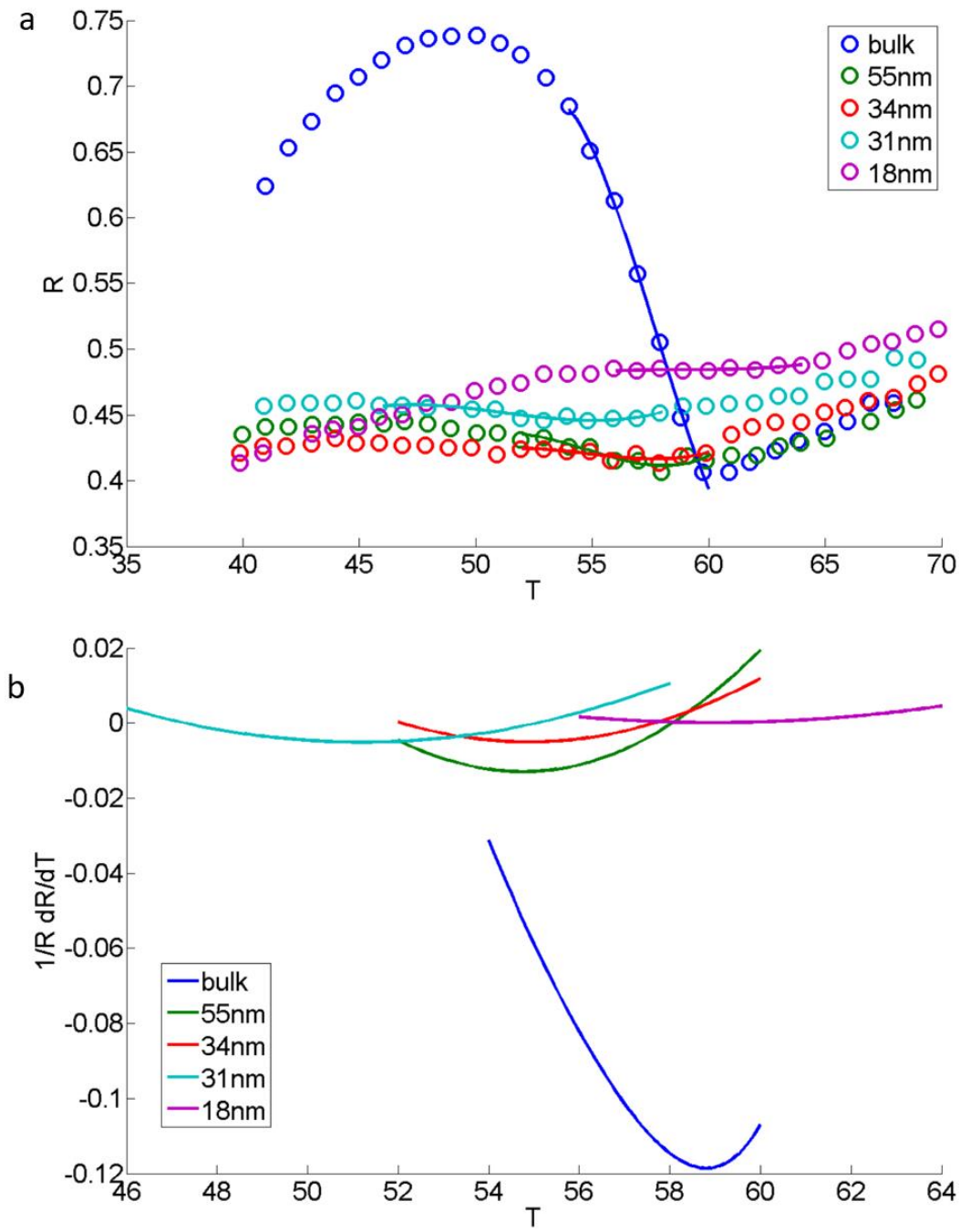

Fig. 6-6 Numerical derivative of lower CDW resistive anomaly.
a) Lower CDW R(T)/R(220) from Fig. 6-4c with 3rd degree polynomial fits. The temperature range for fitting are shown in Table 6-3. b) $\frac{1}{R}\frac{dR}{dT}$ of the fitted polynomials. The temperature corresponding to the minimum of each curve is defined as T_{P2}.

	Upper CDW		Lower CDW	
Thickness (nm)	Fit range (K)	T_{P1}(K)	Fit range (K)	T_{P2}(K)
Bulk	140-148	144	54-61	58
55	137-150	142	50-61	55
34	135-150	141	48-61	54
31	129-151	141	46-59	51
18	135-150	140	54-66	59

Table 6-3 R(T) numerical derivative parameters.
For each sample, the range of temperature used in the polynomial fit in Fig. 6-5 and Fig. 6-6 are shown. T_{P1} and T_{P2} correspond to the CDW transition temperature, defined as the temperature at which $\frac{1}{R}\frac{dR}{dT}$ is minimum.

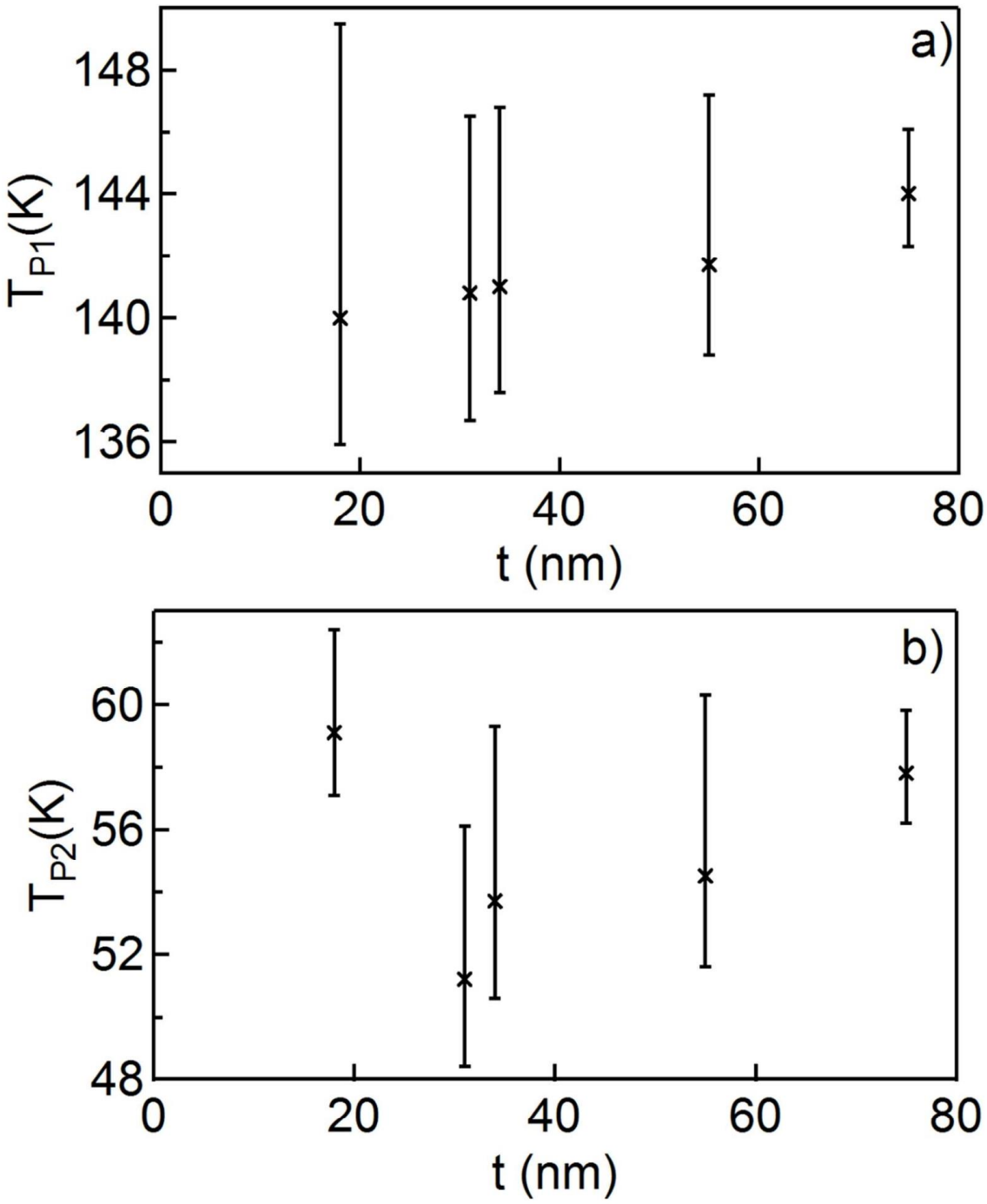

Fig. 6-7 Thickness dependence of T_P.
The x's show a) T_{P1} of the upper CDW and b) T_{P2} of the lower CDW from the minimum of $\frac{1}{R}\frac{dR}{dT}$ in Fig. 6-5b and Fig. 6-6b. The error bars are placed according to the errors from the polynomial fitting process.

6.1.2.2 Threshold field

Previous study [92] has shown that E_T increases as the thickness decreases (see Fig. 6-8). With increase in 1/t (i.e. decrease in t), E_T increases and asymptotes to E_T~1/t for thin samples, as indicated by the dashed lines. The measurements at T=120K (filled symbols) and 50K (open symbols) correspond to E_T of the upper and lower CDW, respectively. While Fig. 6-8 primarily features sample thicknesses on the microscale, subsequent studies [124,192] have confirmed that E_T increases with a decrease in sample size at the nanoscale as well.

Fig. 6-9a shows the differential resistance (dV/dI) of the t=55nm nanoribbon as the electric field bias is swept. The sample is measured at both T=110K and 49K to detect sliding behavior for both the upper and lower CDW behavior, respectively. dV/dI behavior is consistent with sliding CDW (see Fig. 1-11). Similar behavior is seen for the upper CDW in the t=18nm nanoribbon in Fig. 6-9b. However, the lower CDW in t=18nm does not show sliding behavior up to 10^6V/cm. For the upper CDW at 110K, E_T is 0.2V/cm for bulk, 196V/cm for t=55nm and 20,000V/cm for t=18nm. For the lower CDW at 49K, E_T is 0.01V/cm for bulk and 28V/cm for t=55nm. The (lower CDW) E_T for t=18nm, if it exists at all, is $>10^6$V/cm.

Fig. 6-9c shows $E_T(T)$ of bulk and nanoribbons of t=55-18nm, measured by pulse method (see section 6.1.1.2). Each sample shows the divergence near T_P and increase in E_T for $T \rightarrow 0$, consistent with previous study (see section 1.2.2.2). For both the upper and lower CDW, the nanoribbons have E_T higher than the bulk by a factor $>10^2$. For the upper CDW, the increase of E_T with decrease in t can be seen for t=55-18nm. For the lower CDW, E_T for t=34nm is smaller than t=55nm. E_T for t=31 and 18nm could not be measured reliably. It appears that E_T diverges to $E_T>10^6$V/cm for the lower CDW. For bulk, E_T for the upper CDW is greater than that of the lower CDW by an order of magnitude. However, at t=55nm the difference is smaller, although E_T is still greater for the upper CDW. At t=34nm, E_T for the upper and lower CDW states are within the same order of magnitude. As with the resistive anomaly, E_T for lower CDW is more sensitive to the reduction in thickness.

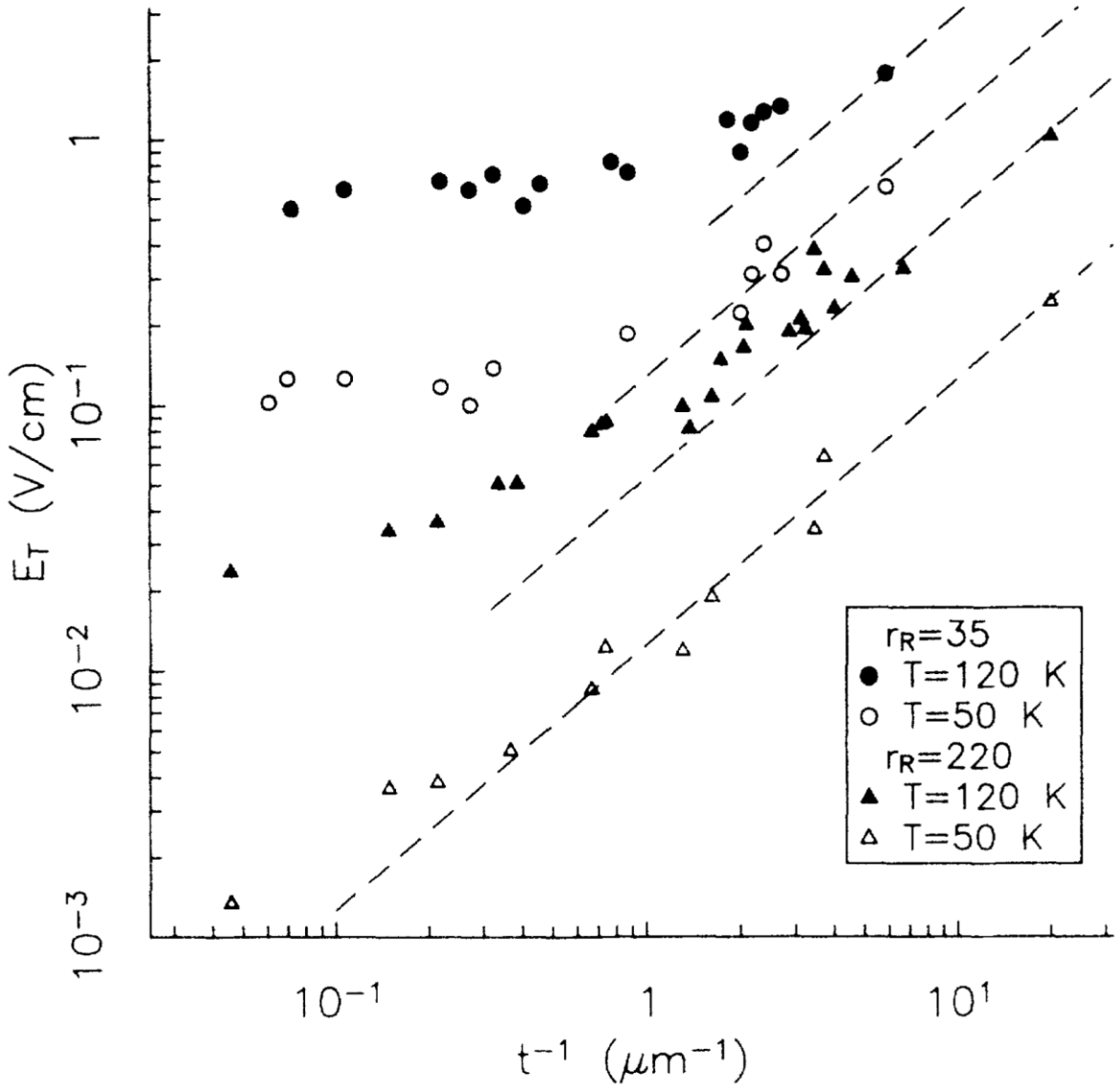

Fig. 6-8 E_T vs thickness of $NbSe_3$.
Fig. 3, McCarten *et al.* [92]. Horizontal axis is the reciprocal of the thickness 1/t. r_R is short for residual resistivity ratio. r_R=35 is Ta-doped and r_R=220 is undoped $NbSe_3$.

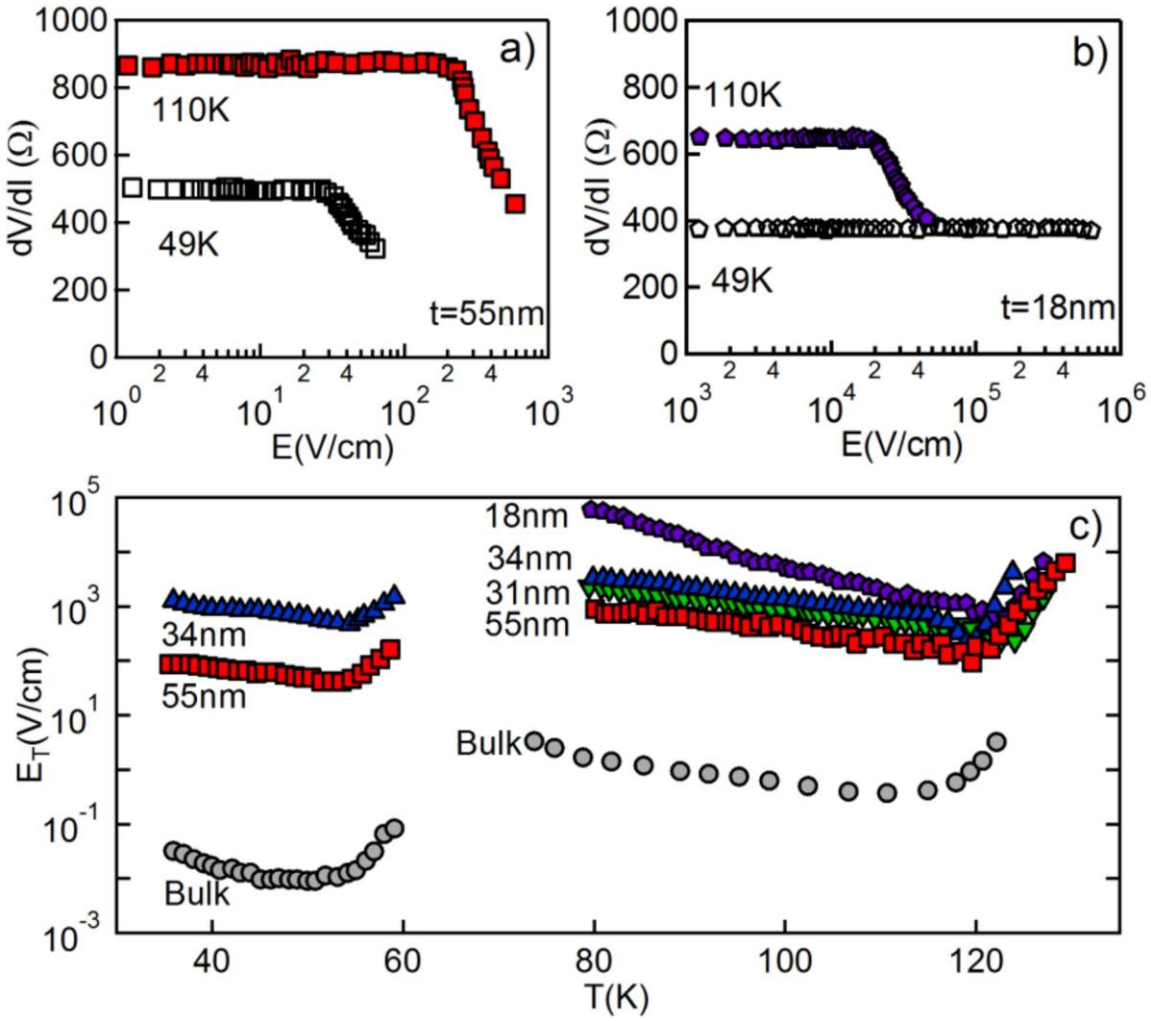

Fig. 6-9 E_T of $NbSe_3$ nanoribbons.
Differential resistance dV/dI of a) t=55nm and b) t=18nm nanoribbons at T=110K and 49K. c) E_T(T) of bulk $NbSe_3$ and nanoribbons. Each point is measured by pulse method.

6.1.2.3 Narrowband noise

The suppression of the CDW resistive anomaly suggests the weakening of the CDW state with reduction in size. However, the sample resistance measures the convolution of the normal state and CDW condensate response. A method to isolate the CDW condensate response would give further insight into the CDW state. For sliding CDW (e.g. $NbSe_3$), narrowband noise measurement is a well-established means to directly probing the CDW order parameter for bulk (see section 1.2.2.3). Here, the same measurement is to $NbSe_3$ nanoribbons.

Fig. 6-10 shows the response of the narrowband noise fundamental frequency (f_{NBN}) to the change in CDW current density (J_{CDW}) for the lower CDW at T=49K. CDW current is obtained by $I_{CDW} = I(E > E_T) - I_{ohmic}$ where I_{ohmic} is the extrapolation from the linear I(V) response at $E<E_T$ (see section 6.1.1.2). For each sample $J_{CDW} = I_{CDW}/A$, where the A is the cross-sectional area $A = \text{width} \times t$. J_{CDW} vs f_{NBN} is linear for bulk $NbSe_3$, as expected, and the linear response still holds for the t=55 and 34nm nanoribbons. The slope is less steep for thinner samples, indicating the decrease in the density of carriers condensed in the CDW state (n_c), according to Eq. 1-21. As summarized in Table 6-4, n_c for t=55nm is significantly suppressed to 0.4 of the bulk value and n_c for t=34nm is further suppressed to 0.19 of the bulk. It appears that thinning down $NbSe_3$ results in the suppression of the CDW order parameter. This interpretation is complicated by the surface pinning effects as discussed in the next section.

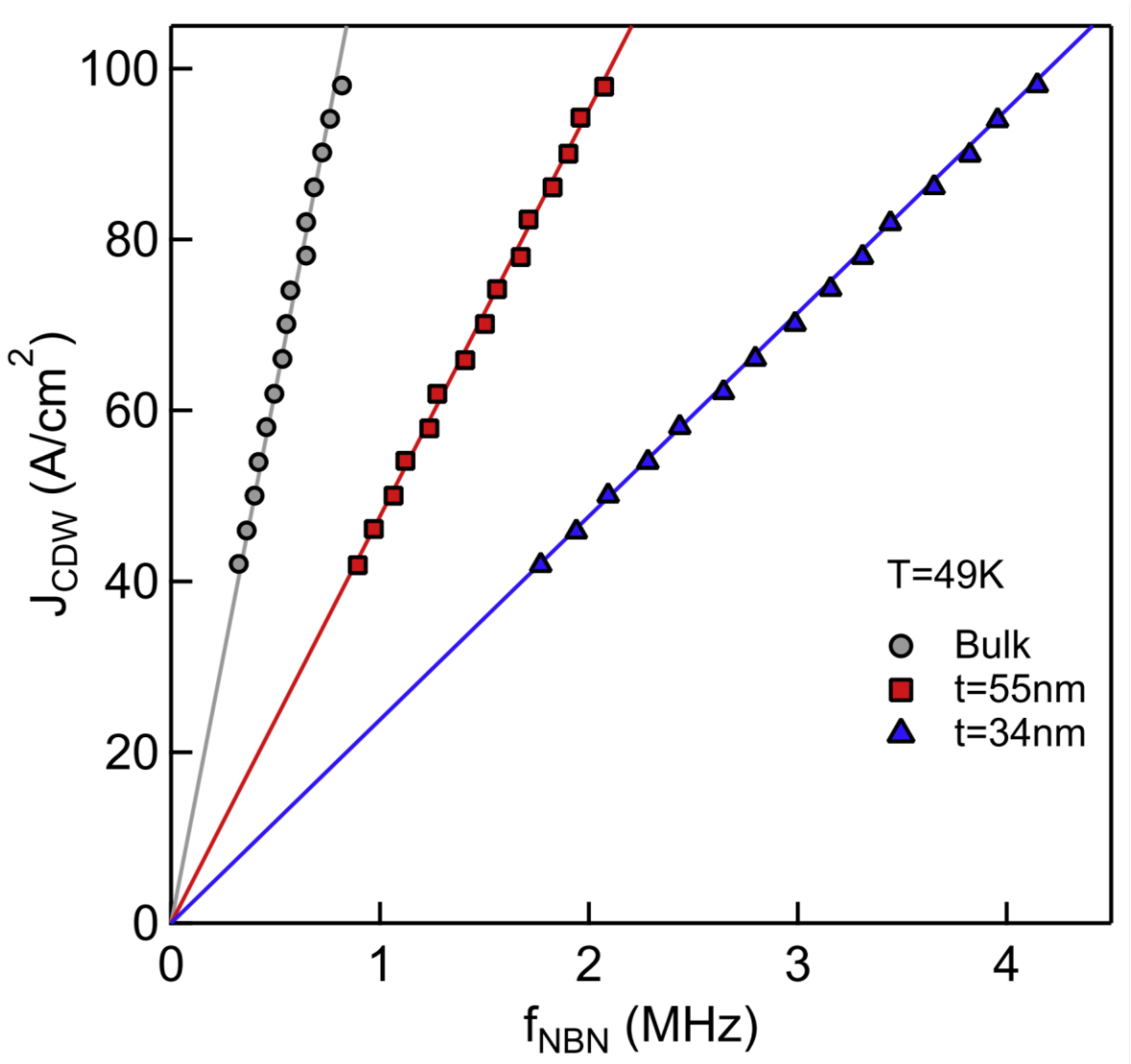

Fig. 6-10 Narrowband noise frequencies for $NbSe_3$ nanoribbons.
Current density of the excess current from sliding CDW (J_{CDW}) vs fundamental frequency of the narrowband noise (f_{NBN}). The lines are linear fits to the data and the slope of each line is used to extract n_c.

6.1.2.4 Order parameter vs surface pinning effects

Fig. 6-11a shows the thickness dependence of E_T for the upper and lower CDW. The minimum E_T from $E_T(T)$ in Fig. 6-9c are shown in red. E_T for the nanoribbons are significantly greater than E_T for bulk, separated by the dashed line and E_T is greater for thinner nanoribbons. E_T for the lower CDW grows with decreasing thickness at a steeper slope and becomes greater than E_T of the upper CDW at t~43nm. It appears that the lower CDW E_T diverges to $E_T>10^6$V/cm for t<34nm, in the region shaded in blue.

An interesting question arises: is the increased E_T in ultrathin samples due to the collapse of the order parameter or enhancement of surface pinning? At first, it seems natural to assume an increase in E_T is caused by the change in pinning conditions. However, E_T diverges as the order parameter collapses (see section 1.2.2.2). The black markers in Fig. 6-11a indicates n_c diminishes as the sample is made thinner. Furthermore, extrapolation to lower t (in the region shaded in blue) suggests $n_c \to 0$ at a finite thickness t~25nm.

Given E_T and n_c, it is possible to calculate the thickness dependence of the static dielectric constant (ε_1) using Eq. 1-19. In bulk, the CDW state results in large ($>10^7$) dielectric constant (see section 1.2.2.3). It is expected that the dielectric constant would significantly decrease with the suppression of the CDW order parameter in ultrathin samples. Fig. 6-11b shows that the ε_1 would fall to 7.2×10^{-5} of the bulk in t=55nm and further down to 2.7×10^{-6} in t=34nm.

There is still a possibility that surface pinning effects are causing the decrease in the measured n_c with thickness. Strong surface pinning could create a layer in which the E_T decays from $E_T^{surface}>E_T^{bulk}$ to E_T^{bulk} over a finite distance, as we move from the surface to the center of the material. This effect would lead to an overestimation of J_{CDW}, as the cross-sectional area should be $A_{eff} < A = \text{width} \times \text{thickness}$. Since the surface/volume ratio is smaller in thinner nanoribbons, this error results in larger f_{NBN} for smaller nanoribbons.

In the study of finite size effects in microscale $NbSe_3$ by McCarten *et al.* [92], surface pinning effects are ruled out based on 1) E_T response to impurity concentration and surface treatment, 2) thickness dependence of small signal ac conductivity, 3) comparison of low field ($E<E_T$) and high field ($E=20E_T$) conductivities and 4) signatures of homogenous sliding CDW from narrowband noise, mode-locking and broad band noise.

Fig. 6-12 shows the imaginary part of the small signal ac conductivity, Im $\sigma(\omega)$, for samples of t=3.7, 0.81 and 0.17μm. As expected from Eq. 1-17, each curve peaks at a particular frequency. The peak moves up in frequency for thinner samples, which is consistent with the increase in E_T. However, it is unusual that the width of the curve does not change with thickness. If the distribution of E_T changes as the sample is made thinner, Im $\sigma(\omega)$ peak should broaden accordingly, as it is sensitive to the spatial distribution of the pinning potential. This observation is used as one of the arguments against surface pinning effects by McCarten *et al.* [92]. A similar measurement should be applied to the mechanically exfoliated $NbSe_3$ nanoribbons in a future study, as it would help distinguish between order parameter collapse and surface pinning enhancement.

Sample thickness (nm)	Upper CDW	Lower CDW			
	E_T(min) (V/cm)	E_T(min) (V/cm)	Slope (A/MHz-cm^2)	$\frac{n_c}{n_{c,Bulk}}$	$\varepsilon_1/\varepsilon_{Bulk}$
Bulk	0.40	0.01	125	1	1
55	100	40	47.6	0.40	7.2×10^{-5}
34	200	500	23.8	0.19	2.7×10^{-6}
31	200	Note 1			
18	800	Note 1			

Table 6-4 Thickness dependence of E_T and f_{NBN} of $NbSe_3$ nanoribbons.
Table 2, Onishi *et al.* [96]. E_T(min) is the minimum E_T for each sample in Fig. 6-9c. Slope of each J_{CDW}/f_{NBN} is obtained from the linear fits in Fig. 6-10. n_c and ε_1 are calculated from Eq. 1-21 and Eq. 1-19, respectively and normalized to the bulk values. Note 1: No E_T found to 10^6V/cm.

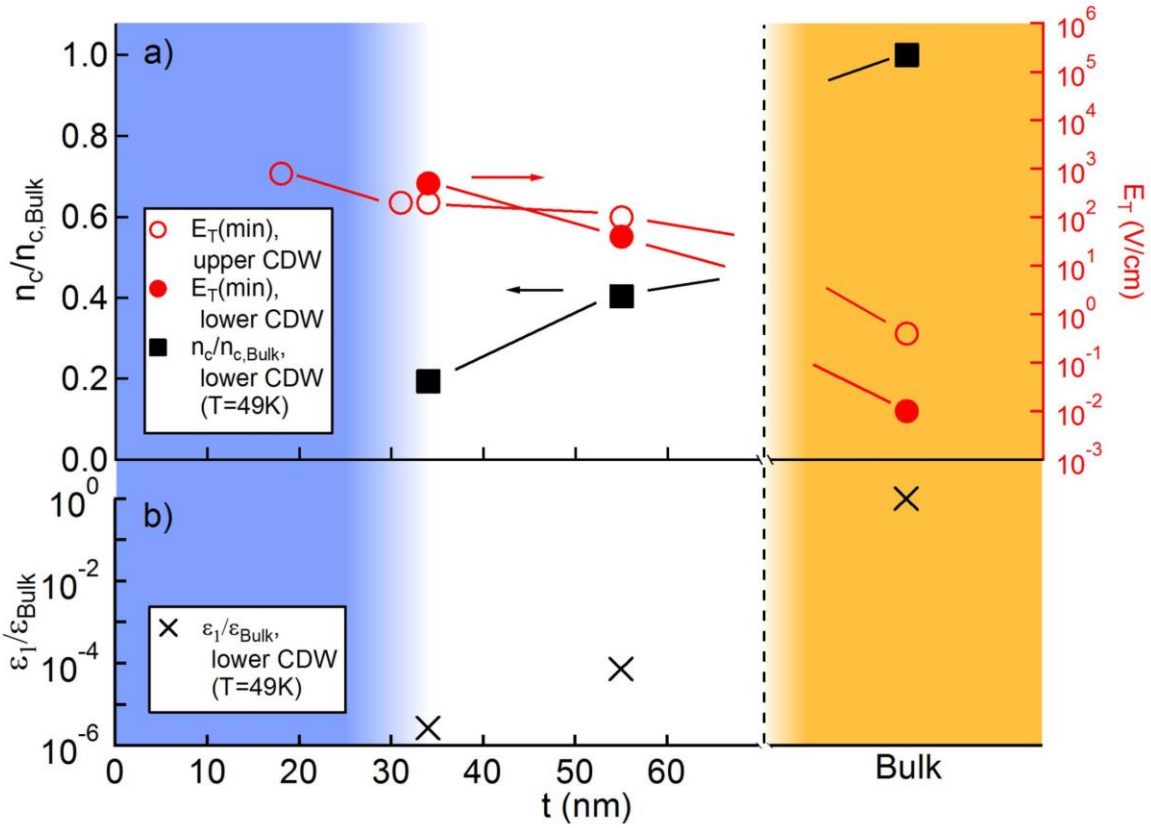

Fig. 6-11 Thickness dependence of CDW dynamics in $NbSe_3$ nanoribbons.
a) Change in E_T (red, right axis) and n_c (black, left axis) with nanoribbon thickness are shown. b) Static dielectric constant (ε_1) calculated from E_T and n_c.

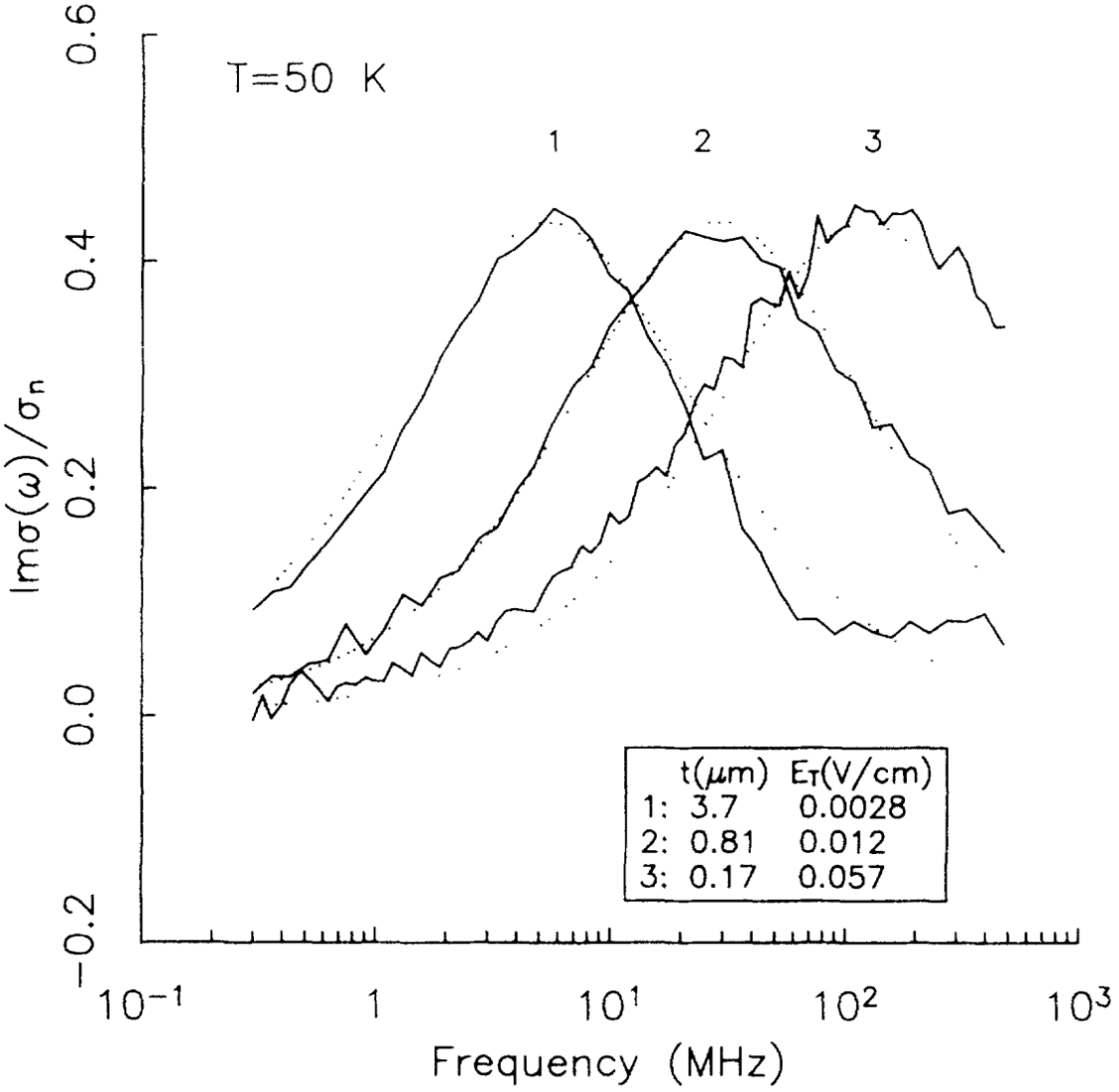

Fig. 6-12 Small signal ac conductivity in microscale $NbSe_3$.
Fig. 20, McCarten *et al.* [92]. Each curve corresponds to a sample of thickness 1) 3.7μm, 2) 0.81μm and 3) 0.17μm.

6.1.2.5 Contact separation and CDW strain

A study with spatially resolved X-ray scattering on bulk $NbSe_3$ [126] found that the CDW within 2mm of an electrical contact is deformed. In Fig. 6-13, the model based on X-ray scattering results shows the current conversion to I_{CDW} is incomplete near the contacts and increases gradually to the equilibrium value over the distance of 1mm. However, a multi-contact transport study [194] found evidence for complete current conversion for $\bar{L}$=20-0.5μm, where $\bar{L}$ is the separation between contacts. In the X-ray study, the CDW is relaxed to its equilibrium state over the $\bar{L}$=4mm distance, whereas in the transport study, the CDW is strained due to $\bar{L}$<2mm. It appears that the current conversion behavior is different for strained and unstrained CDW. For our study, the CDW is strained as $\bar{L}$=7.4-1.1μm and we assume complete current conversion for all samples.

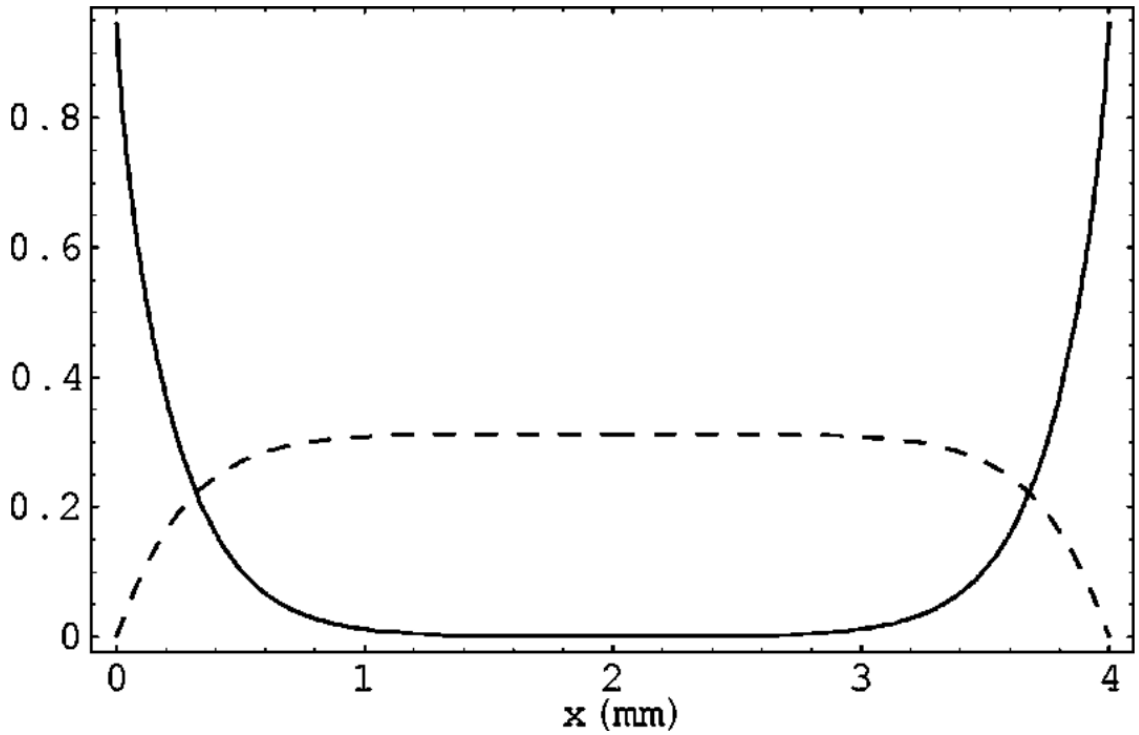

Fig. 6-13 Model of CDW current distribution.
Fig. 7, Brazovskii *et al.* [126]. The electric field (solid line) and CDW current (dashed line) modeled from spatially resolved X-ray scattering measurements on $NbSe_3$ with contacts separated by 4 mm.

6.2 Ionic liquid gating of $NbSe_3$ nanoribbons

Charge carrier concentrations in semiconductors can be modulated by an electric field effect (see Chapter 12). The strength of the electric field is limited by the dielectric strength of the gate dielectric. When the limit is exceeded, dielectric breakdown occurs in the insulator and the gate voltage cannot be sustained. However, liquid gating has emerged as a technique for varying charge carrier concentrations by up to $10^{14}cm^{-2}$ [195], beyond the limit of solid gating. Recently, liquid gating has turned various transition metal dichalcogenides (e.g. MoS_2, $MoSe_2$, WS_2, $MoTe_2$) from a semiconductor to a superconductor, either by strong electric field effect or ion intercalation [108,144].

It would be interesting to extend the narrowband noise measurement to study the effect of liquid gating on the CDW carrier concentration. It is also possible that the liquid gating significantly changes the electronic ground states in $NbSe_3$. The study is in its early stages but preliminary progress is presented. Wu Shi, a post-doctoral researcher in the Zettl group, has started making preliminary measurements. Devices were fabricated by Joey Barreto and Xiyue Wang, undergraduate researchers in the Zettl group.

Fig. 6-14 shows the EBL (see Fig. 9-1) fabrication steps for ionic liquid gating. $NbSe_3$ nanoribbons are transferred on Si/SiO_2 substrate by mechanical exfoliation. A layer of PMMA is deposited on top of the $NbSe_3$ nanoribbons by spin coating. An electron beam pattern exposes the PMMA to write an array of alignment markers. Fig. 6-14a shows the pattern after developing. A ribbon lying horizontally in the center of the image is the target nanoribbon. Unlike CNT, pre-fabricated metal markers and not necessary for alignment (see Fig. 9-3), since the $NbSe_3$ nanoribbons can be identified through the PMMA in an optical microscope.

Fig. 6-14b shows the contact pattern after exposure and developing. In/Cr/Au contacts are deposited immediately after RIE (see section 6.1.1.1). Fig. 6-14c,d show the device after lift-off. The 400μm x 400μm metal pad at the top of the image in Fig. 6-14d is the gate electrode for the gating liquid. Before measurement, the liquid is deposited to cover the gate electrode and the sample area. The gate electrode has a large area compared to the sample to accumulate charge at the sample surface.

In Fig. 6-14d, the metal lines going to the sample are darker than the contact pads because they are covered with a thin layer of deposited SiO_2. They are protected by SiO_2 because the ions in the gating liquid degrades the contact to the sample. Patterning of the SiO_2 mask does not need another step of lithography. After metal deposition (but *before* lift-off), the contact pattern is faintly visible, even though the whole chip is covered by metal. The parts, which should not be covered by the SiO_2 mask (i.e. contact pads and the gate electrode), are painted with a photoresist under a microscope. The SiO_2 layer is then deposited by electron beam evaporation and only the metal contact and SiO_2 mask pattern remain after lift-off.

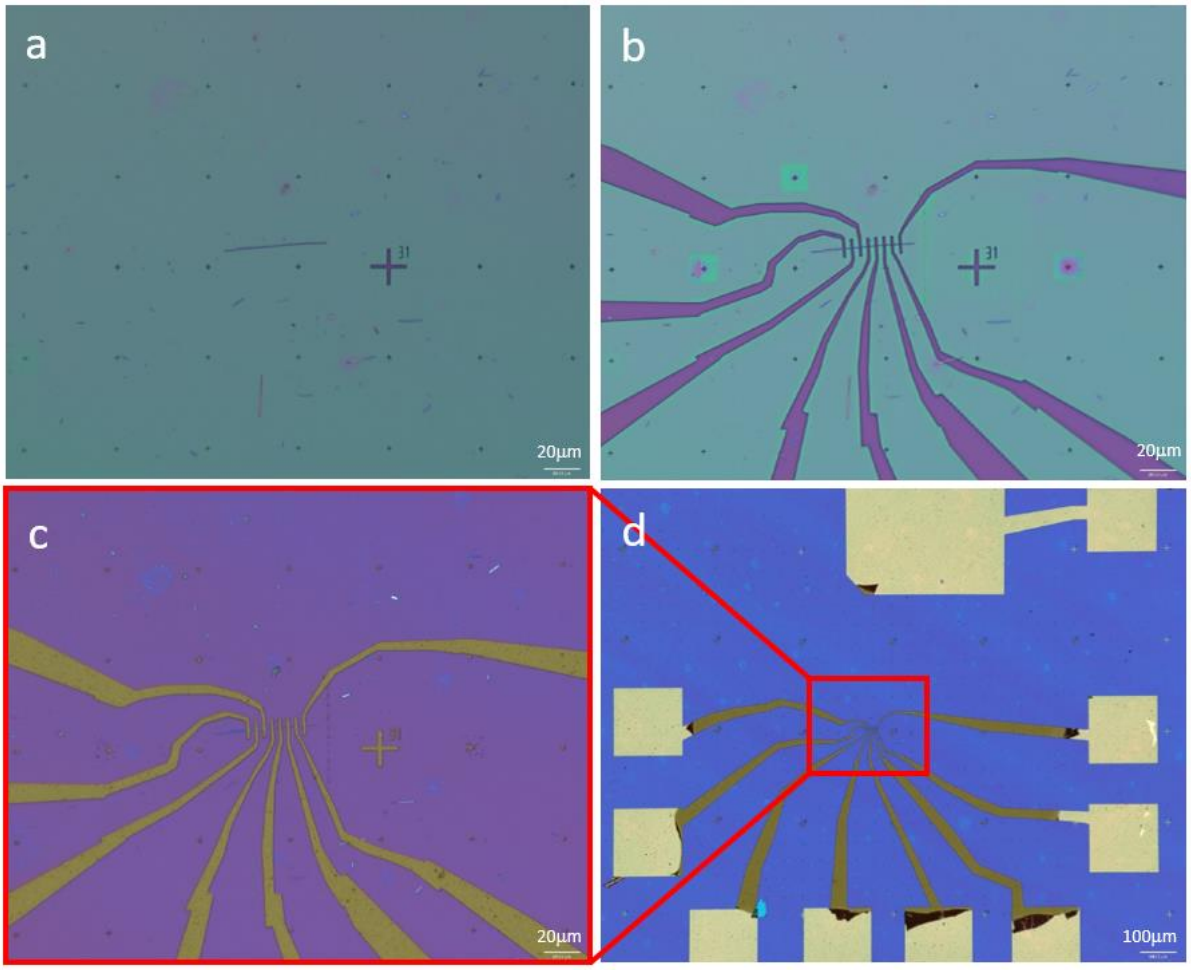

Fig. 6-14 Fabrication of ionic liquid gating device.
Courtesy of Joey Barreto. a) $NbSe_3$ nanoribbon on a grid of alignment markers. b) Contact pattern after electron beam exposure and developing. c) In/Cr/Au pattern after metal deposition and lift-off. d) Overall image of the device with contacts pads. The metal pad at the top is the electrode for liquid gating.

6.3 BNNT encapsulated $NbSe_3$

Thang Pham, a fellow graduate student in the Zettl group, Patrick Stetz, an undergraduate researcher in the Zettl group, and I attempted to grow $NbSe_3$ inside of boron nitride nanotubes (BNNT). Thang provided the BNNT and characterized the samples with TEM and Patrick carried out the synthesis.

$NbSe_3$ has been approaching the single-chain limit through plasma etching [194], ultrasonic cleaving [124], chemical synthesis [192] and mechanical exfoliation [96], but the smallest reported nanoscale $NbSe_3$ samples remain >220 chains [124]. In addition, the study of a material at the single atomic chain limit would require protection from chemical reactions with the environment [124,41]. Learning from studies on layered TMC at the monolayer limit [43], h-BN is a reliable capping layer for encapsulating air sensitive samples and has enabled transport studies by tunneling, despite being an insulator. Similarly, a sheath of h-BN (i.e. BNNT) is a promising candidate for protecting a single chain of $NbSe_3$ from environmental factors, while preserving access to its electrical and optical properties.

Similar to the insertion of C_{60} molecules in BNNT [196], our synthesis method introduces Nb and Se in the vapor phase to BNNT. Nb and Se are loaded with 1:3 stoichiometric ratio in a Ø1.27cm x 20cm long quartz tube, similar to $NbSe_3$ crystal growth (see Table 4-1VI), but BNNT are also added. The BNNT stick to the wall of the quartz tube and makes it difficult to control the BNNT location with respect to Nb and Se. For improved control over BNNT location, we load it inside a short Ø0.64cm quartz tube with both ends open. The BNNT stick to the wall of the Ø0.64cm tube and the tube can slide around within the Ø1.27cm tube. After sealing in vacuum (see section 4.1), the quartz tube is heated at 690^{o}C inside a box furnace (Lindberg 59344) for 120hrs.

Fig. 6-15 shows the BNNT after the synthesis described above. A BNNT runs vertically across the middle of the image. Multiple well-ordered walls of the BNNT are visible. The interior of the tube shows two chains running parallel to the tube. We believe the chain is an $NbSe_x$, which grew inside the BNNT. It is unclear whether the chains are $NbSe_3$ since confinement effects at the interior of nanotubes could result in unique crystal structures [196]. Interestingly, the two chains appear to be twisting with each other multiple times. 1D confinement is prone to creating helical order, as shown from previous studies in other systems [197].

Fig. 6-16 shows an EDS spectrum from TEM of the twisting chains inside the BNNT interior. Clear peaks of both Nb and Se are identified. The silicon contamination is present for all types of samples and believed to originate from the detector. The copper signal is from the TEM grid. Synthesis with only selenium and BNNT as a control experiment yielded BNNT filled with selenium but looked very distinct from the structures shown in Fig. 6-15.

The helical structure of $NbSe_x$ is suggestive of topologically non-trivial states, possibly similar to those observed in Ru_2Sn_3 [198]. As $NbSe_3$ supports a CDW state, the one-dimensional character of the $NbSe_x$ is likely to be driven to a CDW state by Peierls instability. As the interaction of topological insulators and superconductivity has accumulated much interest [199,200], a system with a possible coexistence of CDW and topological effects would be interesting for studying novel collective states.

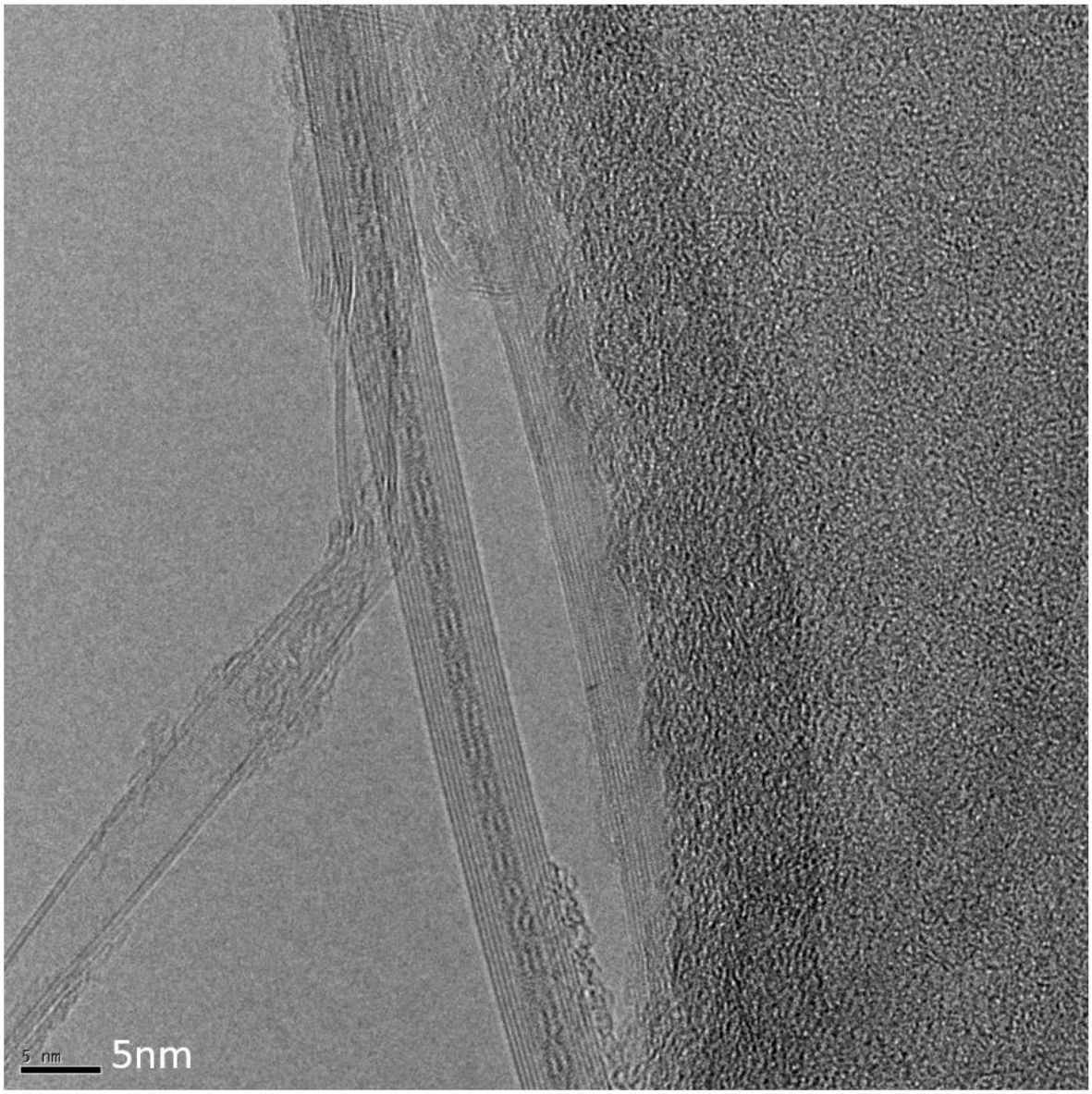

Fig. 6-15 $NbSe_x$ inside boron nitride nanotube.
TEM image courtesy of Thang Pham. A boron nitride nanotube runs vertically across the center of the image. Along the center of the tube, two chains run and twist with each other multiple times.

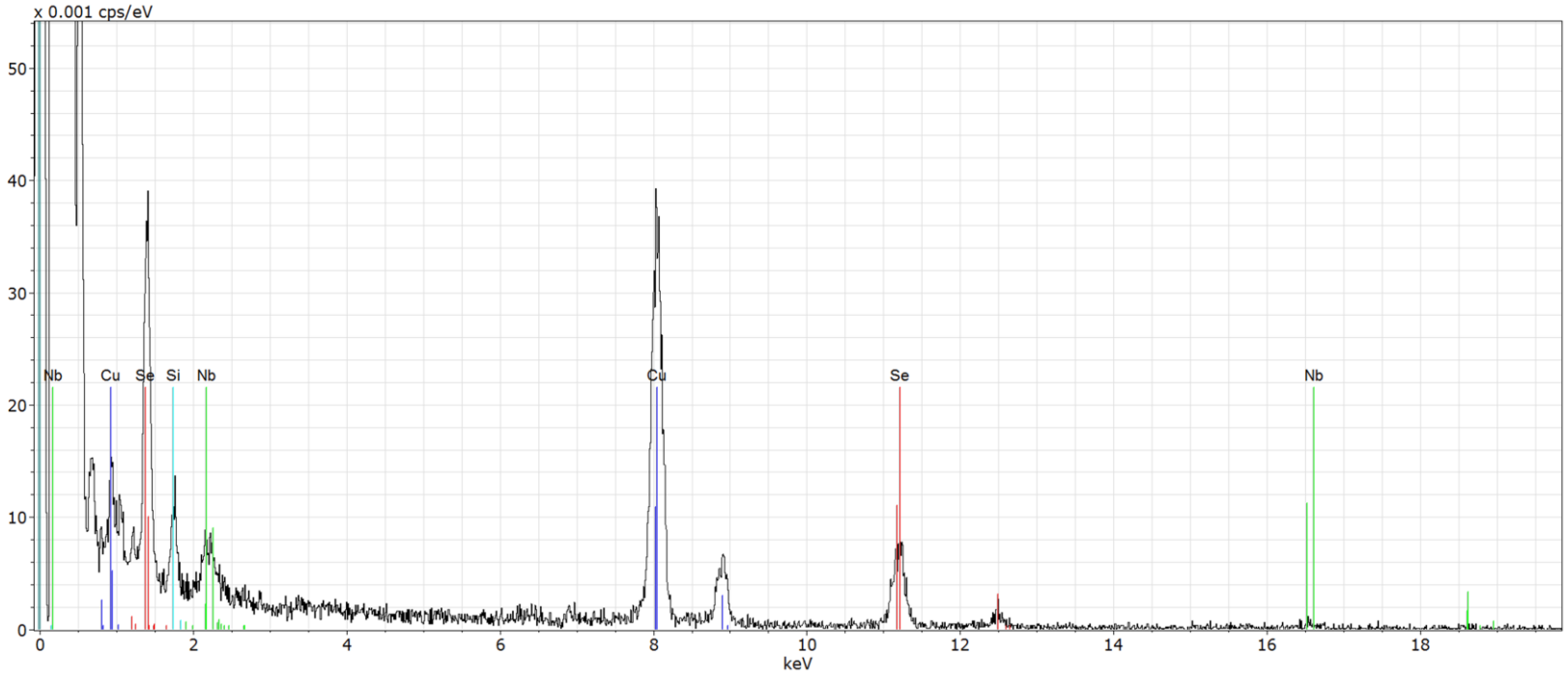

Fig. 6-16 Elemental analysis of $NbSe_x$ inside boron nitride nanotube.
Courtesy of Thang Pham. Spectrum is obtained by energy dispersive X-ray spectroscopy in TEM.

7 Microfabricated contactless measurement platform

Contactless measurement of sample conductivity is a well-established technique for bulk crystals [201]. For layered materials, contactless measurements can offer unique advantages and higher accuracy than the commonly employed four-probe method. We propose to scale down the dimensions of the measurement setup using lithographic techniques to be compatible with nanoscale samples (e.g. van der Waals heterostructures).

The results of my simulations on scaling down the contactless measurement setup to the microscale are presented. Jiyoung Chang, a post-doctoral researcher in the Zettl group, and I designed the microcoils. Jiyoung fabricated the microcoils, using photolithography (Marvell Nanolab). This project is still in progress and will be continued by collaborators. In particular, the next step is to measure the RF characteristics of the fabricated prototypes. Towards this goal, Corey Shih, an undergraduate researcher in the Zettl group, has developed a method of creating copper squares on the microcoils to serve as samples for testing and I have been setting up for RF characterization.

7.1 Contactless measurement

For conductivity measurements, electrical contacts are made on the top surface of the material to flow current and probe the electric field. In layered materials, where the in-plane conductivity is much higher than the out-of-plane conductivity, the current could be limited to only the layer in contact with the electrodes. When this occurs, the assumption that the current (I) is evenly distributed across the cross-sectional area (A) of the sample for finding J=I/A is invalid and leads to errors in conductivity measurements. For some graphite intercalated compounds, the error has been noted and the error was avoided by using a contactless measurement technique [202].

Fig. 7-1 shows the contactless measurement probe developed and used by William Vareka for the study of $Bi_2Sr_2CaCu_2O_x$ [203,204]. Radio frequency (RF) signal of ~50MHz is emitted from the drive coil, located above the sample. The pick-up coil, located below the sample, measures how the sample affects the transmission of the RF signal. Due to the changing electromagnetic fields, eddy currents are induced in the sample and shields some of the RF signal. RF transmission is lower for samples of higher conductivity. The probe is designed to be mounted in a cryostat for measurements down to cryogenic temperatures for its utility in the study of collective ground states. For example, the measurement of both the magnitude and the phase enables the extraction of the superfluid density in superconductors [205]. RF measurements offer great insight into CDW dynamics, as well (see section 6.1.2.3 and 6.1.2.4). Contactless measurements are preferred at high frequency, as contacts introduce uncontrolled impedances [206].

The RF transmission technique is well established on the bulk crystal scale. It would be interesting to apply the technique to the layered materials at the ultrathin limit and van der Waals heterostructures. However, mechanical exfoliation and assembled heterostructures have typical lateral dimensions ~10μm. With machining, it is difficult to fabricate a probe with coil radius <250μm [205]. Coils with dimensions similar or even smaller than the ~10μm sample are required. Analogous to the way lithographic techniques scaled down the 4-point probe measurement for nanoscale samples, we propose to employ lithographically fabricated coils to adapt the contactless measurement technique for nanoscale samples.

The development of contactless measurement for nanomaterials would be interesting as it is non-trivial to find a method to make good contact to the material. Even for graphene, a well-characterized conductor, a special technique to make a one-dimensional contact to its edge is required to make good contact [207]. For air-sensitive samples, making contact is complicated further by the need to encapsulate the material within an insulating matrix [169]. In addition, the coil based inductive coupling scheme of the contactless measurement technique could enable ac susceptibility [208,209] measurements to probe spin dynamics [210] at the single device level of nanomaterials.

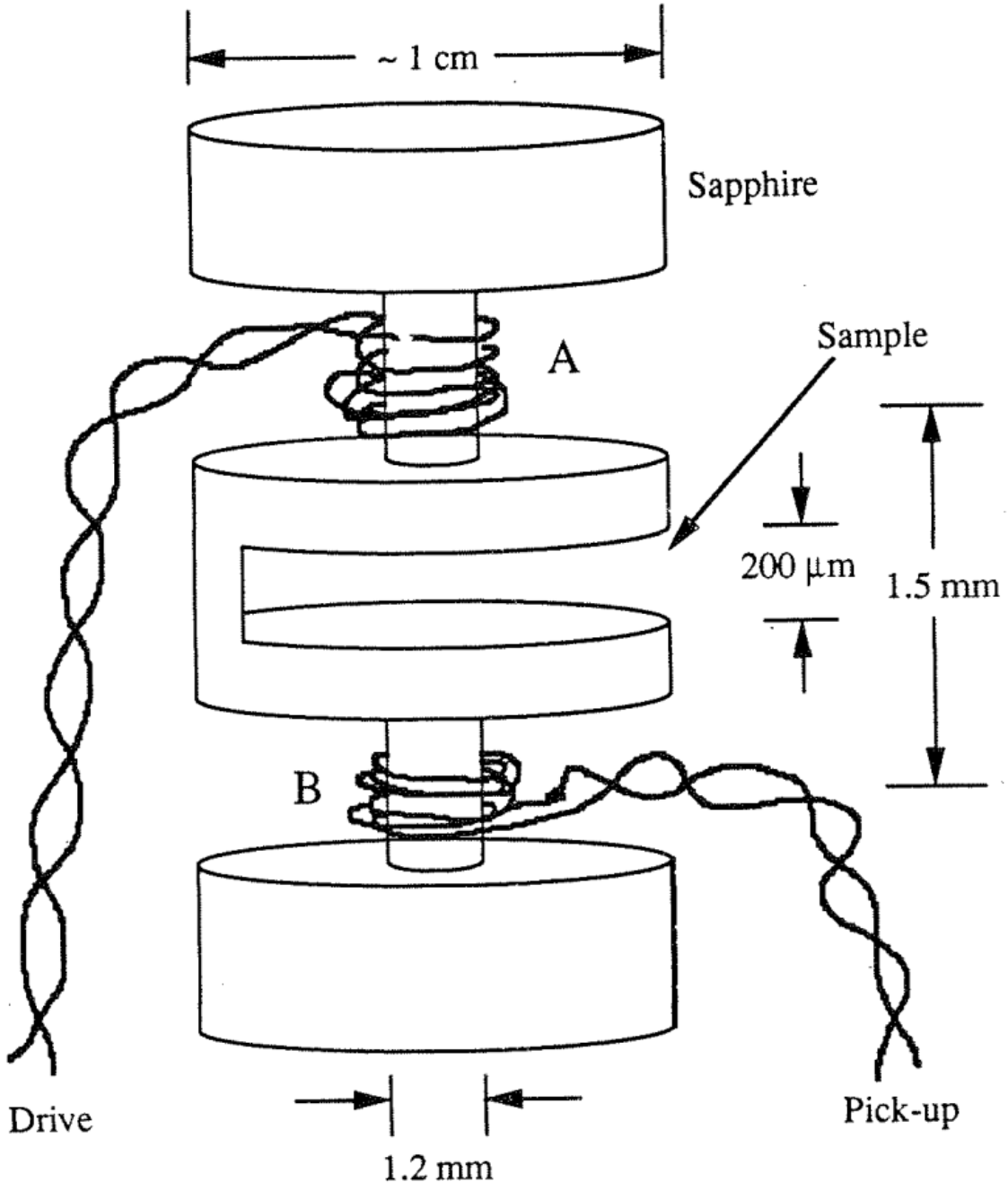

Fig. 7-1 Schematic of contactless measurement probe.
Fig. 5.3, Vareka [204]. The sample is placed in the slot in the middle, between drive and pick-up coils at the top and bottom to measure RF transmission.

7.2 Simulation

The effect of reducing the coil radius and the separation between the coils are simulated with the equation presented in Sakakibara *et al.* [201]. The conductivity (σ) of the sample enters the equation as a modification to the wave vector (k)

$$k'^2 = k^2 + i\omega\mu_0\sigma \qquad \text{Eq. 7-1}$$

where $\omega=2\pi f$ for the frequency (f) and μ_0= the permeability of free space.
As illustrated in Fig. 7-2, the geometry of the probe is parametrized by coil radius (a), separation between the two coils (*l*) and sample thickness (t). Each coil is modeled as a single plane, where the diameter of the wire and the width of the coil is considered negligible. One coil is located at z=-u and the other coil is located at z=-u+*l*. The sample extends from z=0 to z=t. According to Sakakibara *et al.* [201] the RF transmission (T) from the drive coil to the pick-up coil is calculated by

$$T = \frac{\int_0^\infty \frac{4kk' J_1^2(ka) e^{-k(l-t)}}{(k+k')^2 e^{k't} - (k-k')e^{-k't}} dk}{\int_0^\infty J_1^2(ka) e^{-kl} dk} \qquad \text{Eq. 7-2}$$

where $J_1(\ )$ is the first order Bessel function of the first kind.

Using Eq. 7-2, T for various coil dimensions are found by numerically evaluating the integrals (Wolfram Mathematica). Fig. 7-3 shows the programming code for the calculation. The program outputs T as a function of the sample resistivity (ρ) For the parameters used by Vareka [204], the program successfully reproduces previously calculated results (Table 5.1, Vareka [204]).

Fig. 7-4 shows T(ρ) for a single layer of graphene (t=0.35nm) with ρ<7μΩ–cm. As shown on the top axis, the resistivity range corresponds to sheet resistance ≲200Ω. The measurement conditions are: a=100μm, *l*=200nm and f=1GHz (solid line) and 10GHz (dashed line). For both f=1 and 10GHz, T increases sharply as ρ increases from 0 and saturates to T_0=0.806 at higher ρ. The increase is steeper for f=1GHz than f=10GHz. For ρ_{sat} defined by $T(\rho_{sat})=0.999T_0$, ρ_{sat}=0.20μΩ–cm for f=1GHz and ρ_{sat}=1.6μΩ–cm. The sensitivity to sample resistivity rapidly diminishes as the sample resistivity is increased. A highly conductive sample is required to apply the contactless measurement at the monolayer scale. Fig. 7-5 shows the data from Fig. 7-4 as a relative change $(T_0-T)/T_0$.

Fig. 7-6 shows T(ρ) curves with each corresponding to a stack composed of a different layer number of graphene. As the layer number is increased from 1 to 100, the increase to T_0 becomes less steep. Fig. 7-7 shows the corresponding relative change. For higher layer number the range of sensitivity expands to lower ρ and more resistive samples become compatible with the measurement. For a 100 layer sample, $(T_0-T)/T_0$>1% for ρ<5.6 μΩ–cm.

Table 7-1 shows parameters extracted from T(ρ) simulations with a=100, 10 and 1μm for a single layer of graphene similar to Fig. 7-4. Reducing the coil diameter makes the rise to T_0 steeper and narrows the measurable resistivity range. ρ_{sat}=1.89 for a=100μm but ρ_{sat}=0.07 for a=1μm.

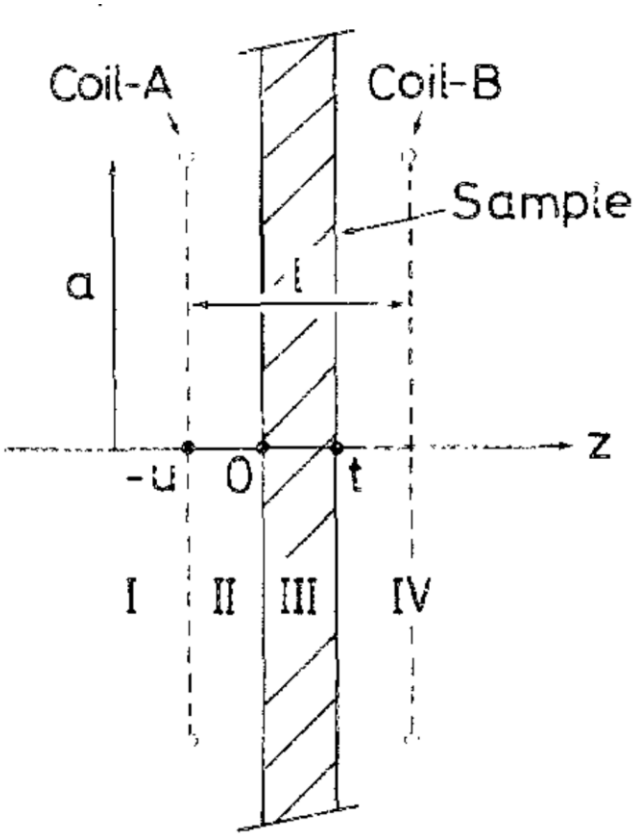

Fig. 7-2 Geometry for RF transmission calculation.
Fig. 2, Sakakibara *et al.* [201]. Side view of the contactless measurement probe. A coil of radius (a) is located at z=-u and z=-u+*l*. The sample of thickness t is located between the two coils.

```
f = 1 * 10^9 (*Hz*)
w = 2 * π * f
l = 200 * 10^-9 (*m*)
a = 100 * 10^-6 (*m*)
n = 1 (*layer number*)
t = n * 3.5 * 10^-10 (*m*)
mu = 4 * π * 10^-7 (*kg*m^2/C^2*)

k = .
kp = Sqrt[k^2 + i * w * mu * sigma]


F2[k_] := (BesselJ[1, k * a])^2 * Exp[-k * l]
V0 = Integrate[F2[k], {k, 0, ∞}]

F1[k_] := (4 * k * kp * (BesselJ[1, k * a])^2 * Exp[-k * (l - t)]) / ((k + kp)^2 * Exp[kp * t] - (k - kp)^2 * Exp[-kp * t])

T = Table[{N[rho],
        sigma = 1 / rho;
        kp = Sqrt[k^2 + i * w * mu * sigma];
        Abs[NIntegrate[F1[k] / V0, {k, 0, 1000000}]]},
       {rho, 0.1 * 10^-9 (*1*t/n*), 2 * 10^-9 (*2*t/n*), 0.01 * 10^-9 (*1*t/n*)}]
ListPlot[T]
T // TableForm
Export["output.xls", T, "XLS"]
```

Fig. 7-3 Mathematica code for simulation of contactless measurement.
Simulation results are obtained for different frequency (f) and layer number (t).

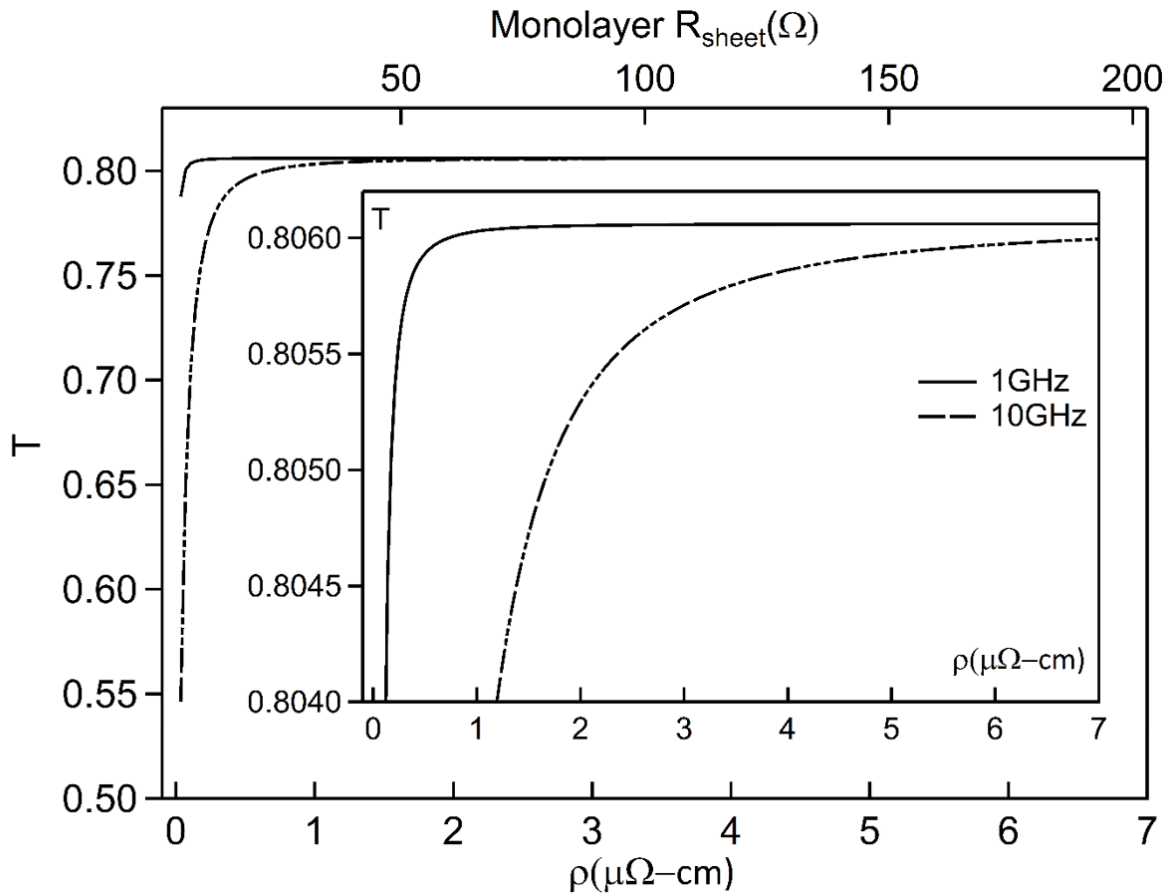

Fig. 7-4 Graphene contactless measurement simulation.
Simulated RF transmission (T) for a t=0.35nm sheet of material with resistivity ρ. Top axis is in units of sheet resistance $R_{sheet}=\rho/t$. a=100μm, *l*=200nm, f=1GHz (solid line) and 10GHz (dashed line).

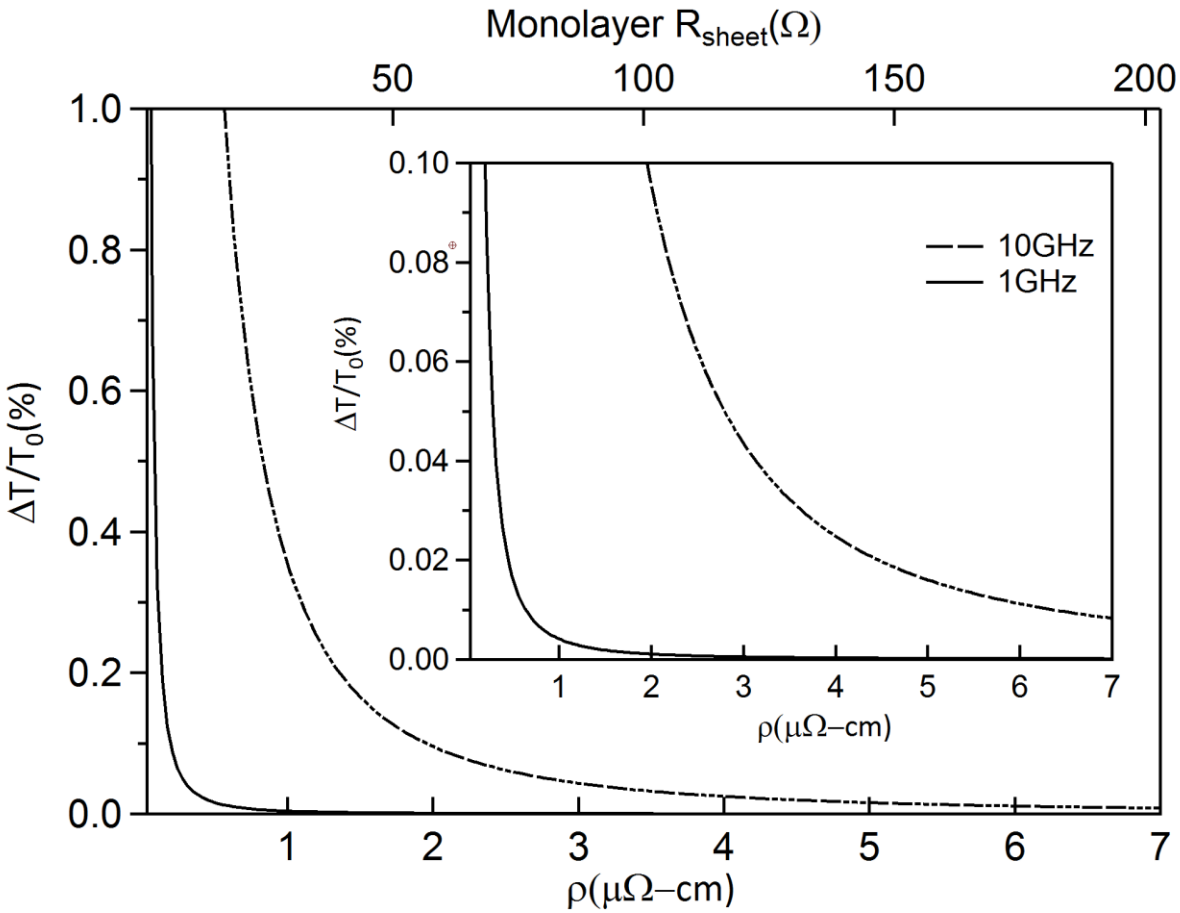

Fig. 7-5 Graphene simulation RF transmission relative change.
The simulation result in Fig. 7-4 displayed as relative change in RF transmission with respect to T_0=0.806.

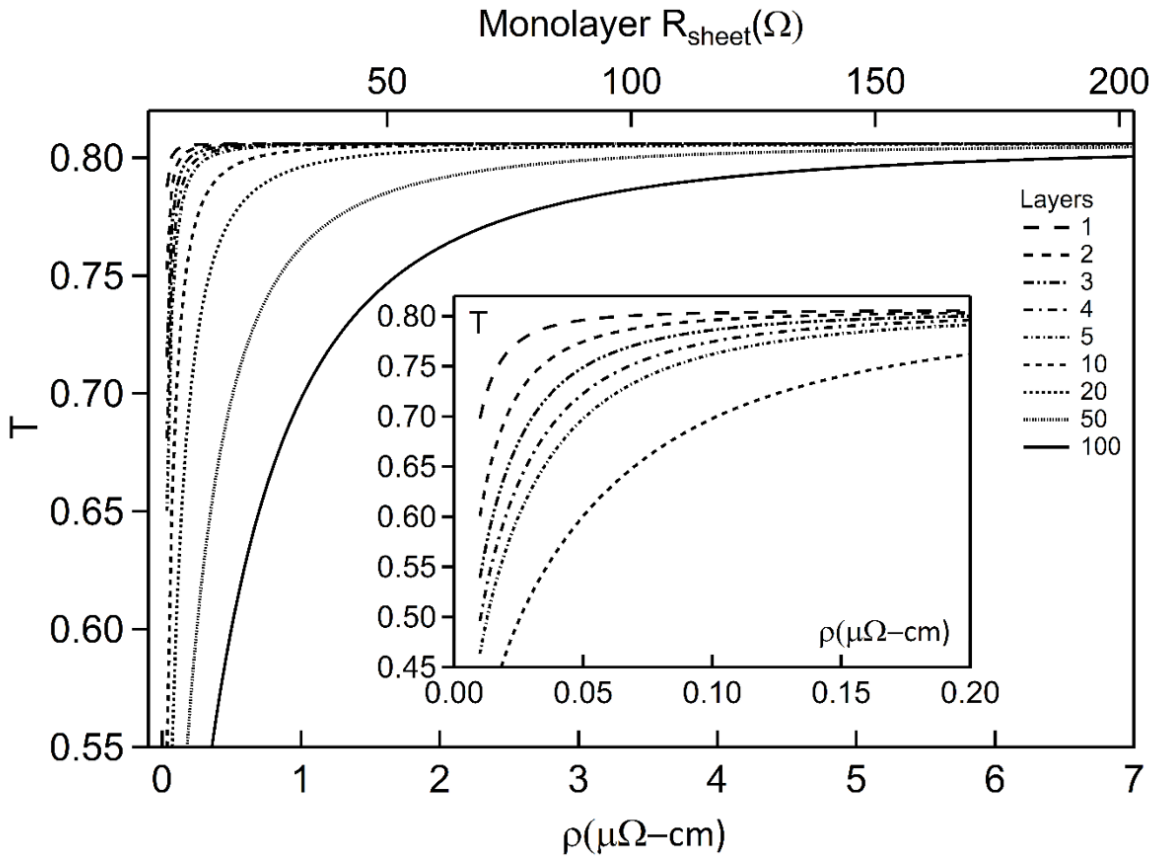

Fig. 7-6 Multi-layer graphene contactless measurement simulation.
Simulated RF transmission (T) for n layers of t=0.35nm sheets. For each curve, n is fixed while the resistivity (ρ) of the material is varied. Top axis is in units of monolayer sheet resistance $R_{sheet}=\rho/t$. *a*=100μm, *l*=200nm, f=1GHz and n=1, 2, 3, 4, 5, 10, 20, 50 and 100.

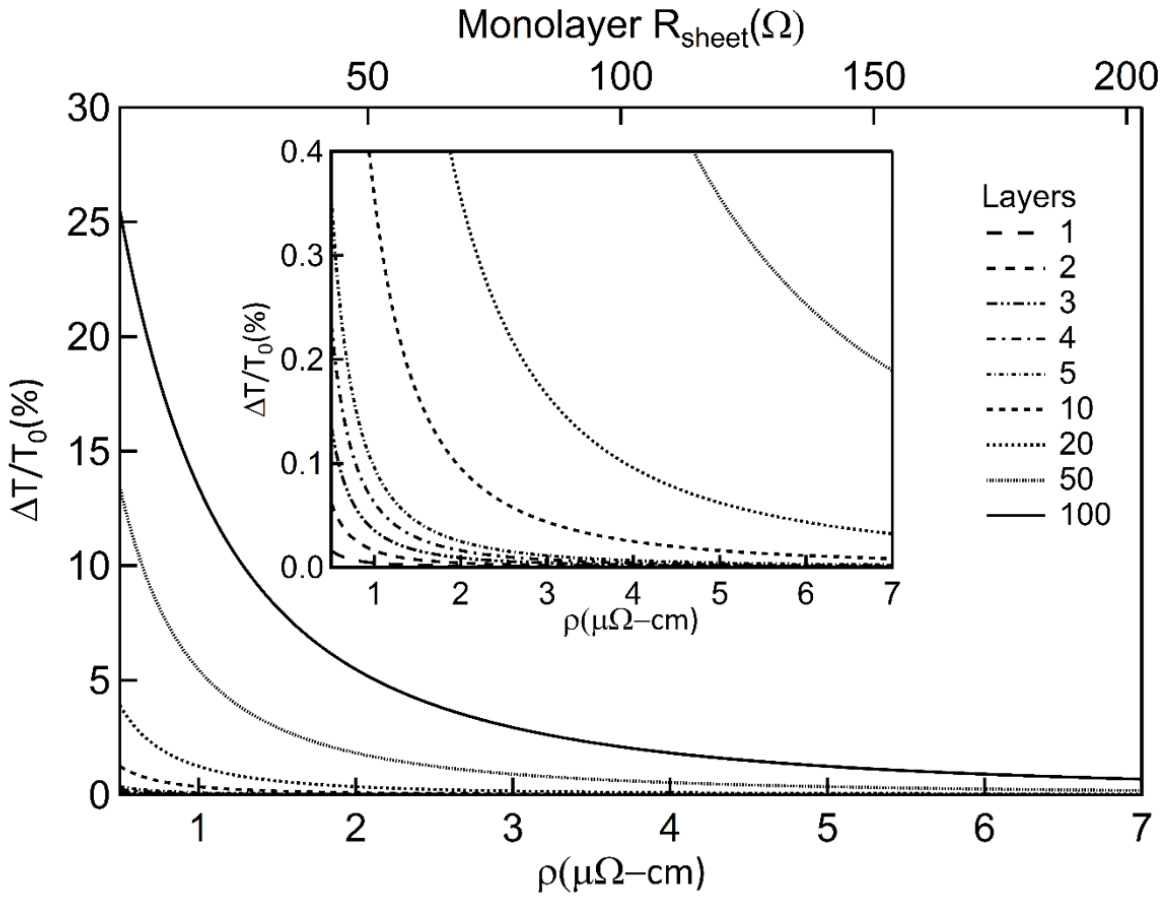

Fig. 7-7 Multi-layer graphene simulation RF transmission relative change.
The simulation result in Fig. 7-6 displayed as relative change in RF transmission with respect to T_0=0.806.

a (μm)	T_0	ρ_{sat} (μΩ-cm)
100	0.8060	1.89
10	0.6975	0.25
1	0.1135	0.07

Table 7-1 Coil radius reduction simulation.
a=coil radius. T(ρ) increases from 0 and saturates to T_0 at high ρ. T(ρ_{sat})=0.999T_0. t=0.35nm, *l*=200nm, f=1GHz.

The simulations assume that the coils are circular but microfabricated coils are actually planar square coils. Calculation of the electromagnetic fields with planar coil geometry is not simple and requires finite element simulations. Instead, we plan to empirically characterize the behavior of the fabricated prototypes by using samples of well-controlled geometry. Evaporated films of copper will be used as test samples. Fig. 7-8 shows the simulation result with a copper film of t=100-1000nm in 100nm increments. There is significant change in T for t=100-500nm, the range easily accessible by standard evaporation techniques. T=0.72 at t=100nm and falls to T=0.42 at t=500nm.

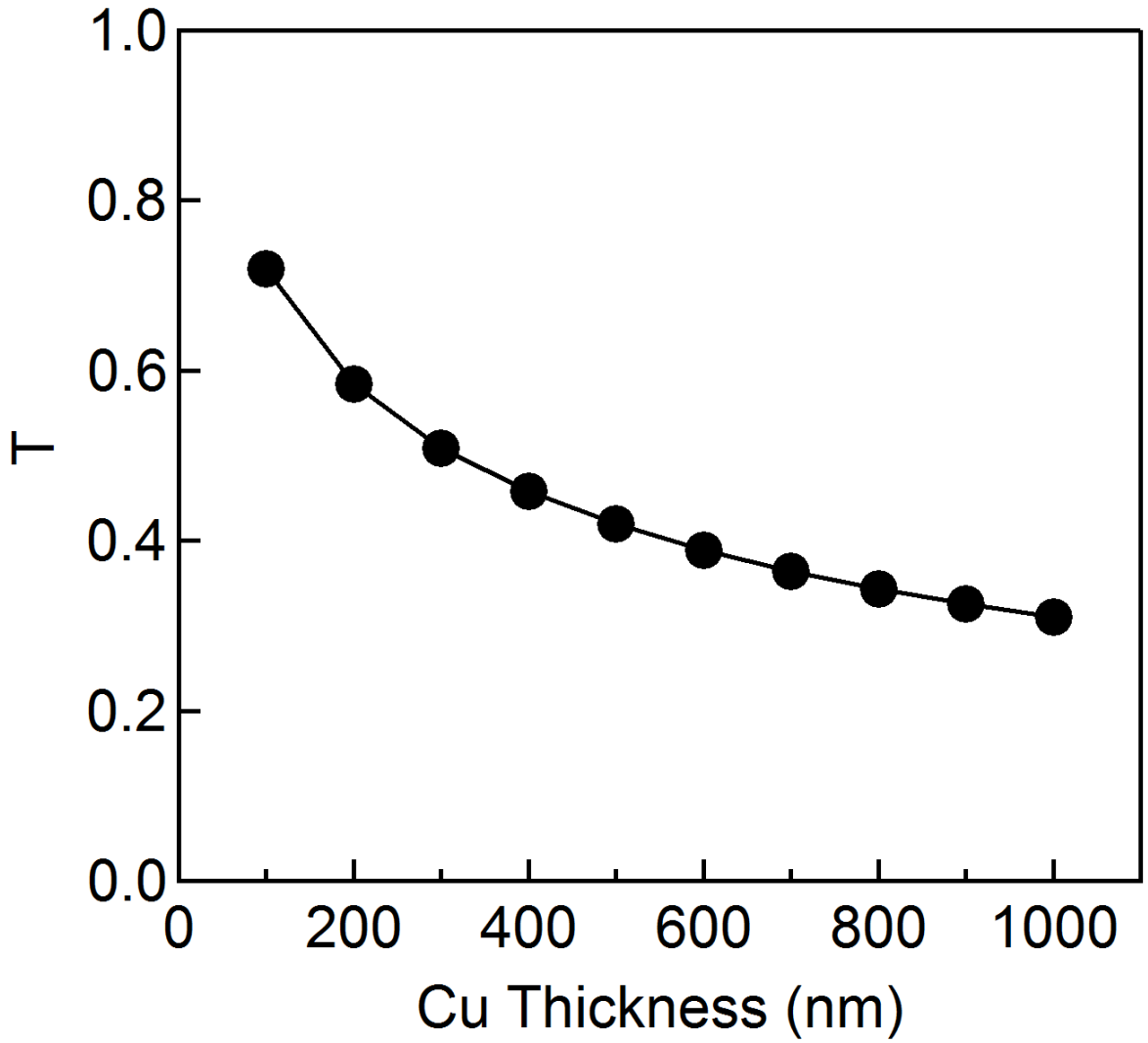

Fig. 7-8 Copper thin film contactless measurement simulation.
f=1GHz, a=100μm and *l*=1μm.

7.3 Microfabricated platforms

Fig. 7-1 shows the lithographic analogs of the contactless measurement probe fabricated by photolithography. The system consists of fused quartz chips patterned with metal. There is a top chip and a bottom chip, each patterned with a planar coil. The sample is placed on the coil of the bottom chip and covered by a top chip. When assembled as designed the coils on the top and bottom chips align. With this flip-chip geometry, the sample is placed between two coils, similar to the machined probe.

Fig. 7-9 shows the microscope image of the bottom chip. At the center, there is a 200μm x 200μm lithographically fabricated planar coil (microcoil). The microcoil starts from the line on the left, makes 3 turns as it spirals to the center. The layer with the microcoil is covered with an insulator (SiO_2) and a contact pad above the insulator (green region) makes contact to the center of the microcoil through a via, which penetrates to the layer below the insulator. Finally, the whole chip is covered with 100nm of SiO_2 to avoid direct electrical contact to the sample. Square holes are etched at the contact pads to allow access by probes.

The four crosses surrounding the microcoil are alignment markers for placing the top chip. The top chip is patterned with a microcoil, two contact pads and four alignment markers. , Similar to the bottom chip, it is also covered with 100nm SiO_2 to prevent shorting. It is slightly smaller than the bottom chip and is placed to fit in the region outlined with the dashed line. When placing the top coil, its position is adjusted with a micromanipulator under a microscope to align the crosses on the top chip with those of the bottom chip. When aligned, the microcoils of the top and bottom chip overlap and the contacts on the top chip touch the lower (upper) half of the T1 (T2) contact pad. A small amount of silver paste is placed at T1 and T2 during the assembly of the two chips to ensure good electrical contact. Both T1 and T2 extend to an area, which is not covered by the top chip. Contacts can be made to the bottom microcoil from B1 and B2 and the top microcoil from T1 and T2. The probe is essentially complete with these four contact pads. The four additional contacts P1, P2, P3 and P4 enable van der Pauw measurement of the sample to compare while characterizing the performance of the device.

Microcoils of various dimensions were fabricated to find the optimum design for contactless measurement. The width of the line composing the coil (w), the separation between the lines (s) and the number of turns in the coil (n_{turns}) are varied. In Fig. 7-10a,b,c n_{turns} is varied to be 1, 3 and 5 respectively, while w=2μm and s=4μm are kept constant. The simulations do not model the dissipation from the finite impedance of the coil wires, however metal at the length scales shown could result in some non-negligible dissipation. The widths of the lines are varied: w=2μm in Fig. 7-10a,b,c; w=4μm in Fig. 7-10d,e; w=5μm in Fig. 7-10f; w=20μm in Fig. 7-10h. The microcoil in Fig. 7-10h is exceptionally large and the alignment markers lie further out, beyond the field of view in this image (see Fig. 7-9) Small s is desired to enable tighter packing of the coil to fit more turns but, as shown in Fig. 7-10g, the narrow gaps cause problems during metal lift-off. The control device with no microcoil, shown in Fig. 7-10i needs to be tested to ensure the signals originate from the microil and the sample.

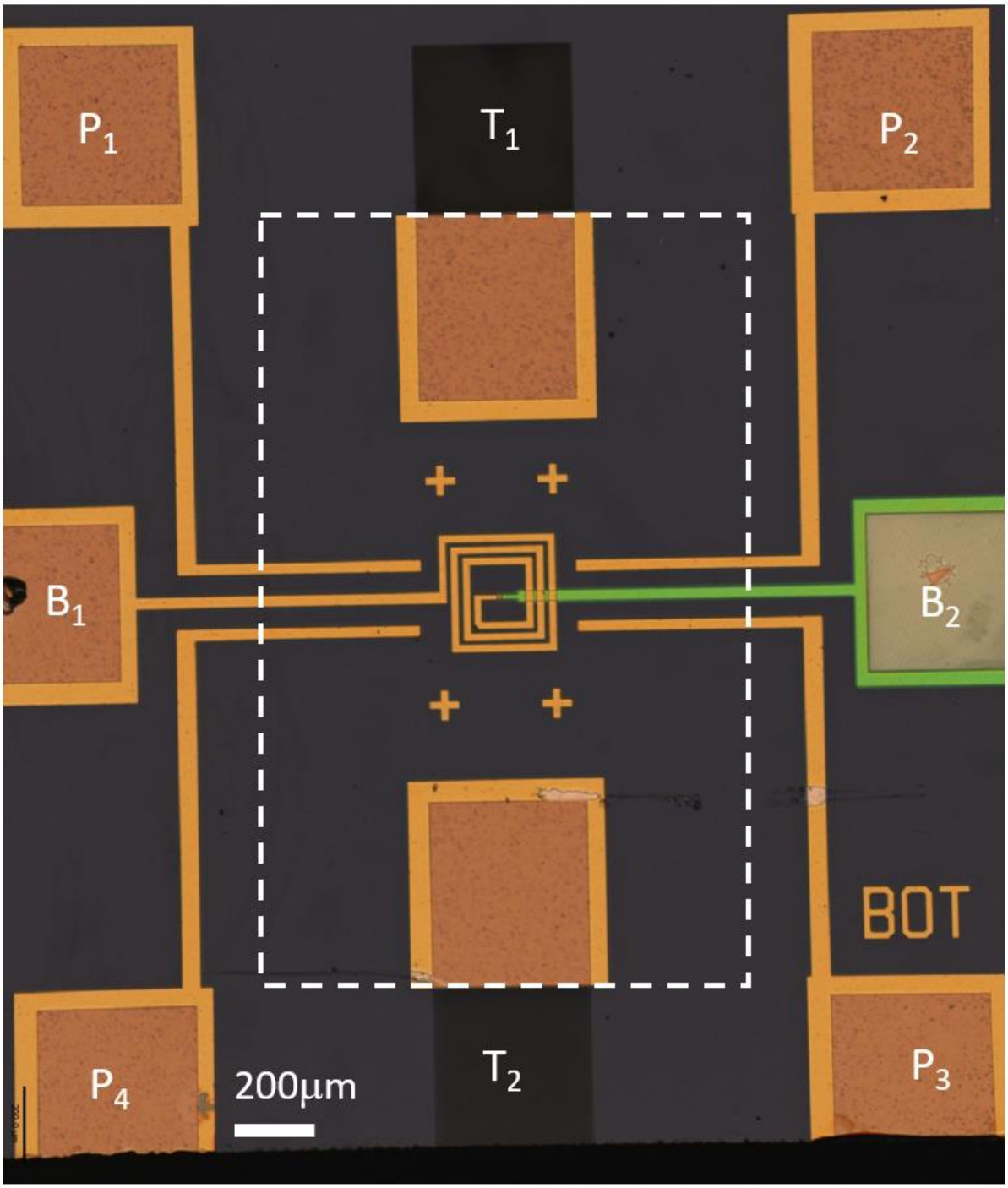

Fig. 7-9 Microfabricated contactless measurement probe.
Courtesy of Corey Shih. Optical image of bottom chip is shown. The rectangle outlined with a dashed line shows the approximate size and position of the top chip. There are contact pads for the bottom coil (B_1, B_2), top coil (T_1, T_2) and 4-probe measurement (P_1, P_2, P_3, P_4). 4-probe measurement is only used for comparison with contactless measurement during testing.

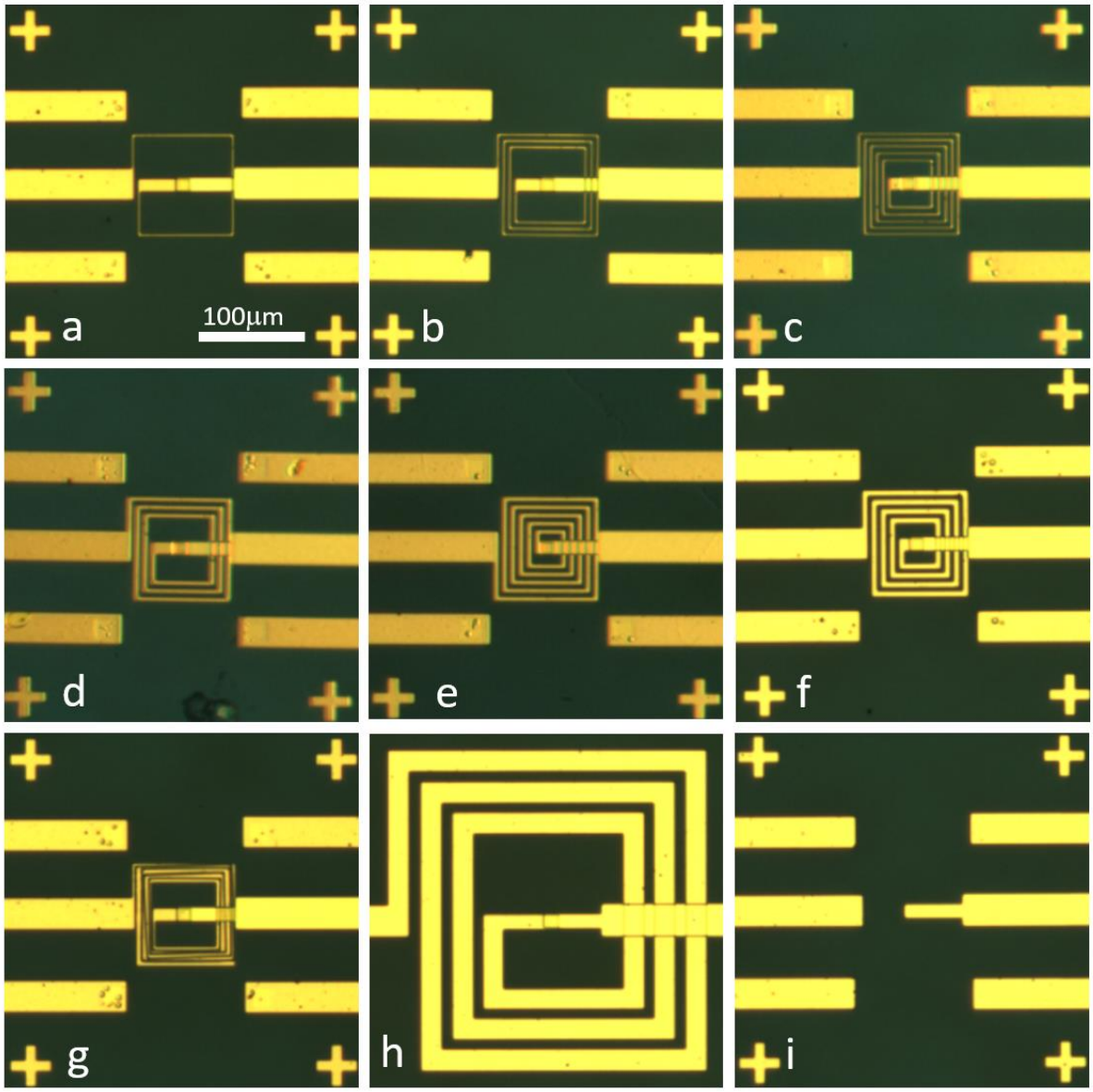

Fig. 7-10 Variation of microcoils.
Images courtesy of Corey Shih. The scale for all images are the same and the scale bar in a) applies to all. The coils in each panel are characterized by: line width (w), line separation (s) and number of turns (n_{turns}). a) w=2µm, s=4µm and n_{turns}=1; b) w=2µm, s=4µm and n_{turns}=3; c) w=2µm, s=4µm and n_{turns}=5; d) w=4µm, s=4µm and n_{turns}=3; e) w=4µm, s=4µm and n_{turns}=5; f) w=5µm, s=4µm and n_{turns}=4; g) w=2µm, s=2µm and n_{turns}=5; h) w=20µm, s=10µm and n_{turns}=3; i) no coil

Fig. 7-11a shows a 100nm thick copper square patterned on the microcoil to provide a test sample. The copper square is produced by patterning the bottom chip with EBL (see section 9.1). Since the chip is made of mostly an insulator (i.e. SiO_2), it would charge up during electron beam exposure and result in errors. To prevent charging, the chip is first coated with 5nm of copper. Subsequently, a 105nm thick copper square is created by electron beam lithography and evaporation. The 5nm thick film of copper is etched off (12s in 10mg/mL $Na_2S_2O_8$) and only the 100nm thick copper square remains on top of the SiO_2 capping layer. The metal lines near the four corners of the copper square each go to contact pads P1, P2, P3 and P4 in Fig. 7-9. To measure the sample resistance by van der Pauw, the metal lines can be extended to the copper square with additional fabrication. The squares on the metal lines are holes in the SiO_2 capping layer to access the metallic layer underneath. So far, we have demonstrated that it is possible to create test samples of copper. For future work, test samples of copper with thickness=100-500nm needs to be created for testing (see Fig. 7-8).

In the testing phase of the project, the RF response of the microcoil with copper squares should be characterized with a network analyzer. To interface the contact pads of the chips with the network analyzer input and output, the chips should be mounted on a printed circuit board (PCB). Fig. 7-11b shows the design of the PCB top surface. The bottom surface is covered with copper to serve as a ground plane. At the left and right edges, SMA (Amphenol 132255) connectors are mounted to interface with the network analyzer. The 0.109inch line, running across the middle, is the signal line where the width is calculated to produce a 50Ω microstrip line. The microcoil chip is mounted in the center of the PCB, where the signal line gaps, and contacted by wirebonding. The PCB is fabricated (Advanced Circuits) from 0.062inch thick FR-4 board with 1oz (i.e. 1.37mil thick) copper on top and bottom.

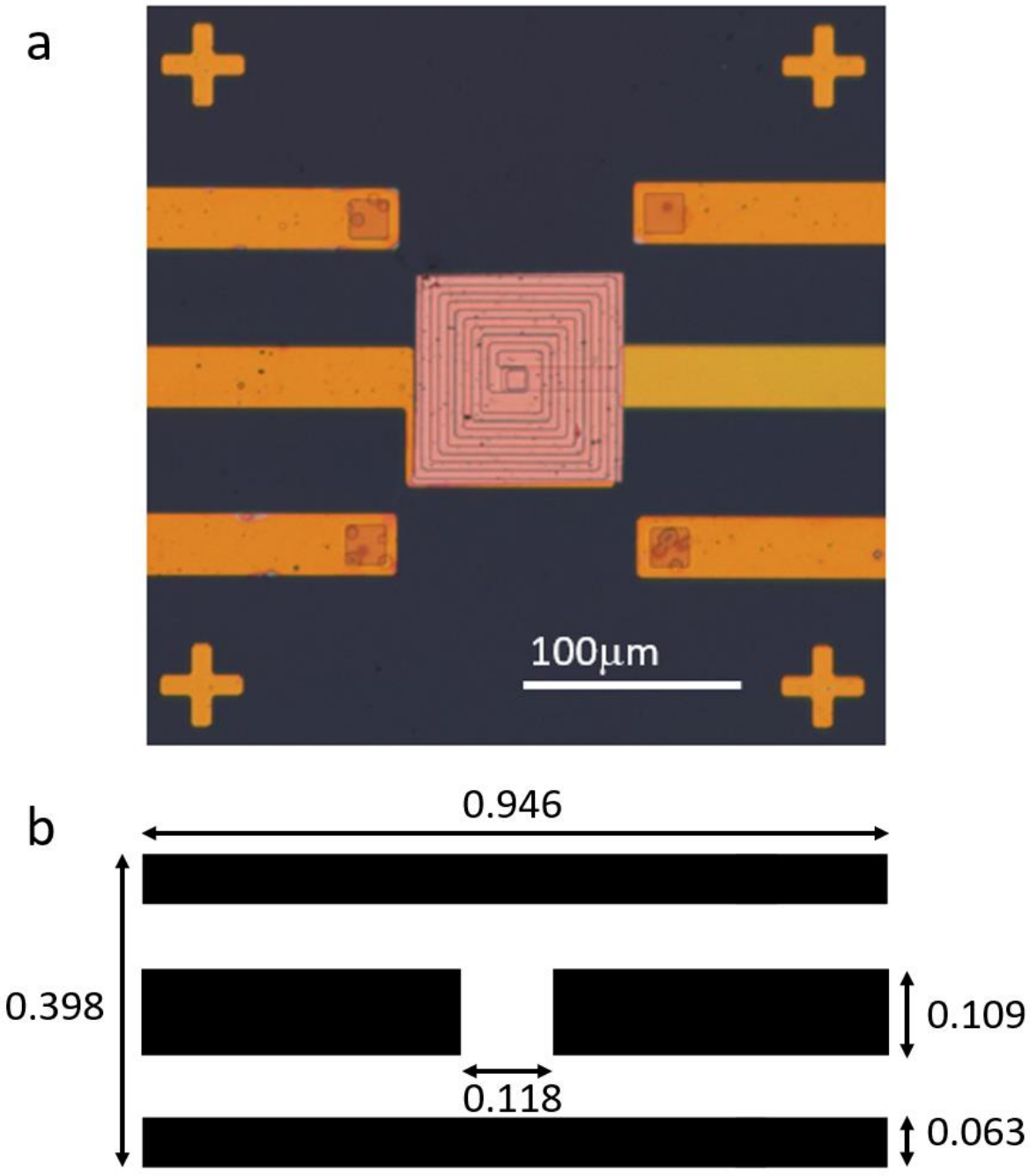

Fig. 7-11 Test sample for microcoil contactless measurement probe.
a) Image courtesy of Corey Shih. Copper square fabricated on top of microcoil by electron beam lithography. b) Printed circuit board design for mounting microcoil chips and interfacing to network analyzer. All dimensions are in inches. Copper covers the black parts.

Part II

Carbon nanomaterials based mechanical resonators

8 Carbon nanomaterials

Microelectromechanical sensors (MEMS) have enjoyed success in the creation of innovative micromachines [211] (e.g. micromotor, micro heaters [212] and micro chemical vapor deposition [213]) using lithographic techniques. At small length scales, the thermal and mechanical response times are fast and even display technology based on shutter motion is possible [214]. Further device innovation is anticipated from expansion of the fabrication domain to the nanoscale. Nanoelectromechanical sensors (NEMS) use the design concepts from MEMS to further scale down the components (e.g. nanomotor [215]). Although the MEMS/NEMS boundary is not strictly defined, NEMS often involves the incorporation of pre-synthesized nanomaterials as components.

Carbon nanomaterials, particularly carbon nanotubes (CNT) and graphene, are popular nanomaterials to use as NEMS components. They are mechanically strong and electrically addressable (i.e. metal, semiconductor or semimetal). In addition, they are chemically robust and compatible with most chemical processes in lithography.

At the "cm" size scale, the crystalline forms of pure carbon are either diamond or graphite. The two allotropes arise because the s and p orbitals of the carbon atoms hybridize differently [7,216]. Diamond is composed of sp^3 bonds, which yields a three dimensionally bonded crystal with strong bonds between atoms in all direction. Graphite is composed of sp^2 bonds, which yield a crystal made of stacked single atom thick layers. Within each layer, the carbon atoms are strongly bonded to their neighbors. The force between the layers are weak van der Waals forces, enabling layers to be peeled off as easily as seen with pencils.

At the nanoscale, sp^2 bonds give rise to a rich group of carbon nanomaterials (i.e. fullerenes, nanotubes and graphene). Theoretically, graphene (the single atom thick sheet in graphite) is the simplest building block among the sp^2 carbon allotropes and the other allotropes can be conceived by manipulating graphene, as shown in Fig. 8-1. When multiple layers of graphene are stacked on top of each other, graphite (bottom right) is obtained. When a small sheet is cut from graphene and rolled up into a tube, a carbon nanotube is produced (bottom middle). The graphene can be cut in a way that the piece rolls up into a ball-like molecule composed of hexagons and pentagons of carbon, called fullerenes (bottom left). The schematic in Fig. 8-1 is presented to simplify theoretical understanding and does not represent the synthesis mechanism. Before the experimental discovery of isolated graphene, graphene was a convenient theoretical construct for the band structure of sp^2 bonded carbon allotropes [24]. Each carbon allotrope was experimentally discovered in their isolated form and was not created out of graphene. Historically, graphite was known as a naturally occurring material and graphene was discovered [23] after fullerenes [217] and CNT [218,219]. The bonds in fullerenes and CNT are not purely sp^2, as the curvature introduces some strains to the bonds. The strained bonds facilitate chemical functionalization [220] and fullerenes have played an important role in the development of organic photovoltaics (see Chapter 15).

CNT can either be a single-walled (SW) CNT, which is as a single rolled up sheet of graphene, or a multi-walled (MW) CNT, which is made of multiple concentric cylinders fitting into each other. The SWCNT and MWCNT diameters vary, with the smallest SWCNT diameter ~0.4nm and largest MWCNT diameter ≥100nm [15]. With optimized synthesis conditions, very large aspect ratios are obtained (e.g. Ø5nm x 1mm MWCNT) [221]. A SWCNT is either a semiconductor or a metal depending on the direction, in which the graphene sheet is rolled up ("chirality of the tube") [15]. In contrast, all MWCNT are metallic.

The fundamental frequency of a mechanical resonator scales as $f_0 \sim \sqrt{\frac{E}{\rho_m}}\frac{t}{L^2}$, where E=Young's modulus, ρ_m=density, t=thickness and L=length [31]. Graphene has a high Young's modulus (E=1.0TPa) [222], low mass density (ρ_m=2200kg/m^3) [31] and is one atom thick (t=0.35nm). High frequency graphene mechanical resonators with f_0=70.5MHz have been demonstrated [31–33]. Table 8-1 compares the Young's moduli (E) between candidate materials for MEMS/NEMS use. Graphene and CNT have higher Young's moduli than materials that are commonly considered "hard" (e.g. SiC and diamond).

The light mass of carbon nanomaterials make them promising for highly sensitive mass sensors. For measurement of deposition rates in thin film deposition, a quartz crystal monitor measures the deposited mass of the material by the change in frequency of a vibrating membrane. The change in frequency of a vibrating beam depends on the change in mass as $\Delta f_0 = -\frac{f_0}{2m_0}\Delta m$, where m_0 is the mass of the beam [223]. A CNT is an excellent material for maximizing the f_0/m_0 ratio and has demonstrated sensitivity to weigh 0.40 gold atoms Hz$^{-1/2}$.

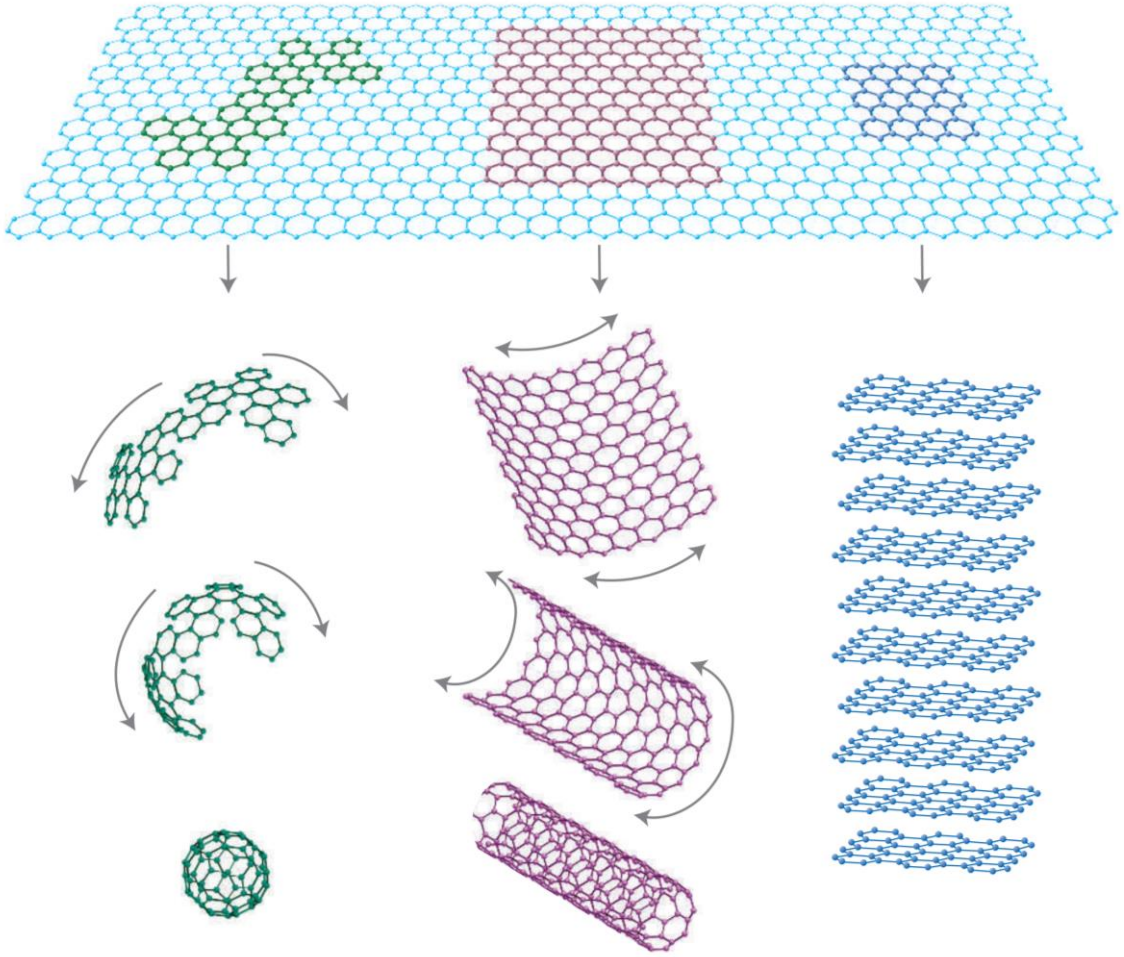

Fig. 8-1 sp^2 carbon allotropes.
Fig. 1, Geim and Novoselov [296]. Schematic of constructing fullerenes (bottom left), nanotubes (bottom middle) and graphite (bottom right) from graphene (top).

Material	E (TPa)	Reference
Graphene	1.0	[222]
CNT	0.27-1.47	
SiC	0.43	[297]
Ultrananocrystalline diamond	0.96	
ta-C	0.80	
Polysilicon	0.16	[242]

Table 8-1 Young's moduli of MEMS/NEMS materials.
Experimentally measured Young's modulus (E). CNT includes both single-walled and multi-walled carbon nanotubes. Wide range of the measured E are reported in literature. Other materials with desirable mechanical properties: silicon carbide (SiC), ultrananocrystalline diamond and hydrogen-free tetrahedral amorphous carbon (ta-C) are listed. Polysilicon is the most commonly used material for MEMS.

9 Fabrication techniques

Fabrication techniques for creating nanomechanical resonators are discussed. Electron beam lithography is relevant to other chapters, where electrical contacts are made to nanoscale samples. Techniques for creating suspended nanostructures are discussed with regard to concepts adopted from micromachining.

9.1 Electron beam lithography

Electron beam lithography (EBL) is used to electrically contact or control the shape of samples. Typically photolithography is limited to 2μm feature sizes and optical imaging is diffraction limited. Using the higher resolution of electron microscopy, EBL allows users to find and precisely align patterns to nanomaterials, providing "eyes" and "hands" for the manipulation of nanomaterials. Since exposure is controlled by the scan pattern of the electron beam, a mask does not need to be fabricated for each new pattern and makes EBL well-suited for versatile fabrication at the laboratory scale. EBL samples requires conducting substrates, since an insulator would accumulate charge from the electron beam and distort the beam path to uncontrolled directions. When patterning an insulator, it should be coated with a thin layer (e.g. ~3nm) of metal to prevent charging (see section 7.3).

EBL is performed with a scanning electron microscope (SEM, Sirion XL30, FEI), modified with a commercial beam controller for lithography purposes (NPGS, JC Nabity Lithography Systems). For EBL, requiring very small resolution, a dedicated EBL writer (e.g. crestec, Marvell Nanolab) is more suited. EBL is often complemented with photolithography: a substrate is first patterned with features of size >2μm and fabrication requiring higher resolution is continued by EBL. Contact pads of ~200 x 200μm and lines from the sample area to the pads are fabricated by photolithography to enable contact by probes or wirebonding. The contact pads are *not* actually "too large" for EBL. For writing small features, the small spot size with low beam current (~28pA) requires a long time for exposing a designated area. For writing large areas (but with lower resolution), a large spot size with large beam current (~2,800pA) can be used. A pattern with four contact pads are exposed in ~20min. Hence, EBL can create a complete device with contacts pads as long as only a few devices are needed. For wafer-scale fabrication, photolithography is much more time efficient.

Fig. 9-1 schematically illustrates the steps in EBL for placing an electrical contact on a nanomaterial. First the target nanomaterial is placed on a substrate (Fig. 9-1a). Typically, the substrate is a silicon chip covered with a layer of SiO_2 to provide an insulating platform for the sample. Silicon chips are frequently used in EBL for the following reasons: 1) it cleaves easily from wafers, 2) wafers are easily available from the semiconducting industry, 3) it is often doped to suitable conductivity, 4) it provides a smooth, flat surface and 5) impurity concentrations are well controlled. Electron beam resist (PMMA[16]) is deposited to cover the substrate and the nanomaterial (Fig. 9-1b).

Electron beam exposes the PMMA in a pattern specified by the design file (Fig. 9-1c). The electron beam cuts the bonds in PMMA and reduces the polymer to shorter units of lower molecular weight, which has a significantly higher solubility in developer than the unexposed PMMA. The developer[17] selectively removes the electron beam exposed PMMA and creates openings in the PMMA layer (Fig. 9-1d). The illustrated procedure is for positive resist (exposed parts open up) and negative resist (e.g. HSQ) would result in an inverse pattern, where the exposed parts remain and the unexposed parts are removed after developing.

During metal deposition, a thin film of metal forms on top of the PMMA but metal is deposited directly on to the nanomaterial and the substrate in areas, where the PMMA layer is

[16] 950 PMMA A4, MicroChem is deposited by spin coating at 3000rpm for 40s and baked at 170°C on a hot plate for 2min

[17] Immersed in 1:3 MIBK:IPA, MicroChem for 90s and rinsed with IPA and water.

open (Fig. 9-1e)[18]. Subsequently, the sample is immersed in acetone to dissolve the PMMA ("lift-off process"). The metal film on the PMMA peels off in solution and only the metal directly deposited on the substrate remains (Fig. 9-1f).

As illustrated in Fig. 9-2, it is important that the thickness of the metal film (t_{metal}) does not exceed the PMMA thickness (t_{PMMA}). When $t_{metal}<t_{PMMA}$ (Fig. 9-2a), acetone enters the gap between the top of metal on the substrate and the bottom of the metal on PMMA to dissolve the PMMA for a successful lift-off. If $t_{metal}>t_{PMMA}$ (Fig. 9-2b), the gap closes and acetone cannot access the PMMA layer. t_{PMMA} varies with spin speeds and composition (e.g. t_{PMMA}~200nm for the parameters described in footnote 16). For the same reason, the deposition method needs to be directional (e.g. electron beam or thermal evaporation) to avoid conformal coating. Practically, the walls of the PMMA opening has rounded corners, which means t_{metal} cannot actually approach the t_{PMMA} limit so closely. To fabricate patterns with thick films, t_{PMMA} is increased by spinning PMMA multiple time to layer them on top of each other. The deposited PMMA is baked only once at the end, as excessive baking could cross link the polymers and make them difficult to dissolve with acetone.

[18] For $NbSe_3$ nanoribbon devices (see section 6.1.1.1), the device is treated with nitrogen plasma after the step in Fig. 9-1d and immediately followed by metal deposition in Fig. 9-1e.

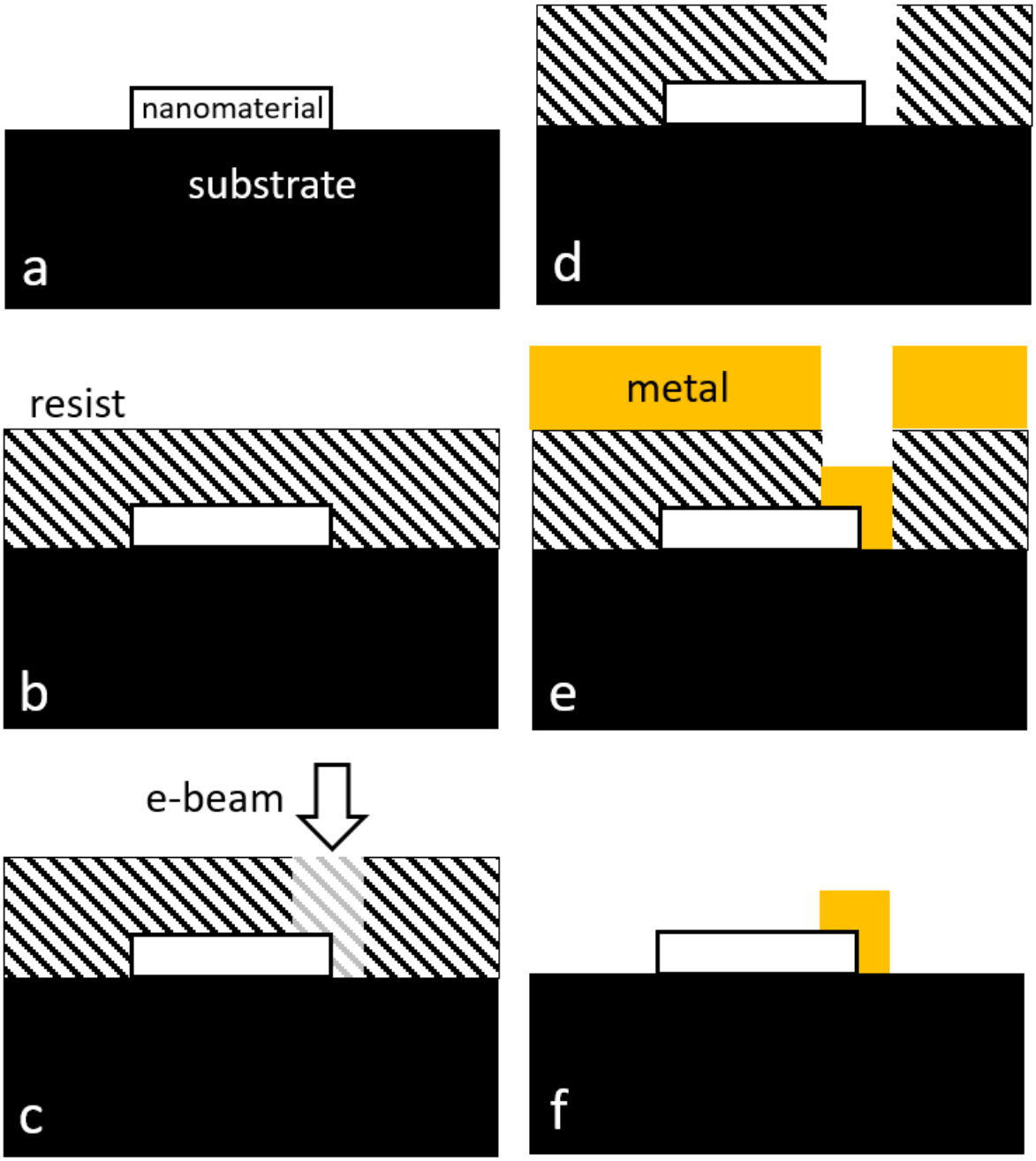

Fig. 9-1 Electron beam lithography steps.
a) Deposit nanomaterial on substrate. b) Coat with electron beam resist (PMMA). c) Expose pattern (aligned to nanomaterial) with electron beams. d) Develop exposed pattern. e) Deposit metal. f) Lift off metal.

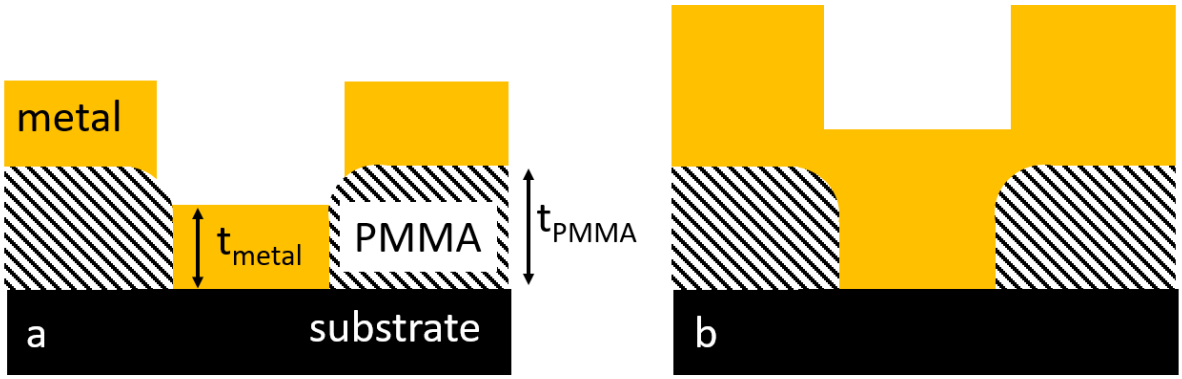

Fig. 9-2 Metal thickness for successful lift-off.
For thickness of metal film (t_{metal}) and thickness of PMMA (t_{PMMA}), a) $t_{metal}<t_{PMMA}$ allows acetone to enter into the PMMA layer (successful lift-off) and b) blocks access to PMMA layer (failed lift-off).

Fig. 9-3 shows the procedure for aligning exposure patterns to nanomaterial location. For the first step, an SEM image of the substrate with the deposited nanomaterial is obtained (Fig. 9-3a). In this example, the substrate is a Si/SiO_2 chip pre-patterned with metal, using photolithography (bright shapes). The 2μm wide lines labeled 1-8 go to contact pads, located outside the field of view. The four pairs of "L-shaped" objects are alignment markers. The target nanomaterials are MWCNT circled in red.

When used for imaging, the SEM scans the whole field of view with the electron beam and creates an image based on the readings from the detector. For lithography, software control of the beam scanning area restricts electron beam exposure to pre-programmed shapes at specified locations in the field of view. The exposure pattern is controlled by a file designed in a CAD program (Fig. 9-3b). The polygons, filled with a yellow stripe pattern, are areas to be exposed. During the exposure process, the field of view is adjusted, so that the "L-shaped" green polygons in the design file and the alignment markers on the substrate overlap. The software writes the pattern at the correct location based on its relative location to the green polygons. When finding the alignment markers, we cannot image the targeted area for writing, since it would expose the entire field of view. Instead, only the vicinity of the expected locations of alignment markers are imaged (alignment windows, outlined by green dashed lines). When optimized, the limited exposure during alignment is negligible and the alignment windows do not open up after developing.

After developing, metal deposition and lift-off (Fig. 9-1d-f), the specified polygons in the design file are realized as metal electrodes (Fig. 9-3c). Fig. 9-3d shows a magnified view of one of the targeted MWCNT. As intended in the design file, the MWCNT is contacted on one end with the bottom electrode, facing an electrode at the opposite side and approached by another electrode from the side. The image demonstrates the precise control over electrode geometry and position with respect to a nanomaterial, enabled by EBL.

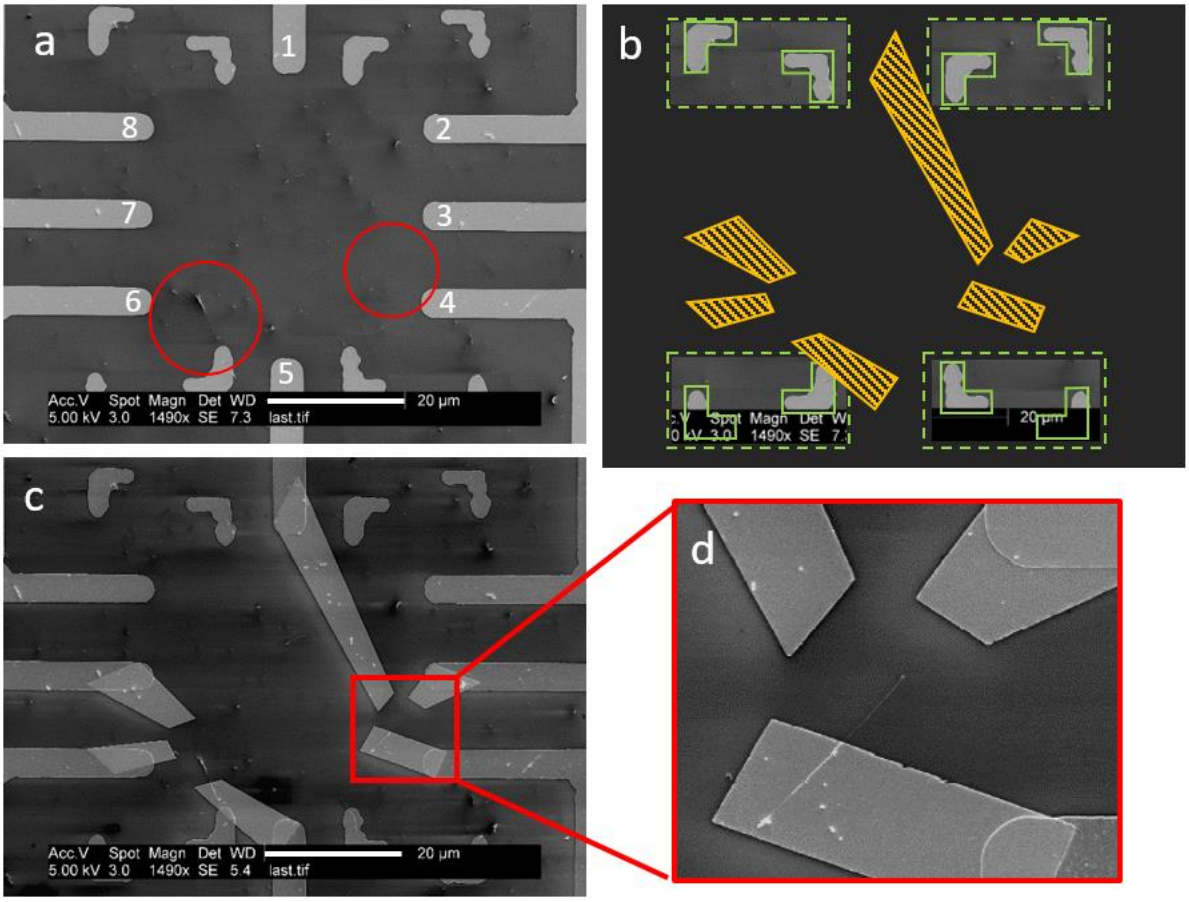

Fig. 9-3 Aligning patterns to nanomaterials.
Procedure for precisely aligning lithographically fabricated features to nanomaterials. a) SEM image of CNT (circled in red) deposited on a substrate before electron beam lithography. b) CAD pattern to control electron beam exposure. Alignment windows (green, dashed outline), alignment markers (green, outline) and exposure patterns (yellow, hatched polygons) are shown. c) Substrate after electron beam lithography according to the CAD pattern and metal deposition. d) Magnified view of CNT with metal electrodes.

9.2 Suspension of nanostructures

Suspended structures are lithographically fabricated with micromachining techniques developed for MEMS. As shown in Fig. 9-4a, an etch layer is the topmost layer of the substrate and the structure to be suspended rests on top of the etch layer. An opening is created in the etch mask by lithography (Fig. 9-1a-d). Etchant [224,225] enters through the opening and etches the etch layer underneath the structure ("release"). Fig. 9-4b shows the suspended structure after release. The etchant does not have any effect on the etch mask material, but the structure after etch mask removal is shown for clarity.

At the micro/nano-scale, capillary forces of drying liquids [226] are strong enough to destroy suspended nanostructures. When a suspended structure is taken out of a liquid, some of the liquid collect in pits or adhere to the surface by surface tension. When drying, the menisci of the liquid moves and pulls suspended structures with it, as illustrated in Fig. 9-4c. To avoid capillary forces, the fabrication process is often designed to make release the last step and the release is performed with a dry etch technique, using either etchants in the vapor phase (e.g. HF vapor, XeF_2) or microwave generated plasma (e.g. reactive ion etcher). HF is commonly used as a wet etchant but there are instruments, which enable HF dry etching by releasing controlled amounts of HF vapor in a chamber (primaxx, Marvell Nanolab). Ethanol is mixed with the HF vapor to capture water, which emerge as a byproduct of the etching reaction.

When using liquid etchants or immersing in liquid after release, suspended structures are dried by critical point drying (CPD). The P-T phase diagram in Fig. 9-5 explains the principle of CPD. The menisci develop when undergoing the liquid-vapor transition across the liquid-vapor phase boundary (solid line). However, the phase boundary ends at a critical point. By going around the critical point in the supercritical region, the liquid is dried without the formation of a meniscus. The standard CPD instruments uses the critical point in CO_2. The device with suspended structures is first immersed in methanol and cooled to exchange methanol with liquid CO_2. Methanol is chosen for its miscibility with liquid CO_2.

Etching processes in micromachining are generally divided into anisotropic and isotropic etching techniques [224,225]. Fig. 9-6a shows anisotropic etching, where etching only occurs in the downward direction and the etched pit does not widen beyond the opened area of the etch mask. In contrast, Fig. 9-6b shows isotropic etching, where etching progresses sideways as well. An undercut below the etch mask opening is created. Most anisotropic etching acquire some degree of isotropic etching quality due to non-idealities. When designing an etch mask pattern, the undercut with respect to etch depth must be considered. KOH etching of silicon is an interesting intermediate between the etching schemes shown in Fig. 9-6a,b, as it selectively etches the (111) plane of silicon. It is often used to create microstructures with silicon nitride (Si_3N_4) windows by etching through ~500μm silicon from the bottom. Fig. 9-6c shows the etch area defined by an etch windows at the bottom. The top is covered by Si_3N_4, which does not get etched by KOH. The etch progresses at a 54.7^o angle and opens up a window at the top.

Fig. 9-7 shows failed fabrication attempts, which highlight the importance of micromachining concepts discussed in this section. Fig. 9-7a,b show structures, which were released by wet etching and dried without CPD. The cantilevered metal films were pulled down by capillary forces (see Fig. 9-4c) and stuck to the bottom. In Fig. 9-7c, the undercut in the etch process was too large and etched the support underneath a significant length of a metal line. The mechanical stress built up during metal deposition caused the metal to peel back.

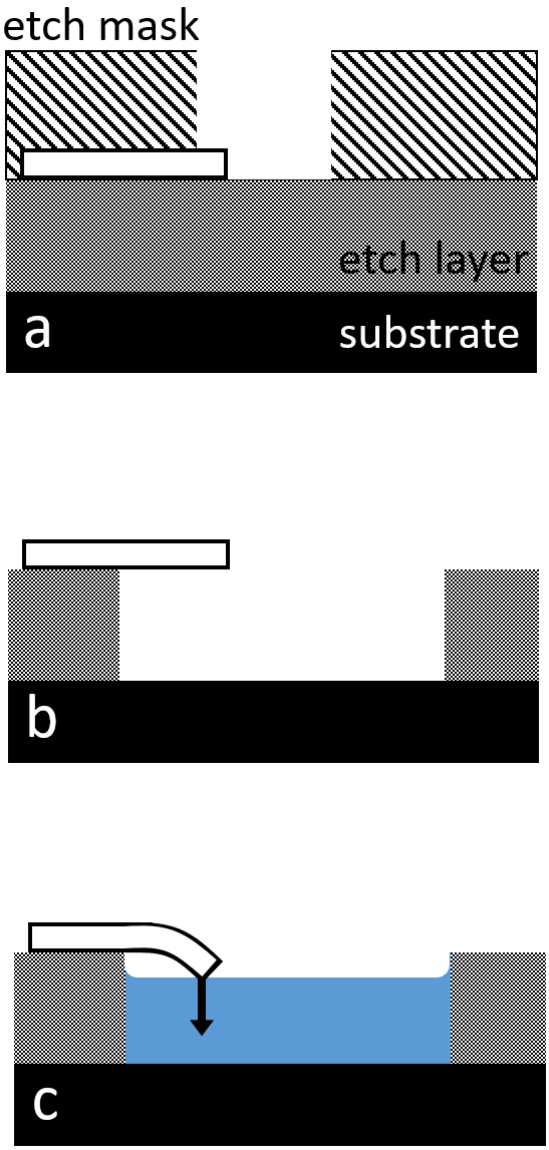

Fig. 9-4 Suspending micro/nano-structures.
a) Structure before suspension (release). b) Suspended structure after release. c) Capillary force while drying from wet etching.

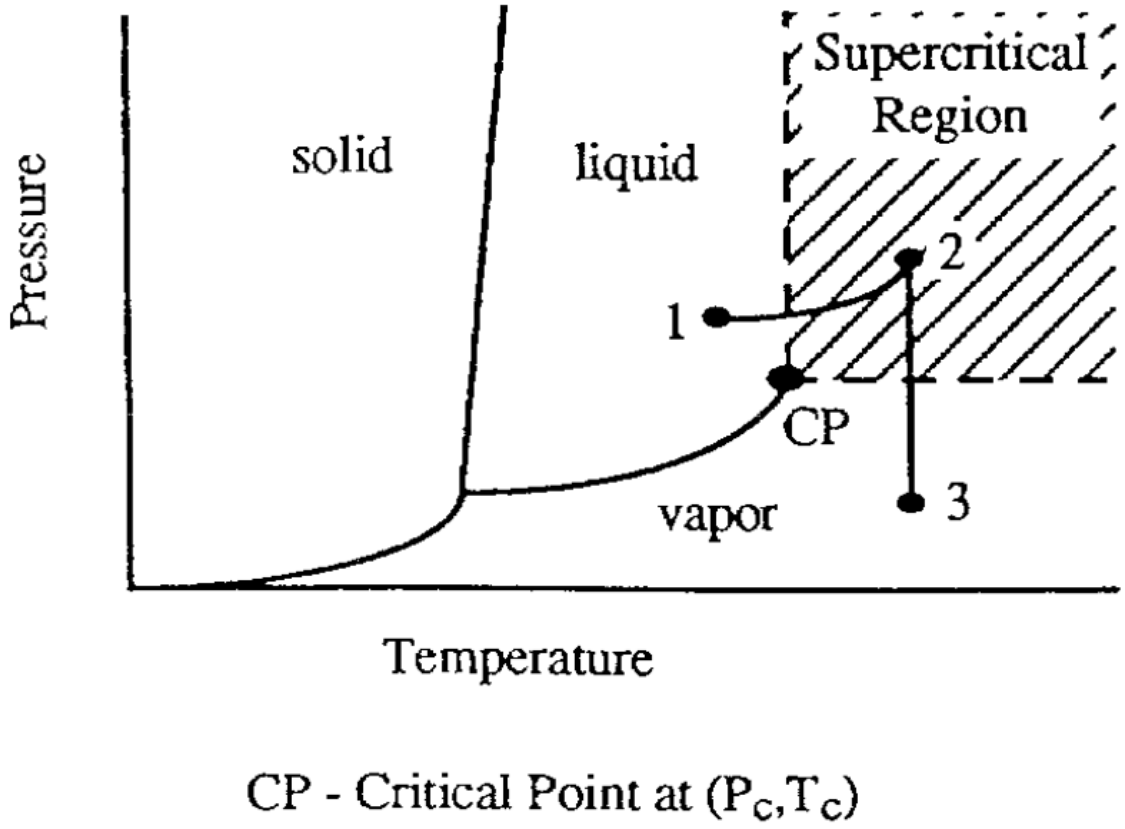

Fig. 9-5 Critical point drying.
Fig. 11, Bustillo, Howe and Muller [226]. Starting from a liquid (1), the system is taken to the supercritical region (2) and turned to vapor (3). This path of liquid-vapor conversion avoids the formation of a meniscus.

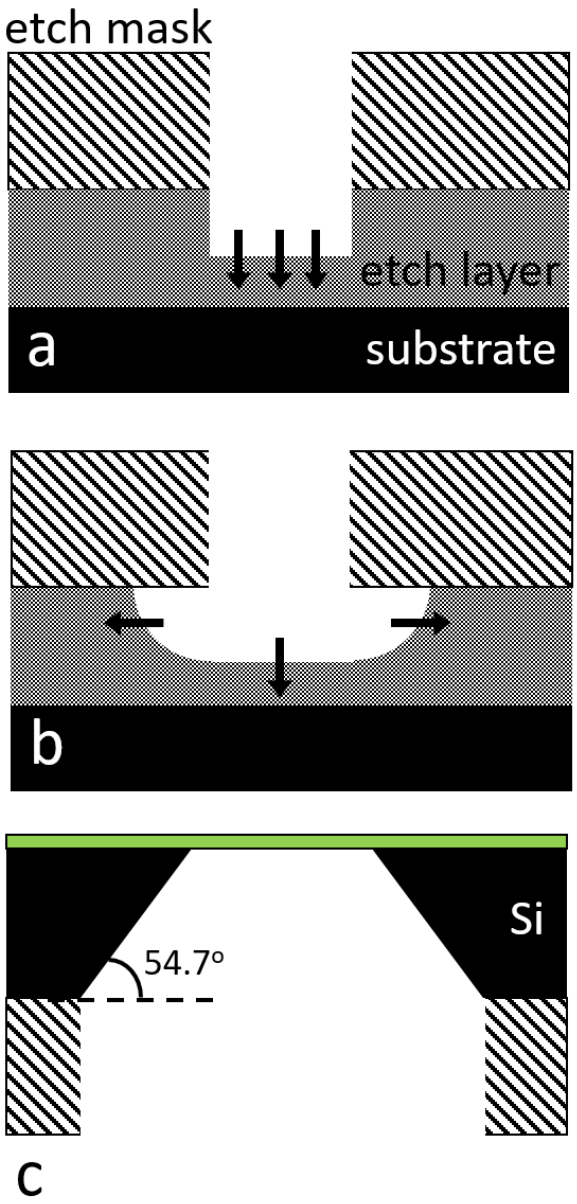

Fig. 9-6 Etching directions in micromachining.
Common types of etching in micromachining. a) Anisotropic etching. b) Isotropic etching. c) KOH etching of silicon.

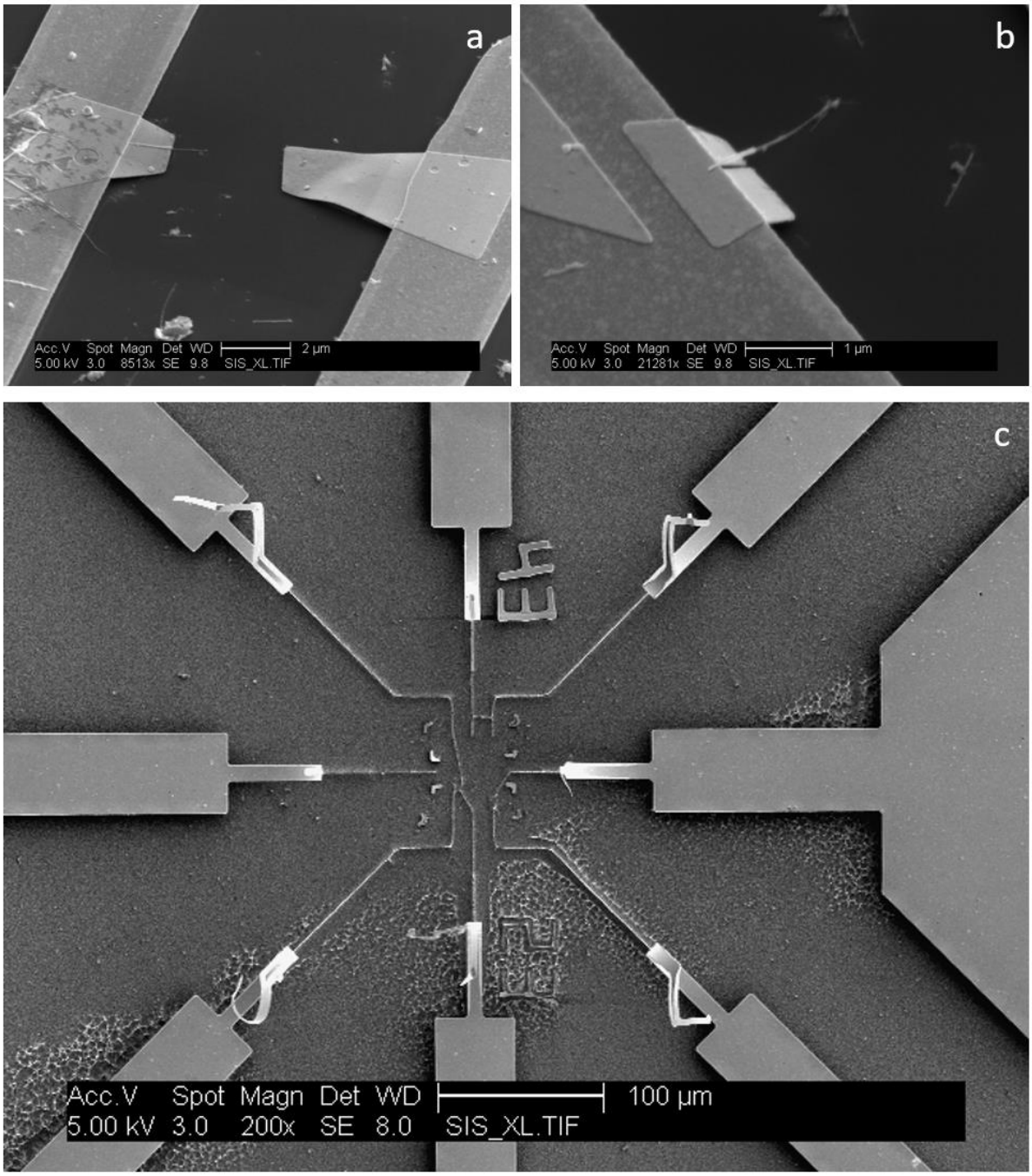

Fig. 9-7 Collapsed and over-etched devices.
a, b) Collapsed metal layer as a result of drying without CPD. c) Delaminated metal layer from excessive undercuts during etching.

10 Field emitting CNT nanomechanical resonator

Most nanomechanical resonators involve nanomaterials clamped on two ends and driven to resonance by a capacitively coupled gate or irradiated by laser light. The CNT resonator discussed in this chapter is a singly clamped CNT. The system strongly couples to electromagnetic fields by field enhancement, characteristic of one dimensional nanostructures, and enables readout of the mechanical motion via modulation of the field emission current. The system realizes an interesting coupling between high frequency nanomechanical resonator, nanoscale antenna and tunneling electrons.

This chapter introduces field emission in relation to carbon nanotubes. Results from previous studies on the singly clamped CNT resonator are summarized (e.g. nanotube radio, atomic and self-oscillation). Benjamín Alemán, a fellow graduate student in the Zettl Group (PhD 2011) began fabrication of an integrated device with a singly clamped CNT nanomechanical resonator. Aidin Fathalizadeh, a fellow graduate student in the Zettl group (PhD 2016), and I continued developing the fabrication method but the project is still in progress as we have encountered obstacles due to high voltage biasing. The devices were also developed to provide samples for a collaboration with Christophe Goze-Bac[19] for enhancement of nuclear magnetic resonance sensitivity with nanoantennae (see section 2.6, Fathalizadeh [227]).

[19] Directeur de Recherche CNRS, BioNanoNMRI, L2C, Université de Montpellier

10.1 Field emission

The work function (φ) of a metal is the energy difference between the Fermi level (E_F) in the metal and the vacuum energy level. For an electron to leave the metal, it must have an energy (E_{e^-}) which overcomes the work function. The model in Fig. 10-1 shows that an electric field (E) makes the energy barrier triangular. The barrier height linearly decreases as we increase the distance (x) from the metal surface. For a strong electric field, the electron tunnels through the barrier into vacuum, despite $E_{e^-} < \varphi$ ("field emission").

Fig. 10-2 shows a CNT of length h and diameter 2ρ in contact to an electrode held at an electric potential V=0. Facing the CNT tip, there is a counter-electrode at $V=V_a$. The counter-electrode is a distance d away from the electrode and *not* in direct contact with the CNT. There is an electric field $E_m=V_a/d$ between the two electrodes. The CNT is effectively a sharp conducting needle that protrudes from a conducting plate and the electric field is enhanced to $E'=\gamma E_m$ at the CNT tip, where $\gamma>1$ is the field enhancement factor. For E' of sufficient strength, electrons from the CNT field emits and are collected at the counter-electrode, resulting in field emission current. γ is calculated by [228]

$$\gamma = 3.5 + \frac{h}{\rho} + O\left(\frac{h}{d}\right)^3 \qquad \text{Eq. 10-1}$$

The result for $h<<d$ can also be derived analytically by using image charges. CNT are good field emitters, as a MWCNT of h=1μm and ρ=10nm results in γ~100. The field emission current is calculated by the Fowler-Nordheim equation [229]

$$I = c_1(\gamma E_m)^2 \exp\left(-\frac{c_2}{\gamma E_m}\right) \qquad \text{Eq. 10-2}$$

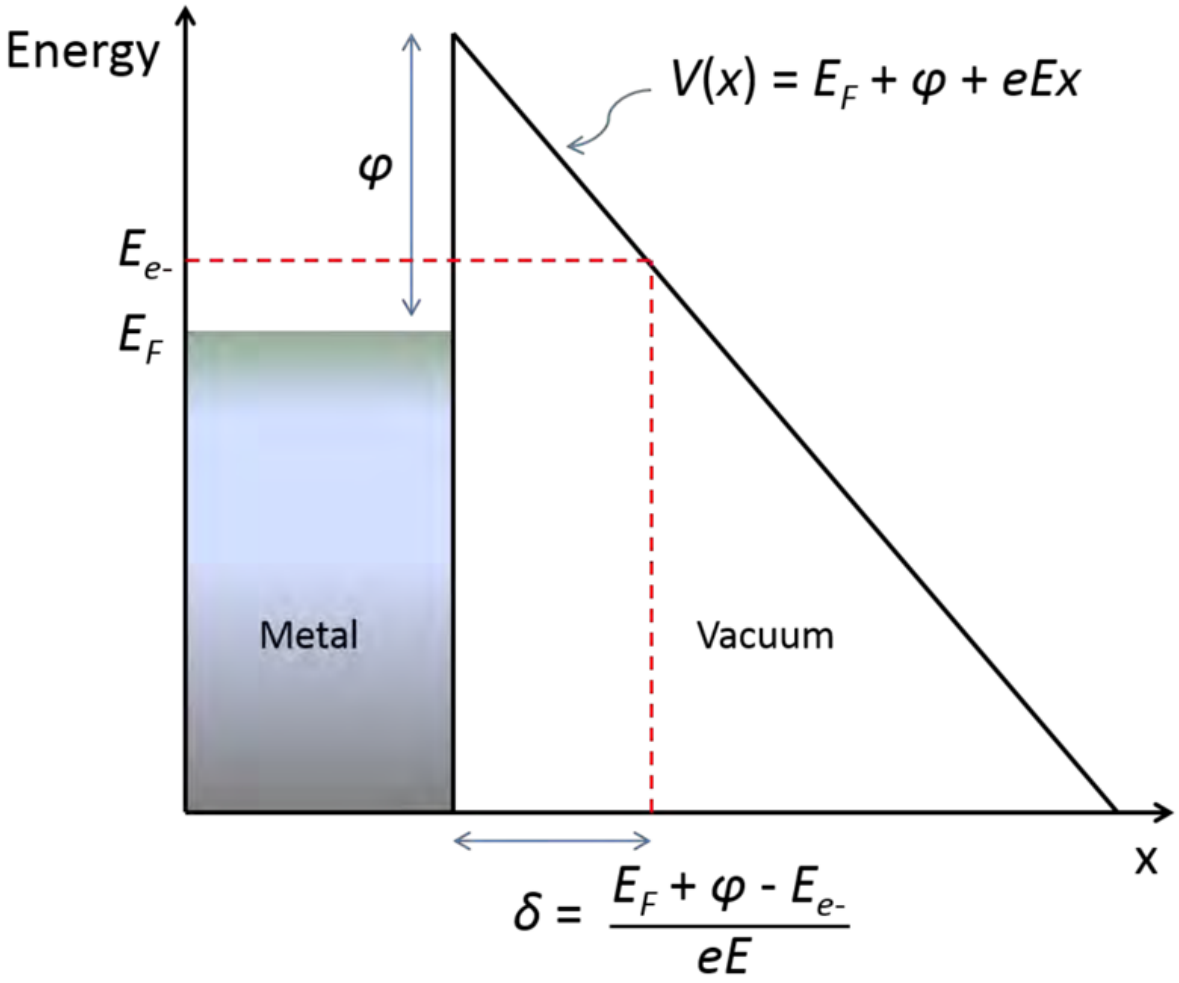

Fig. 10-1 Energy barrier for Fowler-Nordheim tunneling.
Fig. 2.1, Fathalizadeh [227]. Electric field (E) modifies the tunneling barrier height (V) into a function which linearly decreases with distance (x) from the metal surface. This model is used for the derivation of the Fowler-Nordheim tunneling equation. The Fermi energy (E_F), work function (φ) of the metal and the energy of the electron (E_{e-}) are shown.

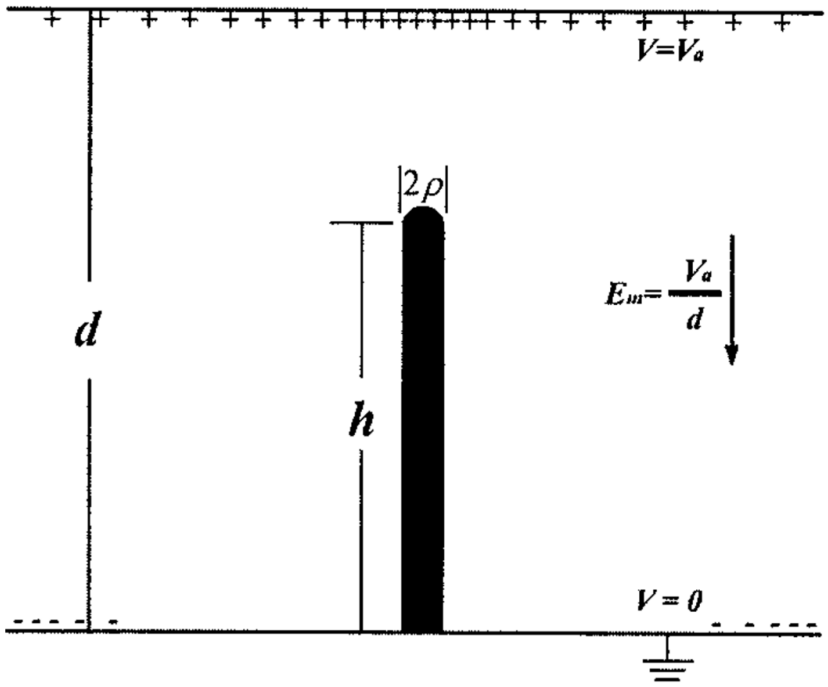

Fig. 10-2 Geometry for field enhancement calculation.
Fig. 1, Wang *et al*. [228]. A CNT is modeled as the black bar of length *h* and diameter 2ρ. The bottom line is the electrode in contact with the CNT and the top line is the counter-electrode, located a distance *d* away from the bottom electrode.

10.2 Nanomechanical resonator

Readout of nanomechanical resonator motion has been successfully demonstrated with capacitive coupling [31,230], optical interferometry [33] and piezoelectric coupling [231]. The field emission current of singly clamped CNT provides another surprising method of detecting nanomechanical motion.

Fig. 10-3a shows the schematic for the nanotube radio [229]. The field enhancement accumulates charge at the tip of the nanotube, which couples to electromagnetic fields. A field oscillating at the same frequency as the mechanical resonance frequency (ω_c) of the cantilevered CNT excites large amplitude mechanical oscillations. The field enhancement factor (γ) at the tip of the CNT is sensitive to the distance from the electrode in contact (h). Mechanical motion modulates h, and hence γ, which modulates the field emission current (Eq. 10-2). As an antenna, the CNT amplifies and modulates the RF signal to readout the RF signal amplitude as dc current.

Fig. 10-3b shows a TEM images of a CNT connected to a metal on the right and facing a counter-electrode on the left (not shown in image). The structure is prepared inside a TEM with a piezomanipulator and observed *in situ*. The CNT does not move when the RF excitation is off resonance (top image) and oscillates when on resonance. Keeping one CNT end free (i.e. not restricting its motion with a second clamp) is important for the observed large amplitude oscillations. The resonance frequency is in the 10-400MHz range. Frequency is fine-tuned by controlling the tension of the CNT with the voltage bias. For coarse-tuning, the CNT shortens when it is strongly biased to field emit at large currents.

Further study in the TEM found that the CNT executes sustained self-oscillations *without* RF excitations when the counter-electrode approaches it from the side [232]. Fig. 10-4 shows the vibrating CNT in the TEM when the counter-electrode (emerging from bottom of image) is biased at 40V with respect to the CNT. While voltage biased, field emission current of 0.1-1μA from the CNT is detected. The CNT for a 0V bias does not oscillate, as shown in the inset. The mechanism behind oscillations is fundamentally different from the nanotube antenna (Fig. 10-3a), since oscillations depend only on dc electric fields. The study proposes a model based on an instability, which occurs in the balance between the CNT's mechanical restoring force and electrostatic forces.

The high fundamental frequency of a nanomechanical resonator enables the ground state of the mechanical motion to be reached by cooling to temperatures achievable by current refrigeration technology [230,233]. Near the ground state, the resonator motion acquires quantum mechanical properties, even though the resonator is a classical object at high temperature. Ground state cooling has been successfully demonstrated with an aluminum nitride based resonator [231] and the field has been opened up for exploring the effects of coupling the quantum mechanical resonators with various physical systems. The singly clamped CNT resonator is an interesting system to study for its coupling of mechanical motion to quantum tunneling.

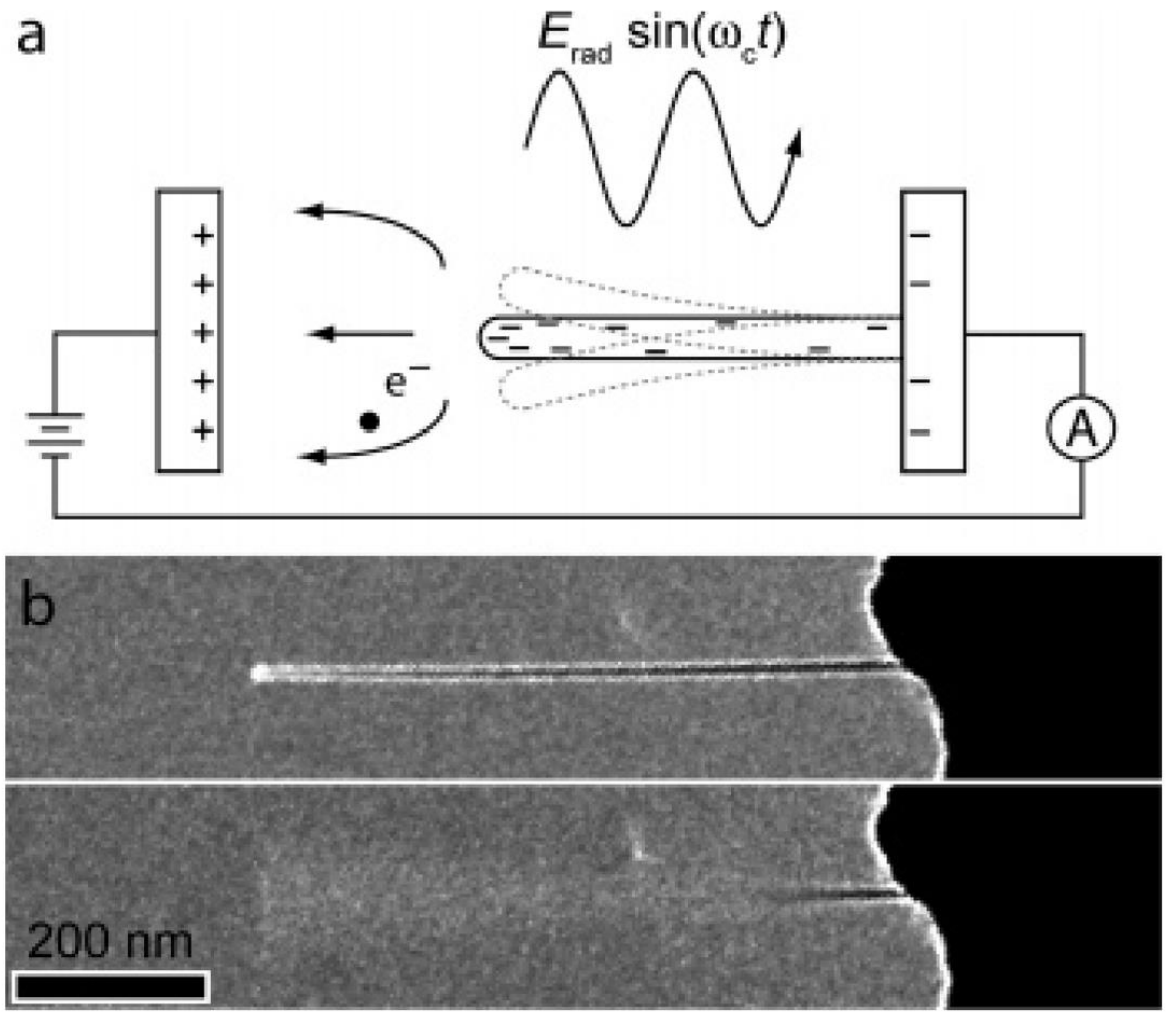

Fig. 10-3 Singly clamped CNT mechanical resonator.
Fig. 2, Jensen *et al*. [229]. a) schematic of the oscillation mechanism of the mechanical resonator. b) CNT viewed in TEM at off resonance (top panel) and on resonance (bottom panel).

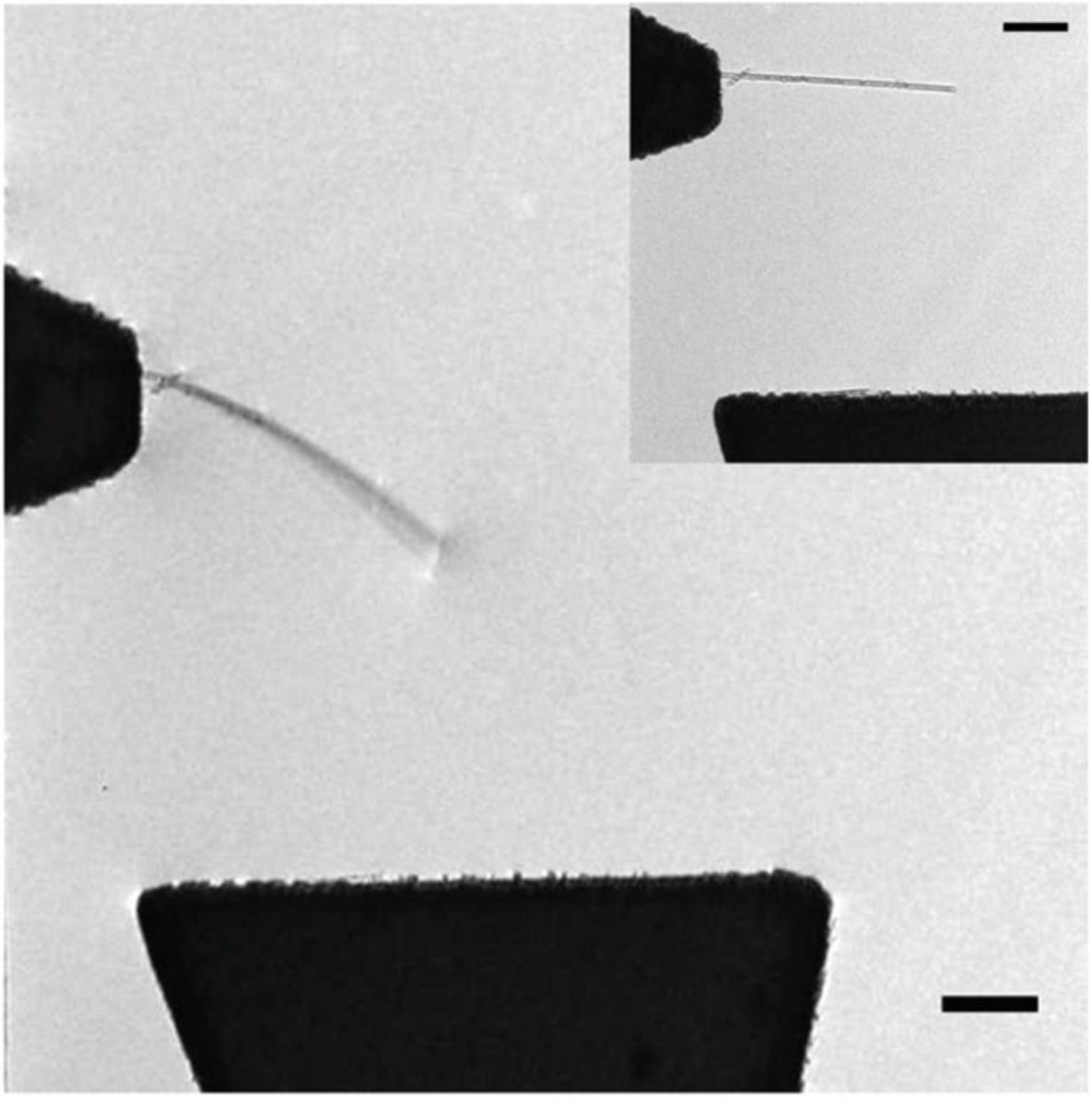

Fig. 10-4 Self-oscillating CNT mechanical resonator.
Fig. 5b, Weldon *et al*. [232]. Scale bar=1μm. TEM image of self-oscillating CNT at 40V bias. Lithographically fabricated electrodes contact the CNT and approach it from the side. Inset: static CNT at 0V bias.

10.3 Device integration

In contrast to the system assembled by a piezoelectric manipulator inside the TEM, the system shown in Fig. 10-4 is fabricated by lithographic techniques prior to loading into the TEM. As a nanofabricated device, the electrode geometry can be more precisely controlled during fabrication and be preserved, while transporting the sample across many characterization techniques. An integrated device allows multiple biases to be introduced simultaneously at multiple electrode locations. The multiple bias geometry is interesting for exploring parametric amplification and noise squeezing [234–236].

To be compatible with TEM, the sample needs to be suspended over a hole, in which the electron beams can go through unobstructed. Fig. 10-5 shows an optical image of the chip with a silicon nitride fabricated by photolithography [237]. The yellow polygons are gold contact pads that provides electrical connection window region in the center, shown in the magnified view. The square in the middle of is a silicon nitride (Si_3N_4) window of 10-200nm thickness. The silicon underneath the Si_3N_4 has been etched down to the bottom of the chip, resulting in a side view similar to Fig. 9-6c.

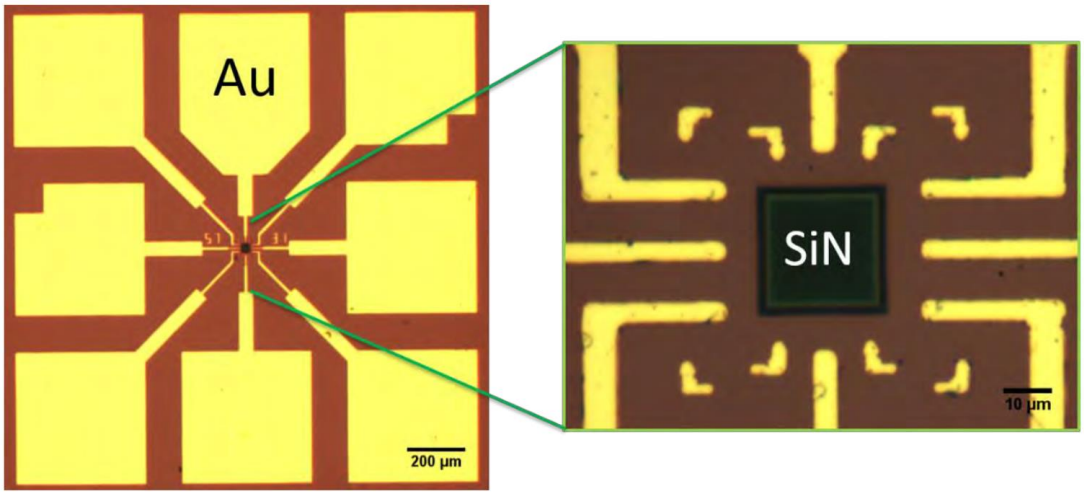

Fig. 10-5 Silicon nitride (Si_3N_4) window chips.
Fig. 2.8, Fathalizadeh [227]. At the center of the chip, a silicon nitride window (10-200nm thick) is surrounded by lines which go to the 6 contact pads (shown in low magnification view). CNT are located on the window (labeled "SiN") and contacted by EBL (see Fig. 9-3). After etching the silicon nitride, features in the window area are suspended over a hole, which goes completely through the whole chip.

MWCNT are deposited on the Si_3N_4 window chip by spin coating from liquid dispersion (10 x10μL drops, while spinning at 2000rpm). Arc-grown MWCNT from Henry Garcia, a former graduate student in the Zettl group, are used, as they contain very few structural defects. The CNT are partially burned while monitoring with thermogravimetric analysis to remove amorphous carbon and dispersed in IPA by sonication. The dispersion is sonicated for ~1min, when left without agitation for >1/2 day to redisperse the CNT. The concentration and deposition conditions are adjusted to place 1-3 MWCNT of 1-2μm length in the Si_3N_4 window region. The deposited MWCNT are located with an SEM image and electrodes, aligned to the MWCNT, are fabricated by EBL (see section 9.1). At the final step, the Si_3N_4 is etched with a reactive ion etcher (200W, 30s, 25sccm SF_6) to produce the CNT and electrodes suspended over a hole. Two-probe devices, with CNT contact electrode and the counter-electrode facing each other, and three probe devices, with a side gate, (see Fig. 9-3d) are fabricated.

Fig. 10-6 shows the I(V) curve of a fabricated device, measured at $P<5\times10^{-7}$Torr[20]. The device show increasing current with voltage, reaching 1μA at ~94V. To distinguish the current from leakage currents, the device is measured again with the voltage bias polarity reversed, which showed I<0.1nA up to -100V. The response is consistent with electrons field emitting from the CNT. For the limit where the counter-electrode is infinitely far away, field emission only occurs when electrons field emit from the CNT to the counter-electrode. For the opposite voltage bias polarity, the lower field enhancement factor of the counter-electrode does not enable electrons to tunnel from the counter-electrode to the CNT. The red line is the fit to the Fowler-Nordheim equation (Eq. 12-4) with fit parameters $c_1=8.9\times10^{-4}A/V^2$ and $c_2=1.5\times10^{11}V/m$. Compared to the fit parameters ($c_1=3.4\times10^{-5}A/V^2$ and $c_2=7.0\times10^{10}V/m$) in Jensen *et al.* [229], c_1 is significantly higher for us and c_2 is on the same order as Jensen *et al.*

[20] Desert Cryogenics TTP4 vacuum probe station and Keithley 2410 source-measure unit.

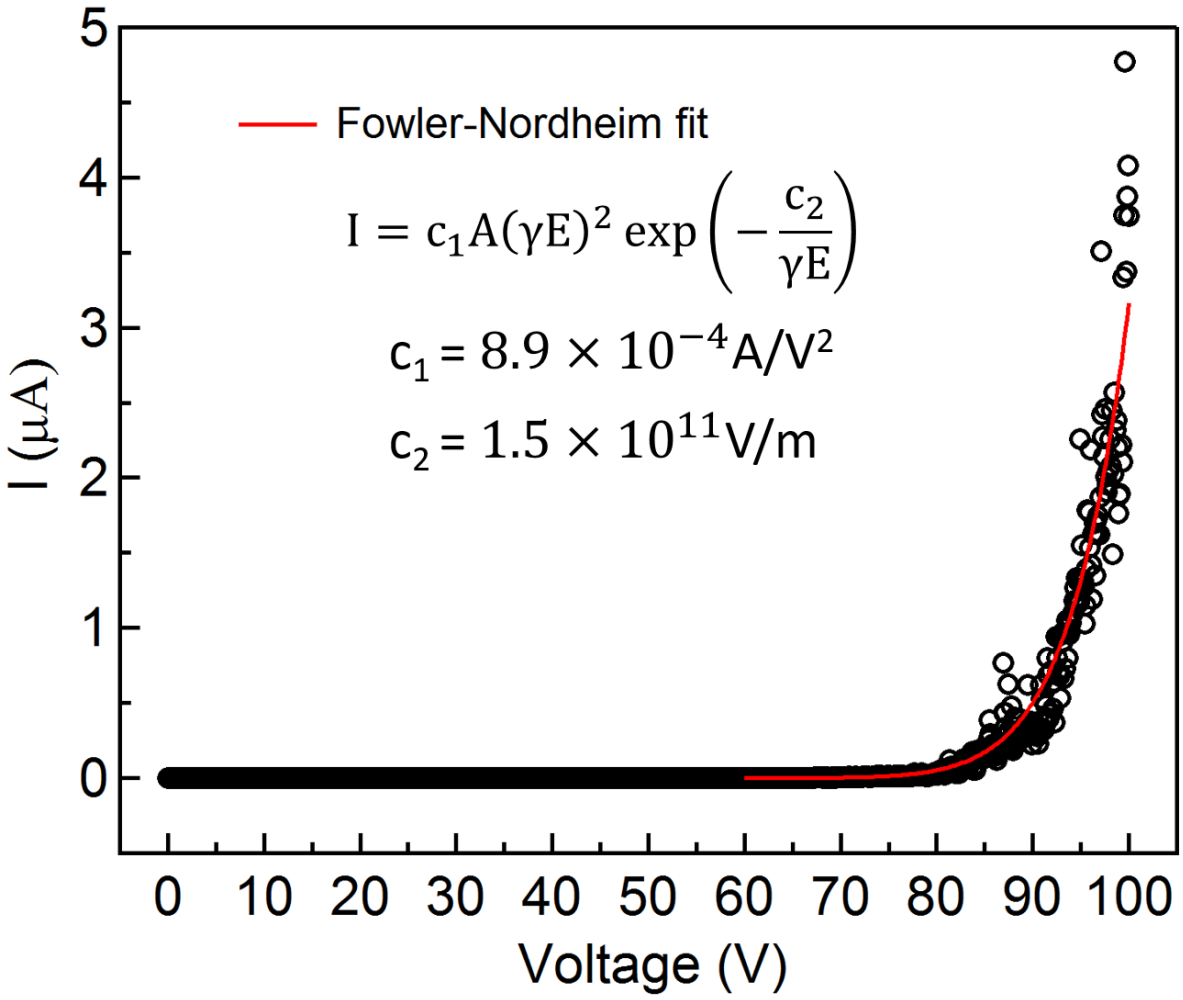

Fig. 10-6 Field emission I(V) curve.
Singly clamped CNT shows current increase with voltage, consistent with the Fowler-Nordheim equation (red line). I<2nA with reversed bias polarity.

The device fabrication does not produce field emitting devices with high yield. Visual inspection with the SEM shows the electrode alignment and release succeeds with high yield. However, many devices show similar current response on the order of ~1μA for both positive and negative voltage biases. In addition, large current spikes appear during voltage sweeps as shown in Fig. 10-7. Two large spikes at 84, 95V appear on increasing voltage (black line). There is a large hysteresis between increasing and decreasing voltage sweeps, in which the current during decreasing voltage sweep is greater, possibly due to increased prevalence of the voltage spikes.

At first, the current spikes were thought to be signatures of contaminants desorbing from the CNT, while it is heated with large field emission current. However, continued operation results in damage to the device. Fig. 10-8 shows and SEM image of a damaged chip. The damage appears to be caused by running excessive current and occur at the metal traces leading to the sample area. Surprisingly, the sample area is completely undamaged. Damage appears on the 20μm wide line at the bottom left corner but the narrower 5μm and 2μm lines are unaffected.

The excessive current is attributed to current leakage from the conducting silicon underneath the Si_3N_4 layer. During high voltage bias, the uncontrolled voltage difference between the silicon and the metal layer results in leakage of large currents caused by dielectric breakdown of the Si_3N_4. The Si_3N_4 thickness in the damaged devices are 20-50nm. To enhance the dielectric strength, devices with 200nm thick Si_3N_4 are fabricated on intrinsic silicon (no dopants). However, the 200nm thick Si_3N_4 devices contained shorts between the metal layer to the silicon with leakage current reaching >1nA at V=30V on the most insulating devices.

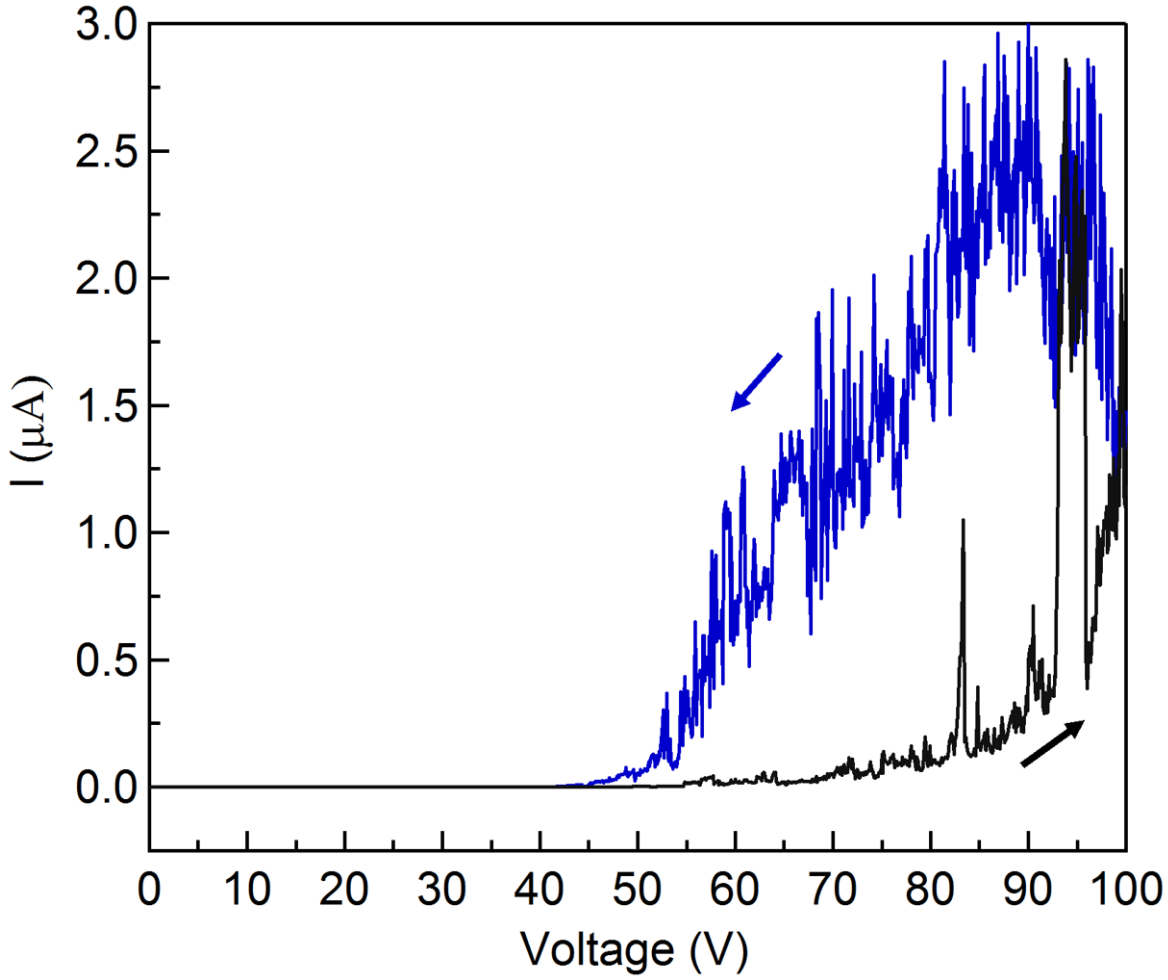

Fig. 10-7 I(V) curve hysteresis.
Voltage sweep up (black) and down (blue).

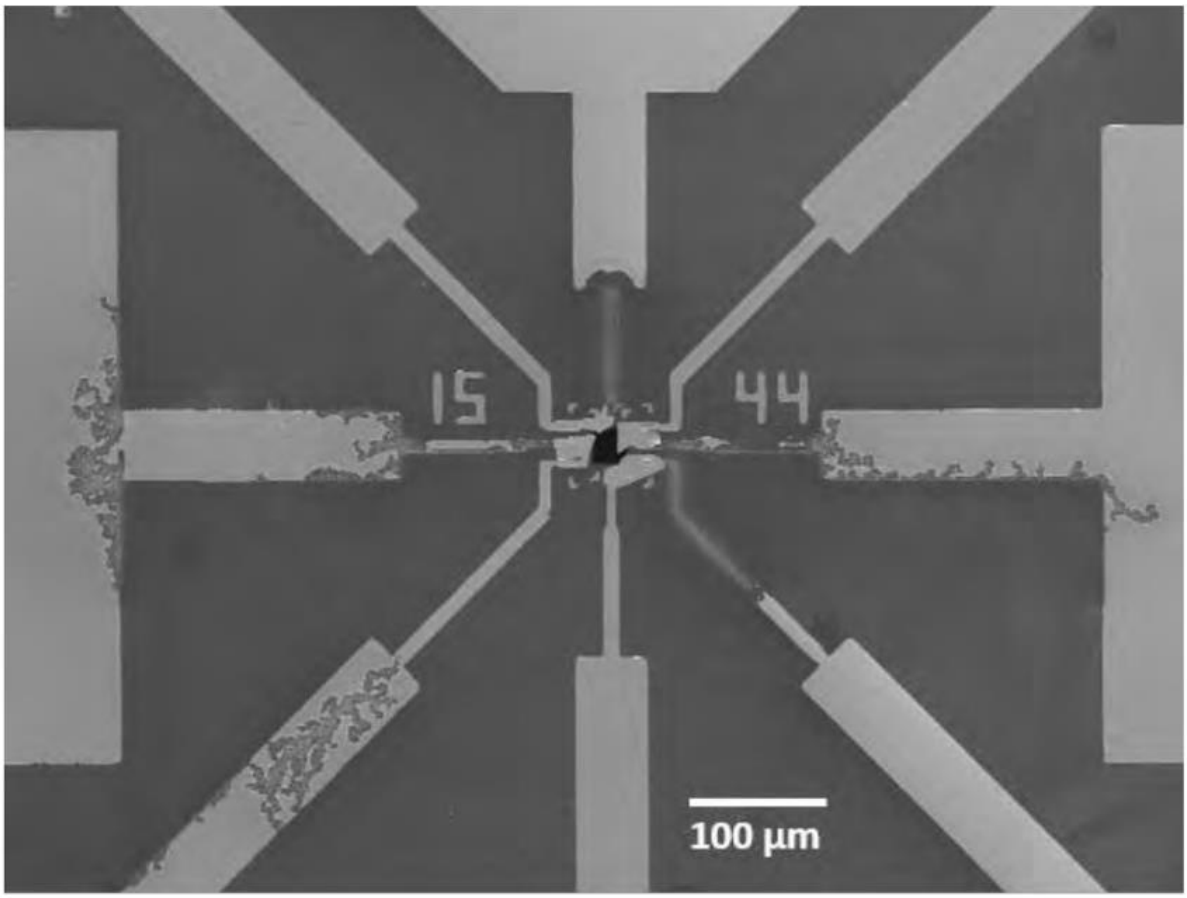

Fig. 10-8 High bias damage on Si_3N_4 window device.
Fig. 2.11, Fathalizadeh [227]. SEM image of Si_3N_4 window (20-50nm thick) based device after biasing at V≤100V.

Fig. 10-9 shows a CNT nanomechanical resonator fabricated on Si/SiO_2. SiO_2 is chosen because it demonstrates reliable dielectric strength, when used as a gate dielectric in FET devices (see Fig. 12-1). The CNT is contacted by the electrode on the top right and faces the counter-electrode on the bottom left. The electrodes and the CNT are cantilevered over a pit etched into silicon. Unlike the Si_3N_4 window devices, the hole does not go through the entire thickness of the chip, making it incompatible for TEM. The CNT and electrodes are placed on a silicon chip with 300nm of thermally grown SiO_2. To release the structures, all of the SiO_2 is etched by HF vapor[21] and a 1.8µm deep pit is etched into Si with XeF_2 vapor[22]. A thick metal layer (50nm Cr, 150nm Au)[23] is used for the electrodes to prevent the electric fields at high voltage from pulling the metal down to the silicon floor of the pit.

The Si/SiO_2 based CNT resonator can be biased to 60V with no leakage current (<0.1nA). For >60V, the device is damaged from SiO_2 dielectric breakdown or collapse of the metal layer to the bottom of the pit. Field emission signals could not be seen with this device, despite visual

[21] primaxx, Marvell Nanolab: 1250sccm N_2; 350sccm ethanol; 310sccm HF; 4×7min.
[22] xetch, Marvell Nanolab: 2torr XeF_2; 5Torr N_2; 15×10s.
[23] 950PMMA A4 spun at 3000rpm, 40s twice and baked 170°C, 2min. Double layer to avoid lift-off problems.

confirmation in SEM that the CNT is successfully contacted and released. Since voltage bias is limited to <60V, the field emission current could be too low and might be detectable with a more sensitive measurement setup (e.g. lock-in amplifier). With both the Si_3N_4 window and Si/SiO_2 based devices, it is challenging to insulate the device's conductors from the conducting bulk silicon underneath. For a careful study of the CNT resonator mechanical motion, fabrication on a substrate containing nor conductors (e.g. SiO_2, Al_2O_3) is recommended to ensure that the only conductors in the device is the metal layer and the CNT.

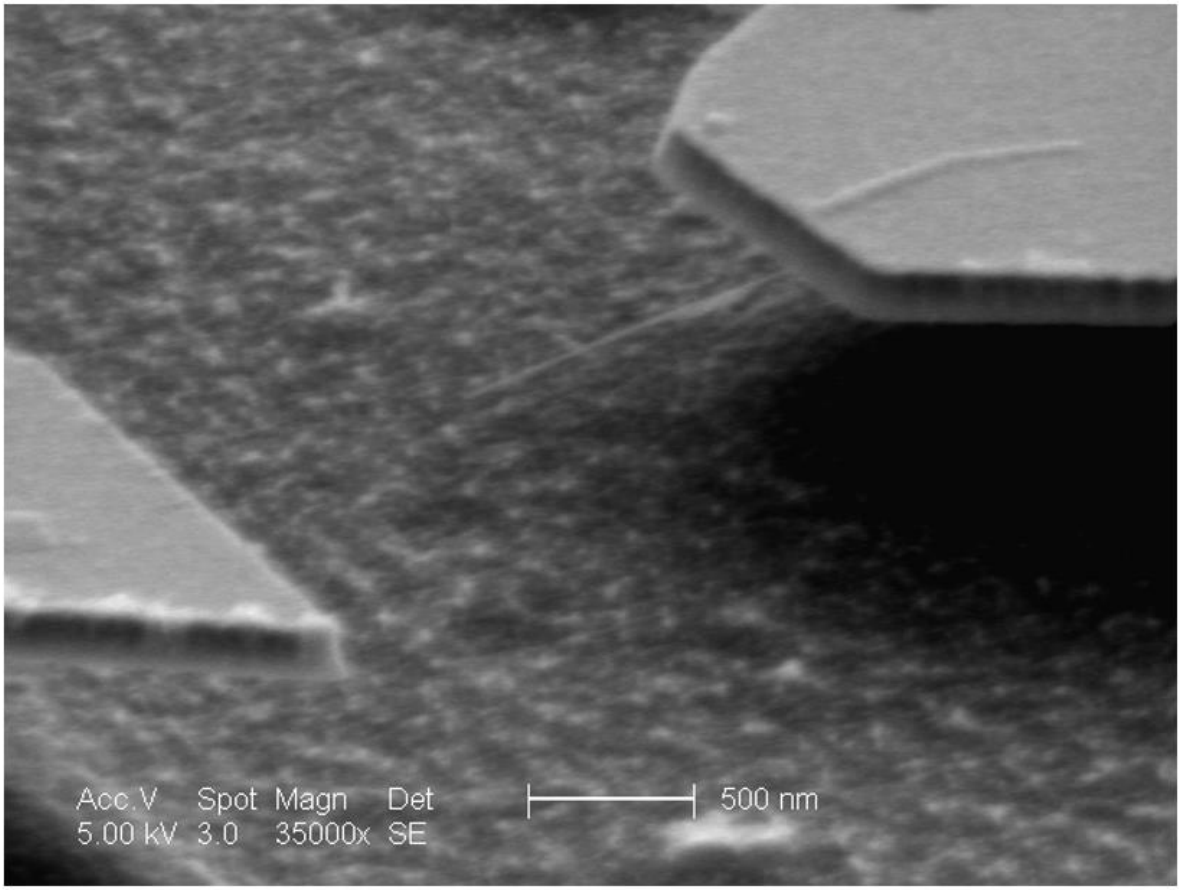

Fig. 10-9 Si/SiO_2 based CNT mechanical resonator.
MWCNT is connected to a metal electrode (top right) and faces a counter-electrode (bottom left). The CNT is cantilevered over a pit etched into silicon.

11 Graphene strain engineering platform

Application of extreme hydrostatic pressure has profound effect on a material's physical properties by changing its lattice parameters [73]. For a system, which is solid at ambient pressure, strain from mechanically pulling or pushing on the material could change the lattice parameter in a similar way. In contrast to hydrostatic pressure, strain from mechanical stress is directional. Hence, the control of strain presents the opportunity to manipulate the lattice symmetry (i.e. break or enhance it), as well as interatomic distances [37,38].

Motivated by the observation of large, strain-induced pseudo-magnetic fields in graphene [238], Qin Zhou, a post-doctoral researcher in the Zettl group, and I have been developing a versatile microfabricated platform for studying strain engineered graphene. Microactuators, a concept borrowed from MEMS design, are introduced and serves as the essential component of the strain platform. Qin designed and fabricated the microactuators by photolithography (Marvell Nanolab) and I fabricated graphene nanomechanical resonators on the strain platform by EBL. Qin led the measurement with the optomechanical detection setup and I assisted.

11.1 Pseudo-magnetic field

The exceptional mechanical strength of graphene allows it to withstand large strains (>15%) without tearing [222,239]. A proposal for "strain engineering", predicted a strain field with threefold symmetry would result in a pseudo-magnetic field. The system was realized and studied with STM in nanobubbles of graphene, which occur when graphene is grown on Pt(111). Scanning tunneling spectroscopy revealed Landau levels, which correspond to pseudo-magnetic fields >300T. Fig. 11-1a shows the topography of the nanobubble measured by STM. The bubble rises to a peak 0.4nm high and has a triangular base. The steep increase to the peak height indicates a highly strained graphene lattice. Fig. 11-1b shows a theoretical simulation for comparison and the overlaid pseudo-magnetic fields support the high fields deduced from Landau levels.

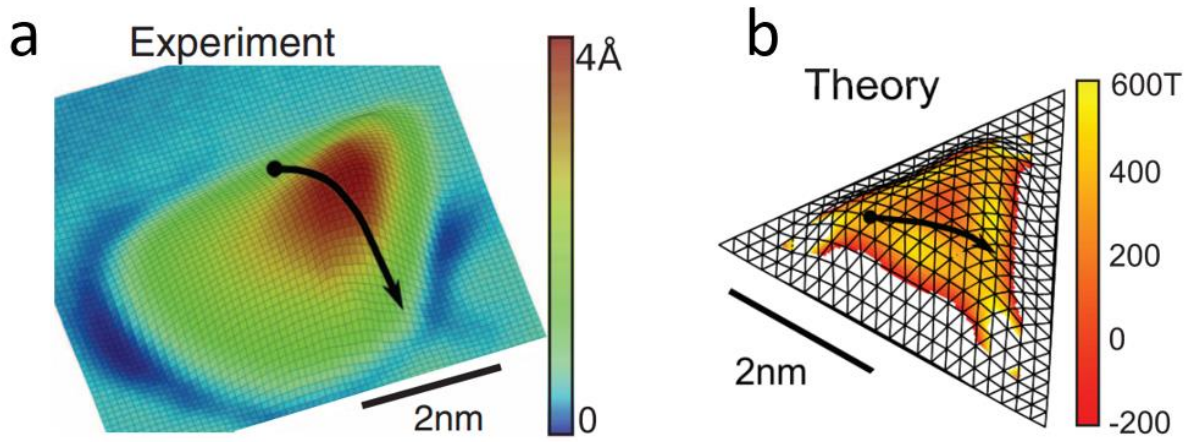

Fig. 11-1 Pseudo-magnetic field in strained graphene.
Fig. 3b,c, Levy *et al.* [238]. Pseudo-magnetic field induced by triangular strain field in a graphene nanobubble. a) Topography of graphene nanobubble measured by STM. Color legend corresponds to sample height. b) Simulated topography of nanobubble (black lines) and color legend corresponds to pseudo-magnetic field strength.

11.2 Microactuators

We propose to develop a platform to controllably create and tune large strain fields for further study of pseudo-magnetic fields in graphene. The strain platform is designed to be transported across a variety of measurement techniques (i.e. transport, optical spectroscopy, electron microscopy) and consists of microactuators, which are fabricated prior to graphene placement. Microactuators have already been used to induce a large uniaxial strain (>10%) in graphene [240]. More complex strain fields than uniaxial strains can be easily created by fabricating, multiple microactuators on one platform. In particular, a triangular strain field can be realized with three microactuators arranged with threefold symmetry. In addition, strain field control at the microscale would be advantageous for avoiding structural defects and grain boundaries [241].

Microactuators are suspended polysilicon beams, which moves in response to an electrical input. Polysilicon is used commonly in MEMS fabrication for its adequate mechanical strength, electrical conductivity [242] and compatibility with fabrication techniques (e.g. it can be deposited and etched). Two types of actuation mechanisms are introduced here: thermal and electrostatic. Both types can push or pull depending on its orientation and bidirectional actuation is possible when actuators of opposite orientation are connected to the same shuttle.

Fig. 11-2 illustrates the operation of the thermal microactuator. The image on the left shows suspended polysilicon beams (red) connecting two contact pads. The beams all have a bend in the middle and connect to another silicon beam, which serves as a shuttle (blue). Actuation occurs when current flows between the contact pads, through the bent beams. Joule heating causes thermal expansion and reduces the bend angle of the beams, resulting in the displacement of the shuttle towards the top of the image. The image on the right shows how the (pulling) force from the actuator is communicated to the sample, which is connected to the other end of the shuttle (black rectangle). The opposite end of the sample is fixed to a load shuttle, which is also suspended and fixed in place by suspended beams of narrower width. When the sample is pulled, the force on the sample is known from the combination of the measured loading shuttle displacement and the restoring force from the supporting beams.

A drawback of the thermal microactuator is the need for large current flow. For sensitive electrical measurements, the flow of large currents near the sample could be a source of significant electrical noise. In the microacutator from a previous study [240], the sample is protected from the high temperatures at the actuator by placing heat sinks along the actuated shuttle. However, for low temperature measurements (e.g. ~10mK by dilution refrigeration), the heat load could overwhelm the cooling power of the cryostat.

A microactuator based on an electrostatic force does not require current flow for actuation. Fig. 11-3 shows a type of electrostatic microactuator called the “comb-drive”. It is composed of two parts of conducting material (polysilicon) with fingers, which face each other in an interdigitating geometry but are never directly in contact. When there is a voltage difference between the two, the suspended moveable part (left) moves towards the stationary electrode (right), which is anchored to the substrate. The interdigitated geometry enhances the capacitance between the two parts. A shuttle connected to the moveable part would be actuated to the right of the image when the microactuator is voltage biased. The comb-drive microactuator has strained graphene up to 1% in a previous study [243]. In principle, the comb-drive microactuators should be able to deliver just as much force as the thermal microactuators.

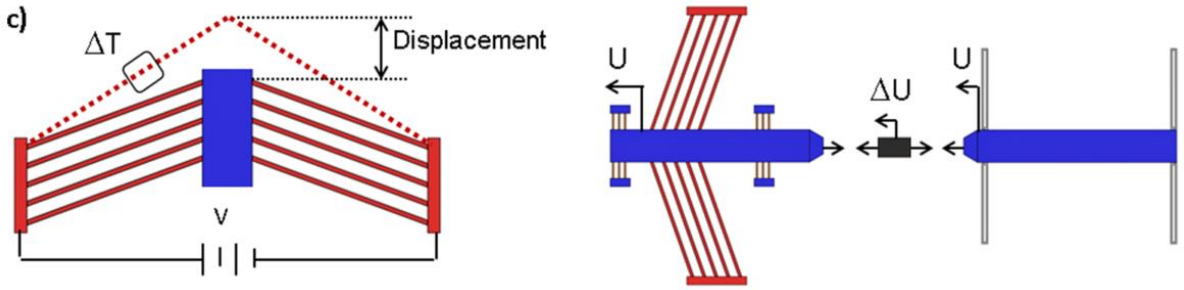

Fig. 11-2 Thermal microactuator.
Fig. 1c, Pérez Garza *et al.* [240]. Left: flowing current through the bent actuator beams (red) causes them to bend more from thermal expansion, leading to the displacement of the shuttle (blue). Right: motion of the microactuator induces a strain (ΔU) on the sample placed between the actuated shuttle (left) and load shuttle (right). Heat sinks also shown on actuated shuttle.

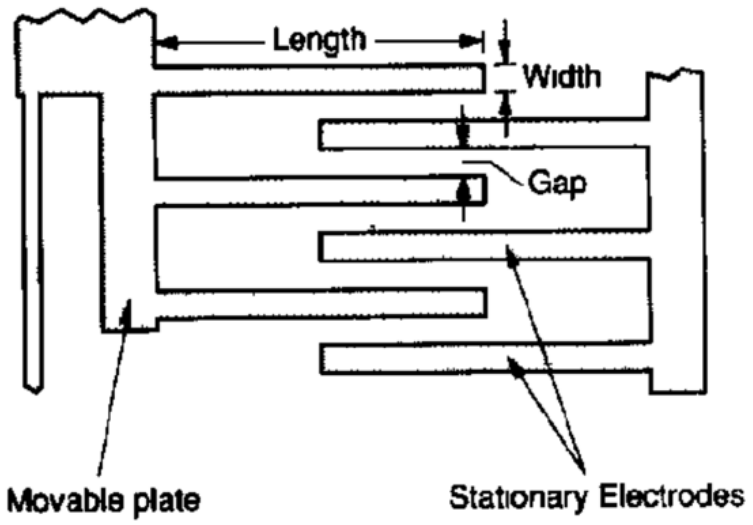

Fig. 11-3 Electrostatic microactuator.
Fig. 3, Tang *et al.* [298]. When voltage is applied between the movable plate and the stationary electrode, the plate is attracted towards the electrode (i.e. move to the right).

11.3 Straining graphene

The strain platform was designed and fabricated by Qin Zhou. Devices with both thermal and comb-drive microactuators were fabricated. The experiments in this section focuses on developing a method of placing graphene on the platform for straining. The devices tested so far consist of a single microactuator per device and uses multilayer (5-10 layer) CVD graphene to simplify testing.

Fig. 11-4a shows the sample area of the strain platform for uniaxial straining. The device is fabricated from suspended polysilicon beams on a silicon substrate, with a layer of SiO_2 between the polysilicon and the substrate. Both the loading shuttle (left) and the actuated shuttle (right) are shown in the middle. They are suspended by polysilicon beams extending from the surrounding anchored structures. The array of holes are etch holes to allow etchant to go in and undercut beneath the structure to completely remove the SiO_2 during release. The actuated shuttle connects to microactuators with the beam extending to the right of the image.

As shown in Fig. 11-4b, the strips of graphene are placed and patterned by nanofabrication to suspend across the actuated and load shuttle. For the sample shown in the image, the filament like structures are graphene strips destroyed during the fabrication process. The sample was intended to be three parallel strips of graphene, similar to the one at the bottom. Details on the nanofabrication procedure are discussed later (see Fig. 11-9).

When graphene is suspended on the strain platform, it can be studied as a nanomechanical resonator. As a first step to characterizing the strain in graphene, the mechanical resonance of the graphene is measured by optical interferometry [31]. Fig. 11-5 shows the schematic of the measurement setup. Mechanical resonance in graphene is excited by capacitively coupling the RF excitation from the network analyzer through the conducting silicon plane underneath the graphene. The graphene and the silicon underneath form a plane, where interference effects make its reflectance sensitive to the distance between graphene and silicon. A dc offset is added to slightly pull down the graphene to the position, where the reflectance is most sensitive to graphene position. The sample is probed with a 633nm laser and the intensity of the reflected beam is measured by a photodiode and fed back into the network analyze. The mechanical resonance in graphene is detected by the modulation of the reflected intensity. The sample is measured in $P<1.5\times10^{-5}$torr vacuum.

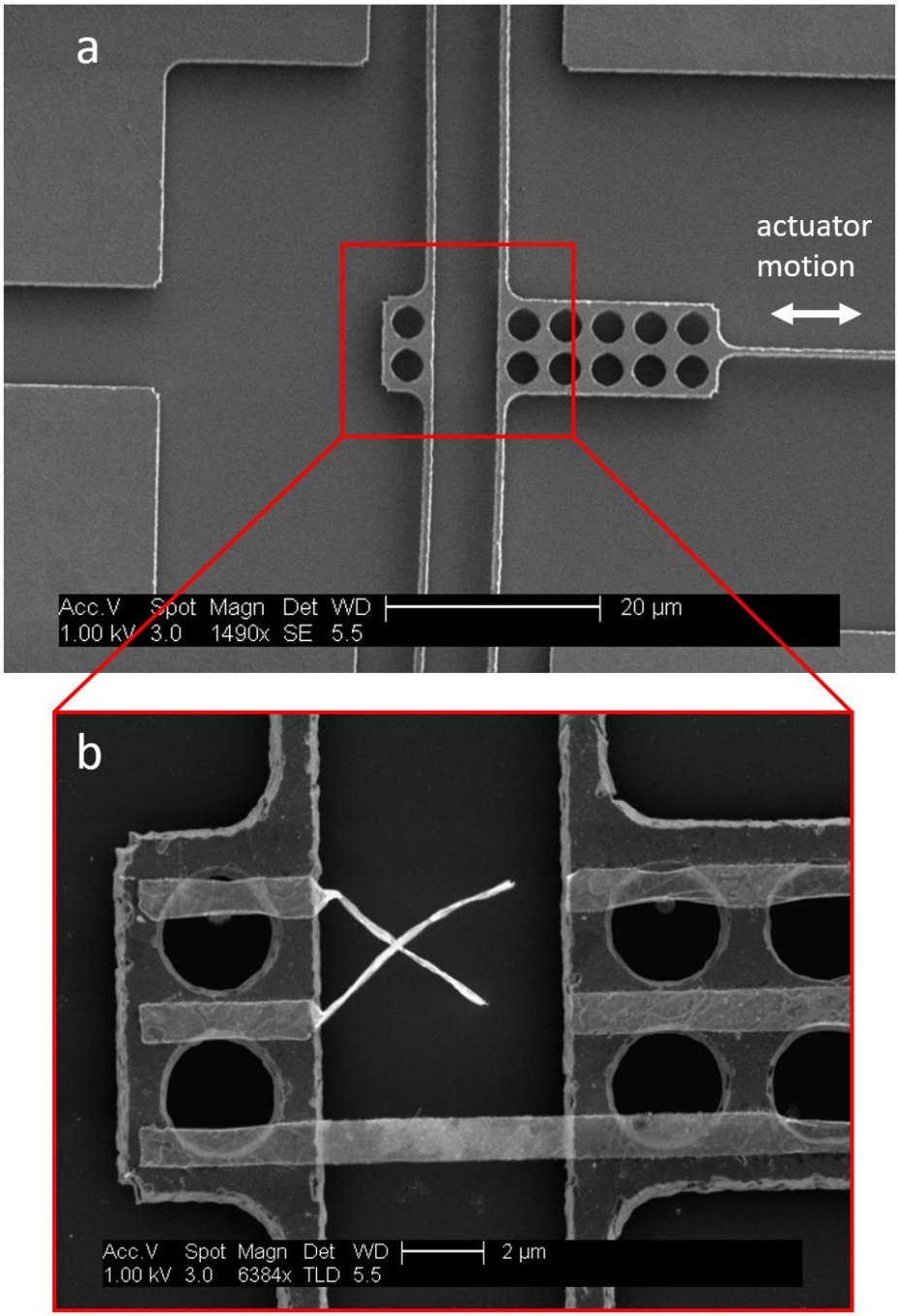

Fig. 11-4 Microactuator-based strain engineering platform.
SEM image of a) sample area (no sample shown in this image). The right shuttle connects to a microactuator (not shown). b) Strips of multi-layer graphene as sample (top two destroyed). The bottom strip bridges across the load (left) and actuated (right) shuttle.

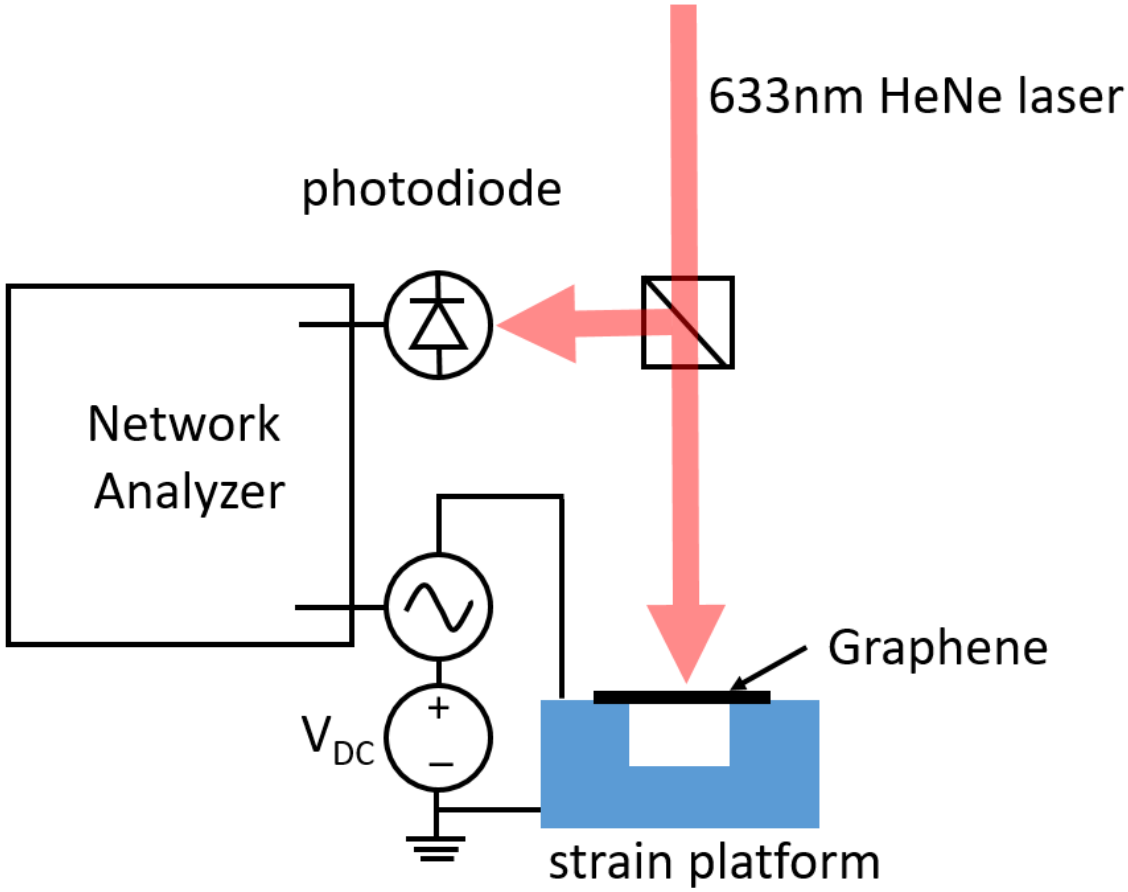

Fig. 11-5 Graphene resonator measurement setup.
Graphene nanomechanical resonator is electrostatically driven and measured by optical interferometry. Strain on graphene is applied with the strain platform.

Fig. 11-6a shows the measured frequency response of the graphene resonator. The Lorentzian peak centered at 17.7MHz is attributed to the resonance frequency of the graphene. There is a feature centered at 12.3MHz where the intensity peaks at lower frequency and dips at higher frequency. The origin of this response is unknown. Since the graphene is 5-10 layers thick, it could be a mode from interlayer coupling.

Fig. 11-6b shows the change in resonance peak, when graphene is tensioned by the microactuator. Each spectrum is shifted vertically with respect to the other spectra for clarity and a lower spectrum corresponds to stronger actuator force. The peak increases from 18MHz to 32MHz, when tensioned with the actuator. However, increasing actuator force beyond this point results in decreasing peak frequency. This effect is explained by slipping at the polysilicon/graphene interface. As shown in Fig. 11-4b, the graphene is fixed to the platform by van der Waals attraction to the polysilicon structure.

To prevent slipping, a layer of metal is evaporated on top of the graphene strips to clamp down on the graphene [33]. Fig. 11-7 shows the device with metal clamps. The strip running horizontally across the middle is graphene and the structures to its left and right are parts of the

strain platform. The metal clamp is false-colored in yellow. We have not characterized the mechanical resonance of the clamped device since we wanted to first develop a clamped device with single layer graphene. For the multilayer, there is ambiguity in how effectively the clamp couples to all the layers.

The microactuator motion is also confirmed by *in situ* actuation in SEM. A strain platform is biased through a feedthrough in the SEM and graphene is imaged as it is pulled by the actuator. Fig. 11-8a shows the graphene before pulling, with some tears in the middle, possibly from damage during fabrication. As the graphene is pulled, Fig. 11-8b,c shows propagation of the tear across the sample as well as another tear, originating from the left side. Finally, Fig. 11-8d shows the graphene completely torn in two. The strain platform could be useful for the study of graphene mechanical properties in response to forces in the lateral directions. The strain platform for this experiment uses a thermal microactuator and the current bias of the microactuator slightly distorts the image with each step in current increase. For best image quality, the electron optics (e.g. focus, beam shift) need to be readjusted for every microactuator displacement. The same (or possibly worse) image distortion effects are expected for the electrostatic actuator.

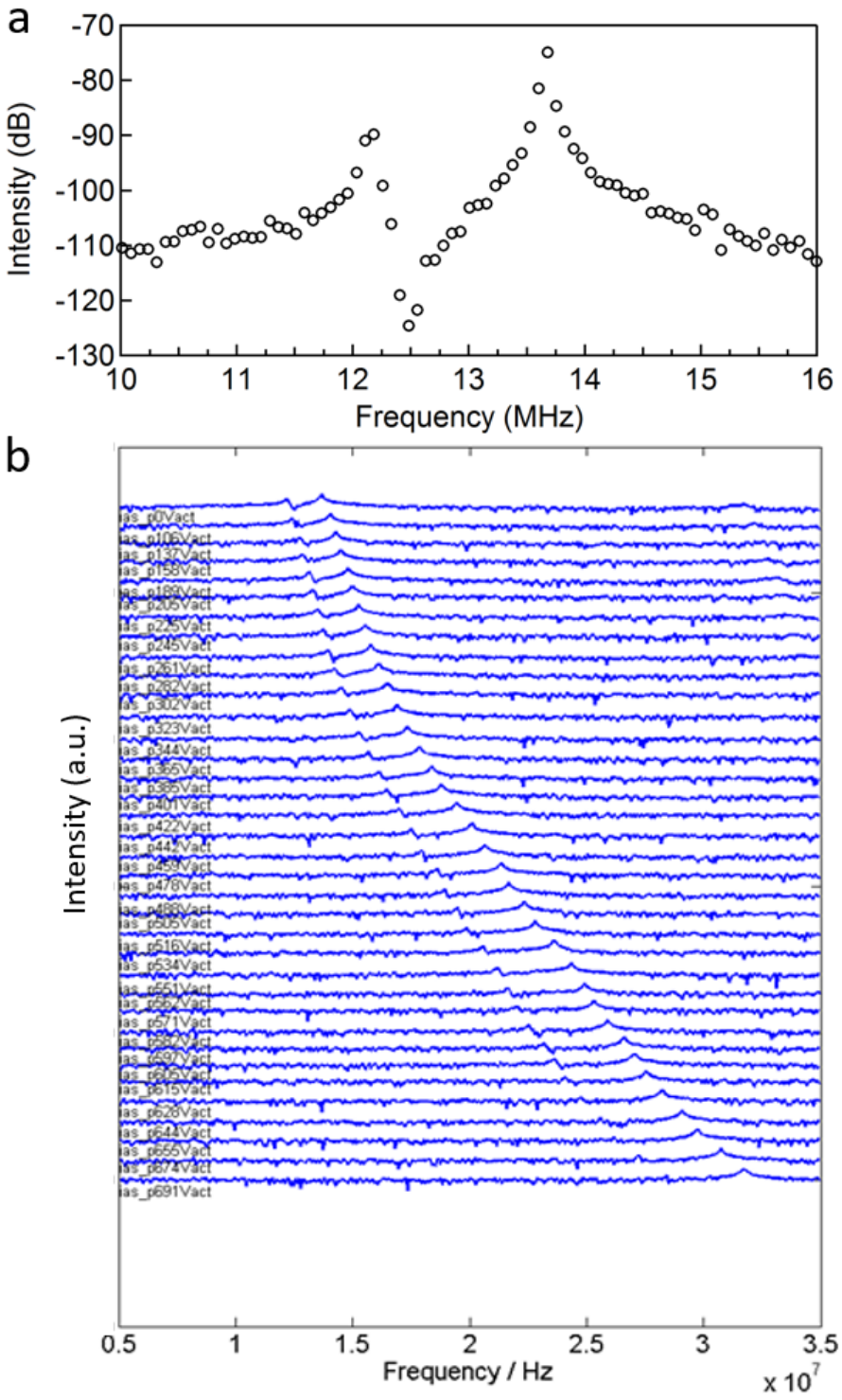

Fig. 11-6 Graphene resonator response.
Courtesy of Qin Zhou. a) Resonator frequency response spectrum with no bias on the microactuator. b) Graphene strain effect on the spectrum. Each spectrum corresponds to a different microactuator bias, with increasing microactuator force for a spectrum located lower.

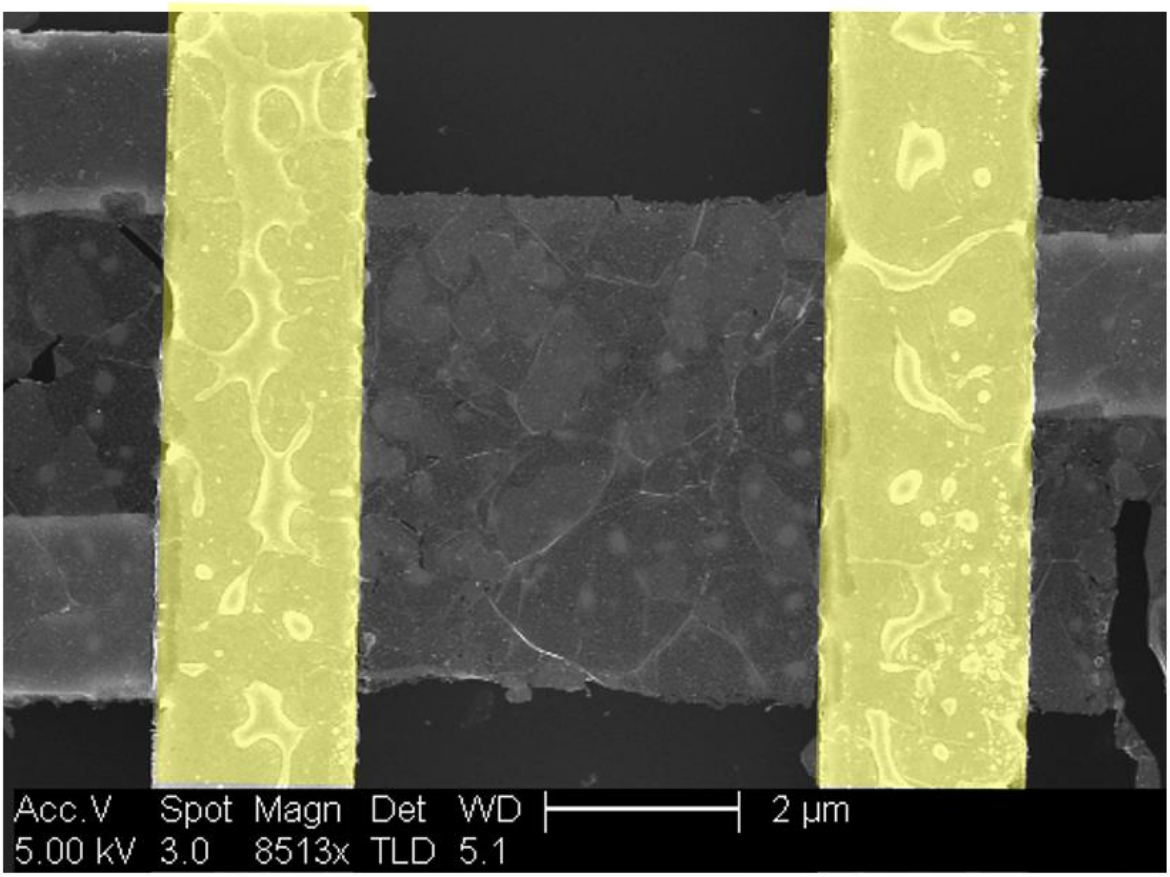

Fig. 11-7 Metal clamps on graphene.
SEM image of multilayer graphene with Cr/Au metal (yellow false color) deposited on top to mechanically clamp down on graphene.

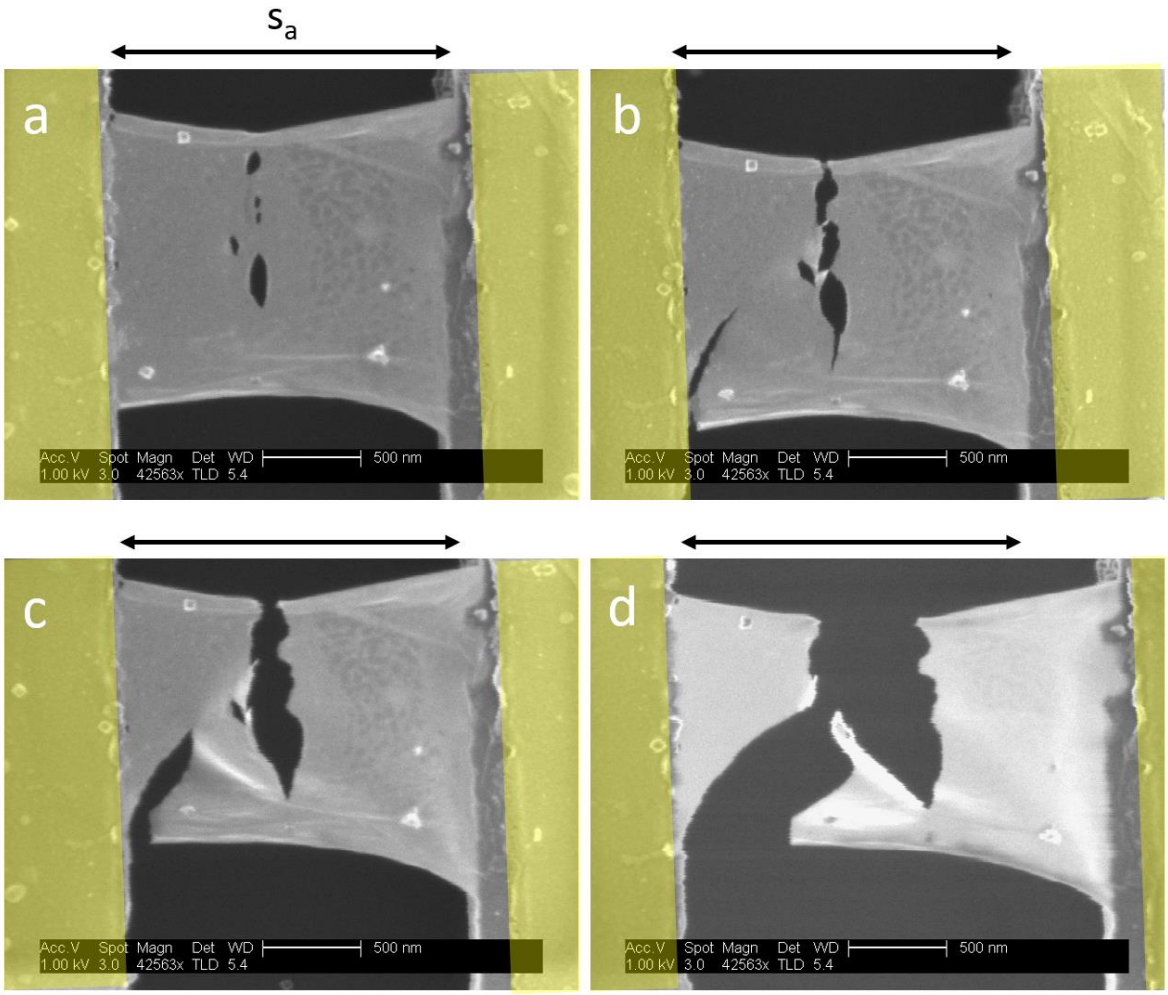

Fig. 11-8 *in situ* observation of tearing graphene.
SEM image of graphene during strain application by microactuator. Metal clamps are false-colored in yellow. a) Multilayer graphene is suspended across the load and actuated shuttle with metal clamps over a separation s_a=1.7μm at zero microactuator bias. Separation is increased to b) s_b, c) s_c and d) s_d, where $s_a<s_b<s_c<s_d$. s_a is shown on top of each panel for comparison.

Fig. 11-9a-g illustrates the nanofabrication process for the graphene nanomechanical resonators on the strain platform. Fig. 11-9h is a legend for the materials in the figure. The fabrication steps are explained below.

1. Fig. 11-9a: the strain platform is microfabricated at wafer scale (Marvell Nanolab). The structure shown is before release and still bound by SiO_2.
2. Fig. 11-9b: CVD graphene is transferred to cover the sample area [244].
3. Fig. 11-9c: 50nm copper etch mask is patterned by EBL (see section 9.1). The position and geometry of the copper should correspond to that of graphene after etching.
4. Fig. 11-9d: unwanted areas of graphene is etched by reactive ion etching (50W, 50sccm O_2, 25s)
5. Fig. 11-9e: etch copper in 100mg/mL $Na_2S_2O_8$ for 2min. Steps 3-5 pattern graphene to a well-controlled geometry. (e.g. three parallel strips suspended across the strain platform).
6. Fig. 11-9f: pattern Cr/Au (1.5nm/50nm) metal clamps on top of the patterned graphene strips.
7. Fig. 11-9g: etch SiO_2 for 125min in "pad etch"[24]. Exchange liquid in order of pad etch, water, methanol and dry by CPD. This step releases the device (see section 9.2).

The fabrication process above needs to be improved, as it does not produce devices with high yield. In particular, graphene is often damaged in the release step. Fig. 11-10a shows patterned multilayer graphene before release. After release, Fig. 11-10b shows the graphene rolls up into filament-like structures. We can confirm that the CPD is successful because the polysilicon beams are suspended. We suspect bubble formation during SiO_2 etching might be causing damage. Changing the etchant to pad etch from the commonly used BHF:HF solution to mitigate bubble formation does not solve the problem. Devices where graphene suspends across 2μm gaps yield some undamaged graphene but graphene rarely survives in devices with 5μm gaps. Devices fabricated from mechanically exfoliated monolayer graphene is also damaged during release. To make progress with prototype testing of the strain platform, the source of graphene damage during fabrication needs to be identified and corrected.

[24] 18% NH_4F, 33% acetic acid, 14% ethylene glycol, 25% H_2O [225,285]

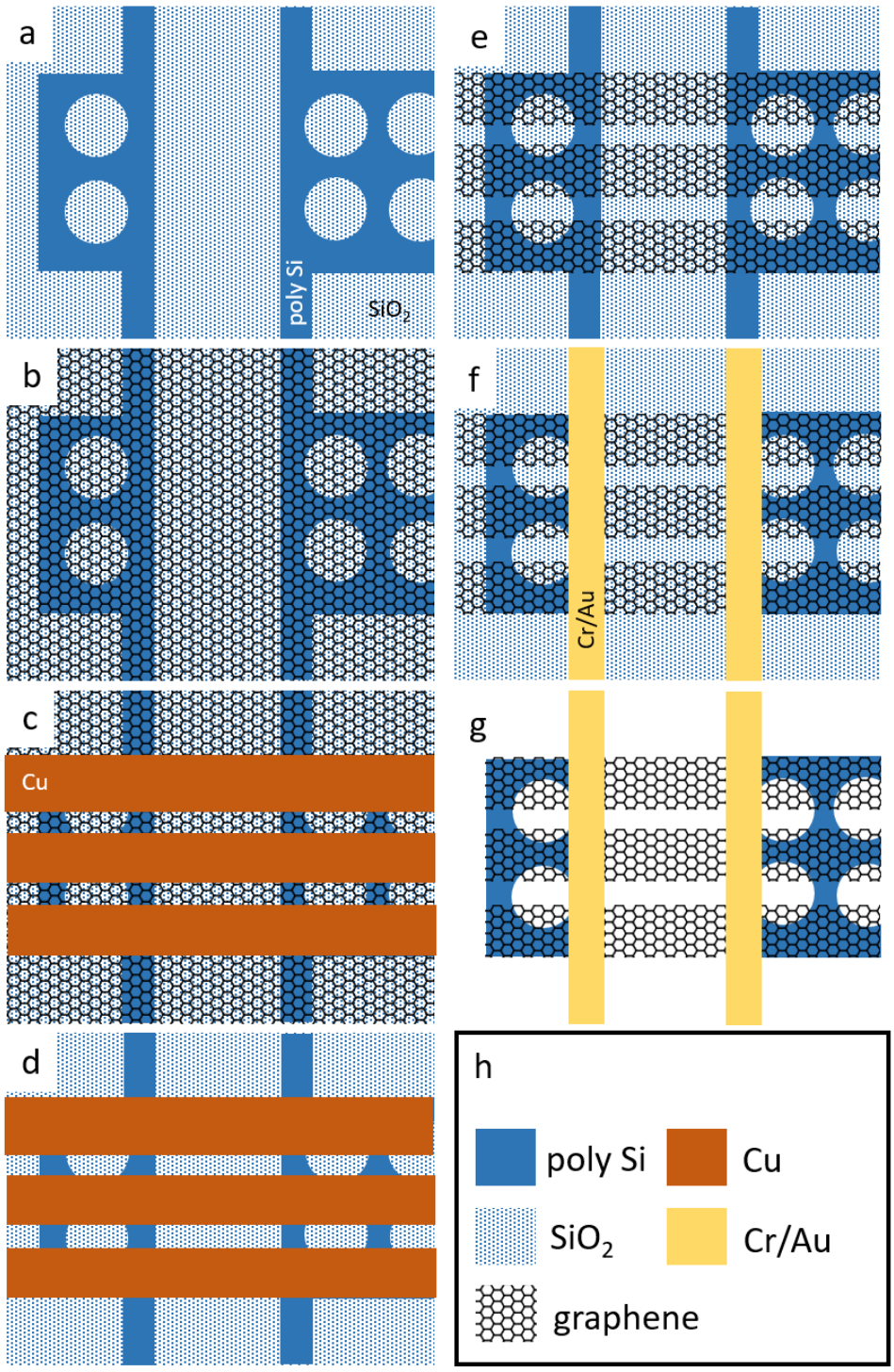

Fig. 11-9 Fabrication of graphene nanomechanical resonator on strain platform.
a) Microfabricated strain platform before release. b) Graphene transferred on platform. c) Etch mask made from patterned copper. d) Graphene etched. e) Strips of graphene after copper is etched off. f) Cr/Au clamps patterned on top of graphene. g) Device released. h) Color/pattern legend of materials illustrated in a-g.

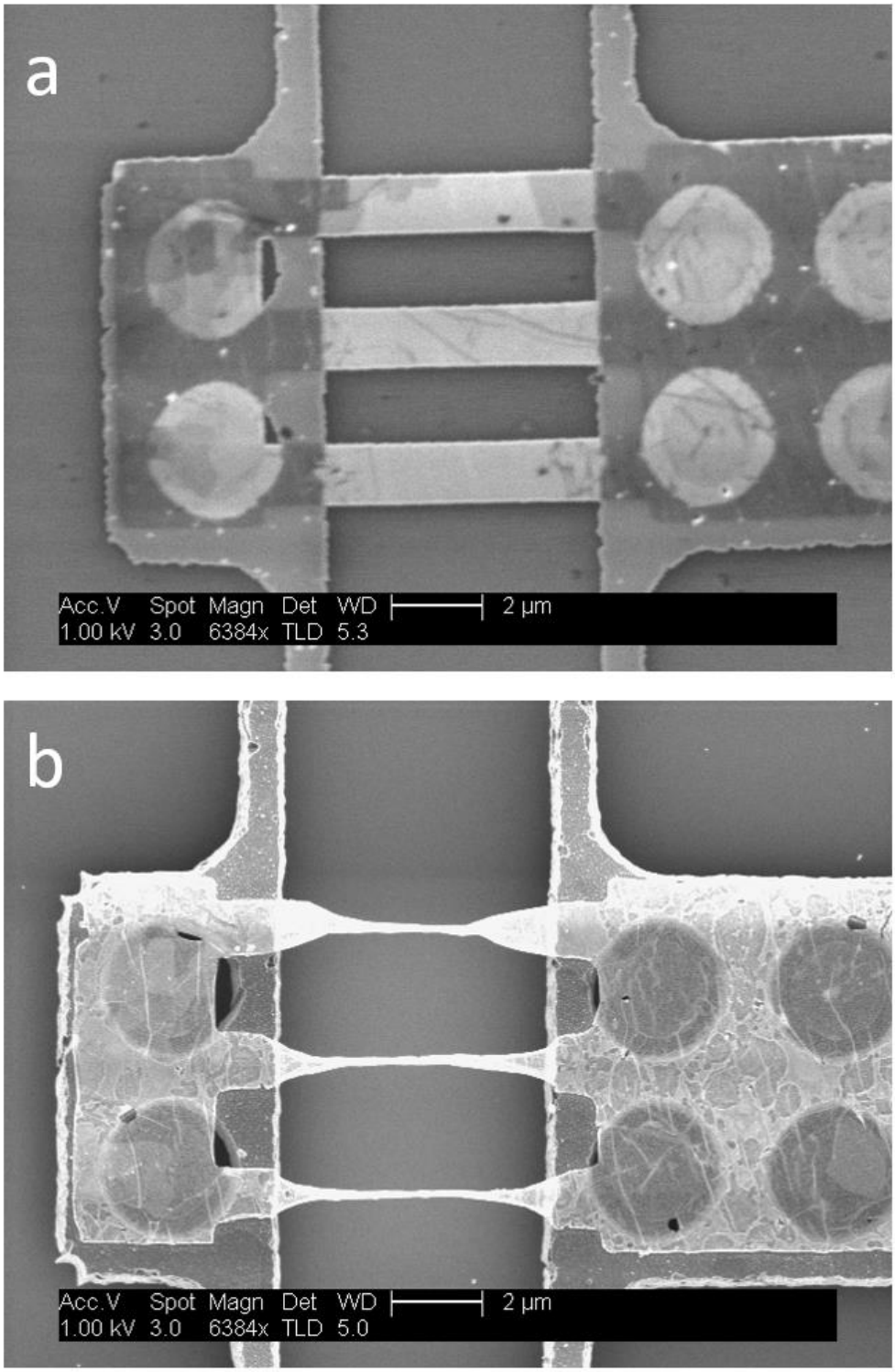

Fig. 11-10 Graphene damage during release.
SEM image of graphene patterned on strain platform a) before release (supported by SiO_2) and b) after release (suspended).

Part III

Organic semiconductors

12 Charge carrier mobility

Mobility is defined by the expression

$$\mu = |v|/\mathrm{E} \qquad \text{Eq. 12-1}$$

where *v* is the charge carrier velocity and E is the electric field driving the charge carrier motion [245]. It is related to a material's conductivity by

$$\sigma = ne\mu_e + pe\mu_h \qquad \text{Eq. 12-2}$$

where *n* and *p* are electron and hole carrier concentrations, respectively, and μ_e and μ_h are electron and hole mobilities, respectively. The mobility corresponds to how quickly the carriers in the material can respond to a change in the electric field. Hence, it determines the signal switching speed between the on and off state when the material is incorporated into an electronic device, such as a transistor. The processing speed of an electronic device is heavily dependent on the semiconductor's mobility [246].

In recent years, the mobility in organic semiconductors have been measured mostly in a field effect transistor (FET) configuration. As shown schematically in Fig. 12-1a, the semiconductor material is placed between source and drain contacts. Conductivity of the semiconductor is measured by an I(V) curve across the source and drain contacts. The gate electrode is placed underneath the semiconductor, separated by the dielectric. When a voltage is applied across the drain contact and the gate electrode, the electric field changes the number of charge carriers in the semiconductor, altering its conductivity. The dielectric insulates the semiconductor from the gate electrode, preventing any leakage current from flowing from the gate to the drain.

In the case of organic semiconductors, the material is insulating when a gate is not applied. The low conductivity of organic semiconductors 10^{-16}-10^{-20} Ω^{-1}-cm^{-1} [247], actually classifies them as insulators (see Fig. 12-2) [248]. However, when a gate voltage is applied, charge carriers are induced in the material and results in a significant enhancement in conductivity. Hence organic semiconductors are "semiconductors" in the sense that its conductivity is modulated by gate voltage in a FET, unlike other insulators such as quartz and diamond. When gate voltage is applied, a continuous sheet of conduction channel forms at the interface of the semiconductor and the dielectric (Fig. 12-1b). This occurs for source-drain voltages, which are much lower than the gate voltage $\mathrm{V_{SD}} \ll \mathrm{V_G}$, in the linear regime. The drain current follows the relation [249]

$$\mathrm{I_{D,lin}} = \frac{\mathrm{W}}{\mathrm{L}}\mathrm{C}\mu\left[(\mathrm{V_G} - \mathrm{V_T})\mathrm{V_{SD}} - \frac{\mathrm{V_{SD}^2}}{2}\right] \qquad \text{Eq. 12-3}$$

where $\mathrm{V_T}$ is the threshold voltage. It is common that $\mathrm{V_T} \neq 0$ due to dopants at the semiconductor/dielectric interface, which could withdraw or induce carriers in the material even when $\mathrm{V_G}=0$.

When $\mathrm{V_{SD}} \sim V_G$, in the saturation regime, the distortion in the electric field causes the conduction channel to be "pinched off", just short of reaching the source contact (Fig. 12-1c). In the saturation regime, any increase in $\mathrm{V_{SD}}$ does not result in increase of $\mathrm{I_D}$ since it only causes the recession of the pinch off point away from the source contact. Instead, the drain current increases as the square of the gate voltage [249]

$$\mathrm{I_{D,sat}} = \frac{\mathrm{W}}{2\mathrm{L}}\mathrm{C}\mu(\mathrm{V_G} - \mathrm{V_T})^2 \qquad \text{Eq. 12-4}$$

From Eq. 12-4, the expression for mobility is derived

$$\mu = \frac{2L}{CW}\left(\frac{d\sqrt{I_{D,sat}}}{dV_G}\right)^2$$ Eq. 12-5

where L is the separation between the source and drain electrodes, W is the width of the conduction channel between the electrodes and C is the capacitance associated with the gate dielectric and $\frac{d\sqrt{I_{D,sat}}}{dV_G}$ is the slope of the linear fit to $\sqrt{I_D}$ vs V_G.

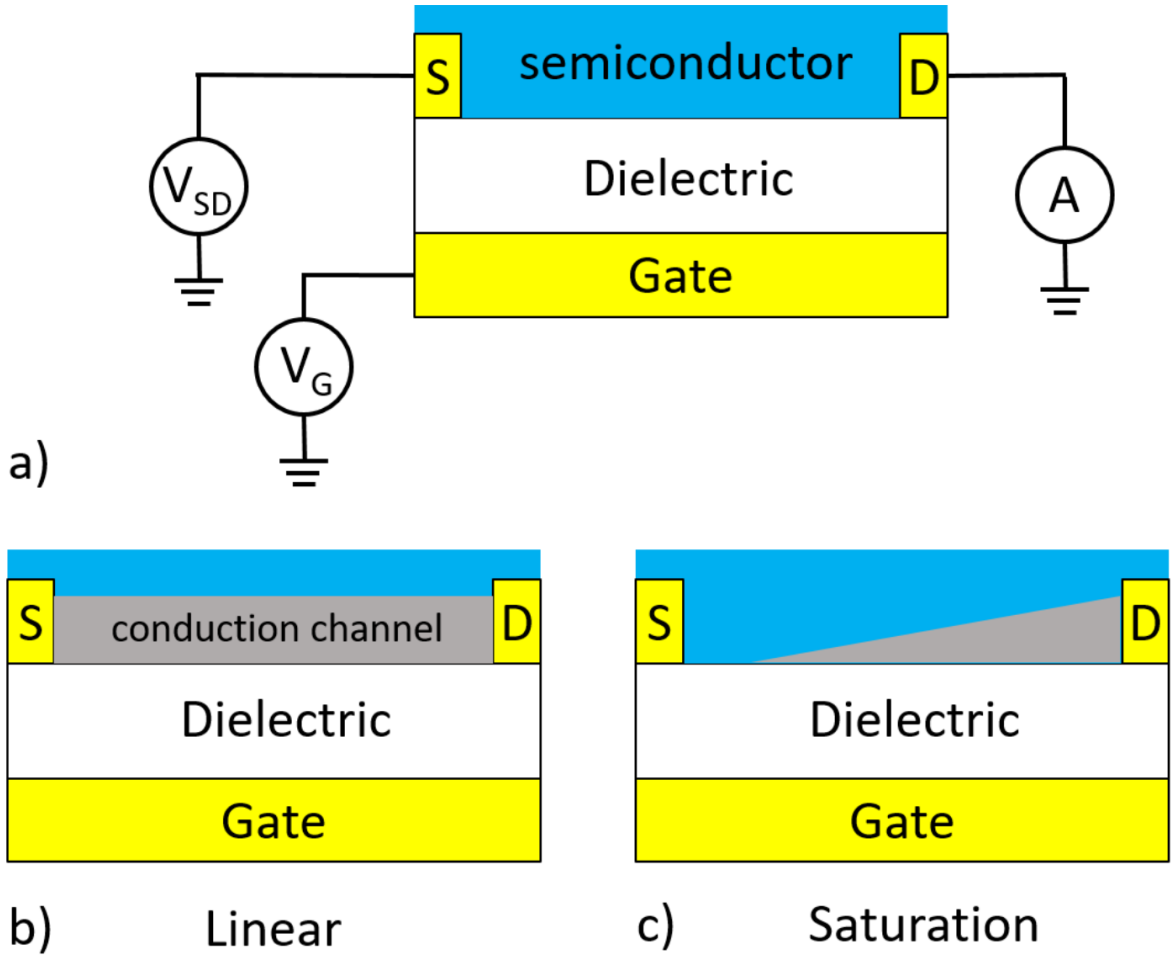

Fig. 12-1 Field effect transistor.
a) FET electrical circuitry. The labels "S" and "D" stand for source and drain contacts, respectively. The source is biased by a source-drain voltage (V_{SD}) and current is measured on the drain contact. The gate voltage (V_G) is applied on the gate to modulate the charge carrier density in the semiconductor. b) FET in the linear response regime. The gray region is the conduction channel formed by the gate electric field. c) FET in the saturation response. The conduction channel (gray region) no longer bridges across the whole source-drain distance, due to the linearly decaying profile of the electric field.

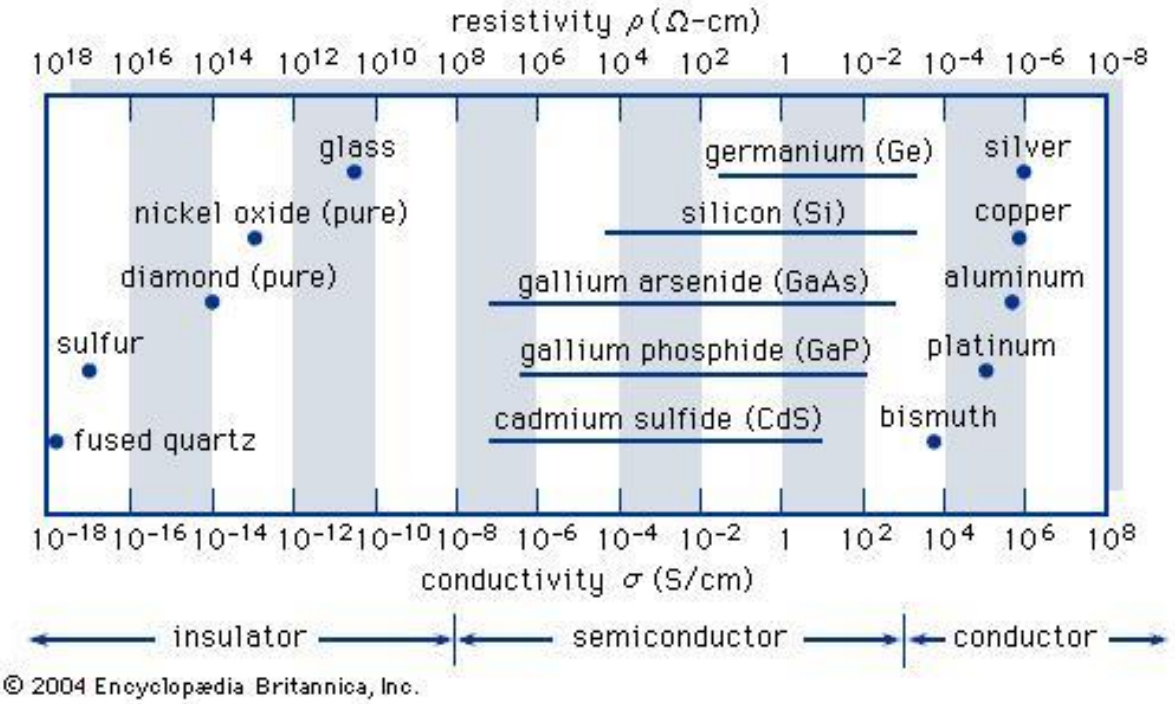

Fig. 12-2 Electrical conductivity classification of materials.
From Encyclopedia Britannica [248].

Fig. 14-7 and Fig. 14-8 show examples of electrical characteristics of an organic semiconductor FET [250]. Fig. 14-7, the "output curve", shows $I_D(V_{SD})$ curves V_G=0 to -60V. I_D increases with V_{SD} in the linear regime and saturates to a constant I_D in the saturation regime. Fig. 14-8 inset, the "transfer curve", shows I_D as a function of V_G for a fixed V_{SD}=80V. The main panel shows $\sqrt{I_D}$ and a linear fit for extracting the mobility in the saturation regime. Mobility is calculated by taking a linear fit to $\sqrt{I_D}$ vs V_G and substituting its slope for $\frac{d\sqrt{I_{D,sat}}}{dV_G}$. Although mobility can be extracted either from the linear regime or the saturation regime, it is more common to use the saturation regime as it yields higher currents for ease of measurement.

The FET configuration is the most common mobility measurement technique for thin films of organic semiconductors. However, the FET measures the in-plane mobility of the film. For solar cells, high out-of-plane mobility is more important than the in-plane mobility. Out-of-plane mobility measurement techniques have been developed for single crystals, such as the measurement of space-charge limited current at high voltage bias [247]. The mobility is extracted by fitting to

$$J = \text{const}\,\mu\frac{V^2}{L^3} \qquad \text{Eq. 12-6}$$

Another method is to induce carriers on the top surface of the material with a pulse of light and measuring the transient electrical response, called "time of flight" measurement. Given the thickness of the sample, the mobility of the photo-induced carriers can be extracted from the decay time of the transient signal [251].

Space-charge limited current and time of flight measurements on thin films of organic semiconductors are complicated for thicknesses ~100nm. The top and bottom electrode separation is small and the surface to bulk ratio carrier photogeneration is reduced. Current extraction by linearly increasing voltage (CELIV) has been developed to serve as a suitable technique in evaluating the out-of-plane mobility for organic thin films [251]. CELIV applies a voltage bias across the top and bottom of the film and increases the voltage linearly in time. The transient response of the current is recorded, while the voltage is ramped up. By analyzing the features in the current transient response, the mobility is extracted. For materials of low conductivity, a pulse of light before the voltage ramp is applied to excite some carriers in "photo-CELIV". Although CELIV has been well-established, FET measurement remains the most common characterization of organic semiconductor mobility.

13 Solids of organic molecules

Organic semiconductors are organic molecules, which contain conjugated bonds. When a chain of carbon atoms are bonded together, such that bonds alternate between double bonds and single bonds, the electron orbitals hybridize into conjugated bonds. The conjugated bonds allow electron delocalization throughout the chain. Such delocalization within the individual organic molecule raises the question whether delocalized electron transport is possible across a crystalline lattice of organic molecules. As demonstrated by polyacetylene [11] and fullerenes [64], organic materials, previously thought to be only insulators, can become metals and even superconductors. For technological applications, it is important to explore whether organic molecules could be made into semiconductors with properties comparable to silicon, which supports the electronics industry today. Organic semiconductors are attractive for their compatibility with low cost manufacturing methods (e.g. inkjet printing [252]). The organic semiconductors can be dissolved in a solvent and simply printed on to a flexible substrate to allow rapid low cost production of flexible electronics. Subsequent research have revealed that they are indeed promising materials for electronic device applications [253].

Organic semiconductors are classified into small molecules and polymers [254] (see Fig. 13-1 and Fig. 13-2). Small molecules are a group of covalently bonded carbon atoms, with one molecule consisting of ~10 carbon atoms and other elements. A polymer consists of many small molecules that are covalently bonded together, such that the small molecules repeatedly appear in a linear chain. In the development of organic semiconductors for electronic device application, various small molecules and polymers have been designed and synthesized. To assess each new material's viability for electronic devices, a new material is often assembled in a field effect transistor configuration and the charge carrier mobility is extracted as a figure of merit.

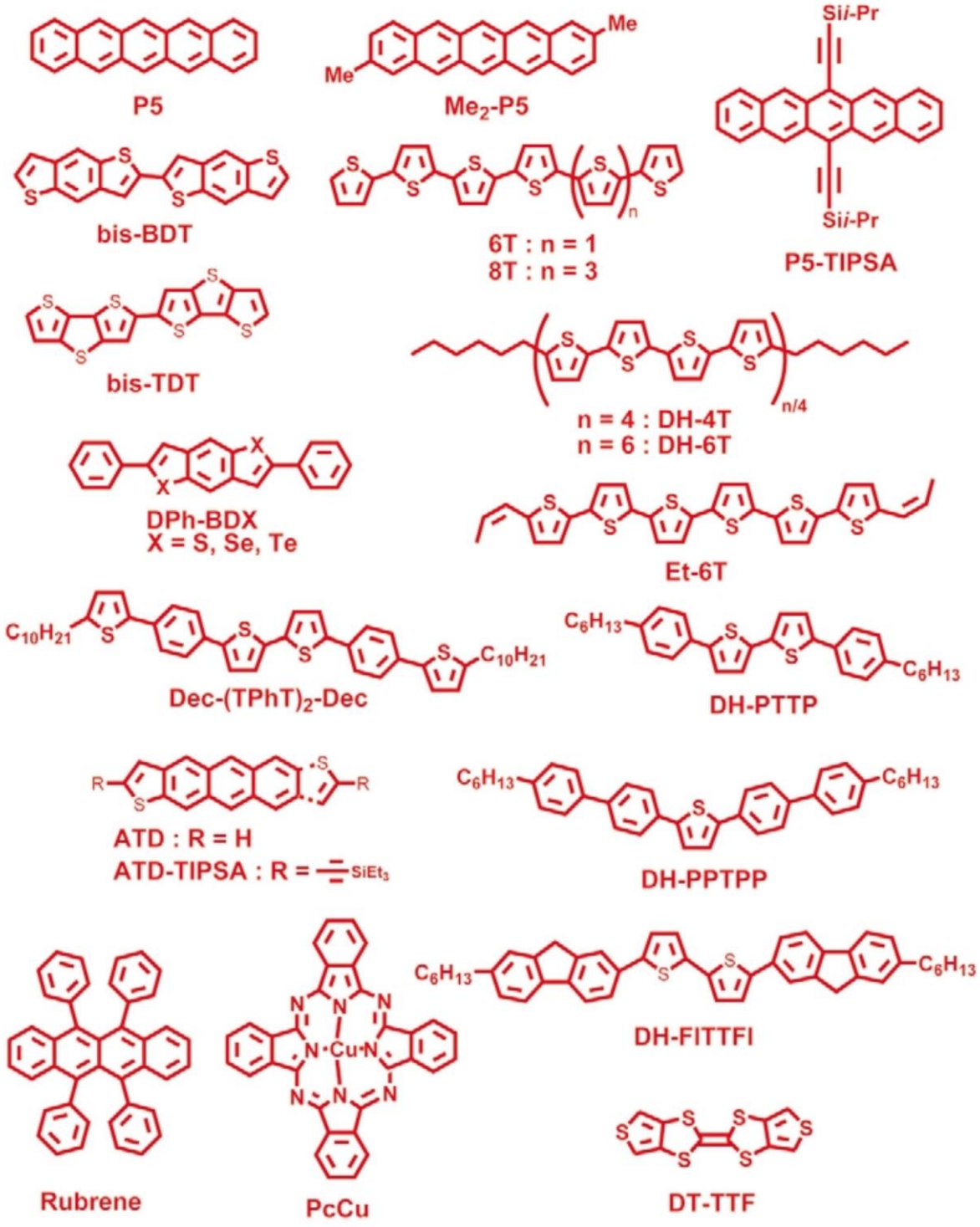

Fig. 13-1 Examples of organic small molecules.
Fig. 3, Facchetti [254]. Small molecule semiconductors.

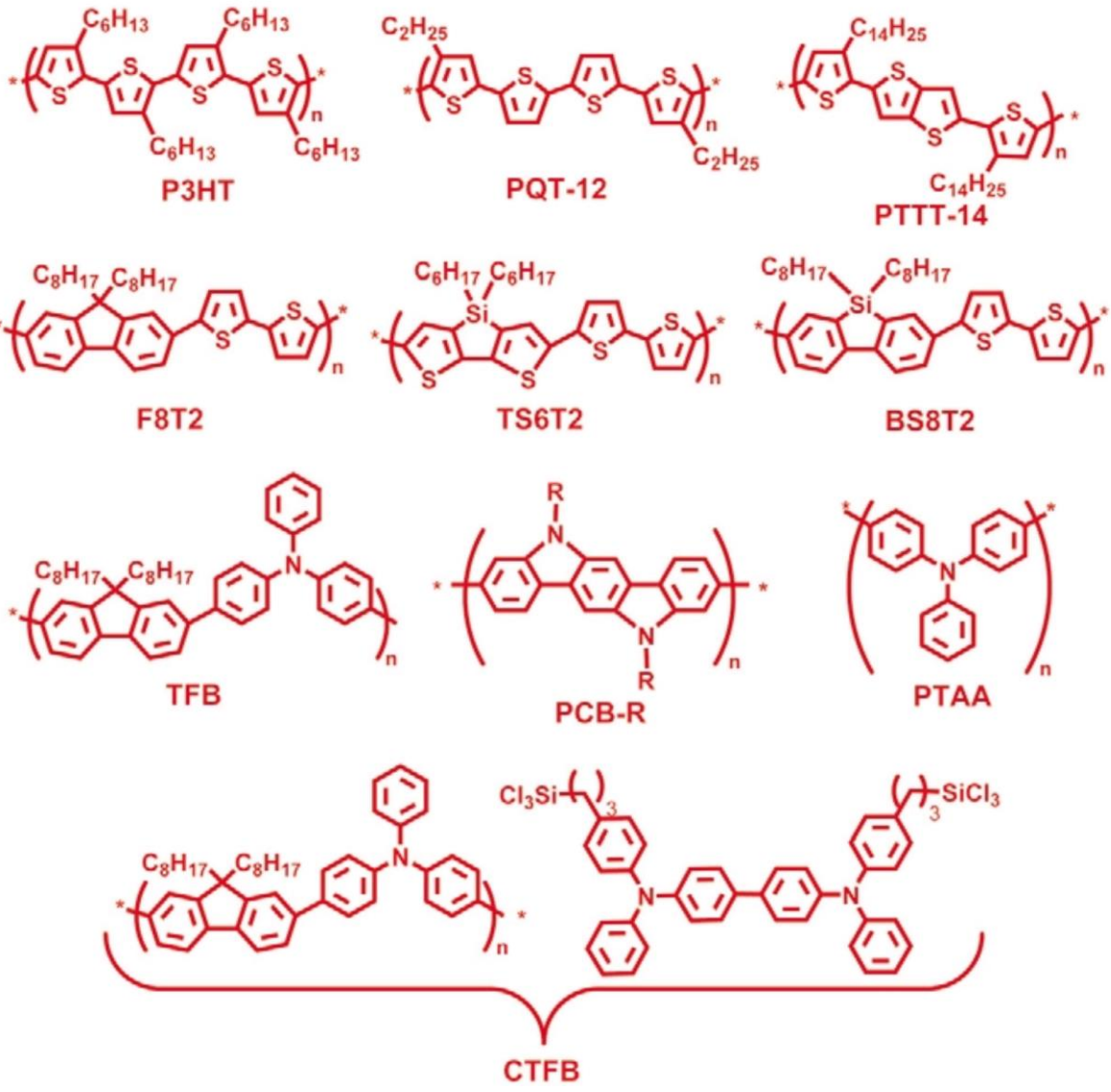

Fig. 13-2 Examples of organic polymers.
Fig. 6, Facchetti [254]. Polymer semiconductors. For each polymer, only one unit is shown. As indicated by the brackets subscripted by n, it is assumed that the polymer unit repeats to form a long covalently linked chain.

13.1 Single crystals

Molecules shown in Fig. 13-1, such as pentacene (P5) and rubrene, are grown into large single crystals by physical vapor transport (see section 4.1.1). Although the study of fragile single crystals does not directly translate to progress in flexible electronics, high quality organic crystals have been studied for understanding fundamental transport mechanisms in van der Waals bonded crystals. High mobility was obtained when the crystal was suspended over a trench of PDMS and vacuum was used as the gate dielectric [255]. As the transport in organic FET is strongly localized to the interface between the crystal and the gate dielectric, mobility is significantly degraded by surface traps at the interface. In the "vacuum-gap" configuration, sample conductivity degraded even when the hot-cathode vacuum gauge was turned on [255].

Typical mobilities in organic single crystals are in ~1cm^2/Vs range, exemplified by 2.2cm^2/Vs in pentacene, but rubrene has an exceptionally high mobility of 20cm^2/Vs [256]. Rubrene is the most extensively studied organic crystal in terms of electrical transport. With very weak interaction between the molecules, it is expected that charge carrier transport occurs via thermally activated hopping. Interestingly, R(T) of rubrene suggests the possibility of delocalized transport [257]. In addition, transport anisotropy in the *a,b* crystallographic plane has been observed [255]. According to the Ioffe-Regel criterion, the mean free path needs to be greater than the inter-molecular distances for delocalized transport [258]. As organic single crystals are below this limit but closely approach it, transport mechanisms in organic single crystals remain a fascinating topic of fundamental interest [255].

To prevent confusion, while reading the literature, it should be noted that there exists reports of gate induced superconductivity and quantum Hall effect in pentacene, which were subsequently revealed to be based on invalid data [259,260].

13.2 Small molecule thin films

For flexible electronics applications, thin films of organic semiconductors have been extensively studied. However, thin film mobilities were initially an order of magnitude lower than their single crystal counterparts. Films prepared by solution processing, such as spin coating, had even lower mobilities. For comparison, the mobility of single crystal pentacene is $2.2 cm^2/Vs$ [256]; vacuum deposited thin film pentacene is $0.62 cm^2/Vs$; spin-coated pentacene is $0.001 cm^2/Vs$ [261]. Most of the promising organic semiconductors from single crystal studies have low solubility in solvents and do not form high quality films, when solution processed. New organic molecules have been designed and synthesized to be highly soluble in solvents. For example, pentacene has been functionalized to 6,13-bis(triisopropylsilylethynyl) (TIPS)-pentacene (labeled as P5-TIPSA Fig. 13-1), which yields spin-coated films with mobilities of $1.2 cm^2/Vs$ [262].

In addition to disorder effects, the mobility in organic semiconductors are significantly dependent on how the molecules stack with each other, as demonstrated by a study on sexithiophene thin films [263]. Sexithiophene (labeled as 6T in Fig. 13-1), functionalized by side-chains at different positions (Fig. 13-3a,b) assemble in different molecular arrangements, as characterized by X-ray diffraction. The mobility varies greatly from $<10\text{-}7 cm^2/Vs$ in β,β'-dihexyl-substituted sexithiophene (Fig. 13-3a) to $0.05 cm^2/Vs$ in α,ω-dihexyl-substituted sexithiophene (Fig. 13-3b), with an intermediate mobility of $0.002 cm^2/Vs$ in the unfunctionalized sexithiophene. Each of the thiophene "pentagons" in the molecule have π orbitals, similar to graphene [264]. When the pentagons are allowed to stack face-to-face in a "π stacking" manner, the orbital overlap is maximized and most favorable for charge carrier transport. In the case of functionalized sexithiophene, X-ray diffraction showed that the molecules in the highest mobility film are π stacked in the plane of the transport direction, as illustrated in Fig. 13-3c. Subsequently, π stacking has been an important component in the design of organic molecules for electronics applications. Organic small molecule semiconductors have undergone dramatic improvement. Mobility in newly developed materials have climbed up to $43 cm^2/Vs$ (with an average of $25 cm^2/Vs$ over 80 devices) [265].

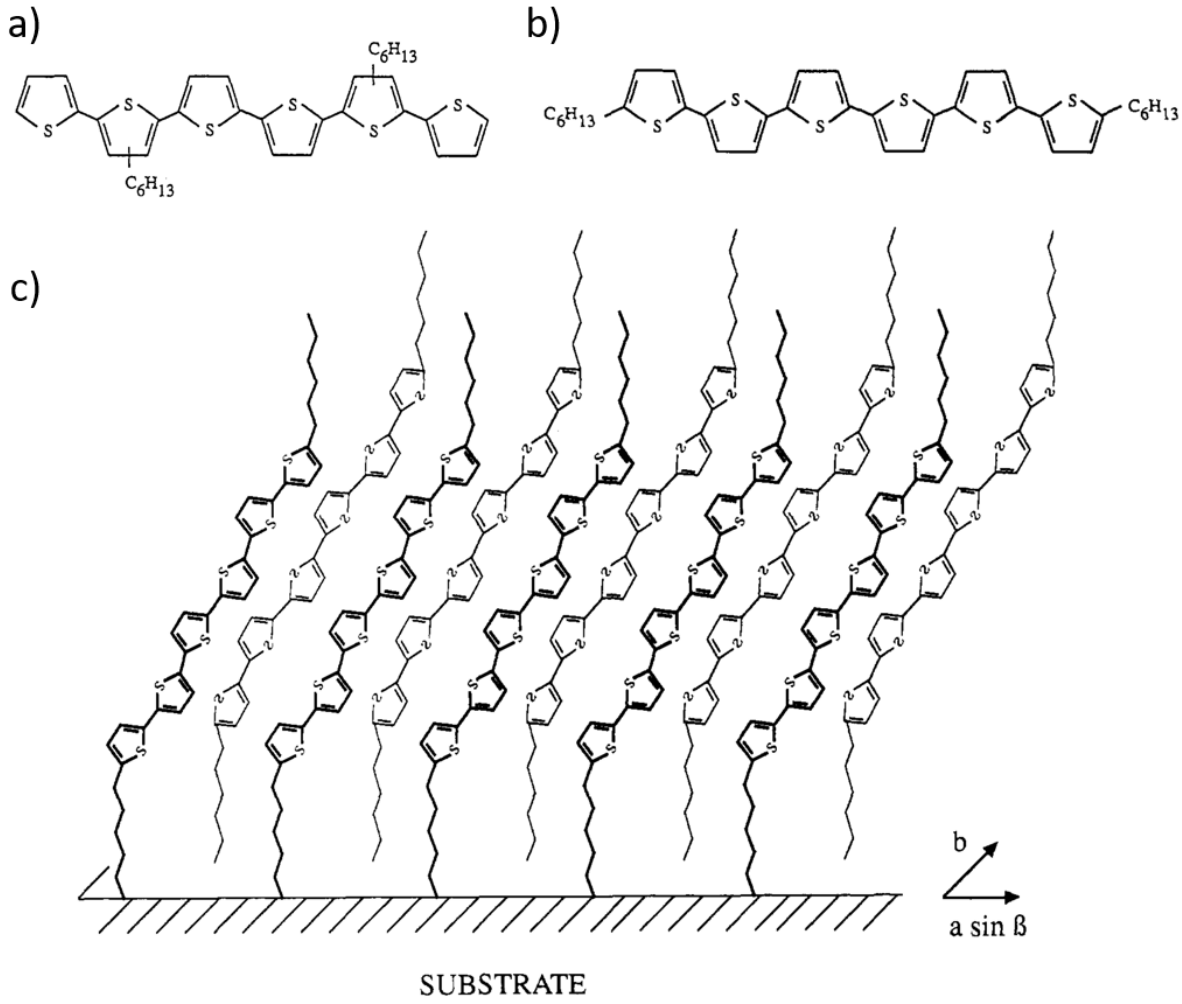

Fig. 13-3 π-stacking of sexithiophene.
Fig. 3, Garnier *et al.* [263]**.** a) β,β'-dihexyl-substituted sexithiophene. Diagram for compound (II), Garnier et. al. [263] b) α,ω-dihexyl substituted sexithiophene. Diagram for compound (III), Garnier et. al. [263] c) Schematic of α,ω-dihexyl substituted sexithiophene self-assembly on a substrate based on X-ray diffraction characterization. The π–π stacking extending in parallel to the substrate plane explains the higher in-plane mobility for α,ω-dihexyl substituted sexithiophene compared to unfunctionalized and β,β'-dihexyl-substituted sexithiophene.

13.3 Polymer

In parallel with small molecules, polymers have been developed for use in flexible electronics. Similar to small molecules, polymer semiconductors have progressed significantly from ~0.01cm^2/Vs to 23.7cm^2/Vs [266]. Unlike the well-defined regular arrangement in a crystalline domain of small molecules, the "spaghetti-like" form of the polymers, do not enable them to form well-ordered crystalline films. However, the polymers still form aggregates with orientational order. Mobility is enhanced if the orientational order is such that it promotes π-π stacking along the direction of transport [250,267]. Despite studies, which demonstrate the robustness of small molecule films to mechanical deformation [268], polymer films have been claimed to possess generally superior mechanical properties for integration into flexible substrates. As polymers are already prevalent in flexible material manufacturing in non-electronic applications, polymer semiconductors could be more readily incorporated into the current manufacturing processes. In particular, the rheological properties of polymers containing solvents can be controlled by synthetically adjusting the molecular weight of the polymer.

The development of high mobility polymers have been essential for organic photovoltaics research. The Frenkel excitons [269] in organic solar cells only dissociate at the interface of donor and acceptor molecules. Given the excitons travel ~10nm before it decays, an interpenetrating network of donor and acceptor materials are required to maximize charge separation. The bulk heterojunction [270] realizes such a structure by utilizing the polymer phase segregation of the acceptor/donor mixture, as illustrated in Fig. 13-6a. High mobility polymers are needed in solar cells for efficient charge carrier extraction. Novel polymers are often characterized simultaneously as solar cells and transistors. For solar cells, there is an added requirement that the polymers have a suitable bandgap for efficiently absorbing the solar spectrum.

13.4 Organic Nanowires

Organic nanowires have emerged as a material, which could exhibit the best of both worlds from small molecules and polymers. Some small molecules self-assemble into nanowires with typical diameters of 0.2-1μm and lengths exceeding 50μm (Fig. 13-4) [271]. Organic nanowires are created both in solution and from vapor phase. Each nanowires consists of small molecules in a crystalline order and the nanowires are easily suspended in solution for solution processing. Delicate changes to the constituent small molecule's optoelectronic property, such as the bandgap by synthetic chemistry can be used to manipulate the optoelectronic properties of the resulting nanowire. Driven by π stacking, the small molecules assemble anisotropically into nanowires. The π orbital overlap is the greatest along the nanowire growth direction leading to favored charge carrier transport along the nanowire growth direction. Mobility in hexathiapentacene nanowire (Fig. 13-4b) is $0.27 cm^2/Vs$, which is six times higher than its thin film form [271]. By functionalizing the small molecule, its self-assembly behavior, in particular the resulting nanowire diameter can be controlled. Hexabenzocoronene has been functionalized with hydrophobic groups on one side and hydrophilic groups on the other. In a non-aqueous solvent, the molecules assemble chirally into a tube to place the hydrophobic part on the outside and the hydrophilic part on the inside of the tube. Well-controlled assembly creates Ø20nm nanotubes with aspect ratio >1000 (Fig. 13-5) [52].

In polymer solar cells (Fig. 13-6a), the charge carriers created at the donor/acceptor interface must go through a percolation path through the random network of polymer domains to reach the electrodes. The carrier extraction can be performed more efficiently if the donor and acceptor domains formed well-ordered structures, which provide direct paths to the electrodes, as shown schematically in Fig. 13-6b. Hence, a vertically aligned array of high mobility organic nanowires, which are backfilled with a complimentary material, would dramatically improve the carrier extraction efficiency.

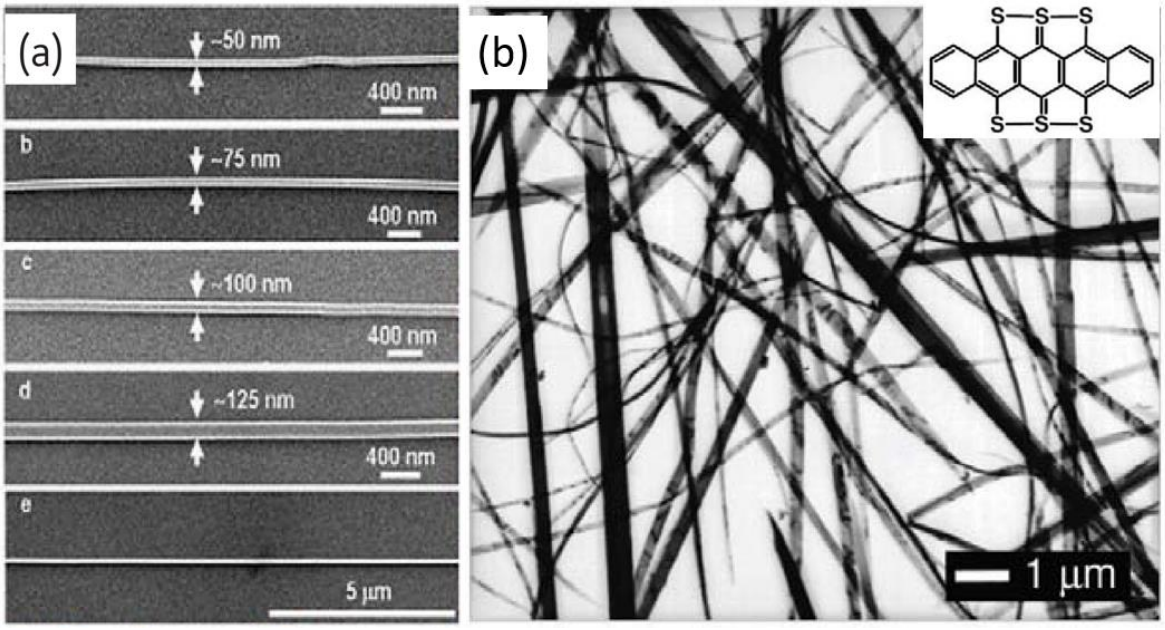

Fig. 13-4 Examples of organic nanowires.
a) Fig. 12a, Briseno *et al*. [271]. Copper phthalocyanine nanowires grown by physical vapor transport. Nanowires of different diameters are obtained by varying the carrier gas flow during synthesis. b) Fig. 4b, Briseno *et al*. [271]. TEM image of hexathiapentacene organic nanowires grown from solution. Inset: molecular diagram of hexathiapentacene.

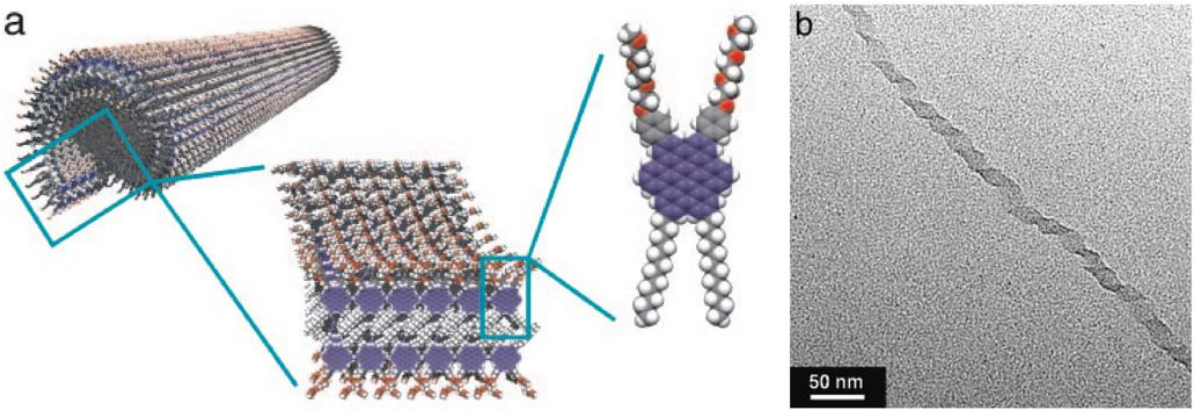

Fig. 13-5 Helically assembled molecular nanotube.
a) Fig 2a, Jin *et al.* [52]. Schematic of helically assembled nanotube of organic small molecules. b) Fig. 6b, Jin *et al.* [52]. TEM image of helically assembled nanotube.

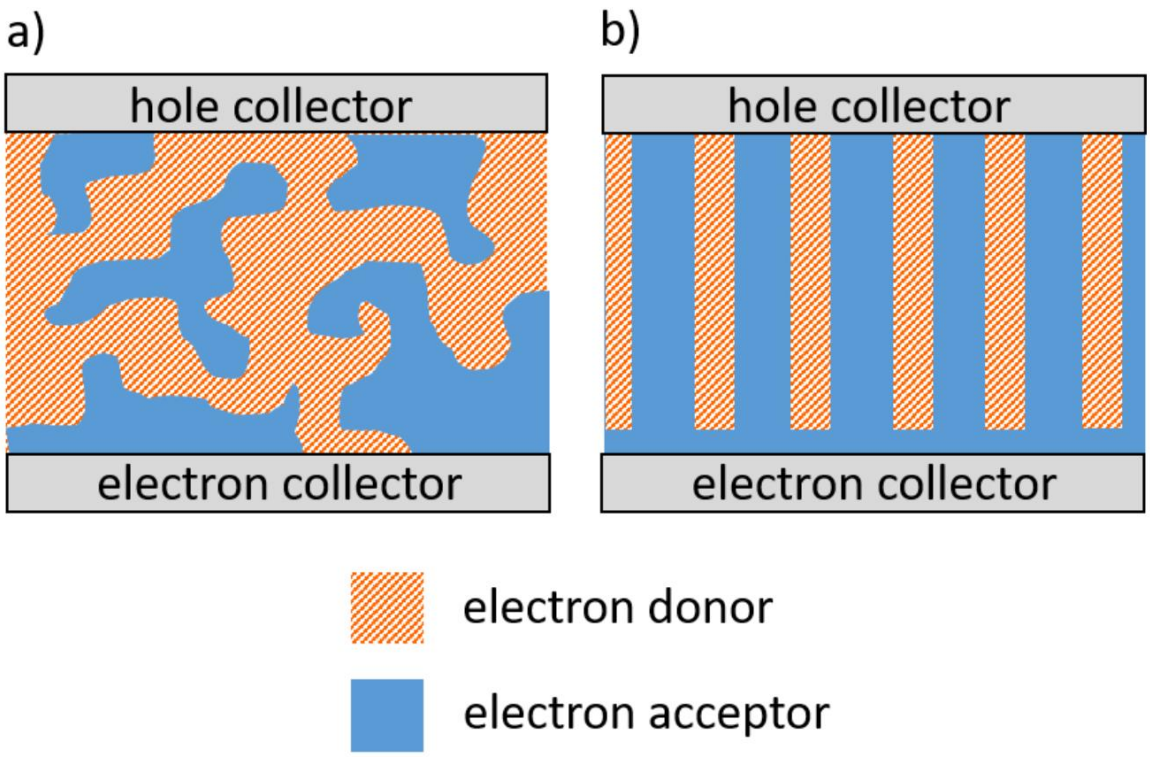

Fig. 13-6 Schematic of organic solar cell architecture.
a) Commonly employed bulk heterojunction structure, in which domains of the acceptor material exists within a matrix of the donor material due to polymer phase segregation. The charge carriers created at the donor/acceptor interface go through a percolation path to the charge collectors. b) Proposed structure, in which an array of vertically aligned nanowires of the donor material is backfilled with the acceptor material. The charge carriers have a direct path to the charge collectors.

14 DPP-TPA organic nanowire

We found that diketopyrrolopyrrole-triphenylamine (DPP-TPA, see Fig. 14-1a) to self-assemble into nanowires. As DPP-TPA has a well matched bandgap to the solar spectrum [53], DPP-TPA nanowires would be a good candidate for incorporation into solar cells. In hindsight, DPP-TPA was a good candidate for obtaining high carrier mobility, as the recent high mobility polymers contain the DPP core [272,273].

The experiments in this section were carried out, when I was a jointly funded graduate student between the Fréchet group and Zettl group. The organic molecules are synthesized by Olivia Lee, a graduate student in the Fréchet group. Jill Millstone, a post-doctoral researcher in the Fréchet group, assisted me with the synthesis of nanowires. The electrical characterization was carried out with Claudia Piliego, a post-doctoral researcher in the Fréchet group.

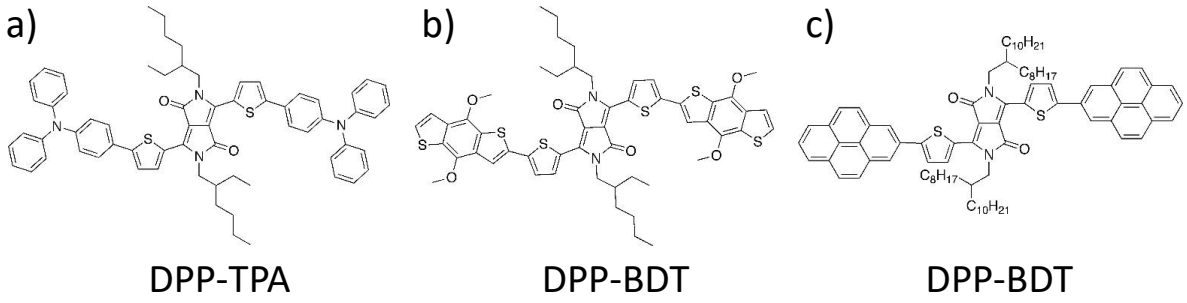

Fig. 14-1 Organic molecules for nanowire formation.
Molecules synthesized by Olivia Lee. All three molecules are composed of the central core diketopyrrolopyrrole (DPP) and end-groups a) triphenylamine (TPA), b) benzo[1,2-*b*;4,5-*b'*]dithiophene (BDT) and c) pyrene. The molecules have bandgaps suitable for efficient absorption of the solar spectrum [53].

14.1 Nanowire formation

DPP-TPA nanowires are formed by dissolving the DPP-TPA in a good solvent (chloroform) and mixing the solution with a poor solvent (ethanol). Quantitatively, 3 drops of 5mg/mol of DPP-TPA in chloroform are added into 5mL of ethanol, while stirring. After 20 minutes, large "cotton-like" aggregates appear in solution. As shown in the SEM image (Fig. 14-2a), the aggregates are made of nanowires. The longest nanowires are >100μm long and Ø~1.8-0.11μm (see Fig. 14-2b).

As exciton diffusion lengths are ~10nm, it is desirable to obtain nanowires with narrower diameters. If the concentration of the DPP-TPA solution is reduced, thinner nanowire could emerge since there are less materials near the nucleation centers. However, a nanowire growth attempt with 0.5mg/mL of DPP-TPA in chloroform yields particles instead of nanowires (see Fig. 14-3a). A closer look at the particles (Fig. 14-3b) shows a row of them starting to join into a wire. The nanowire formation process could be complicated. If the DPP-TPA first forms particles that subsequently join into wires, the lower limit on the minimum nanowire diameter is set by the size of the particle. While we have not found any compelling evidence beyond Fig. 14-3, the nanowire formation mechanism could be investigated further by dynamic light scattering measurement during nanowire formation. Alternatively, organic nanowires could be grown by vapor transport (see section 4.1.1) but DPP-TPA appears to decompose under the heat before it could sublime.

Nanowire formation with other molecules based on DPP are explored [53] (see Fig. 14-1). DPP with benzo[1,2-*b*;4,5-*b'*]dithiophene (DPP-BDT) and DPP with pyrene (DPP-Py) are used for nanowire formation with the same conditions as DPP-TPA. However, DPP-BDT and DPP-Py yielded fibrous aggregates that are mostly amorphous (see Fig. 14-4a, Fig. 14-5a). The solubilities of DPP-BDT and DPP-Py in ethanol are different from DPP-TPA and excess material precipitates as amorphous aggregates under the same condition. When the solution concentration is reduced from 5mg/mL to 0.5mg/mL, DPP-BDT yields nanowires (Fig. 14-4b) and DPP-Py yields dark rods of ~5μm (Fig. 14-5b). The short aspect ratios of DPP-Py is surprising as the sterics of DPP-Py would make it more susceptible to one dimensional stacking than DPP-TPA. The pyrene components in DPP-Py has been shown to π stack in DPP-Py crystallography [53]. In contrast, the TPA components in DPP-TPA are believed to hinder π stacking with its additional rotational degree of freedom.

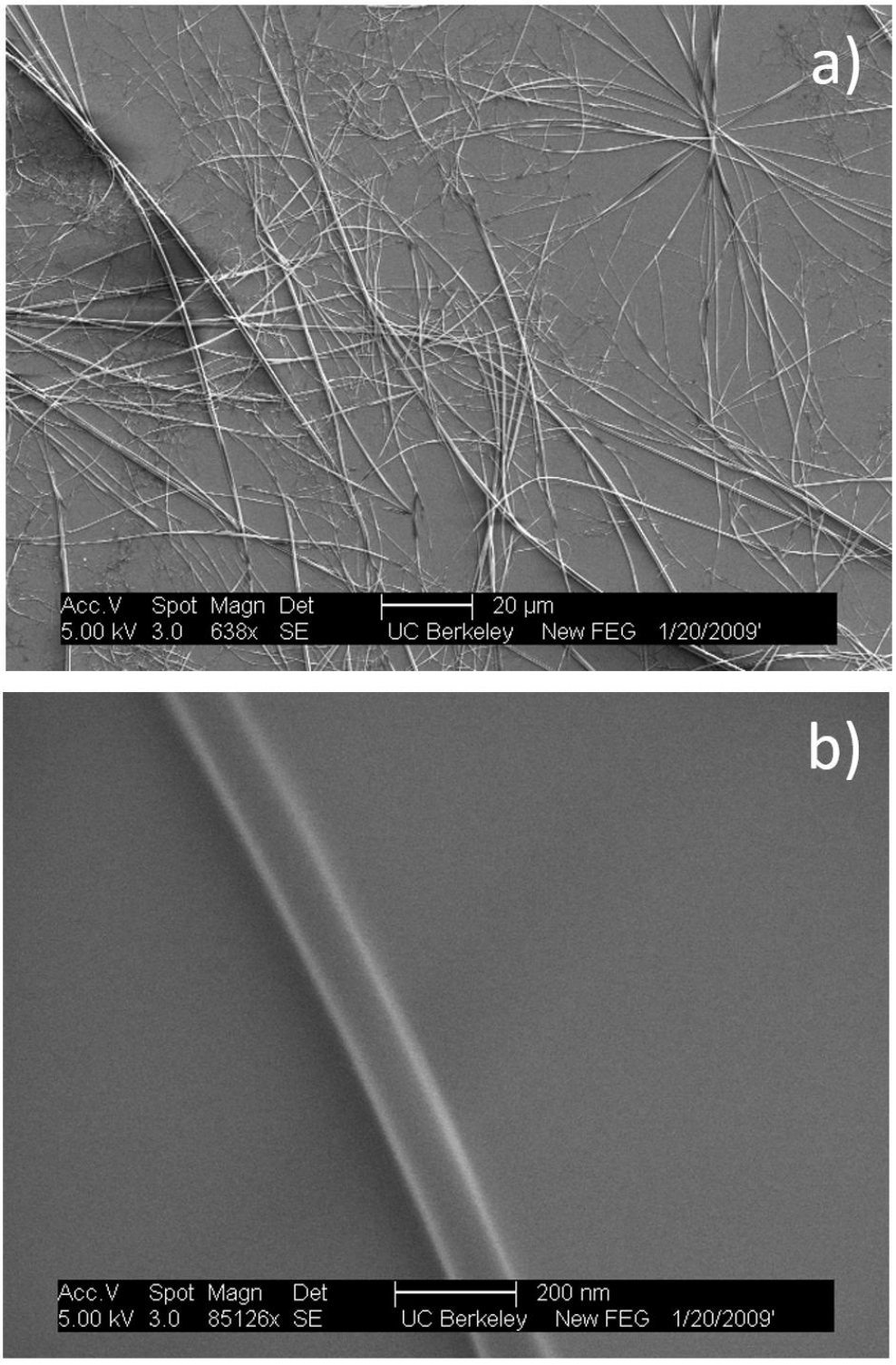

Fig. 14-2 DPP-TPA nanowires.
SEM image of DPP-TPA nanowires (from 5mg/mL DPP-TPA in chloroform) a) Bundles of nanowires. b) Magnified image of a nanowire.

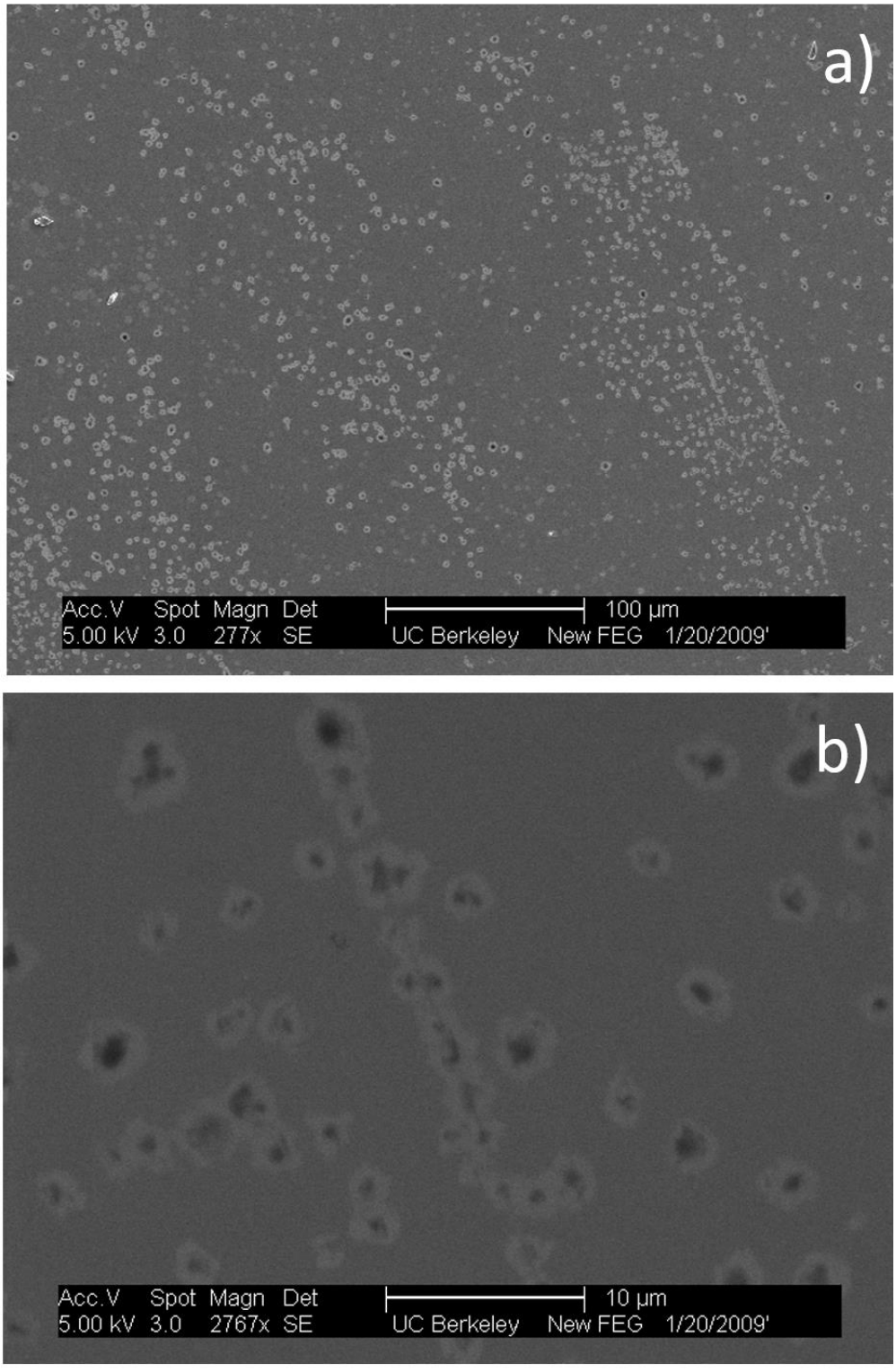

Fig. 14-3 DPP-TPA nanoparticles.
SEM image of DPP-TPA nanoparticles (from 0.5mg/mL DPP-TPA in chloroform) a) Collection of nanoparticles. b) Magnified image of a line of nanoparticles.

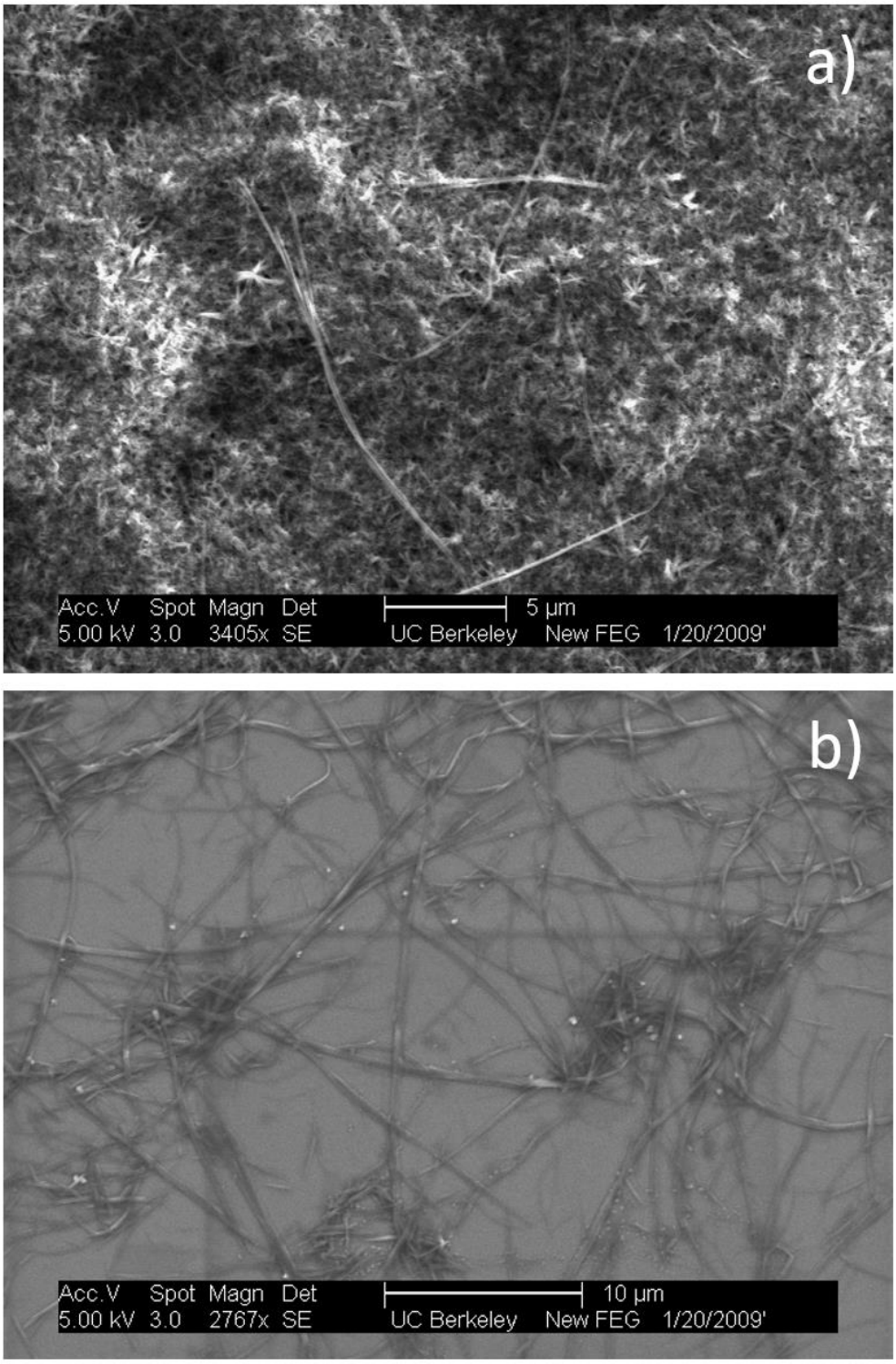

Fig. 14-4 DPP-BDT nanowires.
SEM image of DPP-BDT nanowire from a) 5mg/mL and b) 0.5mg/mL solution in chloroform.

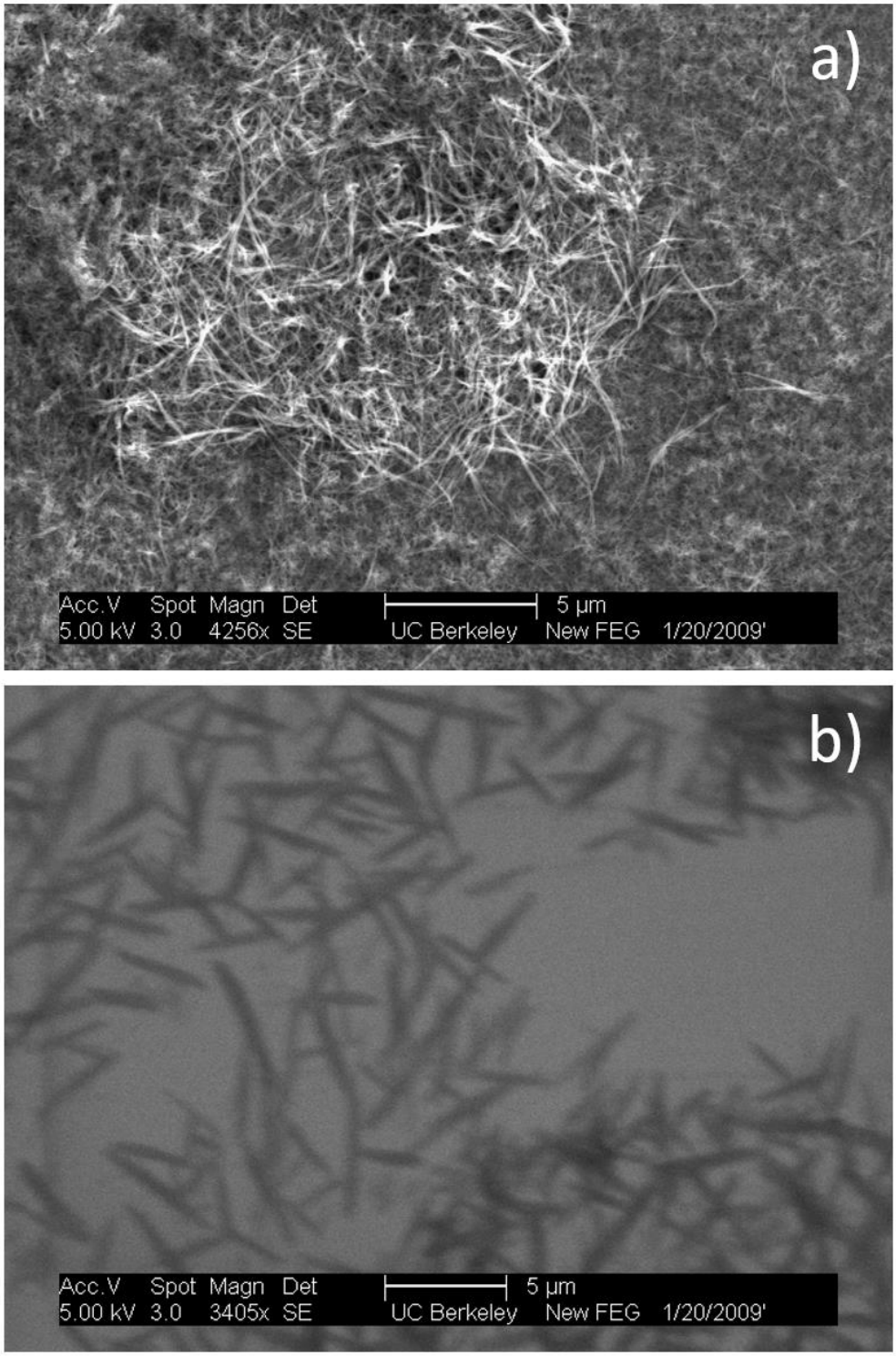

Fig. 14-5 DPP-Py nanowires.
SEM image of DPP-Py nanowire formation from a) 5mg/mL and b) 0.5mg/mL solution in chloroform.

14.2 Nanowire FET

Charge carrier mobility in DPP-TPA nanowires are measured in a FET configuration (see Chapter 12). DPP-TPA nanowires are deposited by spin-coating onto a Si/SiO_2 substrate with 300nm of SiO_2 and gold electrodes fabricated by photolithography. The substrate is treated with UV-ozone prior to nanowire deposition to aid the adhesion of the nanowires on the chip. The silicon is doped to serve as the gate electrode and the SiO_2 functions as a gate dielectric. The gold electrodes serve as source and drain contacts that make bottom contact to the nanowire. Fig. 14-6a shows a nanowire FET, with the lightly shaded part corresponding to the gold electrodes. On the left, a piece of nanowire bridges across the electrodes, bends back and bridges across it again. On the right, another nanowire lays vertically but closer inspection reveals that it does not bridge across the source drain electrodes.

The device shown in Fig. 14-6a is prepared in a glovebox and rapidly transferred to a vacuum probe station and measured at $P<10^{-5}$torr to minimize air exposure. Such precautions are necessary, since most organic semiconductors suffer from degradation in air within 5-10min. While in vacuum, the device is characterized with an Agilent 4155C semiconductor analyzer. The output curves in Fig. 14-7 shows the conductivity across the source-drain electrodes increases with the application of a negative gate voltage. With a positive gate voltage V_G=10V, I_D is negligible. Hence DPP-TPA nanowires exhibit p-type semiconducting behavior.

Fig. 14-8 shows the transfer curve, measured while keeping the source-drain voltage in the saturation regime V_{SD}=80V, and sweeping the gate voltage for V_G=10 to -80V. The inset shows the drain current at each gate voltage. As $I_D \sim V_G^2$ (Eq. 12-4) in the saturation regime, $\sqrt{I_D}(V_G)$ is plotted in the main panel with the black line corresponding to a linear fit. $\sqrt{I_D}$ does not increase until $V_G>V_T$=-13V due to some impurities at the interface, which unintentionally dopes the material. To calculate mobility, $C=13\times10^{-9}$F and L=10μm are extracted from the substrate geometry. A closer look at the nanowire after electrical characterization (Fig. 14-6b,c) shows the two portions bridging the source and drain have widths 667nm and 485nm, hence W=0.667+0.485=1.152μm. Using Eq. 12-5, the hole mobility is $\mu_h = 7.2\times10^{-3}cm^2/Vs$. For the thin film of DPP-TPA cast from solution, the hole mobility measured by Claudia Piliego is $\mu_h=6.5\times10^{-3}cm^2/Vs$. The DPP-TPA nanowire does not have a significantly higher mobility than its thin film form. The thin film mobility is reached after a series of device parameter optimization (e.g. annealing conditions). It is possible that the mobility in nanowire devices will increase significantly with optimized device fabrication.

Another point to be improved is the electrical contact to the sample. The increase at $V_G \sim V_T$ should be sharper in the ideal case. The curvature indicates the presence of energy barriers at the source and drain contacts. Contact resistance is likely a significant problem, since most of the devices that appear to have nanowires across them did not show any electrical response. The contact resistance would be improved by selecting a metal of appropriate work function and evaporating contacts on top of the nanowire instead of bottom contacts. However, DPP-TPA nanowires are unsuitable for patterning contacts with EBL (see section 9.1), as the solutions for chemical processing react with it and electron beams render the material insulating. We propose placing a shadow mask on top of the nanowire with good control over the placement location and evaporating contacts through the shadow mask.

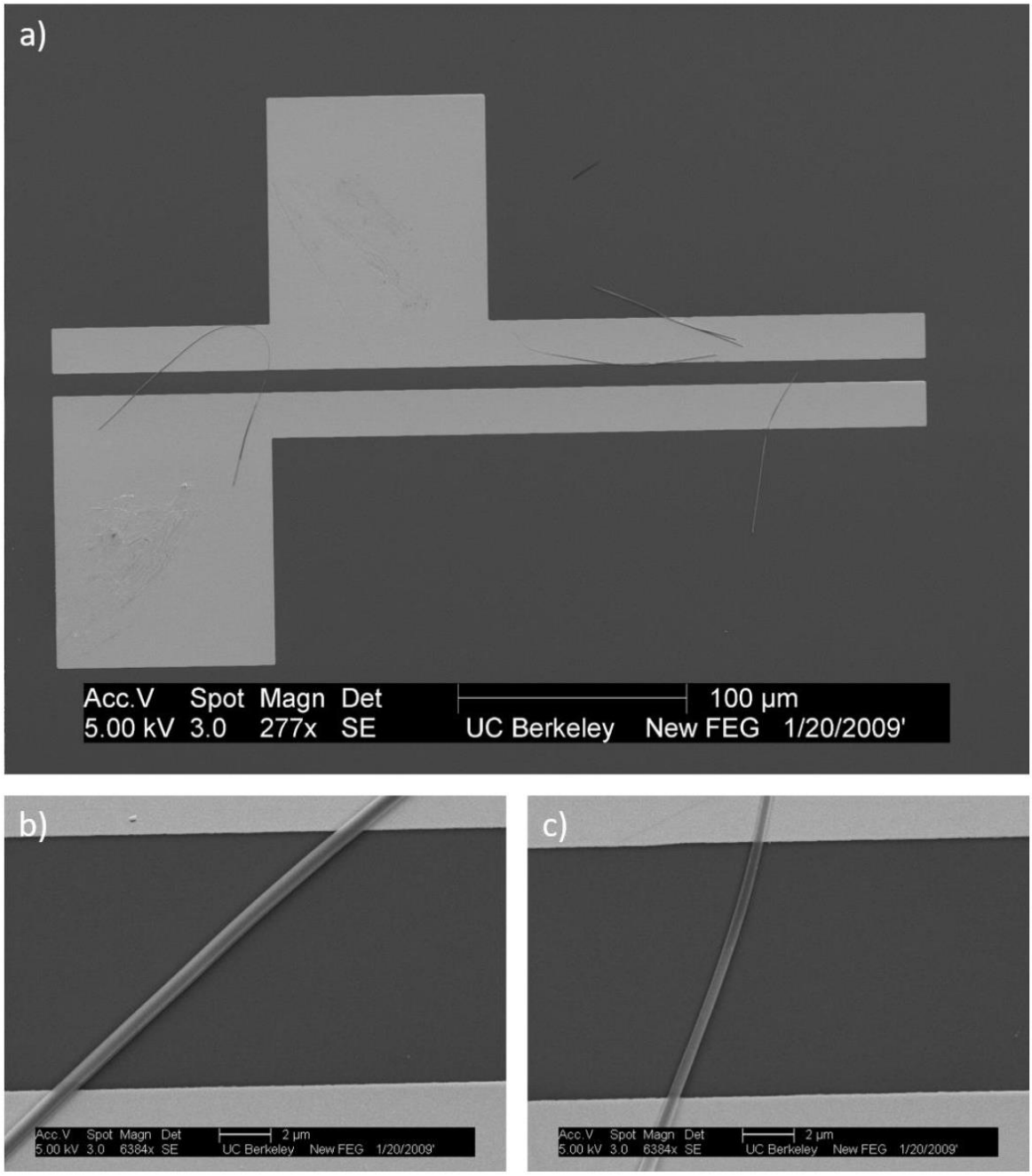

Fig. 14-6 DPP-TPA nanowire FET.
SEM image of DPP-TPA nanowire FET after measurement. a) View of whole nanowire FET device. The nanowire on the right half of the image does not bridge the contacts b, c) Magnified image of the two locations where the nanowire bridges the contacts.

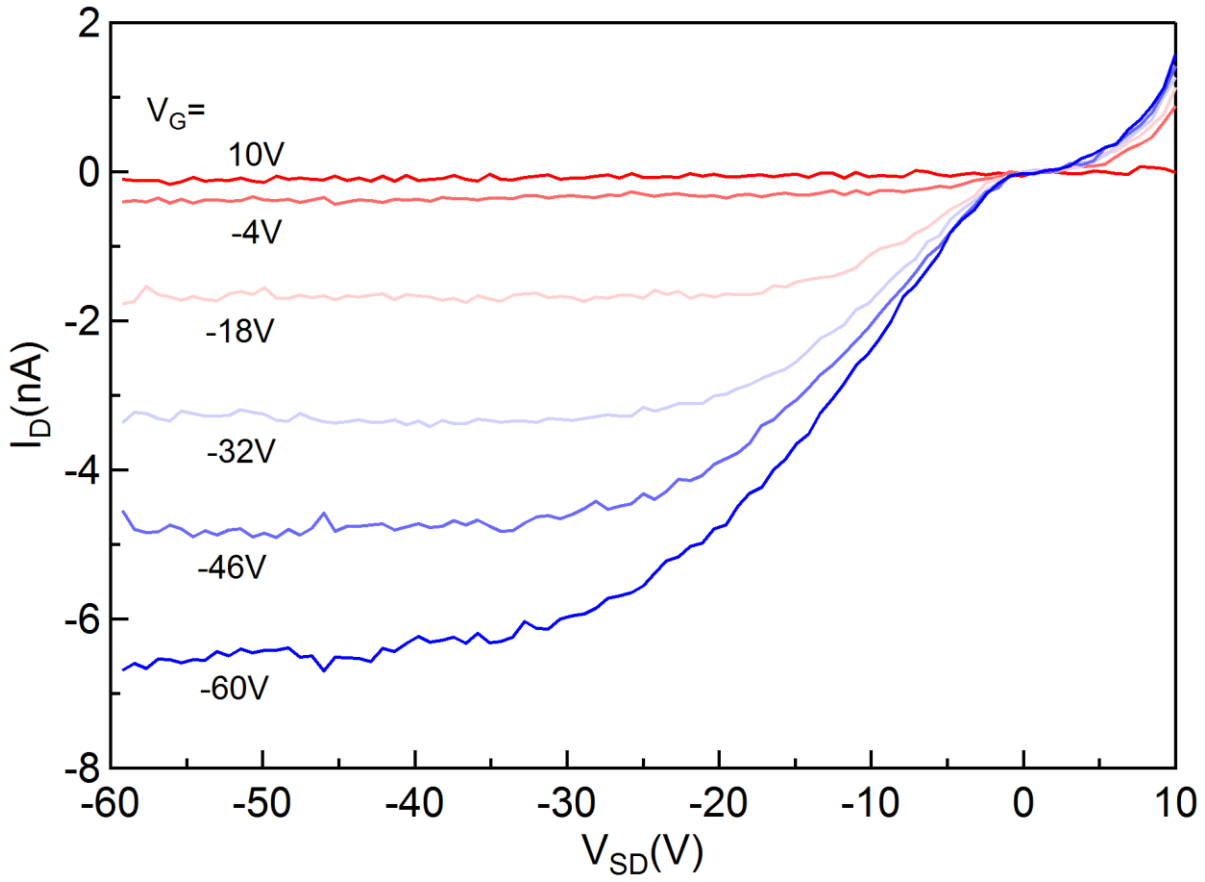

Fig. 14-7 Output curves of DPP-TPA nanowire FET.
Series of I(V) curves across the source-drain contacts for V_G=10 to -60V.

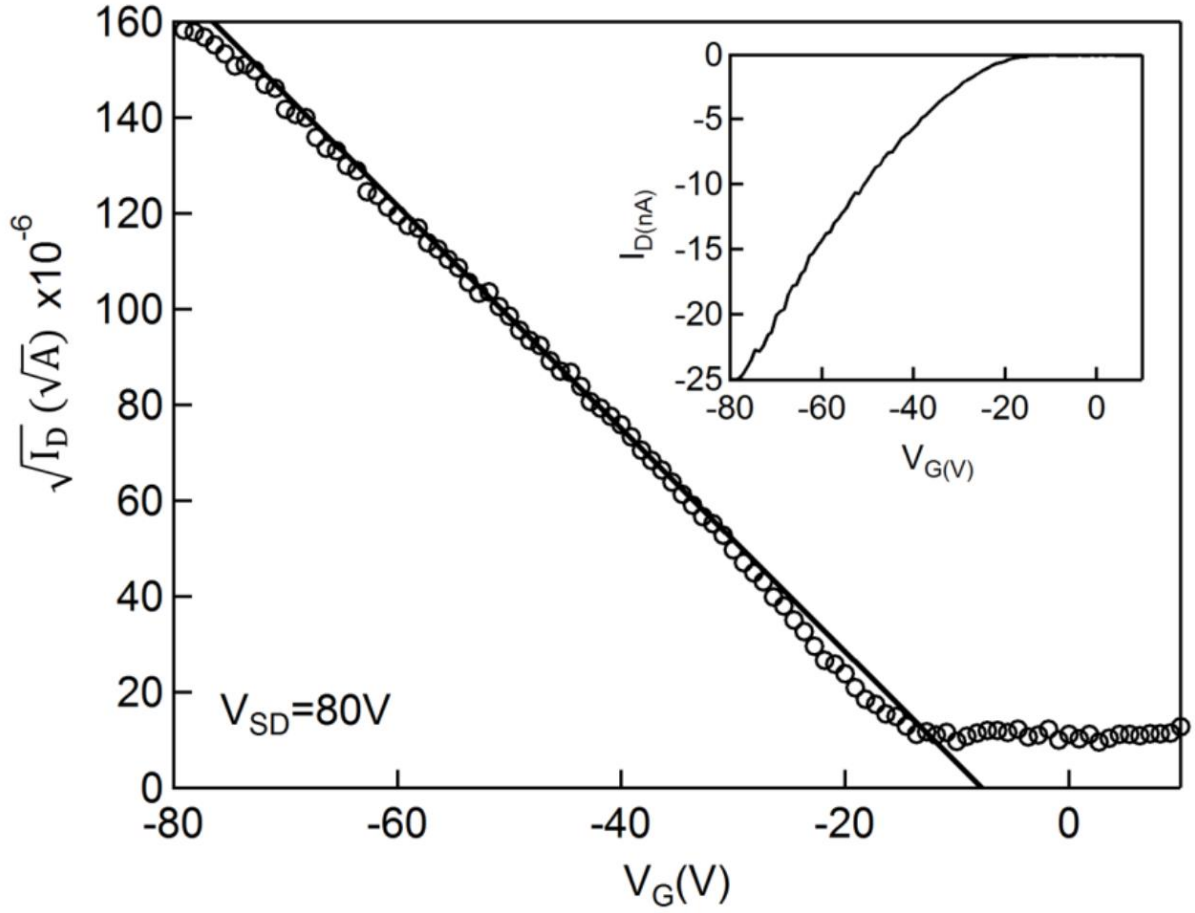

Fig. 14-8 Transfer curve of DPP-TPA nanowire FET.
Inset: drain current for V_G=10 to -80V for fixed V_{SD}=80V. Main panel: square root of the drain current vs V_G. Line is a fit to extract mobility (Eq. 12-5).

15 Rubrene crystals for molecular interface studies

In organic photovoltaics, the interface between the acceptor and donor molecules is essential for charge separation. In particular, C_{60} has been identified as an outstanding acceptor molecule, capable of making charge separation much more efficient compared to other acceptors. Central to understanding the photophysics and device physics of organic solar cells was the "two-layer" solar cell by Tang [274], composed of a layer of acceptor molecules evaporated on top of a thin film of donor molecules. This simple, well-defined structure was a model system for fundamental experiments [274]. I propose to use rubrene as the donor material in a bilayer solar cell to serve as a similar "clean" model system. Compared to the PcCu (Fig. 13-1,"PcCu") thin films used by Tang, the charge transport and exciton diffusion in a single crystal of rubrene is not masked by disorder. Hence, the exciton dynamics and charge separation at the interface could be probed more extensively through the photoconductivity of a rubrene crystal based solar cell. For rubrene, charge transport is extensively characterized and the exciton diffusion has been well studied [275].

Although C_{60} is often used as an acceptor in solar cells for its efficient charge separation [276], it does not absorb strongly for visible light [277]. The power conversion efficiency will significantly improve if we find an acceptor molecule, which strongly absorbs in visible light and enables charge separation as effectively as C_{60}. Rubrene crystals could provide a platform to characterize the exciton and charge carrier dynamics at the interface with novel acceptors developed by the Fréchet group [278]. The fundamental understanding could provide hints for the design of subsequent iterations of molecules.

To assess the viability of my proposal, the photoconductivity of C_{60}/rubrene is characterized. Single crystal rubrene (see section 4.3) is contacted with graphite paint and 10nm of C_{60} is evaporated on the region between the contacts. The sample is rapidly transferred from the evaporator to a glovebox to minimize exposure to air. The sample is characterized by a probe station built inside the glovebox. I(V) curves are measured in the dark and under illumination with a halogen light bulb. As shown in Fig. 15-1, the rubrene crystal shows some enhancement in conductivity with illumination. The sample photoresponse is negligible at zero bias and shows a weak photoresponse at high bias. The I(V) curves are repeatable and no hysteresis is observed for change in voltage. Fig. 15-2 shows the conductivity of the sample increases after C_{60} deposition. Since the dark conductivity increases, it is likely the rubrene is annealed during the unintentional heating effect of the evaporation process. The conductivity enhancement from light is still weak for the C_{60}/rubrene sample and it is difficult to distinguish from the rubrene photoconductivity. It is possible that the bulk conductivity in rubrene is too high and dominates over the conduction by carriers created at the interface. Since rubrene crystals used are ~10μm, thinner crystals can be obtained by tuning the crystal synthesis parameters.

Although C_{60} is compatible with vapor deposition, most molecules for solar cells are not. They are primarily designed for deposition from solution, which is the most attractive route to low cost flexible electronics. The rubrene crystal should be compatible with the deposition of novel acceptor molecules as well. However, the solvents for dissolving the acceptor molecule usually dissolve the rubrene as well. Phenyl-C_{61}-butyric acid methyl ester (PCBM), is a functionalized form of C_{60} to make it easily soluble in organic solvents. When PCBM in chlorobenzene is spun on rubrene at 2000rpm for 40s, the rubrene completely dissolves in the chlorobenzene. To minimize the exposure to chlorobenzene, the PCBM solution is deposited on the rubrene after it is fully accelerated to 2000rpm. However, the deposition does not yield a PCBM film of substantial thickness.

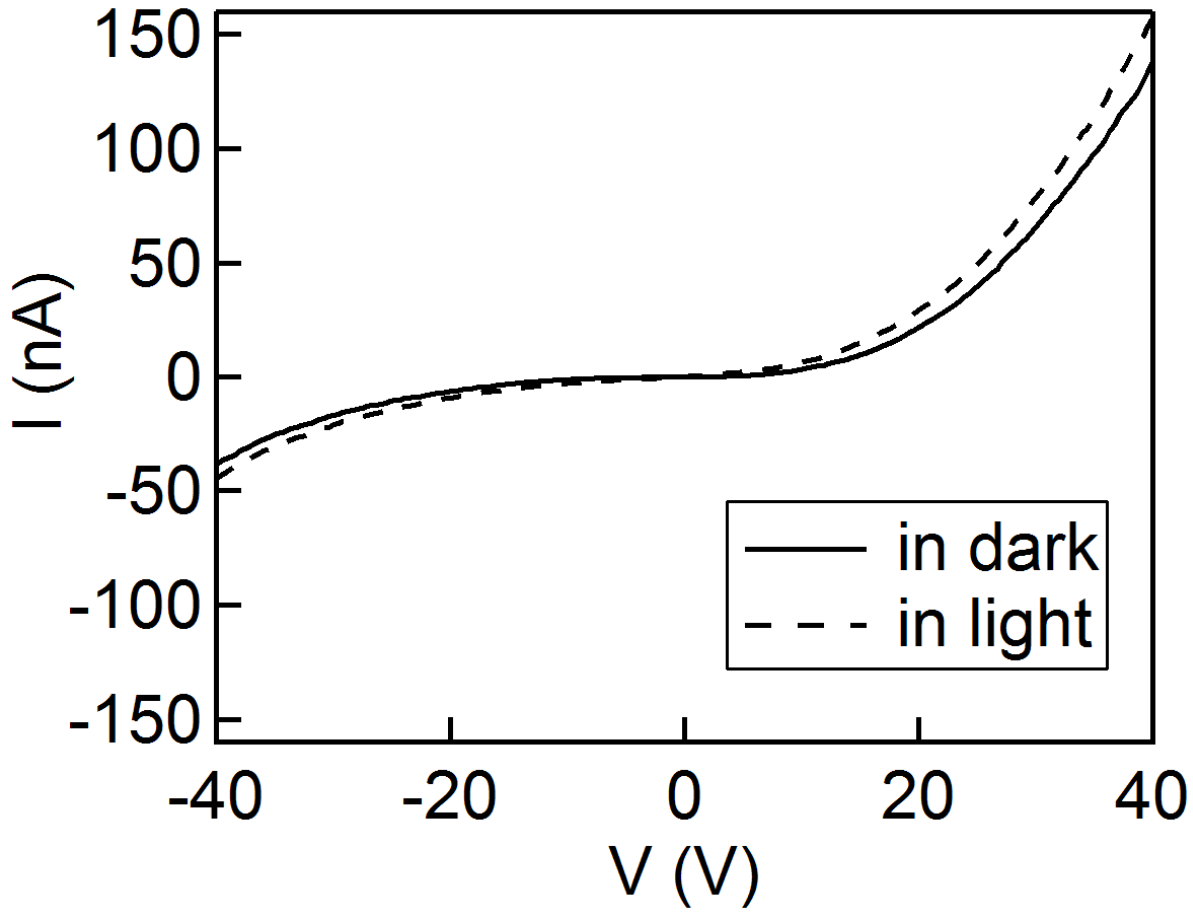

Fig. 15-1 I(V) curves of rubrene crystal.
Before C_{60} deposition. Measurement with no light (solid line) and under halogen light bulb illumination (dashed line) are shown.

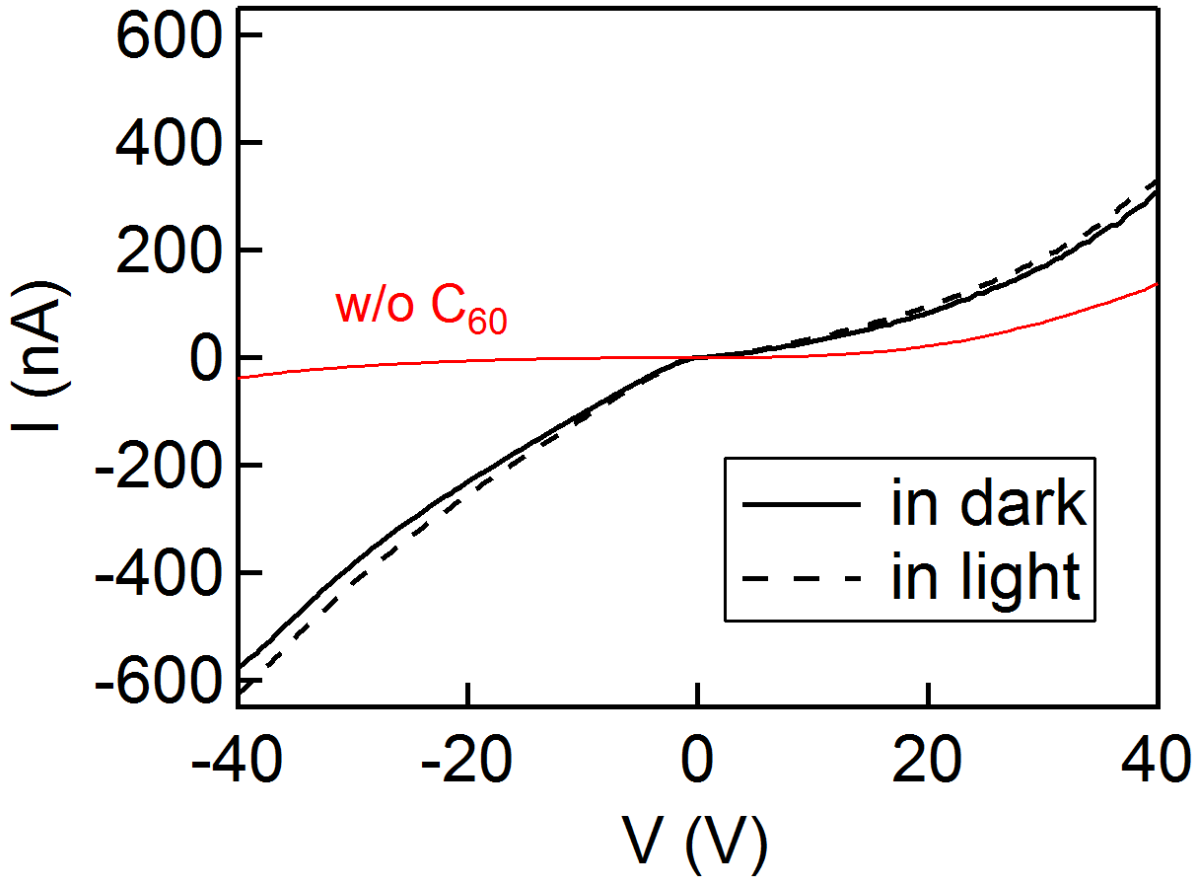

Fig. 15-2 I(V) curves of rubrene crystal+C_{60}.
Measurement with no light (black, solid line), under halogen light bulb illumination (dashed line) and rubrene before C_{60} deposition (thin, red line) are shown.

Conclusion

Transition metal chalcogenides are the most promising system for the study of collective ground states at the 2D and 1D limit. In particular, the mechanical exfoliation is effective for quasi-1D MX_3 materials and calls for further exploration. The TMC possess collective ground states in the bulk and the effect of low dimensionality can be tracked as the thickness is gradually reduced to the atomic low dimensional limit. Currently, it appears that both superconductivity (see Chapter 5) and CDW (see section 6.1) are suppressed at the atomic 2D and 1D limit. This is counter-intuitive for CDW since it is driven by low-dimensional features of a system. It is still unclear if this is a general trend across materials. One counter-example is the enhancement of T_c from 8K in bulk to 100K in monolayer FeSe on $SrTiO_3$. There is still no conclusive evidence whether this effect is due to the interaction with the substrate or not. The report of CDW enhancement in monolayer $NbSe_2$ [48] is in direct conflict with our observations [49]. In our study, the transition temperature remains largely unchanged at the monolayer limit for $NbSe_2$. For $NbSe_3$, the transition temperature also did not change significantly change with confinement but the CDW state was greatly suppressed [96]. The CDW state seems to completely disappear in $NbSe_3$ nanoribbons thinner than 25nm, before reaching the atomic 1D limit. This observation was made with the use of narrowband noise, enabled by the sliding CDW. For materials with sliding CDW, this will continue to be a useful tool for characterizing the CDW order parameter. When using narrowband noise measurements at the nanoscale, it must be controlled against increasing dominance of surface effects with reduction in sample size.

While mechanical exfoliation would provide much insight at the ~10nm scale, it is unclear whether the single chain limit could be reached with this method. 2D monolayers are identified because most of them have lateral dimensions of ~10μm. In contrast, 1D single chains would only be a few atoms wide, which is too narrow to see. It is likely that the analogy with 2D materials break down at that point and more advanced techniques to locate and contact the single chains are needed. Alternatively, the growth of MX_3 inside BNNT seems more promising (see section 6.3). The growth is limited to only a few parallel chains due to the size of the BNNT inner space. The BNNT acts as both a template and protective sheath for the MX_3. The drawback of the MX_3/BNNT is that it would be difficult to compare with the electronic properties of the bulk. The maximum number of chains is set by the nanotube inner diameter and often confinement effects cause materials to adopt different structures than in an open environment. Hence the MX_3/BNNT approach resembles the method of creating and studying a unique 1D nanomaterial, seen with carbon nanomaterials.

The electromechanical measurements of carbon nanomaterials were technically more challenging than transport measurements but still seem achievable with the use of appropriate techniques from micromachining. The carbon nanotube resonator (see Chapter 10) and graphene straining platform (see Chapter 11) are promising because both field emission and strain fields are enhanced as we scale down the sample size. In this respect, it is unclear how well the contactless measurement setup (see Chapter 7) scales down to the nanoscale. While such an analog to the "cm" scale is much desired at the nanoscale, simulations indicate that higher frequencies are required when the setup is scaled down. It is possible that the actual analog of contactless measurements are terahertz measurements [279].

The self-assembly of organic molecules into nanowires is attractive for its simple synthesis method. It can be obtained in solution at room temperature. However, extensive optimization is needed to yield nanowires of narrow diameter and high mobility. While organic molecules offer

tunable control of self-assembly properties, the sensitivity of self-assembly dynamics to functional groups complicates the search for the optimum molecular structure. In addition, it seems difficult to achieve delocalized transport with only π orbital overlap. Even organic semiconductors with the highest charge carrier mobility are at the border between delocalized and hopping transport. However, this may be complimented by introducing dopants (e.g. alkali metals, iodine) to increase the carrier density (see section 3.2.3).

Finally, experimental work with three classes of materials (i.e. TMC, carbon nanomaterials and organic semiconductors) highlighted the importance of chemical stability. When looking at the historical evolution of successful low-dimensional materials, it is easy to overlook the importance of chemical stability. However, initial efforts to handle monolayer TMC similarly to graphene was hindered by degradation in air for many materials. For organic molecules, the rich variation in functional groups would offer a great library of low dimensional nanostructures but their sensitivity to temperature, chemicals and radiation render them incompatible with many of the nanofabrication techniques developed for carbon nanomaterials. It is tempting to regard carbon nanomaterials as an anomalously successful case due to their robustness against temperature, chemicals and mechanical forces. However, innovative techniques to protect other materials have expanded the library of 2D materials and similar developments are anticipated for 1D materials.

Bibliography

1 Dirac P.A.M. Quantum Mechanics of Many-Electron Systems. *Proceedings of the Royal Society A: Mathematical, Physical and Engineering Sciences* (1929) **123** 714–733.

2 Skocpol W.J., Tinkham M. Fluctuations near superconducting phase transitions. *Reports on Progress in Physics* (1975) **38** 1049–1097.

3 Ising E. Beitrag zur Theorie des Ferromagnetismus. *Zeitschrift für Physik* (1925) **31** 253–258.

4 Onsager L. Crystal statistics. I. A two-dimensional model with an order-disorder transition. *Physical Review* (1944) **65** 117–149.

5 Voit J. One-dimensional Fermi liquids. *Reports on Progress in Physics* (1995) **58** 977–1116.

6 Phillips P., Dalidovich D. The elusive Bose metal. *Science* (2003) **302** 243–247.

7 Robertson J. Amorphous carbon. *Advances in Physics* (1986) **35** 317–374.

8 Little W.A. Possibility of Synthesizing an Organic Superconductor. *Physical Review* (1964) **134** A1416–A1424.

9 Jérome D., Schulz H.J. Organic conductors and superconductors. *Advances in Physics* (1982) **31** 299–490.

10 Grüner G., Zettl A. Charge density wave conduction: A novel collective transport phenomenon in solids. *Physics Reports* (1985) **119** 117–232.

11 Etemad S., Heeger A.J., MacDiarmid A.G. Polyacetylene, (CH)x: The Prototype Conducting Polymer. *Annual Review of Physical Chemistry* (1982) **33** 443–469.

12 Yuen J.D., Menon R., Coates N.E., Namdas E.B., Cho S., Hannahs S.T. *et al.* Nonlinear transport in semiconducting polymers at high carrier densities. *Nature Materials* (2009) **8** 572–575.

13 Troisi A. Organic conductors: Polymers as one-dimensional metals. *Nature Materials* (2009) **8** 538–539.

14 Requist R., Baruselli P.P., Smogunov A., Fabrizio M., Modesti S., Tosatti E. Metallic, magnetic and molecular nanocontacts. *Nature Nanotechnology* (2016) **11** 499–508.

15 Baughman R.H. Carbon Nanotubes--the Route Toward Applications. *Science* (2002) **297** 787–792.

16 Bockrath M., Cobden D.H., Lu J., Rinzler A.G., Smalley R.E., Balents L. *et al.* Luttinger-liquid behavior in carbon nanotubes. *Nature* (1999) **397** 598–601.

17 Haviland D.B., Liu Y., Goldman A.M. Onset of superconductivity in the two-dimensional limit. *Physical Review Letters* (1989) **62** 2180–2183.

18 Yazdani A., Kapitulnik A. Superconducting-insulating transition in two-dimensional a-MoGe thin films. *Physical Review Letters* (1995) **74** 3037–3040.

19 Tsui D.C., Stormer H.L., Gossard A.C. Two-dimensional magnetotransport in the extreme quantum limit. *Physical Review Letters* (1982) **48** 1559–1562.

20 Laughlin R.B. Anomalous quantum Hall effect: An incompressible quantum fluid with fractionally charged excitations. *Physical Review Letters* (1983) **50** 1395–1398.

21 Wilson J.A., Di Salvo F.J., Mahajan S. Charge-density waves and superlattices in the metallic layered transition metal dichalcogenides. *Advances in Physics* (1975) **24** 117–201.

22 Frindt R. Superconductivity in ultrathin NbSe2 layers. *Physical Review Letters* (1972) **28** 299–301.

23 Novoselov K.S., Geim A.K., Morozov N., Jiang D., Zhang Y., Dubonos S. V *et al.* Electric Field Effect in Atomically Thin Carbon Films. *Science* (2004) **306** 666–669.
24 Castro Neto A.H., Guinea F., Peres N.M.R., Novoselov K.S., Geim A.K. The electronic properties of graphene. *Reviews of Modern Physics* (2009) **81** 109–162.
25 Yan B., Zhang S.-C. Topological materials. *Reports on Progress in Physics* (2012) **75** 96501.
26 Oura K., Lifshits V.G., Saranin A.A., Zotov A.V., Katayama M. Surface Science An Introduction. *Springer Verlag* (2003) 179.
27 Blake P., Hill E.W., Castro Neto A.H., Novoselov K.S., Jiang D., Yang R. *et al.* Making graphene visible. *Applied Physics Letters* (2007) **91** 0–3.
28 Wang F., Cho D.J., Kessler B., Deslippe J., Schuck P.J., Louie S.G. *et al.* Observation of excitons in one-dimensional metallic single-walled carbon nanotubes. *Physical Review Letters* (2007) **99** 1–4.
29 Shi Z., Hong X., Bechtel H.A., Zeng B., Martin M.C., Watanabe K. *et al.* Observation of a Luttinger-liquid plasmon in metallic single-walled carbon nanotubes. *Nature Photonics* (2015) **9** 515–519.
30 Hone J., Whitney M., Piskoti C., Zettl A. Thermal conductivity of single-walled carbon nanotubes. *Physical Review B* (1999) **59** R2514–R2516.
31 Bunch J.S., van der Zande A.M., Verbridge S.S., Frank I.W., Tanenbaum D.M., Parpia J.M. *et al.* Electromechanical Resonators from Graphene Sheets. *Science* (2007) **315** 490–493.
32 Chen C., Rosenblatt S., Bolotin K.I., Kalb W., Kim P., Kymissis I. *et al.* Performance of monolayer graphene nanomechanical resonators with electrical readout. *Nature nanotechnology* (2009) **4** 861–867.
33 Van Der Zande A.M., Barton R.A., Alden J.S., Ruiz-Vargas C.S., Whitney W.S., Pham P.H.Q. *et al.* Large-scale arrays of single-layer graphene resonators. *Nano Letters* (2010) **10** 4869–4873.
34 Bourne L.C., Zettl A. Elastic properties of charge-density-wave conductors in applied electric fields. *Physical Review B* (1987) **36** 2626–2637.
35 Sengupta S., Solanki H.S., Singh V., Dhara S., Deshmukh M.M. Electromechanical resonators as probes of the charge density wave transition at the nanoscale in NbSe2. *Physical Review B* (2010) **82** 155432.
36 Struck P.R., Wang H., Burkard G. Nanomechanical readout of a single spin. *Physical Review B* (2014) **89** 45404.
37 Hicks C.W., Brodsky D.O., Yelland E.A., Gibbs A.S., Bruin J.A.N., Barber M.E. *et al.* Strong Increase of Tc of Sr2RuO4 Under Both Tensile and Compressive Strain. *Science* (2014) **344** 283–285.
38 Steppke A., Zhao L., Barber M.E., Scaffidi T., Jerzembeck F., Rosner H. *et al.* Strong peak in T c of Sr 2 RuO 4 under uniaxial pressure. *Science* (2017) **355** eaaf9398.
39 Mas-Ballesté R., Gómez-Navarro C., Gómez-Herrero J., Zamora F. 2D materials: to graphene and beyond. *Nanoscale* (2011) **3** 20–30.
40 Sheneve Z. Butler, Shawna M. Hollen, Linyou Cao, Yi Cui J.A.G. Opportunities in Two-Dimensional Materials Beyond Graphene. *ACS Nano* (2013) **7** 2898–2926.
41 Geim A.K., Grigorieva I. V. Van der Waals heterostructures. *Nature* (2013) **499** 419–25.
42 Radisavljevic B., Radenovic A., Brivio J., Giacometti V., Kis A. Single-layer MoS2 transistors. *Nature Nanotechnology* (2011) **6** 147–150.

43 Cao Y., Mishchenko A., Yu G.L., Khestanova E., Rooney A.P., Prestat E. *et al.* Quality heterostructures from two-dimensional crystals unstable in air by their assembly in inert atmosphere. *Nano Letters* (2015) **15** 4914–4921.
44 Kessler B.M., Girit Ç.Ö., Zettl A., Bouchiat V. Tunable Superconducting Phase Transition in Metal-Decorated Graphene Sheets. *Physical Review Letters* (2010) **104** 47001.
45 Morpurgo A.F. Gate-Controlled Superconducting Proximity Effect in Carbon Nanotubes. *Science* (1999) **286** 263–265.
46 Goli P., Khan J., Wickramaratne D., Lake R.K., Balandin A.A. Charge density waves in exfoliated films of van der waals materials: Evolution of raman spectrum in TiSe2. *Nano Letters* (2012) **12** 5941–5945.
47 Tsen A.W., Hovden R., Wang D., Kim Y.D., Okamoto J., Spoth K. a *et al.* Structure and control of charge density waves in two-dimensional 1T-TaS2. *Proceedings of the National Academy of Sciences* (2015) **112** 15054–15059.
48 Xi X., Zhao L., Wang Z., Berger H., Forró L., Shan J. *et al.* Strongly enhanced charge-density-wave order in monolayer NbSe2. *Nature Nanotechnology* (2015) **10** 765–769.
49 Ugeda M.M., Bradley A.J., Zhang Y., Onishi S., Chen Y., Ruan W. *et al.* Characterization of collective ground states in single-layer NbSe2. *Nature Physics* (2015) **12** 92–97.
50 Island J.O., Molina-Mendoza A.J., Barawi M., Biele R., Flores E., Clamagirand J.M. *et al.* Electronics and optoelectronics of quasi-1D layered transition metal trichalcogenides. *2D Materials* (2017) **4** 22003.
51 Curtis M.D., Cao J., Kampf J.W. Solid-State Packing of Conjugated Oligomers: From π-Stacks to the Herringbone Structure. *Journal of the American Chemical Society* (2004) **126** 4318–4328.
52 Jin W., Fukushima T., Niki M., Kosaka A., Ishii N., Aida T. Self-assembled graphitic nanotubes with one-handed helical arrays of a chiral amphiphilic molecular graphene. *Proceedings of the National Academy of Sciences of the United States of America* (2005) **102** 10801–10806.
53 Lee O.P., Yiu A.T., Beaujuge P.M., Woo C.H., Holcombe T.W., Millstone J.E. *et al.* Efficient Small Molecule Bulk Heterojunction Solar Cells with High Fill Factors via Pyrene-Directed Molecular Self-Assembly. *Advanced Materials* (2011) **23** 5359–5363.
54 Lenes M., Kooistra F.B., Hummelen J.C., Van Severen I., Lutsen L., Vanderzande D. *et al.* Charge dissociation in polymer:fullerene bulk heterojunction solar cells with enhanced permittivity. *Journal of Applied Physics* (2008) **104** 114517.
55 Anderson P.W. More Is Different. *Science* (1972) **177** 393–396.
56 Kittel C. Introduction to solid state physics. *8th ed. John Wiley & Sons Inc.* (2005) p161-218.
57 Novoselov K.S., Geim A.K., Morozov S. V, Jiang D., Katsnelson M.I., Grigorieva I. V *et al.* Two-dimensional gas of massless Dirac fermions in graphene. *Nature* (2005) **438** 197–200.
58 Xu S.-Y., Belopolski I., Alidoust N., Neupane M., Bian G., Zhang C. *et al.* Discovery of a Weyl fermion semimetal and topological Fermi arcs. *Science* (2015) **349** 613–617.
59 Lv B.Q., Weng H.M., Fu B.B., Wang X.P., Miao H., Ma J. *et al.* Experimental Discovery of Weyl Semimetal TaAs. *Physical Review X* (2015) **5** 31013.
60 Kittel C. Introduction to solid state physics. *8th ed. John Wiley & Sons Inc.* (2005) p279.
61 Tinkham M. Introduction to superconductivity. *2nd ed. Dover Publications, Inc.* (1996) p43-108.

62 Norman M.R. The Challenge of Unconventional Superconductivity. *Science* (2011) **332** 196–200.
63 Kittel C. Introduction to solid state physics. *8th ed. John Wiley & Sons Inc.* (2005) p258-264.
64 Xiang X.-D., Hou J.G., Crespi V.H., Zettl A., Cohen M.L. Three-dimensional fluctuation conductivity in superconducting single crystal K3C60 and Rb3C60. *Nature* (1993) **361** 54–56.
65 Griffiths D.J. Electricity and Magnetism. *3rd ed. Prentice-Hall, Inc.* (1999) p303.
66 Tinkham M. Introduction to superconductivity. *2nd ed. Dover Publications, Inc.* (1996) p135-138.
67 Gurevich A. Challenges and Opportunities for Applications of Unconventional Superconductors. *Annual Review of Condensed Matter Physics* (2014) **5** 35–56.
68 Clogston A.M. Upper Limit for the Critical Field in Hard Superconductors. *Physical Review Letters* (1962) **9** 266–267.
69 Chandrasekhar B.S. A note on the maximum critical field of high-field superconductors. *Applied Physics Letters* (1962) **1** 7–8.
70 Kittel C. Introduction to solid state physics. *8th ed. John Wiley & Sons Inc.* (2005) p261.
71 Matthias B.T., Geballe T.H., Compton V.B. Superconductivity. *Reviews of Modern Physics* (1963) **35** 1–22.
72 Conder K. A second life of the Matthias's rules. *Superconductor Science and Technology* (2016) **29** 80502.
73 Drozdov A.P., Eremets M.I., Troyan I.A., Ksenofontov V., Shylin S.I. Conventional superconductivity at 203 K at high pressures. *Nature* (2015) **525** 73.
74 Moussa J.E., Cohen M.L. Two bounds on the maximum phonon-mediated superconducting transition temperature. *Physical Review B* (2006) **74** 94520.
75 Wu M.K., Ashburn J.R., Torng C.J., Hor P.H., Meng R.L., Gao L. *et al.* Superconductivity at 93 K in a new mixed-phase Y-Ba-Cu-O compound system at ambient pressure. *Physical Review Letters* (1987) **58** 908–910.
76 Paglione J., Greene R.L. High-temperature superconductivity in iron-based materials. *Nature Physics* (2010) **6** 645–658.
77 Saito Y., Nojima T., Iwasa Y. Highly crystalline 2D superconductors. *Nature Reviews Materials* (2016) **2** 16094.
78 Monceau P. Electronic crystals: an experimental overview. *Advances in Physics* (2012) **61** 325–581.
79 Thomson R.E., Burk B., Zettl A., Clarke J. Scanning tunneling microscopy of the charge-density-wave structure in 1T-TaS2. *Physical Review B* (1994) **49** 16899–16916.
80 Chaussy J., Haen P., Lasjaunias J.C., Monceau P., Waysand G., Waintal A. *et al.* Phase transitions in NbSe3. *Solid State Communications* (1976) **20** 759–763.
81 Harper J.M.E., Geballe T.H., Di Salvo F.J. Heat capacity of 2H-NbSe2 at the charge density wave transition. *Physics Letters A* (1975) **54A** 27–28.
82 Zybtsev S.G., Pokrovskii V.Y., Nasretdinova V.F., Zaitsev-Zotov S. V., Pavlovskiy V. V., Odobesco A.B. *et al.* NbS3 : A unique quasi-one-dimensional conductor with three charge density wave transitions. *Physical Review B* (2017) **95** 35110.
83 Mihaila B. Lindhard function of a d-dimensional Fermi gas. (2011) arXiv:1111.5337 [cond-quant-gas].
84 Johannes M.D., Mazin I.I. Fermi surface nesting and the origin of charge density waves in

metals. *Physical Review B - Condensed Matter and Materials Physics* (2008) **77** 1–8.
85 Rice T.M., Scott G.K. New Mechanism for a Charge-Density-Wave Instability. *Physical Review Letters* (1975) **35** 120–123.
86 Weber F., Rosenkranz S., Castellan J.P., Osborn R., Hott R., Heid R. *et al.* Extended phonon collapse and the origin of the charge-density wave in 2H-NbSe2. *Physical Review Letters* (2011) **107** 1–5.
87 Frohlich H. On the Theory of Superconductivity: The One-Dimensional Case. *Proceedings of the Royal Society A: Mathematical, Physical and Engineering Sciences* (1954) **223** 296–305.
88 Schmalian J. Failed theories of superconductivity. *Modern Physics Letters B* (2010) **24** 2679–2691.
89 Bardeen J., Cooper L.N., Schrieffer J.R. Theory of superconductivity. *Physical Review* (1957) **108** 1175–1204.
90 Le Bolloc'H D., Sinchenko A.A., Jacques V.L.R., Ortega L., Lorenzo J.E., Chahine G.A. *et al.* Effect of dimensionality on sliding charge density waves: The quasi-two-dimensional TbTe3 system probed by coherent x-ray diffraction. *Physical Review B - Condensed Matter and Materials Physics* (2016) **93** 1–5.
91 Flemming R., Moncton D., McWhan D. X-ray scattering and electric field studies of the sliding mode conductor NbSe3. *Physical Review B* (1978) **18** 5560–5563.
92 McCarten J., DiCarlo D.A., Maher M.P., Adelman T.L., Thorne R.E. Charge-density-wave pinning and finite-size effects in NbSe3. *Physical Review B* (1992) **46** 4456–4482.
93 Maki K. Thermal fluctuations of the order parameter in charge-density waves. *Physical Review B* (1986) **33** 2852–2854.
94 Maki K., Virosztek A. Phase Hamiltonian and depinning electric field in the charge-density wave and the spin-density wave. *Physical Review B* (1990) **42** 655–659.
95 Lee P., Rice T. Electric field depinning of charge density waves. *Physical Review B* (1979) **19** 3970–3980.
96 Onishi S., Jamei M., Zettl A. Narrowband noise study of sliding charge density waves in NbSe 3 nanoribbons. *New Journal of Physics* (2017) **19** 23001.
97 Edwards J., Frindt R.F. Anisotropy in the resistivity of NbSe2. *J. Phys. Chem. Solids* (1971) **32** 2217–2221.
98 Dean C.R., Young a F., Meric I., Lee C., Wang L., Sorgenfrei S. *et al.* Boron nitride substrates for high-quality graphene electronics. *Nature Nanotechnology* (2010) **5** 722–726.
99 Springer Materials. (2016).http://materials.springer.com (accessed 1 Jan2017).
100 Bechstedt F., Käckell P., Zywietz A., Karch K., Adolph B., Tenelsen K. *et al.* Polytypism and properties of silicon carbide. *Physica Status Solidi (B)* (1997) **202** 35–62.
101 Staley N.E., Wu J., Eklund P., Liu Y., Li L., Xu Z. Electric field effect on superconductivity in atomically thin flakes of NbSe2. *Physical Review B* (2009) **80** 184505.
102 Woollam J.A., Somoano R.B., O'Connor P. Positive curvature of the Hc2-versus-Tc boundaries in layered superconductors. *Physical Review Letters* (1974) **32** 712–714.
103 Morris R.C., Coleman R. V., Bhandari R. Superconductivity and magnetoresistance in NbSe2. *Physical Review B* (1972) **5** 895–901.
104 Muto Y., Toyota N., Noto K., A H. Temperature dependence of ratio, Hc2parallel/Hc2perp, for NbSe2. *Physics Letters A* (1973) **45A** 99–100.

105 Toyota N., Nakatsuji H., Noto K., Hoshi A., Kobayashi N., Muto Y. *et al.* Temeprature and angular dependences of upper critical fields for the layer structure supercionductor 2H-NbSe2. *Journal of Low Temperature Physics* (1976) **25** 485–499.
106 Wilson J. a., Di Salvo F.J., Mahajan S. Charge-density waves and superlattices in the metallic layered transition metal dichalcogenides. *Advances in Physics* (1975) **24** 117–201.
107 Thompson A.H., Gamble R.F., Revelli J.F. Transitions between semiconducting and metallic phases in 1-T TaS2. *Solid State Communications* (1971) **9** 981–985.
108 Yu Y., Yang F., Lu X.F., Yan Y.J., Cho Y.-H., Ma L. *et al.* Gate-tunable phase transitions in thin flakes of 1T-TaS2. *Nature nanotechnology* (2015) **10** 270–276.
109 Naylor C.H., Parkin W.M., Gao Z., Kang H., Noyan M., Wexler R.B. *et al.* Large-area synthesis of high-quality monolayer 1T'-WTe2 flakes. *2D Materials* (2017) **4** 21008.
110 Kabashima S. Electrical properties of tungsten-ditelluride WTe2. Journal of the Physical Society of Japan. (1966) **21** 945–948.
111 Ashcroft N.W., Mermin N.D. Solid State Physics. *Holt, Rinehart and Winston* Philadelphia, (1976).
112 Ali M.N., Xiong J., Flynn S., Tao J., Gibson Q.D., Schoop L.M. *et al.* Large, non-saturating magnetoresistance in WTe2. *Nature* (2014) **514** 205.
113 Fallah Tafti F., Gibson Q., Kushwaha S., Krizan J.W., Haldolaarachchige N., Cava R.J. Temperature−field phase diagram of extreme magnetoresistance. *Proceedings of the National Academy of Sciences* (2016) **113** E3475–E3481.
114 Soluyanov A.A., Gresch D., Wang Z., Wu Q., Troyer M., Dai X. *et al.* Type-II Weyl semimetals. *Nature* (2015) **527** 495–498.
115 Wu Y., Mou D., Jo N.H., Sun K., Huang L., Bud'ko S.L. *et al.* Observation of Fermi arcs in the type-II Weyl semimetal candidate WTe2. *Physical Review B* (2016) **94** 121113.
116 Thoutam L.R., Wang Y.L., Xiao Z.L., Das S., Luican-Mayer A., Divan R. *et al.* Temperature-Dependent Three-Dimensional Anisotropy of the Magnetoresistance in WTe2. *Physical Review Letters* (2015) **115** 46602.
117 Hsu F.-C., Luo J.-Y., Yeh K.-W., Chen T.-K., Huang T.-W., Wu P.M. *et al.* Superconductivity in the PbO-type structure alpha-FeSe. *Proceedings of the National Academy of Sciences of the United States of America* (2008) **105** 14262–14264.
118 Wang A.F., Ying J.J., Yan Y.J., Liu R.H., Luo X.G., Li Z.Y. *et al.* Superconductivity at 32 K in single-crystalline RbxFe2-ySe2. *Physical Review B - Condensed Matter and Materials Physics* (2011) **83** 1–4.
119 Wang Q.-Y., Li Z., Zhang W.-H., Zhang Z.-C., Zhang J.-S., Li W. *et al.* Interface-induced high-temperature superconductivity in single unit-cell FeSe films on SrTiO3. *Chinese Physics Letters* (2012) **29** 37402.
120 Ge J.-F., Liu Z.-L., Liu C., Gao C.-L., Qian D., Xue Q.-K. *et al.* Superconductivity above 100 K in single-layer FeSe films on doped SrTiO3. *Nature Materials* (2014) **14** 1–5.
121 Li Z.-X., Wang F., Yao H., Lee D.-H. What makes the Tc of monolayer FeSe on SrTiO3 so high: a sign-problem-free quantum Monte Carlo study. *Science Bulletin* (2016) **61** 925–930.
122 Lee J.J., Schmitt F.T., Moore R.G., Johnston S., Cui Y.-T., Li W. *et al.* Interfacial mode coupling as the origin of the enhancement of Tc in FeSe films on SrTiO3. *Nature* (2014) **515** 245–248.
123 Fan Q., Zhang W.H., Liu X., Yan Y.J., Ren M.Q., Peng R. *et al.* Plain s-wave

superconductivity in single-layer FeSe on SrTiO3 probed by scanning tunnelling microscopy. *Nature Physics* (2015) **11** 946–952.
124 Slot E., Holst M.A., Van Der Zant H.S.J., Zaitsev-Zotov S. V. One-dimensional conduction in charge-density-wave nanowires. *Physical Review Letters* (2004) **93** 1–4.
125 Fleming R.M., Grimes C.C. Sliding-Mode Conductivity in NbSe3: Observation of a Threshold Electric Field and Conduction Noise. *Physical review letters* (1979) **42** 1423–1426.
126 Brazovskii S., Kirova N., Requardt H., Nad F., Monceau P., Currat R. *et al.* Plastic sliding of charge density waves: X-ray space resolved-studies versus theory of current conversion. *Physical Review B* (2000) **61** 10640–10650.
127 Isakovic A.F., Evans P.G., Kmetko J., Cicak K., Cai Z., Lai B. *et al.* Shear modulus and plasticity of a driven charge density wave. *Physical Review Letters* (2006) **96** 1–4.
128 Thompson A.H., Zettl A., Grüner G. Charge-Density-Wave Transport in TaS3. *Physical Review Letters* (1981) **47** 64–67.
129 Novoselov K.S., Jiang D., Schedin F., Booth T.J., Khotkevich V. V, Morozov S. V *et al.* Two-dimensional atomic crystals. *Proceedings of the National Academy of Sciences of the United States of America* (2005) **102** 10451–10453.
130 Xi X., Wang Z., Zhao W., Park J.-H., Law K.T., Berger H. *et al.* Ising pairing in superconducting NbSe2 atomic layers. *Nature Physics* (2016) **12** 139–143.
131 Girit Ç.Ö. Conductance Characterization og Massless Dirac Fermions and the Synthesis, Characterization, and Manipulation of Graphene, Doctoral Dissertation. *University of California, Berkeley* (2010) 9–17.
132 Castellanos-Gomez A., Agra?t N., Rubio-Bollinger G. Optical identification of atomically thin dichalcogenide crystals. *Applied Physics Letters* (2010) **96** 213116.
133 You Y., Zhang X.-X., Berkelbach T.C., Hybertsen M.S., Reichman D.R., Heinz T.F. Observation of biexcitons in monolayer WSe2. *Nature Physics* (2015) **11** 477–481.
134 Mak K.F., Lee C., Hone J., Shan J., Heinz T.F. Atomically thin MoS2: A new direct-gap semiconductor. *Physical Review Letters* (2010) **105** 2–5.
135 Hunt B., Sanchez-Yamagishi J.D., Young A.F., Yankowitz M., LeRoy B.J., Watanabe K. *et al.* Massive Dirac Fermions and Hofstadter Butterfly in a van der Waals Heterostructure. *Science* (2013) **340** 1427–1430.
136 Dean C.R., Wang L., Maher P., Forsythe C., Ghahari F., Gao Y. *et al.* Hofstadter's butterfly and the fractal quantum Hall effect in moiré superlattices. *Nature* (2013) **497** 598–602.
137 Wang L., Meric I., Huang P.Y., Gao Q., Gao Y., Tran H. *et al.* One-dimensional electrical contact to a two-dimensional material. *Science* (2013) **342** 614–7.
138 Castellanos-Gomez A., Buscema M., Molenaar R., Singh V., Janssen L., van der Zant H.S.J. *et al.* Deterministic transfer of two-dimensional materials by all-dry viscoelastic stamping. *2D Materials* (2014) **1** 11002.
139 Efetov D.K., Wang L., Handschin C., Efetov K.B., Shuang J., Cava R. *et al.* Specular interband Andreev reflections at van der Waals interfaces between graphene and NbSe2. *Nature Physics* (2015) 1–5.
140 Rigosi A.F., Hill H.M., Li Y., Chernikov A., Heinz T.F. Probing Interlayer Interactions in Transition Metal Dichalcogenide Heterostructures by Optical Spectroscopy: MoS2/WS2 and MoSe2/WSe2. *Nano Letters* (2015) **15** 5033–5038.
141 McMillan W.L. Transition temperature of strong-coupled superconductors. *Physical*

Review (1968) **167** 331–344.
142 Gubin A.I., Il'in K.S., Vitusevich S.A., Siegel M., Klein N. Dependence of magnetic penetration depth on the thickness of superconducting Nb thin films. *Physical Review B* (2005) **72** 64503.
143 Nuckolls K.P. Characterization and electrical transport measurements of chemically-doped graphene aerogels, BA Honor Senior Thesis. *University of California, Berkeley*, (2017).
144 Shi W., Ye J., Zhang Y., Suzuki R., Yoshida M., Miyazaki J. *et al.* Superconductivity Series in Transition Metal Dichalcogenides by Ionic Gating. *Scientific Reports* (2015) **5** 12534.
145 Fuhrer M.S. Electronic properties of high-temperature superconductors and novel carbon-based conductors and superconductors, Doctoral Disseration. *University of California, Berkeley* (1998).
146 Ojeda-Aristizabal C., Santos E.J.G., Onishi S., Yan A., Rasool H.I., Kahn S. *et al.* Molecular Arrangement and Charge Transfer in C 60 /Graphene Heterostructures. *ACS Nano* (2017) **11** 4686–4693.
147 Kittel C., Kroemer H. Thermal Physics. *2nd ed. W.H. Freeman and Company* (1980) p341-345.
148 McElfresh M. Fundamentals of magnetism and magnetic measurements. *Quantum Design Application Note* (1994).
149 Charles K. Introduction to Solid State Physics. *8th ed. John Wiley & Sons Inc.* (2005) p167-168, 173.
150 Mott N.F., Davis E.A. Electronic processes in non-crystalline materials. *2nd ed. Oxford University Press* (1979) p15-22.
151 Winter M. WebElements. https://www.webelements.com/ (accessed 3 Jan2017).
152 Lieth R.M.., Terhell J.C.J.M. Transition metal dichacogenides. In: Lieth RMA (ed). *Preparation and crystal growth of materials with layered strcutures*. *D. Reidel Publishing Company, Inc.* Hingham, (1977), pp 184–185.
153 Analytis J.G., Chu J.-H., McDonald R.D., Riggs S.C., Fisher I.R. Enhanced Fermi-Surface Nesting in SuperconductingBaFe2(As1−xP)2 Revealed by the de Haas-van Alphen Effect. *Physical Review Letters* (2010) **105** 207004.
154 Wu Y., Jo N.H., Ochi M., Huang L., Mou D., Bud'Ko S.L. *et al.* Temperature-Induced Lifshitz Transition in WTe2. *Physical Review Letters* (2015) **115** 1–6.
155 Laudise R.., Kloc C., Simpkins P.., Siegrist T. Physical vapor growth of organic semiconductors. *Journal of Crystal Growth* (1998) **187** 449–454.
156 Podzorov V. Charge Carrier Transport in Single-Crystal Organic Field-Effect Transistor. In: Bao Z, Lockin J (eds). *Organic Field-Effect Transistors*. (2007), p 32.
157 Enomoto H., Kawaguchi M., Lerner M.M. Syntheses and Characterizations of Polymer/TaS2 Layered Nanocomposites. (2003) **5223** 241–248.
158 Di Salvo F.J., Bagley B.G., Voorhoeve J.M., Waszczak J.V. Preparation and properties of a new polytype of tantalum disulfide (4Hb-TaS2). *Journal of Physics and Chemistry of Solids* (1973) **34** 1357–1362.
159 Wang Z.Z., Monceau P., Renard M., Gressier P., Guemas L., Meerschaut A. Charge density transport in a novel halogened transition metal tetrachalcogenide (NbSe4)3.33I. *Solid State Communications* (1983) **47** 439–443.
160 Keum D.H., Cho S., Kim J.H., Choe D.-H., Sung H.-J., Kan M. *et al.* Bandgap opening in

few-layered monoclinic MoTe2. *Nature Physics* (2015) **11** 482–486.
161 Koz C., Schmidt M., Borrmann H., Burkhardt U., Röβler S., Carrillo-Cabrera W. *et al.* Synthesis and Crystal Growth of Tetragonal β-Fe1.00Se. *Zeitschrift für anorganische und allgemeine Chemie* (2014) **640** 1600–1606.
162 Zhang S.B., Sun Y.P., Zhu X.D., Zhu X.B., Wang B.S., Li G. *et al.* Crystal growth and superconductivity of FeSex. *Superconductor Science and Technology* (2009) **22** 15020.
163 X-ray crystallography performed and analyzed by Dr. Antonio DiPasquale at College of Chemistry X-ray Crystallography Facility, University of California, Berkeley. .
164 Harada T. Transport Properties of Iron Dichalcogenides FeX2 (X=S, Se and Te). *Journal of the Physical Society of Japan* (1998) **67** 1352–1358.
165 Fischer G. FeSe2, A semiconductor containing iron. *Canadian Journal of Physics* (1958) **36** 1435–1438.
166 Kar'kin A.E., Titov A.N., Shkvarina E.G., Titov A.A., Goshchitskii B.N. Synthesis, single-crystal growth, and superconducting properties of Fe-Se system. *The Physics of Metals and Metallography* (2012) **113** 932–937.
167 Cullity B.D. Introduction to magentic materials. *Addison-Wesley Publishing Company, Inc.* (1972) p156-168.
168 Morris R.C., Coleman R. V. Anisotropic superconductivity in layer compounds. *Physical Review B* (1973) **7** 991–1001.
169 Cao Y., Mishchenko A., Yu G.L., Khestanova E., Rooney A.P., Prestat E. *et al.* Quality Heterostructures from Two-Dimensional Crystals Unstable in Air by Their Assembly in Inert Atmosphere. *Nano Letters* (2015) **15** 4914–4921.
170 Saito Y., Nakamura Y., Bahramy M.S., Kohama Y., Ye J., Kasahara Y. *et al.* Superconductivity protected by spin–valley locking in ion-gated MoS_2. *Nature Physics* (2016) **12** 144–149.
171 Foner S., McNiff E.J. Upper critical fields of layered superconducting NbSe2 at low temperatures. *Physics Letters A* (1973) **45A** 429–430.
172 Nader A., Monceau P. Critical field of 2H-NbSe2 down to 50mK. *SpringerPlus* (2014) **3** 16.
173 Myers G.E., Montet G.L. Light-induced oxidation of NbSe2 single crystals. *Journal of Physics and Chemistry of Solids* (1971) **32** 2645–2646.
174 El-Bana M.S., Wolverson D., Russo S., Balakrishnan G., Paul D.M., Bending S.J. Superconductivity in two-dimensional NbSe2 field effect transistors. *Superconductor Science and Technology* (2013) **26** 125020.
175 Tsen A.W., Hunt B., Kim Y.D., Yuan Z.J., Jia S., Cava R.J. *et al.* Nature of the quantum metal in a two-dimensional crystalline superconductor. *Nature Physics* (2016) **12** 208–213.
176 Xi X., Berger H., Forró L., Shan J., Mak K.F. Gate Tuning of Electronic Phase Transitions in Two-Dimensional NbSe2. *Physical Review Letters* (2016) **117** 1–6.
177 Gurevich A., Patnaik S., Braccini V., Kim K.H., Mielke C., Song X. *et al.* Very high upper critical fields in MgB2 produced by selective tuning of impurity scattering. *Superconductor Science and Technology* (2004) **17** 278–286.
178 Godeke A., Jewell M.C., Fischer C.M., Squitieri A.A., Lee P.J., Larbalestier D.C. The upper critical field of filamentary Nb3Sn conductors. *Journal of Applied Physics* (2005) **97** 93909.
179 Ni N., Bud'ko S.L., Kreyssig A., Nandi S., Rustan G.E., Goldman A.I. *et al.* Anisotropic

thermodynamic and transport properties of single crystalline Ba1-xKxFe2As2 (x = 0 and 0.45). (2008) **2** 1–9.
180 Fuchs G., Drechsler S.L., Kozlova N., Behr G., Köhler A., Werner J. *et al.* High-field pauli-limiting behavior and strongly enhanced upper critical magnetic fields near the transition temperature of an arsenic-deficient LaO0.9F0.1FeAs1-δ superconductor. *Physical Review Letters* (2008) **101** 1–4.
181 Zhu X., Yang H., Fang L., Mu G., Wen H.-H. Upper critical field, Hall effect and magnetoresistance in the iron-based layered superconductor LaFeAsO0.9F0.1-delta. (2008) **105001** 10.
182 Hunte F., Jaroszynski J., Gurevich A., Larbalestier D.C., Jin R., Sefat A.S. *et al.* Two-band superconductivity in LaFeAsO0.89F0.11 at very high magnetic fields. *Nature* (2008) **453** 903–5.
183 Laboratories T.B., Hill M. Electronic Transport Properties of K3C6o Films. (1992) **68** 1054–1057.
184 Rullier-Albenque F., Alloul H., Tourbot R. Disorder and transport in cuprates: weak localization and magnetic contributions. *Physical review letters* (2001) **87** 157001.
185 Mauri F., Errea I., Calandra M. Anharmonic matter: charge density waves in dichalcogenide and hydrogen sulfide superconductor. In: *XXXth International Winterschool on Electronic Properties of Novel Materials*. (2016).
186 Aoki H. Private communication at International Workshop on Superconductivity and Related Functional Materials. (2016).
187 Kosterlitz J.M., Thouless D.J. Ordering, metastability and phase transitions in two-dimensional systems. *Journal of Physics C: Solid State Physics* (2002) **6** 1181–1203.
188 Mermin N.D., Wagner H. Absence of ferromagnetism or antiferromagnetism in one- or two-dimensional isotropic Heisenberg models. *Physical Review Letters* (1966) **17** 1133–1136.
189 Aseev P.P., Artemenko S.N. Stabilization of the surface CDW order parameter by long-range Coulomb interaction. *Physica B: Condensed Matter* (2012) **407** 1835–1838.
190 Yoshida M., Suzuki R., Zhang Y., Nakano M., Iwasa Y. Memristive phase switching in two-dimensional 1T-TaS2 crystals. *Science Advances* (2015) **1** e1500606–e1500606.
191 Aslan O.B., Chenet D.A., Van Der Zande A.M., Hone J.C., Heinz T.F. Linearly Polarized Excitons in Single- and Few-Layer ReS2 Crystals. *ACS Photonics* (2016) **3** 96–101.
192 Hor Y.S., Xiao Z.L., Welp U., Ito Y., Mitchell J.F., Cook R.E. *et al.* Nanowires and nanoribbons of charge-density-wave conductor NbSe 3. *Nano Letters* (2005) **5** 397–401.
193 Jamei M. Electronic properties of low-dimensional materials under periodic potential. (2015).
194 Mantel O., Chalin F., Dekker C., van der Zant H., Latyshev Y., Pannetier B. *et al.* Charge-Density-Wave Current Conversion in Submicron NbSe3 Wires. *Physical Review Letters* (2000) **84** 538–541.
195 Yuan H., Shimotani H., Tsukazaki A., Ohtomo A., Kawasaki M., Iwasa Y. High-density carrier accumulation in ZnO field-effect transistors gated by electric double layers of ionic liquids. *Advanced Functional Materials* (2009) **19** 1046–1053.
196 Mickelson W., Aloni S., Han W., Cumings J., Zettl A. Packing C 60 in Boron Nitride Nanotubes. *Society* (2003) **300** 467–469.
197 Fujimori T., dos Santos R.B., Hayashi T., Endo M., Kaneko K., Tom?nek D. Formation and Properties of Selenium Double-Helices inside Double-Wall Carbon Nanotubes:

Experiment and Theory. *ACS Nano* (2013) **7** 5607–5613.
198 Gibson Q.D., Evtushinksy D., Yaresko A.N., Zabolotnyy A.B., Ali M.N., Fuccillo M.K. *et al.* Quasi One Dimensional Dirac Electrons on the Surface of Ru$_2$Sn$_3$. *Scientific reports* (2014) **4** 5168.
199 Nadj-Perge S., Drozdov I.K., Li J., Chen H., Jeon S., Seo J. *et al.* Observation of Majorana fermions in ferromagnetic atomic chains on a superconductor. *Science* (2014) **346** 602–607.
200 Mourik V., Zuo K., Frolov S.M., Plissard S.R., Bakkers E.P.A.M., Kouwenhoven L.P. Signatures of Majorana Fermions in Hybrid Superconductor-Semiconductor Nanowire Devices. *Science* (2012) **336** 1003–1007.
201 Sakakibara T., Goto T., Miura N. Contactless transport measurement of metals in pulsed high magnetic fields. *Review of Scientific Instruments* (1989) **60** 444–449.
202 Dresselhaus M.S., Dresselhaus G. Intercalation compounds of graphite. *Advances in Physics* (2006) **30** 139–326.
203 Xiang X.-D., Vareka W.A., Zettl A., Corkill J.L., Cohen M.L., Kijima N. *et al.* Metallization of the resistivity tensor in Bi2Sr2CaCu2Ox through epitaxial intercalation. *Physical Review Letters* (1992) **68** 530–533.
204 Vareka W.A. Intercalation in high-temperature oxide and fullerene superconductors, Doctoral Dissertation. *University of California, Berkeley* (1993).
205 Božović I., He X., Wu J., Bollinger A.T. Dependence of the critical temperature in overdoped copper oxides on superfluid density. *Nature* (2016) **536** 309–311.
206 Došlić M., Pelc D., Požek M. Contactless measurement of nonlinear conductivity in the radio-frequency range. *Review of Scientific Instruments* (2014) **85**. doi:10.1063/1.4890557.
207 Wang L., Meric I., Huang P.Y., Gao Q., Gao Y., Tran H. *et al.* One-dimensional electrical contact to a two-dimensional material. *Science (New York, N.Y.)* (2013) **342** 614–7.
208 Casimir H.B.G., du Pré F.K. Note on the thermodynamic interpretation of paramagnetic relaxation phenomena. *Physica* (1938) **5** 507–511.
209 de Haas W.J., du Pré F.K. Paramagnetic relaxation in iron ammonium alum at low temperatures. *Physica* (1938) **5** 501–506.
210 Bałanda M. AC Susceptibility Studies of Phase Transitions and Magnetic Relaxation: Conventional, Molecular and Low-Dimensional Magnets. *Acta Physica Polonica A* (2013) **124** 964–976.
211 Judy J.W. Microelectromechanical systems (MEMS): fabrication, design and applications. *Smart Materials and Structures* (2001) **10** 1115–1134.
212 Mickelson W., Sussman A., Zettl A. Low-power, fast, selective nanoparticle-based hydrogen sulfide gas sensor. *Applied Physics Letters* (2012) **100** 173110.
213 Zhou Q., Liu K., Xiong S., Wang F., Lin L. Direct synthesis of self-aligned single-walled carbon nanotubes on paper. *Carbon* (2012) **50** 1179–1185.
214 Ma J. Advanced MEMS-based technologies and displays. *Displays* (2015) **37** 2–10.
215 Fennimore a M., Yuzvinsky T.D., Han W., Fuhrer M.S., Cumings J., Zettl A. Rotational actuators based on carbon nanotubes. *Nature* (2003) **424** 408–410.
216 Heeger A.J., Kivelson S., Schrieffer J.R., Su W.P. Solitons in conducting polymers. *Reviews of Modern Physics* (1988) **60** 781–850.
217 Kroto H.W., Heath J.R., O'Brien S.C., Curl R.F., Smalley R.E. C60: Buckminsterfullerene. *Nature* (1985) **318** 162–163.

218 Iijima S. Helical microtubules of graphitic carbon. *Nature* (1991) **354** 56–58.
219 Monthioux M., Kuznetsov V.L. Who should be given the credit for the discovery of carbon nanotubes? *Carbon* (2006) **44** 1621–1623.
220 Hummelen J.C., Knight B.W., LePeq F., Wudl F., Yao J., Wilkins C.L. Preparation and Characterization of Fulleroid and Methanofullerene Derivatives. *The Journal of Organic Chemistry* (1995) **60** 532–538.
221 Ajayan P.M. Nanotubes from Carbon. *Chemical Reviews* (1999) **99** 1787–1800.
222 Lee C., Wei X., Kysar J.W., Hone J. Measurement of the Elastic Properties and Intrinsic Strength of Monolayer Graphene. *Science* (2008) **321** 385–388.
223 Jensen K., Kim K., Zettl A. An atomic-resolution nanomechanical mass sensor. *Nature Nanotechnology* (2008) **3** 533–537.
224 Williams K.R., Muller R.S. Etch rates for micromachining processing. *Journal of Microelectromechanical Systems* (1996) **5** 256–269.
225 Williams K.R., Gupta K., Wasilik M. Etch rates for micromachining processing-part II. *Journal of Microelectromechanical Systems* (2003) **12** 761–778.
226 Bustillo J.M., Howe R.T., Muller R.S. Surface micromachining for microelectromechanical systems. *Proceedings of the IEEE* (1998) **86** 1552–1574.
227 Fathalizadeh A. Synthesis, Characterization, and Fabrication of Boron Nitride and Carbon Nanomaterials, their Applications, and the Extended Pressure Inductively Coupled Plasma Synthesis of Boron Nitride Nanotubes, Doctoral Dissertation. *University of California, Berkeley* (2016).
228 Wang X.Q., Wang M., He P.M., Xu Y.B., Li Z.H. Model calculation for the field enhancement factor of carbon nanotube. *Journal of Applied Physics* (2004) **96** 6752–6755.
229 Jensen K., Weldon J., Garcia H., Zettl A. Nanotube radio. *Nano Letters* (2007) **7** 3508–3511.
230 Rocheleau T., Ndukum T., Macklin C., Hertzberg J.B., Clerk A.A., Schwab K.C. Preparation and detection of a mechanical resonator near the ground state of motion. *Nature* (2010) **463** 72–75.
231 O?Connell A.D., Hofheinz M., Ansmann M., Bialczak R.C., Lenander M., Lucero E. *et al.* Quantum ground state and single-phonon control of a mechanical resonator. *Nature* (2010) **464** 697–703.
232 Weldon J.A., Alema?n B., Sussman A., Gannett W., Zettl A.K. Sustained Mechanical Self-Oscillations in Carbon Nanotubes. *Nano Letters* (2010) **10** 1728–1733.
233 Schwab K.C., Roukes M.L. Putting Mechanics into Quantum Mechanics. *Physics Today* (2005) **58** 36–42.
234 Rugar D., Grütter P. Mechanical parametric amplification and thermomechanical noise squeezing. *Physical Review Letters* (1991) **67** 699–702.
235 Suh J., LaHaye M.D., Echternach P.M., Schwab K.C., Roukes M.L. Parametric Amplification and Back-Action Noise Squeezing by a Qubit-Coupled Nanoresonator. *Nano Letters* (2010) **10** 3990–3994.
236 Alemán B.J., Sussman A., Mickelson W., Zettl A. A Carbon Nanotube-based NEMS Parametric Amplifier for Enhanced Radio Wave Detection and Electronic Signal Amplification. *Journal of Physics: Conference Series* (2011) **302** 12001.
237 Begtrup G. Silicon Nitride Membranes for Electrical and Thermal Transport Studies of Nanotubes, Doctoral Dissertation. *University of California, Berkeley* (2008).
238 Levy N., Burke S.A., Meaker K.L., Panlasigui M., Zettl A., Guinea F. *et al.* Strain-

Induced Pseudo-Magnetic Fields Greater Than 300 Tesla in Graphene Nanobubbles. *Science* (2010) **329** 544–547.
239 Guinea F., Geim A.K., Katsnelson M.I., Novoselov K.S. Generating quantizing pseudomagnetic fields by bending graphene ribbons. *Physical Review B - Condensed Matter and Materials Physics* (2010) **81** 1–5.
240 Pérez Garza H.H., Kievit E.W., Schneider G.F., Staufer U. Controlled, reversible, and nondestructive generation of uniaxial extreme strains (>10%) in graphene. *Nano Letters* (2014) **14** 4107–4113.
241 Kim K., Lee Z., Regan W., Kisielowski C., Crommie M.F., Zettl A. Grain Boundary Mapping in Polycrystalline Graphene. *ACS Nano* (2011) **5** 2142–2146.
242 Sharpe W.N., Jackson K.M., Hemker K.J., Xie Z. Effect of specimen size on Young's modulus and fracture strength of polysilicon. *Journal of Microelectromechanical Systems* (2001) **10** 317–326.
243 Goldsche M., Khodkov T., Kaienburg P., Neumann C., Stampfer C., Goldsche M. *et al.* Low-temperature compatible electrostatic comb-drive actuators with integrated graphene. In: *The 9th IEEE International Conference on Nano/Micro Engineered and Molecular Systems (NEMS). IEEE*, (2014), pp 251–255.
244 Li X., Colombo L., Ruoff R.S. Synthesis of Graphene Films on Copper Foils by Chemical Vapor Deposition. *Advanced Materials* (2016) **28** 6247–6252.
245 Kittel C. Introduction to Solid State Physics. *8th ed. John Wiley & Sons Inc.* (2005) p208.
246 Subramanian V. Radio Frequency Identification Tags. In: Bao Z, Locklin J (eds). *Organic Field-Effect Transistors*. *CRC Press Taylor & Francis Group*, (2007), pp 480–505.
247 Helfrich W. Space-charge-limited and volume controlled currents in organic solids. In: Fox D, Labes MM, Weissberger A (eds). *Physics and chemistry of the organic solid state volume III*. *John Wiley & Sons Inc.*, (1967), pp 2–58.
248 electrical conductivity: range of conductivity, illustration. Encyclopædia Britannica Online. (2017).https://www.britannica.com/science/semiconductor?oasmId=139 (accessed 17 Jun2017).
249 Horowitz G. Charge Transport in Oligomers. In: Bao Z, Locklin J (eds). *Organic Field-Effect Transistors*. *CRC Press Taylor & Francis Group*, (2007), pp 73–101.
250 Chen M.S., Lee O.P., Niskala J.R., Yiu A.T., Tassone C.J., Schmidt K. *et al.* Enhanced Solid-State Order and Field-Effect Hole Mobility through Control of Nanoscale Polymer Aggregation. *Journal of the American Chemical Society* (2013) **135** 19229–19236.
251 Pivrikas A., Sariciftci N.S., Juška G., Österbacka R. A review of charge transport and recombination in polymer/fullerene organic solar cells. *Progress in Photovoltaics: Research and Applications* (2007) **15** 677–696.
252 Arias A.C. Inkjet Printed Organic Thin Film Transistors. In: Bao Z, Locklin J (eds). *Organic Field-Effect Transistors*. (2007), pp 419–432.
253 Sirringhaus H. 25th anniversary article: Organic field-effect transistors: The path beyond amorphous silicon. *Advanced Materials* (2014) **26** 1319–1335.
254 Facchetti A. Semiconductors for organic transistors. *Materials Today* (2007) **10** 28–37.
255 Podzorov V. Charge Carrier Transport in Single-Crystal Organic Field-Effect Transistors. In: Bao Z, Locklin J (eds). *Organic Field-Effect Transistors*. *CRC Press Taylor & Francis Group*, (2007), pp 27–72.
256 Reese C., Bao Z. Organic single-crystal field-effect transistors. *Materials Today* (2007) **10** 20–27.

257 Podzorov V., Menard E., Rogers J.A., Gershenson M.E. Hall effect in the accumulation layers on the surface of organic semiconductors. *Physical Review Letters* (2005) **95** 1–4.
258 Mott N.F., Davis E.A. Electronic Processes in Non-Crystalline Materials. 2nd ed. *Oxford University Press*, (2012).
259 Bao Z., Batlogg B., Berg S., Dodabalapur A., Haddon R.C., Hwang H. *et al.* Retraction. *Science* (2002) **298** 961–961.
260 Schön J.H., Kloc C., Batlogg B. retraction: Superconductivity in molecular crystals induced by charge injection. *Nature* (2003) **422** 93–93.
261 Horowitz G. Organic field-effect transistors. *Advanced Materials* (1998) **10** 365–377.
262 Sakanoue T., Sirringhaus H. Band-like temperature dependence of mobility in a solution-processed organic semiconductor. *Nature materials* (2010) **9** 736–40.
263 Garnier F., Yassar A. Molecular engineering of organic semiconductors: design of self-assembly properties in conjugated thiophene oligomers. *Journal of American Chemical Society* (1993) **115** 8716–8721.
264 Saito R., Dresselhaus G., Dresselhaus M.S. Physical properties of carbon nanotubes. *Imperial College Press* (1998) p25-33.
265 Yuan Y., Giri G., Ayzner A.L., Zoombelt A.P., Mannsfeld S.C.B., Chen J. *et al.* Ultra-high mobility transparent organic thin film transistors grown by an off-centre spin-coating method. *Nature communications* (2014) **5** 3005.
266 Tseng H.-R., Phan H., Luo C., Wang M., Perez L.A., Patel S.N. *et al.* High-Mobility Field-Effect Transistors Fabricated with Macroscopic Aligned Semiconducting Polymers. *Advanced Materials* (2014) **26** 2993–2998.
267 Sirringhaus H., Brown P.J., Friend R.H., Nielsen M.M., Bechgaard K., Langeveld-Voss B.M.W. *et al.* Two-dimensional charge transport in self-organized, high-mobility conjugated polymers. *Nature* (1999) **401** 685–688.
268 Yi H.T., Payne M.M., Anthony J.E., Podzorov V. Ultra-flexible solution-processed organic field-effect transistors. *Nature Communications* (2012) **3** 1259.
269 Kittel C. Introduction to Solid State Physics. *8th ed. John Wiley & Sons Inc.* (2005) p437-440.
270 Huang Y., Kramer E.J., Heeger A.J., Bazan G.C. Bulk heterojunction solar cells: Morphology and performance relationships. *Chemical Reviews* (2014) **114** 7006–7043.
271 Briseno A.L., Mannsfeld S.C.B., Jenekhe S.A., Bao Z., Xia Y. Introducing organic nanowire transistors. *Materials Today* (2008) **11** 38–47.
272 Back J.Y., Yu H., Song I., Kang I., Ahn H., Shin T.J. *et al.* Investigation of Structure–Property Relationships in Diketopyrrolopyrrole-Based Polymer Semiconductors via Side-Chain Engineering. *Chemistry of Materials* (2015) **27** 1732–1739.
273 Ji Y., Xiao C., Wang Q., Zhang J., Li C., Wu Y. *et al.* Asymmetric Diketopyrrolopyrrole Conjugated Polymers for Field-Effect Transistors and Polymer Solar Cells Processed from a Nonchlorinated Solvent. *Advanced Materials* (2016) **28** 943–950.
274 Tang C.W. Two-layer organic photovoltaic cell. *Applied Physics Letters* (1986) **48** 183–185.
275 Irkhin P., Biaggio I. Direct Imaging of Anisotropic Exciton Diffusion and Triplet Diffusion Length in Rubrene Single Crystals. *Physical Review Letters* (2011) **107** 17402.
276 Sariciftci N.S., Smilowitz L., Heeger A.J., Wudl F. Photoinduced Electron Transfer from a Conducting Polymer to Buckminsterfullerene. *Science* (1992) **258** 1474–1476.
277 Wienk M.M., Kroon J.M., Verhees W.J.H., Knol J., Hummelen J.C., van Hal P.A. *et al.*

Efficient methano[70]fullerene/MDMO-PPV bulk heterojunction photovoltaic cells. *Angewandte Chemie (International ed. in English)* (2003) **42** 3371–5.
278 Douglas J.D., Chen M.S., Niskala J.R., Lee O.P., Yiu A.T., Young E.P. *et al.* Solution-processed, molecular photovoltaics that exploit hole transfer from non-fullerene, n-type materials. *Advanced Materials* (2014) **26** 4313–4319.
279 Horng J., Chen C.F., Geng B., Girit C., Zhang Y., Hao Z. *et al.* Drude conductivity of Dirac fermions in graphene. *Physical Review B - Condensed Matter and Materials Physics* (2011) **83** 1–5.
280 Zadik R.H., Takabayashi Y., Klupp G., Colman R.H., Ganin A.Y., Potocnik A. *et al.* Optimized unconventional superconductivity in a molecular Jahn-Teller metal. *Science Advances* (2015) **1** e1500059–e1500059.
281 Shi W., Wang Z., Zhang Q., Zheng Y., Ieong C., He M. *et al.* Superconductivity in bundles of double-wall carbon nanotubes. *Scientific Reports* (2012) **2** 625.
282 Ekimov E.A., Sidorov V.A., Bauer E.D., Mel'nik N.N., Curro N.J., Thompson J.D. *et al.* Superconductivity in diamond. *Nature* (2004) **428** 542–545.
283 http://supercon.nims.go.jp/index_en.html/. National Institute of Materials Science (Japan).
284 Einaga M., Sakata M., Ishikawa T., Shimizu K., Eremets M.I., Drozdov A.P. *et al.* Crystal structure of the superconducting phase of sulfur hydride. *Nature Physics* (2016) **12** 1–5.
285 Bühler J., Steiner F.-P., Baltes H. Silicon dioxide sacrificial layer etching in surface micromachining. *Journal of Micromechanics and Microengineering* (1997) **7** R1–R13.
286 Jensen Ray P. Structural investigation of La(2-x)Sr(x)CuO(4+y) - Following staging as a function of temperature. (2015). doi:10.6084/m9.figshare.2075680.v2.
287 Kittel C. Introduction to solid state physics. *8th ed. John Wiley & Sons Inc.* (2005).
288 Gressier P., Meerschaut a, Guemas L., Rouxel J. Characterization of the New Series of Quasi One-Dimensional Compounds (MX & Y (M = Nb , Ta ; X = S , Se ; Y = Br , I). (1984) **151** 141–151.
289 Novoselov K.S., Castro Neto a H. Two-dimensional crystals-based heterostructures: materials with tailored properties. *Physica Scripta* (2012) **T146** 14006.
290 Naik I., Rastogi A.K. Transport properties of 2H-NbSe2: Effect of Ga-intercalation. *Physica B: Condensed Matter* (2010) **405** 955–957.
291 Iwaya K., Hanaguri T., Koizumi A., Takaki K., Maeda A., Kitazawa K. Electronic state of NbSe2 investigated by STM/STS. *Physica B: Condensed Matter* (2003) **329**–**333** 1598–1599.
292 Oglesby C.S., Bucher E., Kloc C., Hohl H. Growth of faceted niobium diselenide. *Journal of Crystal Growth* (1994) **137** 289–294.
293 Okamoto H. The fese (ironselenium) system. *Journal of Phase Equilibria* (1991) **12** 383–389.
294 Terzieff P., Komarek K.L. The antiferromagnetic and ferrimagnetic properties of iron selenides with NiAs-type structure. *Monatshefte fur Chemie* (1978) **109** 1037–1047.
295 Onishi S., Ugeda M.M., Zhang Y., Chen Y., Ojeda-Aristizabal C., Ryu H. *et al.* Selenium capped monolayer NbSe 2 for two-dimensional superconductivity studies. *physica status solidi (b)* (2016) **253** 2396–2399.
296 Geim A.K., Novoselov K.S. The rise of graphene. *Nature Materials* (2007) **6** 183–191.
297 Espinosa H.D., Peng B., Moldovan N., Friedmna T.A., Xiao X., Mancini D.C. *et al.* Comparison of mechanical properties of three MEMS materials-silicon carbide, ultrananocrystalline diamond, and hydrogen-free tetrahedral amorphous carbon (Ta-C). In:

11th International Conference on Fracture 2005, ICF11. Turin, Italy, (2005), p 3806–30`11.
298 Tang W.C., Nguyen T.-C.H., Judy M.W., Howe R.T. Electrostatic-comb drive of lateral polysilicon resonators. *Sensors and Actuators A: Physical* (1990) **21** 328–331.